A petrological and geochemical cross section of lower crust at the Wadi Gideah (Samail ophiolite): Implications for the crustal accretion at fast-spreading mid-ocean ridges

Tim Mueller

THÈSE
Pour obtenir le grade de
Docteur

Délivré par **l'Université de Montpellier**

Préparée au sein de l'école doctorale SIBAGHE
Et de l'unité de recherche Géosciences Montpellier

Spécialité : **Géosciences**

Présentée par **Tim Mueller**

A petrological and geochemical cross section of lower crust at the Wadi Gideah (Samail ophiolite): Implications for the crustal accretion at fast-spreading mid-ocean ridges

---

Soutenue le 23 Novembre 2015 devant le jury composé de

Wolfgang BACH, Professeur, Univ. Bremen		Rapporteur
Georges CEULENEER, DR CNRS, Univ. Toulouse		Rapporteur
Ulrich HEIMHOFER, Professeur, Univ. Hannover (Président)		Examinateur
Benoît ILDEFONSE, DR CNRS, Univ. Montpellier		Co-directeur
Juergen KOEPKE, Professeur, Univ. Hannover		Co-directeur

Table of Content

Chapter B

Implications for Crustal Accretion at Fast-Spreading Mid-Ocean Ridges: Crystallographic Preferred Orientations from the Wadi Gideah Cross Section

Chapter C

Anatomy of a Frozen Axial Melt Lens from a Fast-Spreading Paleo-Ridge (Wadi Gideah, Oman Ophiolite)

Abstract

A cross section of fast-spreading mid-ocean crust lithologies was sampled at the Wadi Gideah, which is located in the Wadi Tayin Massif in the southern part of the Oman ophiolite. A coherent data set for advancing our understanding of crustal accretion processes at fast-spreading mid-ocean ridges was created by performing different analytical and structural investigations on the same suite of samples.

Major and trace element studies from Wadi Gideah lower crust reveal an up section trend of chemical evolution. Although it is slight within the layered gabbros, it becomes more distinctive at the layered/foliated gabbro transition. In the upper foliated gabbro section it is accompanied by the first occurrences of mineral zonation and late magmatic phases. Petrological modeling in a chemical system corresponding to Wadi Gideah reveals that the overall up section trend of chemical evolution can be produced by hydrous fractional crystallization. Melt H_2O content is estimated to be ~0.8 wt% and 0.8 to 1.2 wt% by modeling for lower and upper crust, respectively. Hydrous modeling combined with a very steep bulk Zr/Hf vs. Zr gradient, a high F and Cl content for magmatic amphibole, a general Nb-Ta depletion of Wadi Gideah melts in comparison with normal mid-ocean ridge basalt (NMORB), and a Sr^{87}/Sr^{86} ratio generally higher in comparison with modern East Pacific Rise (EPR) crust indicate that the Wadi Gideah layered gabbros accreted by in situ crystallization within sills in a subduction initiation setting. Evidence for reactive porous flow is not observed. The distinctive change in the chemical trend of evolution associated with a distinctive change in average grain sizes at layered/ foliated gabbro transition is probably related to a horizon of enhanced cooling below the axial melt lens (AML), considering deep crust hydrothermal cooling. Upper foliated gabbros represent a ~500 m thick transition with evidence for both subsidence of crystals from the AML above and upward flow of melt from below. In summary, Wadi Gideah lower crust displays a formation history similar to hybrid accretion models proposed by previous studies. Hydrothermal cooling, required for heat extraction from deep crystallization, was probably facilitated by channeled hydrothermal flows, preserved today in multiple, up to 100 m wide zones of extensively altered former layered gabbro which cut host rock layering. These metagabbros display significantly high Sr^{87}/Sr^{86} ratios, late stage phases, and evidence for high temperature partial melting.

Lower crust hybrid accretion is supported by plagioclase crystallographic preferred orientations (CPO), which show very low intra-mineral misorientation and no significant crystal-plastic deformation down to mantle/crust boundary. Furthermore, clinopyroxene fabric strength shows a lack of continuous increase down section associated with high scatter. Upper foliated gabbro plagioclase displays random or very weak CPO, similar to that in the varitextured gabbro, reflecting the transition zone character. A slight but nevertheless apparent increase of plagioclase fabric strength with depth, observed for the complete lower crust, is possibly related to increased shear flow caused by an impact of active plastic mantle flow below.

The outcrop of the frozen AML on top of lower crust, at the gabbro/dike transition, includes varitextured gabbro bearing relics of very primitive poikilitic clinopyroxene. These gabbros are intruded by masses of oceanic plagiogranites bearing relics of assimilated sheeted dikes, which in turn are cut by trondhjemite dikes. All lithologies are cut by basaltic dikes with

chilled margins. Time constraints on the sequence of intrusions, modeling of AML melt fractional crystallization and comparison to previous partial melting experiments give evidence that these Wadi Gideah lithologies were formed as a consequence of episodic vertical movements of the AML, probably caused by changes in AML replenishment rates.

Zusammenfassung

Für diese Arbeit wurden in einem geologischen Profil alle Horizonte der schnell-spreizenden mittelozeanischen Kruste beprobt. Das Profil befindet sich im Wadi Gideah des Wadi Tayin Massivs, welches dem südlichen Oman Ophiolith angehört. Durch die Anwendung unterschiedlicher Analysemethoden konnte ein kohärenter Datensatzerstellt werden, der hervorragend geeignet, um unser Wissen über die Entstehungsprozesse der schnell-spreizenden ozeanischen Kruste zu verbessern.

Die Ergebnisse der Haupt- und Spurenelementanalysen zeigen mit abnehmender Profiltiefe einen positiven Entwicklungstrend der Geochemie für die untere Kruste. Der Trend ist in den Layered Gabbros schwach ausgeprägt, verstärkt sich jedoch direkt am Übergang zu den Foliated Gabbros. In den oberen Foliated Gabbros kommt es zudem zu Mineralzonierung und dem ersten Auftreten spät-magmatischer Phasen. Die Ergebnisse einer petrologischen Modellierung, in einem dem Wadi Gideah ähnlichen chemischen System, zeigen, dass der chemische Entwicklungstrend sehr gut mit wasserreicher fraktionierter Kristallisation reproduziert werden kann. Der Wasseranteil der Schmelze beträgt dabei ca. 0,8 Gew% für die untere und 0,8 bis 1,2 Gew% für die obere Kruste. Mehrere Beobachtungen zeigen, dass die Layered Gabbros des Wadi Gideah in einen angehendem Subduktions-Setting in situ in Schmelzlinsen kristallisiert sind: die wasserreiche Modellierung; ein steiler Gradient für Zr/Hf gegen Zr; ein hoher Fluor- und Chlorgehalt der magmatischen Amphibole; eine konstante negative Nb-Ta Anomalie der Wadi Gideah Schmelzen im Vergleich zu normalem mittelozeanischen Rücken Basalt; und deutlich erhöhte Sr^{87}/Sr^{86} Raten im Vergleich mit der moderne Kruste vom Ostpazifischem Rücken. Anzeichen für Porous Flow sind nicht erkennbar. Die Zunahme des chemischen Entwicklungstrends am Übergang von Layered Gabbros zu den Foliated Gabbros wird von einer deutlichen Abnahme der durchschnittlichen Mineralgrößen begleitet. Es ist möglich, dass dies auf eine erhöhte Abkühlrate unterhalb der axialen Schmelzlinse zurückzuführen ist, was jedoch eine hydrothermale Kühlung der unteren Kruste voraussetzt. Die oberen Foliated Gabbros entsprechen einer ca. 500 m dicken Übergangszone, in welcher aufsteigende Schmelzen und aus der Schmelzlinse absinkende auseinandertreffen. Zusammengefasst zeigt die untere Kruste des Wadi Gideah kombinierte Entstehungsprozesse, ähnlich zu Modellen früherer Veröffentlichungen. Die Kühlung, welche zu Abfuhr der Kristallisationswärme benötigt wird, könnte durch hydrothermale Kanäle gegeben worden sein. Diese treten heute im Wadi Gideah als ca. 100 m weite Zonen mit verstärkter hydrothermaler Alteration ehemaliger Layered Gabbros zu Tage. Diese Metagabbros haben hohe Sr^{87}/Sr^{86} Raten, beinhalten spätmagmatische Phasen und zeigen Anzeichen für das partielle Schmelzen bei hoher Temperatur.

Das kombinierte Entstehungsmodell wird durch die bevorzugte kristallographische Orientierung (CPO) der Plagioklase untermauert. Die Plagioklase zeigen eine geringe intrakristalline Missorientierung und haben keine Anzeichen für plastische Verformung nahe dem Übergang von Kruste zum Mantel. Zudem zeigen die Ergebnisse keine systematische Zunahme sondern nur eine starke, unsystematische Variation der Stärke des Klinopyroxen-Gefüges mit zunehmender Profiltiefe. Die Plagioklase der oberen Foliated Gabbros haben eine zufällige oder gar keine CPO. Das ist vergleichbar mit den Plagioklasen der darüber

gelegenen der Varitextured Gabbros und ist ein weiterer Hinweis für den Übergangcharakter des Bereiches. Die Stärke des Plagioklas-Gefüges nimmt mit zunehmender Profiltiefe leicht zu und könnte auf einen erhöhten Scherfluss zurückzuführen sein, welcher wiederum eine Konsequenz des Einflusses des plastischen Mantelflusses unter der Kruste ist.

Direkt am Übergang von Varitextured Gabbros zu Sheeted Dikes befindet sich ein einzigartiger Aufschluss, der eine Vielfalt an Lithologien aufweist. Der Aufschluss beinhaltet Varitextured Gabbros mit stark alterierten primitiven poikilitischen Klinopyroxenen. In den Gabbro ist ein ozeanischer Plagiogranit intrudiert, welcher Relikte von ehemaligen - nun assimilierten - Sheeted Dikes beinhaltet. Der Plagiogranit wird von trondhjemitischen Gängen durchlagen. Alle Lithologien werden zusätzlich von basaltischen Gängen durchschlagen. Rückschlüsse auf den zeitlichen Verlauf der Intrusionen lassen darauf schließen, dass die aufgeschlossenen Lithologien auf Grund vertikaler Bewegungen der axialen Schmelzlinse entstanden sind. Dies kann durch die Modellierung fraktionierter Schmelzen und dem Vergleich mit früheren Experimenten mit partiellen Schmelzen untermauert werden.

Stichworte: schnell-spreizende mittelozeanische Rücken, Krustenbildung, Oman Ophiolith, Wadi Gideah, lagige Gabbros, Hauptelemente, Spurenelemente, bevorzugte kristallographische Orientierung, axiale Schmelzlinse

Background and Objectives

1. Fast-Spreading Mid-Ocean Ridges

Mid-ocean ridges, underwater boundaries of tectonic plates, are the largest mountain range on earth, with a total length of about 60.000 km. They generally represent the place of birth for oceanic crust, which covers about 2/3 of Earth´s surface. The crust is formed by solidification of basaltic melts (Mid Ocean Ridge Basalt; MORB), derived by decompression melting of the earth´s mantle. The crust constantly drifts away from ridge axis and becomes destroyed at subduction zones, by moved under continental crust, which is lower in density. Hence, oceanic crust formation plays a major role in Earth´s tectonic and geochemical cycle. Both the ridge and the accreted oceanic crust are defined by the present spreading rate, which can be generally divided into slow- and fast-spreading ($\leq$30 mm year^{-1} and $\geq$80 mm year^{-1} full spreading rate, respectively; e.g. Coogan, 2014). Fast-spreading oceanic crust (e.g. from East Pacific Rise; EPR), in contrast to slow-spreading one (e.g. from Mid Atlantic Ridge; MAR), exhibits a uniform seismic stratigraphy and can be regarded as relatively homogeneous and layered (e.g. Canales et al., 2003). Theoretical models on magmatic accretion, thermal models, mass balance calculations or general alteration models of and for the oceanic crust therefore generally only exist for fast-spreading systems. Experimental, petrological, and geochemical studies gave evidence for low pressure crystallization of MORB (e.g., Grove et al., 1992), with a crystallization sequence of olivine $\rightarrow$ olivine + plagioclase $\rightarrow$ olivine + plagioclase + clinopyroxene $\rightarrow$ plagioclase + clinopyroxene + magmatic late stage phases, at mid-ocean ridges. Away from the ridge, where melt is solidified, fast-spreading oceanic crust features a lower crust of 3-5 km thick gabbro section, overlain by 1-2 km upper crust composed of sheeted dikes, with another 1-2 km of sheeted flows and pillow basalts on top. Geophysical studies revealed the presence of an Axial Melt Lens (AML) at mid-crust level (tens to hundreds of meter high and <1-2 km wide; Sinton and Detrick, 1992), overlying a crystal mush zone (e.g. Detrick et al., 1987; Hussenoeder et al., 1996; Sinton and Detrick, 1992; Vera et al., 1990).

2. Accretion of Fast-Spreading Oceanic Crust

The discovery of the AML gave reason to rethink the model for fast-spreading crust accretion, to explain, how such a small-dimensioned melt lens can account for ~7 km of crustal material. Before, the so called "infinite onion" model (Cann, 1974) was well established, assuming large magma chambers (up to 4 km in height and 20 km in width) to feed dikes and lavas above by ejected melts, and to form lower oceanic crust by minerals plating their margins (Fig. 1a). The gabbro-glacier model was developed (e.g., Henstock et al., 1993; Quick and Denlinger, 1993; Morgan and Chen, 1993) assuming that minerals, precipitated within the AML, subside below the melt lens bottom, where they are transported down to the mantle/crust boundary by suspension flow (Fig. 1b). Flow lines are vertical directly below the AML, becoming horizontal with increasing stratigraphic depth and distance from ridge axis. This change accounts to the observation at Oman ophiolite that lower gabbros reveal graded

layering and foliation parallel to Moho Transition Zone below (MTZ), whereas upper gabbros reveal steep foliation, with graded layering absent. The sheeted-sills model (e.g., Kelemen et al., 1997; Korenaga and Kelemen, 1997, 1998; Natland and Dick, 2009) was developed as an alternative accretion model, after observation of gabbro-sill intrusions into Oman ophiolite MTZ. It assumes that crystallization of lower crust minerals doesn´t take place within the AML, but in situ, directly from ascending mantle derived melts in sills, which intrude into already solidified gabbroic cumulate (Fig. 1c). Both aforementioned models are generally described as end member models, whereas a hybrid accretion, featuring lower crust to relate to both subsidence of crystals and deep crystallization to a variable proportion is also discussion (e.g., Bédard et al., 1988; Boudier et al., 1996; Fig. 1d).

The major difference between the end member models, next to location of crystallization, is the amount of hydrothermal convection required and the depth where it takes place. For the gabbro-glacier model, crystallization heat at the AML is extracted by hydrothermal convection with the upper crust, with lower crust cooled generally conductively. In contrast, the sheeted-sills model requires hydrothermal convection down to the mantle/crust boundary, to sufficiently extract heat of deep crystallization, as shown by thermal modeling (e.g. Maclennan et al., 2004). It is still in discussion, if and how intense lower crustal cooling is
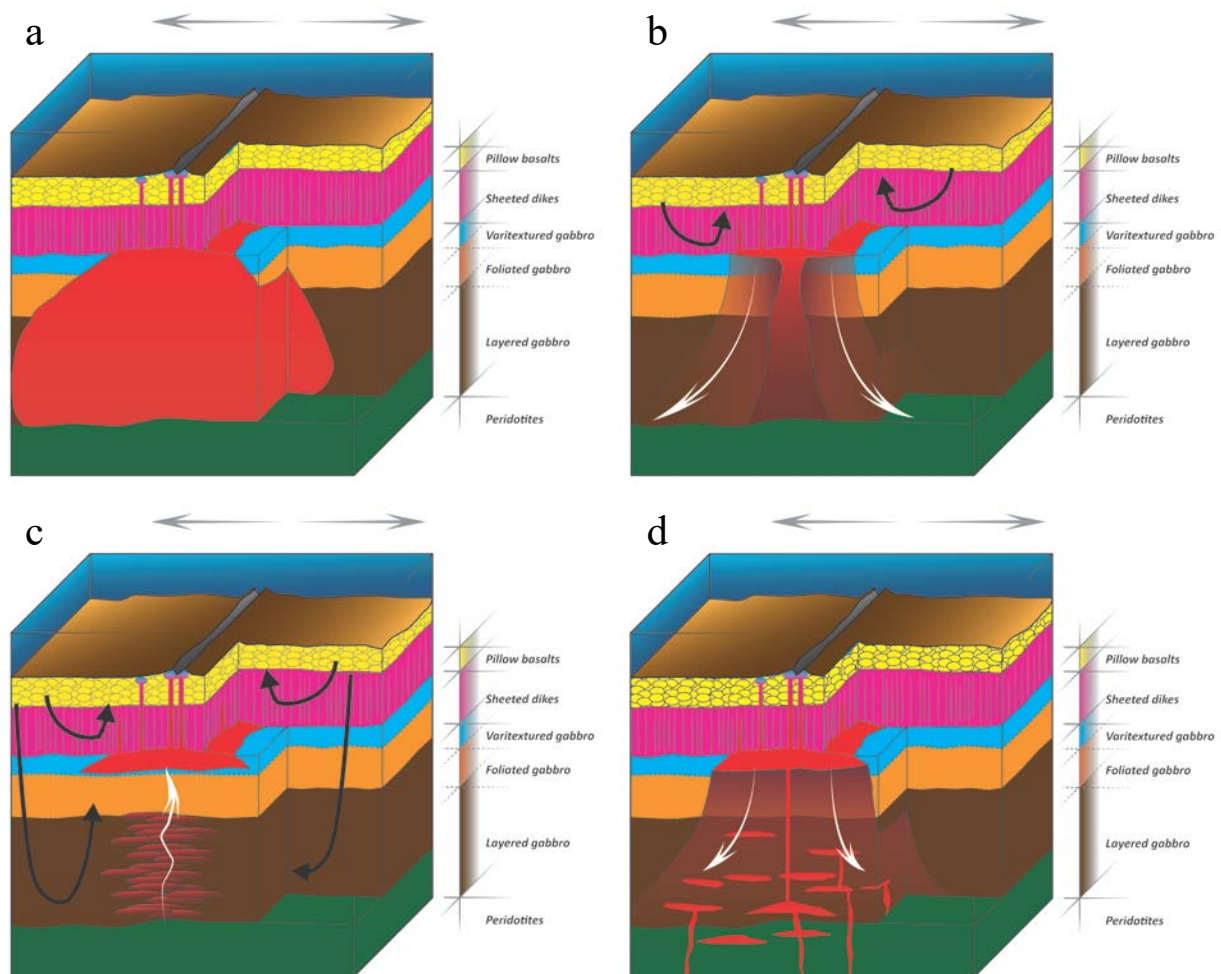
Figure 1. Models for formation of the lower fast-spreading oceanic crust: a) The "infinite onion" model (Cann, 1974). Lower crust is formed by an ever-present magma chamber. b) The "gabbro-glacier" model (e.g., Henstock et al., 1993; Quick and Denlinger, 1993; Morgan and Chen, 1993). Lower crust is formed by crystal subsidence from the axial melt lens. Black arrows indicate hydrothermal cooling. c) The "sheeted-sills" model (e.g., Kelemen et al., 1997; Korenaga and Kelemen, 1997, 1998; Natland and Dick, 2009). Lower crust is formed by crystallization in multiple sill injections. Black arrows indicate hydrothermal cooling. d) The "hybrid" model (e.g., Bédard et al., 1988; Boudier et al., 1996). Lower crust is formed by crystallization in sills at the bottom and by crystal subsidence from the axial melt lens at the top.

enabled. Earlier studies of the southern Oman ophiolite (e.g., Bosch et al., 2004; Manning et al., 2000; Nicolas et al., 2003) described the occurrence of micro crack networks reaching down to MOHO level. It is, however, uncertain if such a permeability network would extract heat efficiently enough, to enable deep crust cooling (e.g., Manning et al., 2000). Other authors observed zones of intense hydrothermal high- and low temperature alteration in Oman ophiolite lower crust, proposing possible focused seawater flow down to mantle/crust boundary (Coogan et al., 2006). A clear evidence for deep crust hydrothermal cooling is rare so far and, hence, type of accretion of fast-spreading lower oceanic crust still under debate.

3. Oman Ophiolite

In spite of tremendous efforts by ship-based research, a complete modern chemical and/or petrological profile based on natural samples is still missing, due to a lack of exposures and drilled sections of the deeper parts of fast-spread crust. Most promising drilling sites have either reached only first tens of meters of gabbro so far (IODP Site 1256D) or returned short sections from multiple holes (Hess Deep). Ophiolites are regarded as the best analogue to fast-spreading mid ocean crust (e.g. Nicolas, 1989). Earth's largest and most widely studied ophiolite is the Oman-Union Arab Emirates ophiolite (Samail ophiolite). The Samail ophiolite was formed during the Creatious Period (~95 Ma for youngest rocks; Rioux et al., 2013;
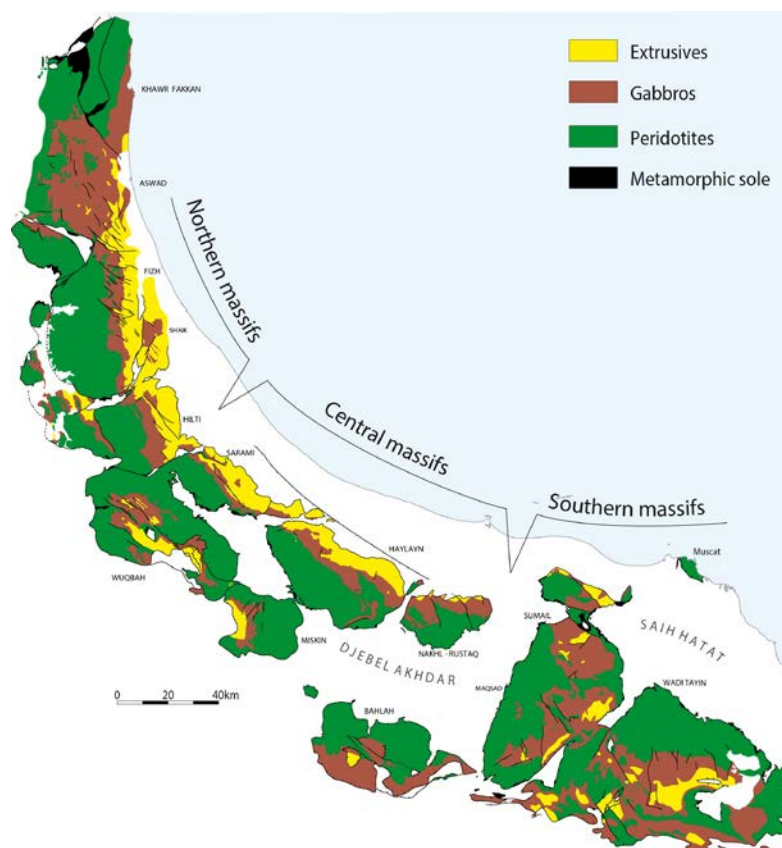
**Figure 2.** Simplified lithological map of the Samail ophiolite (after Nicolas et al., 2000a). The ophiolite is generally divided into 3 main massifs (norther, central, and southern) with late stage magmatism more apparent in the north and widely absent in the south (V2 or Phase 2, see text). Map shows mantle peridotites, lower crust gabbros, and upper crust extrusives, colored in different shades.

Tilton et al., 1981; Warren et al., 2005) as part of the Neothethys seafloor. Its obduction onto the Arabic Peninsula started ~1 Ma after formation of youngest rocks (e.g., Hacker, 1994; Hacker et al., 1997; Warren et al., 2005), with peak metamorphic conditions at ~82-79 Ma (e.g. Warren et al., 2003; Warren et al., 2005).

Today, Samail ophiolite forms a large mountain range along the northern coast of the Arabic Peninsula. It is ~600 km long, covers ~20.000 km^2, and is separated in to 12 tectonic blocks, as a result of the obduction process (Lippard et al., 1986; Fig. 2). The obducted crust was tilted during obduction. The Samail ophiolite has up to 4.6 km of lower crust, underlain by up to 9 km of mantle, and overlain by ~2 km of sheeted dikes and ~1.5 km of sheeted flows and pillow basalts (Lippard et al., 1986; Nicolas et al., 1996). The lower crust is subdivided in layered gabbros (1-4 km), which includes a Moho transition zone (MTZ), few tens to hundreds of meters thick (e.g. Korenaga and Kelemen, 1997), foliated gabbros (0.3-2 km), and varitextured gabbros (0-1 km; also designated as high-level or isotropic gabbro). Layered gabbros have the characteristic cumulate layering and a foliation parallel to the mantle/crust boundary below, with plagioclase, clinopyroxene, and olivine representing the most abundant minerals (e.g. Pallister and Hopson, 1981). The MTZ, which represents the transition from mantle harzburgite to lower crust gabbro, is generally composed of dunite and gabbro sills (e.g., Korenaga and Kelemen, 1997). Foliated gabbros, which overlie layered gabbros, are marked by an absence of cumulate layering and by foliations perpendicular to the MTZ, with plagioclase, clinopyroxene, and olivine still representing the most abundant mineral phases (e.g. Pallister and Hopson, 1981). The varitextured gabbros on top present high variety of grain sizes and textures, with absence of any foliation, a general lack of olivine, and presence of late stage magmatic phases. This horizon can be considered as remnant of former AML horizon (e.g., MacLeod and Yaouancq, 2000; Koepke et al. 2011).
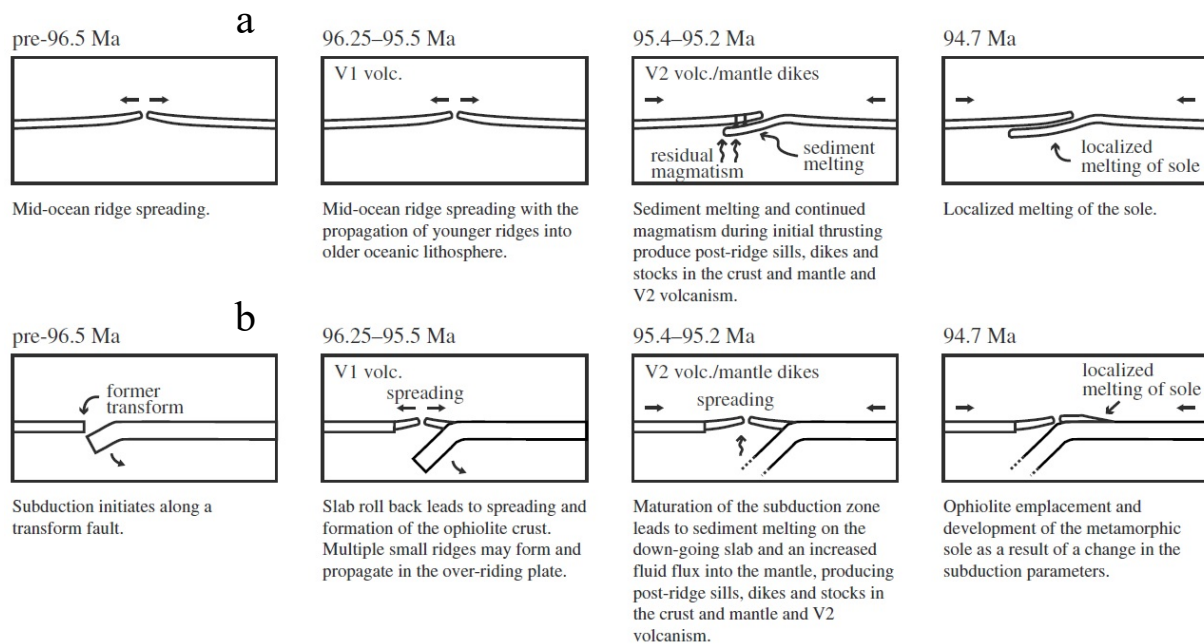
Figure 3. The tectonic settings and time constraints for Oman ophiolite accretion from Rioux et al. (2013). a) Formation at a normal fast-spreading mid-ocean ridge setting (e.g. Coleman, 1981). b) Formation at a setting of subduction zone initiation (e.g. Bloomer et al., 1995), where the crust is obducted relatively fast after the initiation. Note the different mechanisms and time constraints, proposed for V2 formation by either normal mid-ocean ridge- or subduction initiation setting.

The ophiolite crust was originally considered to relate to normal mid-ocean ridge magmatism (Coleman, 1981; Fig. 3a). However, assumption arose, that the ophiolite is rather related to subduction initiation or even arc magmatism (e.g. Bloomer et al., 1995; Pearce et al., 1981; Fig. 3b), since petrological and geochemical observations revealed late intrusions and rock chemical transitions into direction of arc volcanism (e.g., Alabaster et al., 1982; Godard et al., 2003; Goodenough et al., 2010, 2014; Juteau et al., 1988; Lippard et al., 1986; MacLeod et al., 2013; Pearce et al., 1981; Rioux et al., 2013). Ophiolite magmatism was subdivided into a first stage and a second stage (V1, "Geotimes lavas", or Phase 1 and V2, "Lassai lavas", or Phase 2; e.g., Godard et al., 2003; Goodenough et al., 2014). The impact of late stage magmatism is relatively strong at the northern Oman ophiolite and becomes weaker into southern direction. Some authors still tend to a setting of normal mid-ocean ridge magmatism, proposing that the observed late stage magmas, different to NMORB in chemistry, possibly result from late stage seawater injection (e.g. Abily and Ceuleneer, 2013; Boudier et al., 2000; Nicolas et al., 2003) or a second stage of mantle melting (e.g., Ernewein et al., 1988; Godard et al. 2006). To summarize, Samail ophiolite tectonic setting, like lower crust accretion, is still under debate. However, similarity to modern fast-spreading crust and good accessibility make it a unique place, to study fast-spreading mid-ocean ridge processes.

4. Objectives of the Study

As aforementioned, many processes like fast-spreading crust accretions, deep crust hydrothermal cooling, and the tectonic setting of Oman ophiolite are still under discussion. This study aims to shed some new light on these points in three chapters:

Chapter A is a detailed petrological and geochemical study of the fast-spreading paleo-crust lithologies, exposed at Wadi Gideah (Wadi Tayin Massif; Samail ophiolite), using petrography, major and trace element chemistry, and bulk isotopy. Aim of the study is to get new implications for fast-spreading lower mid-ocean crust accretion, possible deep crust hydrothermal cooling, and the overall southern Oman ophiolite tectonic setting. It is revealed that Wadi Gideah lower crust was accreted in a subduction initiation setting, mostly by crystallization at depth and with downward suspension flow only apparent in the uppermost part. Required deep crust cooling could be provided by channeled hydrothermal flow down to mantle/crust boundary. The trace element analysis of clinopyroxene from this chapter was developed in collaboration with the Master thesis of MSc. Laura Bähre (Bähre, 2015).

Chapter B is a complementary study to the petrological and geochemical investigation of chapter A, using electron back scattered diffraction to determine variation of plagioclase crystallographic preferred orientations (CPO) symmetries and strength. Aim of the study is to acquire further information on Wadi Gideah lower crust formation. It is revealed that hybrid accretion model of chapter A is supported by plagioclase CPO, which shows low intra-mineral misorientation and no significant crystal plastic-deformation down to mantle/crust boundary. It is additionally revealed

that Wadi Gideah lower crust may have suffered increased shear flow with increasing depth as an impact of mantle plastic flow from below.

Chapter C is a detailed petrological and geochemical study of an exceptional exposure (Gideah South) from Wadi Gideah axial melt lens (AML) horizon. Aim of the study is to get further insights into possesses in AMLs at fast-spreading mid-ocean ridges. It is revealed that Gideah South lithologies (varitextured gabbro, xenolith bearing plagiogranite, trondhjemite dikes, and basaltic dikes) formed as a consequence of episodic vertical AML movement, which is shown by time constraints on intrusions, major and trace element analysis, and petrological modeling.

Chapter A

Implications for the Crustal Accretion at Fast-Spreading Mid-Ocean Ridges:

Petrology and Geochemistry from the Wadi Gideah Cross Section

A.1 Introduction

As aforementioned, the Samail ophiolite is separated into 12 blocks, generally summarized as the northern, central, and southern Massifs (Fig. 2). Late stage magmatism, also designated as V2 or Phase 2 (e.g. Godard et al., 2003 and Goodenough et al., 2014), is more common in the northern Massifs and widely absent in the southern ones. Hence, the latter are well suitable for studying more primary fast-spreading mid-ocean ridge accretion processes (e.g., Garrido et al., 2001; Koga et al., 2001; VanTongeren et al., 2008). So far, only few profiles from Wadi Khafifah, Wadi Kadir, Wadi Gideah, and Wadi Imrad were described by Pallister and Hopson (1981) based on an intensive US mapping project in the 1970´s in the complete Ibra area of
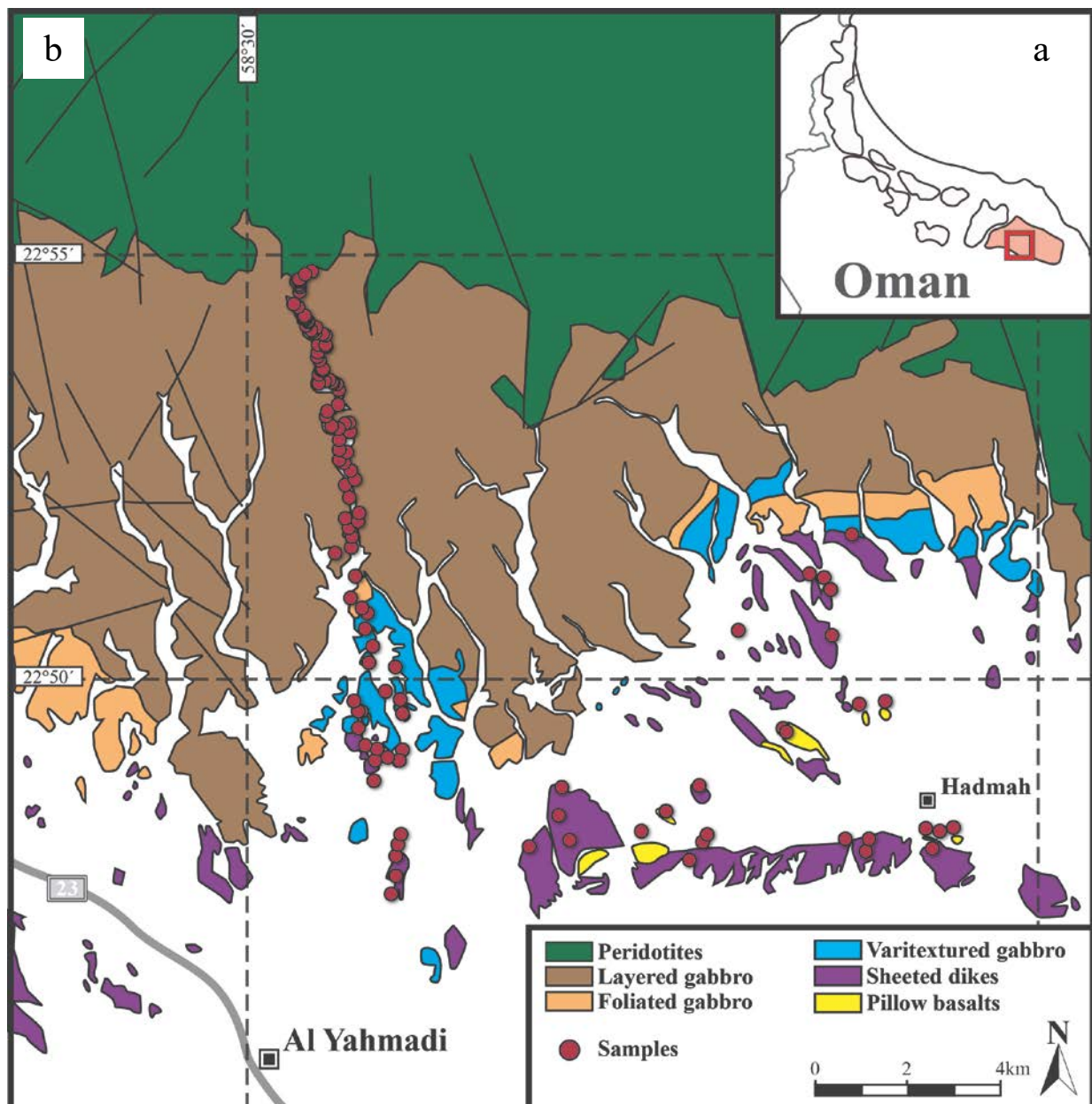

Figure A1. a) Sketch of the Oman Ophiolite with the southeast Wadi Tayin Massif colored in red. The location of b) is marked by the red rectangle. b) Geological map of the southern Wadi Tayin Massif of the Samail ophiolite modified and simplified after Peters et al. (2008). Red marks indicate positions of samples, which were taken for this study.

Wadi Tayin. Additional profiles lacked completeness or coherency since they generally focused on special issues of crust accretion or hydrothermal cooling (e.g., Browning, 1982; Coogan et al., 2002b; Garrido et al., 2001; MacLeod and Yaouancq, 2000; VanTongeren et al., 2008). Hence, in order to shed some new light on fast-spreading mid-ocean crust accretion and to establish a complete and coherent reference profile for modern fast-spreading mid-ocean ridge crust, a cross section was sampled for this study at the Wadi Gideah, in the Wadi Tayin Massif of Samail ophiolite (224 samples; Fig A1). The Wadi Tayin is the southeastern Massif of Samail ophiolite, with the plutonic and extrusive section exposed at its southern flank and late-stage magmatism widely absent. Since the thickness of the plutonic section is ~3 to 5 km (Pallister and Hopson, 1981), in well agreement with observations from modern fast-spreading oceanic crust, a cross section can be considered to have an excellent reference character. Wadi Gideah cuts into Wadi Tayin ~10 km north of Ibra in north-northwest direction. All lithologies of the fast-spreading paleo-crust are well exposed at a Wadi length of ~12 km, with an average dip of 28° (Pallister and Hopson, 1981) into southern direction. Dip angle is slightly higher in the northern Wadi parts and become lower to the south, related to a syncline structure. Wadi Gideah was, next to the work of 1970´s group, also studied by France et al. (2009) who described in detail the gabbro/dike transition and found a clear correspondence to drilled gabbros from IODP Site 1256D, supporting the reference character of Wadi Gideah. In this chapter, I focus on the investigation of coherent Wadi Gideah sample suite for vertical variations by petrography, major and trace element geochemistry, and bulk isotopy, to obtain new insight into fast-spreading ridge lower crust accretion, possible hydrothermal deep crust cooling, and the tectonic setting of Wadi Gideah.

A.2 General Terms and Calculations

A.2.1 General Terms for this Study

The designation of fast-spreading oceanic crust lithologies and rocks may vary in literature although referring to the same objective. Wadi Gideah crust lithologies are designated as layered-, foliated-, varitextured-, sheeted dike-, and pillow basalt section within this study. In terms of geochemical description and the concluding discussion, lithologies are subdivided into lower- and upper foliated gabbro- and lower and upper sheeted dike section. The term "section" comprises all rock types within the referred lithology whereas a general rock type including designation of the lithology (e.g. varitextured gabbro) does not comprise the complete section in turn. Wadi Gideah layered gabbro section comprises layered gabbro and metagabbro (see A.5.1.4 for description). Wadi Gideah varitextured gabbro section comprises varitextured gabbro and basaltic dikes in varitextured gabbro. Wadi Gideah pillow basalts are also referred to a pillow lavas. Layered-, foliated-, plus varitextured gabbro section are referred to as gabbroic section, plutonic section, and lower crust. Sheeted dike- and pillow basalt sections are referred to as basaltic section, extrusive section, or upper crust. A list of all Wadi Gideah lithologies is given in Table A1.

A.2.2 Calculation of Tilt Adjustment, Lithology Thicknesses, and Sample Depths

The Oman ophiolite was tilted during its obduction onto the continental crust of the Arabic peninsula, which led to today´s unique exposure of fast-spreading oceanic crust at Earth´s surface. However, it requires recalculation of sample field coordinates in order to obtain representative crustal thickness and valid sample depths within the Wadi Gideah profile. Hence, coordinates of field samples taken for this study were adjusted for both distance from profile axis and tilt of ophiolite lithologies. GPS coordinates obtained in field were transformed to UTM system (Universal Transverse Mercator) to simplify adjustment calculations.

Table A1. List of Wadi Gideah lithologies with abbreviation and thickness.

Section/lithology		Abbreviation	Thickness [m][a]
Extrusive section	Pillow basalts	PB	~ 600[a]
	Upper sheeted dikes	USD	~ 1500[a]
	Lower sheeted dikes	LSD	
Varitextured gabbro section	Basaltic dikes cutting varitextured gabbros	BDVG	~1000[b]
	Varitextured gabbros	VG	
Foliated gabbro section	Upper foliated gabbros	UFG	~1400[b]
	Lower foliated gabbros	LFG	
Layered gabbro section	Layered gabbros	LG	~ 2600[b]
	Moho transition zone	MTZ	

[a] estimated from literature (Nicolas et al., 1996)
[b] calculated for this study

As a natural system Wadi Gideah does neither follow a straight line nor does Wadi axis display general N-S orientation of exposed lithologies. Hence, sample coordinates in UTM system were shifted to a fixed N-S axis by changing all x-coordinates to a single fixed value. Wadi Gideah Mohorovičić discontinuity (Moho) location on profile axis was defined as the average y-coordinate of the last lower crust- and the first mantle sample (OM10_Gid_A32 and OM10_Gid_A33, respectively). Referring to Moho position, all sample coordinates were expressed as "Height above Moho" (H.a.M.) using equation

$$\mathrm{H.\,a.\,M.}_{\mathrm{sample}} = y_{\mathrm{sample}} - y_{\mathrm{Moho}}$$

Y represents UTM y-coordinate. The stratigraphic sample height is referred as "sample depth" throughout the study, although designation includes "height". Sample depths for the lower crust were corrected for Wadi Gideah tilt (respectively dip) using equation

$$\mathrm{H.\,a.\,M.}_{\mathrm{sample\ final}} = \mathrm{H.\,a.\,M.}_{\mathrm{sample}} * \sin(\alpha)$$

The dip angle α was set to 28° as an average of dip angles given by Pallister and Hopson (1981) for Wadi Gideah lithologies (23 values from 12 to 50°). The syncline structure, in the south of Wadi Gideah, was not taken into account to simplify calculation, with focus on well-grounded but comprehensible sample depths. The altitude of Wadi Gideah sample was not taken into account, since samples were taken generally from the Wadi bed. Location of lithology transitions was defined as an average of depths from last and first sample taken in field from lower- and upper lithology, respectively. Wadi Gideah lower crust lithology thicknesses, obtained by aforementioned calculations, are ~2630 m for layered-, ~1390 m for foliated-, and ~1000 m for varitextured gabbro section. Since the upper crust is rarely preserved in the field, lithology thicknesses are estimated to be ~1500 m for sheeted dike- and ~600 m of pillow basalt section (based on estimations by Nicolas et al., 1996), with a total thickness of ~7100 m for Wadi Gideah fast-spreading crust (~6.8 km for EPR crust; Canales et al. 2003). The depths of samples, which were taken out of Wadi Gideah (see A.3.5; Fig. A.1), were fixed, independent from their original location, to 6300 m and 6600 m H.a.M. for sheeted dikes and pillow basalts, respectively. Results of sample depth calculations are given in Table 1 (appendix).

A.3 Field Description

A.3.1 Layered Gabbro Section

Wadi Gideah layered gabbro section represents the thickest lithology of this study including the ~300 m thick Moho transition zone (MTZ). Layered gabbros have the eye-catching and name giving cumulus layering in field. It is parallel to underlying mantle/crust boundary (Pallister and Hopson, 1981), with a variation in scale from centimeters to meters (Fig. A2a). Single layers can only be tracked for several meters, with striking similarities with gabbro sill intrusions observed in the MTZ, which are interpreted by some authors as layered complexes (e.g. Boudier et al., 1996; Kelemen et al., 1997; Van Tongeren et al., 2008). Cumulus layers have variations in dip angle but can be generally described with an average dip angle of 28° (Pallister and Hopson, 1981; see A.2.2). Layered gabbros are foliated parallel to the cumulus layering. A feature of Wadi Gideah lower layered gabbro section is the lack of wherlite intrusions near the MTZ, which were observed at other locations of Oman ophiolite (e.g. Boudier and Nicolas, 1995; Koga et al., 2001; Pallister and Hopson, 1981). Larger displacement faults are rare and are only observed near the MTZ (Pallister and Hopson, 1981).

A.3.2 Foliated Gabbro Section

The layered gabbro section passes into foliated gabbro section ~2600 m above the Moho with a relatively thin transition zone of <60 m. Foliated gabbros in the field show a lack of cumulus layering in comparison with layered gabbro section below, which is associated with mineral foliations perpendicular to Moho (e.g., France et al., 2009). These significant changes at the layered to foliated gabbro transition zone are still heavily discussed in literature and gave foundation (amongst other evidences) for theoretical models concerning the formation fast-spreading oceanic crust. The most frequent mineral phases of foliated gabbros are plagioclase, clinopyroxene and olivine, with a smaller grain size in comparison with layered gabbro minerals. The amount of olivine decreases up section, which is associated with the first appearance of opaque oxides.

A.3.3 Varitextured Gabbro Section

The foliated gabbro section passes into the varitextured gabbro section ~4000 m above the Moho with a wide and smooth transition zone of 200 to 500 m. The varitextured gabbros show an intense heterogeneity in grain size and modal proportions (suggesting the term "varitextured"; for definition see MacLeod and Yaouancq, 2000), with fine- to medium grained gabbro, gabbronorite, and hornblende gabbro, which systematically lack any mineral foliation (Fig. A2d). Up section, textures become more homogenous. A feature of Wadi Gideah is the occurrence of multiple well preserved outcrops at the gabbro/dike transition including an exceptional outcrop, designated as Gideah South. The outcrop exhibits

spectacular interconnection of spotty gabbro (poikilitic clinopyroxenes enclosed by smaller grained whitish, granular matrix) bearing varitextured gabbro, intruded and assimilating xenolith bearing plagiogranite, and crosscutting trondhjemite and basaltic dikes. This outcrop is referred to as Gideah South outcrop, which is described and discussed in detail in chapter C (including definition of rock types mentioned).
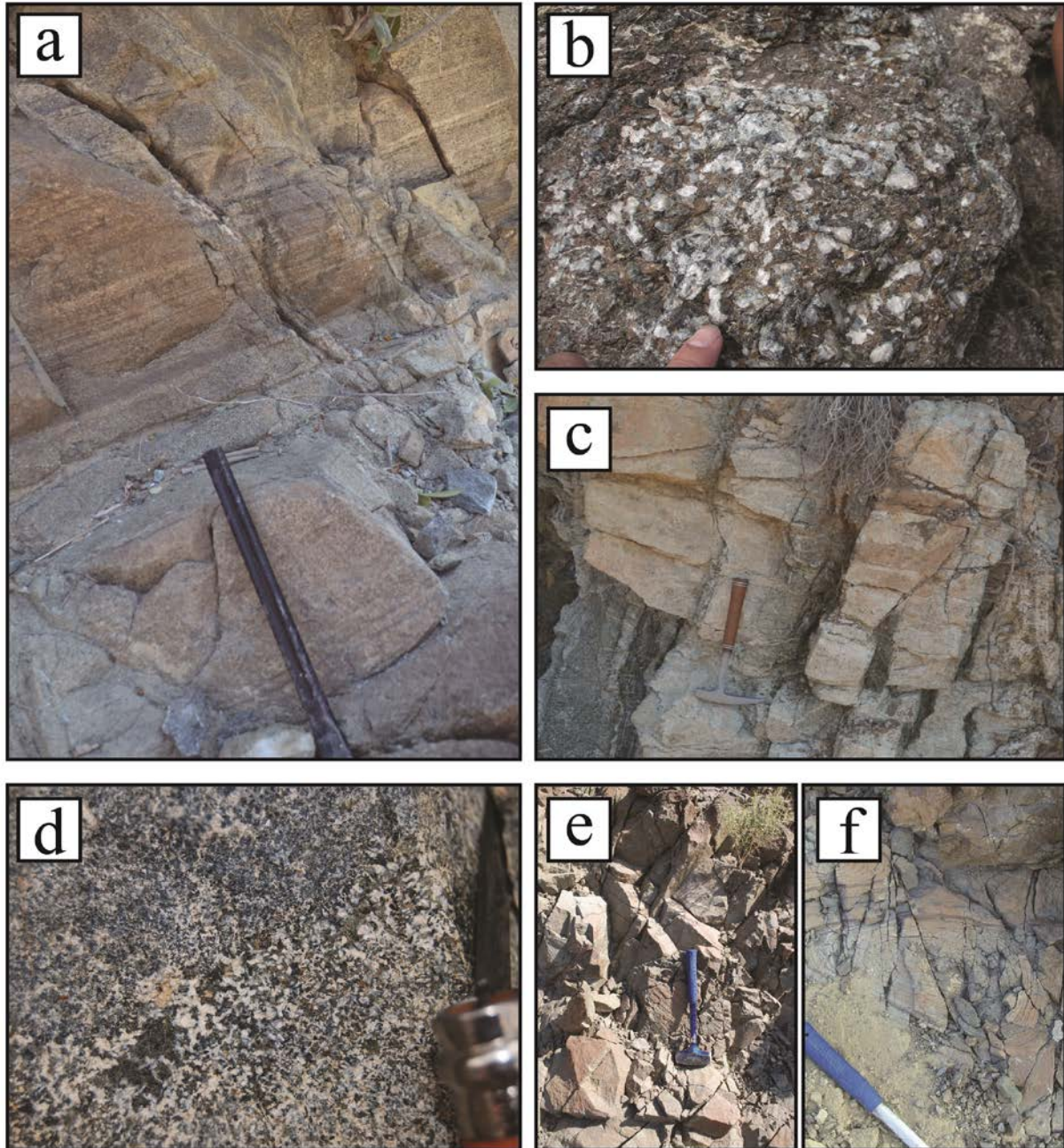

Figure A2. a) Layered gabbro cumulus layering with variation in centimeter scale. Whitish zones are poor in olivine and pyroxene b) Heterogeneous gabbro from hydrothermal fault zone with mostly large plagioclase minerals and large pyroxenes c) Heavily altered layered gabbro with preserved layering ("ghost layering") from hydrothermal fault zone. d) Heterogeneous varitextured gabbro from Gideah South outcrop. e) Sheeted dikes in the southern part of south of Wadi Gideah cross section. Outcrops are generally rare with sizes from some meters to only decimeters. f) Pillow basalts out of the Wadi Gideah area. All material is heavily altered.

A.3.4 Hydrothermal Fault Zones

A special feature of the Wadi Gideah lower crust is the occurrence of multiple hydrothermal fault zones, which cut layered gabbro generally perpendicular to its layering (Fig. A2b, c), similar to "focused fluid flow zones" (FFFZ) observed by Coogan et al. (2006) in Wadi Abyad (Rustaq-Nakhl Massif) and Wadi Namarah (Wadi Tayin Massif). These fault zones have width to more than 100 m, in short distance down to 100 m, and appear within the complete layered gabbro section down to the Moho. This section comprises large amounts of former layered gabbro rock ("ghost layering"; Fig. A2c), which is intensely hydrothermally altered into amphibolite to greenschist facies. These rocks are referred to as metagabbro in this study. These areas have a bright appearance in color, which is well observable in field and also on aerial images. Since distinctive transitions are hard to identify, it is questionable if these 100 m wide zones actually represent a single large fault zone or rather multiple smaller ones with narrow spacing. Within altered layered gabbro, very heterogeneous hornblende gabbros, highly variable in grain size (up to pegmatitic; Fig. A2b), can be identified in the fault zone centers (heavily imprinted by greenschist alteration though). Referring to Coogan et al. (2006), these zones are proposed by this study to represent possible evidence in field for the channeling of focused hydrothermal flow down to mantle/crust boundary during lower crust accretion (see A.7.4).

A.3.5 Sheeted Dike Section and Pillow Basalt Section

The varitextured gabbro section passes into the sheeted dike complex ~5000 m above the Moho. The gabbro/dike transition zone is marked by the occurrence of recrystallized hydrated varitextured gabbro, basaltic dikes cutting gabbro rock, dike in dike intrusions, and remnants of granoblastic margins. The sheeted dike section exhibits up to meter thick, fine grained doleritic dikes with chilled margins versus adjacent dikes. Appearance, alteration, weathering, and dike N-S orientation perpendicular to mantle/crust boundary are similar to other dike sections, which were described for the southern Oman ophiolite (e.g., France et al., 2009; Pallister and Hopson, 1981; Nicolas et al., 2008). Up section, Wadi Gideah sheeted dike section is rarely preserved and only observable at discontinuous outcrops (sometimes of decimeter scale only; Fig. A2e). Therefore, for this study sampling was extended multiple kilometers into eastern direction where sheeted dikes are well preserved in outcrops at a scale of tens of meters. Wadi Gideah sheeted dike- to pillow basalt transition is not distinctive in field with pillow basalts rarely preserved and only available multiple kilometers east (similar to sheeted dikes). They are highly altered, up to 30 cm wide, and red in color (Fig. A2f).

A.4 Methods

A detailed list of Wadi Gideah sample suite and the performed analysis for each sample is given in Table 1.

A.4.1 Sample Selection and Sample Preparation

A.4.1.1 Field Sampling

Wadi Gideah rock suite was sampled during three field campaigns in 2010, 2011, and 2012 (Fig. A1). The total number of samples is 224, with 41 samples taken out of Wadi Gideah (sheeted dikes and pillow basalts). Sample sizes varied from centimeter to decimeter scale. The average spacing between the sampling sites for Wadi Gideah profile is 63 m (calculated stratigraphic height; see A.2.2), whereas spacing varies from 1 m to 276 m between single locations of sampling.

A.4.1.2 Sample Preparation

Thin sections were prepared for 220 samples. Rock samples were cut and sliced using a steel circular saw to remove impact of high weathering.

Sample powders for bulk rock analysis were prepared for 161 field samples. Samples, cut for thin section preparation, were crushed using a jaw-crusher. Rock chips which had been in direct contact with either steel saw or the jaw-crusher were excluded from milling to avoid sample contamination. The remaining chips were cleaned for 20 min in ultrasonic bath for dust removal in a warm mixture of 50 % ethanol and 50 % distilled water. Cleaned chips were crushed to millimeter size, using a stainless-steel mortar, and homogenized and milled for 1 h in an oscillating agate disc mill to grain sizes <40 μm.

Powder from 136 samples was dissolved with acid digestion at the Institute for Geosciences of the CAU University Kiel, following the protocol of Garbe-Schönberg (1993), to enable bulk chemistry and isotopy analysis (see A.4.2.2, A.4.2.3, and A.4.2.5). For each sample 100 mg powder were successively digested in Teflon crucibles by a solution of 0.5 ml ultrapure water (ELGA; >18.5MΩcm^{-1}) and 8 ml nitrohydrochloric acid (1 ml HNO_3 + 2 ml HCl + 4 ml HF), perchloric acid ($HClO_4$) as needed, and 3 ml nitric acid (HNO_3). The Teflon crucibles were closed and heated at 160 °C to accelerate the powder dissolution by rise of temperature and internal pressure. The sample solutions were fully vaporized between acid treatments. The dilution factor for analysis was either 200 or 500. Although perchloric acid was used to enhance acid digestion, results from ICP-MS indicated an unsystematic underestimation of especially Zr and Hf for some samples, which was presumably related to incomplete dissolution of accessory minerals like zircon (see A.4.2.3).

Nano-particulate powder tablets were produced from sample powder at the Institute for Geosciences of the CAU University Kiel, following the protocol of Garbe-Schönberg and Müller (2014), to improve trace element analysis (see A.4.2.4). For each sample 2 g sample powder were grinded in a high power planetary ball mill (Fritsch Pulverisette 7 classic line), with addition of 8 ml ultrapure water (ELGA; >18.5 MΩcm^{-1}), freeze-dried (Alpha 1-2 LD, Martin Christ GmbH), and pressed into a tablet form (Specac Atlas 15 t manual). For further details see Garbe-Schönberg and Müller (2014).

A.4.2 Analytics

A.4.2.1 Electron Probe Micro Analysis

Electron probe micro analysis (EPMA) was used for the determination of mineral major element concentrations and performed at the Institute for Mineralogy of the University of Hannover. A Cameca SX100 electron microprobe system with five spectrometers (TAP, LIF, PET, and LPET used as diffracting crystals), the software "PeakSight" (Cameca), Kα emission for all elements (Al, Ca, Cl, Cr, F, Fe, K, Mg, Mn, Na, Ni, Si, Ti, and V), a focused beam, an acceleration potential of 15 kA, a beam current of 15 nA, and an analyses time per element of 10 s was used for analyses. The matrix-correction was performed after Pochou and Pichoir (1991; PAP). F and Cl were analyzed with a beam current of 40 nA and an analysis time of 30 s per element. The microprobe-internal standards used for calibration were albite (Na), Al$_2$O$_3$ (Al), Cr$_2$O$_3$ (Cr), Fe$_2$O$_3$ (Fe), MgO (Mg), Mn$_2$O$_3$ (Mn), NaCl (Cl), orthoclase (K), SrF$_2$ (F); wollastonite (Si and Ca), and V$_2$O$_3$ (V). Plagioclase and clinopyroxene minerals were generally probed separately for core and rim composition. The detection limits for minerals analyzed by EPMA are given in Table 2.

A.4.2.2 Inductively Coupled Plasma Optical Emission Spectrometry

Inductively coupled plasma optical emission spectrometry (ICP-OES) was used for the determination of bulk rock major element concentrations and performed at the Institute for Geosciences of the CAU University Kiel by the working group of Dr. Dieter Garbe-Schönberg. A SPECTRO Ciros SOP ICP-OES with a 10-fold diluted digest sample solution (see A.4.1.2) spiked with 5 ppm Y for the internal standardization was used for analysis. The digest solutions of international rock standards used for calibration were AC-E, BE-N, BHVO-2, BIR-1, JGb-2, RGM-1, and UB-N. The precision of the results is estimated to be better than 1 % relative standard deviation (RSD). The concentration of bulk rock SiO$_2$ was determined by the difference of the analyzed element concentrations and the loss on ignition (L.O.I.) from a total of 100 %. The results for the analysis of standard material are given in Table 3.

A.4.2.3 Inductively Coupled Plasma Mass Spectrometry

Inductively coupled plasma mass spectrometry (ICP-MS) was used for the determination of bulk rock trace element concentrations and performed at the Institute for Geosciences of the CAU University Kiel by the working group of Dr. Dieter Garbe-Schönberg. An Agilent 7500cs ICP-MS with a 10 to 20 fold sample solution (see A.4.1.2), spiked with 2.5 ppb Be, Y, and Re for the internal standardization, was used for analysis of 39 trace elements (Li, Sc, V, Cr, Co, Ni, Cu, Zn, Ga, Rb, Sr, Y, Zr, Nb, Mo, Sb, Cs, Ba, la, Ce, Pr, Nd, Sm, Eu, Gd, Tb, Dy, Ho, Er, Tm, Yb, Lu, Hf, Ta, W, Pb, Th, U, and Sn). The digest solutions of international rock standards used for calibration were BHVO-2, BIR-1, JGb-1, and JGb-2. The precision of the results is estimated to be better than 2 % (RSD). A significant lower precision was identified for Zr, Hf, Cr, and Ni. This is presumably related to an incomplete dissolution of accessory minerals during acid digestion (see A.4.1.2). A significant lower precision was also identified for Mo, Pb, and W (>10% RSD), with unsystematic variation of Pb content independent from sample depths. Although contamination was minimized as good as possible during powder preparation (see A.4.1.2), low precision and high scatter is presumably related to sample contact with steel saw or jaw-crusher alloys. Hence, Pb is excluded from trace element results of this study. The results for Zr, Hf and few ultra-trace elements (Dy, Er, Ho, Nb, Lu, Ta, Tb, Tm, Y, and Yb) were replaced by results from laser ablation inductively coupled plasma mass spectrometry (LA-ICP-MS) of powder tablets, additionally offering lower detection limits (see A.4.2.4). The results for the analysis of standard material are given in Table 4.

A.4.2.4 Laser Ablation Inductively Coupled Plasma Mass Spectrometry

Laser ablation inductively coupled plasma mass spectrometry (LA-ICP-MS) was used for the determination of bulk trace element concentrations for elements affected by incomplete dissolution of accessory minerals during acid digestion (Zr and Hf) or of ultra-trace character (Dy, Er, Ho, Nb, Lu, Ta, Tb, Tm, Y, and Yb; see A.4.2.3) and determination of clinopyroxene trace element compositions (Ba, Ce, Dy, Er, Eu, Gd, Hf, Ho, La, Lu, Nb, Nd, Pb, Pr, Rb, Sc, Sm, Sr, Ta, Tb, Th, Tm, U, Y, Yb, and Zr). All analyses were performed at the Institute for Geosciences of the CAU University Kiel by the working group of Dr. Dieter Garbe-Schönberg. A GeoLasPro Plus 193 nm ArF excimer laser ablation system, coupled to a Zurich-type low dispersion high capacity laser ablation cell (LDHCLAC; Fricker et al., 2011), was used for analysis of nano-particulate pressed sample powder tablets (see A.4.1.2) or clinopyroxene. The laser pulse length was 10 to 20 ns, with a pulse frequency of 10 to 15 Hz and an ablation spot size of 80 µm (tablets) or 8 to10 Hz and an ablation spot size of 24 to 60 µm (pyroxene). The ablation cell was flushed with $1 \, \text{L min}^{-1}$ He as carrier gas and sensitivity increased by addition of $14 \, \text{mL min}^{-1}$ H_2 gas, before entering the ablation cell. International rock standards, used for calibration, were AC-E, BHVO-2, GA, JGb-2, and UB-N for tablet- and GOR128-G, GOR132-G, JGb-1, NIST-SRM-610, SRM-612, and St.Hs6/80-G for pyroxene analysis. The precision of the results is estimated to be better than 5 % (RSD) and detection limits are estimated to be in the low ppb-range (Garbe-Schönberg and Müller, 2014). Data reduction and visualization was done with the GLITTER software package

(Griffin et al., 2008). The NIST SRM612 standard was used for an external calibration and ^{48}Ca for an internal standardization (Jochum et al., 2011).

A.4.2.5 Multi Collector inductively coupled plasma mass spectrometry

Multi Collector inductively coupled plasma mass spectrometry (MC-ICP-MS) was used for the determination of ^{87}Sr/^{86}Sr, ^{176}Hf/^{177}Hf, and ^{143}Nd/^{144}Nd isotope ratios, and performed at the Institute of Mineralogy of the University of Hannover. For analysis approximately 25 ml of sample digest solutions (see A.4.1.2) were separated for Hf, Sr, and Nd, following Lazarov et al. (2009), Münker et al. (2001), and Pin et al. (1994). The analyses were carried out with a ThermoFinnigan Neptune MC-ICP-MS, coupled to a Cetac Aridus-II-Desolvator (for Hf and Nd analysis only) and an ESI SC2-DX-Autosampler. International standards, used for precision monitoring, were AMES, BIR-1, JGB-2, JMC, and NIST SRM 987. ^{86}Sr and ^{87}Sr were corrected for ^{86}Kr and ^{87}Rb interferences and ^{87}Sr/^{86}Sr corrected for mass fractionation. The interference and mass fractionation correction for ^{176}Hf/^{177}Hf and ^{143}Nd/^{144}Nd were done automatically by Neptune software package. ^{87}Sr/^{86}Sr displayed an average deviation of 0.001 % (RSD), εNd of 0.012 % (RSD), and εHf of 0.007 % (RSD).

A.4.2.6 X-Ray Fluorescence Spectrometry

X-Ray fluorescence spectrometry (XRF; Vogel and Kuipers, 1987) was used for determination of bulk major element concentrations and performed at the Institute for Mineralogy and Petrography of the University Hamburg by the working group of Prof. Dr. Stefan Jung. Concentration of 20 trace elements (Ba, Ce, Co, Cr, Cu, Ga, La, Nb, Nd, Ni, Pb, Rb, Sc, Sr, Th, U, V, Y, Zn, and Zr) was also determined. A wavelength dispersive spectrometer PANalytical MagiX PRO, with a 4 kV Rh-anode coupled to a PW 2540 VC sample changer, was used for analysis of pellets, consisted of 0.6 g sample powder (see A.4.1.2) and 3.6 g lithium tetraborate ($Li_2B_4O_7$). The L.O.I. was determined gravimetrically (Lechler and Desilets, 1987). The analytical accuracy for major elements is estimated to be ≤0.01 wt%. The analytical accuracy for trace elements is estimated to be <5 ppm, except for Ba (10 ppm), Ce (20 ppm), Co (15 ppm), Nd (10 ppm) and La (20 ppm). The results from XRF are not included in the final Wadi Gideah profile data set, due to a lower precision for trace element analysis in comparison with ICP-MS (see A.4.2.4; A.4.2.7).

A.4.2.7 Comparison between XRF, ICP-OES, and ICP-MS

A set of 60 samples from all Wadi Gideah lithologies were analyzed for major- and trace element compositions by XRF, ICP-OES, and ICP-MS. This enabled a detailed comparison of both techniques, regarding precision and data correlation.

The XRF data was normalized to 100 % for a comparison of bulk major element concentrations, after subtraction of the L.O.I. and SO_3 content (not analyzed by ICP-OES). The ICP-OES data was normalized to 100 % after subtraction of the L.O.I.. Both techniques

were directly compared for their analysis results of nine major element oxides (SiO_2, Al_2O_3, Fe_2O_3, MnO, MgO, CaO, Na_2O, K_2O, and TiO_2) and generally found to be in well agreement (Fig. A3). Results revealed that XRF analysis slightly overestimated concentrations of MnO and K_2O. Hence, all further bulk rock major element analyses were performed by ICP-OES.

The XRF and ICP-MS data were directly compared concerning their analysis results of 20 trace elements (Ba, Ce, Co, Cr, Cu, Ga, La, Nb, Nd, Ni, Pb, Rb, Sc, Sr, Th, U, V, Y, Zn, and Zr; Fig. A3). The data revealed that the XRF analysis tended to a general overestimation of the trace element concentration, especially at a range <150 ppm, referring to the higher detection limits of XRF (see A.4.2.6) in comparison with ICP-MS (see A.4.2.4). Hence, further bulk rock trace element analyses were performed by ICP-MS. The ICP-MS data revealed, however, an intense underestimation of Zr content. This is presumably related to an incomplete dissolution of accessory minerals during acid digestion (see A.4.1.2). Hence, results for affected trace elements were replaced by more precise and dissolution independent LA-ICP-MS data.
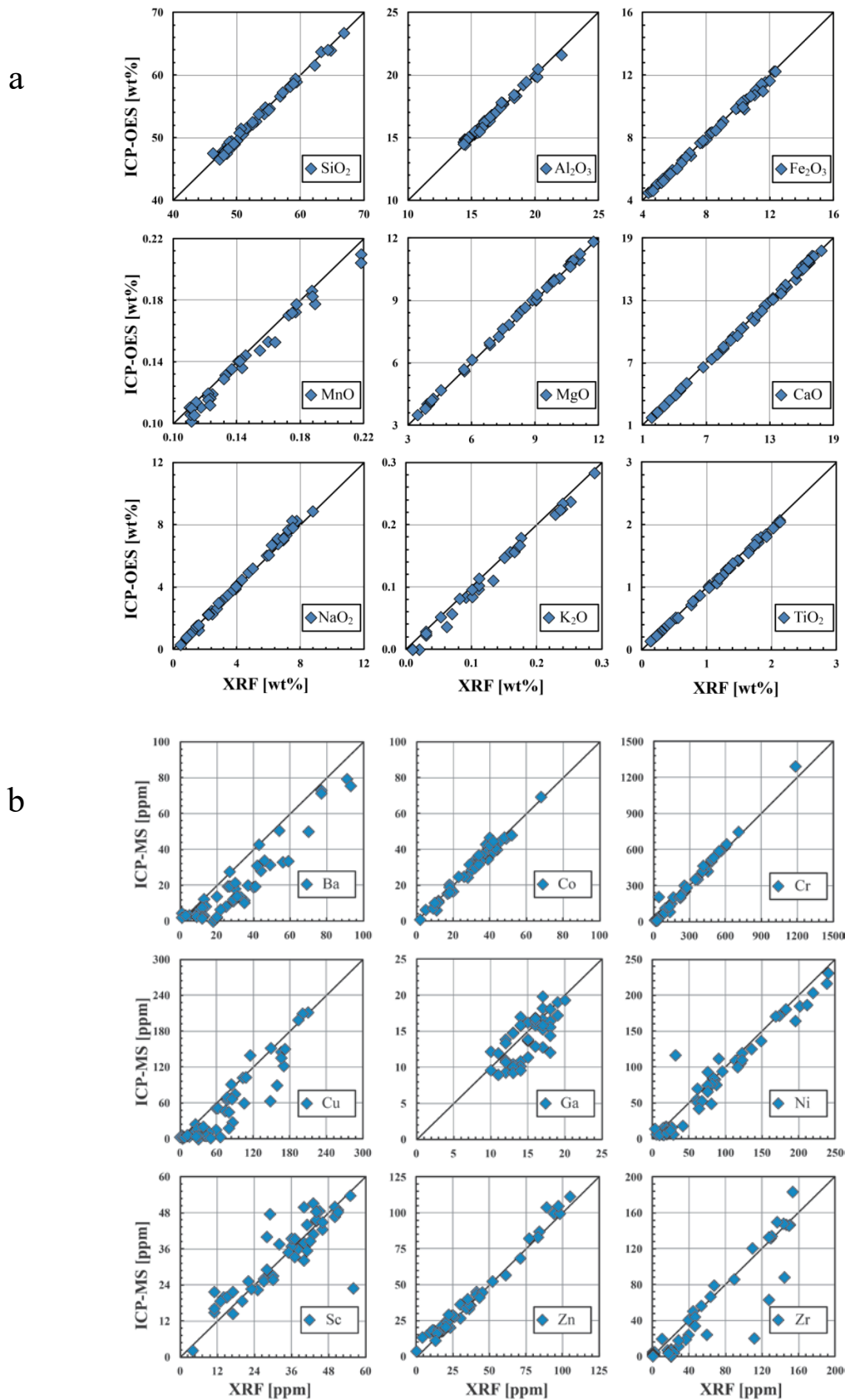
Figure A3. a) Comparison between XRF and ICP-OES major element concentrations. Each point represents one sample with well correlation near 1:1 line. b) Comparison between XRF and ICP-MS trace element concentrations. Each point represents one sample. XRF reveals overestimation for very low abundant elements, probably related to higher detection limit in comparison with ICP-MS. Hence, ICP-MS was favored for further analysis. Note, however, the deviation of ICP-MS for Zr, which may relate to incomplete dissolution of accessory minerals.

A.5 Results

A.5.1 Petrography

A set of 140 thin sections from Wadi Gideah profile was examined by transmitted and reflected light microscopy, in order to obtain detailed information about modal proportions, grain sizes, accessory minerals, special textural features, and the degree of pervasive and vein related alteration. This study follows the methods from Gillis et al. (2014; IODP expedition 345 proceedings volume) in terms of petrographic designations. The results of the petrographic description are given in Table 5.

The accuracy of visual estimation of modal proportions was tested for 6 representative samples from the layered- and foliated gabbro section by additional point-counting. The step size was 0.25 mm in x- and y direction, leading to a total amount of 7800 to 9000 points per thin section. The standard deviation was calculated after Van der Plas and Tobi (1965). By comparison, modal proportions, determined by visual estimation, are revealed to display relative uncertainties of 5.8±2.8 % for plagioclase and 4.1±2.8 % for clinopyroxene (both highly abundant; ~45 vol%), 13.1±4.4 % for olivine (low abundant; ~5 vol%), and 71.1±47.8 % for mineral alteration or accessory minerals (very low abundant; ~0.7 vol%), well acceptable for this study. The results of point counting are given in Table 6.

A.5.1.1 Layered Gabbros

Layered gabbros generally comprise gabbros and olivine gabbros, composed of a fine to medium grained equigranular cumulate network of euhedral to subhedral, tabular- to lath shaped, not zoned plagioclase associated, with subhedral prismatic clinopyroxene, and subhedral to anhedral prismatic olivine (Fig. A4). Plagioclase, clinopyroxene, and olivine are coexistent in all samples, taken for this study (lowest at 50 m H.a.M.). Orthopyroxene is generally absent and if present, only in amounts <1 vol%. Layered gabbros have an average modal proportion of 51 vol% plagioclase, 44 vol% clinopyroxene, and 5 vol% olivine, similar to observations for gabbros from lower recent fast-spreading oceanic crust (Coogan, 2014; Fig. A10) and from Oman (Yaouancq and MacLeod, 2000). The modal proportion of olivine is highly variable, depending on the sample location within the cumulate layering (see A.3.1). The estimated crystallization order is olivine prior to plagioclase prior to clinopyroxene. All samples show generally slight pervasive and/or vein related alteration to minerals of amphibolite or greenschist facies, like actinolite, iddingsite, chlorite, epidote, secondary hornblende, serpentine, and sometimes talc. A few samples display a very high degree of alteration, up to 80 vol%, generally associated with an increased occurrence of veins. The intensity of mineral foliation is weak to moderate.
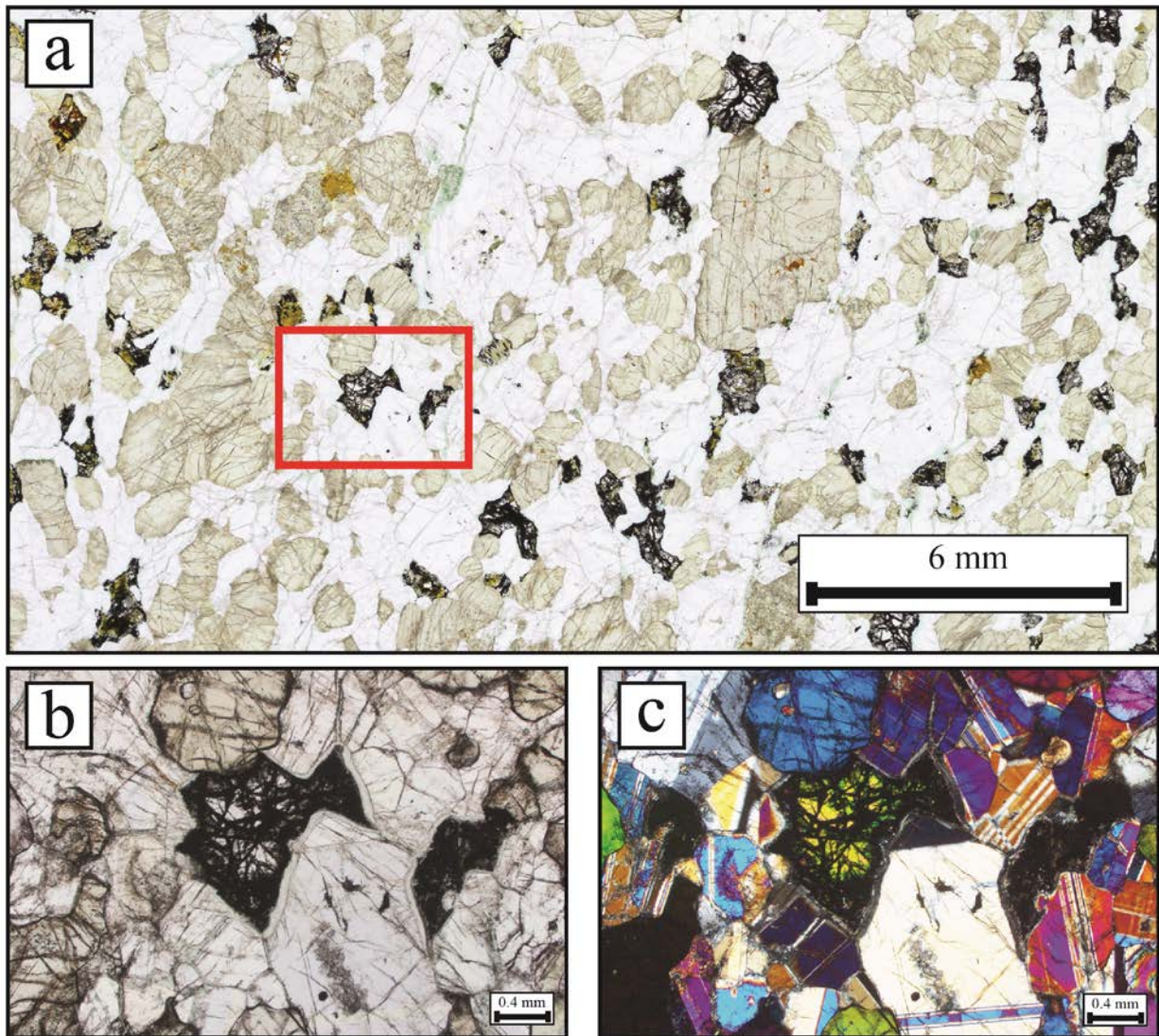
Figure A4. a) Thin section scan of Wadi Gideah layered gabbro (OM10_Gid_A26; 1079 m) composed of plagioclase, clinopyroxene, and olivine. Position of b) and c) are marked by the red rectangle. b) Microphotograph of the layered gabbro at plane-polarized light. c) Same as b) at cross-polarized light. Olivine is generally heavily altered with well visible serpentinisation cracks for the cumulate network. Upper left clinopyroxene in b) and c) has typical inclusions of plagioclase indicating plagioclase crystallization prior to clinopyroxene one.

A.5.1.2 Foliated Gabbros

Foliated gabbros generally comprise gabbros and olivine gabbros, composed of a fine to medium grained cumulate network of euhedral to subhedral and lath shaped plagioclase, associated with subhedral to anhedral prismatic clinopyroxene, and subhedral to anhedral prismatic olivine (Fig. A5). Olivine proportion decreases in the upper foliated gabbro section, associated with the first systematic appearance of orthopyroxene, interstitial amphibole, and interstitial oxides (Fig. A6). Plagioclase zonation is rare in lower foliated gabbros and becomes common in upper foliated gabbros. Foliated gabbros have an average mineral
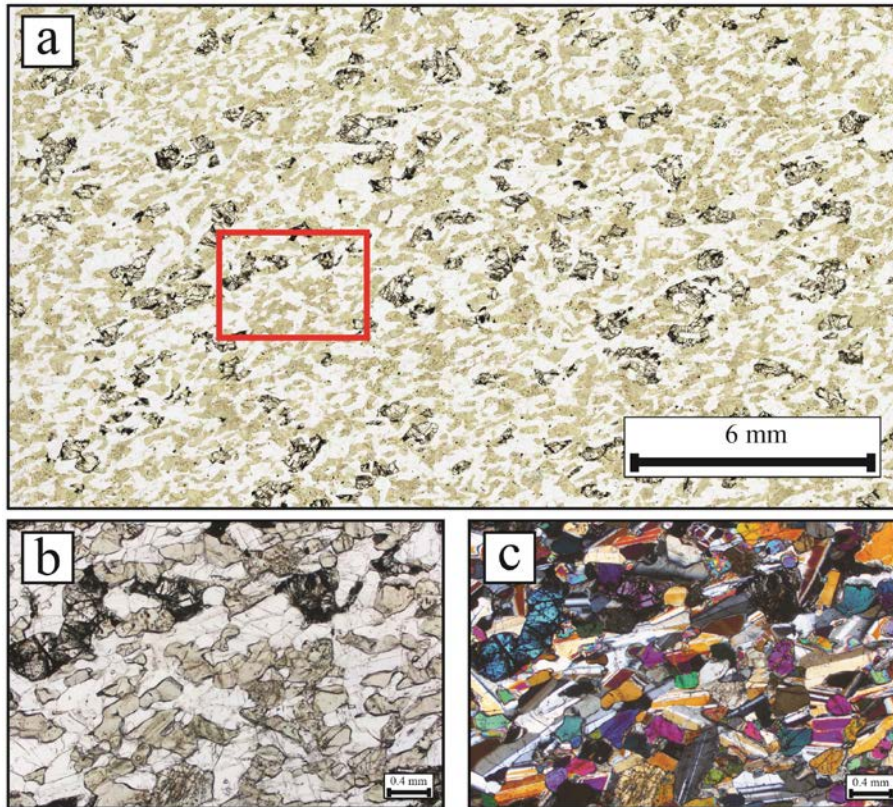
Figure A5. a) Thin section scan of Wadi Gideah fine grained lower foliated gabbro (OM10_Gid_A19; 2700 m) composed of plagioclase, clinopyroxene, and olivine with typical small grain sizes. Position of b) and c) are marked by the red rectangle. b) Microphotograph of the foliated gabbro at plane-polarized light. c) Same as b) at cross-polarized light. Note that grain sizes are generally smaller than 0.5 mm.
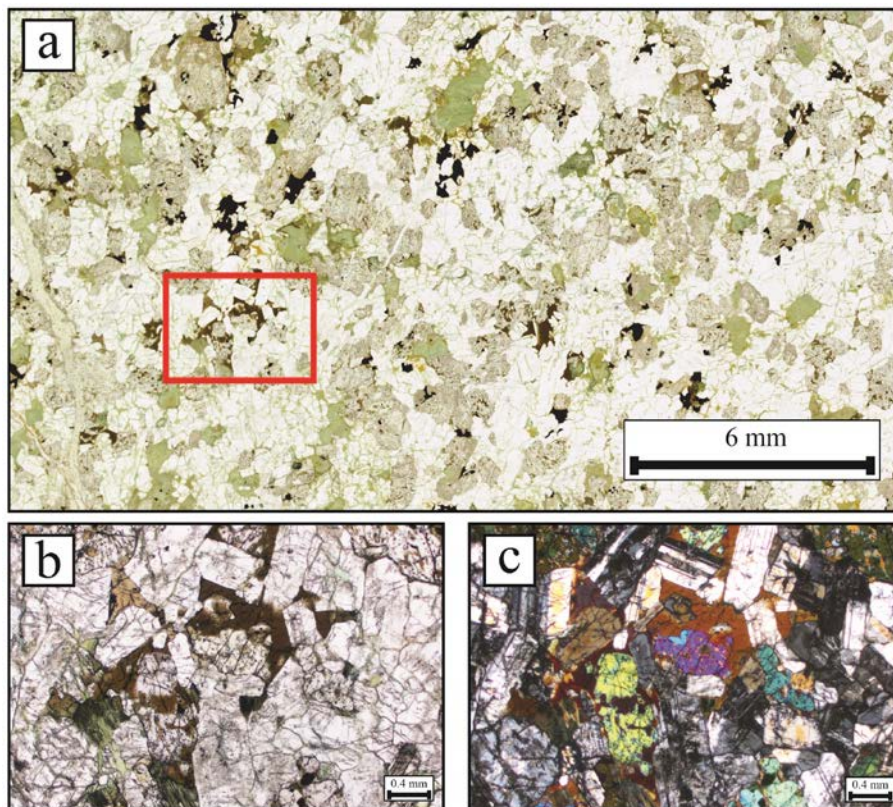
Figure A6. a) Thin section scan of medium grained Wadi Gideah upper foliated gabbro (OM10_Gid_A17; 3734 m) composed of plagioclase, clinopyroxene, brown and green amphibole, and oxides. Texture and phases vary obviously from lower foliated gabbros with a tendency to a heterogeneous appearance, similar to varitextured gabbro above (A.7). Position of b) and c) are marked by the red rectangle. b) Microphotograph of the foliated gabbro at plane-polarized light. c) Same as b) at cross-polarized light. Interstitial amphibole (brown) and oxides (opaque), both magmatic late stage phases, are common.

assemblage of 59 vol% plagioclase, 33 vol% clinopyroxene, 6 vol% olivine, and 2 vol% oxides for the complete foliated gabbro section (Fig. A10). All samples show slight pervasive and/or vein related alteration to minerals of the amphibolite or greenschist facies, like actinolite, iddingsite, chlorite, epidote, secondary hornblende, serpentine, and sometimes talc. Clinopyroxene and olivine display inclusions of plagioclase, with an estimated crystallization order of plagioclase prior to olivine and clinopyroxene. The intensity of mineral foliation is moderate to high. Foliated gabbros show significant petrographic differences to layered gabbros with a smaller average grainsize and a more "flow-like" appearance of the plagioclase network, associated with additional mineral zonation and appearance of later stage phases up section.

A.5.1.3 Varitextured Gabbros

Varitextured gabbros generally comprise gabbros and some gabbronorite. They have a fine to medium grained isotropic granular to doleritic texture, and are mainly composed of euhedral to subhedral, tabular to lath shaped, often strongly zoned plagioclase, associated with subhedral to anhedral prismatic clinopyroxene, brown to green hornblende (sometimes poikilitic), and interstitial granular oxides (Fig. A7). Some samples include up to 5 vol% orthopyroxene. Samples display an average mineral proportion of 57 vol% plagioclase, 36 vol% clinopyroxene, 5 vol% primary amphibole, and 2 vol% oxides for the complete varitextured gabbro section (Fig. A10). Varitextured gabbros show alteration to minerals of the amphibolite and greenschist facies, like actinolite, chlorite, epidote, secondary hornblende, and occasionally titanite. Plagioclase is observed as inclusions in clinopyroxene and primary amphibole, leading to a crystallization order of plagioclase prior to clinopyroxene prior to amphibole. Varitextured gabbro section comprises, next to gabbro and gabbronorites, also plagiogranites and basaltic dikes cutting the gabbro. They are generally related to the Gideah South outcrop and described in detail in chapter C.

A.5.1.4 Metagabbros

Metagabbros generally represent layered gabbros, as described above, affected by intense pervasive alteration at amphibolite-, greenschist-, or prehnite pumpellyite facies conditions. They are sometimes highly affected by high temperature vein alteration. The intensity of alteration is highly variable, comprising only small areas with layered gabbro host rock generally well preserved (<50 % total alteration) or complete thin sections (>90 % total alteration). Veins and adjacent areas may include interstitial brown amphibole (pargasite to hornblende), orthopyroxene, and interstitial oxides (Fig. A8). The layered gabbro host rock can have microstructures related to hydrous partial melting (e.g., Wolff et al., 2013). Some samples show pegmatitic-like textures, with plagioclase grain sizes >5 mm and large green-to-brown amphiboles.
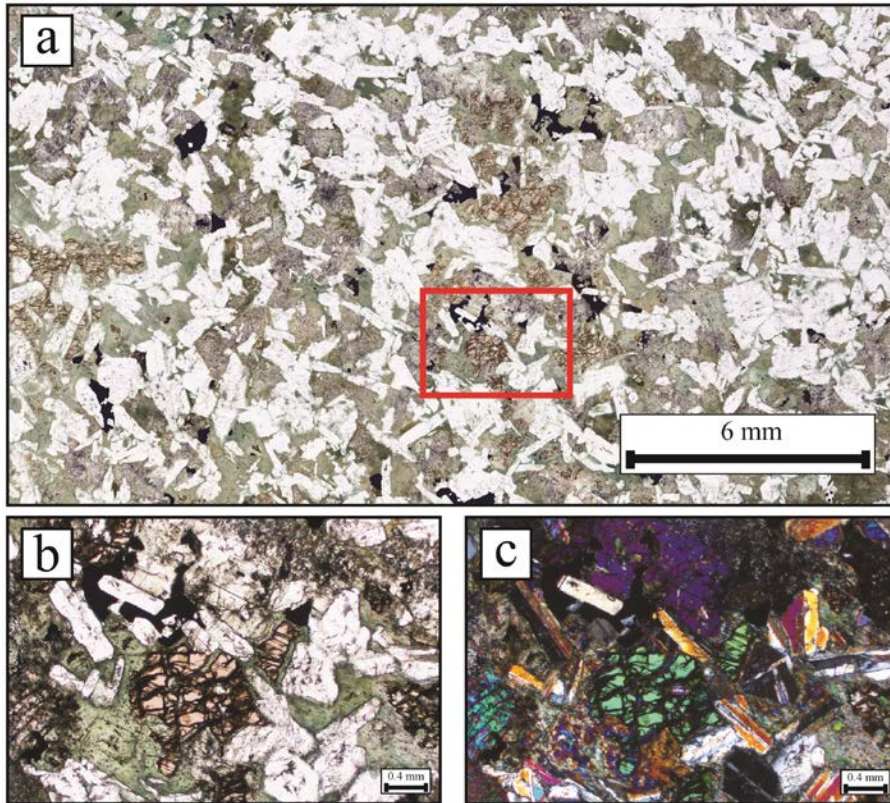
Figure A7. a) Thin section scan of Wadi Gideah medium grained varitextured gabbro (OM10_Gid_A13; 4602 m) composed of plagioclase, clinopyroxene, orthopyroxene, amphibole and oxides. Position of b) and c) are marked by the red rectangle.
b) Microphotograph of the varitextured gabbro at plane-polarized light with nice pink orthopyroxene. Interstitial oxides are common, with clinopyroxene and former brownish amphibole generally altered to greenish amphibole.
c) Same as b) at cross-polarized light.
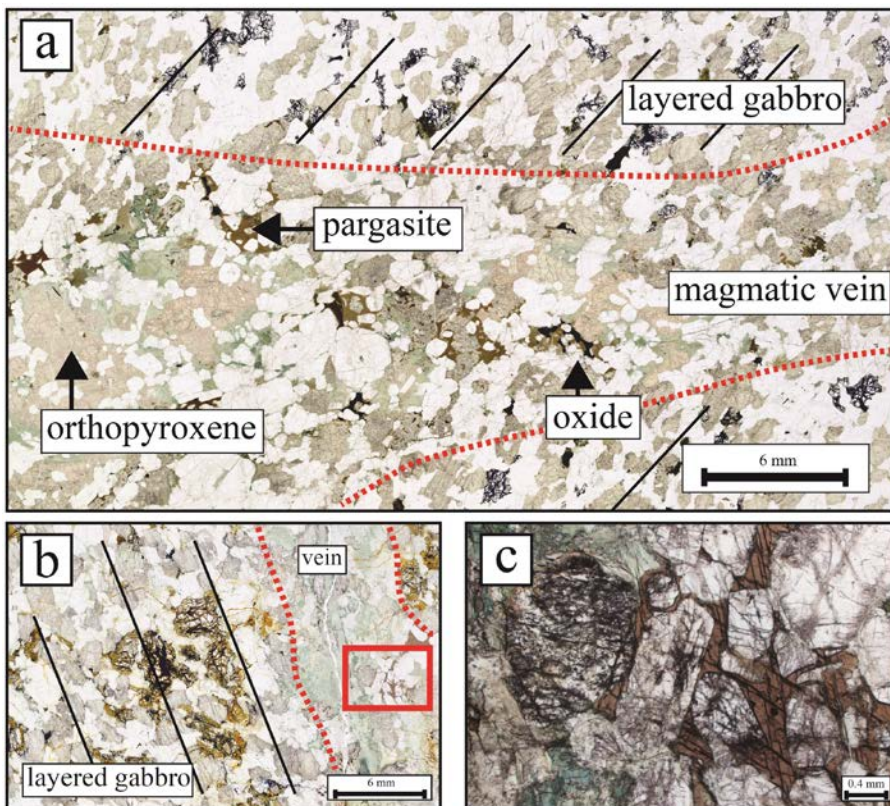
Figure A8. a) Thin section scan of Wadi Gideah layered gabbro cut by a magmatic vein (OM12_Gid_A27; 1222 m). Layering of host rock is indicated by black lines. Magmatic vein includes high temperature amphibole, interstitial oxides, and high amounts of orthopyroxene, which are all very uncommon for Wadi Gideah lower crust.
b) Thin section scan of Wadi Gideah metagabbro cut by a hydrothermal vein (OM12_Gid_Hy038; 1190 m). Layering of host rock is indicated by black lines. Position of c) is marked by red rectangle.
c) Microphotograph of heterogeneous domain including primary magmatic amphibole next to a hydrothermal vein at plane-polarized light.

A.5.1.5 Sheeted Dikes and Pillow Basalts

Wadi Gideah sheeted dikes and pillow basalts are highly to completely altered and recrystallized. They correspond to former microcrystalline to fine grained basalts with an intergranular texture and are mainly composed of subhedral, lath-shaped, often strongly zoned plagioclase, former clinopyroxene, completely converted into green to brown-green amphibole, and interstitial oxides. Few plagioclase oikocrysts appear (Fig. A9). The metamorphic overprint was pervasively to minerals of the amphibolite to greenschist facies, like actinolite, calcite, chlorite, green to brown hornblende, oxides, titanite, and quartz.
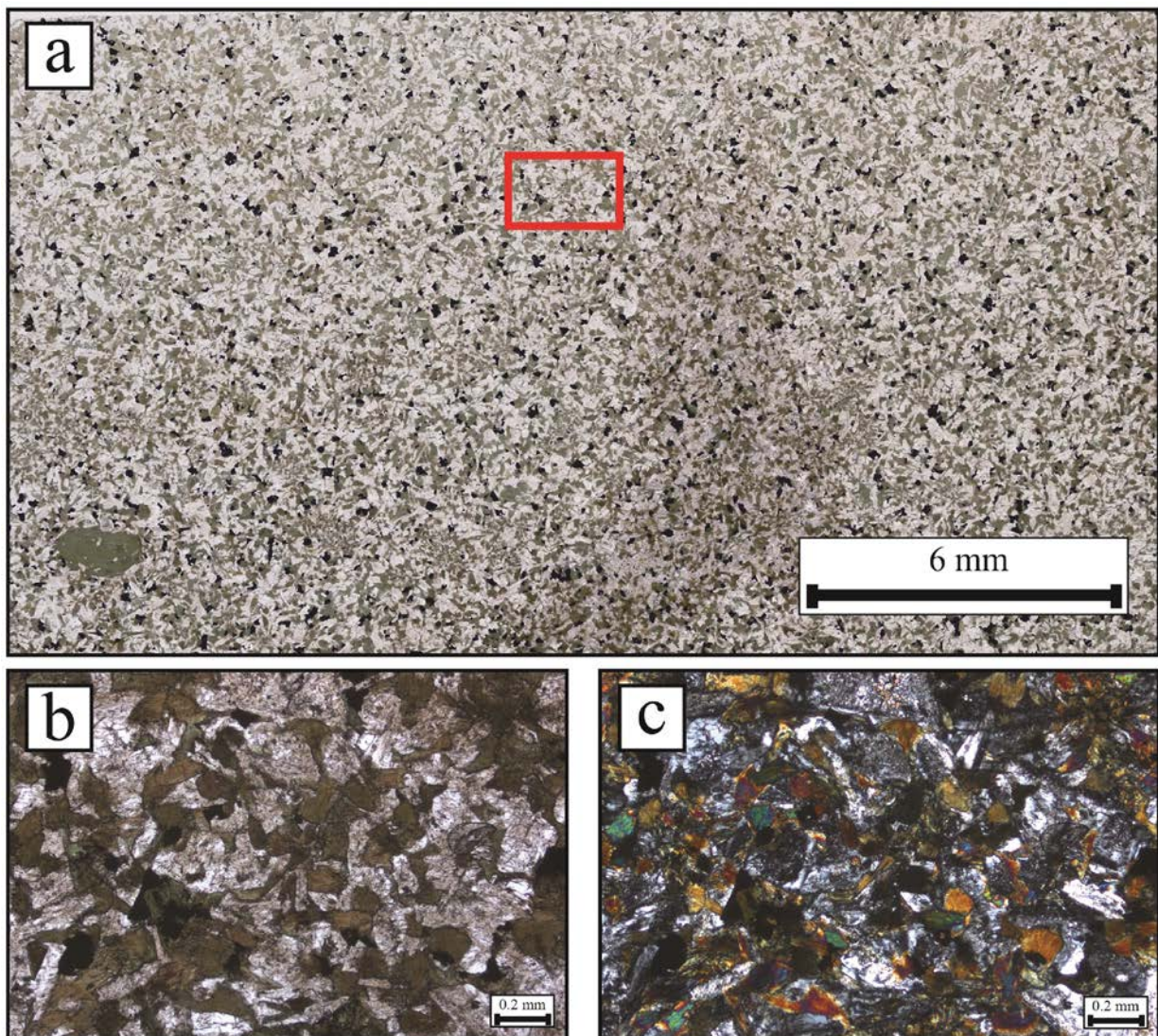
Figure A9. a) Thin section scan of Wadi Gideah lower sheeted dike (OM10_Gid_A10; 5321 m) composed of plagioclase, clinopyroxene (completely converted), green to brown hornblende, and oxides. Position of b) and c) are marked by the red rectangle. b) Microphotograph of the sheeted dike at plane-polarized light. c) Same as b) at cross-polarized light.
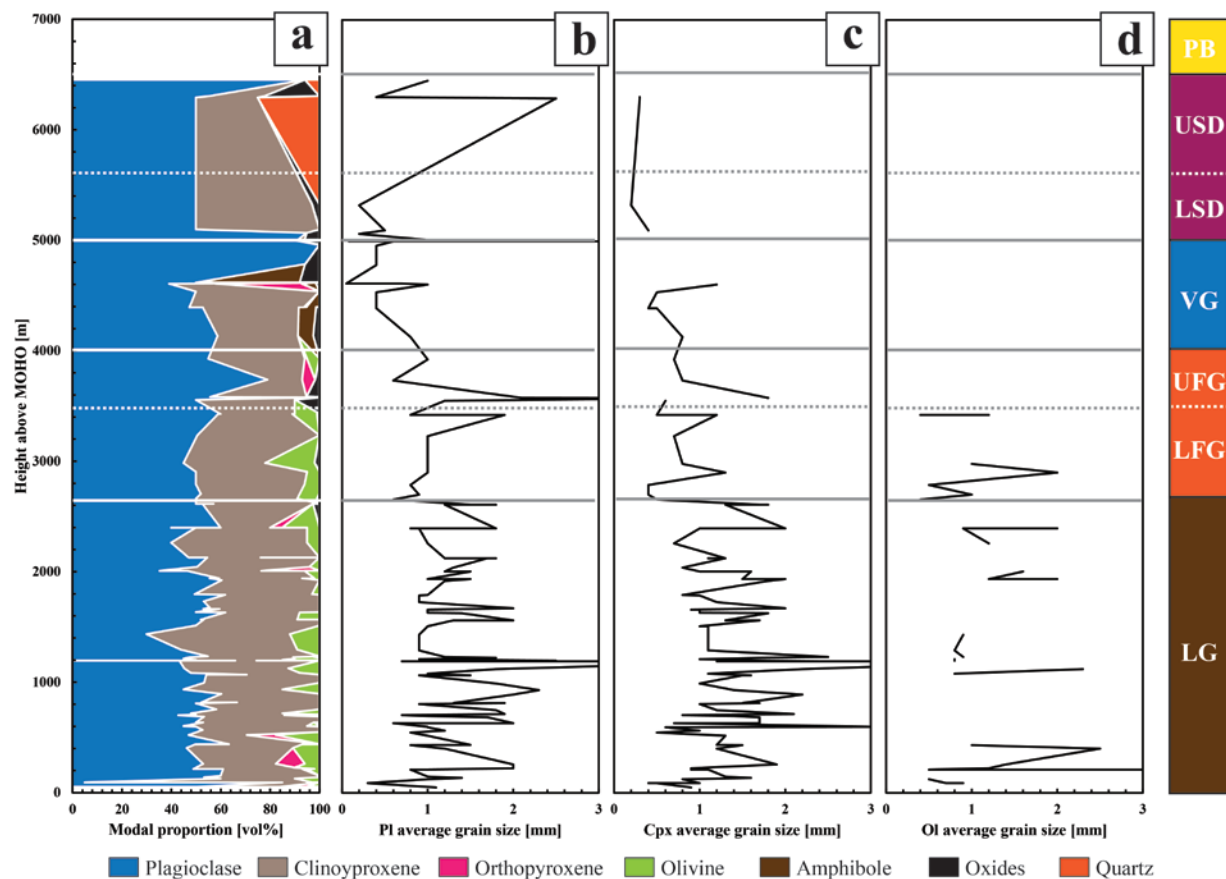
Figure A10. a) Depth log of the average modal proportion of Wadi Gideah samples. All primary phases were normalized to 100 vol% for correction of sample alteration. b-d) Depth log of average grain size of Wadi Gideah b) plagioclase, c) clinopyroxene, and d) olivine. Abbreviation for Wadi Gideah lithologies follows Table A1. Note the significant shift to smaller average grain sizes directly at the layered/foliated gabbro transition.

A.5.2 Bulk Rock Chemistry

The bulk rock major- and trace element concentrations were determined by ICP-OES, ICP-MS, and LA-ICP-MS (see A.4.2.2 to A.4.2.4) for 136 samples from all Wadi Gideah lithologies, in order to obtain information about compositional variation with depth and hence formation processes. Bulk rock strontium, neodymium, and hafnium isotopy was determined by MC-ICP-MS (see A.4.2.5) for 88 (Sr) and 66 (Nd, Hf) samples, in order to obtain information about impact of hydrothermal seawater fluids at depths during formation, to verify a single Wadi Gideah magma source, and to improve the classification of the tectonic setting.

A.5.2.1 Bulk Rock Major Element Compositions

The bulk rock major element compositions were normalized to a total of 100 wt%, after subtraction of L.O.I. and calculation of FeO_{tot} (FeO_{tot} [wt%] = 0.899* Fe_2O_3 [wt%]). The results for bulk rock major element analyses are given in Table 7.

Layered gabbros show primitive cumulate compositions in comparison with NMORB (Gale et al., 2013), with an average content of ~48 wt% SiO_2, ~0.25 wt% TiO_2, and ~1 wt% Na_2O (51 wt% SiO_2, 1.5 wt% TiO_2, and 2.9 wt% Na_2O for NMORB; Fig. A11). The average Mg# $(MgO/(MgO+FeO_{tot})*100)$ is ~80. The bulk rock major elements show correlated element variations, with a vertical wavelength (Fig. A11a-c) of some hundred meters, similar to cycles of mineral major element variations observed by Browning (1984) for Oman ophiolite layered gabbros (Wadi Abyad). Although superposed by these cycles, an overall slight normal trend (negative with height for compatible and positive with height for incompatible elements) of chemical evolution is shown (change in Mg# of ~82 to ~78 from lowest to highest layered gabbros, respectively; Fig. A11a-c). Metagabbros from the layered gabbro section reveal bulk rock major element compositions, similar to layered gabbros (Mg# of ~81; Fig. A11).

Layered gabbros reveal compositions generally in range of Hess Deep layered series (Gillis et al., 2014; Fig. A11a-c, g, h).Wadi Gideah layered gabbros are slightly evolved revealed by average lower Mg# and higher TiO_2 content (Mg# of ~83, TiO_2 of ~0.2 wt%). Nevertheless, they are depleted in Na_2O in comparison with Hess Deep average compositions (Na_2O of ~1.4 wt%), which reflects the higher anorthite content of Wadi Gideah layered gabbro plagioclase in comparison (see A.5.4). Wadi Gideah layered gabbros are well in the range of compositions from other Oman ophiolite gabbros at a similar stratigraphic height (Wadi Abyad, Wadi Khafifah, and Wadi Namarah), compiled by Coogan (2014; Mg# of ~80), although these gabbros display no trend of chemical evolution.

Foliated gabbros show slightly evolved cumulate compositions in comparison with layered gabbros, with similar average content of SiO_2 but ~0.8 wt% TiO_2 and ~2 wt% Na_2O (Fig. A11). The average Mg# is ~67. The overall normal trend of chemical evolution up section, observed for layered gabbros, becomes more distinctive for lower foliated gabbros at the layered/foliated gabbro transition (change in Mg# from ~76 to ~52 and Na_2O from ~1.3 to ~2.6 wt% from layered/foliated gabbro transition to lower/upper foliated gabbro transition; Fig. A11a-c). The trend becomes reversed in the upper foliated gabbros (change in Mg# from ~52 to 75 and Na_2O from ~2.6 to ~1 wt% from lower/upper gabbro transition to uppermost sample; Fig. A11a-c). The lowest Mg# and highest TiO_2 content is slightly exaggerated by the appearance of Fe-Ti oxides (Fig. A11d).

Foliated gabbros show a slightly wider range in composition in comparison with Hess Deep shallow series gabbros (Gillis et al., 2014; Fig. A11a-c, g, h) with a similar average bulk composition. Wadi Gideah foliated gabbros are evolved in average composition in comparison with of other Oman ophiolite gabbros from similar stratigraphic height (Mg# ~77; Coogan, 2014).

Varitextured gabbros show average bulk compositions of ~51 wt% SiO_2, ~1.1 wt% TiO_2, and ~2.8 wt% Na_2O), with average Mg# of 60 (Fig. A11). The compositional range is wide, from primitive to evolved (Mg# 71 to 41 and TiO_2 of 0.5 to 2.5; Fig. A11). Varitextured gabbros correspond to basaltic, basaltic-andesitic, and basaltic-trachyandesitic compositions in total-alkali-silica diagram (TAS; Le Bas and Streckeisen, 1991; Fig. A12), considering them to represent frozen AML melts (e.g., MacLeod and Yaouanaq, 2000 and Koepke et al., 2011). A general trend of chemical evolution up section is not shown, although the uppermost gabbros

(Gideah South) have most evolved compositions. *Basaltic dikes*, cutting varitextured gabbro, show two populations. A more evolved one (Mg# ~48; basaltic, basaltic andesitic and andesitic compositions in TAS diagram; Fig. A11, Fig. A12) is observed at the medium level of the varitextured gabbro section. A second, more primitive one (Mg# of ~59; basaltic and basaltic andesitic compositions; Fig. A11, Fig. A12) is observed in association with the uppermost gabbros (Gideah South; see chapter C for details). Therefore, evolved dikes cut relative primitive gabbros, while primitive dikes above cut relatively evolved gabbros.

Varitextured gabbros are slightly more primitive in comparison with average composition of IODP Site 1256D varitextured gabbros (Mg# of ~57, TiO_2 of ~1.4 wt%, and Na_2O of ~2.6 wt%; Neo et al., 2009; Fig. A11a-c, e, f), with both locations showing a very high variation in composition though. Wadi Gideah varitextured gabbros show similar compositions in comparison with of other Oman ophiolite gabbros from similar stratigraphic height (average Mg# of~61, with a range from 80 to 36; Coogan, 2014).

Sheeted dikes show two populations, with one located near the varitextured gabbro section (designated as lower dikes), and one further up section near pillow basalts (designated as upper dikes). Lower dikes show basaltic to basaltic-andesitic compositions (at Mg# of ~58), similar to the basaltic dikes from below, which cut varitextured gabbro (Fig. A11, Fig. A12). Upper sheeted dikes show more evolved trachy-andesitic compositions (at Mg# of ~36; Fig. A11a, Fig. A12). It can be suggested, that a trend of chemical evolution is existent from the lower to the upper sheeted dikes. This transition is, however, not shown since this area lacks a sufficient amount of samples. Sheeted dikes, samples out of Wadi Gideah, show compositions similar to Wadi Gideah upper sheeted dikes (Fig. A11a-c, e, f, A12). *Pillow basalts* (all samples out of Wadi Gideah) show andesitic, trachy-andesitic, and dacitic compositions (at Mg# of ~31), slightly evolved in comparison with the underlying upper sheeted dikes (Fig. A11, Fig. A12).

Extrusive rocks have little correlation with bulk compositions of Hess Deep and IODP Site1256D basaltic rocks (Neo et al., 2009; Steward et al., 2002; Wilson et al., 2003). These are, in relation to MgO in element variation diagrams, generally depleted in Al_2O_3 and enriched in TiO_2 and FeO_{tot} (Fig. A11e, f). Wadi Gideah extrusives correlate well with the range of composition of dikes and lavas (including Oman V1-lavas) from other locations of the Oman ophiolite (compiled by MacLeod et al., 2013; Fig. A11e, f).
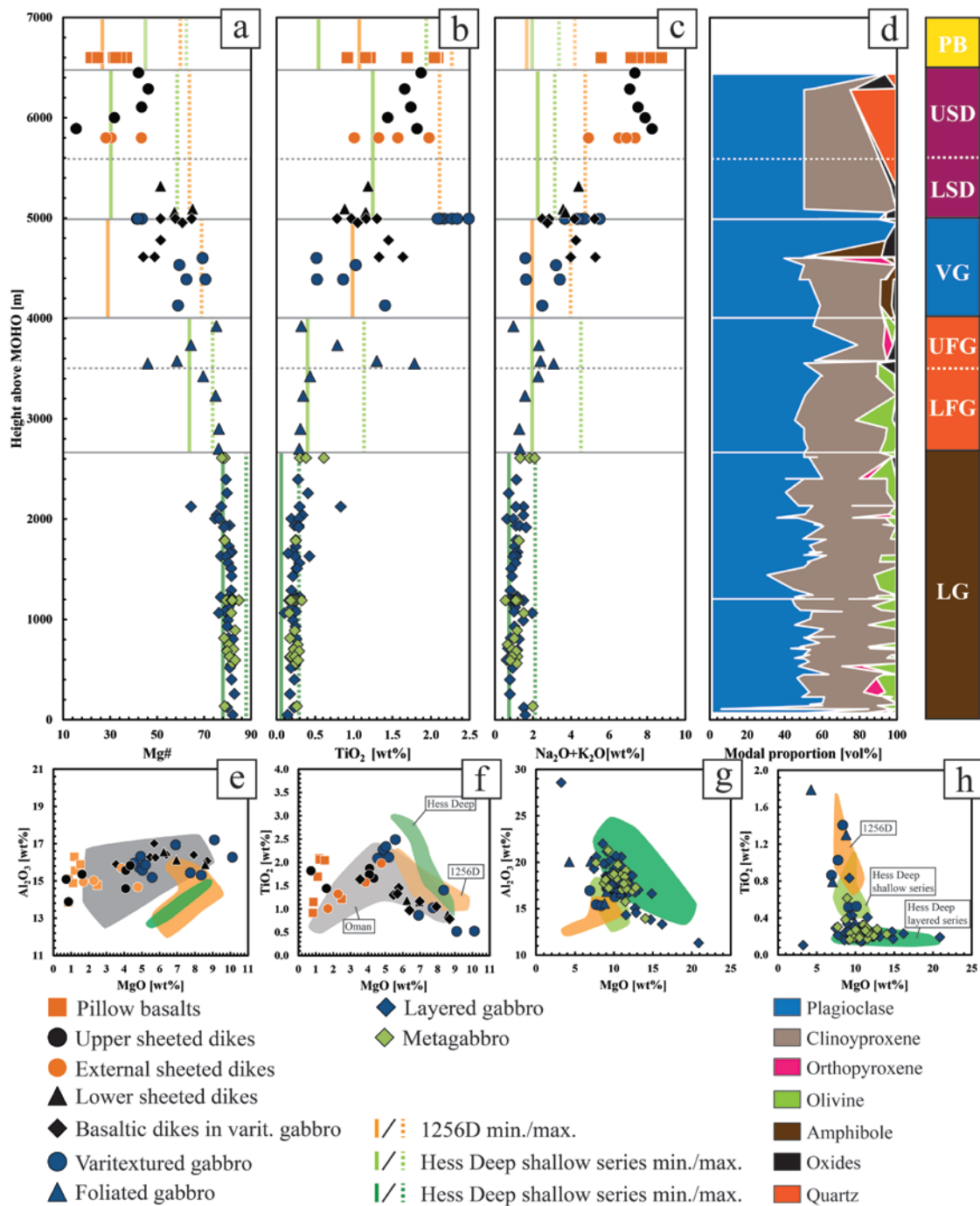
Figure A11. a-c) Geochemical depth logs for bulk rock major element compositions with a) Mg#, b) TiO$_2$ and c) Na$_2$O+K$_2$O. d) Depth log of the average modal proportion of Wadi Gideah samples for comparison. See Table A1 for the abbreviations of the lithologies. e-f) Element variation diagram for Wadi Gideah extrusive section with e) MgO vs. Al$_2$O$_3$ and f) MgO vs. TiO$_2$. g-h) Element variation diagram for Wadi Gideah plutonic section with g) MgO vs. Al$_2$O$_3$ and h) MgO vs. TiO$_2$. Data for IODP Site 1256D and Hess Deep are from Gillis et al., 2014; Neo et al., 2009; Steward et al., 2002; and Wilson et al., 2003. Data for Oman ophiolite are from MacLeod et al., 2013. Abbreviation for Wadi Gideah lithologies follows Table A1. A trend of chemical evolution is well shown by downhole plots. The trend is only slight for layered gabbros but becomes much more apparent directly at the layered/foliated gabbro transition. Since Wadi Gideah extrusives are in well range of other Oman ophiolite extrusives, they also deviate in element variation diagrams from range of EPR extrusives.
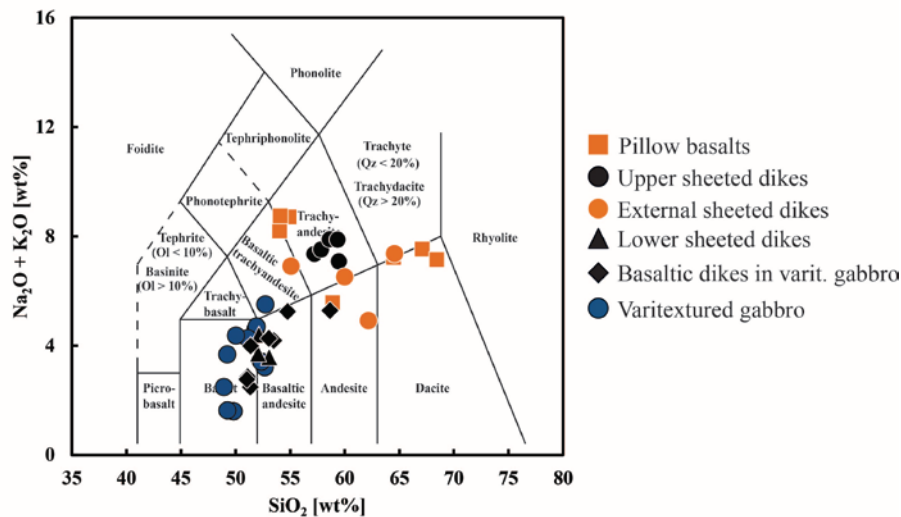
Figure A12. TAS classification (Le Bas and Streckeisen, 1991) for samples from Wadi Gideah varitextured gabbro- and extrusive section.

A.5.2.2 Bulk Rock Trace Element Compositions

The results for bulk rock trace element analyses are given in Table 7.

Layered gabbros show trace element concentrations, which are highly depleted in comparison with NMORB (Gale. et al., 2013; Fig. A13b, c), which reflects well the cumulate character (Pallister and Knight, 1981). This correlates with primitive major element compositions (see A.5.2.1). A slight trend of chemical evolution is present (change from ~0.14 to ~0.27 ppm La from for lowermost and uppermost samples, respectively; Fig. A14). Gabbros show a positive anomaly of Sr and Eu and a negative anomaly of Zr, Hf, and Nb in comparison with neighbor elements in trace element diagrams (Fig. A13b, c). Positive Sr- and Eu-anomaly can be related to an increased plagioclase affinity in comparison with other trace elements (partition coefficient Kd of 1.3 and 0.71, respectively; Bédard et al., 2001). Zr-Hf, as well as Nb-Ta, are highly incompatible elements (e.g. Bédard et al., 2001) which are additionally fractionated in plagioclase (e.g. Bédard et al., 2001), clinopyroxene (e.g., compiled by Pfänder et al., 2007; see A.5.4) and olivine (e.g. Bédard et al., 2001).

Foliated gabbros show a medium depletion of all trace elements in comparison with NMORB (Gale et al., 2013) in NMORB-normalized diagram (Fig. A13b, c). They are evolved in comparison with layered gabbro, which correlates well with observations from major element analysis (see A.5.2.1). Bulk rocks display a positive anomaly of Sr and Eu and a negative anomaly of Zr-Hf and Nb-Ta in comparison with neighbor elements in trace element diagrams, similar to layered gabbros, but lower in intensity (Fig. A13b, c). The slight trend of chemical evolution up section, observed for layered gabbros, becomes more distinctive within the lower foliated gabbros at the layered/foliated gabbro transition (change from 0.26 to 1.04 ppm La from for lowermost and uppermost samples, respectively; Fig. A14), and is

reversed in the upper foliated gabbros (change from 1.04 to 0.26 ppm La from for lowermost and uppermost samples, respectively; Fig. A14).

Varitextured gabbros show trace element concentrations slightly depleted in comparison with NMORB (Gale et al., 2013; Fig. A13) and range of V1 lavas (Godard et al., 2003). V1 lavas (Beurrier, 1987; Ernewein et al., 1988), also called "Geotimes" (Alabaster et al., 1982; Lippard et al., 1986; Pearce et al., 1981), represent the most exposed extrusives sequence from Oman ophiolite. These extrusives represent compositions close to MORB and hence correspond to the Phase 1 accretion of Oman ophiolite crust (Goodenough et al., 2014). Gabbros show a slight positive Sr anomaly and a negative Nb-Ta anomaly in comparison with neighbor elements in trace element diagrams (Fig. A13). A slight negative Zr-Hf anomaly is shown only for slightly more primitive samples. A systematic trend of chemical evolution is not present, although uppermost gabbros directly below sheeted dikes show most evolved compositions (Fig. A14). Varitextured gabbros correlate to basaltic compositions in immobile TAS proxy diagram (Pearce, 2014; Fig. A14). Immobile TAS proxy diagram considers the high fluid mobility of Si, Na, and K, which impacts TAS classification of rocks heavily affected by amphibolite or greenschist alteration, by an exchange of TAS SiO_2 by Zr/Ti and TAS Na_2O+K_2O by Nb/Y (Floyd and Winchester, 1975; Pearce, 2014). *Basaltic dikes*, cutting varitextured gabbro, show trace element composition similar to varitextured rocks.

Lower sheeted dikes have trace element concentrations very similar to varitextured gabbro, slightly depleted in comparison with NMORB (Gale et al., 2013) and range of V1 lavas (Godard et al. 2013), with a positive Sr and negative Nb-Ta anomaly (Fig. A13a, c). A trend of chemical evolution up section may be present (change from 2.72 to 3.34 ppm La for lowermost and uppermost sample, respectively; Fig. A14). However, the amount of samples is too low for clear evidence (# of 3). The lower sheeted dikes correlate to basaltic and basaltic andesitic compositions in the immobile trace element TAS proxy diagram (Fig. A14), which is in well agreement with the standard TAS classification (see A.5.2.1).

Upper sheeted dikes, external dikes, and pillow basalts show very similar trace element compositions. They are slightly evolved in comparison with NMORB (Gale et al., 2013) and well in range of V1 lavas (Godard et al., 2003; Fig. A13a, c). Anomalies are generally absent, except for a negative Zr-Hf anomaly for external dikes and a general negative Nb-Ta anomaly for all extrusives (Fig. A13a, c). There is no explanation here for the Zr-Hf anomaly, but Nb-Ta anomaly may be related to an influence of a subduction zone setting, since both elements are generally subduction zone immobile (e.g., Pearce 2014). Wadi Gideah dikes and lavas have basaltic to andesitic compositions in immobile TAS proxy diagram (Pearce et al., 2014; Fig. A14). This is in disagreement with standard TAS classification, which proposes more evolved rock compositions (see A.5.2.1). The disagreement could be evidence that intense amphibolite and greenschist alteration, observed for extrusive samples, indeed affected the sample geochemistry.
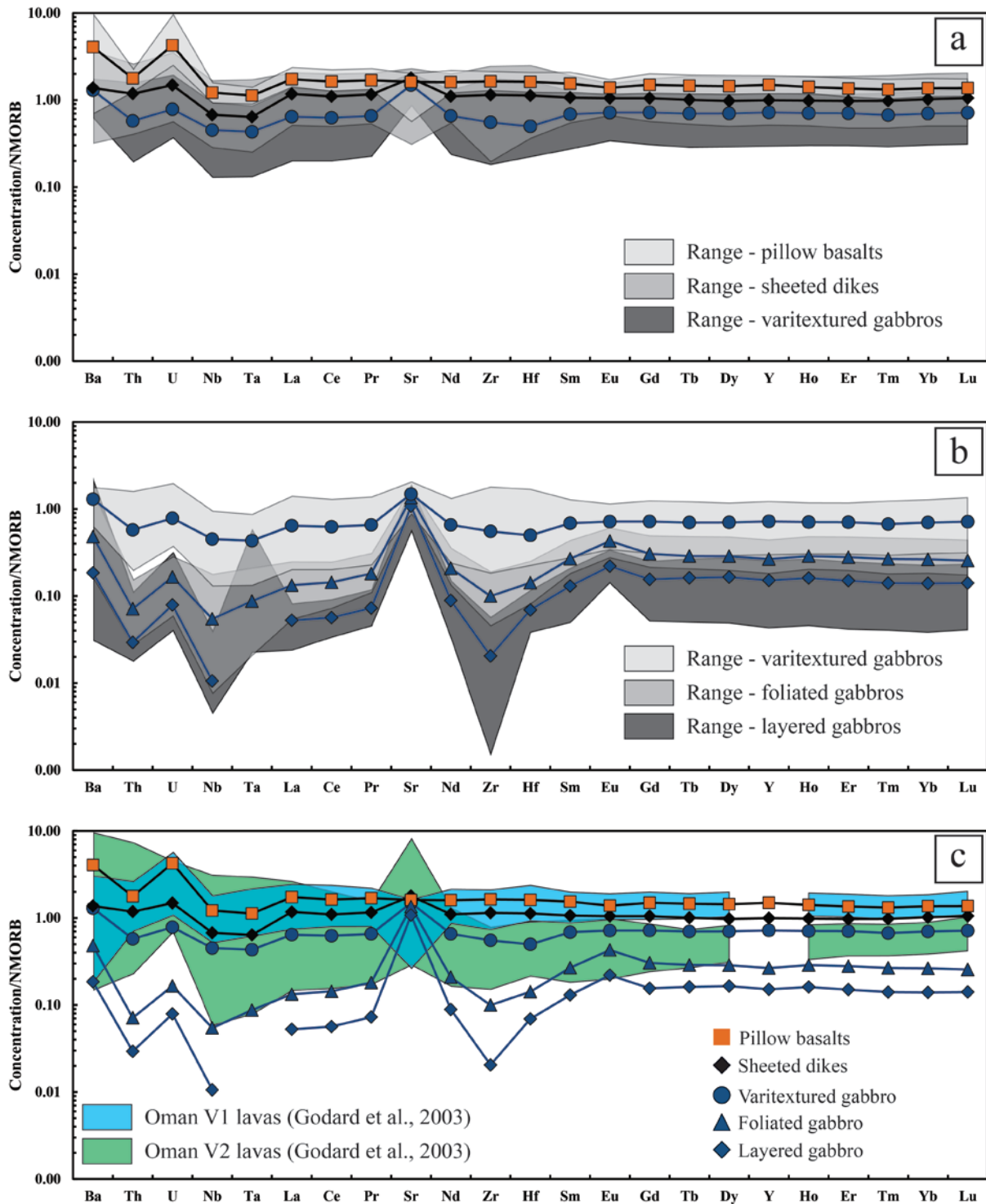
Figure A13. a) Average trace element composition and compositional range of Wadi Gideah varitextured gabbro- and extrusive section. b) Average trace element composition and compositional range of Wadi Gideah plutonic section. c) Average trace element composition of Wadi Gideah plutonic- and extrusive section in comparison to range of V1 and V2 (Godard et al., 2003). Note, that layered and foliated gabbros represent cumulate compositions. Hence, variation and evolution in cumulate does only gives evidence for variation and evolution of the host melt. All compositions are normalized to NMORB (Gale et al., 2013), with pillow basalts well in V1-range. The trend of chemical evolution, revealed by bulk major elements, is also well shown by bulk trace elements. The Zr-Hf anomaly may be related to the high fractionation of both elements in clinopyroxene, which is a major phase in the layered and foliated gabbro cumulates. Hence, the anomaly is not observed for the frozen melts above. However, a distinctive negative Nb-Ta anomaly is observed for both cumulate from Wadi Gideah lower crust and frozen melts from Wadi Gideah upper crust.
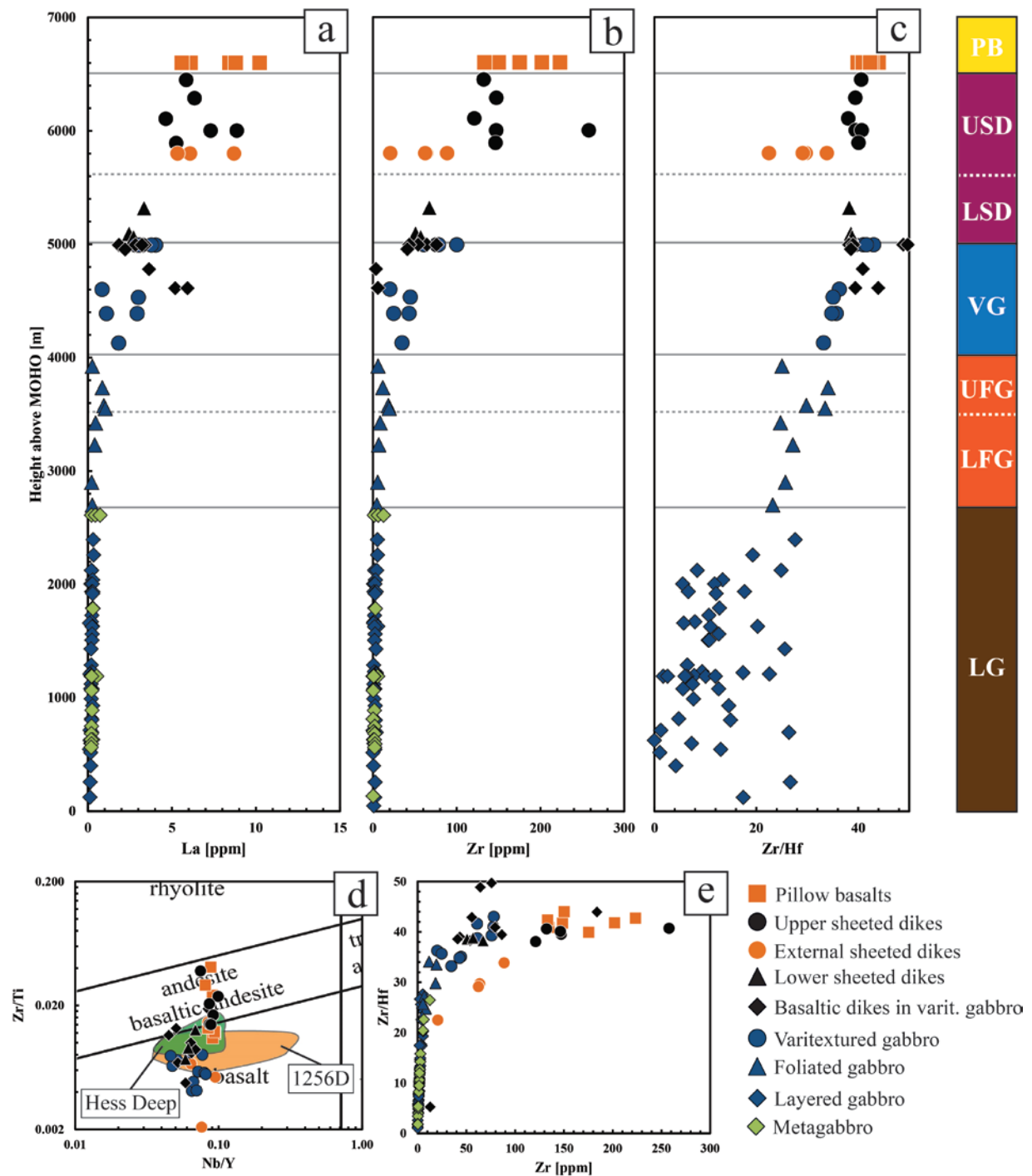
Figure A14. a-c) Geochemical depth logs for bulk rock trace element compositions with a) La, b) Zr, and c) Zr/Hf ratio. d) Immobile TAS proxy classification (e.g., Pearce, 2014) for samples from Wadi Gideah varitextured gabbro- and extrusive section in comparison with range of IODP Site 1256D and Hess Deep extrusive section. Data of IODP Site 1256D and Hess Deep are from Neo et al. (2009) and Stewart et al. (2002). f) Element variation diagram for Wadi Gideah crust with Zr vs. Zr/Hf. A steep trend is evidence for in situ crystallization (Langmuir, 1989). Abbreviation for Wadi Gideah lithologies follows Table A1.

A.5.2.3 Bulk Rock Isotopy

The εNd and εHf of Wadi Gideah bulk rocks were calculated following Allègre (2008), using $(^{143}Nd/^{144}Nd)_{CHUR}$ and $(^{176}Hf/^{177}Hf)_{CHUR}$ given by Bouvier et al. (2008). Wadi Gideah initial $^{87}Sr/^{86}Sr$ and $^{143}Nd/^{144}Nd$ ratios were calculated, following Bosch et al. (2004), assuming an age of 96 Ma (e.g., Rioux et al., 2013; Tilton et al., 1981; Warren et al., 2005). The water rock ratios (W/R) were calculated for $^{87}Sr/^{86}Sr$ following McCulloch et al. (1980), using $^{87}Sr/^{86}Sr_{ini}$ and $C_{Sr\ Seawater}$ given by these authors, $^{87}Sr/^{86}Sr_{Seawater}$ given by Burke et al. (1982), and $C_{Sr\ MORB}$ given by Höfig et al. (2014). The results for bulk rock isotopy are given in Table 8a-c.

Wadi Gideah oceanic crust shows Nd and Hf isotope ratios in a range from 0.512993 to 0.513178 and 0.283097 to 0.283388, respectively (Fig. A15c, d). The average εNd is ~8.46 in a range from 7.08 to 10.69, with average εNd$_{(96\ Ma)}$ ~7.95 in a range from 5.83 to 10.7. Three layered gabbro samples show significantly higher εNd in comparison to other Wadi Gideah rocks. Nd isotope ratios are similar to other Oman ophiolite crustal rocks (εNd$_{(96\ Ma)}$ from ~6.9 to ~7.88 from Rioux et al., 2012; εNd$_{(130\ Ma)}$ of 7.5 to 8.6 from McCulloch et al., 1980; Fig A15f). Wadi Gideah average $^{143}Nd/^{144}Nd_{(96\ Ma)}$ is significantly lower in comparison with NMORB (9-10°N; ~0.51311; Waters et al., 2011) and EPR rocks from IODP Site 1256D (~0.513089 with range from 0.53037 to 0.513110).

Wadi Gideah Sr isotope ratios have a higher variation compared with Nd and Hf ones (Fig. A15a). The $^{87}Sr/^{86}Sr_{ini}$ is ~0.7033 in a range from 0.7030 to 0.7037 for layered and foliated gabbros, with a very low W/R ratio. Two foliated gabbros, directly at the lower/upper foliated gabbro transition, show relatively high $^{87}Sr/^{86}Sr_{ini}$ of 0.7041 and 0.7046. Note, that these samples show also most evolved bulk major element compositions and higher proportion of Fe-Ti oxides, which may be an indication for increased hydrothermal cooling in that area. Excluding these two samples, layered and foliated gabbros show little variation and no distinctive trend. Metagabbros from the layered gabbro section contrast host rock ratios with a significantly increased $^{87}Sr/^{86}Sr_{ini}$ of ~0.7042 in a range from 0.7035 to 0.7046 (Fig. A15a). The transition between gabbros and dikes is represented by the varitextured gabbro section, with a range in $^{87}Sr/^{86}Sr_{ini}$ from 0.7035 (at the bottom) to 0.7057 (at the top). Wadi Gideah extrusive section above shows $^{87}Sr/^{86}Sr_{ini}$ of ~0.7054 in a range from 0.7038 to 0.7064, significantly higher in comparison with layered and foliated gabbros, and with a slight trend of evolution up section (Fig. A15a). Wadi Gideah crust reveals slightly increased average $^{87}Sr/^{86}Sr_{ini}$ in comparison with both Hess Deep layered- and shallow series (0.7027±0.0004 and 0.7025 to 0.7043, respectively; Gillis, 1996 and Gillis et al., 2014) and IODP 1256D varitextured gabbro and extrusive section (0.7034±0.0006 and 0.7035±0.0007, respectively; Harris et al., 2015; Höfig et al., 2014; Fig. A15a), correlating with the slightly decreased $^{143}Nd/^{144}Nd_{ini}$ in comparison with EPR MORB and IODP 1256D rocks (see above; Fig. A15e). Since the W/R ratio is very low in average for Wadi Gideah layered and foliated gabbros (~0.81), increased average $^{87}Sr/^{86}Sr_{ini}$ is presumably not related to alteration, but can be considered to have been apparent in Wadi Gideah melts before lower crust formation.

The striking higher $^{87}Sr/^{86}Sr_{ini}$ of metagabbros, in comparison with well-preserved layered gabbro host rock, is not accompanied by variation of εNd or εHf (Fig. A15a, c, d). The general variations in $^{87}Sr/^{86}Sr_{ini}$ of layered gabbro section rocks (layered gabbro and

metagabbro) correlates roughly with the degree of sample alteration. However, variations in $^{87}Sr/^{86}Sr_{ini}$ do generally (two samples excluded) not correlate with bulk rock Sr content (Fig. A15g).
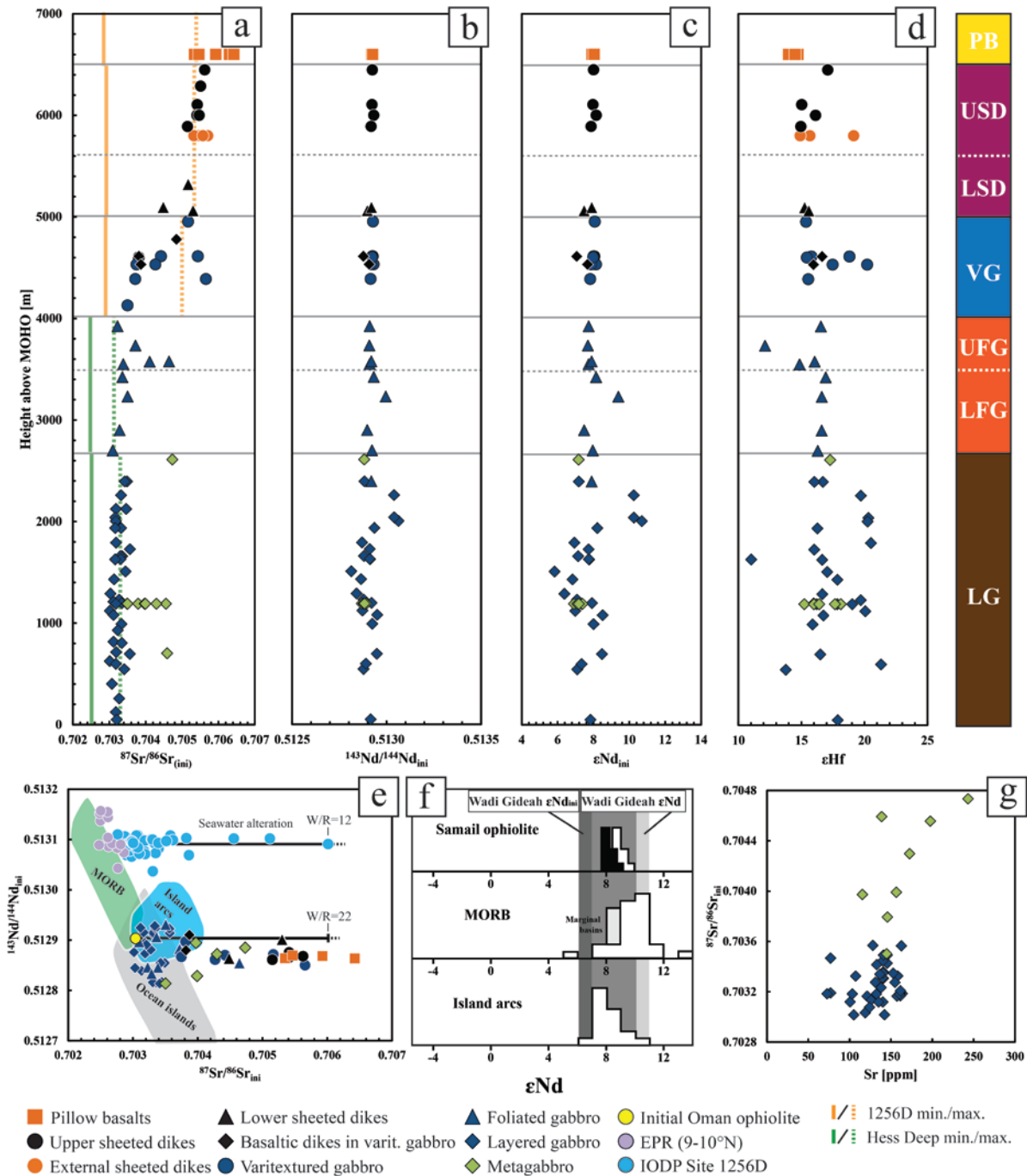
Figure A15. a-d) Depth logs for Wadi Gideah bulk isotopy with a) $^{87}Sr/^{86}Sr_{ini}$, with range from Hess Deep and 1256D added for comparison b) $^{143}Nd/^{144}Nd_{ini}$, c) εNd_{ini}, and d) εHf_{ini}, with ini=96 Ma (Rioux et al. 2013). Isotope variation plot with $^{87}Sr/^{86}Sr_{ini}$ vs. $^{143}Nd/^{144}Nd_{ini}$ and calculated water/rock ratios (W/R). Wadi Gideah data is compared with range of MORB, island arcs, and ocean islands (all taken from McCulloch et al., 1980), and isotope data from EPR (9-10°N; Waters et al., 2011) and IODP Site 1256D (Höfig et al., 2014). Initial value for Oman ophiolite was taken from McCulloch et al. (1980). e) Histogram (taken and simplified from McCulloch et al., 1980) comparing εNd data from Samail ophiolite with MORB and Island arcs. Range of εNd and εNd_{ini} of this study were added for comparison. f) Variation diagram with Sr vs. $^{87}Sr/^{86}Sr_{ini}$ for Wadi Gideah layered gabbros and metagabbros. Abbreviation for Wadi Gideah lithologies follows Table A1.

A.5.3 Mineral Major Element Chemistry

Mineral major element compositions were determined by EPMA (see B.4.2.1) for 136 samples from most Wadi Gideah lithologies (extrusive section minerals were hardly analyzable), in order to obtain information about possible vertical compositional variation within Wadi Gideah profile. For minerals with core and rim dataset, the enrichment factor ($EF_{element}=conc_{rim}/conc_{core}$) was calculated, with a value >1 indicating enrichment and <1 indicating depletion of rim- compared with core area.

A.5.3.1 Plagioclase

Plagioclase minerals were generally analyzed for core and rim composition separately. All results for plagioclase major element compositions given in Table 9.

Layered gabbro plagioclases show an average $An_{82\pm4}$ (anorthite content in mol%; Fig. A15a). The Ca# (Ca/(Ca+Na)) is used as an equivalent for An in terms of calculation in this study, since the amount of K_2O is generally low in all minerals. Some of the lowermost samples at depths <147 m H.a.M. show plagioclase $An_{<76}$. The plagioclases show a slight normal trend of chemical evolution up section, with a change from average An_{86} to An_{81} for lowest and highest samples, respectively (aforementioned samples <147 m H.a.M. are excluded). A distinctive chemical zonation between mineral cores and rims is not observed (EF_{An} 0.98±0.15; Fig. A15a-c, f). Metagabbro plagioclases from layered gabbro section show compositions similar to layered gabbro minerals ($An_{81\pm10}$), with a higher scatter though (Fig. A15a-e). Plagioclases from layered gabbro section (layered gabbro and metagabbro) have generally similar average compositions to minerals from Hess Deep (Koepke, unpublished; Lissenberg et al., 2013; Fig. A15a, c, d, e). It has to be noted, however, that Wadi Gideah plagioclase has higher anorthite content ($An_{77\pm7}$ for Hess Deep) in comparison, related to depletion in Na_2O and enrichment in CaO. Layered gabbro section plagioclases show a similar range of data in comparison with other Oman ophiolite gabbro minerals (Abily, 2011; Browning, 1982; Koga et al., 2001; Korenaga and Kelemen, 1997; Yamasaki et al., 2006; Fig. A15d, e).

Foliated gabbro plagioclases minerals show an average $An_{74\pm9}$ and are evolved in comparison with layered gabbro minerals (Fig. A15a-f). The slight normal trend of chemical evolution up section, observed for layered gabbros, becomes distinctive for the lower foliated gabbros at the layered/foliated gabbro transition, shown by a change from An_{78} to An_{60} for lowest and highest minerals, respectively. A distinctive chemical zonation is not observed (EF_{An} 1.01±0.01; Fig. A15a-c, f). The normal trend becomes reversed in the upper gabbros at the lower/upper foliated gabbro transition, shown by change from An_{59} to An_{83} for lowest and highest sample, respectively, and is associated with first distinctive mineral chemical zonation (EF_{An} 0.94±0; Fig. A15a-f). Foliated gabbro plagioclases show a similar average major element composition in comparison with minerals from Hess Deep lower shallow series (Lissenberg et al., 2013; Fig. A15a, c, d, e), including the normal and reversed trend of chemical evolution up section (assuming recalculated sample depths, given by the authors, to be correct in approximation). Wadi Gideah foliated gabbro plagioclases are well in range of

other Oman ophiolite gabbro plagioclases (Abily, 2011; Browning, 1982; Koga et al., 2001; Korenaga and Kelemen, 1997; Yamasaki et al., 2006; Fig. A15d, e).

Plagioclases form *varitextured gabbro* show a strong variability in compositions (An_{16} to An_{86}), typical for these highly heterogeneous rocks (Fig. A15a-f). A distinctive trend, as observed for underlying layered and foliated gabbros, is not apparent, although uppermost gabbros (Gideah South), near sheeted dikes section, show most evolved compositions. Minerals show an intense chemical zonation between core and rim (EF_{An} 0.53 ±0.26) independent from sample depth (Fig. A15a-c, f). Plagioclases from basaltic dikes cutting varitextured gabbro show no difference in plagioclase compositions in comparison to varitextured gabbro minerals. Plagioclases from varitextured gabbro section show major element compositions, similar to slightly evolved in comparison with minerals from Hess Deep upper shallow series (Lissenberg et al., 2013; Miller et al., 1996; Natland and Dick, 1996) and IODP Site 1256D (Koepke et al., 2011; Fig. A15a, c, d, e). The range of composition is similar to other Oman ophiolite gabbro plagioclases (Abily, 2011; Browning, 1982; Koga et al., 2001; Korenaga and Kelemen, 1997; Yamasaki et al., 2006; Fig. A15d, e).

Sheeted dikes contain only few primary plagioclases of good quality. These have $An_{61\pm2}$ for lower sheeted dikes and $An_{46\pm11}$ for external sheeted dikes, with EF_{An} 0.54 and ~0.45, respectively (Fig. A15a-f).
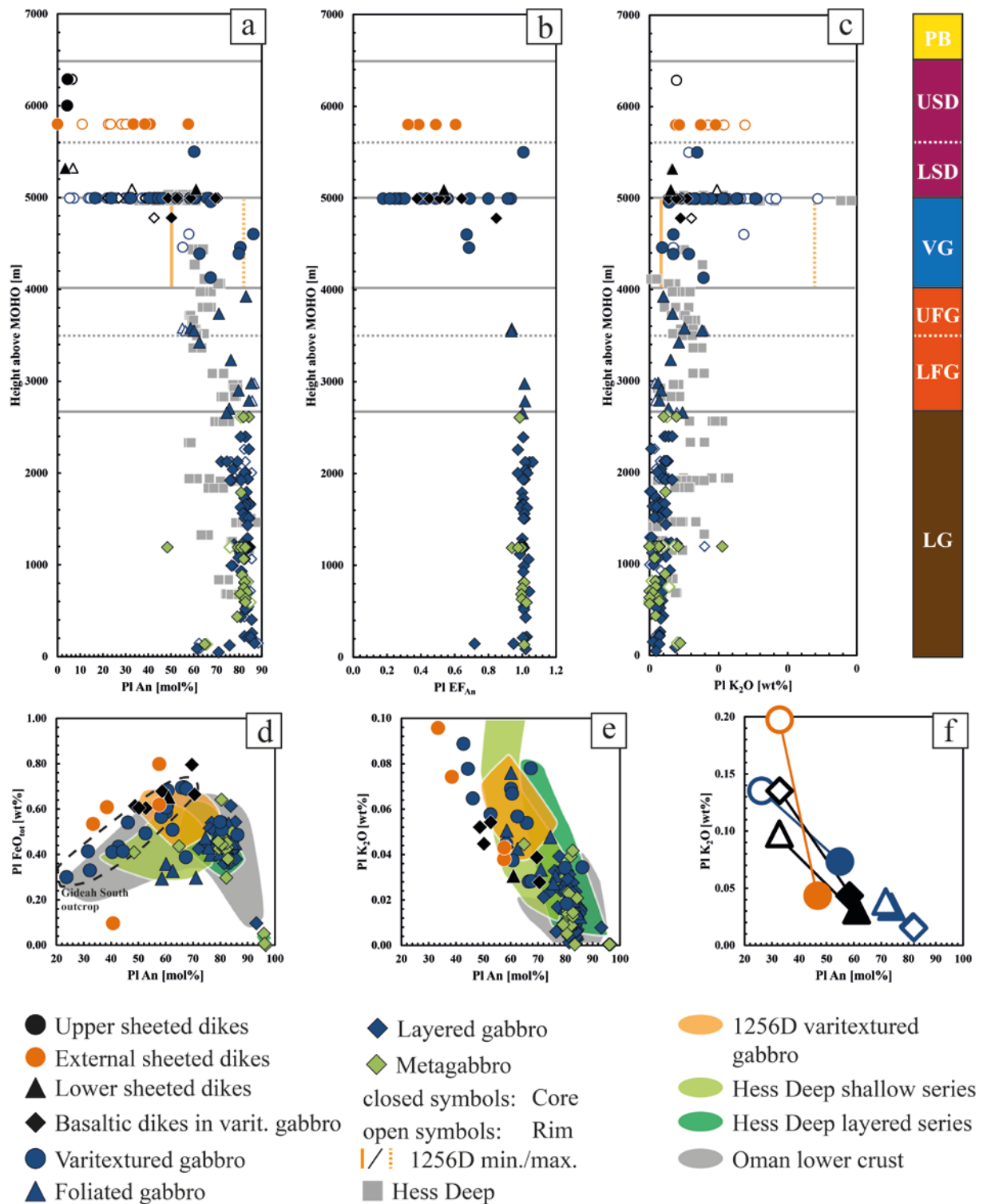
Figure A16. a-c) Geochemical depth logs for average mineral major element content with a) Pl An, b) Pl EF$_{An}$, and c) Pl K$_2$O. d-e) Major element variation diagrams with d) Pl An vs. Pl FeO$_{tot}$ and e) Pl An vs. K$_2$O. f) Major element variation diagram for plagioclase rim and core from Wadi Gideah lithologies with Pl An vs. Pl K$_2$O. Data for Hess Deep plagioclase are from Koepke (unpublished); Lissenberg et al., 2013; Miller et al., 1996; and Natland and Dick, 1996. Data for IODP Site 1256D plagioclase are from Koepke et al., 2011. Data for Oman ophiolite plagioclase are from Abily, 2011; Browning, 1982; Koga et al., 2001; Korenaga and Kelemen, 1997; and Yamasaki et al., 2006. Abbreviation for Wadi Gideah lithologies follows Table A1.

A.5.3.2 Pyroxene

The general lack of orthopyroxene in any lithology is an important feature of the Wadi Gideah profile (see A.5.1). Only few samples (three layered and one varitextured gabbro) could be analyzed. Therefore, the following section will focus on clinopyroxene only, with orthopyroxene results added but not described separately. If minerals are generally referred to as pyroxene they are always referred to as clinopyroxene. Clinopyroxene minerals were analyzed for core and rim composition separately. Orthopyroxene minerals were analyzed for average composition only. All results for clinopyroxene and orthopyroxene major element compositions are given in Table 9.

Layered gabbro clinopyroxenes display average Mg# (MgO/(MgO+FeO)*100) of ~83 in a range from 85 to 76 (Fig. A17a). The same three samples <147 m H.a.M., which also show relatively low plagioclase An content, show clinopyroxene Mg# <80. The cycles of mineral major element variations, observed by Browning (1984) for Oman ophiolite layered gabbros (Wadi Abyad), are well displayed by correlated element variations of Wadi Gideah clinopyroxenes. Also supposed by these cycles, an overall normal trend of chemical evolution is present, shown by change in Mg# ~85 to ~81 for lowest and highest samples, respectively (aforementioned pyroxene <147 m excluded; Fig. A17a, c-g). A chemical zonation is not observed for pyroxenes (Fig. A17b). Minerals from layered gabbro section *metagabbros* show similar major element compositions in comparison with layered gabbro minerals (Fig. A17a-g). Layered gabbro clinopyroxenes show generally similar major element composition in comparison with minerals from Hess Deep layered series with TiO_2 slightly enriched (average Mg# ~84; Koepke, unpublished; Lissenberg et al., 2013; Fig. A17a-f). Clinopyroxenes show also a compositional range in comparison with minerals from other Oman ophiolite gabbros (Browning, 1982; Coogan et al., 2002; Koga et al., 2001; Korenaga and Kelemen, 1997; Yamasaki et al., 2006; Fig. A17e, f). Layered gabbro orthopyroxenes show a similar major element contents in comparison with minerals from Hess Deep layered series (Koepke, unpublished), except for a striking enrichment in FeO_{tot} (decreasing average Mg#) and depletion in CaO.

Clinopyroxenes from the *foliated gabbro* section show average Mg# of ~79 in a range from 83 to 74, evolved in comparison with the layered gabbro pyroxenes (Fig. A17a). The slight normal trend of chemical evolution up section, observed for layered gabbro section, becomes more distinctive in the lower foliated gabbros at the layered/foliated gabbro transition (shown by a change in Mg# from ~81 to ~76 for lowest and highest samples, respectively), and is reversed in the upper foliated gabbros at the lower/upper foliated gabbro section (shown by a change in Mg# from ~76 to ~80 for lowest and highest samples, respectively; Fig A17a, c-g). A chemical zonation between mineral cores and rims is not observed for pyroxenes ($EF_{Mg\#}$ 1±0.01; Fig. A17b). Foliated gabbro clinopyroxenes show a slightly evolved average major element composition in comparison with minerals from Hess Deep lower shallow series (average Mg# of ~81; Lissenberg et al., 2013; Fig. A17a-g). The normal and reversed trend, observed for Wadi Gideah minerals, is also shown by Hess Deep minerals (assuming recalculated sample depths, given by these authors, to be correct in approximation). Wadi Gideah pyroxenes show a similar compositional range in comparison with minerals from

other Oman ophiolite gabbros (Browning, 1982; Coogan et al., 2002b; Koga et al., 2001; Korenaga and Kelemen, 1997; Yamasaki et al., 2006; Fig. A17e-f).

Varitextured gabbro clinopyroxenes have high variability in composition, with average Mg# ~76 in a range from 88 to 71 (Fig. A17a). Some pyroxenes show very low Al_2O_3 and TiO_2 contents, probably related to crystallization in a relatively cool environment (Fig. A17e). A single pyroxene at the medium level of the horizon is noteworthy, showing most primitive clinopyroxene composition from all Wadi Gideah gabbros (Mg# of 88; Fig. A17a). This is supported by very primitive pyroxene trace element composition, showing even impact by mantle signature (see also A.5.4). Varitextured gabbro pyroxenes show generally no or weak chemical zonation ($EF_{Mg\#}$ 0.98±0.03; Fig. A17b). Aforementioned most primitive pyroxene shows intense zonation ($EF_{Mg\#}$ 0.9; Fig. A17b). Varitextured gabbro orthopyroxenes show average Mg# of ~71 (Fig. A17a). Varitextured gabbro clinopyroxenes reveal compositions generally similar to minerals from Hess Deep upper shallow series (average Mg# of ~75; Coogan et al., 2002a; Dick and Natland, 1996; Koepke, unpublished; Lissenberg et al., 2013; Miller et al., 1996; Natland and Dick, 1996; Fig. A17a-g) and similar to slightly evolved in comparison with minerals from IODP Site 1256D gabbro dike 1 and 2 (average Mg# of ~76; Koepke et al., 2011; Fig. A17e, f). Pyroxenes show also similar compositions in comparison with other minerals from Oman ophiolite gabbros (Browning, 1982; Coogan et al., 2002b; Koga et al., 2001; Korenaga and Kelemen, 1997; Yamasaki et al., 2006; Fig. A17e, f). Varitextured gabbro orthopyroxenes displays similar major element contents in comparison with Hess Deep upper shallow series minerals (Koepke, unpublished), except for a striking depletion in TiO_2 and CaO.

An upper *sheeted dike* clinopyroxene displays an average Mg# of 73 and mineral zonation ($EF_{Mg\#}$ 0.96), slightly evolved in comparison with varitextured gabbro minerals (Fig. A17a-f).
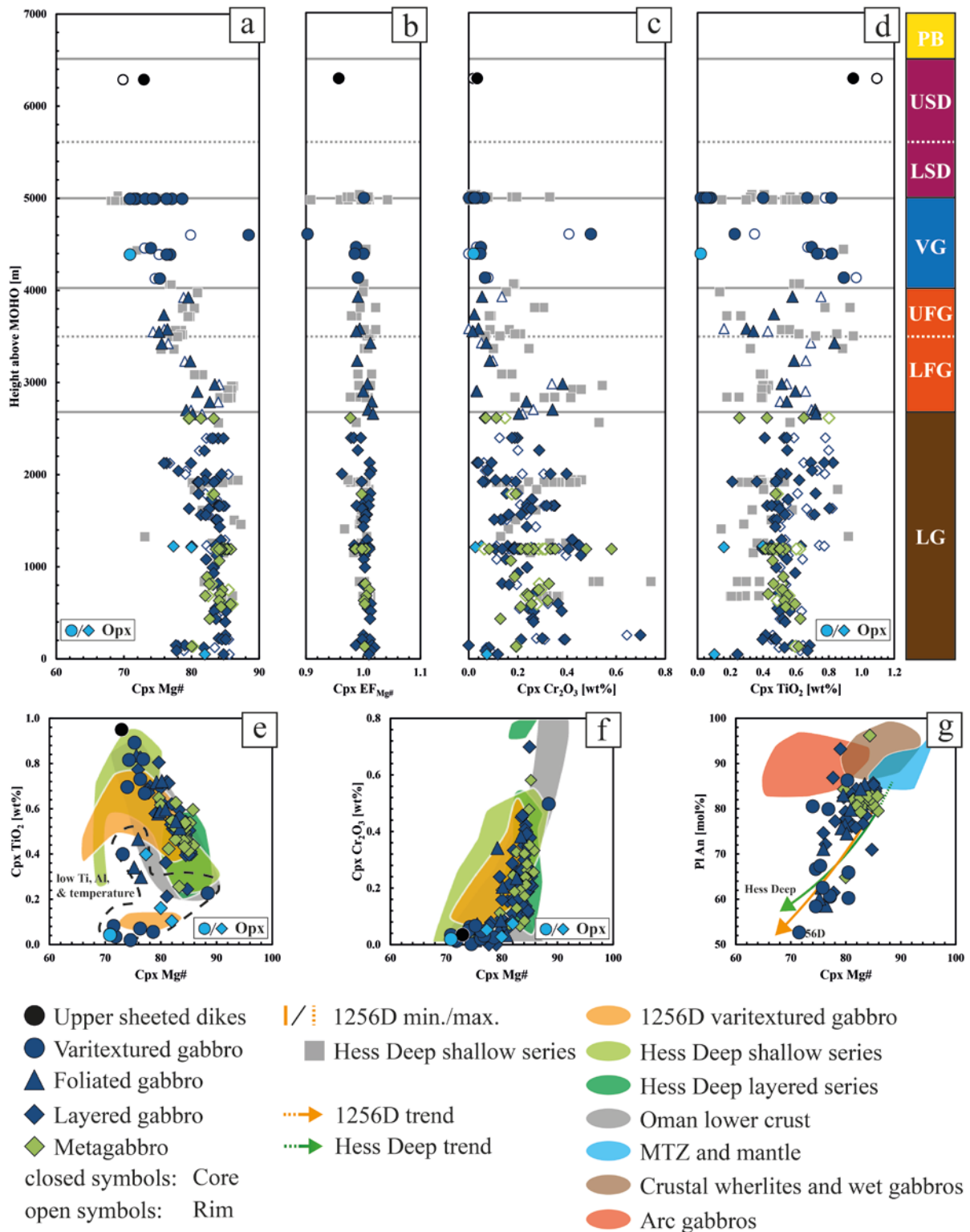
Figure A17. a-d) Geochemical depth logs for average mineral major element content with a) Cpx Mg#, b) Cpx EF$_{Mg\#}$, c) Cpx Cr$_2$O$_3$, and d) Cpx TiO$_2$. e-g) Major element variation diagrams with e) Cpx Mg# vs. Cpx TiO$_2$, f) Cpx Mg# vs. Cpx Cr$_2$O$_3$, and g) Cpx Mg# vs. Pl An. Data for Hess Deep clinopyroxene and plagioclase are from Coogan et al., 2002a; Dick and Natland, 1996; Koepke (unpublished); Lissenberg et al., 2013; Miller et al., 1996; and Natland and Dick, 1996. Data for IODP Site 1256D clinopyroxene and plagioclase are from Koepke et al., 2011. Data for Oman ophiolite clinopyroxene are from Browning, 1982; Coogan et al. 2002b; Koga et al., 2001; Korenaga and Kelemen, 1997; and Yamasaki et al., 2006. Mineral data for MTZ and mantle are from Koga et al., 2001; and Korenaga and Kelemen, 1997. Mineral data for crustal wherlites and wet gabbros are from Abiliy, 2011 (Sarimi, Hilti, and Bahla). Mineral data for fore arc gabbros are from Burns (1985). Abbreviation for Wadi Gideah lithologies follows Table A1.

A.5.3.3 Olivine

Olivine minerals were analyzed for an average composition only. All results for olivine major element compositions are given in Table 9.

Layered gabbro olivines have an average NiO content of ~0.11 wt% and Mg# of ~79 in a range from 82 to 71 (Fig. A18a, b). A slight normal trend of chemical evolution up section is present, shown by a change of Mg# from ~80 to ~77 for lowest and highest samples, respectively (Fig. A18a-f). Olivines have slightly evolved compositions in comparison with minerals from Hess Deep layered series (average Mg# of ~81; Koepke, unpublished; Lissenberg et al., 2013; Fig. A18a-f) and compositions similar to other minerals from Oman ophiolite gabbros (Abily, 2011; Browning, 1982; Korenaga and Kelemen, 1998; Fig. A18b-f).

Olivines from *foliated gabbro* section show average NiO contents of ~0.08 wt% and Mg# of ~74 in a range from 79 to 67 (Fig. A18a, b), which is more evolved in comparison with layered gabbro minerals. The slight normal trend of chemical evolution up section, observed for layered gabbro olivines, becomes apparently more distinctive at the layered/foliated gabbro transition, shown by a change of Mg# from ~75 to ~70 for lowest and highest samples, respectively (Fig. A18a-f). It cannot be determined, if the trend is reversed at some level (like observed for plagioclase and clinopyroxene; see A.5.3.1 and A.5.3.2), since the density of olivine bearing samples becomes lower up section. Foliated gabbro olivines have slightly evolved major element compositions in comparison with minerals from Hess Deep lower shallow series (average Mg# of ~78; Lissenberg et al., 2013; Fig. A18a-f) and compositions similar to other minerals from Oman ophiolite gabbros (Abily, 2011; Browning, 1982; Korenaga and Kelemen, 1998; Fig. A18d-f).

Varitextured gabbro olivines are very rare (two samples only). They reveal average NiO content of 0.05 wt% and Mg# of ~66 (Fig. A18a, b), which is more evolved in comparison to layered and foliated gabbro minerals. Olivines have major element compositions similar to minerals from Hess Deep upper shallow gabbro series (average Mg# of ~66; Koepke, unpublished; Lissenberg et al., 2013; Fig. A18a-f) and IODP Site 1256D gabbro dike 1 and 2 (average Mg# of ~66; Koepke et al., 2011 Fig. A18d-f).
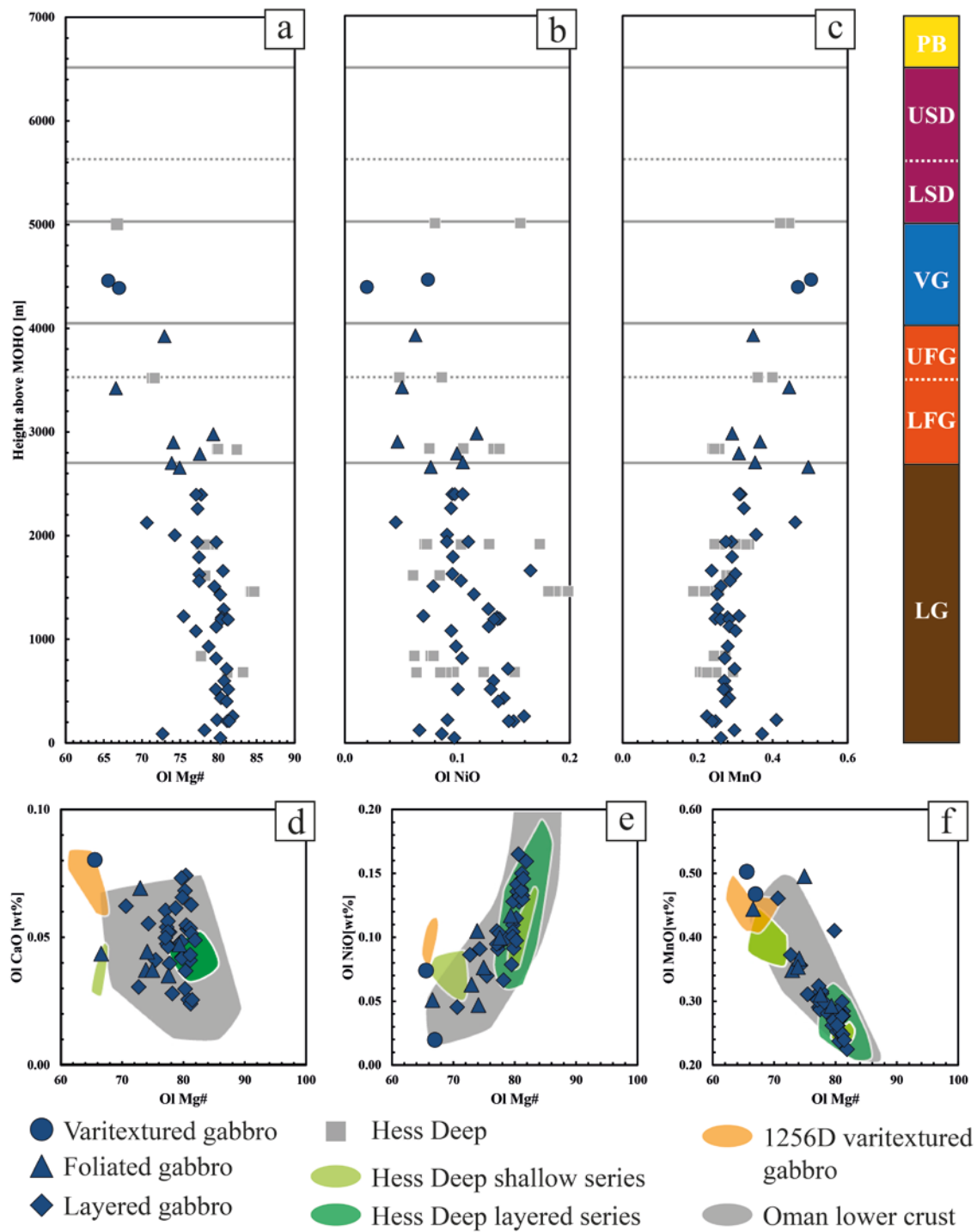
Figure A18. a-c) Geochemical depth logs for average mineral major element content with a) Ol Mg#, b) Ol NiO, and Ol MnO. d-e) Major element variation diagrams with d) Ol Mg# vs. Ol CaO, e) Ol Mg# vs. Ol NiO, and f) Ol Mg# vs. Ol MnO. Data for Hess Deep olivine are from Koepke (unpublished); and Lissenberg et al., 2013. Data for IODP 1256D olivine are from Koepke et al., 2011. Data for Oman ophiolite olivine are from Abiliy, 2011a; Browning, 1982; and Korenaga and Kelemen, 1997. Abbreviation for Wadi Gideah lithologies follows Table A1.

A.5.3.4 Amphibole

Wadi Gideah amphibole structural formula was calculated after Robinson (1982) and minerals classified for Ca-amphiboles after Leake et al. (1997), using Ca_A, Ca_B, $(Na+K)_A$, Ti, Si in formula and XMg (Mg/(Mg+Fe)), assuming 23 oxygen atoms per half unit cell. The amphibole formation temperatures were estimated by semi quantitative Ti-in-amphibole thermometer of Ernst and Liu (1998). All amphiboles were analyzed for an average composition only. All results for amphibole major element compositions are given in Table 9.

Amphibole data sets used for comparison are compiled from Koepke et al. (2011) for IODP Site 1256D and Abily (2011) and Browning (1982) for Oman ophiolite.

Layered gabbro amphiboles are generally pargasites (+ 1 hornblende), with Mg# of ~75 in a range from 79 to 70 (Fig. A19a). The estimated formation temperature is ~924°C in a range from 1006 to 839°C (Fig. A19d). It is noteworthy that all amphiboles show neither a defined magmatic nor hydrothermal signature, following F-Cl amphibole classification by Coogan et al. (2001; Fig A19f). Instead, they reveal a high F content (up to 1774 ppm) generally related to magmatic formation, and high Cl content (up to 2402 ppm) generally related to secondary interaction with seawater-derived fluids (Coogan et al., 2001). Since pargasites are interpreted to retain their magmatic compositions, it can be assumed, that Cl-rich fluids were present during crystallization from the corresponding melt. This could be related to a tectonic setting of subduction initiation, since the degree of alteration (see A.5.1) and W/R ratios (see A.5.2.3) for layered gabbros are generally low. A trend of chemical evolution up section is not observed. Amphiboles from metagabbros within the layered gabbro section are pargasite, edenite, and magnesio-hornblende, with Mg# of ~73 in a range from 80 to 76 (Fig. A19a). Pargasite and edenite show formation temperatures of ~864°C in a wide range from 1014°C to ~510°C for few amphiboles with low Ti (Fig. A19d). Magnesio-hornblende shows formation temperatures ~686°C in a range from 813 to 541°C (Fig. A19d). Metagabbros show high F (up to 1903 ppm) and Cl (up to 2481 ppm) content for amphibole, neither related to a defined magmatic nor hydrothermal signature (Coogan et al., 2001), and in a range similar to minerals from layered gabbro host rock (Fig. A19f).

Amphiboles from the *foliated gabbro* section are pargasite and edenite with average Mg# of ~69 in a range from 74 to 64 (Fig. A19a), with high F and Cl content (up to 1957 ppm and 1559 ppm, respectively; Fig. A19f). The average formation temperature is ~928°C in a range from 999 to 880°C (Fig. A19d). A slight normal trend of chemical evolution up section is present for the lower foliated gabbros (change of Mg# from ~73 to ~64 for lower and upper samples, respectively), which is apparently reversed at the lower/upper foliated gabbro transition (change in Mg# from 64 to 72 for lowest and highest upper foliated gabbro samples, respectively (Fig. A19a). This is similar to observations from plagioclase (see A.5.3.1) and clinopyroxene (see A.5.3.2).

Varitextured gabbro amphiboles are pargasite, edenite, magnesio-hornblende, and actinolite, with average Mg# of ~66 in a range from 71 to 61 (Fig. A19a). Pargasite and edenite reveal an average formation temperature of 951°C in a range from 982 to 880°C (Fig. A19d). Magnesio-hornblende gives an average formation temperature of 664°C in a range from 727

to 574°C, and actinolite a temperature of 623°C in a range from 660 to 578°C (Fig. A19d). All amphiboles, including pargasites, which are interpreted to retain their magmatic composition, show high F (up to 2657 ppm) and high Cl (up to 2723 ppm) concentrations (Fig. A19f). Amphiboles in the basaltic dikes, cutting varitextured gabbro, show compositions of actinolitic to magnesio-hornblende, with F and Cl content up to 2102 and 939 ppm, respectively (Fig. A19f). Varitextured gabbro pargasites show major element composition similar to the range of primitive amphiboles from other Oman ophiolite gabbros (Abily, 2011; Browning, 1982; Fig. A19e). The edenite is similar to primitive amphiboles from Site 1256D gabbro 1 and 2 (Koepke et al., 2011; Fig. A19e). Magnesio-hornblende and actinolite display compositions similar to range of evolved amphiboles from other Oman ophiolite gabbros and Site 1256D gabbro dike 1 and 2, although they display a slight shift to lower Al_2O_3 content (Fig. A19a-c, e).

Extrusive section amphibole was only possible to analyze in external sheeted dike samples, giving compositions of actinolite to ferro-actinolite, with average Mg# of ~52 in a range from 62-39 (Fig. A19a). They are generally more evolved in comparison with amphiboles from varitextured gabbro section. Average actinolite formation temperature is ~564°C with a narrow range from 595 to 537°C (Fig. A19d).
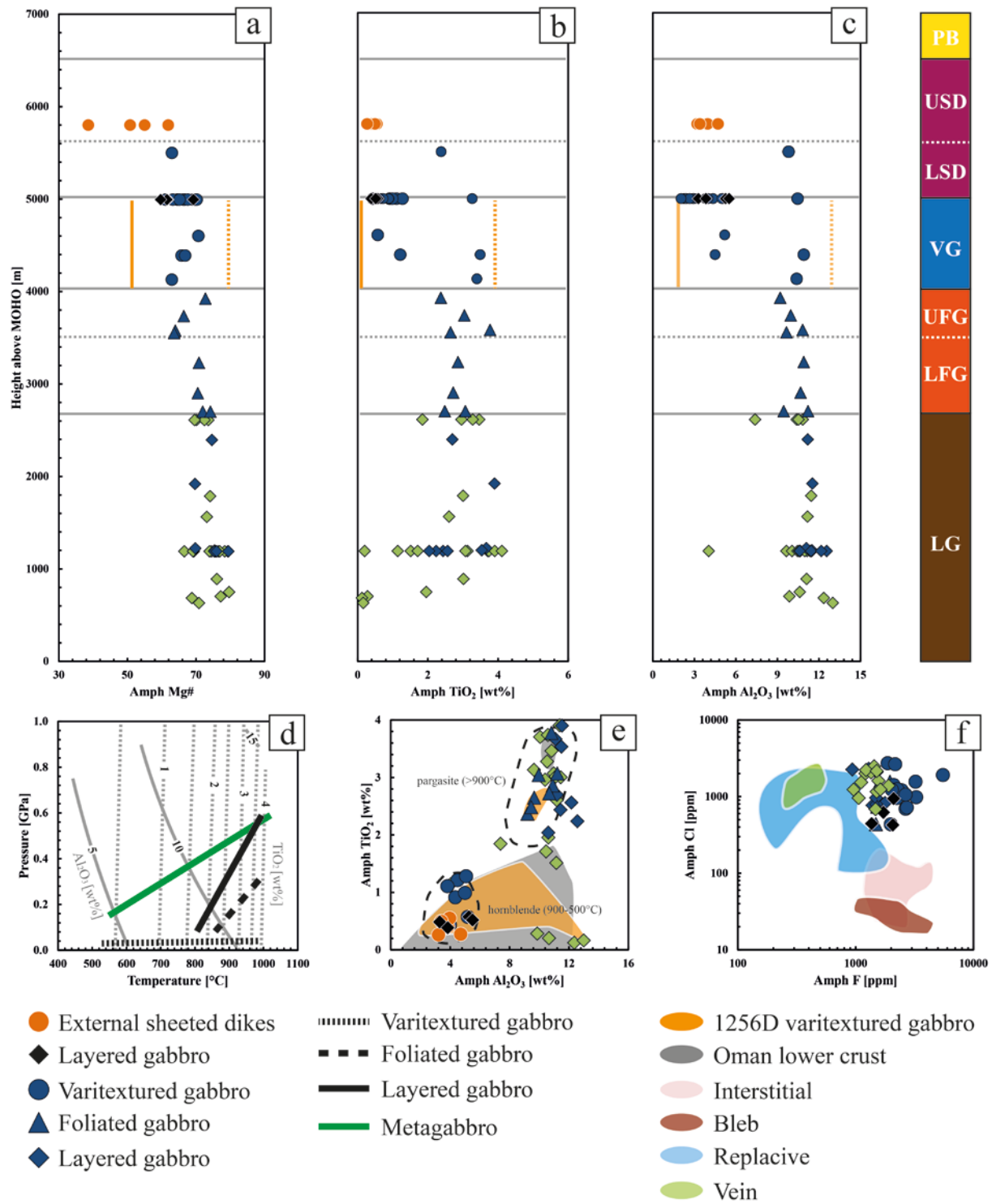
Figure A19. a-c) Geochemical depth logs for average mineral major element content with a) Amph Mg#, b) Amph TiO$_2$, and c) Amph Al$_2$O$_3$. d) Semi quantitative Ti-in-amphibole thermometer of Ernst and Liu (1998). Lines connect highest and lowest temperature given by amphibole of the lithology. e) Major element variation diagram with Amph Al$_2$O$_3$ vs. Amph TiO$_2$. Dashed lines represent fields for pargasite and hornblende. f) Element variation diagram for Amph F vs. Amph Cl. Fields represent ranges for amphibole which are generally related to magmatic formation (interstitial and bleb) or generally related to secondary interaction with seawater-derived fluids (replacive and vein) from Coogan et al., 2001. Data from IODP Site 1256D amphibole are from Koepke et al., 2011. Data from Oman ophiolite amphibole are from Abily, 2011; and Browning, 1982. Abbreviation for Wadi Gideah lithologies follows Table A1.

A.5.4 Mineral Trace Element Chemistry

Mineral trace element compositions were determined for clinopyroxenes by LA-ICP-MS (see A.4.2.4) for 25 selected samples from all Wadi Gideah lower crust lithologies, in order to obtain detailed information about chemical variation between mineral cores and rims, as well as a general vertical compositional variation within the Wadi Gideah profile. Multiple grains per sample were analysed to qualify intra-sample variations. The results were normalized to NMORB (Gale et al., 2013) and equilibrium melts calculated for core and rim, using a compiled data set of partition coefficients (K_D) from Dorais and Tubrett (2008) and Pfänder et al. (2007; Zr and Hf only). The enrichment factor ($EF_{element}=conc_{rim}/conc_{core}$) was calculated, with a value >1 indicating enrichment and <1 indicating depletion of rim in comparison with core. Zr, Hf, and La are used as representatives in the following paragraph to display trace element content for minerals of the different lithologies. The results for clinopyroxene trace element compositions are given in Table 10 and 11. The clinopyroxene dataset, used for comparison, was published by Lissenberg et al. (2013) for Hess Deep layered- and shallow gabbro series.

Layered gabbro clinopyroxenes cores have Zr concentrations of ~7.46 ppm and Hf of ~0.38 ppm, with a Zr/Hf ratio of 19.19±3.53. A trend of chemical evolution up section is not observed (Fig. A20a-d). The lowest sample (50 m H.a.M.) has striking primitive trace element content, with an impact of mantle signature (Fig. A20f). This, like major and bulk trace element from samples within MTZ at depths <147 m (see A.5.2 and A.5.3), gives evidence for an impact of mantle processes on mineral crystallization, which hence was more likely at depth directly at the mantle/crust transition and not within AML. Clinopyroxene rims show slightly evolved composition in comparison with mineral cores, with an average EF_{Zr} of 1.39±0.54 and highest EF_{Zr} of 3.77 (Fig. A20d). Pyroxene cores give trace element compositions generally similar to minerals from Hess Deep layered series (~ 7.76 ppm Zr; Lissenberg et al., 2013; Fig. A20a-d), while Hess Deep mineral rims are significantly more enriched (average EF_{Zr} of 2.52±1.94 with highest EF_{Zr} of 10.63; Lissenberg et al., 2013; Fig. A20d). Wadi Gideah lower gabbro equilibrium melts (for core and rim) have compositions slightly primitive in comparison with NMORB (Gale et al., 2013), associated with a slight negative Zr-Hf anomaly, which may, however, be related to the K_D values used for calculation (Fig. A20e).

Clinopyroxene cores from *foliated gabbro* section show content of ~14.28 ppm Zr, ~0.63 ppm Hf, and a Zr/Hf ratio of ~22.97 (Fig. A20a-d). A normal trend of chemical evolution is present within the lower foliated gabbros (change in Zr from ~14 to ~27 ppm for lowest and highest minerals, respectively). The trend is reversed within the upper foliated gabbros at the lower/upper foliated gabbro transition (change in Zr from ~27 to ~7 ppm for lowest and highest minerals, respectively), which is similar to mineral major element chemistry (see A.5.3). Pyroxene rims are similar in composition to cores within the lower foliated gabbro section (EF_{Zr} 1.01±0.07) but become more evolved in comparison within the upper foliated gabbros (EF_{Zr} 2.35±0.86; Fig. A20d). Pyroxene cores reveal compositions generally more primitive in comparison with Hess Deep lower shallow series minerals (~ 37.72 ppm Zr; Lissenberg et al., 2013), with significantly lower vertical variation (Fig. A20a-d). The

chemical evolution up section, normal and reversed, is also present for Hess Deep minerals, with an average EF_{Zr} 1.76±1.21. The calculated Wadi Gideah equilibrium melts show compositions similar to NMORB (Gale et al. 2013), at lower range of Oman V1-lavas (Godard et al., 2003), and associated with a slight negative Zr-Hf anomaly, also displayed by pyroxene equilibrium melts from layered gabbro section (Fig. A20e).

Varitextured gabbro clinopyroxenes cores have ~12.02 ppm Zr, ~0.63 ppm Hf, and a Zr/Hf ratio of ~1.32 (Fig. A20a-d). They are slightly primitive in comparison to minerals from foliated gabbro section (see above) and have a slight chemical zonation (EF_{Zr} 1.32±0.45; Fig. A20d). A single sample (OM10_Gid_A13), however, gives very primitive pyroxene trace element compositions similar to the lowermost layered gabbro, with an impact of mantle signature (Fig. A20e). This correlates with this sample´s very high Mg# of 88 (see A.5.3.2). Pyroxenes have more primitive compositions in comparison with Hess Deep minerals from upper shallow gabbro series (~47.22 ppm Zr; Lissenberg et al., 2013; Fig. A20a-d) but a similar intensity of chemical zonation (EF_{Zr} 1.26±0.42). The calculated Wadi Gideah equilibrium melts are similar to NMORB (Gale et al., 2013), at lower range of Oman V1-lavas (Godard et al., 2003), and associated with the negative Zr-Hf anomaly also observed for other Wadi Gideah gabbro sections (Fig. A20e).
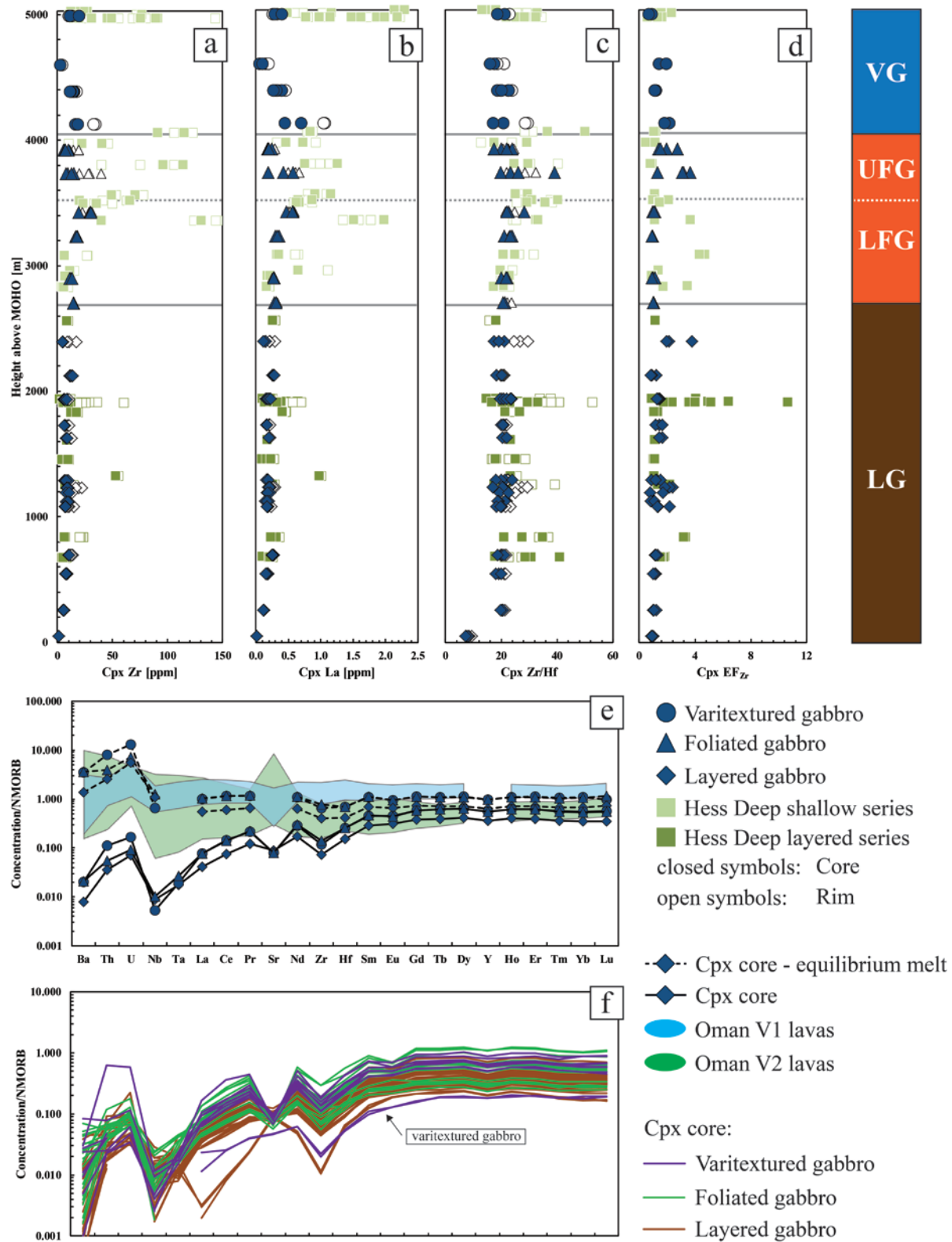
Figure A20. a-d) Geochemical depth logs for clinopyroxene with a) Cpx Zr, b) Cpx La, c) Cpx Zr/Hf ratio, and Cpx EF$_{Zr}$. e) Average trace element composition of clinopyroxene cores and calculated equilibrium melts in comparison with range of V1- and V2 lavas (Godard et al., 2003). f) Trace element compositions of all analyzed clinopyroxenes. Note the primitive, mantle signature affected pattern of pyroxenes from varitextured sample OM10-Gid-A13. All compositions are normalized to NMORB (Gale et al., 2013). Abbreviation for Wadi Gideah lithologies follows Table A1.

A.6 Modeling Fractional Crystallization

Wadi Gideah gabbros show a trend of chemical evolution up section, slight for layered gabbros and more distinctive for lower foliated gabbros (see B.5.2 to B.5.5). It is additionally observed, that plagioclase anorthite content is higher at similar clinopyroxene Mg# in comparison with minerals from modern EPR crust. This could be related to an enriched water content of Wadi Gideah melts in comparison to EPR ones. With the assumption that the overall trend of evolution was derived by fractional crystallization within the layered and lower foliated gabbro section, MELTS software (Ghiorso and Sack, 1995) was used to reproduce the Wadi Gideah trend of chemical evolution, with a variation of the initial melt composition and melt H_2O content. In order to use a system, which is chemically similar to Wadi Gideah, multiple compositions related to the Wadi Gideah bulk analyses were used as initial melt compositions. This included the calculated Wadi Gideah bulk crust (GBC), following Gillis et al., 2014 (for Hess Deep). GBC takes into account the average bulk major element compositions of Wadi Gideah lithologies, in dependency of their proportion on the complete profile (assuming 29 % extrusive section, 11 % varitextured gabbro, 20 % foliated gabbro, and 40 % of layered gabbro section; Table 12). However, GBC displays iron content, which is too low. Better results for modeling were obtained, using the composition of a primitive Wadi Gideah basaltic dike (A11_1U; Table 12). NMORB (Gale et al., 2013) was used, to model a LLD more valid for EPR. The calculations were done for quartz-fayalite-magnetite buffer (QFM) conditions at a fixed pressure of 2 kbar for gabbro-related and 0.5 kbar for AML- and basalt-related modeling. Little effect for a buffer variation between QFM±1 was shown by additional modeling. The amount of H_2O in the melt was increased in steps of 0.2 wt% from an anhydrous state to total H_2O_{melt} content of 1.4 wt%. The results for MELTS modeling are given in Table 12.

MELTS software was used to approximatively calculate the variation of plagioclase and clinopyroxene compositions in dependence of the total H_2O_{melt} content. Results reveal that the plagioclase anorthite content increases at similar clinopyroxene Mg# with a rise in H_2O_{melt} content (Fig. A21a). It is shown that Wadi Gideah trend of chemical evolution up section is best reproduced for an H_2O_{melt} content of ~0.8 wt% (Fig. A21a). In contrast, evolutionary trend from Hess Deep lower and shallow gabbro series and IODP Site 1256D gabbro dikes 1 and 2 are best modeled generally water free or only with very low amounts of H_2O_{melt} (0 % to 0.4 % H_2O; Fig. A21a).

MELTS software was also used to approximatively calculate LLD for Wadi Gideah extrusive section, with variation of H_2O_{melt} content, following the approach of MacLeod et al. (2013). Results reveal that Wadi Gideah lower and generally upper sheeted dikes are well reproduced with an H_2O_{melt} of 0.8 to 1.0 wt% (Fig. A21b-d). Pillow basalts, external sheeted dikes, and some upper sheeted dikes give very low MgO contents, not reproduced by any modeled LLD. These samples, however, display high alteration under amphibolite and greenschist facies (A.5.1.5). This is likely to impact content of highly fluid mobile Mg (e.g., Pearce, 2014).

Dikes and lavas from Hess Deep (Stewart et al., 2002) and IODP Site 1256D (Neo et al., 2009) are best modeled with H_2O_{melt} contents of 0 to 0.4 wt% (Fig. A21b-d).
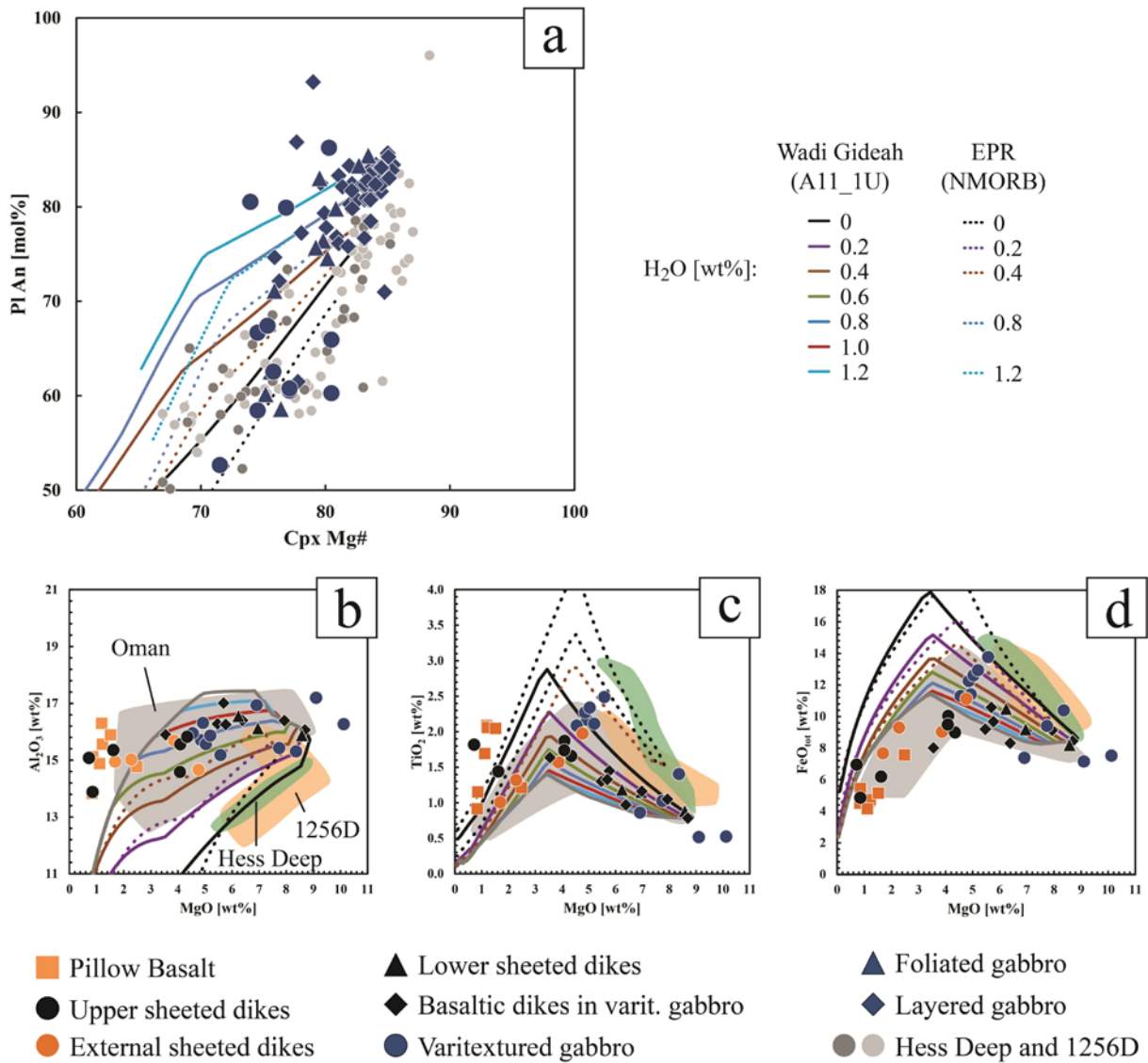
Figure A21. Liquid lines of descent obtained by MELTS modeling (Ghiorso and Sack, 1995) with variation of H_2O_{melt} for a chemical system similar to Wadi Gideah (A11_1U = melt$_{ini}$) and EPR (NMORB [Gale et al., 2013] = melt$_{ini}$) for a) plutonic section (Cpx Mg# vs. Pl An) and b-d) extrusive section (Cpx MgO vs. Al_2O_3, TiO_2, and FeO_{tot}). Data for IODP Site 1256D and Hess Deep are from Gillis et al., 2014; Koepke et al., 2011; Lissenberg et al., 2013; Neo et al., 2009; Steward et al., 2002; and Wilson et al., 2003. Data for Oman ophiolite are from MacLeod et al., 2013.

A.7 Discussion

A.7.1 Sample Quality in Terms of Alteration

Alteration is an important process, which potentially affects the chemical composition of sampled rocks. It is related to the change of mineral phases at or near the location of its formation in depth by variation of environmental parameters, like pressure or temperature (more relevant for this study), in presence of water. Intense hydrothermal rock alteration under amphibolite to greenschist facies was observed for many Wadi Gideah sheeted dikes (see A.3.5). A simple classification, to observe or identify the impact of weathering or alteration on basaltic rock geochemical results, referred to by Pearce (2014) and based on observations by Cann (1970), is the direct comparison of fluid- and not fluid mobile elements. Cann discovered during the analysis of fresh and altered rocks that some elements were likely to be affected by alteration (e.g. Si, Na, K), designated as "mobile elements", while other were unlikely to be affected (e.g. Zr and Ti), designated as "immobile elements". In a diagram with Zr plotted versus Ti (both immobile elements), bulk rock analyses therefore should generally follow the crystallization vector. If Zr is plotted versus K (mobile), results will deviate from the crystallization vector to more positive values for an impact by amphibolite facies alteration and negative values for impacted by greenschist facies alteration.

Wadi Gideah bulk compositions reveal that some samples from external- and sheeted dikes as well as pillow basalts deviate from the general crystallization vector in the Zr vs. Ti diagram (Fig. A22a). This gives evidence that they do not to represent undisturbed "frozen" melt or that they are affected by other processes It is also shown in the Zr vs. K diagram that some basaltic dikes in varitextured gabbros, lower- and external sheeted dikes, and pillow basalts are slightly to moderately affected by amphibolite facies alteration, while some upper sheeted dikes samples and single pillow basalts are highly affected by greenschist facies (Fig. A22b).
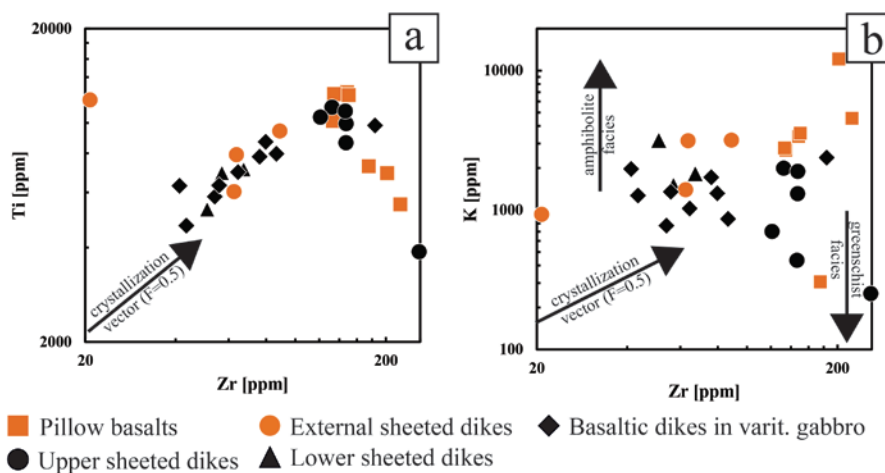
Figure A22. Element variation diagram (after Cann, 1970; Pearce, 2014) for a) with bulk Zr vs. bulk Ti (both immobile) and b) bulk Zr (immobile) vs. K (mobile) for Wadi Gideah extrusive section. Arrows indicate the compositional shift supposed for impact of amphibolite and greenschist alteration (Pearce, 2014).

The impact of amphibolite and greenschist facies alteration on samples does not imply that the analytical results are generally negligible or invalid. Nevertheless, the impact has to be kept in mind for interpretations, which refer to fluid mobile elements, like Mg (used for bulk major element Harker diagrams) and Si, Na, and K (used for rock classification in TAS diagram; see A.5.2.1). Additionally, rock classifications using immobile element TAS proxy diagram (Pearce, 2014; see A.5.2.2) should be preferred to classification using standard TAS (Le Bas and Streckeisen, 1991; see A.5.2.1) for altered, upper crust rocks.

A.7.2 Tectonic Setting

It is still under debate if and how intense Samail ophiolite is related to supra-subduction magmatism rather than to normal mid-ocean ridge magmatism (see objectives and background). Several observations from this chapter give evidence that Wadi Gideah crust does not relate to a normal mid-ocean ridge setting in contrast to crust from e.g. Hess Deep and IODP Site 1256D:

(1) Wadi Gideah bulk trace elements reveal a distinctive Nb-Ta anomaly, independent from lithology, in comparison with neighbor elements in NMORB-normalized diagram (see A.5.2.2; Fig. A13). Therefore, it is considered that mantle derived melts, forming Wadi Gideah crust, were already depleted in Nb-Ta. Taking into account the knowledge that both Nb and Ta are subduction immobile (e.g. Pearce, 2014), this is clear evidence for a tectonic setting of supra-subduction (e.g., Pearce et al., 1981; Peate and Pearce, 1998). Since Nb-Ta anomaly is relatively low in intensity, the setting could be narrowed to subduction initiation, maybe at a marginal basin (e.g., MacLeod et al., 2013).

(2) Wadi Gideah basaltic samples show a shift away from the range of NMORB (including Hess Deep and IODP Site 1256D crust) to the range of oceanic arcs (Fig. A23) in the Nb/Yb vs. Th/Yb diagram. This classification (e.g. Pearce, 2014; Peate and Pearce, 1998) is based on the decoupling of subduction mobile Th and subduction immobile Nb (also displayed by negative Nb anomaly in NMORB-normalized diagram; see above). Since the deviation is relatively small, equivalent to intensity of Nb-Ta anomaly, a setting of subduction zone initiation is considered here.
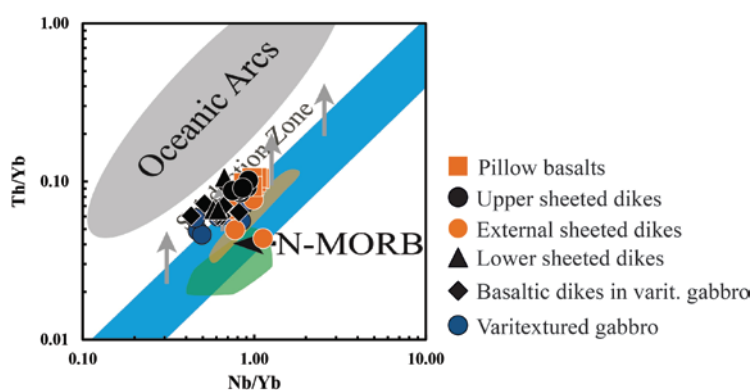
Figure A23. Discriminant diagram for Wadi Gideah varitextured gabbro- and extrusive section with Nb/Yb vs. Th/Yb. Range of NMORB is marked in blue. Wadi Gideah samples reveal a clear shift into direction of subduction zone (initiation). Data for range of NMORB and Oceanic Arcs are from Pearce, 2014. Data of IODP Site 1256D and Hess Deep are from Neo et al. (2009) and Stewart et al. (2002).

(3) Wadi Gideah plagioclases from layered and foliated gabbro sections show increased anorthite contents in comparison to minerals from Hess Deep at similar Mg# in clinopyroxene (see A.5.3.1 and A.5.3.2). It is revealed by the MELTS calculations, that the increase in anorthite content can be well produced with fractional crystallization of a melt, containing ~0.8 wt% H_2O (see A6). Since $^{87}Sr/^{86}Sr$ is generally constant for Wadi Gideah layered and foliated gabbros (see A.5.2.3), it is considered here that mantle derived melts were already enriched in water before crystallization. This supports the assumption of a subduction initiation setting, since water content is too low for pure arc magmatism (> 3 wt%; e.g., Ushioda et al., 2014). The assumption is further supported by the lack of gabbronorites, pyroxenites, and hornblendites at Wadi Gideah, which are all rock units supposed and observed for arc related magmatism (e.g., Behn and Kelemen, 2006; Henjes-Kunst et al., 2014; Jagoutz et al., 2007).

(4) Wadi Gideah layered and foliated gabbros show $^{87}Sr/^{86}Sr_{ini}$ ratios significantly enriched in comparison with $^{87}Sr/^{86}Sr$ ratios from Hess Deep layered and shallow series (see A.5.2.3). $^{87}Sr/^{86}Sr$ could be raised by isotopic exchange during low temperature hydrothermal alteration. However, $^{87}Sr/^{86}Sr_{ini}$ ratios are generally constant for Wadi Gideah lower crust, with a significant increase only observed for metagabbros (see also A.7.4). Additionally the alteration of Wadi Gideah layered gabbros is relatively low, W/R ratios are very small (~ 0.81), and a raise in $^{87}Sr/^{86}Sr$ should be also observed for Hess Deep, implying similar mechanisms. Therefore, there is no evidence for a significant increase of Wadi Gideah layered gabbro $^{87}Sr/^{86}Sr_{ini}$ by hydrothermal alteration during the lower crust accretion. It could be hence considered that the high ratio was already present in later crystallizing melts, most likely by an impact of subduction zone fluids.

(5) Wadi Gideah high temperature magmatic amphiboles from lower crust show both high F and Cl content (see A5.3.4), with first generally related to magmatic formation and latter generally related to secondary interaction with seawater-derived fluids (Coogan et al., 2001). Since the average Cl content of layered and foliated gabbro amphibole is generally constant, independent from the stratigraphic height, it is considered here that the chlorine enrichment of mantle derived melts is related to subduction zone fluids, rather than hydrothermal introduction.

In summary, aforementioned evidences most likely point towards a subduction initiation-related accretion of the Wadi Gideah crust, which corresponds to assumptions made by previous authors. Goodenough et al. (2014) subdivided the Oman ophiolite crust into Phase 1 crust and Phase 2 crust, based on petrologic observations (correlating to V1 and V2 magmatism, respectively; Alabaster et al., 1982; Ernewein et al., 1988). While Phase 1 crust is related to a normal spreading center postdated intrusive Phase 2 crust (with occurrence of e.g. wherlites) is related to a subduction zone development. Haase et al. (2015) described that Haylayn felsic intrusions into the mantle represent partial melts of sediment. Therefore, these authors support a model of subduction initiation. MacLeod et al. (2013) modeled fractional crystallization of experimental MORB parental melt and revealed that Oman "Geotimes"

magmas must have been significantly enriched in H_2O content (up to 1 wt%). These authors concluded that the Oman ophiolite formed in a marginal basin above a type of subduction zone, hence assuming that also lower crust forming melts displayed enriched H_2O content. This assumption is supported by modeling of this study, which reveals an H_2O_{melt} content of ~0.8 wt% for Wadi Gideah lower crust forming melts (see A.6).

A.7.3 Accretion of Wadi Gideah Lower Crust

Several observations from this chapter give evidence for deep crust crystallization during the accretion of the Wadi Gideah lower crust. Following observations reveal that an accretion of Wadi Gideah lower crust exclusively by downward suspension flow from the AML mighty be unlikely:

(1) Wadi Gideah lower crust shows a distinctive, normal trend of geochemical evolution up section for major and trace elements (see A.5.2.1, A.5.2.2, A.5.3, and A.5.4). The trend is slight for the layered gabbro section and becomes distinctive above at the layered/foliated gabbro transition. This feature is unlikely to be derived from a downward suspension flow since differentiation occurs exclusively in the AML. The overall trend of chemical evolution up section is additionally superposed by cyclic co-variations in Wadi Gideah mineral major element data, with wavelength of few hundred meters. This is similar to observations of Browning (1984) from Wadi Abyad. Korenaga and Kelemen (1998) showed in a numerical approach that these covariations are unlikely to be generated by porous flow. Therefore, they proposed that mantle derived melts ascend rather by focused flow (e.g. Kelemen and Aharonov, 1998). They additionally proposed that a suspension downward flow from the AML to the mantle/crust boundary is unlikely since the inter-cumulus melts should somehow react with the lower crust. Since these kinds of co-variations were also observed in this study, a suspension downward flow may be considered to be also unlikely for Wadi Gideah lower crust accretion.

(2) Wadi Gideah layered and lower foliated gabbro minerals show no systematic, distinctive chemical zonation. If a zonation is observed, it is weak, independent from sample depth, and normal or reversed (see A.5.3.1, A.5.3.2, and A.5.4). The first appearance of a distinctive, systematic chemical zonation is shown for upper foliated gabbros, which correlates well with the observed trend of chemical evolution up section. The lack of a chemical zonation for layered gabbro minerals but the appearance of a chemical zonation for upper foliated gabbro minerals is unlikely for a downward suspension flow.

(3) Wadi Gideah mineral grain sizes are similar in average within the single lower crust lithologies. However, the average grain size shows a distinctive step directly at the layered/foliated gabbro transition to smaller grain sizes for foliated gabbros (see A.5.1.2), which is unlikely for a downward suspension flow. This "stepping" in the average grain size was also observed at the nearby Wadi Khafifah section (Wadi

Tayin Massif) by Garrido et al., 2001, who studied in detail the crystal size distributions (CSD).

(4) Wadi Gideah lower layered and upper foliated gabbro section generally have no magmatic late stage phases. These appear only within the upper foliated gabbros (see A.5.1). Assuming a suspension flow from AML to mantle/crust boundary, however, the phases should be present also at greater depths.

Observations from this chapter give evidence that the accretion of Wadi Gideah layered- and foliated gabbros could be better explained by crystallization at depth in lateral intrusions (respectively sills; e.g. Kelemen and Korenaga, 1997). The chemical evolution trend up section, revealed by lower crust major and trace elements, is well reproduced by a modeled hydrous fractional crystallization (~0.8 wt% H_2O) in a system chemically similar to Wadi Gideah (see A.6). Therefore, a deep crystallization in sills is well applicable to explain the formation of the layered- and lower foliated gabbro section. This is additionally supported by the occurrence of gabbroic sills, which intrude dunite in the MTZ (e.g., Kelemen et al. 1997; Kelemen and Aharonov, 1998; Korenaga and Kelemen., 1997). These sills are unlikely to be formed by downward suspension flow. The crystallization at depth, with a slight fractionation of host melt, is unlikely to produce a reverse trend of chemical evolution up section at any stratigraphic depth, which is, however, observed within the Wadi Gideah upper foliated gabbro section (see A.5.2.1, A.5.2.2, A.5.3, and A.5.4). It could be assumed that this section instead represents a ~500 m thick transition zone, which combines AML crystallization processes from above (gabbro-glacier like) and fractionating melts from below (sheeted-sills like). This indicates a hybrid accretion model for the complete Wadi Gideah lower crust, similar to the model by Boudier et al. (1996). Some mechanisms of Wadi Gideah hybrid accretion model are discussed in detail in the following:

Lack of mineral zonation in the layered gabbros: It is shown in this study that Wadi Gideah layered gabbro minerals (plagioclase and clinopyroxene) generally have no distinctive chemical zonation (see A.5.3.1, B.5.3.2, and A.5.4). If a chemical zonation is observed, it is weak, independent from depth, unsystematic, and either normal or reversed. It is proposed here that this feature reflects crystallization processes in layered gabbro sill intrusions. Kelemen et al. (1997) and Kelemen and Aharonov (1998), who studied sill intrusions into the MTZ, propose that sill formation may relate to melt trapping below permeability barriers. These barriers could be a consequence of e.g. crystallization of anorthositic bands, reduction of porosity caused by increased crystallization rates for porous flow liquids at a level of pl-cpx-opx saturation, or simple cumulate compaction after melt extraction. Trapped melts accumulate and intrude laterally into adjacent rocks, driven by an increasing sill internal pressure, which is related to the subsequent melt replenishment from below. At some point, the permeability barrier is fractured sufficiently due to the sill internal high pressure, and the trapped melt is ejected. Assuming this scenario for Wadi Gideah sill intrusions, a constant flux of primitive melt would cause a continuous melt flow through the sills, while cumulate precipitates in situ at the margins (Langmuir, 1989). Therefore, the ascending melts would display an overall trend of chemical evolution up section, while precipitated minerals would lack a chemical zonation. Assuming that sills and ascending melt flows form a complex

sequence of replenishment, ejection, and bypassing, the unsystematic normal or reversed mineral zonation could be related to slight variations in the composition of melts passing the sills.

Distinctive changes at the layered/foliated gabbro transition: It can be considered that the degree of crystallization was significantly higher in the lower foliated gabbros in comparison with the layered gabbros. This takes into account that the trend of overall chemical evolution up section becomes very distinctive at the layered/foliated gabbro transition, associated with a sudden decrease in the otherwise constant average grain sizes. Garrido et al. (2001), who also observed the shift in average grain sizes at Wadi Khafifah, proposed that the Wadi Khafifah upper gabbros may have crystallized 1.5 to 2 times faster in comparison with the lower gabbros, in a system with a hydrothermally cooled environment. Maclennan et al. (2004, 2005) did thermal modeling for gabbro-glacier, sheeted-sills, and hybrid models. They combined conductive and deep crust hydrothermal cooling and referred to both EPR (half spreading rate set to 55mm/yr) and also Oman ophiolite. They proposed that the accretion of lower crust in hybrid models is generally possible in terms of heat removal, when taking into account deep crust hydrothermal cooling. The thermal model of crustal accretion displayed a 1.5 to 2 km thick, low temperature zone below the AML, directly at ridge axis, for the assumption that 33 % of the lower crust is formed by gabbro-glacier and 67 % is formed by sheeted-sills model (Fig. A24). The thickness of this low-temperature zone matches generally well the thickness of the Wadi Gideah foliated gabbro section (~1400 m; see A.2.2). This could be evidence for a possibly enhanced crystallization of these gabbros. With the lack of sills in the foliated gabbro section, crystallization takes place directly within the upward melt flow, enhanced by the relatively low environmental temperatures, and with a fast decreasing amount of melt fraction. Therefore, layered gabbro channel-like flow (e.g., Kelemen et al., 1997; Korenaga and Kelemen, 1998) becomes porous-like flow at the layered/foliated gabbro transition. MacLeod and Yaouancq (2000), who investigated the Wadi Abyad profile (Rustaq-Nakhl Massif), proposed that upward trajectory flow (crystal orientation by melt flow) could possibly cause steep foliations observed for foliated gabbros. This might be a consequence of a change from suspension to grain flow (crystals transported in melt and melt flowing through crystal matrix, respectively) with a decrease of melt fraction to <40 %. Since melt upward flow and increasing crystallization rates are assumed for Wadi Gideah lower foliated gabbros here, trajectory flow, as proposed by MacLeod and Yaouancq (2000), could potentially be a
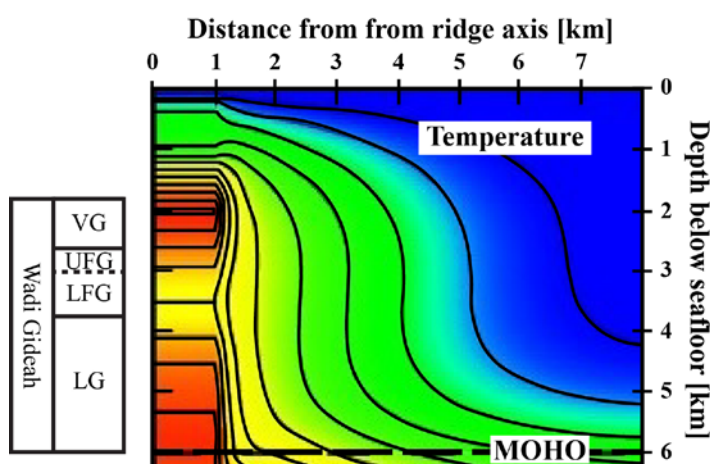
Figure A24. Thermodynamic model from Maclennan et al. (2005) for fast-spreading crust accretion assuming 33% gabbro-glacier at the top and 66% sheeted-sills at the bottom of lower crust, with deep crust hydrothermal cooling. Thermal gradients are steep near ridge axis (red = high temperature and blue = low temperature), with enhanced cooling below the AML at depths similar to the stratigraphic height of Wadi Gideah foliated gabbro section. Abbreviation for Wadi Gideah lithologies follows Table A1.

mechanism for steepening Wadi Gideah mineral foliation.

Reactive porous flow: Lissenberg et al. (2013) published a study on multiple samples from Hess Deep layered- and shallow series, discussing anomalies in mineral core and rim element compositions. The authors observed a difference in the chemical evolution path of mineral cores and rims (Pl An vs. Cpx Mg#) and a poor correlation of clinopyroxene fractionation indices (Mg#, TiO_2, and Cr_2O_3 with rims having up to 1.35 wt% TiO_2). Additionally, they observed a high fractionation of incompatible trace elements in clinopyroxene, with very high zircon enrichment factors (>10), which may even cause a positive Zr anomaly of the calculated rim equilibrium melts in NMORB-normalized diagram. These authors proposed that inter-cumulus melts, continuously evolving by fractional crystallization, may ascend in a reactive porous flow in the lower crust where they heavily affect the compositions of passed mineral rims. As a consequence, mineral rims and cores up section reveal an increased disequilibrium with standard MORB fractionation. The reactive porous flow does not refer to a general lower crust formation model (e.g. sheeted-sills or gabbro-glacier), since only the presence of a cumulus-melt mush is required, independent from a crystal precipitation within the AML or in situ at depth. Geochemical results of this study for Wadi Gideah lower crust reveal no difference in the chemical evolution of mineral cores and rims (see A.5.3.1 and A.5.3.2), covariation of clinopyroxene Mg# and TiO_2 (see A.5.3.2) and no or only poor incompatible trace element fractionation in clinopyroxene (see A.5.4). The highest TiO_2 content from Wadi Gideah lower crust clinopyroxene rims is ~0.82 wt%, with highest EF_{Zr} observed ~3.77. Therefore, it can be assumed that features of Wadi Gideah lower crust mineral (and hence bulk) chemistry relate only to in situ crystallization of ascending melts, with no significant impact of reactive porous flow.

Wadi Gideah varitextured gabbros include many features described by previous authors in terms of petrography and geochemistry (e.g., France et al., 2009; Koepke et al., 2011; MacLeod and Yaouancq, 2000; Nicolas et al., 2008). The gabbros have high variations in grain size, no foliation, an absence of olivine, an appearance of late stage phases, heavy mineral zonation, and enhanced alteration under amphibole facial *P-T* conditions (see A.3.3, A.5.1.3, A.5.2.1, and A.5.2.2). The chemical variation is large, with bulk Mg# from 70 to 42 (letter for gabbro/dike transition). Although Wadi Gideah varitextured gabbros correlate with observations from Oman and modern fast-spreading oceanic crust, some unique features should be noted. First, the Wadi Gideah transition from lower crust layered- and foliated gabbros into AML varitextured gabbros is not distinctive but better described as continuous and smooth in contrast to better defined gabbro/dike transition from AML roof (see A.3.5). This fact, together with changes of chemical trends up section (see A.5), is presumed to represent the gabbro-glacier proportion of a hybrid lower crust accretion. Second, Wadi Gideah varitextured gabbro $^{87}Sr/^{86}Sr$ ratios show a significant increase from lower varitextured gabbro to upper varitextured gabbros (from 0.7035 to 0.7052, respectively), which is coupled to an increase of Sr content (from 153 to 298 ppm; see A.5.2.2). This gives evidence for an increased impact of induced seawater (e.g., Lecuyer and Reynard, 1996), which correlates with the modeled H_2O_{melt} content. H_2O_{melt} is ~0.8 wt% for layered and foliated gabbros below and 0.8 to 1 wt% for sheeted dikes above varitextured gabbros. The difference in H_2O_{melt} content is similar to the modeled 0 to 0.4 wt% water concentrations for

EPR melts from the sheeted dikes section (see A.6). EPR lower crust melts give best results when models were calculated on an anhydrous base. This gives evidence for similar processes of H_2O_{melt} enrichment for Wadi Gideah AML and modern EPR AML. Processes causing H_2O_{melt} enrichment are most likely seawater introduction by synmagmatic normal faulting (Abily et al., 2011), through tensile-stress-driven cracks (Nicolas et al., 2008), or stoping and assimilation of hydrated AML roof material, as proposed by previous authors (e.g., France et al., 2009; Koepke et al., 2008; Wilson et al., 2006) and well displayed by the Gideah South outcrop (see chapter C). Third, the Wadi Gideah varitextured gabbro includes a sample with very primitive bulk compositions (see A.5.2), very primitive mineral compositions (see A.5.3), and clinopyroxene trace element concentrations with a mantle signature. This could be evidence that either minerals, formed near the mantle/crust boundary, were transported into the AML by the ascending mantle derived melts, or that the here proposed complex system of sill intrusions (see above) was indeed bypassed by highly primitive, unfractionated melts, as assumed (see above).

A.7.4 Deep Crust Hydrothermal Cooling

It is revealed in this chapter that the Wadi Gideah lower crust could be related to a hybrid accretion model. The accretion of the layered and lower foliated gabbros is assumed to relate to a sheeted-sills like formation model whereas the accretion of the upper foliated gabbros is assumed to relate to a mix of upward melt flow and minerals subsiding from the AML above (gabbro glacier like model). The heat of crystallization for the gabbro-glacier model could be efficiently extracted by hydrothermal convection in sheeted dike section at the AML roof. Instead, the crystallization in layered intrusions requires an extensive hydrothermal circulation throughout the entire lower crust, down to the Moho, to extract a sufficient amount of heat (e.g., Maclennan et al., 2004). Although thermal modeling for a hybrid model exists (e.g., Maclennan et al., 2004, 2005; Fig. A24), evidence is rare how a significant deep crust cooling should take place at mid ocean ridges. Earlier studies from the southern Oman ophiolite (e.g., Bosch et al., 2004; Manning et al., 2000; Nicolas et al., 2003) described the occurrence of micro crack networks reaching down to the Moho. However, it is unclear if such a permeable network would extract heat efficiently enough to enable deep crust cooling (e.g., Manning et al., 2000). Coogan et al. (2006) studied zones of gabbro in Wadi Abyad and Wadi Namarah (Wadi Tayin Massif), which are highly hydrothermally altered and comprise high temperature veins. These authors propose the veins to represent channels of hydrothermal focused fluid flow (focused fluid flow zones). It was shown that altered gabbros (by them designated as wall rocks) have significantly increased $^{87}Sr/^{86}Sr$ ratios in comparison with well-preserved layered gabbros and decreased Cu content in comparison with the assumed magmatic range. Similar hydrothermal fault zones were observed for the Wadi Gideah lower crust, down to the Moho, for this study. These zones are wider and higher in frequency as the ones reported by Coogan et al. (see B.3.2). Wadi Gideah hydrothermally altered fault zone gabbros (designated as metagabbro in this study) have strong variations in texture, grain sizes into poikilitic range, high temperature amphiboles (formation temperature up to 1000 °C; see A.5.3.4) in and near cross cutting veins, and even appearance of orthopyroxene usually highly uncommon for Wadi Gideah lower crust (see A.5.1). All these characteristics are evidences for high

temperature hydrous partial melting (Koepke et al., 2014). Geochemical results display significantly increased $^{87}Sr/^{86}Sr$ and W/R ratios as well as systematically low Cu content for metagabbros in comparison with adjacent, well preserved layered gabbros. This indicates an increased presence of seawater, which initiated isotopic exchange (since seawater $^{87}Sr/^{86}Sr$ ratio is significantly above magmatic range [e.g. Coogan et al., 2006]) and Cu leaching at relatively high temperatures (as proposed by petrographic features). Coogan et al. (2006) supposed in a rough calculation that a 10 m wide focused fluid flow zone could be capable of cooling ~170 m of adjacent lower crust by 600 °C (see Coogan et al., 2006 for details). Taking into account the appearance of fault zones up to 100 m wide and sometimes down to 100 m in spacing in the Wadi Gideah lower crust, it is proposed here that channeled hydrothermal fluid flow may have been capable to sufficiently extract the heat of deep crust crystallization, required by sheeted-sills accretion model.

A.7.5 Comparison with Other Studies from Southern Oman

The geochemical dataset for the Wadi Gideah profile is unique, since never before all lithologies of especially lower fast-spreading oceanic crust were sampled in such coherency and detail for a single study. However, Wadi Gideah profile is not the first profile, published for the southern Oman ophiolite. Cutting-edge work has been done in 1980´s by authors like Browning, Pallister, and Hopson who published and discussed petrologic and geochemical profiles for e.g. Wadi Bani (also known as Wadi Abyad), Wadi Khafifah, and also Wadi Gideah (e.g., Browning, 1982; Hopson and Pallister, 1981; Pallister and Hopson, 1981). Although field descriptions and petrography were very detailed, geochemical results lacked a sufficient amount of analyzed samples. MacLeod and Yaouancq (2000) complemented the Wadi Abyad dataset. This dataset contrasts the observations from this study, since the Wadi Abyad layered- and foliated gabbros reveal no trend of chemical evolution up section (Fig. A25a). By focusing on mineral compositions, however, it is revealed that Wadi Abyad layered gabbro plagioclases in comparison with Wadi Gideah ones are highly depleted in anorthite content whereas clinopyroxenes reveal only a slight depletion in Mg# (Fig. A.25b).This implies that either Wadi Abyad mantle derived liquids were different in composition or nearly anhydrous in comparison with Wadi Gideah ones. However, the feature is not present in the foliated gabbros. A direct explanation for these deviations cannot be given here. Nevertheless, it has to be noted that Wadi Abyad lower crust has a thickness of only ~2.4 km (which is nearly the size of only Wadi Gideah varitextured- and foliated gabbro section), which might be too thin for normal fast-spreading oceanic crust. It could be argued that Coogan et al. (2014) published a compilation of geochemical profile datasets, obtained so far for southern Oman ophiolite from Wadi Namarah, Wadi Khafifah, and Wadi Abyad (see above), also not showing any trend of chemical evolution up section (Fig. A.25a). However, the data sets (which generally lack a detailed description of the calculation of lithology thicknesses) were normalized to a relative depth from 0 (base of sheeted dike complex) to 1 (base of crust), whereas the origin of some data is unclear. In contrast, Wadi Gideah shows a crustal thickness similar to modern oceanic crust (see A.2.2) with a dataset unique in coherency. Hence, a more detailed study of aforementioned profiles is suggested, to further

enhance our knowledge of fast-spreading crust accretion by correlation and comparison with the observations from Wadi Gideah cross section.

A.7.6 Comparison with Modern Fast-Spreading Oceanic Crust

Most advanced drilling sites for deep see drilling into fast-spreading oceanic crust are Hess Deep and IODP Site 1256D for EPR. Even though data for lower crust is rare from these locations, since only first meters of varitextured gabbro were drilled at IODP Site 1256D and the combination of different drilling sites affects coherency and detailed sample depths within the lower crust for Hess Deep, some conclusions can be made by direct comparison with results from this study. Wadi Gideah bulk and mineral, major and trace element compositions are generally similar to Hess Deep and IODP Site 1256D lower and upper crust (see A.5.2 to A.5.4). This includes that Hess Deep shallow series is generally more evolved in comparison with layered series, and that Hess Deep shallow series reveals normal and reverse trends of chemical evolution up section. However, some exceptions must be made. Hess Deep layered- and shallow series generally have lower plagioclase anorthite content (see A.5.3.1). The negative Nb-Ta anomaly, always apparent for Wadi Gideah lithologies, is absent for both Hess Deep and IODP Site 1256D. Additionally Wadi Gideah crust has a higher $^{87}Sr/^{86}Sr$ ratio. All these features are proposed here to relate to the major difference in the tectonic setting (subduction zone initiation vs. normal mid-ocean ridge; see A.7.2) between Oman ophiolite and drilled EPR fast-spreading oceanic crust. This is well shown by the MELTS calculations in this study, which reveals that drilled lower- and upper EPR crust were formed by nearly
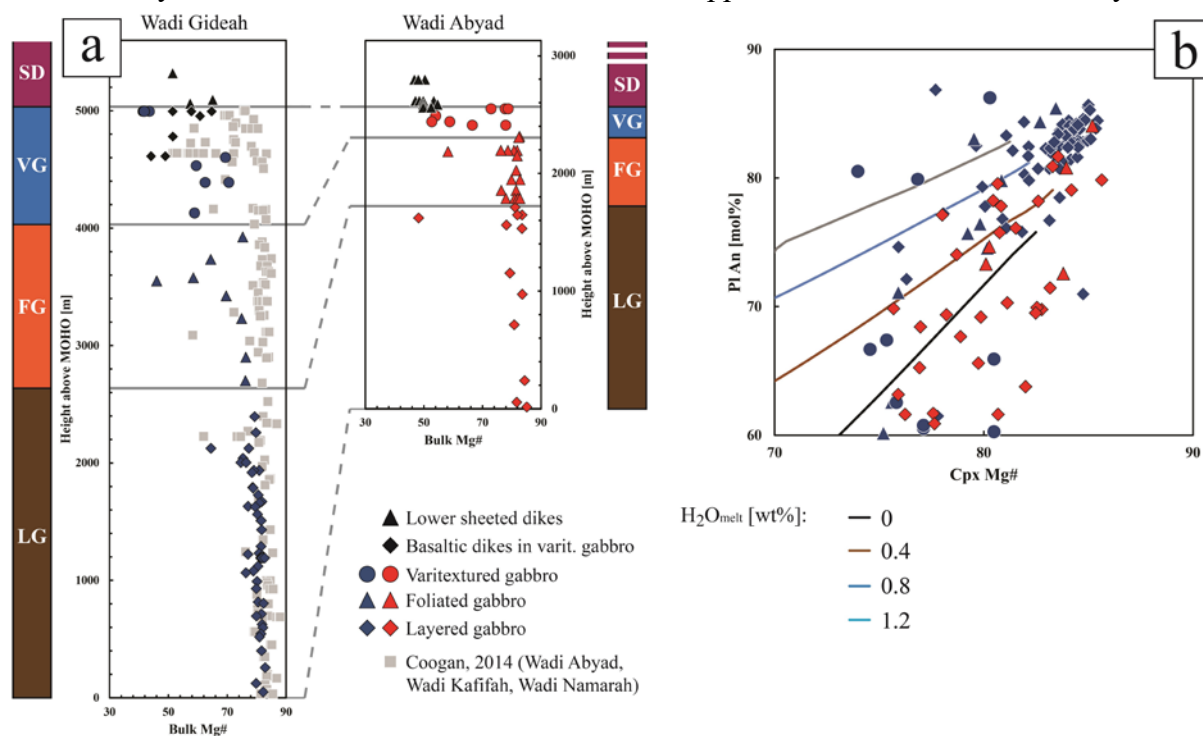
Figure A25. a) Comparison of depth logs with Mg# for Wadi Gideah and Wadi Abyad crust (data from MacLeod and Yaouancq, 2000). The compiled dataset for Wadi Abyad, Wadi Khafifah, and Wadi Namarah from Coogan, 2014, was additionally added to Wadi Gideah depth log (normed to thickness of Wadi Gideah lower crust). Note the difference in lower crust thickness between Wadi Gideah and Wadi Abyad. b) Major element variation diagram with Cpx Mg# vs. Pl An for Wadi Gideah and Wadi Abyad lower crust samples. Added are the liquid lines of descent from MELTS calculation for variation in H_2O_{melt} (see A.6). Abbreviation for Wadi Gideah lithologies follows Table A1.

anhydrous melts (see A.6). In contrast, southern Oman ophiolite crust formed by melts containing ~0.8 to ~1.2 wt% H_2O (in well agreement with MacLeod et al., 2013). It is still uncertain though, why Hess Deep lower crust has orthopyroxene appearance as a general feature, while it is nearly absent in Oman ophiolite lower crust (Gillis et al., 2012) and why reactive porous flow (Lissenberg et al., 2013) is not displayed for Wadi Gideah (see A.7.3). These questions may be answered by further study of the Wadi Gideah, the modern ERP crust (by drilling), and by further comparison of the obtained datasets.

A.8 Conclusion

The previous sections discussed the formation of the Wadi Gideah lower crust, based on petrological and geochemical observations described in this chapter. To summarize, petrography, bulk and mineral major and trace element chemistry, bulk isotopy, and petrological modeling give evidence for a hybrid accretion model (Fig. A26), in a tectonic setting of subduction initiation:

Crystallization at depth. Observations from this study give evidence that most of the Wadi Gideah lower curst (layered and lower foliated gabbros) were formed by crystallization at depth, rather than by downward suspension flow. Major and trace elements reveal a normal, overall trend of chemical evolution up section, slight in the layered gabbros, but becoming much more distinctive in the lower foliated gabbros directly at the layered/foliated gabbro transition. The trend can be reproduced well by modeling hydrous fractional crystallization (~ 0.8 wt% H_2O) in a system that is chemically similar to Wadi Gideah. The change in trend intensity at the layered/foliated gabbro transition is associated with a shift to lower average grain sizes, a change in mineral foliation from parallel to perpendicular to mantle/transition, and an absence of sill intrusions. The overall trend of chemical evolution is superposed by cycles of element covariation in layered gabbro minerals, which lack a systematic and distinctive chemical zonation. All these features imply crystallization at depth since they are unlikely to derive from downward suspension flow. It is assumed here that layered gabbro accretion is related to a complex system of multiple sill intrusions, connected and bypassed by ascending mantle derived melts (Fig. A26a, b). Gabbros show an overall chemical evolution, with systematic chemical zonation absent, since crystallization took place in situ near the sill margins at a constant flux of ascending melt (Fig. A26a). The layered/foliated gabbro transition represents a significant change in environmental parameters. Here it is assumed that there is enhanced hydrothermal cooling below the AML, based on thermal modeling (e.g., Maclennan et al., 2004) and similar observations from former studies (Garrido et al., 2001), forcing faster crystallization and smaller grain sizes (Fig. A26e). The steepening in mineral foliation may derive from trajectory flow, as proposed by MacLeod and Yaouancq (2000), since minerals no longer crystallized in sills but directly from the ascending melt, in a system with a rapidly decreasing melt proportion. It is noteworthy that no clear evidence for this process can be given here, except for the verification of mineral crystallization from an ascending melt. Steep foliation of lower foliated gabbros derived by downward suspension flow is unlikely, since neither the absence of magmatic late stage phases nor the chemical evolution up section are compatible with this process. However, downward suspension flow is not excluded from Wadi Gideah lower crust formation. Upper foliated gabbros show a reversed trend of chemical evolution up section associated with the presence of magmatic late stage phases. Hence, upper foliated gabbros could represent a ~500 m thick transition zone with both ascending melt flux and subsiding minerals precipitated in the AML above (Fig. A26f). In summary, it is proposed here that theWadi Gideah lower crust accreted in a model

similar to other hybrid models (e.g., Boudier et al. 1996), with most of the lower crust related to crystallization at depth with additional downward suspension flow at the very top.

Deep crust hydrothermal cooling. Lower crust hydrothermal cooling, required for sheeted-sills-like model, may have been facilitated by channeled hydrothermal flow down to the mantle/crust boundary (Fig. A26c). These zones are preserved at Wadi Gideah as up to 100 m wide hydrothermal fault zones (Coogan et al., 2006), which are closely spaced and cut across the layered gabbro foliation (Fig. A26d). Heavily altered metagabbros (former layered gabbros) show very high $^{87}Sr/^{86}Sr_{ini}$ (up to 0.7046) in comparison with well-preserved host rocks. Additionally, strong variations in grain size, high temperature primary amphibole, and the presence of orthopyroxene all provide evidence for high temperature hydrothermal fluid/rock interaction. Referring to the back-of-the-envelope calculation of Coogan et al. (2006), Wadi Gideah hydrothermal fault zones were wide and frequent enough to presumably extract the latent heat of deep crust crystallization. However, a detailed calculation or thermal modeling cannot be given here.

Tectonic setting. Observations from this study give evidence for a crustal accretion in a tectonic setting of subduction initiation (Fig. A26d). Evidence is given by the presence of a distinctive negative Nb-Ta anomaly in all Wadi Gideah lithologies, Nb/Yb vs. Th/Yb classification showing a shift of Wadi Gideah lithologies away from normal mid-ocean ridge magmatism to subduction initiation, and an enriched water content of ~0.8 wt% for Wadi Gideah lower crust forming melts. These observations are supported by a significantly higher lower crustal $^{87}Sr/^{86}Sr_{ini}$ in comparison with lower crust from modern EPR, as well as high F (related to magmatic formation) and Cl (related to secondary interaction with seawater derived fluid) contents of lower crust high temperature, magmatic amphiboles. An impact of hydrothermal alteration can be excluded, since layered gabbro alteration is relatively low, calculated W/R ratios are only ~0.81, $^{87}Sr/^{86}Sr_{ini}$ shows no covariation with Sr content, and neither $^{87}Sr/^{86}Sr_{ini}$ nor Cl in amphibole show any increase up section. Therefore, mantle derived ascending melts must have been affected by subduction zone fluids before the crystallization of Wadi Gideah lower crust.
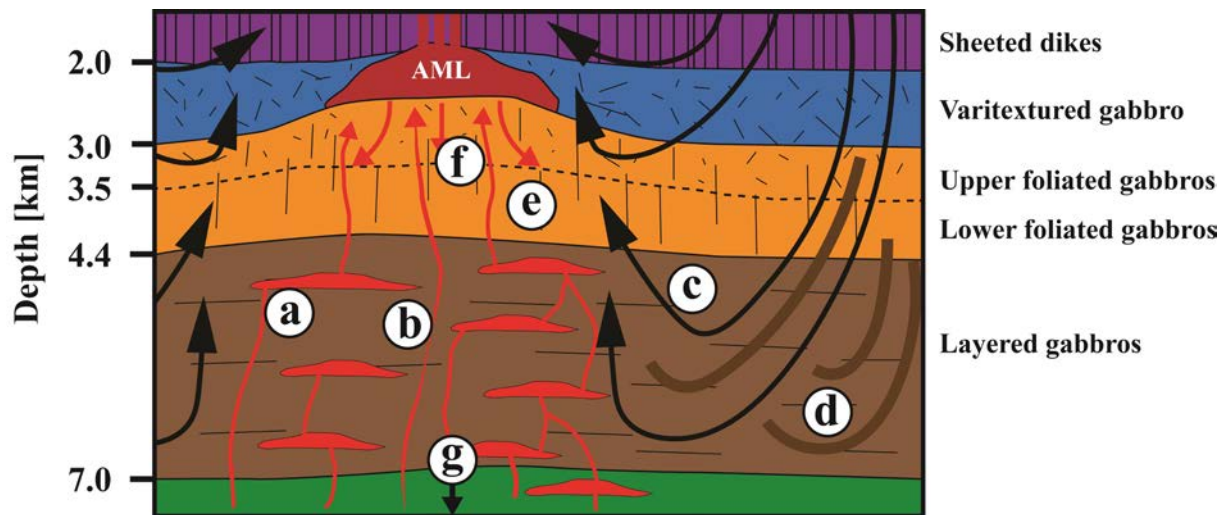
Figure A26. Schematic cross section for the supposed magmatic system during formation of Wadi Gideah lower fast-spreading mid-ocean ridge crust. The depth is based on the thickness of Wadi Gideah lithologies (Table A1). Black lines represent the foliation, which is parallel to the mantle/crust boundary for the layered gabbros, perpendicular to the mantle/crust boundary for the foliated gabbros, and isotropic for the varitextured gabbros. a) Formation of the layered gabbros by in situ crystallization in sills. The sills are connected and bypassed by replenishing melts. b) Primitive mantle melts can bypass all sills to directly feed the AML. c) Latent heat of crystallization is extracted by channeled hydrothermal flow down to mantle/crust boundary. d) The former hydrothermal channels are preserved as zones of heavily altered, former layered gabbros, which show evidence for high temperature partial melting. e) Hydrothermal cooling of the lower crust causes a low temperature zone below the AML (e.g. Maclennan, 2004) forcing faster crystallization of the lower foliated gabbros. f) Upper foliated gabbros represent a transition zone with both ascending melt flux and subsiding minerals precipitated in the AML above. g) Wadi Gideah lower crust is accreted in a setting of subduction initiation with H_2O_{melt} of ~0.8% for the mantle derived melts. See text for further discussion. The formation setting is similar to the mixed settings proposed by former studies (e.g., Boudier et al., 1996) but assumes a downward suspensions flow only for first few hundred of meters below the AML.

Chapter B

Implications for the Crustal Accretion at Fast-Spreading Mid-Ocean Ridges:

Crystallographic Preferred Orientations from the Wadi Gideah Cross Section

B.1 Introduction

Chapter A focused heavily on geochemistry (supported by petrological observations) to identify stratigraphic variation of especially the Wadi Gideah lower crust. It was assumed that Wadi Gideah layered and lower foliated gabbros were formed by deep crystallization. The upper foliated gabbro section was formed instead by suspension flow of minerals precipitated within the AML possibly interacting with melt upward flow feeding the AML. Hence, a hybrid formation for Wadi Gideah lower crust was proposed (see A.7.7). Hydrothermal cooling required by deep crust crystallization was assumed to be given by deep crust channel hydrothermal fluid flow as a major process. Remnants of these flows are preserved and exhibited at Wadi Gideah today in form of up to hundred meter wide zones containing heavily altered former layered gabbro. These metagabbros, superposed by intense greenschist facies alteration, display the appearance of high temperature magmatic amphibole (up to 1000°C), high temperature partial melting, varitextured domains, and orthopyroxene (uncommon for Wadi Gideah lower crust; see A.5.1).

However, in addition to geochemistry, the variability of mineral crystallographic preferred orientation (CPO) with depth can give further evidence for lower crust accretion. Unfortunately, cross-sections though complete lower fast-spread oceanic crust are rare. They are even nonexistent for deep see drilling at all since the only dilled fast-spread crust, at Hess Deep, returned short sections from multiple holes. The only three major publications for southern Oman ophiolite are from Morales et al. (2011), Nicolas et al. (2009) and Van Tongeren et al. (2015). Morales et al. (2011) and Nicolas et al. (2009) studied multiple small cross sections from the gabbro/dike transition to a few hundred meters below. They interpret their results as evidence for gabbro-glacier flow in the upper gabbros. Van Tongeren et al. (2015) studied a cross section through the lower crust (Wadi Khafifah), and sheeted-sills model for the formation of layered gabbros. They proposed the steepening of the foliated gabbro crystal foliation to be possibly related to upward melt migration as proposed by MacLeod and Yaouancq (2000). In this study the availability of a large number of samples from all lithologies of Wadi Gideah lower crust was used to investigate crystal CPO's in terms of depth in greater details.

I focus on plagioclase CPO in this chapter as they are the main constituent phase. Plagioclase has a triclinic symmetry, and its CPO is best described by the pole figures of the [100] axis, the (010) planes, and the (001) planes. The aspect ratio of plagioclase grains is most cases relatively high, with elongated along a-axes [100] and short b-axes [010]. Hence, due their tabular shape, plagioclase generally display a point maximum of (010) poles-to-planes (defining the foliation) with a preferred orientation of [100] that varies from a point (lineation) to a girdle maximum for magmatic flow (Axial-B to type P CPOs; Satsukawa et al., 2013). CPOs resulting from plastic flow are more variable in style, with all possible combination of the Axial-B, P type, and Axial-A styles (Satsukawa et al., 2013). CPO of plagioclase should record any variation of intensity with depth, which is expected for example if crystals have been involved in increasing sub-magmatic and/or crystal-plastic flow with

depth (as predicted by the gabbro-glacier model). In this chapter, I present the plagioclase CPO from a subset of 48 samples from Wadi Gideah, and discuss these results in comparison with aforementioned studies, and with the petrology and geochemistry results presented in the previous chapters.

B.2 Methods

B.2.1 Sample Selection and Preparation

In order to identify and quantify the plagioclase CPOs in the lower crust of the Wadi Gideah profile, 48 samples (Fig. B1) were analyzed by electron backscatter diffraction (EBSD). They include 7, 8, and 33 samples from the varitextured gabbro, foliated gabbro, and layered gabbro sections, respectively (Table 13, appendix). The average distance between two sample locations in the profile is ~107 m, though generally lower for layered and higher for foliated and varitextured gabbros. Thin sections were re-polished at Geosciences Montpellier.
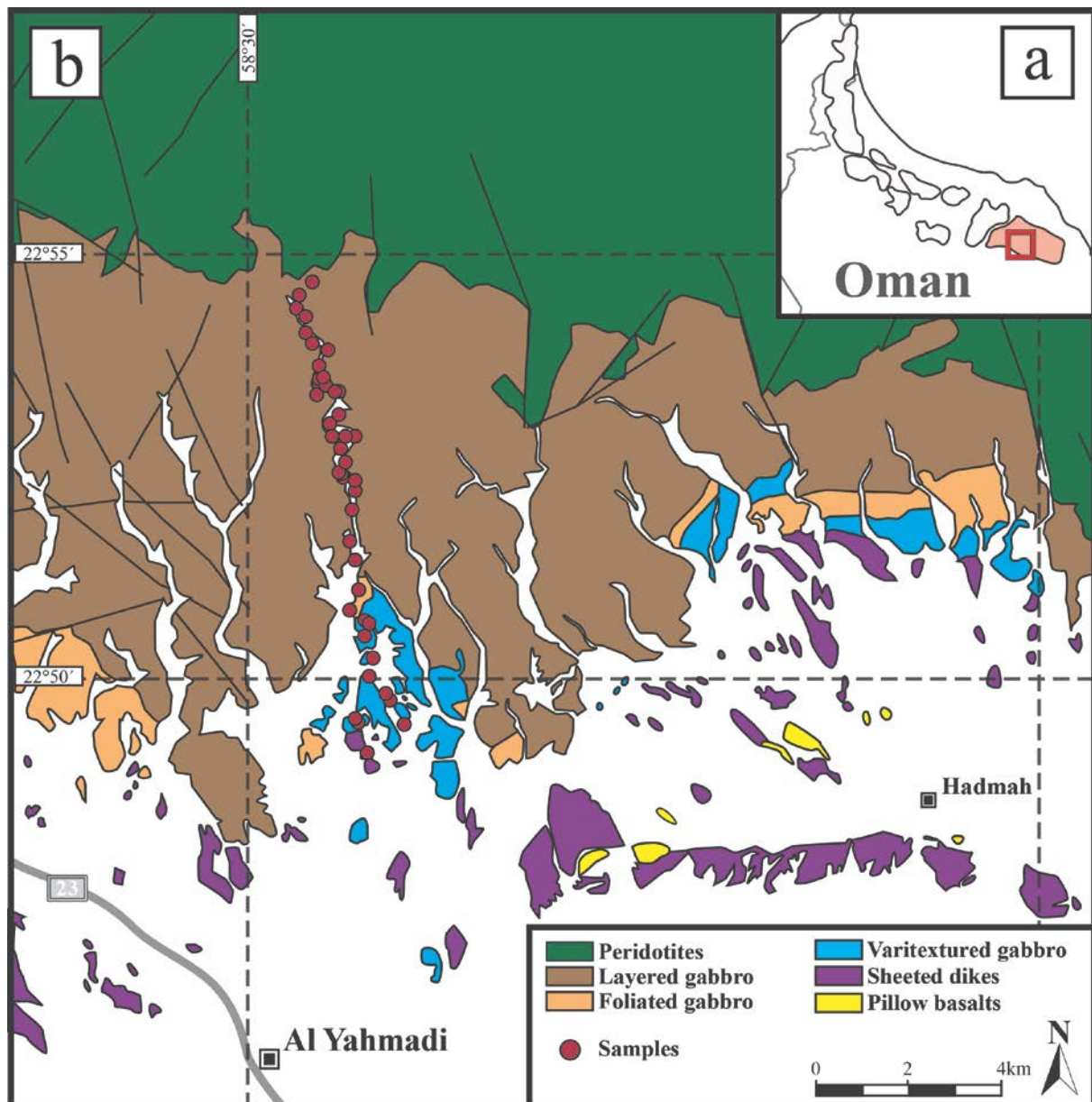
Figure B1. a) Sketch of the Oman ophiolite after Nicolas et al., 2000a and b) geological map of Ibra and Wadi Gideah area after Peters et al. (2008). The figure is equal to Fig. A1, except for marked sample positions, which indicate here only locations for samples analyzed by EBSD.

B.2.2 EBSD Analysis

EBSD was done at Geosciences Montpellier. A JEOL JSM 5600 scanning electron microscope (SEM) with a Tungsten filament source (accelerating voltage 15 kV) was used with a 70° tilted eucentric x-y sample stage. The system is equipped with Oxford/Nordlys EBSD detectors; the diffraction patterns were collected and processed using the Channel 5® suite of programs. The EBSD map step size varied between 14 and 30 μm, depending on the sample average grain size. Minerals taken into account for indexing were plagioclase (bytownite; Pl), clinopyroxene (diopside; Cpx), orthopyroxene (enstatite; Opx), olivine (forsterite; Ol), magnetite, ilmenite (combines with magnetite to "oxides"; Ox), hornblende (Hbl), and actinolithe (Act). The RAW data contained indexed pixels with a mean angular deviation (MAD; angular difference between the acquired diffraction pattern and the indexing solution proposed by the acquisition software) <1.3°. The RAW data indexing rate was between 50 % and 80 % excluding two heavily altered samples (OM10_Gid_A11 and OM12_Gid_A035). Thin sections were not carbon-coated; they were mounted on the sample holder with conductive carbon tape. The RAW data was post-processed in Channel 5 ® suite´s Tango software to enhance data quality by extrapolating well indexed neighboring points (minimum of 5 neighbors) to non-indexed points and removing isolated pixels, correcting for pseudosymmetry in olivine, and removing grains smaller than four times the related analysis step size. Pole figures can be calculated using either the grid data set from EBSD mapping, or the average crystallographic orientation for each grain. Grains were identified assuming that a misorientation >10° between two adjacent pixels of the phase represented a grain boundary. The average crystallographic orientation was preferred here to calculate the pole figures to avoid the overrepresentation of larger grains when the grain size distribution is heterogeneous at the thin section scale. An open source MatLab toolbox was used for analyzing and modeling CPO (Hielscher and Schaeben, 2008; Bachmann et al., 2010). MTEX was used to calculate J-Index of both pole figures (pfJ) and the orientation distribution function (ODF J), using the grid data. PfJ represents the distribution density of the principal crystallographic axis in a pole figure and ODF J the CPO strength based on the distribution density of crystal orientations within the sample (e.g. Bunge, 1982; Mainprice and Silver, 1993). Both vary from 1 to infinity, for random distribution to single crystal, respectively. To define pole figure symmetry P- (Point), G- (Girdle), and R- (Random) indexes were calculated with $P=\lambda_1-\lambda_3$, $G=2(\lambda_2-\lambda_3)$, and $R=3\lambda_3$. P and G were then used for calculating the plagioclase BA-Index defined as $0.5*(2-(P_{(010)}/(G_{(010)}+P_{(010)}))-(P_{[100]}/(G_{[100]}+P_{[100]})))$ to characterize (010) and [100] pole figure symmetry (Mainprice et al., 2014; Satsukawa et al., 2013; Vollmer, 1990). BA-index of 0 refers to a perfect oblate Axial-B fabric (planar), of 0.5 to a perfect P-type fabric, and 1 to a perfect prolate Axial-A fabric (linear). The classification for CPO into Axial-A, Axial-B, and P-type fabric is defined in Satsukawa et al. (2013). A pole figure Axial-A fabric is defined by a point maximum in [100] with perpendicular girdle distributions of (010) and (001), an Axial-B fabric is defined by a point maximum in (010) and perpendicular girdle distribution of [100] and (001), and an Axial-P fabric is defined by point maxima in [100], (010), and (001). Samples with a CPO that result from magmatic flow very commonly display an Axial-B, or a combination of Axial-B and P-type CPO.

B.3 Results

B.3.1 Modal Proportion and Grain Size

Varitextured gabbro samples display average modal amounts of 72.2±18.7 % Pl, 9.9±9 % Cpx, 0.5±0.8 % Opx, 0.4±0.7 % Ox, 8.8±5.9 % Hbl, and 8.1±5.9 % Act normed to 100 % after excluding 36±7 % of not indexed area (NI), foliated gabbro samples display average modal amounts of 59.2±6.1 % Pl, 34.9±5.2 % Cpx, 0.4±0.5 % Opx, 0.2±0.5 % Ox, 3.2±3.4 % Ol, 1.3±1.3 % Hbl, and 0.7±0.5 % Act normed to 100 % after excluding 26.2±5.3 % NI, and layered gabbro samples display average modal amounts of 56.8±11.4 % Pl, 38±12.3 % Cpx, 0.3±1.1 % Opx, 4.1±4.3 % Ol, 0.5±0.8 % Hbl, and 0.4±0.7 % Act normed to 100 % after excluding 26±10.9 % NI (Fig. B2) shown by post-processed RAW mapping data (not 1ppg). It is noticeable that orthopyroxene is generally present only in very small amounts. The general absence of orthopyroxene in the lower crust is well known for the southern Oman. Contrasting observations were made at Hess Deep. There it is present in higher proportions, leading to a relatively high amount of gabbronorite for the Hess Deep sample suit (e.g., Gillis et al. 2014). Varitextured gabbro samples display an average mean grain size of 184 µm for Pl, 151 µm for Cpx, and 93 µm for Ol. The average maximum grain size is 1324 µm for Pl, 735 µm for Cpx, and 124 µm for Ol. Foliated gabbro samples display an average mean grain size of 247 µm for Pl, 259 µm for Cpx, and 231 µm for Ol. The average maximum grain size is 1556 µm for Pl, 1224 µm for Cpx, and 778 µm for Ol. Layered gabbro samples display an
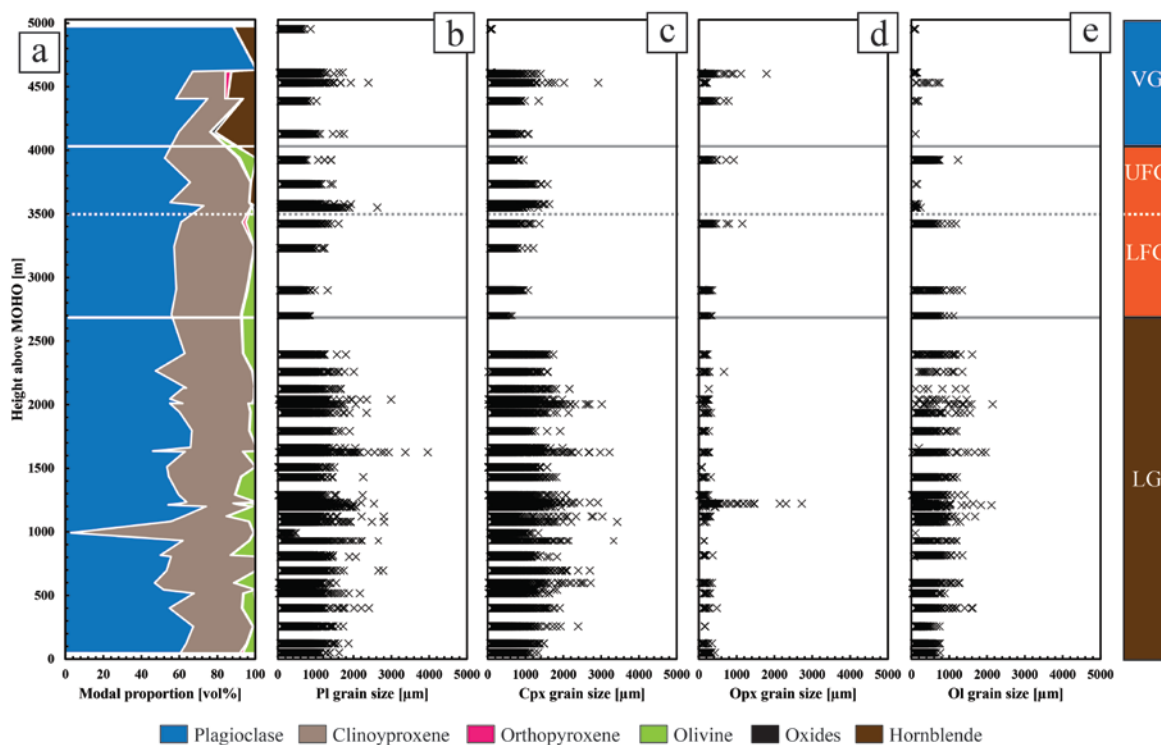
Figure B2. a) Modal proportions of primary phases for Wadi Gideah samples with depth, determined by EBSD analysis b-e) Grain sizes for a) Pl, b) Cpx, c) Opx, and d) Ol of Wadi Gideah samples with depth. Each cross represents a single grain. Grains were determined by EBSD data, assuming that misorientation above a 10° threshold between two adjacent pixels represent a grain boundary. Abbreviation for lithologies follows Table A1.

average mean grain size of 320 μm for Pl, 460 μm for Cpx, and 371 μm for Ol. The average maximum grain size is 2094 μm for Pl, 2141 μm for Cpx, and 1180 μm for Ol. While the variation of average and maximum mineral grain sizes is independent from sample depths for single lithologies, a significant stepping (see Garrido et al., 2001) is observed at the lithology transitions (Fig. B2).

B.3.2 CPO Symmetry and Strength

Varitextured gabbro plagioclases show an average pfJ of 1.19±0.2 for [100], 1.29±0.35 for (010), and 1.07±0.08 for (001). Foliated gabbro plagioclases have an average pfJ of 2.02±0.82 for [100], 2.98±1.99 for (010), and 1.4±0.38 for (001). Layered gabbro plagioclases show an average pfJ of 2±0.72 for [100], 2.31±0.94 for (010), and 1.24±0.27 for (001). A slight shift in average pfJ intensity is revealed for varitextured and foliated gabbros. However, a continuous, distinctive change of plagioclase pfJ down section is not observed (Fig. B3a-c). Plagioclase pole figures display a systematic P-type fabric (point maximum in [100], (010), and (001)) for varitextured and upper foliated gabbros changing rapidly to Axial-B fabrics (point maximum in (010) and girdle in [100] and (001)) at the upper to lower foliated gabbro transition (Fig. B4). The fabric changes smoothly towards Axial-A type down section (point maximum in [100] and girdle in (010)) at medium level of the layered gabbro section (Fig. B4). Clinopyroxene pole figures reveal a correlation, typical for magmatic flow, with Cpx (010) parallel to Pl (010) and Cpx [001] parallel to Pl [100] (Fig. B5). The transitions are well quantified by the plagioclase BA-index (Fig. B3d). The BA-index is relatively stable for the varitextured and upper foliated gabbro section (0.39±0.13) and rapidly decreases at the upper to lower foliated gabbro transition (0.07 for OM10_Gid_A18_1). Below, the BA-index increases continuously (up to 0.5±0.09 for the lower 600 m of layered gabbro section). The CPO strength, quantified here using the ODF J index, regularly increases down section from top of the varitextured gabbros to bottom of layered gabbros (Fig. B3e). The ODF J-index for clinopyroxene has also been calculated (Fig. B3f). There is a clear distinction between the upper part of the lower crust (varitextured and foliated gabbros), in which J tends to decrease down section, with more scattering in the varitextured gabbros, and the lower part of the lower crust (layered gabbros), in which J is much higher in average, and much more scattered (Fig. B3f). The transition from foliated to layered gabbros is marked by a pronounced change in the Cpx fabric strength.
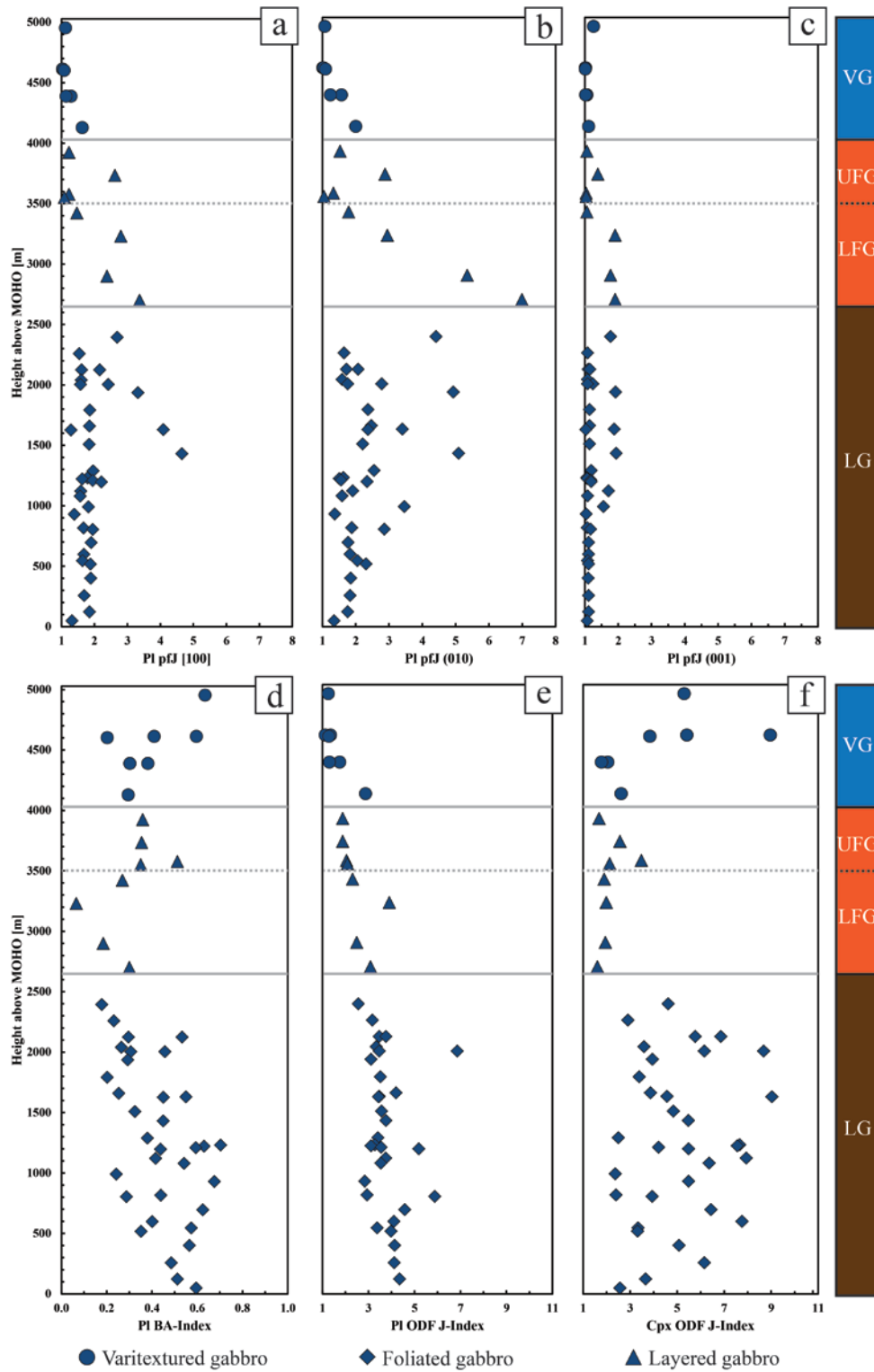
Figure B3. a-c) Plagioclase pfJ for a) [100], b) (010), and c) (001) with depth. d) Plagioclase BA-index with depth. e) Plagioclase fabric strength, quantified by ODF J, with depth. f) Clinopyroxene fabric strength, quantified by ODF J, with depth.
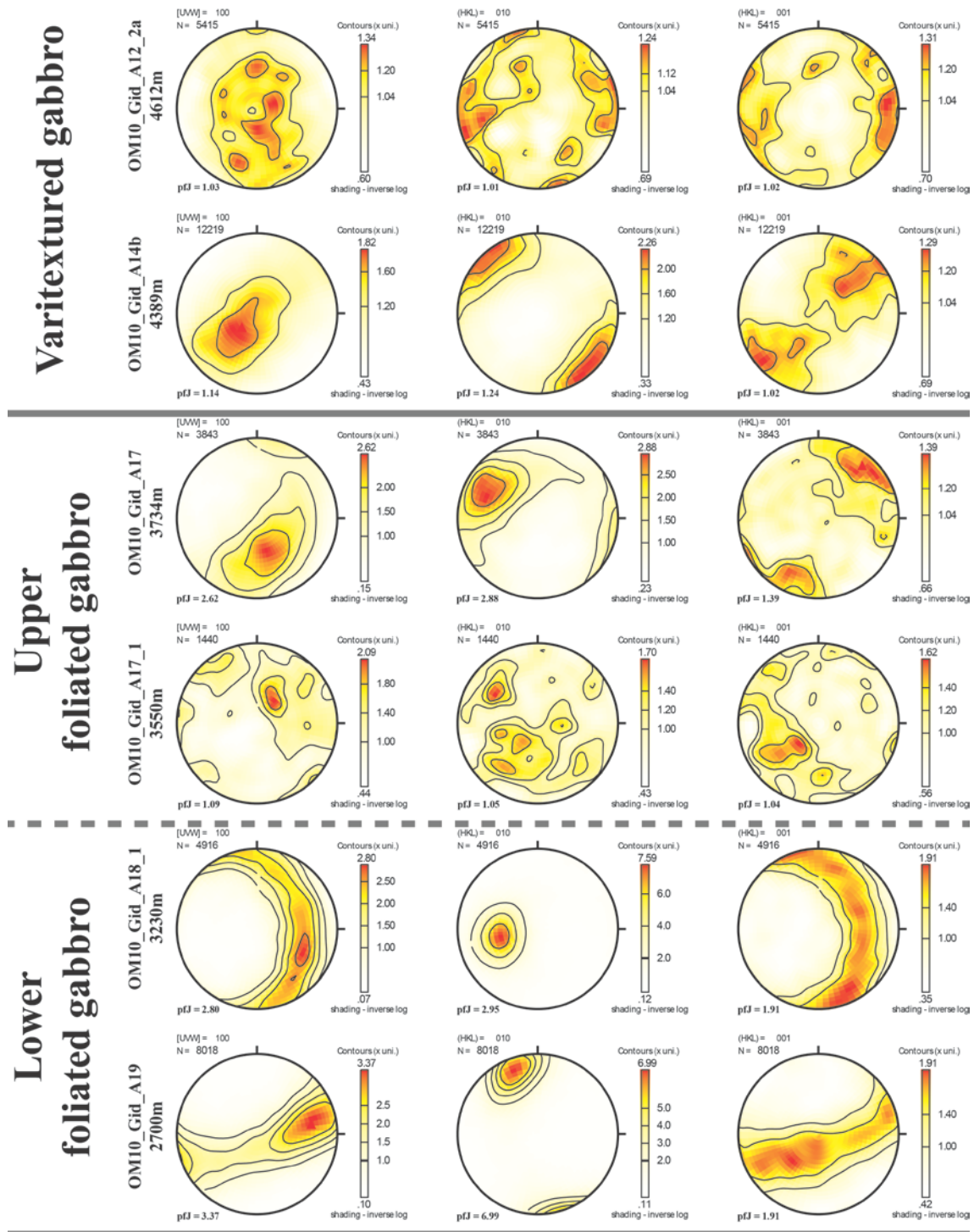
Figure B4. Crystallographic preferred orientation of plagioclase [100] axes and poles to (010) and (001) for representative samples arranged for depth. Lower hemisphere. N is the number of measurements. MAD <1.3°. The calculated pfJ is added.
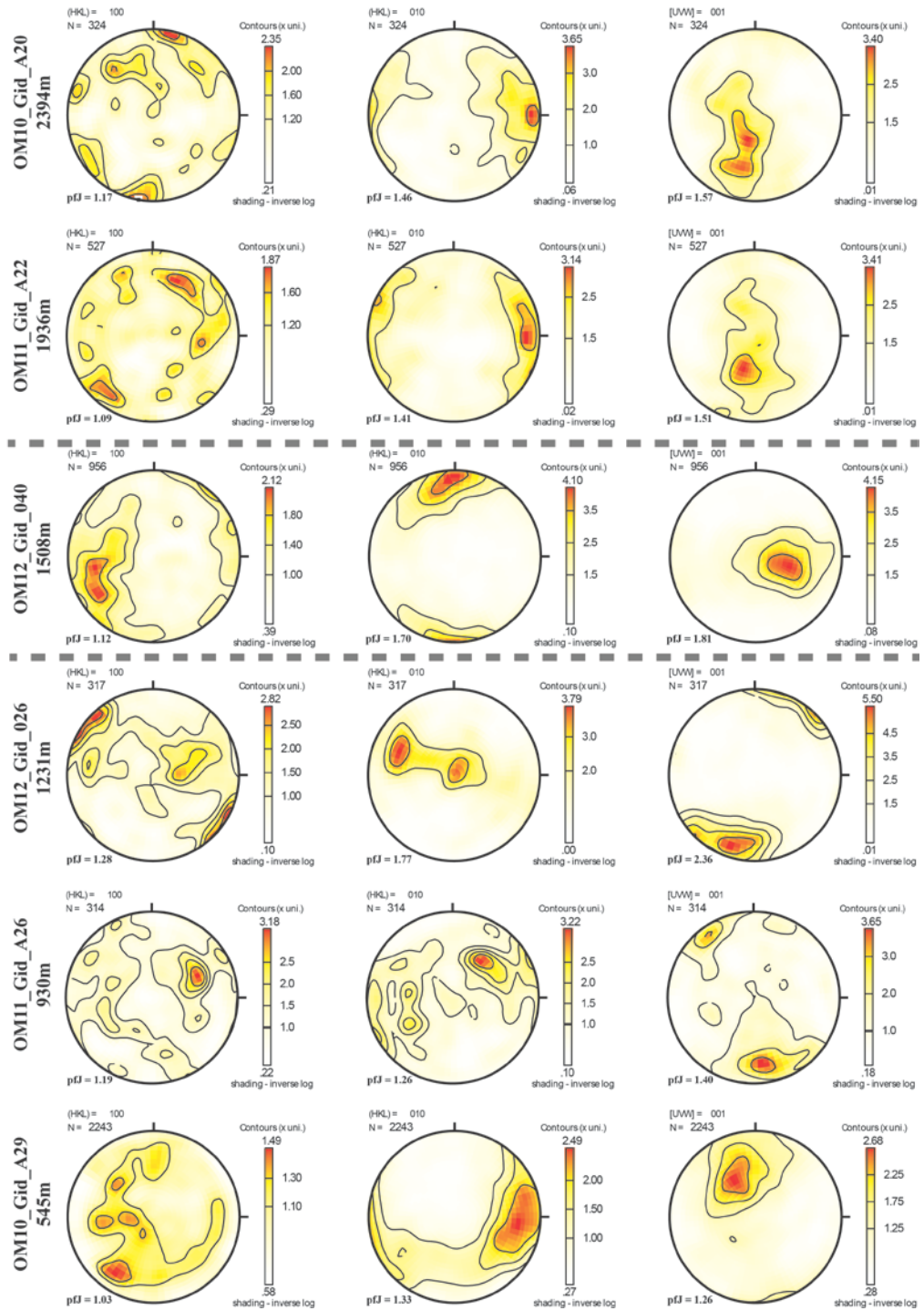
Figure B4. *continued*
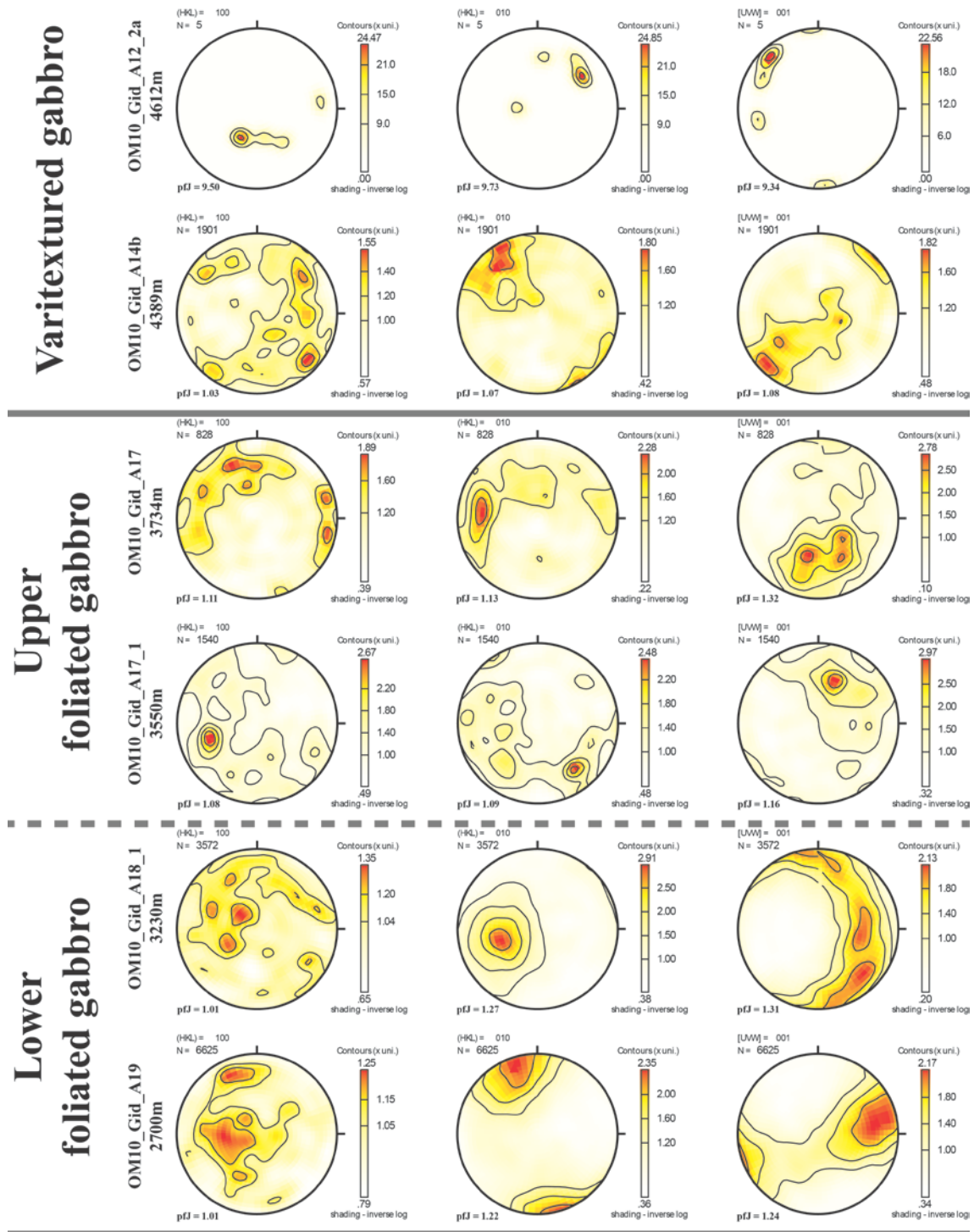
Figure B5. Crystallographic preferred orientation of clinopyroxene poles to (100) and (010) and [001] axis for representative samples arranged for depth (same samples as for Fig. B4). Lower hemisphere. N is the number of measurements. MAD <1.3°. The calculated pfJ is added.
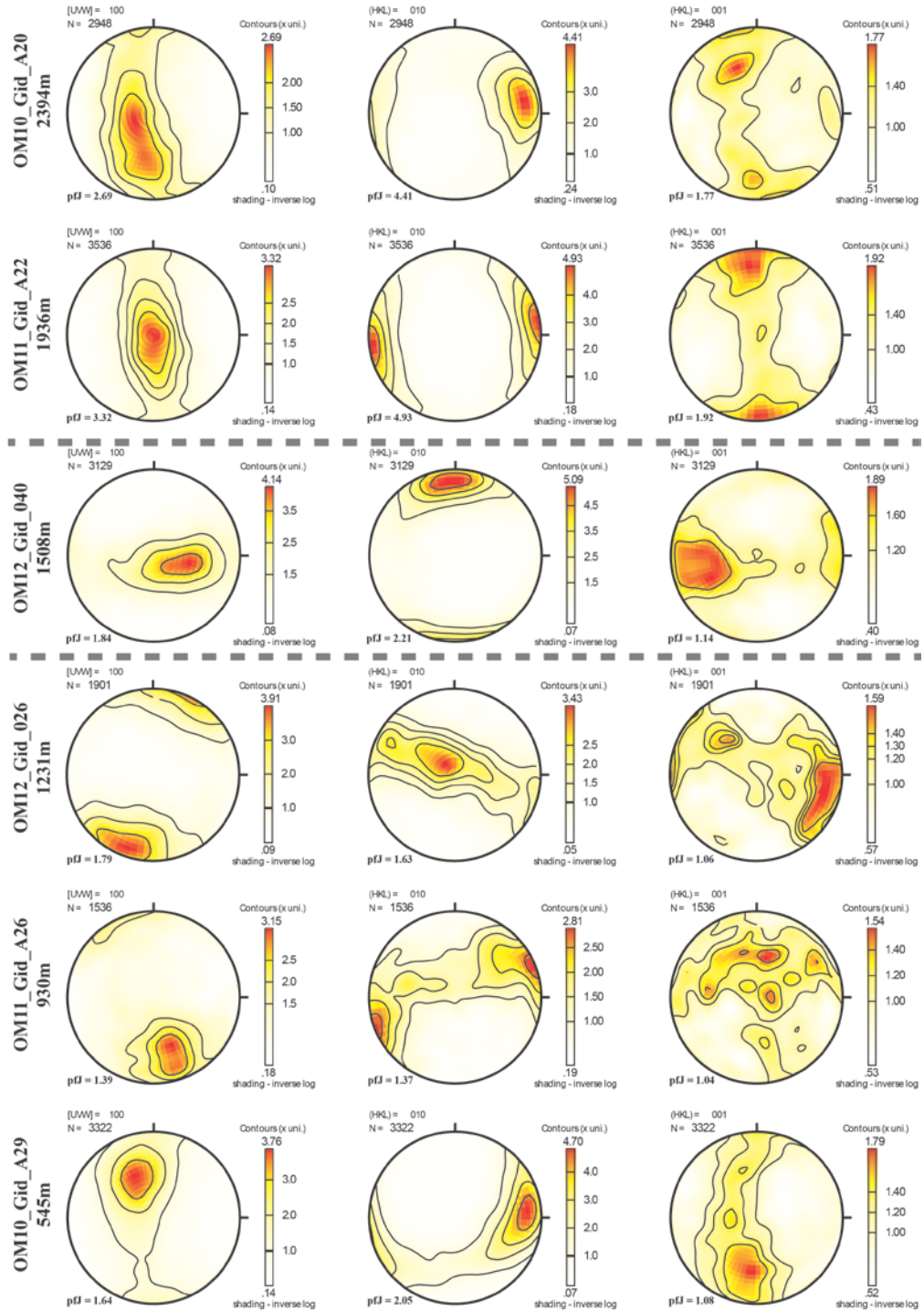
Figure B5. *continued*

B.4 Discussion

B.4.1 CPO Variation with Depth

The continuous increase of the plagioclase J-index down section (Fig. B3e) could be used as an argument to support a gabbro glacier model. However, it should be noted that the range of J-index values (from 1.1 to 6.8, with a mean of 3.2) remains relatively modest, and that there is no significant increase of solid-state, crystal-plastic deformation down section. The absence of significant crystal-plastic deformation (and hence the confirmation that the textures and fabrics are magmatic) is confirmed by the very low misorientation inside the grains, which never exceeds an average of 0.5° (average misorientation to the mean orientation of the grain) in plagioclase, clinopyroxene, or olivine. A down section increasing strength, as predicted by the numerical models (e.g., Phipps Morgan and Chen, 1993), would probably result in either stronger magmatic fabrics (the plagioclase J-index of strong magmatic fabrics reported in the compilation of Satsukawa et al. [2013], commonly extend to values of ~10) or progressively stronger misorientation in the grains if flow was accommodated by crystal-plastic deformation. This is not observed; hence it is difficult to reconcile the observed down section overall J increase with a simple gabbro glacier model. Several other observations are unlikely to be consistent with a continuous downward flow model, and call for combining several processes at the scale of the studied section:

(1) The average and maximum grain size of major mineral plagioclase, clinopyroxene, and olivine display no trend of continuous increase down section but only a single shift directly at the layered- to foliated gabbro transition (see B.3.1, Fig. B2b-e). This decoupling of layered- and foliated gabbros favors a rapid change or modification of the formation processes.

(2) Clinopyroxene ODF J displays no obvious trend of continuous increase down section but a shift at the layered- to foliated gabbro transition with higher values for layered gabbros, and also much stronger scattering (see B.3.2, Fig. B3f). In particular, the high scattering of J values in the lower gabbro section favors a strong dependence of mineral and texture on local factors (rather than a single crustal section-scale predominant process).

(3) Plagioclase pfJs in the lower foliated gabbro section are different from those in the varitextured, upper foliated, and layered gabbro section. They are relatively higher with values >2 for the [100], (010), and (001). More generally, there is a general increasing trend for the three pfJs downsection to the bottom of the foliated gabbros, also shown by the plagioclase ODF J-index (Fig. B3e). It has to be noted though that only this three samples of the sample suit display that behavior. However, this progressive increase could result from downward flow of a magmatic mush (e.g., Morales et al, 2011; Nicolas et al., 2009). Nevertheless, this interpretation cannot extend beyond the base of the foliated gabbro section. Alternatively, the plagioclase preferred orientation in the upper part of the profile could be related to upward melt flow as proposed by MacLeod and Yaouancq (2000), with minerals aligned by the

melt flow in a porous flow like regime. However, the reason for a decreasing intensity upward in this scenario is unclear.

Now assuming mineral crystallization in sills in the lower, layered gabbros, the end-member sheeted sill model fails to explain the progressive increase of plagioclase CPO strength. A possible explanation could arise from considering the impact of active mantle flow at fast-spreading mid ocean ridges. Jousselin et al. (2012) did a detailed study on gabbro lenses from MTZ of Maqsad Diapir region observing four types of gabbro: unlayered with random fabric (type 1); weak shape fabric and planar CPO defined by plagioclase (010) axis (type 2); strong shape with linear CPO defined by plagioclase [100] axis (type 3); and very strong fabric with linear CPO defined by plagioclase [100] axis (type 4). These authors defined type 2 to relate to compaction (pure shear), type 3 to increased simple shear in a suspension flow, and type 4 to high simple shear at the magmatic-plastic flow transition (where melt fraction becomes too low for suspension flow). Jousselin et al. (2012) described the impact of mantle flow along a flow line parallel to the Moho in the Mantle Transition Zone. In Wadi Gideah, we may see the impact of active mantle flow upward, with progressive increase of J down section (Fig. B3e). The upper layered gabbros hence would record simple compaction pure shear with an increasing influence of magmatic suspension flow and/or upward melt percolation down section. Assuming that the lower crust J index reflects an impact of active mantle flow, however, continuity between both, mantle and crust, is required. This is supported by previous authors like Ceuleneer et al. (1998), Jousselin et al. (1998), and Ildefonse et al. (1995). These authors clearly displayed that the lower crust cumulate mixture suffered a shear flow impacted by below mantle plastic flow, based on observations from the Maqsad diapir area (Jousselin et al.) and Hilti Massif (Ildefonse et al.), or on compiled observations from all asthenospheric flow pattern recognized in Oman mantle peridotites and above gabbros (Ceuleneer et al.). Hence it is here proposed that Wadi Gideah profile may record the impact of active mantle flow, not only at the MTZ level as suggested by Van Tongeren et al. (2015), but also above, with a much weaker gradient (Fig. B6).

The textural observations and CPO characteristics reported here support the hybrid formation model (e.g. Boudier et al., 1996) already derived from the geochemical and petrological study (see A.7 for detailed discussion and description):

(1) The upper foliated gabbro section can be regarded as a ~500 m thick transition zone with generally random or very weak CPO and a tendency for a stronger alignment of plagioclase laths at depth, starting at the varitextured to upper foliated gabbro transition, possibly related to downward flow as predicted by the gabbro glacier model (Fig. B6).

(2) Minerals in the lower foliated gabbro section are aligned by continuing downward flow (Morales et al, 2011; Nicolas et al., 2009) and/or upward melt migration (MacLeod and Yaouncq, 2000). It is revealed in chapter B that Wadi Gideah lower crust shows a trend of chemical evolution up section, very distinctive in the lower foliated gabbro section and associated with absence of any late magmatic phases. Hence, suspension downward flow might be unlikely for Wadi Gideah lower foliated

gabbros hardly matching these features. An alignment by upward flow, however, could be taken into account, well matching these features.

(3) In the layered gabbro section, minerals crystallize in situ in layered intrusions as predicted by the sheeted sill model. Increasing fabric intensity down section results from increasing compaction and/or simple shear of the magmatic mush, caused by active mantle flow underneath (Fig. B6).
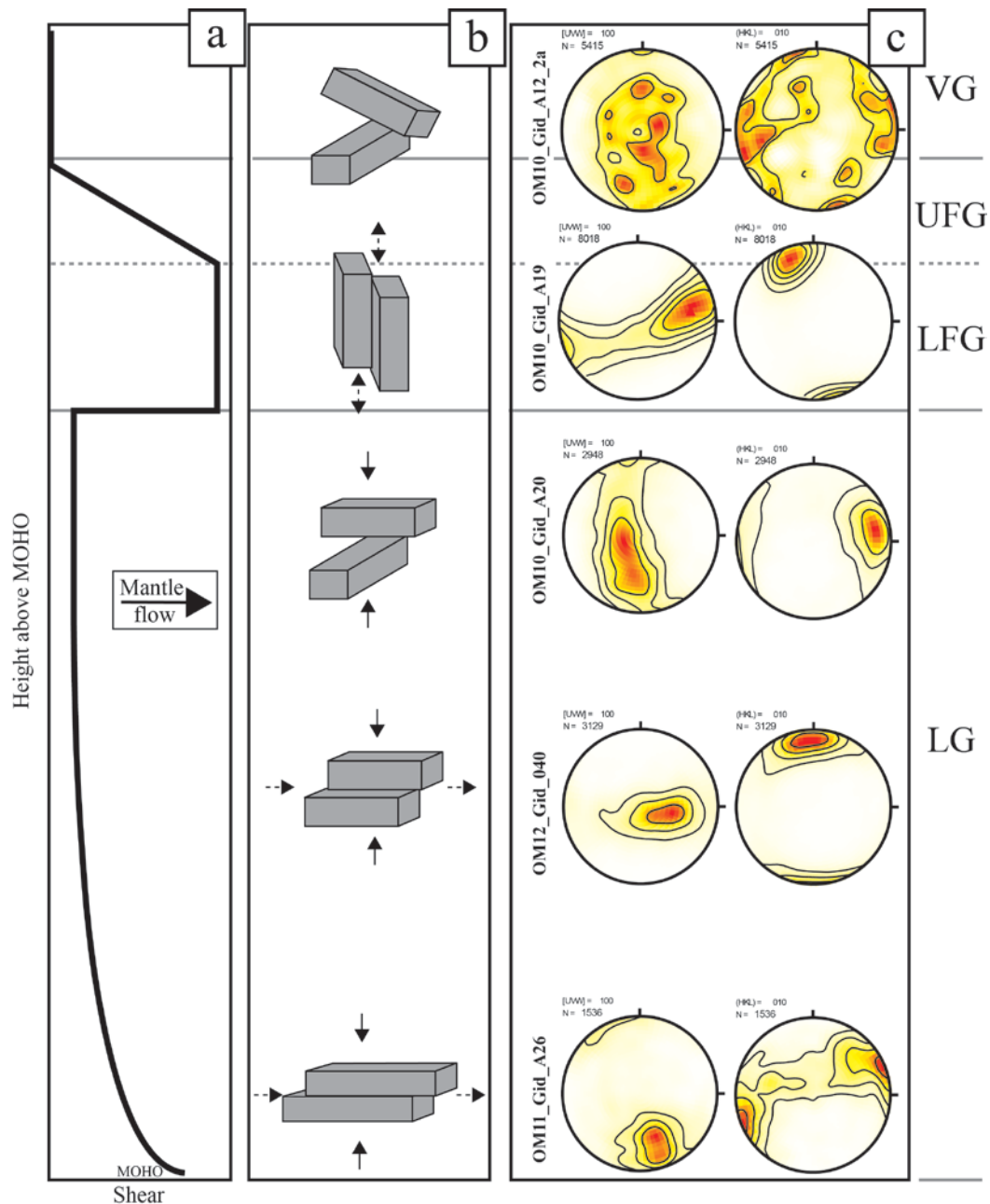
Figure B6. Schematic model for variations on Wadi Gideah plagioclase CPO. a) Approximate absolute shear with depth, b) Schematic alignment of plagioclase minerals with depth. Dotted arrow represent simple shear, full colored arrows compaction. c) Representative pole figures for plagioclase [100] axis and (010) plane with depth. Plagioclase shows no or little CPO for varitextured gabbros (VG), increasing in the upper foliated gabbros to a maximum in lower foliated gabbros (by upward magmatic flow). This is well shown by [100] girdle in pole figure. The plagioclase CPO decreases directly at the layered/foliated gabbro transition when minerals crystallize from melt intrusions (see A.8 for discussion). The downward increase in shear for lower gabbro plagioclase results from increased compaction and/or simple shear as a consequence of mantle dragging.

B.4.2 Comparison with Other Studies from Oman Ophiolite

Nicolas et al. (2009) studied multiple profiles for the first hundred meters of gabbro below the gabbro/dike transition (designated as "root zone of sheeted dike complex"; RZSDC). These authors concluded that steep magmatic foliation of foliated gabbro plagioclase is related to the subsidence of crystals settled on the floor of the AML due to crustal spreading. They showed plagioclase pole figures from 5 samples at different depths below RZSDC (0 m, 10 m, 45 m, 80 m, and 365 m; Fig. 5 of their study) with distinctive CPOs only displayed by samples at 45 m and 80 m. In comparison with results of this study, the lower four pole figures presented by these authors are very similar to plagioclase pole figures from 4612 m, 4389 m, 3734 m, and 3550 m H.a.M. (Height above Wadi Gideah Moho) presented in this chapter (Fig. B4). However, the assumption by Nicolas et al. (2009) that their results generally disprove the possible generation of plagioclase preferred orientation by an upward melt migration in the foliated gabbro section (e.g., MacLeod and Yaouancq, 2000) is not shared here since their dataset only comprises the upper 400 m of foliated gabbro, while the possible influence of melt migration may occur deeper as shown in this study (see A.7.3 and B.4.1). Hence, results by Nicolas et al. (2009) can be regarded as a solid argument for a gabbro glacier component exclusively in the uppermost gabbro section. Morales et al. (2011) worked in the same regions as Nicolas et al. (2009), and studied in detail a set of anorthosites from the first hundred meters below the RZSDC, complemented by a few samples from the layered gabbro section. These authors described and discussed in detail the occurrence of anorthisitic layers below the RZSDC, foliated parallel (generally East Nakhl section) or perpendicular (Jebel Dihm section) to the Moho, and representing either dynamics of the melt lens or crystal subsidence below the AML floor. They describe all their samples to display generally Axial-B fabrics with an increase in ODF J and (010) axis density until 750 m below RZSDC (Fig. 8 of their study), similar to observations from this study, interpreted by these authors as evidence for downward flow. Data from layered gabbro section are rare with the lowermost sample from 2000 m below the RZSDC. They all show generally Axial-B fabric and foliation planes parallel to modal layering, similar to observations from upper to medium layered gabbros in this study, with no indication for an increasing J down section. Van Tongeren et al. (2015) studied in detail the foliated- and layered gabbros of the Wadi Khafifah section in the Wadi Tayin block, observing only the known change from plagioclase [100] alignment perpendicular to alignment parallel to the Moho at the upper- (foliated) to lower (layered) gabbro transition, with no significant differences in pfJ and overall J with depth. Van Tongeren et al. (2015) regard this as a strong support for a sheeted sill type of accretion model. It is questionable why Wadi Khafifah displays no increasing strength with depth while Wadi Gideah does. Part of this difference with the study presented here may be partly related to the different ways to calculate the intensity J (to be discussed in a coming article), to the much lower number of measurement points per sample in their study, and/or to the smaller number of samples measured in the entire section. However, the bulk major elements (see A.7.6) in Wadi Khafifah show no trend of geochemical evolution up section while Wadi Gideah does. This is similar to observations from Wadi Abyad section in Nakhl Rustaq block, where MacLeod and Yaouancq (2000) did geochemical, and Yaouancq and MacLeod (2000) petrofabric investigation on the gabbro section. These authors described plagioclase from both

foliated and layered gabbros to display generally Axial-B fabric, with no systematic change in foliation or lineation intensity down section. This is accompanied with no geochemical evolution up section for bulk major elements (see A.7.6). There is no clear explanation to be given at this point for the apparent differences between Wadi Gideah, Wadi Khafifah, and Wadi Abyad section. However, none of the three profiles support a simple gabbro glacier model with continuous flow downward.

D.5 Conclusion

Crystallographic preferred orientations symmetry and strength (essentially plagioclase for this study) support the hypothesis that the Wadi Gideah lower crust formation is best explained by a hybrid model, with gabbro-glacier flow-like crystal subsidence for upper foliated gabbro section and sheeted-sills-like formation for rocks below (e.g. Boudier et al. 1996; see A.8). The lower foliated gabbro section may be assumed to be related to magmatic flow (subsidence and/or upward melt migration) and the upper layered gabbros to simple compaction pure shear with an increasing influence of magmatic suspension flow and/or upward melt percolation down section. The increasing fabric intensity down section in the layered gabbro, together with the progressively more linear fabric, may result from a combination of an increasing compaction with depth (pure shear) and the influence of active mantle flow below the crystallizing gabbros (simple shear).

Chapter C

The following chapter has been submitted as a paper to LITHOS

T. Müller [a], J. Koepke [a], C.-D. Garbe-Schönberg [b],
M. Dietrich [a], U. Bauer [a], P.E. Wolff [a]

[a] Institute for Mineralogy, Leibniz University of Hannover, Callinstrasse 3, 30167 Hannover, Germany

[b] Institute of Geosciences, CAU Kiel University, Ludewig-Meyn-Strasse 10, 24188 Kiel, Germany

Anatomy of a Frozen Axial Melt Lens from a Fast-Spreading Paleo-Ridge (Wadi Gideah, Oman Ophiolite)

C.1 Abstract

At fast-spreading mid-ocean ridges, axial melt lenses (AMLs) sandwiched between the sheeted dike section and the uppermost gabbros are assumed to be the major magma source of crust formation. Here, we present our results from a field study based on a single outcrop of a frozen AML in the Samail ophiolite in the Sultanate of Oman which presents a whole suite of different lithologies and complex cutting relationships: varitextured gabbro-bearing relics of very primitive poikilitic clinopyroxene are intruded upon by masses of oceanic plagiogranite-bearing relics of assimilated sheeted dikes, which in turn are cut by trondhjemite dikes. The whole is cut by basaltic dikes with chilled margins. The geochemical evolutionary trend of the varitextured gabbros, including some of the plagiogranites, can be best modeled by fractional crystallization of a parental Mid-Ocean Ridge Basalt (MORB) melt typical for the Southern Samail ophiolite containing 0.4 to 0.8 wt% H_2O. Patchy varitextured gabbros containing domains of primitive poikilitic clinopyroxene and evolved granular networks represent the record of in situ crystallization. Other plagiogranites, often with xenoliths of sheeted dikes and exceptionally high Al_2O_3 contents, show a bulk trace element pattern more in accord with melts generated by experimental partial melting of dike material. Highly evolved, crosscutting trondhjemite dikes show typical trace element patterns implying formation by partial melting of granoblastic hornfelses formed by an earlier event of partial dike melting. The late basaltic dikes with chilled margins crosscutting all other lithologies show a relatively depleted geochemical character with pronounced negative Nb-Ta anomalies implying a genetic relationship to the second phase of magmatic Oman paleo-ridge activity (V2). The field relationships in combination with the petrological/geochemical trends reveal multiple sequences of MORB-type magma cooling (resulting in fractional crystallization) and re-heating (producing partial melting) during the formation of this special horizon; these are best explained by alternating cycles of vertical AMLs. Since the investigated outcrop shows many characteristic lithological and petrographic features that are well-known from the uppermost gabbros drilled at Site 1256 by the International Ocean Drilling Program (IODP) in the equatorial Eastern Pacific, our results based on 3-D observation in the field help to elucidate the geological observations obtained from the 1-D drill core.

C.2 Introduction

Oceanic crust that forms at fast-spreading rates exhibits a relatively uniform seismic stratigraphy (e.g., Canales et al., 2003) and is regarded as layered and relatively homogeneous. Multichannel seismic studies revealed the presence of an AML in the mid-crust beneath fast-spreading MORs, which is underlain by crystal melt mush in the lower crust (e.g., Detrick et al., 1987; Vera et al., 1990; Hussenoeder et al., 1996; Sinton et al., 1992). The role of the AML, which is sandwiched between the sheeted dike and the gabbro sequence, is known to be vital, but it is still not known with certainty whether this melt body is the source for the complete lower, gabbroic crust (e.g., Henstock et al., 1993; Morgan and

Chen, 1993; Quick and Denlinger, 1993), or if it only serves as a source for a distinct portion of the lower crust, while other, significant parts originate from in situ crystallization in the deep crust (e.g., Bédard et al., 1988; Boudier et al., 1996; Kelemen et al., 1997; Natland and Dick, 2009).

There are only a few locations worldwide where rocks from such horizons, interpreted as parts of frozen AML systems, have been investigated. The most important are a section of EPR crust drilled by the IODP at Site 1256 (Eastern Equatorial Pacific) and the Samail ophiolite in the Sultanate of Oman. The ODP/IODP multi-leg campaign at IODP Site 1256 provides the first continuous in situ sampling of fast-spreading oceanic crust from extrusive lavas, through the sheeted dikes, down into the uppermost gabbros, which were interpreted as parts of an AML system. The drilled plutonic rocks from IODP Site 1256 are a suite of heterogeneous, varitextured gabbroic rocks spanning a wide range of compositions including gabbros, oxide gabbros, orthopyroxene-bearing gabbros, olivine-bearing gabbros, and highly-differentiated rocks like quartz-rich oxide diorites and trondhjemite dikelets (for details see France et al., 2009; Teagle et al., 2006; Erdmann et al., 2015). Koepke et al. (2011) showed that at least a part of the heterogeneous features recorded there (i.e., the "spotty" gabbros) was the result of in situ crystallization, where domains of poikilitic gabbro crystallized from a primitive, high-temperature MORB melt, differentiated into domains of granular, evolved gabbro, consistent with a magma evolution by crystal fractionation, up to ~ 80 % crystallization.

France et al. (2009) compared the drilled gabbros from Site 1256 and overlying contact-metamorphic hornfelses to corresponding lithologies from the gabbro/dike transition of the Samail ophiolite of the Sultanate of Oman (Ibra area; Wadi Tayin Massif), and found an excellent correspondence between these two localities. These authors concluded that the AML in fast-spreading systems is a very dynamic horizon characterized by upward and downward migration as a consequence of eruption/replenishment stages, recrystallization in the overlying sheeted dikes, and assimilation of the roof rocks.

Another location within the Oman ophiolite where typical rocks of the melt lens horizon are exposed is the Wadi Abyad in the Rustaq block of the Oman ophiolite. Here, MacLeod and Yaouancq (2000) and Coogan et al. (2002) interpreted the isotropic, so-called varitextured gabbros at the base of the sheeted dike complex as a rock suite corresponding to a fossilized AML. Based on their observations, they suggested that the varitextured gabbro horizon can be regarded as the highly-differentiated end product of MORB liquid crystallization at the margins of an AML.

Here we present detailed petrographic, petrological, and geochemical results from one exceptional exposure from the Oman ophiolite melt lens horizon located in the Ibra area (Wadi Tayin Massif). This outcrop presents many characteristic lithological and petrographic features well-known from IODP Hole 1256D. In contrast to the 1-D drilling at Site 1256, the investigated outcrop in the Wadi Gideah opens interesting perspectives for fine-scale mapping and focused 3-D sampling, in order to shed new light on the complex magmatic and metamorphic processes related to a freezing AML from fast-spreading MORs.

C.3 Field Observations

The Gideah South outcrop is located in the southern part of the Wadi Gideah about 10 km north of Ibra (Wadi Tayin Massif; Fig. C1a, b); at this outcrop, a coherent section of the oceanic crust from the Moho transition zone to sheeted dikes is exposed (e.g., Pallister and Hopson, 1981; Müller et al., 2014). This crustal section is regarded as nearly undisturbed and is considered to be a good analog of typical EPR crust representing rocks formed during the magmatic phase 1 of the paleo-ridge accretion according to Goodenough et al. (2014). Typical rocks of magmatic phase 2 of Goodenough et al. (2014) which are believed to be related to an
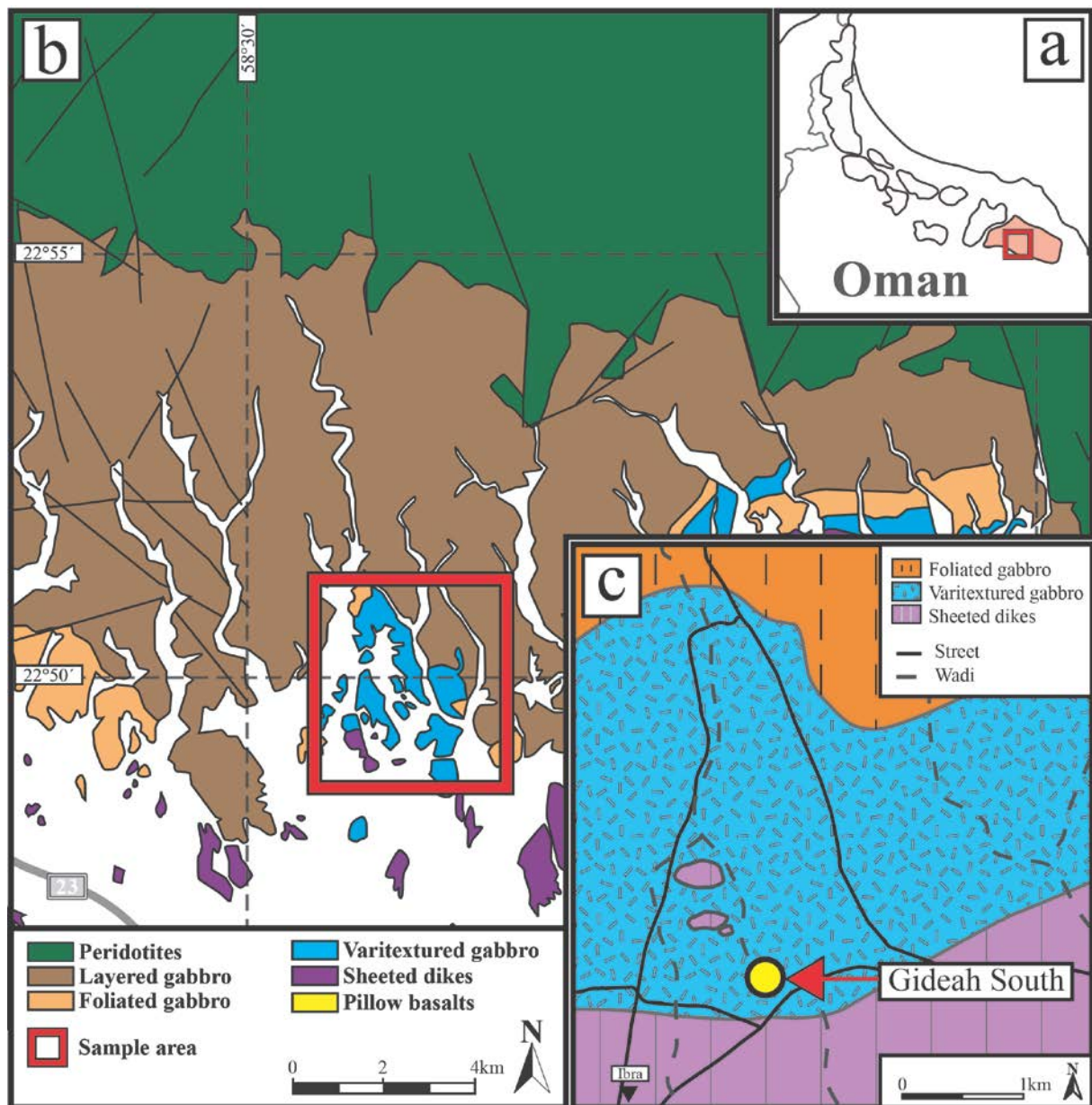
Figure C1. a) Sketch map of the Oman ophiolite with southeast Wadi-Tayin Massif colored in red. The location of b) marked by the rectangle. **b)** Geological map of the southern Wadi-Tayin Massif of the Samail ophiolite of the Sultanate of Oman modified and simplified from Peters et al. (2008). Location of c) in Wadi Gideah is marked by the red rectangle. **c)** Detailed geological map of the southern part of Wadi Gideah modified from France et al. (2009) including the marked location of the Gideah South outcrop.
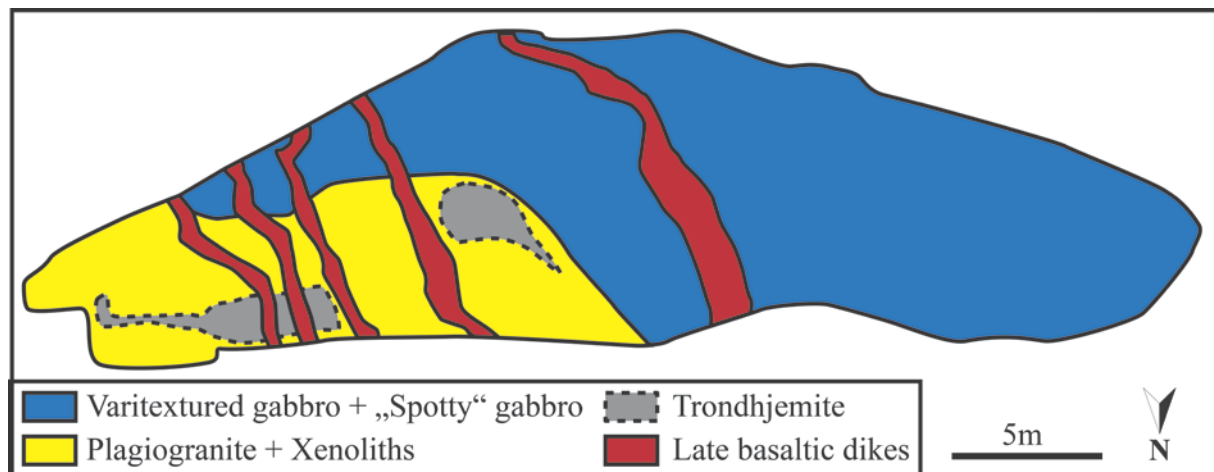
Figure C2. Sketch of the Gideah South outcrop. The present lithologies are marked in different colors. Spotty and "normal" varitextured gabbros (right side) were intruded upon by xenolith-bearing plagiogranite (left side) which was in turn crosscut by trondhjemite dikes. All lithologies were crosscut later by basaltic dikes.

advanced subduction zone initiation, like crustal wehrlites, gabbronorite intrusions, and large plagiogranitic bodies, are widely absent in this part of the Wadi Tayin Massif (see also the discussion of Van Tongeren et al., 2008). Gideah South is located in the working area of France et al. (2009; Fig. C1c), but was not included for detailed mapping or sampling by those authors. Recently our group re-investigated the Wadi Gideah section (Müller et al., 2014), which also includes the Gideah South outcrop (location A11_1) representing the uppermost location for gabbros in this section. Gideah South, with a length of ~35 m and a height of ~14 m, is located at the termination of the Wadi Gideah where the Ibra-Hadmah road cuts the Wadi (22.819°N, 58.527°E). In the map of France et al. (2009), the outcrop is assigned to the unit of varitextured gabbro, directly at the contact with the sheeted dikes (Fig. C1c). It basically consists of three components: (1) varitextured gabbro (Fig. C2, right part), which is cut by (2) a very heterogeneous, xenolith-bearing plagiogranitic complex (Fig. C2, left part). Both units are cut by (3) late, more-or-less parallel basaltic dikes (Fig. C2).

(1) The varitextured gabbro is a very heterogeneous suite of evolved gabbros, consisting of isotropic gabbros, which may be olivine-, orthopyroxene-, and/or oxide-bearing, and which are characterized by a wide variability in texture, grain size, and chemical composition on a centimeter-to-several-decimeter scale, suggesting the term "varitextured" gabbro (for definition see MacLeod and Yaouancq, 2000). These gabbros are fine- to coarse-grained (Fig. C3e), sometimes pegmatitic, with granular-to-intergranular textures including the presence of leucogabbroic schlieren. Characteristic are patches in which the gabbro shows a marked spotty appearance (Fig. C3i). The spotty gabbro shows dark, millimeter- to centimeter-sized spots consisting of poikilitic clinopyroxene surrounded by a whitish granular matrix. These gabbros appear very similar to those spotty gabbros described by Koepke et al. (2011) from the uppermost gabbros drilled at IODP Site 1256.

(2) The varitextured gabbro is cut by an intrusion of oceanic plagiogranite which consists of a plagiogranitic matrix bearing countless xenoliths from centimeter- to decimeter-scale consisting of fragments of basaltic dikes and fine- to medium-grained isotropic gabbro. The term plagiogranite is used here according to the definition of Koepke et al. (2007) to describe the whole suite of evolved, SiO_2-enriched plutonic rocks within the lower oceanic crust in a

very broad sense, including diorites, quartz diorites, and tonalites. The plagiogranite displays small apophyses intruding into the varitextured gabbro (Fig. C3d). The xenoliths show a considerable variation of shapes from highly angular to rounded, mostly with diffuse, lobed contacts to the matrix rock (Fig. C3b, g, h). In the left part of the outcrop, decimeter-sized coherent blocks of former sheeted dikes are visible which were brecciated in situ by a net of plagiogranite veins. Here, the geometry of the contacts between blocks and matrix clearly corresponds to brittle fracturing which has produced spectacular brickwork with plagiogranite as joint filling (Fig. C3g). At other places the proportion of interstitial plagiogranite increases while the rectangular dike clasts become more and more rounded, developing a typical "vinaigrette" texture (Juteau et al., 1988; Fig. C3h). At this stage, centimeter-wide reaction zones between the xenoliths and the plagiogranite matrix become common. The xenolith-bearing plagiogranite complex is cut by several decimeter- to meter-wide homogenous trondhjemite dikes (Fig. C3f) showing relatively sharp contacts to the plagiogranitic breccia (without chilled margins) with small apophyses intruding into the host rock.

(3) Both plagiogranite complex and varitextured gabbro are crosscut by subparallel basaltic dikes (Fig. C3c), which are oriented SSE-NNW corresponding to the overall orientation of the sheeted dike complex in this area (e.g., France et al., 2009; Pallister and Hopson, 1981). Since these dikes are microcrystalline to fine-grained in grain size with well-developed chilled margins, they are definitely late, and were emplaced when the surrounding rocks had cooled down significantly (<450 °C, Nicolas et al., 2000b). After this diking event, all lithologies were cut by brittle fault zones, which are also characterized by strong weathering.
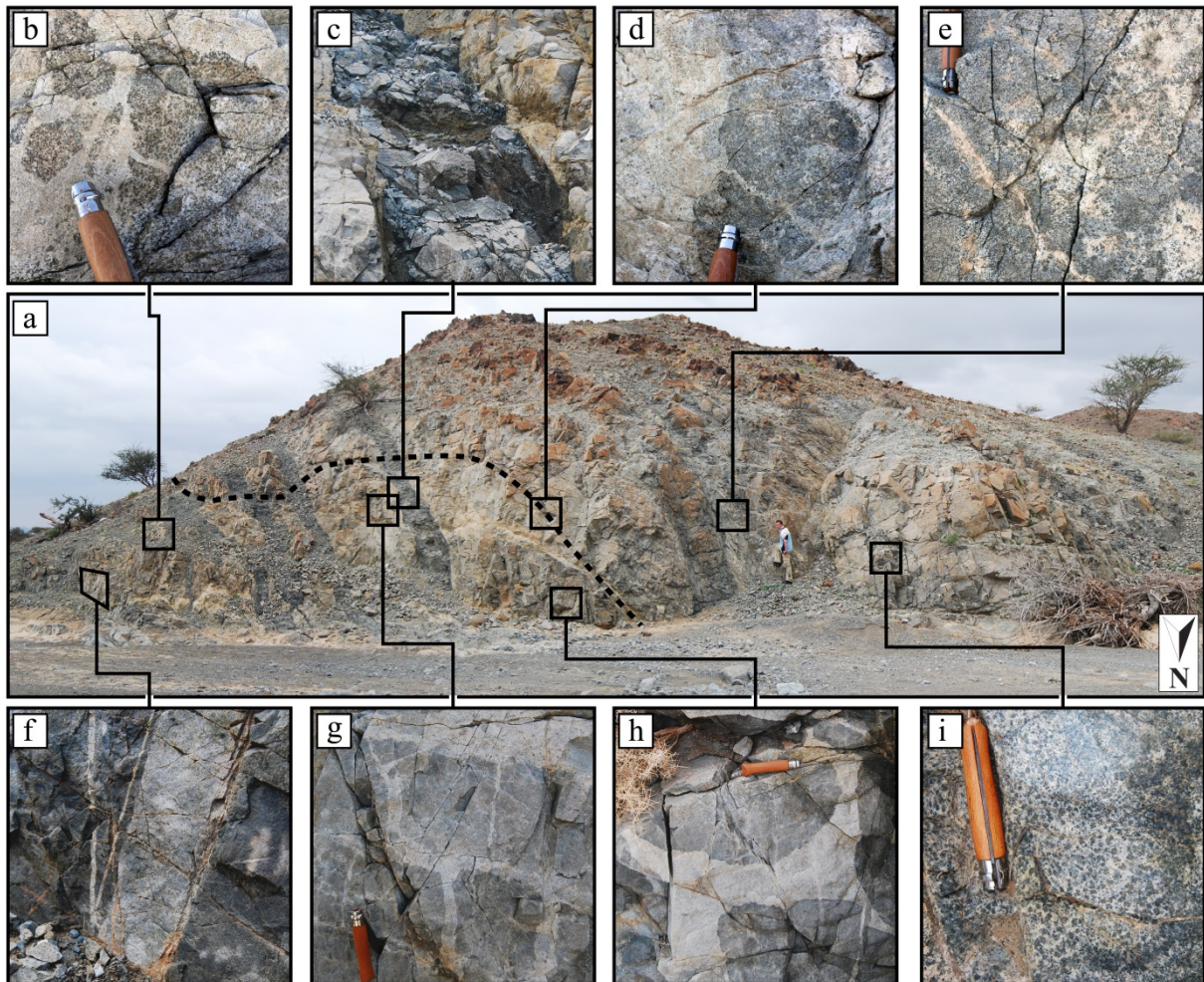
Figure C3. a) The Gideah South outcrop exposing a portion of a fossil AML with magnified images representing different types of characteristic lithologies. **b)** Light plagiogranite matrix, net-veining xenoliths of basaltic dike, and varitextured gabbro. **c)** Late basaltic dike with chilled margins crosscutting xenolith-bearing plagiogranite. **d)** Sharp contact between xenolith-bearing plagiogranite (left) and varitextured gabbro (right). Note the apophyses of plagiogranite within the varitextured gabbro indicating that the plagiogranite intruded later. **e)** Varitextured gabbro. **f)** Late trondhjemite dikes intruding upon xenolith-bearing plagiogranite with sharp contacts. **g)** Early stage of sheeted dike complex basalt assimilation by plagiogranite, producing a net-veining plagiogranite matrix and basaltic xenolith brickwork. **h)** Like g, but in an advanced assimilation stage with rounded xenoliths displaying a higher degree of assimilation. **i)** Spotty gabbro with spots of rather primitive poikilitic clinopyroxene domains surrounded by patches of an evolved granular matrix.

C.4. Methods

For the petrographic description in terms of rock names, textures, and qualifiers we follow Gillis et al. (2014).

EPMA was performed at the Institute for Mineralogy of the University of Hannover using a Cameca SX100 electron microprobe with five spectrometers, "Peak Sight" software (Cameca), Kα emission for all elements, a focused beam, 15kA acceleration potential, beam current of 15 nA, 10 s analysis time per element, and the "PAP" matrix correction (Pouchou and Pichoir, 1991). F and Cl were analyzed with an acquisition time of 30 s and with higher beam current. We generally analyzed both core and rim compositions of the minerals.

Bulk rocks trace element analysis was performed by LA-ICP-MS at the Institute of Geosciences of the CAU Kiel University on nano-particulate pressed powder tablets in a Zurich-type LDHCLAC (Fricker et al., 2011) with a 193 nm ArF excimer laser ablation system (GeoLasPro Plus, Coherent) coupled to an Agilent 7500s ICP-MS and "GLITTER" software (for details see Garbe-Schönberg and Müller, 2014). The laser pulse length was 10-20 ns with a pulse frequency of 10-15Hz and an ablation spot size of 80 μm. Precision was <5 % (RSD).

RFA was performed at the Mineralogical-Petrographic Institute at the University of Hamburg with a Panalytical MagiX PRO wavelength dispersive spectrometer with a PW 2540 VC sample changer, an Rh-anode, and pellets with 0.6 g sample powder plus 3.6 g lithiumtetraborate. Detection limit for major elements was ≤ 0.01 wt%. Detection limits for trace elements were 20 ppm for Ce and La, 15 ppm for Co, 10 ppm for Ba and Nd, and <5 ppm for others.

C.5 Results

C.5.1 Petrography

Twenty-two samples from all lithologies were investigated for petrography. A summary of the results including modal amounts are given in Table 5 (appendix).

The varitextured gabbros are mainly composed of plagioclase (euhedral to subhedral, lath-shaped to tabular, often strongly zoned), often associated with clinopyroxene (subhedral, prismatic to poikilitic), primary brown-green hornblende (sometimes poikilitic), and interstitial granular oxide. The textures vary within a wide range from isotropic granular to doleritic with grain sizes mostly from fine grained to medium grained (Fig. C4a). The varitextured gabbros are strongly (sometimes completely) pervasively altered into minerals of
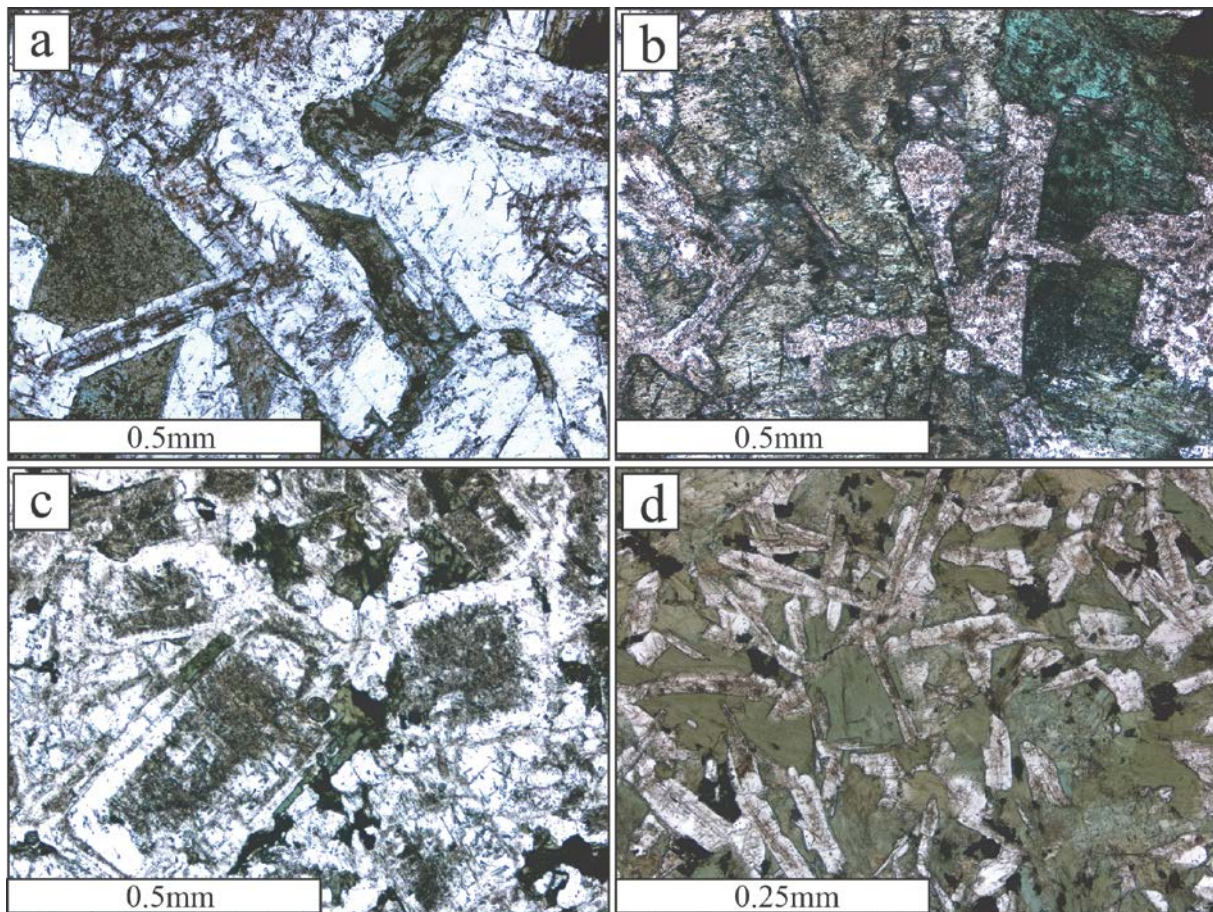
Figure C4. Photomicrographs showing principle lithologies of "Gideah South". See text for details. **a)** Coarse-grained framework of colorless prismatic plagioclase and clinopyroxene in a varitextured gabbro showing strong greenschist facies alternating with clinopyroxene (plane-polarized light; A11_1b). **b)** Subophitic texture of spotty gabbro showing mm-sized clinopyroxene oikocrysts enclosing whitish skeletal plagioclase chadacrysts (cross-polarized light; A11_1x). **c)** Medium- to coarse-grained granular framework, mainly consisting of colorless plagioclase and interstitial mafic phases in a plagiogranite. Plagioclases show sponge-like cores filled with cloudy alteration products. Interstitial phases are smaller colorless quartz with few interstitial oxides, and amphibole with relics of former clinopyroxene now strongly altered into greenschist facies (plane-polarized light; A11_1ib). **d)** Former microcrystalline intergranular to doleritic texture of a basaltic dike, now recrystallized to a granoblastic framework of plagioclase and green amphibole (plane-polarized light; A11_1u).

the amphibolite and greenschist facies (secondary hornblende, actinolite, chlorite, epidote, titanite).

Within the varitextured gabbros are patches of spotty gabbros, which are composed of subophitic domains up to 6 mm wide surrounded by more felsic domains of fine- to medium-grained granular networks (Fig. C4b). The subophitic domain consists of mm-sized clinopyroxene oikocrysts enclosing subhedral to anhedral lath-shaped, often zoned plagioclase chadacrysts (average size of ~0.4 mm). The granular network is composed mainly of subhedral, lath-shaped to tabular, strongly-zoned plagioclase (average grain size ~0.8 mm). Interspaces are filled with granular oxides up to 2 mm in size; the primary amphibole (now nearly completely changed to secondary amphibole) contains relics of clinopyroxene. The subophitic patches appear dark due to a high content of secondary amphibole, contrasting with the whitish color of the plagioclase-rich granular groundmass which results in the spotty appearance of this rock (Fig. C3i). The transition between domains is gradual. Very similar gabbros with spotty appearance and the same petrographic features were described by Koepke et al. (2011) for the uppermost gabbros drilled at Site 1256 by IODP.

The main component of the plagiogranites is subhedral to anhedral, lath to tabular shaped, 0.6-mm- to 3-mm-sized, and often strongly-zoned plagioclase. Other primary minerals are prismatic brown-green amphibole, sometimes poikilitic, granular oxides, and quartz. The most common rocks are diorites, quartz diorites, and tonalites. The textures are granular to doleritic (Fig. C4c). Most samples display different domains recognizable by slight variation in average grain size and mode, indicating possible intermingling of different plagiogranitic melts at cm-scale. The contact between plagiogranite and xenoliths is mostly sutured with a smooth transition between lithologies. Most xenoliths correspond to formerly sheeted dikes with originally intergranular textures which are now transformed to fine-grained to microcrystalline granular textures composed of plagioclase and brown-green amphibole. Some plagiogranites show microgranular domains very similar to those described by France et al. (2009) and Koepke et al. (2011) from the 1256D gabbros drilled by IODP, which were interpreted as relics from assimilated dikes.

The trondhjemites are composed of plagioclase and quartz with small amounts of brown-green amphibole and oxides. Accessory minerals in the plagiogranites and trondhjemites are apatite and sometimes zircon. Most of the plagiogranites are pervasively altered into secondary minerals of mainly greenschist or amphibolite facies.

The basaltic dikes correspond to former microcrystalline to fine-grained basalts with probably intergranular to intersertal texture, which are now fully recrystallized to granoblastic amphibolitic assemblages, composed of subhedral, lath-shaped, zoned plagioclase and green or brown-green amphibole, oxides, and titanite (Fig. C4d). The metamorphic overprint was pervasively minerals of the amphibolite to greenschist facies (hornblende, actinolite, chlorite, oxides, and titanite). All primary mafic minerals are converted to amphibole. One sample displays a few larger relictic plagioclases interpreted as former phenocrysts.

C.5.2 Bulk Chemistry

C.5.2.1 Major Elements

Varitextured and spotty gabbros display basaltic to basaltic-andesitic compositions (Fig. C5) with bulk Mg# of 41 to 44 and are significantly evolved compared to NMORB (Gale et al., 2013) as expressed by higher amounts of Al_2O_3, K_2O, and TiO_2 (Fig. C6).

Plagiogranites display dacitic to trachydacitic compositions (Fig. C5) with bulk Mg# of 28 to 37. They fall within the range of data for plagiogranites from several places within the Wadi Tayin Massif of the Oman ophiolite analyzed by Freund (2014), except for Al_2O_3 which is generally enriched in the plagiogranites from Gideah South (Fig. C6). The crosscutting trondhjemite dike shows a rhyolitic composition in the TAS diagram (Le Bas and Streckeisen, 1991; Fig. C5) with an SiO_2 content which is significantly enriched compared to the plagiogranites (74.51 wt%). The analyzed mafic xenolith in a plagiogranitic matrix interpreted as former basalt of the sheeted dike complex displays an andesitic composition and is in many aspects very similar to plagiogranites, although slightly less evolved. We interpret this as an effect of assimilation of dike basalts by the plagiogranite melt which infiltrated the basalt resulting in a mix of these two components.

Basaltic dikes display basaltic to basaltic-andesitic composition with a bulk Mg# of 51 to 65. Major element compositions fit well to NMORB (Gale et al., 2013; Fig. C6) except for a small enrichment in Al_2O_3 (MV=16.42 wt%) and depletion in TiO_2 (MV=1.05 wt%) and P_2O_5 (MV=0.08 wt%).

Major element data for all lithologies of Gideah South follow a clear evolutionary trend of (1) basaltic dikes, (2) varitextured including spotty gabbro, (3) xenoliths of basaltic dike, (4) plagiogranite, and (5) trondhjemite. This trend correlates well with other data for extrusives from the Oman ophiolite including the Geotimes (V1) lava compositions (MacLeod et al., 2013). However, our data show little correlation with the compositional range of present-day EPR extrusives from Hess Deep and IODP Hole 1256D (Neo et al., 2009; Steward et al., 2002; Wilson et al., 2003; Fig. C6), which is very probably the
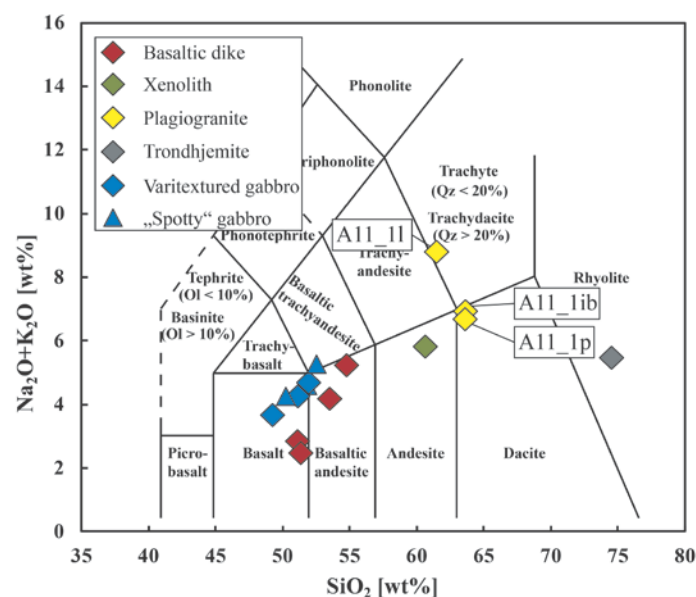
Figure C5. Classification of Gideah South lithologies using the TAS diagram after Le Bas and Streckeisen (1991).

consequence of an influence of increased water content in the primary melts of the Oman paleo-ridge system due to subduction zone initiation (see MacLeod et al., 2013 and below). Major element bulk analyses are given in Table 14..

C.5.2.2 Trace elements

NMORB-normalized bulk trace element patterns follow the general trend of compositional evolution formed by major elements. Varitextured gabbros including spotty gabbros show bulk element concentrations slightly more depleted than NMORB, a negative Nb-Ta, slightly negative Zr-Hf and Eu, and
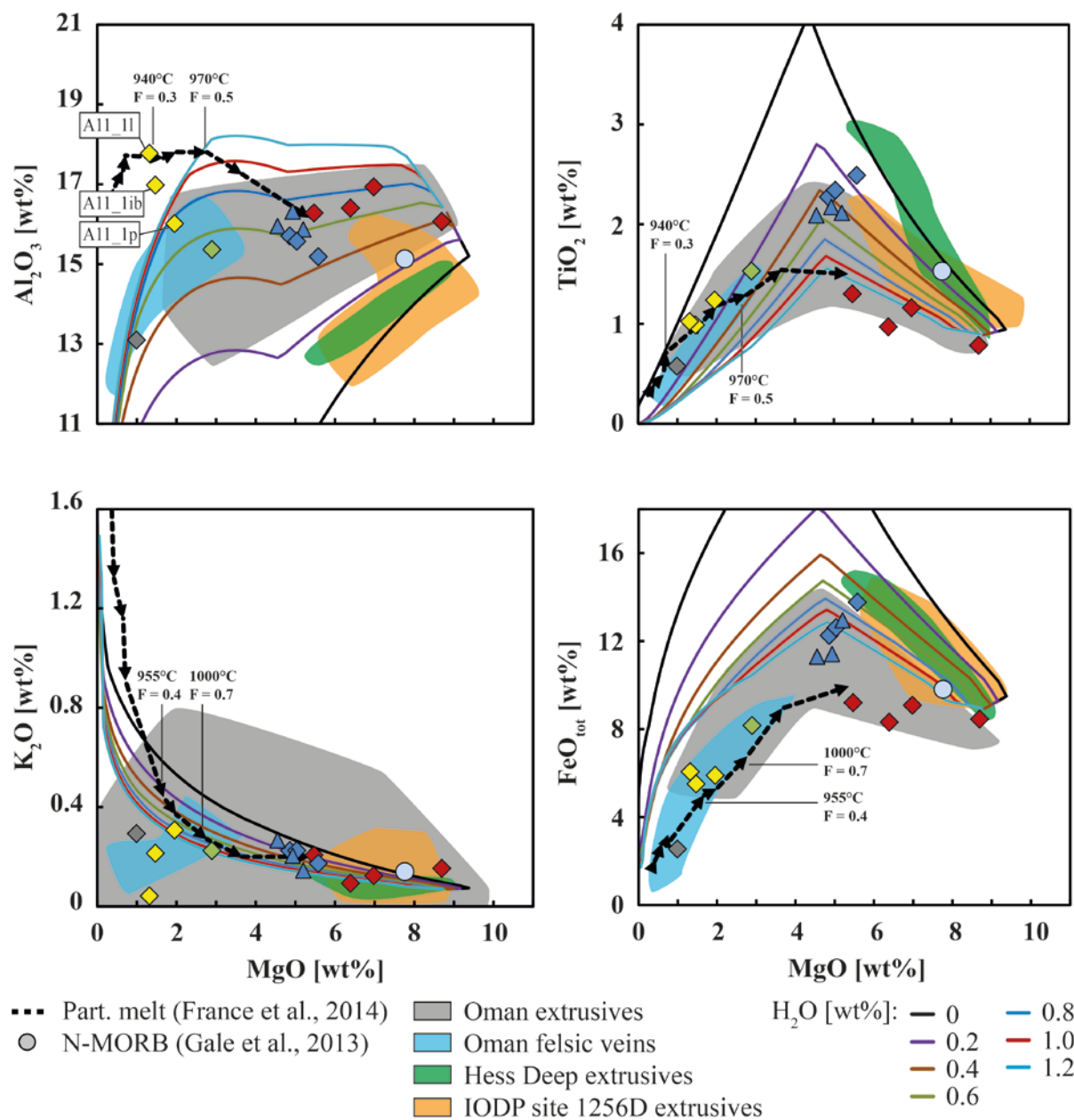
Figure C6. Harker diagrams (MgO vs. oxides) for bulk composition of Gideah South lithologies compared to data from MacLeod et al. (2013) for Oman extrusive rocks (including V1-lavas), Freund (2014) for Wadi-Tayin P1-plagiogranite, Neo et al. (2009) and Wilson et al. (2003) for IODP Site 1256D extrusive section, Steward et al. (2002) for Hess Deep extrusive section, and Gale et al. (2013) for NMORB. Symbols are the same as in Figure C5. Solid lines represent calculated LLDs for varying melt H_2O content (see text for further details). Dashed line represents compositional evolution of partial melts experimentally obtained by France et al. (2010, 2014) including labeling for temperature and associated melt fraction F.
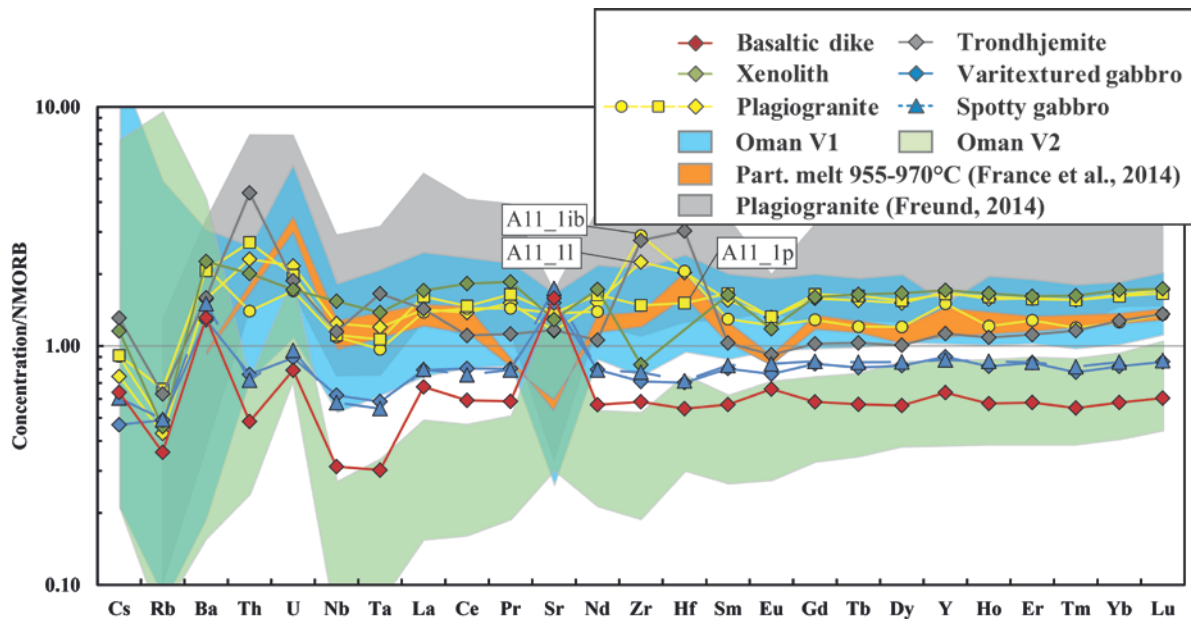
Figure C7. Spider diagram (trace element concentrations normalized to NMORB of Gale et al., 2013) for bulk compositions of Gideah South lithologies compared to data from Godard et al. (2003) for Oman V1- and V2-lavas, Freund (2014) for Wadi-Tayin P1-plagiogranite, and partial melts experimentally obtained by France et al. (2010, 2014) between 955 and 970 C.

positive Sr anomalies (Fig. 7). While the incompatible elements including light and medium REE correlate with the Oman V1 extrusives, the heavy REE are more compatible with the Oman V2 lavas. A marked positive Sr anomaly implies a relationship to Oman V2 lavas. However, this element, and Ba which also shows a strong positive anomaly, is often strongly affected by hydrothermal alteration (e.g., Godard et al., 2003; Pearce, 2014) and thus this evidence must be interpreted with caution because all varitextured gabbros are heavily altered. Low Nb and Ta concentrations, however, are believed to be unaffected by secondary alteration processes, supporting an origin related to subduction zone initiation (e.g., Pearce, 2014) rather than a "normal" MOR; this hypothesis is supported by MacLeod et al. (2013) based on major element chemistry.

Plagiogranite including the basaltic dike xenolith represents the most evolved lithology of Gideah South; it generally displays positive Th, U, and Zr-Hf, negative Sr and Eu, and slightly negative Nb-Ta anomalies (Fig. C7). The most primitive sample (A11_1p) lacks the Zr-Hf anomaly. The evolved character of these rocks as well as anomalies observed on an NMORB-normalized diagram is within the compositional range of Wadi Tayin plagiogranite as described by Freund (2014). On the other hand, the trace element patterns of the two more-evolved samples (A11_1l, A11_1ib) are generally similar to trace element patterns from melts obtained by experimental partial melting of hydrated Oman basaltic dike material (France et al., 2010, 2014; Fig. C7). This leads to a discussion of whether the Gideah South plagiogranite represents partial melts from a prior anatectic event or late products of fractional crystallization; both are influenced by assimilation processes (see discussion). The crosscutting trondhjemite shows a trace element pattern that is strikingly similar to patterns of experimental partial melt (France et al., 2014) including the positive Zr-Hf anomaly and negative Eu anomaly. The hornfelsic dike xenolith, enclosed and partly assimilated by plagiogranite, displays a trace element pattern similar to that of plagiogranite except for a Zr
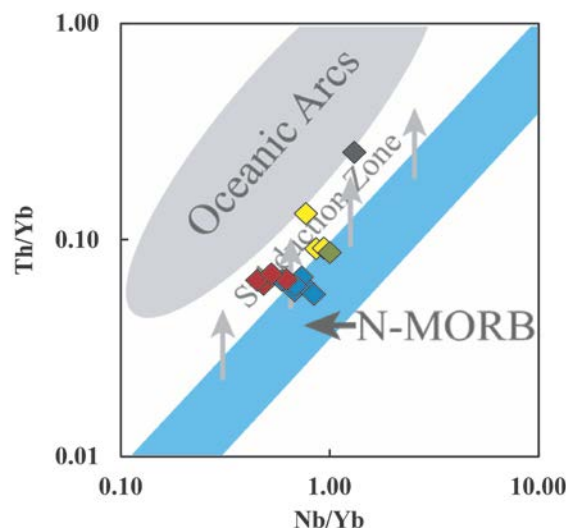
Figure C8. Classification of Gideah South lithologies using Th/Nb diagram of Pearce (2014).

anomaly that is strikingly negative compared to its neighbor elements (Fig. C7). We interpret this as a result of element equilibration during assimilation with highly incompatible Zr being depleted in xenolith and enriched in the plagiogranitic melt.

Basaltic dikes represent the most primitive lithology of Gideah South"; they are more primitive than NMORB (Gale et al., 2013) and exhibit negative Nb-Ta, positive Sr, and slightly-positive Eu anomalies (Fig. C7). Although Sr concentration may be influenced by alteration processes, the trace element concentrations and anomalies observed are generally more similar to the range of Oman V2 lavas rather than to V1 lavas, as described by Godard et al. (2003). These lavas correspond to arc or MOR magmatism, respectively. The strong relationship to arc magmatism, which is also supported by the marked Nb-Ta anomaly, is also shown in the classification diagram exhibiting Pearce's (2014) immobile element ratios and displaying a clear shift from NMORB to an SSZ relationship, while the varitextured gabbros plot more into the NMORB field (Fig. C8). Results of bulk trace element analyses are given in Table 15.

C.5.3 Mineral chemistry

Major element mineral analyses are given in Table 16.. Plagioclase in varitextured gabbros except for those patchy domains of spotty gabbro (see below) show, in general, a strong variability in An contents with 53 to 16 mol% in the cores and 29 to 7 mol% in the rims (Fig. C9a, b). A strong zonation is documented by a difference in An content of up to 28 mol% between core and rim within single grains (Fig. C10a). In contrast to the broad compositional range in plagioclase, Mg# of varitextured gabbro clinopyroxene varies only slightly from 71 to 75 (Fig. C11). Amphiboles in the varitextured gabbros, although texturally identified as primary, have mostly actinolitic composition due to resetting of the composition by secondary alteration with one exception where compositions of magnesio-hornblende and pargasite were recorded. In the classification related to F and Cl following Coogan et al. (2001), all amphiboles from varitextured gabbros display neither a defined hydrothermal nor a

magmatic signature (Fig. C12). Instead, they display both; high F contents (up to 3270 ppm), generally related to magmatic formation, and high Cl contents (up to 1563 ppm), generally related to a secondary interaction with seawater-derived fluids (Coogan et al., 2001). However, since those brownish pargasites which are interpreted to retain their magmatic compositions also show high F and Cl contents, we assume that Cl-rich fluids were present during the crystallization of the corresponding melt. This presence could be derived from either assimilation of previously-altered sheeted dikes or from subduction-zone-related fluids.

Plagioclase from the granular matrix of the spotty gabbros displays compositions generally similar to varitextured gabbros with An contents of 61 to 32 mol% in cores and 5 to26 mol% in rims and a clinopyroxene Mg# of ~73. However, plagioclase chadacrysts from the subophitic domain show a more primitive composition with An contents of 46 to 67 mol% in cores and 39 to 26 mol% in rims (Fig. C9). The Mg# of clinopyroxene oikocrysts of these domains ranges from 80 to 76 (Fig. C11). Thus, the subophitic domains represent much more depleted compositions implying a crystallization history in which the subophitic domain crystallized first (forming the spots of the "spotty gabbro"), followed by the more evolved granular matrix of the spotty gabbros, and finally the common varitextured gabbro in which only a granular matrix is common and subophitic domains are not present. Hence, both the order of crystallization and the composition of subophitic and granular domains correlate well with observations of spotty gabbros from IODP Hole 1256D by Koepke et al. (2011), implying similar magmatic processes in a freezing AML during crustal accretion of the Oman paleo-ridge and the modern EPR crust.
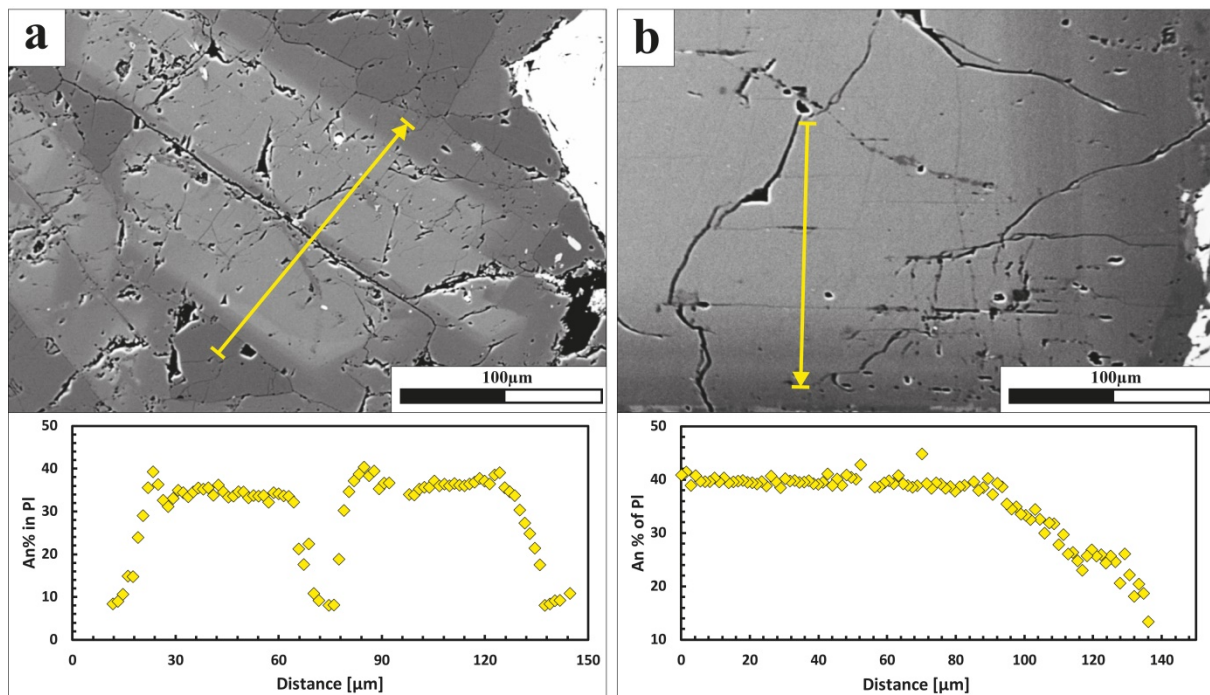
Figure C10. BSE images of plagioclase and related electron probe profiles for An% vs. distance [μm]. Yellow arrows represent location of profiles for **a)** plagiogranite (A11_1o) and **b)** varitextured gabbro (A11_1e).
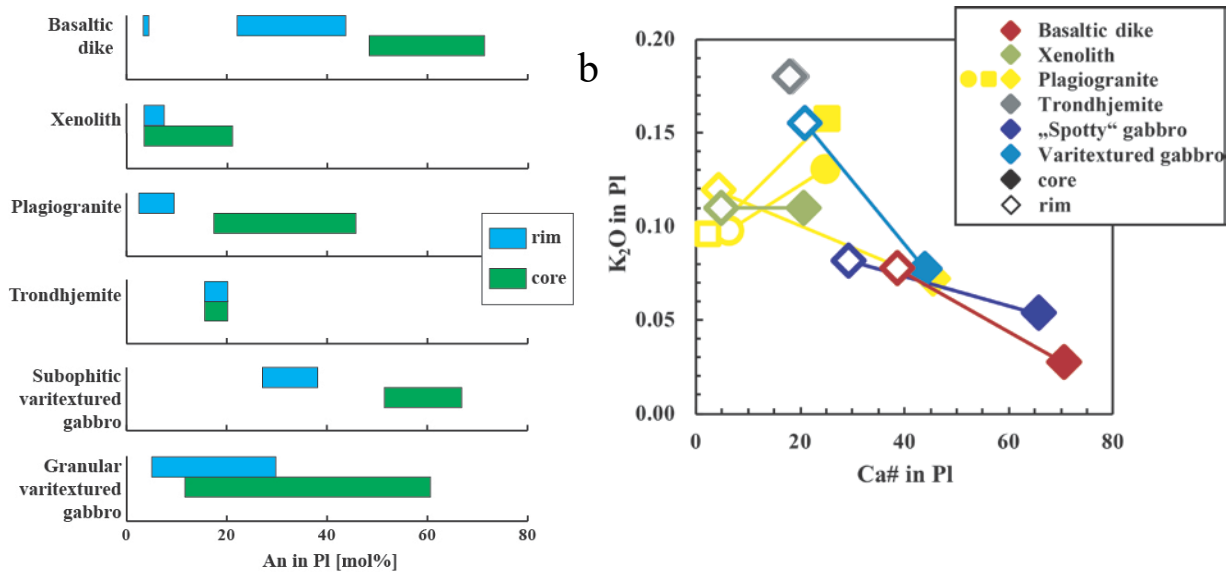
Figure C9. a) Range of core and rim An% for plagioclase from Gideah South lithologies. **b)** Compositional range (An% vs. K$_2$O) of representative plagioclases from Gideah South lithologies. Closed symbols represent core and open symbols rim composition.

Plagiogranitic plagioclase generally displays An contents of 46 to 17 mol% in the cores and 10 to 3 mol% in the rims (Fig. C9). Zonation in plagioclase is strong with a variation in An content of up to 21 mol% between cores and rims of single crystals (Fig. C10b). Plagioclases in the xenoliths representing former basalts from the sheeted dike complex show the same composition (20 to 23 mol% An in cores and 3 to 7 mol% in rims) as those of the plagiogranitic matrix, implying that the basaltic precursor material was obviously equilibrated with the plagiogranitic melt. Amphiboles of plagiogranites and basaltic xenoliths are of actinolitic composition and display the same high F and Cl contents (up to 5033 and 1556 ppm, respectively) observed for the varitextured gabbro (Fig. C12).

Compared to the plagiogranitic plagioclase, the trondhjemitic plagioclase lacks any zonation with an An content of ~18 mol%. The trondhjemitic amphibole displays the highest F content (9742 ppm) and a generally high Cl content (1236 ppm) (Fig. C12).

An content of plagioclase in the basaltic dike amphibolitic matrix varies from 70 to 49 mol% in the cores and 44 to 22 mol% in the rims. In some places which are strongly affected by secondary overgrowth the An content of the rims approaches pure albite composition (Fig. C9a). Relictic plagioclase phenocrysts which survived the secondary overprint show an extremely high An content of 82 mol%. Amphiboles in the basaltic dike are
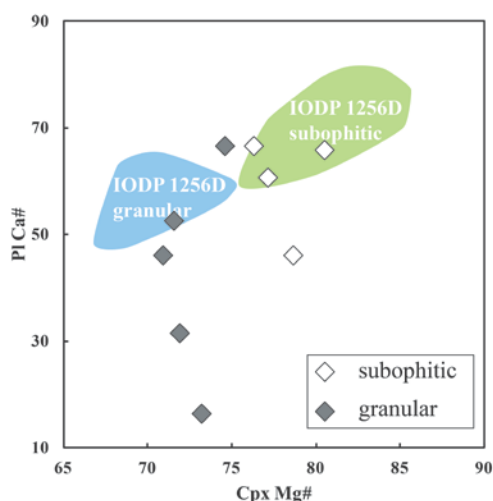
Figure 11 Clinopyroxene Mg# vs. plagioclase An% for Gideah South spotty gabbro subophitic and granular domains. Green field represents subophitic and blue-field range of data for granular domain of IODP Site 1256D spotty gabbro published by Koepke et al. (2011).

of actinolitic to magnesio-hornblenditic composition with high F and Cl content (up to 2102 and 939 ppm, respectively).
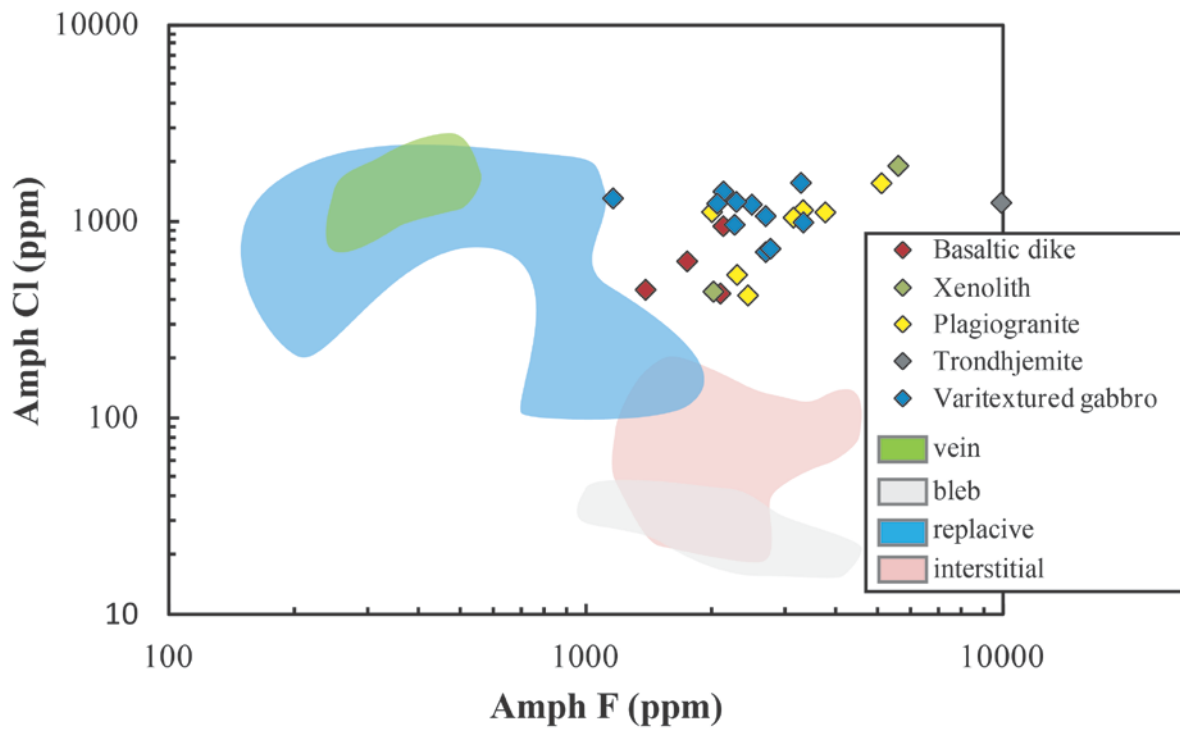
Figure C12. F vs. Cl for Gideah South amphiboles. Colored fields are from Coogan et al. (2001) for amphiboles related to either magmatic (bleb, interstitial) or hydrothermal (vein, replacive) formations evaluated for amphiboles from mid-Atlantic ridge gabbros. Note that Gideah South amphiboles show both high F and high Cl content and do not fall into one of the discrimination fields of Coogan et al. (2001).

C.6 Discussion

C.6.1 Modeling Liquid Lines of Descent

To identify the differentiation mechanism of the Gideah South lithologies, the MELTS program (Ghiorso and Sack, 1995) was used to model LLDs with a variation of melt water content from 0 to 1.6 wt% following MacLeod et al. (2013). As parental melt composition, the most primitive dike composition from the SDC (sample OM01 74) of the Wadi Tayin Massif published by MacLeod et al. (2013) was used with an oxygen fugacity corresponding to the quartz-fayalite-magnetite oxygen buffer. Crystallization pressure was fixed to 1 kbar and water content varied in steps of 0.2 wt%. Calculated LLDs were directly compared with the trends obtained for the bulk major element data (Fig. C6).

The results of the MELTS calculations revealed that the LLDs generally correlate well with the Gideah South bulk major element trends for water contents from 0.4 to 0.8 wt%, implying that fractional crystallization within an AML was the general magmatic process which produced the lithologies of Gideah South. The relatively high water contents are in clear contrast to modern EPR dikes and lavas for which differentiation trends can be best modeled in a nearly water-free system (Fig. C6). This result is also in good agreement with MacLeod et al. (2013) who estimated that those parental melts which formed the Geotimes (or V1) dikes and lavas within the Oman ophiolite contained 0.2 to 1 wt% of water. Details on the origin of water are discussed in the following.

C.6.2 Directly Visible: Details of Assimilation Processes at the Roof of the AML

A very interesting feature of Gideah South is the appearance of centimeter- to decimeter-wide basaltic xenoliths within the plagiogranite intrusions, similar to observations by France et al. (2009) from outcrops of the dike/gabbro transition in the Ibra area. The homogenous, very-fine-grained texture suggests that these basaltic xenoliths correspond to former sheeted dikes, which were intruded upon by felsic melts. The shape and the size of these xenoliths vary dramatically. Early stages of plagiogranite infiltration produced a net-veining plagiogranitic matrix and brickwork of basaltic xenoliths (Fig. C3g). In an advanced infiltration stage these brick-like xenoliths become more and more rounded (Fig. C3h), approaching a structure that was termed "vinaigrette" by Oman field geologists (e.g., Juteau et al., 1988). While this term implies the presence of two apparently-immiscible liquids of plagiogranitic and melanodoleritic composition, any formation by liquid immiscibility is not considered here, since it is obvious from the continuous textural observation that this texture is related to an advanced stage of basaltic dike dissolution with increasing disaggregation and assimilation of the dike material. In the upper parts of the outcrop, plagiogranite forms the matrix of a typical magmatic breccia with fist-sized, rounded xenoliths of basalts and varitextured gabbro in equal proportions, often with cm-wide dark-colored reaction rims. All

these features are the record of assimilation of sheeted dike basalts and varitextured gabbro by a plagiogranitic melt which developed from an initial to an advanced stage; one benefit of this outcrop is that all these different stages are directly visible.

We assume that the low density and compositionally highly-evolved plagiogranitic melts produced both by fractional crystallization and by partial melting (see section C5.4) formed the top of an upward-moving AML (e.g., Christensen, 1977) intruding upon, assimilating, and re-equilibrating with overlaying sheeted dikes and varitextured gabbros generated during an earlier AML event.

C.6.3 Origin of AML Water Content

Several processes are believed to result in a possible enrichment of water within the AML. Based on studies on the Oman ophiolite, several authors argue that hydrothermal cooling can be supposed to be responsible for inducing penetration of water directly into the AML or into the ascending melts within the lower crust before they feed the AML (e.g., Boudier et al., 2000; Nicolas et al., 2003). Based on detailed mapping of the gabbro/dike transition in the Oman ophiolite, Nicolas et al. (2008) modeled the introduction of seawater through tensile-stress-driven cracks into the AML. Moreover, Abily et al. (2011) presented a model deduced from the Oman ophiolite that directly introduces water into the MORB magma chambers via synmagmatic normal faulting. When applying these models to a modern fast-spreading MOR setting like the EPR, we would expect MORBs to display hydrous fractionation; however, this has not been observed. Instead, their LLDs are generally best modeled at water contents <0.2 wt% (see above; e.g., MacLeod et al., 2013; Fig. C6). Moreover, due to the assumed high water activities in the corresponding melts, involved plagioclases in gabbros from the Oman ophiolite are often strongly enriched in An (e.g., Abily et al., 2011, Benoit et al., 1999, France et al., 2013) and sometimes also show a clinopyroxene-before-plagioclase crystallization order (Abily et al., 2011, Koepke et al., 2009; Lippard et al., 1986) which is also not observed in the modern EPR (e.g., Coogan, 2014). Independent of whether these models are correct, this clearly shows that the Oman paleo-ridge was not like the modern EPR, but was instead related to the initiation of a subduction zone, an environment which introduced water into the parental melts which was obviously derived from subduction-zone-related fluids (e.g., MacLeod et al., 2013). Incompatible trace element signatures from this study support this assumption (Fig. C8), leading to the implication that ascending mantle melts already contained >0.2 wt% water derived from subduction-related fluids before feeding the AML.

Another possibility that would enhance the AML water content is the assimilation of previously-altered sheeted dikes by the AML roof during upward migration of a melt lens or volume inflation of the AML. The record of this process was observed both in the Oman ophiolite (France et al., 2009) and at the EPR IODP Site 1256 (e.g., Wilson et al., 2006; Koepke et al., 2008), where this process was identified to be responsible for the water content during the crystallization of the varitextured gabbros in the AML (Koepke et al., 2011). It should be noted that only very small amounts of water are necessary for establishing wet crystallization conditions in an AML (<1 wt%), due to the low water solubility at very low pressures (e.g., less than 1 kbar for the dike/gabbro transitions of modern fast-spreading

ridges; for details see discussion in Nicolas et al., 2008). It is obvious that this process was also very important for Gideah South, since the process of increasingly assimilating dike basalt fragments can directly be seen in the outcrop (Fig. C3g, h). It was shown both from modern EPR IODP Site 1256 (e.g., Koepke et al., 2008; Alt et al., 2010) and from the Oman ophiolite (France et al., 2009) that the sheeted dikes above the AML roof, prior to the assimilation, were first hydrated by hydrothermal alteration and then metamorphosed into granoblastic hornfelses, so it can be concluded that the assimilation process introduced seawater-derived fluids into the AML, in addition to intrinsic, subduction-zone-related water which was present in the parental melts. Thus, it is obvious that we are dealing with two completely different sources from which water was introduced into the AML. Since all analyzed amphiboles in the varitextured gabbros show relatively high amounts of F (Fig. C12), which is regarded to be of pure magmatic origin (e.g., Coogan et al., 2001), it can be concluded that significant amounts of primary magmatic, subduction-zone-related fluids were present. On the other hand, in addition to high F contents all amphiboles also show high Cl concentrations (Fig. C12), which could be derived either from seawater or from a subduction-zone-related fluid; both are known to be strongly enriched in Cl (e.g., Kent et al., 2002). The methods applied in this study cannot distinguish between these two processes.

C.6.4 Formation of Plagiogranite

For the formation of felsic melts within the oceanic crust, several processes have been discussed, most often extreme differentiation or partial melting of mafic lithologies (see Koepke et al., 2007 for review). Recently, models for AFC were proposed (e.g., Freund et al., 2013; Wanless et al., 2010). For the two major processes, partial melting of dikes at the roof of an AML (France et al., 2010, 2014, Erdmann et al., 2015) and differentiation of MORB, major and trace element concentrations for the resulting felsic melts are generally comparable except for differences in Al_2O_3, K_2O, Zr, and Hf concentration. As shown in Fig. C6 and C7 one of three analyzed plagiogranite samples, A11-1p, which is relatively low in Al_2O_3 and K_2O, fits the LLD calculated by "MELTS" for 0.6 to 0.8 wt% water perfectly (Fig. C6). In addition, in a NMORB-normalized spider diagram this sample does not show a positive Zr-Hf anomaly, implying that this rock was produced by simple fractional crystallization of a typical parental Oman MORB.

The other two samples (A11-1ib and A11-1l) are too enriched in Al_2O_3 and depleted in K_2O for an origin via fractional crystallization of MORB (Fig. C6). Moreover, the NMORB-normalized spider diagram of these rocks (Fig. C7) shows a distinct positive Zr-Hf anomaly suggesting an origin by partial melting of hydrated sheeted dike basalt. This hypothesis is based on an experimental study of France et al. (2010, 2014) who showed that the partial melting of typical hydrated Oman basalt leads to anatectic melts with high bulk Al_2O_3 content (Fig. C6) and Zr- and Hf-enriched trace element compositions (Fig. C7) similar to the two A11-1ib and A11-il plagiogranites from the Gideah South outcrop (referring to experimental melt produced below 1000°C at a relatively low degree of partial melting). The bulk K_2O contents of these two samples, however, are in disagreement with a model of partial melting of hydrated dike basalts, since the experimental partial melts are highly enriched in K_2O, while the K_2O content of these two samples is rather low (Fig. C6). However, this effect is

attributed to the relatively high bulk K_2O content of 0.2 wt% of the starting material used by France et al. (2010, 2014), whereas the average K_2O content of typical sheeted dikes from the Ibra area is much lower (e.g., ~0.07 wt% K_2O for the most primitive basalt of this area from the compilation of MacLeod et al., 2013 used for the MELTS modeling; see section C5.1). Erdmann et al. (2015) showed experimentally that partial melting of highly hydrothermally-altered basaltic dikes from IODP Site 1256 (11 and 27 % alteration) with a low bulk K_2O (0.07 and 0.11 wt%) results in partial melts with nearly constant low bulk K_2O.

To summarize, bulk major and trace element characteristics reveal that the two plagiogranite samples A11-1ib and A11-1l can be assumed to be more related to partial melting of altered dikes, while the plagiogranite A11-1p better fits a model of fractional crystallization. However, since it is obvious that the initial plagiogranitic melt was significantly modified by massive assimilation of sheeted dike basalt (see section C5.2), all these evaluations related to pure endmember processes must be considered with caution. It should be noted that the high Al_2O_3 content observed in two plagiogranite samples cannot be the result of complex assimilation processes, since the addition of typical Oman sheeted dike basalt, altered or fresh, cannot result in an increase of Al_2O_3 to such high values. Given the great variability in texture and the compositional heterogeneity of the Gideah South plagiogranites, the general good fit with the calculated LLD in a hydrous system of typical Oman MORB, and both the high Al_2O_3 contents and the positive Zr-Hf anomalies, a model of formation is implied in which simultaneous coexistent fractional crystallization, partial melting, assimilation, and mixing occurred at a relatively small scale. That the partial melting of hydrated basalts played a significant role is also indicated by the presence of typical granoblastic two-pyroxene hornfelses which show characteristic depleted trace element patterns and which were identified as residues after partial melting of sheeted dikes (France et al., 2010, 2014, Erdmann et al., 2015). However, we did not find these hornfelses within the Gideah South outcrop but rather some hundred meters farther north (see also France et al., 2009, 2014), in a crustal stratigraphy about 200 meters below the frozen AML investigated here; this reflects the general dip of the Wadi Gideah crustal sequences (see Pallister and Hopson, 1981). The record of residues after hydrous partial melting of dikes in that structural level could explain the generation of felsic melts which then moved up into higher parts of the AML system, infiltrating already-frozen sheeted dikes and intruding into nearly-frozen varitextured gabbro.

The Gideah South trondhjemite dike displays a bulk trace element signature in NMORB-normalized spider diagrams strikingly similar to that of partial melts obtained experimentally by France et al. (2010, 2014) (Fig. C7). However, an enrichment of bulk Al_2O_3 related to partial melting of hydrated dikes, like for those most-evolved plagiogranites, is not observed. Hence, we assume that the trondhjemite is eventually produced by partial melts derived by reheating Al_2O_3-depleted granoblastic hornfelses after the dikes have partially melted in a first phase, i.e., after partial melts corresponding to the more-evolved Gideah South plagiogranite were produced. Another possibility could be the partial melting of hydrated dikes, but under reduced water activity as discussed by Erdmann et al. (2015).

C.6.5 In Situ Crystallization within the Varitextured Gabbros

Another feature from Gideah South is the appearance of a varitextured gabbro subtype very similar to spotty gabbros observed and described by Koepke et al. (2011) for IODP Site 1256 (EPR). The dark appearance of a subophitic domain consisting of clinopyroxene oikocrysts highly altered to minerals of amphibolite and greenschist facies contrasts with a whitish, plagioclase-rich granular domain and gives these rocks their typical patchy appearance (Fig. C3i). Koepke et al. (2011) defined five main characteristics to distinguish EPR spotty from "normal" varitextured gabbro: (1) the major and trace mineral data reveal that the subophitic domain crystallized from a more primitive melt while the granular domain crystallized from a liquid which was much more evolved; (2) the transition between granular matrix and subophitic patches is continuous, implying temporarily simultaneous crystallization; (3) the granular matrix includes relics of clinopyroxene oikocrysts and plagioclase chadacrysts from subophitic patches; (4) the granular matrix plagioclases display a wider range of more-evolved compositions compared to plagioclase chadacrysts of the subophitic domain; and (5) the crystallization of the granular matrix started at temperatures <900 °C, whereas the crystallization of the subophitic domains started at much higher temperatures. Hence, these authors presented the following model for the formation of the spotty gabbros. Crystallization starts with the first plagioclase before clinopyroxene in mushy zones (e.g., at the margin of the AML) which form the subophitic domains. Under decreasing temperatures, the subophitic domains continue to crystallize, forming a well-connected framework. The evolved residual melt is then trapped within the subophitic network, and crystallizes to a granular matrix under continuously decreasing temperatures.

The spotty gabbros from Gideah South are very similar to those patchy gabbros from IODP Site 1256, showing the same textural features such as clinopyroxene oikocrysts enclosing skeletal plagioclase chadacrysts and a continuous transition between domains as well as similar chemical compositions for clinopyroxene and plagioclase (Fig. C11). Minerals from the granular domain display generally more-evolved compositions compared to subophitic ones. Hence we assume a formation scenario for the Gideah South spotty gabbros very similar to the one described by Koepke et al. (2011), implying that some of the complex crystallization processes recorded in Gideah South correlate well with modern EPR AML processes, in spite of higher water content in those melts feeding the Gideah South AML.

C.6.6 Comparison with Modern Oceanic Crust

Authors of previous studies (e.g., MacLeod et al., 2013) pointed out that models of rock formation and crust accretion based on field work in the Oman ophiolite should be transferred with caution to modern fast-spreading MOR settings due to the possible influence of a subduction zone initiation. While we are in full agreement with that statement, which was confirmed by our study, we realize striking similarities between the AML horizon at the termination of the Wadi Gideah and a modern EPR AML, as manifested in the IODP drill core recovered at Site 1256: (1) The presence of spotty gabbro-bearing domains of poikilitic clinopyroxene and plagioclase chadacrysts representing remnants of primitive MORB

delivered to the AML; (2) the presence of felsic melts produced by partial melting of dikes triggered by the heat of upward-moving melt lenses (France et al., 2010, 2014, Erdmann et al., 2015); (3) the visible assimilation of dikes; (4) the occurrence of granoblastic two-pyroxene hornfelses about 100 m north of Gideah South (France et al., 2009, and our sampling); (5) the presence of relatively small felsic dikes within these hornfelses which can be interpreted as products of partial melting (France et al., 2010, 2014); (6) the direct record of a very dynamic AML with the potential of upward and downward motion (see next section). It is an important observation that all felsic intrusions in the dike/gabbro transition of the Wadi Gideah are of small size (maximum meter-scale) and are geochemically related to the early V1 magmatism (e.g., Godard et al., 2003), while other felsic intrusives in the Samail ophiolite that form much larger bodies (often 100-meter scale) are related to the later V2 magmatism, which is clearly subduction-zone-related with a geochemical character not known from any recent ridge system (Freund, 2014; Haase et al., 2015).

Thus, we conclude that the results and implications related to the AML-magmatic processes of this study are generally applicable to modern fast-spreading MOR systems. The study presented here related to the Gideah South outcrop, as well as other studies on the same topic performed nearby (France et al., 2009, 2014), are a useful complement to the IODP efforts at Site 1256 at the EPR, where for the first time the dike/gabbro transition was penetrated in an intact sequence of oceanic crust through lavas and dikes into the uppermost gabbros. Unfortunately, the drilling at Site 1256 terminated after cutting two screens of varitextured gabbro within the hornfelses of the conducting boundary layer (Teagle et al., 2012), so that this and similar investigations on the dike/gabbro transition of the Wadi Gideah can be regarded as an essential step towards unraveling the geological processes operating at this horizon; this understanding will allow us to constrain the controls on heat and mass transfer within the uppermost plutonic oceanic crust.

C.6.7 A Dynamic Model for Magmatic Processes in a Dying Axial Magma Chamber

Observations from this study, such as the general sequence of intrusions, the occurrence of basaltic dikes with chilled margins, the presence of trondhjemite dikes with sharp contacts, the brecciation of sheeted dikes by infiltrating felsic melts, and the record of several partial melting events, suggest that one AML steady-state system for the Gideah South formation is highly unlikely. Our observations and results, instead, require multiple sequences of heating and cooling events, and are best explained by a vertical migration of the AML, including upward motion after replenishment and downward motion after a volcanic eruption at the seafloor (for details see Gillis and Coogan, 2002; Gillis, 2008; France et al., 2009). This is the basis for a dynamic model presented in the following which summarizes the different modes of magmatic accretion in an open AML system during the Oman paleo-ridge accretion. Based on the complex field relationships observed in Gideah South and in our petrographic and geochemical results, we present here a formation scenario related to multiple sequences of melt lens migration including four identified stages as illustrated in Fig. C13.

Stage (1), t = t_0. After migrating upward, perhaps as a consequence of replenishment, the AML establishes a new steady state at a relatively high position, thereby intruding upon previously altered sheeted dikes. Local stoping and assimilation of hydrothermally-altered roof material may increase melt water content. Only the varitextured gabbro, visible in the outcrop, remains from this stage; the record from a higher level above the gabbro is missing. This scenario is well-recorded from IODP Site 1256, where varitextured gabbro intruded into previously-altered dikes. The steady-state situation is followed by a downward migration of the AML. Temperature within the AML decreases quickly due to reduced heat supply from below and convective cooling from above, leading to at least partial freezing of the AML starting with the formation of the spotty gabbro domains followed by the formation of the granular domains and the normal varitextured gabbro. This freezing situation is depicted in Fig. 13a. In the outcrop, this situation is visible in the right part where a coherent body of varitextured gabbro identified as the oldest part of the outcrop exists, including those characteristic spotty domains (Fig. C3 e, i).

Stage (2), t = t_1. At a deeper level, after a phase of minor replenishment, thermal metamorphism in the AML roof leads to hydrous partial melting of basaltic dikes forming low-density plagiogranitic melts, which migrate upwards (e.g., Christensen, 1977) and mix with evolved melts produced by MORB differentiation. At the top of the AML, these evolved melts assimilate sheeted dikes (Fig. C3g, h) and finally intrude into the varitextured gabbros which are still not completely frozen at this stage, as indicated by apophyses from the plagiogranitic melt in the varitextured gabbro (Fig. C3d). At this stage, the plagiogranitic melts also infiltrate the varitextured gabbro, as evident from xenoliths of varitextured gabbro within the plagiogranite (Fig C3b). This very complex situation is depicted in Fig. C13b. The granoblastic residuum shown in Fig. 13b, lower left is not visible in the outcrop. Typical two-pyroxene hornfelses, interpreted as residues remaining after partial melting of dikes, are exposed about 100 m farther north (France et al., 2009, 2014) corresponding to a deeper level of the melt lens horizon, beneath the Gideah South outcrop.

Stage (3), t = t_3. This stage is solely constrained by the presence of those trondhjemite dikes cutting the plagiogranite with very sharp contacts (Fig. C3f), implying that the plagiogranite was cooled down to relatively low temperatures during the trondhjemite intrusion, probably by hydrothermal convection, enabling cracking in a brittle regime. Because the geochemical results imply that this trondhjemite was formed by hydrous partial melting of a hornfelsic residuum produced during a previous partial melting event, we assume that after another replenishment the AML moved up again but persisted at a crustal height below the outcrop level. Thermal metamorphism in the granoblastic hornfelses induced by the heat of the AML led to hydrous partial melting, forming the trondhjemitic veins which intruded upwards and filled cracks both within the plagiogranite and in the varitextured gabbro.

Stage (4), t = t_4. This stage reflects the last primary event visible in the Gideah South outcrop: the intrusion of basaltic dikes which cut all other lithologies including the so-far-latest formation, the trondhjemite dikes (Fig. C3a, c). Since these basaltic dikes show well-preserved chilled margins at the contact to all host rocks, it is obvious that these dikes were emplaced in a brittle regime when the surrounding rocks were significantly cooled down by

hydrothermal convection. Because we observed five basaltic dikes within the relatively small area exposed in the outcrop, it is obvious that this event is related to another replenishment of the AML which must be located in a much deeper crustal level than that of the outcrop level. This situation is depicted in Fig. C13d.

Since the model of a vertically-migrating dynamic melt lens presented above is a direct consequence of the contact relationships between the different intrusions (i.e., sutured, sharp, presence of chilled margins) which are clearly visible in the outcrop, our interpretation seems quite robust. Although the field relationships allow us to identify at least three different stages of upward movement (heating) and downward movement (cooling by hydrothermal convection), we are not able to reliably estimate the absolute time scale for these processes. France et al. (2009) reviewed the literature available at that time on this topic and concluded that multidisciplinary investigations mostly performed at the EPR revealed indirect constraints on time scales for the vertical fluctuations of an AML ranging from a few tens of years to 100,000 years. To quantify the cooling rate above a frozen AML at EPR IODP Site 1256, Zhang et al. (2014) estimated recent cooling rates by using a forward modeling approach based on CaAl-NaSi interdiffusion in plagioclase from two-pyroxene hornfelses representing recrystallized sheeted dikes. Their results show that cooling from the peak thermal overprint at 1000–1050 °C to 600 °C occurs within about 10–30 years as a result of hydrothermal circulation above a melt lens during magma starvation. Using the recently-estimated paleo spreading rate for the Oman ophiolite based on high-precision U/Pb zircon geochronology (50–100 km/Ma full spreading rate; Rioux et al., 2012) and an AML width of 2 km (Sinton and Detrick, 1992), it is possible to roughly calculate how long a volume element created at the center of the AML stays within the molten regime before leaving due to seafloor spreading; 10,000 to 20,000 years. Thus, when using the replenishment rate of 10-30 years estimated by Zhang et al. (2014) for the AML at IODP Site 1256, 350 to 2000 replenishment cycles can be calculated for a typical AML during the accretion of the Oman ophiolite paleo-ridge. When considering this high number of replenishments, it is obvious that only the last cycles could be frozen and visible in any outcrop, when the AML is moving out of the on-axis area for a final freezing, and this is obviously the record we can observe in Gideah South.

One surprising outcome of this study is that the basaltic dikes cutting all other lithologies show a geochemical character typical of the V2 magmatic stage, which is related to a supra-subduction setting or the development of a proto-arc system (e.g., Goodenough et al., 2010, 2014; Rioux et al., 2013), while the other lithologies more closely correspond to the V1 magmatic stage, which is related to the initiation of subduction. According to Rioux et al. (2013), the V2 activity started ≤250,000 – 500,000 years after the on-axis formation of most of the crust by the V1 magmatism that probably is related to spreading during slab roll back. Thus, it is possible that the gabbros and felsic rocks of Gideah South were formed in the early V1 stage in a ridge setting similar to what we observe today at the EPR, and that the late basaltic dikes intruded much later, with several 10,000 year delays, in a situation which was still tectonically dominated by extension, but in the environment of a proto-arc evolution.
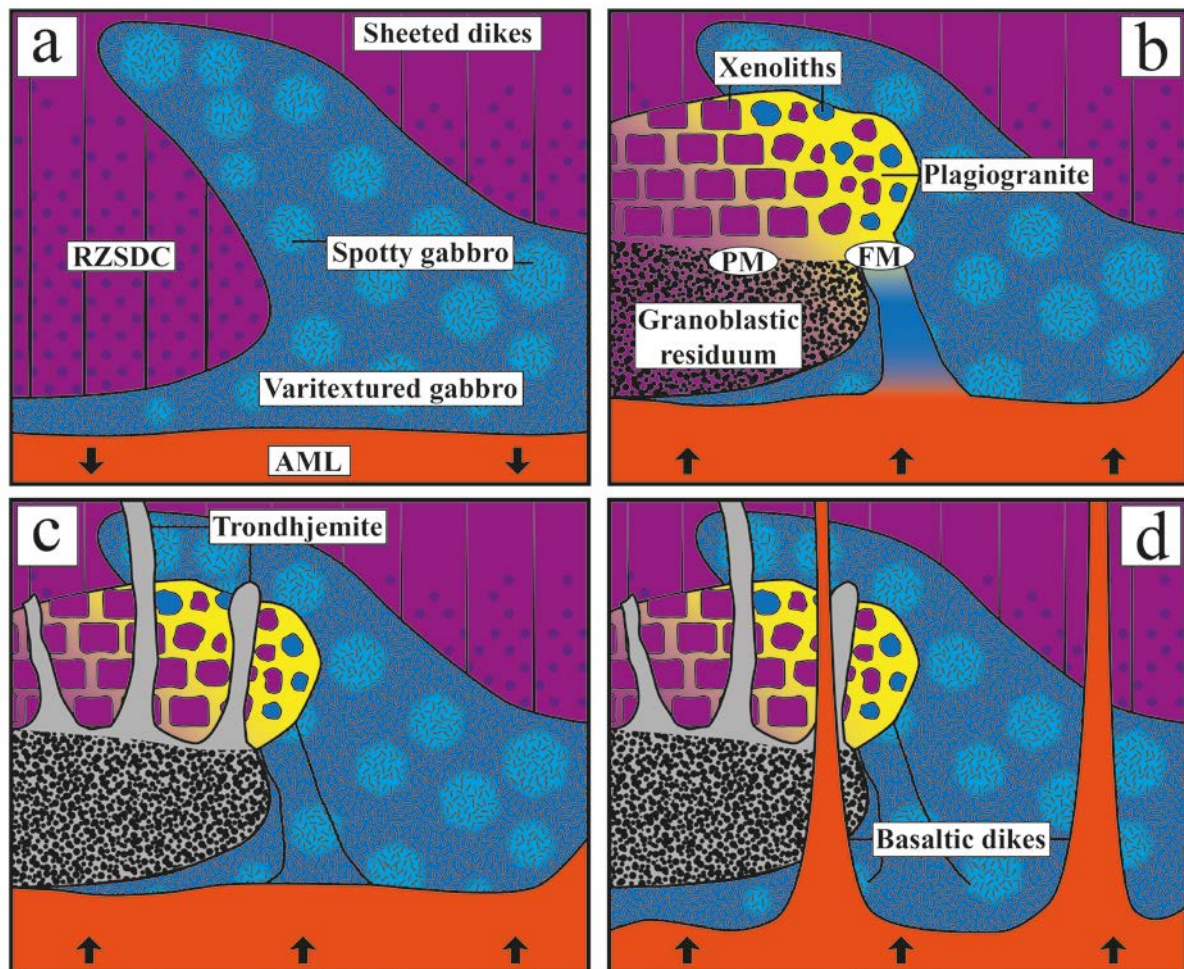
Figure C13. Schematic model for melt lens migration and formation of Gideah South lithologies. Black arrows represent movement direction of AML roof. a) Stage (1) $t=t_o$. Formation of spotty gabbro domains followed by formation of granular domains and normal varitextured gabbro in a frozen situation after AML downward migration. b) Stage (2) $t=t_1$. Plagiogranitic melts formed by hydrous partial melting of basaltic dikes (PM) and MORB differentiation (FM) mix together after upward AML movement and migrate upwards, thereby assimilating sheeted dikes and infiltrating the varitextured gabbro above, integrating xenoliths of basaltic dikes and varitextured gabbro. This leads to "brick-" (left) or "vinaigrette-like" (right; Juteau et al., 1988) texture for frozen xenolith-bearing plagiogranite, depending on the grade of assimilation. c) Stage (3) $t=t_3$. Trondhjemitic dikes are formed by hydrous partial melting of granoblastic residuum at the depth produced in stage (2) after AML upward migration, cutting plagiogranite from above which had already cooled down allowing the formation of cracks in which the trondhjemite intrudes. d) Stage (4) $t=t_4$. Basaltic dikes crosscut all other lithologies after they have significantly cooled down, allowing the formation of distinct chilled margins. For further details see text.

C.7 Conclusion

Field observations, petrography, bulk and mineral major and trace element chemistry, and petrological modeling for the Gideah South lithologies reveal the following implications:

(1) The Gideah South lithologies were formed as a consequence of episodic vertical movements of the AML probably caused by changes in AML replenishment rates.

(2) The spotty gabbro can be regarded as equivalent to those spotty gabbros described for IODP Site 1256 by Koepke et al. (2011). We suppose a similar formation mechanism based on in situ crystallization in a freezing AML.

(3) The varitextured gabbros can mostly be regarded as frozen melts and were formed by crystallization within the AML of a melt containing ~0.4 to 0.8 wt% H_2O. In agreement with the results of MacLeod et al. (2013) for the Oman extrusives we conclude that the presence of water is derived from subduction-zone-related fluids during a phase of subduction initiation.

(4) The observed plagiogranites were formed by a complex magmatic process, which involved simultaneous fractional crystallization, partial melting of dikes, and assimilation at a relatively small scale.

(5) The Gideah South and other outcrops exposing the dike/gabbro transition at the termination of the Wadi Gideah are, in general, a good analog to modern EPR fast-spreading oceanic crust in terms of general magmatic formation processes.

(6) The late basaltic dikes cutting all other lithologies exhibit a distinct geochemical evolution compared to the gabbros and felsic rocks, and are probably related to the V2 magmatic stage in an extensional setting, likely associated with the formation of a proto-arc.

References

Abily, B. (2011). Caractéristiques pétrographique, géochimique et structurale de la section crustale profonde de l'ophiolite d'Oman: Implications pour la genèse des magmas et le fonctionnement des chambres magmatiques à l'aplomb d'un centre d'expansion océanique (Doctoral dissertation, Université Paul Sabatier-Toulouse III).

Abily, B., Ceuleneer, G., & Launeau, P. (2011). Synmagmatic normal faulting in the lower oceanic crust: Evidence from the Oman ophiolite. Geology, 39(4), 391-394.

Abily, B., & Ceuleneer, G. (2013). The dunitic mantle-crust transition zone in the Oman ophiolite: Residue of melt-rock interaction, cumulates from high-MgO melts, or both?. Geology, 41(1), 67-70.

Alabaster, T., Pearce, J. A., & Malpas, J. (1982). The volcanic stratigraphy and petrogenesis of the Oman ophiolite complex. Contributions to Mineralogy and Petrology, 81(3), 168-183.

Allègre, C. J. (2008). Isotope geology (p. 512). Cambridge: Cambridge University Press.

Alt, J. C., Laverne, C., Coggon, R. M., Teagle, D. A., Banerjee, N. R., Morgan, S., ... & Galli, L. (2010). Subsurface structure of a submarine hydrothermal system in ocean crust formed at the East Pacific Rise, ODP/IODP Site 1256. Geochemistry, Geophysics, Geosystems, 11(10).

Bachmann, F., Hielscher, R., & Schaeben, H. (2010). Texture analysis with MTEX–free and open source software toolbox. Solid State Phenomena, 160, 63-68.

Bähre, L. (2015). Major and trace element chemistry of minerals in gabbros from a complete profile through the oceanic crust in the Wadi Gideah (Sumail Ophiolite, Sultanate Oman). Master´s Thesis

Bédard, J. H., Sparks, R. S. J., Renner, R., Cheadle, M. J., & Hallworth, M. A. (1988). Peridotite sills and metasomatic gabbros in the Eastern Layered Series of the Rhum complex. Journal of the Geological Society, 145(2), 207-224.

Bédard, J. H. (2001). Parental magmas of the Nain Plutonic Suite anorthosites and mafic cumulates: a trace element modelling approach. Contributions to Mineralogy and Petrology, 141(6), 747-771.

Behn, M. D., & Kelemen, P. B. (2006). Stability of arc lower crust: Insights from the Talkeetna arc section, south central Alaska, and the seismic structure of modern arcs. Journal of Geophysical Research: Solid Earth (1978–2012), 111(B11).

Benoit, M., Ceuleneer, G., & Polvé, M. (1999). The remelting of hydrothermally altered peridotite at mid-ocean ridges by intruding mantle diapirs. Nature, 402(6761), 514-518.

Beurrier, M., Geologie de la nappe ophiolitique de Samaildans les parties orientales et centrales des montagnesd'Oman, Univ. e Pierre et Marie Curie, Paris VI, Paris, France, 1987.

Boudier, F., & Nicolas, A. (1995). Nature of the Moho transition zone in the Oman ophiolite. Journal of Petrology, 36(3), 777-796.

Boudier, F., Nicolas, A., & Ildefonse, B. (1996). Magma chambers in the Oman ophiolite: fed from the top and the bottom. Earth and Planetary Science Letters, 144(1), 239-250.

Boudier, F., Godard, M., & Armbruster, C. (2000). Significance of gabbronorite occurrence in the crustal section of the Semail ophiolite. Marine Geophysical Researches, 21(3-4), 307-326.

Bouvier, A., Vervoort, J. D., & Patchett, P. J. (2008). The Lu–Hf and Sm–Nd isotopic composition of CHUR: constraints from unequilibrated chondrites and implications for the bulk composition of terrestrial planets. Earth and Planetary Science Letters, 273(1), 48-57.

Bosch, D., Jamais, M., Boudier, F., Nicolas, A., Dautria, J. M., & Agrinier, P. (2004). Deep and high-temperature hydrothermal circulation in the Oman ophiolite—petrological and isotopic evidence. Journal of Petrology, 45(6), 1181-1208.

Browning, P. (1982). The petrology, geochemistry and structure of the plutonic rocks of the Oman ophiolite (Doctoral dissertation, Open University).

Browning, P. (1984). Cryptic variation within the cumulate sequence of the Oman ophiolite: magma chamber depth and petrological implications. Geological Society, London, Special Publications, 13(1), 71-82.

Bloomer, S. H., Taylor, B., MacLeod, C. J., Stern, R. J., Fryer, P., Hawkins, J. W., & Johnson, L. (1995). Early arc volcanism and the ophiolite problem: a perspective from drilling in the western Pacific. Active margins and marginal basins of the western Pacific, 88, 1-30.

Bunge, H. J. Texture analysis in materials science'; 1982. Butterworth's, London.

Burke, W. H., Denison, R. E., Hetherington, E. A., Koepnick, R. B., Nelson, H. F., & Otto, J. B. (1982). Variation of seawater 87Sr/86Sr throughout Phanerozoic time. Geology, 10(10), 516-519.

Burns, L. E. (1985). The Border Ranges ultramafic and mafic complex, south-central Alaska: cumulate fractionates of island-arc volcanics. Canadian Journal of Earth Sciences, 22(7), 1020-1038.

Canales, J. P., Detrick, R. S., Toomey, D. R., & Wilcock, W. S. (2003). Segment-scale variations in the crustal structure of 150–300 kyr old fast spreading oceanic crust (East Pacific Rise, 8 15′ N–10 5′ N) from wide-angle seismic refraction profiles. Geophysical Journal International, 152(3), 766-794.

Cann, J. R. (1970). Rb, Sr, Y, Zr and Nb in some ocean floor basaltic rocks.Earth and Planetary Science Letters, 10(1), 7-11.

Cann, J. R. (1974). A model for oceanic crystal structure developed. Geophysical Journal International, 39(1), 169-187.

Ceuleneer, G., Nicolas, A., & Boudier, F. (1988). Mantle flow patterns at an oceanic spreading centre: the Oman peridotites record. Tectonophysics,151(1), 1-26.

Christensen, N. I. (1977). The geophysical significance of oceanic plagiogranite. Earth and Planetary Science Letters, 36(2), 297-300.

Coleman, R. G. (1981). Tectonic setting for ophiolite obduction in Oman.Journal of Geophysical Research: Solid Earth (1978–2012), 86(B4), 2497-2508.

Coogan, L. A., Wilson, R. N., Gillis, K. M., & MacLeod, C. J. (2001). Near-solidus evolution of oceanic gabbros: Insights from amphibole geochemistry.Geochimica et Cosmochimica Acta, 65(23), 4339-4357.

Coogan, L. A., Gillis, K. M., MacLeod, C. J., Thompson, G. M., & Hékinian, R. (2002a). Petrology and geochemistry of the lower ocean crust formed at the East Pacific Rise and exposed at Hess Deep: A synthesis and new results. Geochemistry, Geophysics, Geosystems, 3(11), 1-30.

Coogan, L. A., Thompson, G., & MacLeod, C. J. (2002b). A textural and geochemical investigation of high level gabbros from the Oman ophiolite: implications for the role of the axial magma chamber at fast-spreading ridges. Lithos, 63(1), 67-82.Coogan, L.A. (2014). The lower oceanic crust; 2nd Edition. Turekian, K., Holland, H.D. (Eds.), Treatise on Geochemistry. Elsevier, Amsterdam, pp. 497-541

Coogan, L. A., Howard, K. A., Gillis, K. M., Bickle, M. J., Chapman, H., Boyce, A. J., ... & Wilson, R. N. (2006). Chemical and thermal constraints on focussed fluid flow in the lower oceanic crust. American Journal of Science,306(6), 389-427.

Coogan, L. A., (2014). The lower oceanic crust. In Turekian, K., and Holland, H. D. (eds.), Treatise on Geochemistry, 2nd edn. Amsterdam: Elsevier, doi:10.1016/B978-0-08-095975-7.00316-8.

Danyushevsky, L. V. (2001), The effect of small amounts of H2O on crystallisation of mid-ocean ridge and backarc basin magmas, J. Volcanol. Geotherm. Res., 110, 265–280,doi:10.1016/S0377-0273(01)00213-X.

Danyushevsky, L. V., & Plechov, P. (2011). Petrolog3: Integrated software for modeling crystallization processes. Geochemistry, Geophysics, Geosystems,12(7).

Detrick, R. S., Buhl, P., Vera, E., Mutter, J., Orcutt, J., Madsen, J., & Brocher, T. (1987). Multi-channel seismic imaging of a crustal magma chamber along the East Pacific Rise. Nature, 326(6108), 35-41.

Dick, H. J., & Natland, J. H. (1996). Late-stage melt evolution and transport in the shallow mantle beneath the East Pacific Rise. In proceedings-ocean drilling program scientific results (pp. 103-134). National Science Foundation.

Dorais, M. J., & Tubrett, M. (2008). Identification of a subduction zone component in the Higganum dike, Central Atlantic Magmatic Province: A LA-ICPMS study of clinopyroxene with implications for flood basalt petrogenesis. Geochemistry, Geophysics, Geosystems, 9(10).

Erdmann, M., Fischer, L. A., France, L., Zhang, C., Godard, M., & Koepke, J. (2015). Anatexis at the roof of an oceanic magma chamber at IODP Site 1256 (equatorial Pacific): an experimental study. Contributions to Mineralogy and Petrology, 169(4), 1-28.

Ernewein, M., Pflumio, C., & Whitechurch, H. (1988). The death of an accretion zone as evidenced by the magmatic history of the Sumail ophiolite (Oman).Tectonophysics, 151(1), 247-274.

Ernst, W. G., & Liu, J. (1998). Experimental phase-equilibrium study of Al-and Ti-contents of calcic amphibole in MORB-A semiquantitative thermobarometer.American Mineralogist, 83, 952-969

Floyd, P. A., & Winchester, J. A. (1975). Magma type and tectonic setting discrimination using immobile elements. Earth and Planetary science letters,27(2), 211-218.

France, L., Ildefonse, B., & Koepke, J. (2009). Interactions between magma and hydrothermal system in Oman ophiolite and in IODP Hole 1256D: Fossilization of a dynamic melt lens at fast spreading ridges. Geochemistry, Geophysics, Geosystems, 10(10).

France, L., Koepke, J., Ildefonse, B., Cichy, S. B., & Deschamps, F. (2010). Hydrous partial melting in the sheeted dike complex at fast spreading ridges: experimental and natural observations. Contributions to Mineralogy and Petrology, 160(5), 683-704.

France, L., Ildefonse, B., & Koepke, J. (2013). Hydrous magmatism triggered by assimilation of hydrothermally altered rocks in fossil oceanic crust (northern Oman ophiolite). Geochemistry, Geophysics, Geosystems, 14(8), 2598-2614.

France, L., Koepke, J., MacLeod, C. J., Ildefonse, B., Godard, M., & Deloule, E. (2014). Contamination of MORB by anatexis of magma chamber roof rocks: Constraints from a geochemical study of experimental melts and associated residues. Lithos, 202, 120-137.

Freund, S., Beier, C., Krumm, S., & Haase, K. M. (2013). Oxygen isotope evidence for the formation of andesitic–dacitic magmas from the fast-spreading Pacific–Antarctic Rise by assimilation–fractional crystallisation. Chemical Geology, 347, 271-283.

Freund, S., (2014). The generation of felsic magmas in the oceanic crust: assimilation-fractional crystallization processes versus re-melting of the crust. PhD-Thesis

Fricker, M. B., Kutscher, D., Aeschlimann, B., Frommer, J., Dietiker, R., Bettmer, J., & Günther, D. (2011). High spatial resolution trace element analysis by LA-ICP-MS using a novel ablation cell for multiple or large samples. International Journal of Mass Spectrometry, 307(1), 39-45.

Gale, A., Dalton, C. A., Langmuir, C. H., Su, Y., & Schilling, J. G. (2013). The mean composition of ocean ridge basalts. Geochemistry, Geophysics, Geosystems, 14(3), 489-518.

Garbe-Schönberg, C. D. (1993). Simultaneous determination of thirty-seven trace elements in twenty-eight international rock standards by ICP-MS. Geostandards Newsletter, 17(1), 81-97.

Garbe-Schönberg, D., & Müller, S. (2014). Nano-particulate pressed powder tablets for LA-ICP-MS. Journal of Analytical Atomic Spectrometry, 29(6), 990-1000.

Garrido, C. J., Kelemen, P. B., & Hirth, G. (2001). Variation of cooling rate with depth in lower crust formed at an oceanic spreading ridge: Plagioclase crystal size distributions in gabbros from the Oman ophiolite. Geochemistry, Geophysics, Geosystems, 2(10).

Ghiorso, Mark S., and Sack, Richard O. (1995) Chemical Mass Transfer in Magmatic Processes. IV. A Revised and Internally Consistent Thermodynamic Model for the Interpolation and Extrapolation of Liquid-Solid Equilibria in Magmatic Systems at Elevated Temperatures and Pressures. Contributions to Mineralogy and Petrology, 119, 197-212

Gillis, K. M. (1996). Rare earth element constraints on the origin of amphibole in gabbroic rocks from site 894, Hess Deep. In proceedings-ocean drilling program scientific results (pp. 59-76). National Science Foundation.

Gillis, K. M., & Coogan, L. A. (2002). Anatectic migmatites from the roof of an ocean ridge magma chamber. Journal of Petrology, 43(11), 2075-2095.

Gillis, K. M. (2008). The roof of an axial magma chamber: A hornfelsic heat exchanger. Geology, 36(4), 299-302.

Gillis, K., Snow, J.E., and Klaus, A., 2012. Hess Deep plutonic crust: exploring the plutonic crust at a fast-spreading ridge: new drilling at Hess Deep. IODP Sci. Prosp., 345. doi:10.2204/iodp.sp.345.2012

Gillis, K. M., Snow, J. E., Klaus, A., Guerin, G., Abe, N., Akizawa, N., ... & Gjesvold, R. (2014). Hess deep plutonic crust: exploring the plutonic crust at a fast-spreading ridge: new drilling at Hess Deep. Integrated Ocean Drilling Program: Preliminary Reports, (345), 1-89.

Godard, M., Dautria, J. M., & Perrin, M. (2003). Geochemical variability of the Oman ophiolite lavas: Relationship with spatial distribution and paleomagnetic directions. Geochemistry, Geophysics, Geosystems, 4(6).

Godard, M., Bosch, D., & Einaudi, F. (2006). A MORB source for low-Ti magmatism in the Semail ophiolite. Chemical Geology, 234(1), 58-78.

Goodenough, K. M., Styles, M. T., Schofield, D., Thomas, R. J., Crowley, Q. C., Lilly, R. M., ... & Carney, J. N. (2010). Architecture of the Oman–UAE ophiolite: evidence for a multi-phase magmatic history. Arabian Journal of Geosciences, 3(4), 439-458.

Goodenough, K. M., Thomas, R. J., Styles, M. T., Schofield, D. I., & MacLeod, C. J. (2014). Records of ocean growth and destruction in the Oman–UAE ophiolite. Elements, 10(2), 109-114.

Griffin, W.L., Powell, W.J., Pearson, N.J. and O'Reilly, S.Y. 2008. GLITTER: data reduction software for laser ablation ICP-MS. In Laser Ablation–ICP–MS in the Earth Sciences (P. Sylvester, ed.). Mineralogical Association of Canada Short Course Series Volume 40, Appendix 2, 204-207.

Grove, T.L., Kinzler, R.J., and Bryan, W.B., (1992), Fractionation of mid-ocean ridge basalt (MORB), in Phipps Morgan, J., et al., eds., Mantle fl ow and melt generation at mid-ocean ridges: American Geophysical Union Geophysical Monograph 71, p. 281–310, doi:10.1029/GM071p0281

Haase, K. M., Freund, S., Koepke, J., Hauff, F., & Erdmann, M. (2015). Melts of sediments in the mantle wedge of the Oman ophiolite. Geology, 43(4), 275-278.

Hacker, B. R. (1994). Rapid emplacement of young oceanic lithosphere: argon geochronology of the Oman ophiolite. Science, 265(5178), 1563-1565.

Hacker, B. R., Mosenfelder, J. L., & Gnos, E. (1997). Rapid ophiolite emplacement constrained by geochronology and thermal considerations. Tectonics, 15, 1230-1247.

Harris, M., Coggon, R. M., Smith-Duque, C. E., Cooper, M. J., Milton, J. A., & Teagle, D. A. (2015). Channelling of hydrothermal fluids during the accretion and evolution of the upper oceanic crust: Sr isotope evidence from ODP Hole 1256D. Earth and Planetary Science Letters, 416, 56-66.

Henjes-Kunst, F., Koepke, J., Läufer, A., Estrada, S., Phillips, G., Piepjohn, K., & Kosanke, D. (2014). The Ross-Orogenic Tiger Gabbro Complex (Northern Victoria Land, Antarctica): Insights into the Lower Crust of a Cambrian Island Arc. herausgegeben vom Alfred-Wegener-Institut Helmholtz-

Zentrum für Polar-und Meeresforschung und der Deutschen Gesellschaft für Polarforschung e. V., 84(1), 23-38.

Henstock, T. J., Woods, A. W., & White, R. S. (1993). The accretion of oceanic crust by episodic sill intrusion. Journal of Geophysical Research: Solid Earth (1978–2012), 98(B3), 4143-4161.

Hielscher, R., & Schaeben, H. (2008). A novel pole figure inversion method: specification of the MTEX algorithm. Journal of Applied Crystallography, 41(6), 1024-1037.

Hussenoeder, S. A., Collins, J. A., Kent, G. M., & Detrick, R. S. (1996). Seismic analysis of the axial magma chamber reflector along the southern East Pacific Rise from conventional reflection profiling. Journal of Geophysical Research: Solid Earth (1978–2012), 101(B10), 22087-22105.

Höfig, T. W., Geldmacher, J., Hoernle, K., Hauff, F., Duggen, S., & Garbe-Schönberg, D. (2014). From the lavas to the gabbros: 1.25 km of geochemical characterization of upper oceanic crust at ODP/IODP Site 1256, eastern equatorial Pacific. Lithos, 210, 289-312.

Hopson, C. A., Coleman, R. G., Gregory, R. T., Pallister, J. S., & Bailey, E. H. (1981). Geologic section through the Samail Ophiolite and associated rocks along a Muscat-Ibra Transect, southeastern Oman Mountains. Journal of Geophysical Research: Solid Earth (1978–2012), 86(B4), 2527-2544.

Ildefonse, B., Billiau, S., & Nicolas, A. (1995). A detailed study of mantle flow away from diapirs in the Oman ophiolite. In Mantle and Lower Crust Exposed in Oceanic Ridges and in Ophiolites (pp. 163-177). Springer Netherlands.

Jagoutz, O., Müntener, O., Ulmer, P., Pettke, T., Burg, J. P., Dawood, H., & Hussain, S. (2007). Petrology and mineral chemistry of lower crustal intrusions: the Chilas Complex, Kohistan (NW Pakistan). Journal of Petrology.

Juteau, T., Beurrier, M., Dahl, R., & Nehlig, P. (1988). Segmentation at a fossil spreading axis: The plutonic sequence of the Wadi Haymiliyah area (Haylayn Block, Sumail Nappe, Oman). Tectonophysics, 151(1), 167-197.

Jochum, K. P., Weis, U., Stoll, B., Kuzmin, D., Yang, Q., Raczek, I., ... & Enzweiler, J. (2011). Determination of reference values for NIST SRM 610–617 glasses following ISO guidelines. Geostandards and Geoanalytical Research, 35(4), 397-429.

Jousselin, D., Nicolas, A., & Boudier, F. (1998). Detailed mapping of a mantle diapir below a paleo-spreading center in the Oman ophiolite. Journal of Geophysical Research: Solid Earth (1978–2012), 103(B8), 18153-18170.

Jousselin, D., Morales, L. F., Nicolle, M., & Stephant, A. (2012). Gabbro layering induced by simple shear in the Oman ophiolite Moho transition zone. Earth and Planetary Science Letters, 331, 55-66.

Kelemen, P. B., Koga, K., & Shimizu, N. (1997). Geochemistry of gabbro sills in the crust-mantle transition zone of the Oman ophiolite: implications for the origin of the oceanic lower crust. Earth and Planetary Science Letters, 146(3), 475-488.

Kelemen, P. B., & Aharanov, E. (1998). Periodic formation of magma fractures and generation of layered gabbros in the lower crust beneath oceanic spreading ridges. Geophysical Monograph-American Geophysical Union, 106, 267-290.

Kent, A. J., Peate, D. W., Newman, S., Stolper, E. M., & Pearce, J. A. (2002). Chlorine in submarine glasses from the Lau Basin: seawater contamination and constraints on the composition of slab-derived fluids. Earth and Planetary Science Letters, 202(2), 361-377.

Koepke, J., Berndt, J., Feig, S. T., & Holtz, F. (2007). The formation of SiO2-rich melts within the deep oceanic crust by hydrous partial melting of gabbros. Contributions to Mineralogy and Petrology, 153(1), 67-84.

Koepke, J., Christie, D. M., Dziony, W., Holtz, F., Lattard, D., Maclennan, J., ... & Yamazaki, S. (2008). Petrography of the dike-gabbro transition at IODP Site 1256 (equatorial Pacific): The evolution of the granoblastic dikes. Geochemistry, Geophysics, Geosystems, 9(7).

Koepke, J., Schoenborn, S., Oelze, M., Wittmann, H., Feig, S. T., Hellebrand, E., ... & Schoenberg, R. (2009). Petrogenesis of crustal wehrlites in the Oman ophiolite: Experiments and natural rocks. Geochemistry, Geophysics, Geosystems, 10(10).

Koepke, J., France, L., Müller, T., Faure, F., Goetze, N., Dziony, W., & Ildefonse, B. (2011). Gabbros from IODP Site 1256, equatorial Pacific: Insight into axial magma chamber processes at fast spreading ocean ridges.Geochemistry, Geophysics, Geosystems, 12(9).

Koepke, J., Mueller, T., Linsler, S., Schuth, S., Garbe-Schoenberg, C. D., & McCaig, A. M. (2014, December). Invasion of Seawater-Derived Fluids at Very High Temperatures in the Oman Ophiolite-a Key for Cooling the Deep Crust at Fast-Spreading Ridges. In AGU Fall Meeting Abstracts (Vol. 1, p. 03).

Koga, K. T., Kelemen, P. B., & Shimizu, N. (2001). Petrogenesis of the crust-mantle transition zone and the origin of lower crustal wehrlite in the Oman ophiolite. Geochemistry, Geophysics, Geosystems, 2(9).

Korenaga, J., & Kelemen, P. B. (1997). Origin of gabbro sills in the Moho transition zone of the Oman ophiolite: implications for magma transport in the oceanic lower crust. Journal of Geophysical Research: Solid Earth (1978–2012), 102(B12), 27729-27749.

Korenaga, J., & Kelemen, P. B. (1998). Melt migration through the oceanic lower crust: a constraint from melt percolation modeling with finite solid diffusion. Earth and Planetary Science Letters, 156(1), 1-11.

Langmuir, C. H. (1989). Geochemical consequences of in situ crystallization. Nature, 340(6230), 199-205.

Lazarov, M., Brey, G. P., & Weyer, S. (2009). Time steps of depletion and enrichment in the Kaapvaal craton as recorded by subcalcic garnets from Finsch (SA). Earth and Planetary Science Letters, 279(1), 1-10.

Leake, B. E., Woolley, A. R., Arps, C. E. S., Birch, W. D., Gilbert, M. C., Grice, J. D., Hawthorne, F. C., Kato, A., Kisch, H. J., Krivovichev, V. G., Linthout, K., Laird, J., Mandarino, J. A. Maresch, W. V., Nickel, E. H., Rock, N. M. S., Schumacher, J. C., Smith, D. C., Stephenson, N. C. N., Ungaretti, L., Whittaker E. J. W., and Youzhi, G. (1997). Nomenclature of amphiboles: report of the Subcommittee on Amphiboles of the International Mineralogical Association, Commission on New Minerals and Mineral Names in The Canadian Mineralogist, vol. 35, 1997, pp. 219-246.

Le Bas, M. J., & Streckeisen, A. L. (1991). The IUGS systematics of igneous rocks. Journal of the Geological Society, 148(5), 825-833.

Lechler, P. J., & Desilets, M. O. (1987). A review of the use of loss on ignition as a measurement of total volatiles in whole-rock analysis. Chemical Geology,63(3), 341-344.

Lecuyer, C., & Reynard, B. (1996). High-temperature alteration of oceanic gabbros by seawater (Hess Deep, Ocean Drilling Program Leg 147): Evidence from oxygen isotopes and elemental fluxes. Journal of Geophysical Research: Solid Earth (1978–2012), 101(B7), 15883-15897.

Lippard, S. J., Shelton, A. W., & Gass, I. G. (1986). The Ophiolite of northern Oman. Geological Society of London, Memoir 11.

Lissenberg, C. J., MacLeod, C. J., Howard, K. A., & Godard, M. (2013). Pervasive reactive melt migration through fast-spreading lower oceanic crust (Hess Deep, equatorial Pacific Ocean). Earth and Planetary Science Letters,361, 436-447.

McCulloch, M. T., Gregory, R. T., Wasserburg, G. J., & Taylor, H. P. (1980). A neodymium, strontium, and oxygen isotopic study of the Cretaceous Samail ophiolite and implications for the petrogenesis and seawater-hydrothermal alteration of oceanic crust. Earth and Planetary Science Letters, 46(2), 201-211.

Maclennan, J., Hulme, T., & Singh, S. C. (2004). Thermal models of oceanic crustal accretion: Linking geophysical, geological and petrological observations. Geochemistry, Geophysics, Geosystems, 5(2).

Maclennan, J., Hulme, T., & Singh, S. C. (2005). Cooling of the lower oceanic crust. Geology, 33(5), 357-366.

MacLeod, C. J., & Yaouancq, G. (2000). A fossil melt lens in the Oman ophiolite: Implications for magma chamber processes at fast spreading ridges. Earth and Planetary Science Letters, 176(3), 357-373.

MacLeod, C. J., Lissenberg, C. J., & Bibby, L. E. (2013). "Moist MORB" axial magmatism in the Oman ophiolite: The evidence against a mid-ocean ridge origin. Geology, 41(4), 459-462.

Mainprice, D., & Silver, P. G. (1993). Interpretation of SKS-waves using samples from the subcontinental lithosphere. Physics of the Earth and Planetary Interiors, 78(3), 257-280.

Mainprice, D., Bachmann, F., Hielscher, R., & Schaeben, H. (2014). Descriptive tools for the analysis of texture projects with large datasets using MTEX: strength, symmetry and components. Geological Society, London, Special Publications, 409, SP409-8.

Manning, C. E., MacLeod, C. J., & Weston, P. E. (2000). Lower-crustal cracking front at fast-spreading ridges: Evidence from the East Pacific Rise and the Oman ophiolite. Special Papers-Geological Society of America, 261-272.

Miller, D. J., Iturrino, G. J., & Christensen, N. I. (1996). Geochemical and petrological constraints on velocity behavior of lower crustal and upper mantle rocks from the fast-spreading ridge at Hess Deep. In proceedings-ocean drilling program scientific results (pp. 477-492). National Science foundation.

Morales, L. F., Boudier, F., & Nicolas, A. (2011). Microstructures and crystallographic preferred orientation of anorthosites from Oman ophiolite and the dynamics of melt lenses. Tectonics, 30(2)

Morgan, J. P., & Chen, Y. J. (1993). The genesis of oceanic crust: Magma injection, hydrothermal circulation, and crustal flow. Journal of Geophysical Research: Solid Earth (1978–2012), 98(B4), 6283-6297.

Müller, T., Koepke, J., Garbe-Schoenberg, C. D., Schuth, S., & Wolff, P. E. (2014, December). Oman Ophiolite: Petrological and Geochemical Investigation of Fast-Spreading Crust Formation Processes. In AGU Fall Meeting Abstracts(Vol. 1, p. 4727).

Münker, C., Weyer, S., Scherer, E., & Mezger, K. (2001). Separation of high field strength elements (Nb, Ta, Zr, Hf) and Lu from rock samples for MC-ICPMS measurements. Geochemistry, Geophysics, Geosystems, 2(12).

Natland, J. H., & Dick, H. J. (1996). Melt migration through high-level gabbroic cumulates of the East Pacific Rise at Hess Deep: the origin of magma lenses and the deep crustal structure of fast-spreading ridges. In proceedings-ocean drilling program scientific results (pp. 21-58). National Science Foundation.

Natland, J. H., & Dick, H. J. (2009). Paired melt lenses at the East Pacific Rise and the pattern of melt flow through the gabbroic layer at a fast-spreading ridge. Lithos, 112(1), 73-86.

Neo, N., Yamazaki, S., & Miyashita, S. (2009). Data report: Bulk rock compositions of samples from the IODP Expedition 309/312 sample pool, ODP Hole 1256D. Teagle, DAH, Alt, JC, Umino, S., Miyashita, S., Banerjee, NR, Wilson, DS, the Expedition, 309, 312.

Nicolas, A. (1989). Structures of ophiolites and dynamics of oceanic lithosphere), 367 pp., Kluwer Acad., Norwell, Mass, 1989

Nicolas, A., Boudier, F., & Ildefonse, B. (1996). Variable crustal thickness in the Oman ophiolite: implication for oceanic crust. Journal Of Geophysical Research-All Series-, 101, 17-941.

Nicolas, A., Boudier, F., Ildefonse, B., & Ball, E. (2000a). Accretion of Oman and United Arab Emirates ophiolite–Discussion of a new structural map. Marine Geophysical Researches, 21(3-4), 147-180.

Nicolas, A., Ildefonse, B., Boudier, F., Lenoir, X., & Ismail, W. B. (2000b). Dike distribution in the Oman-united Arab Emirates ophiolite. Marine Geophysical Researches, 21(3-4), 269-287.

Nicolas, A., Mainprice, D., & Boudier, F. (2003). High-temperature seawater circulation throughout crust of oceanic ridges: A model derived from the Oman ophiolites. Journal of Geophysical Research: Solid Earth (1978–2012), 108(B8).

Nicolas, A., Boudier, F., Koepke, J., France, L., Ildefonse, B., & Mevel, C. (2008). Root zone of the sheeted dike complex in the Oman ophiolite. Geochemistry, Geophysics, Geosystems, 9(5).

Nicolas, A., Boudier, F., & France, L. (2009). Subsidence in magma chamber and the development of magmatic foliation in Oman ophiolite gabbros. Earth and Planetary Science Letters, 284(1), 76-87.

Pallister, J. S., & Hopson, C. A. (1981). Samail ophiolite plutonic suite: field relations, phase variation, cryptic variation and layering, and a model of a spreading ridge magma chamber. Journal of Geophysical Research: Solid Earth (1978–2012), 86(B4), 2593-2644.

Pallister, J. S., & Knight, R. J. (1981). Rare-earth element geochemistry of the Samail Ophiolite near Ibra, Oman. Journal of Geophysical Research: Solid Earth (1978–2012), 86(B4), 2673-2697.

Pearce, J. A., Alabaster, T., Shelton, A. W., & Searle, M. P. (1981). The Oman ophiolite as a Cretaceous arc-basin complex: evidence and implications. Philosophical Transactions of the Royal Society of London A: Mathematical, Physical and Engineering Sciences, 300(1454), 299-317.

Pearce, J. A. (2014). Immobile element fingerprinting of ophiolites. Elements,10(2), 101-108.

Peters, Tj., El Amin, O., Blechschmid I., & Al-Busaidi, S. (2008) Geological Map Oman 1:50000, Sheet NF 40-8A1. Sultanate of Oman: Ministry of Commerce and Industry

Peate, D. W., & Pearce, J. A. (1998). Causes of spatial compositional variations in Mariana arc lavas: Trace element evidence. Island Arc, 7(3), 479-495.

Pfänder, J. A., Münker, C., Stracke, A., & Mezger, K. (2007). Nb/Ta and Zr/Hf in ocean island basalts—implications for crust–mantle differentiation and the fate of Niobium. Earth and Planetary Science Letters, 254(1), 158-172.

Pin, C., Briot, D., Bassin, C., & Poitrasson, F. (1994). Concomitant separation of strontium and samarium-neodymium for isotopic analysis in silicate samples, based on specific extraction chromatography. Analytica Chimica Acta, 298(2), 209-217.

Pouchou, J. L., & Pichoir, F. (1991). Quantitative analysis of homogeneous or stratified microvolumes applying the model "PAP". In Electron probe quantitation (pp. 31-75). Springer US.

Quick, J. E., & Denlinger, R. P. (1993). Ductile deformation and the origin of layered gabbro in ophiolites. Journal of Geophysical Research: Solid Earth (1978–2012), 98(B8), 14015-14027.

Rioux, M., Bowring, S., Kelemen, P., Gordon, S., Dudás, F., & Miller, R. (2012). Rapid crustal accretion and magma assimilation in the Oman-UAE ophiolite: High precision U-Pb zircon geochronology of the gabbroic crust. Journal of Geophysical Research: Solid Earth (1978–2012), 117(B7).

Rioux, M., Bowring, S., Kelemen, P., Gordon, S., Miller, R., & Dudas, F. (2013). Tectonic development of the Samail ophiolite: High-precision U-Pb zircon geochronology and Sm-Nd isotopic constraints on crustal growth and emplacement. Journal of Geophysical Research: Solid Earth, 118(5), 2085-2101.

Robinson, P., Spear, F. S., Schumacher, J. C., Laird, J., Klein, C., Evans, B. W., & Doolan, B. L. (1982). Phase relations of metamorphic amphiboles; natural occurrence and theory; Introduction, Reviews in Mineralogy and Geochemistry, 9(1), 1.3.

Satsukawa, T., Ildefonse, B., Mainprice, D., Morales, L. F. G., Michibayashi, K., & Barou, F. (2013). A database of plagioclase crystal preferred orientations (CPO) and microstructures-implications for

CPO origin, strength, symmetry and seismic anisotropy in gabbroic rocks. Solid Earth, 4(2), 511-542.

Sinton, J. M., & Detrick, R. S. (1992). Mid-ocean ridge magma chambers. Journal of Geophysical Research: Solid Earth (1978–2012), 97(B1), 197-216.

Stewart, M. A., Klein, E. M., & Karson, J. A. (2002). Geochemistry of dikes and lavas from the north wall of the Hess Deep Rift: Insights into the four-dimensional character of crustal construction at fast spreading mid-ocean ridges. Journal of Geophysical Research: Solid Earth (1978–2012), 107(B10), EPM-4.

Teagle, D.A.H., Alt, J.C., Umino, S., Miyashita, S., Banerjee, N.R., Wilson, D.S., and the Expedition 309/312 Scientists (2006). Proceedings of the Integrated Ocean Drilling Program, Volume 309/312

Teagle, D. A., Ildefonse, B., Dick, H. J., Endo, D., Ferré, E. C., France, L., ... & Deans, J. (2012). IODP expedition 335: deep sampling in ODP hole 1256D.Scientific Drilling, 13, 28-34.

Tilton, G. R., Hopson, C. A., & Wright, J. E. (1981). Uranium-lead isotopic ages of the Samail Ophiolite, Oman, with applications to Tethyan ocean ridge tectonics. Journal of Geophysical Research: Solid Earth (1978–2012), 86(B4), 2763-2775.

Ushioda, M., Takahashi, E., Hamada, M., & Suzuki, T. (2014). Water content in arc basaltic magma in the Northeast Japan and Izu arcs: an estimate from Ca/Na partitioning between plagioclase and melt. Earth, Planets and Space,66(1), 1-10.

Van der Plas, L., & Tobi, A. C. (1965). A chart for judging the reliability of point counting results. American Journal of Science, 263(1), 87-90

VanTongeren, J. A., Kelemen, P. B., & Hanghøj, K. (2008). Cooling rates in the lower crust of the Oman ophiolite: Ca in olivine, revisited. Earth and Planetary Science Letters, 267(1), 69-82.

VanTongeren, J. A., Hirth, G. R. E. G., & Kelemen, P. B. (2015). Constraints on the accretion of the gabbroic lower oceanic crust from plagioclase lattice preferred orientation in the Samail ophiolite. Earth and Planetary Science Letters, 427, 249-261

Vera, E. E., Mutter, J. C., Buhl, P., Orcutt, J. A., Harding, A. J., Kappus, M. E., ... & Brocher, T. M. (1990). The structure of 0-to 0.2-my-old oceanic crust at 9 N on the East Pacific Rise from expanded spread profiles. Journal of Geophysical Research: Solid Earth (1978–2012), 95(B10), 15529-15556.

Vogel, W. & Kuipers, G. (1987). A pre-calibrated program for geological applications. Phillips New Developments in X-Ray Spectrometry, 11, 2–8.

Vollmer, F. W. (1990). An application of eigenvalue methods to structural domain analysis. Geological Society of America Bulletin, 102(6), 786-791.

Wanless, V. D., Perfit, M. R., Ridley, W. I., & Klein, E. (2010). Dacite petrogenesis on mid-ocean ridges: evidence for oceanic crustal melting and assimilation. Journal of Petrology, 51(12), 2377-2410.

Warren, C. J., Parrish, R. R., Searle, M. P., & Waters, D. J. (2003). Dating the subduction of the Arabian continental margin beneath the Semail ophiolite, Oman. Geology, 31(10), 889-892.

Warren, C. J., Parrish, R. R., Waters, D. J., & Searle, M. P. (2005). Dating the geologic history of Oman's Semail ophiolite: Insights from U-Pb geochronology.Contributions to Mineralogy and Petrology, 150(4), 403-422.

Waters, C. L., Sims, K. W., Perfit, M. R., Blichert-Toft, J., & Blusztajn, J. (2011). Perspective on the genesis of E-MORB from chemical and isotopic heterogeneity at 9–10 N East Pacific Rise. Journal of Petrology, 52(3), 565-602.

Wilson, D. S., Teagle, D. A. H., & Acton, G. D. (2003). An in situ section of upper oceanic crust formed by superfast seafloor spreading. In Proceedings of the Ocean Drilling Program Initial Reports (Vol. 206).

Wilson, D. S., Teagle, D. A., Alt, J. C., Banerjee, N. R., Umino, S., Miyashita, S., ... & Yamasaki, T. (2006). Drilling to gabbro in intact ocean crust. Science,312(5776), 1016-1020.

Wolff, P. E., Koepke, J., & Feig, S. T. (2013). The reaction mechanism of fluid-induced partial melting of gabbro in the oceanic crust. European Journal of Mineralogy, 25(3), 279-298.

Yaouancq, G., & MacLeod, C. J. (2000). Petrofabric investigation of gabbros from the Oman ophiolite: comparison between AMS and rock fabric. Marine Geophysical Researches, 21(3-4), 289-306.

Yamasaki, T., Maeda, J., & Mizuta, T. (2006). Geochemical evidence in clinopyroxenes from gabbroic sequence for two distinct magmatisms in the Oman ophiolite. Earth and Planetary Science Letters, 251(1), 52-65.

Zhang, C., Koepke, J., Kirchner, C., Götze, N., & Behrens, H. (2014). Rapid hydrothermal cooling above the axial melt lens at fast-spreading mid-ocean ridge. Scientific reports, 4.

Appendix

Table A1. List of Wadi Gideah samples used in the study with sample depth, sample lithology, sample sub-lithology, and analytical techniques applied.

Sample	Depth[1]	Lithology[2]	Sub-Lithology[3]	Qualifier[4]	XRF	EPMA	EBSD	ICP OES ICP-MS	LA-ICP-MS	^{87}Sr/^{86}Sr	^{176}Hf/^{177}Hf	^{143}Nd/^{144}Nd
OM10_Gid_B01a	6600	PB		ext.	x			x		x	x	x
OM10_Gid_B01b	6600	PB		ext.	x			x		x	x	x
OM10_Gid_B04a	6600	PB		ext.	x			x		x	x	
OM10_Gid_B04c	6600	PB		ext.	x			x		x	x	
OM10_Gid_B04e	6600	PB		ext.	x			x		x	x	x
OM10_Gid_B05a	6600	PB		ext.				x				
OM10_Gid_B05b	6600	PB		ext.	x			x		x	x	x
OM10_Gid_A02	5500	SD	USD		x			x		x	x	x
OM10_Gid_A03	5500	SD	USD		x	x		x		x		
OM10_Gid_A04	5500	SD	USD		x			x		x	x	x
OM10_Gid_A05a	5500	SD	USD		x	x		x		x	x	x
OM10_Gid_A05b	5500	SD	USD					x		x		
OM10_Gid_A06	5500	SD	USD		x			x		x	x	x
OM10_Gid_B00	5500	SD		ext.	x			x		x	x	x
OM10_Gid_B02	5500	SD		ext.	x			x		x	x	x
OM10_Gid_B03	5500	SD		ext.	x			x		x		
OM10_Gid_B06	5500	SD		ext.	x			x		x	x	x
OM10_Gid_A10	5321	SD	LSD		x	x		x		x		
OM10_Gid_A11_3	5094	SD	LSD		x	x		x		x	x	x
OM10_Gid_A11_2	5062	SD	LSD		x			x		x	x	x
OM10_Gid_A11_1a	4994	ML	SG			x		x				
OM10_Gid_A11_1b	4994	ML	VG			x		x				
OM10_Gid_A11_1c	4994	ML	VG			x		x				
OM10_Gid_A11_1d	4994	ML	VG			x		x				
OM10_Gid_A11_1e	4994	ML	XE			x						
OM10_Gid_A11_1f	4994	ML	BDVG			x		x				
OM10_Gid_A11_1i	4994	ML	XE			x		x				
OM10_Gid_A11_1j	4994	ML	BDVG			x		x				
OM10_Gid_A11_1l	4994	ML	PG					x				
OM10_Gid_A11_1m	4994	ML	PGXE			x						
OM10_Gid_A11_1n	4994	ML	PGXE			x		x				
OM10_Gid_A11_1o	4994	ML	PGXE			x						
OM10_Gid_A11_1p	4994	ML	PG			x		x				
OM10_Gid_A11_1q	4994	ML	VG			x						
OM10_Gid_A11_1r	4994	ML	VG			x						
OM10_Gid_A11_1s	4994	ML	BDVG			x						
OM10_Gid_A11_1t	4994	ML	BDVG			x		x				
OM10_Gid_A11_1u	4994	ML	BDVG			x		x				
OM10_Gid_A11_1v	4994	ML	SG			x		x				
OM10_Gid_A11_1w	4994	ML	SG			x		x				
OM10_Gid_A11_1x	4994	ML	SG			x		x				
OM10_Gid_A11	4954	ML			x	x	x	x		x	x	x
OM10_Gid_A12_3	4780	SD			x	x		x		x		
OM10_Gid_A13	4602	VG			x	x	x	x		x	x	x
OM10_Gid_A12_2c	4612	SD	BDVG					x		x	x	x
OM10_Gid_A12_2a	4612	ML			x		x	x		x	x	x
OM10_Gid_A12_2b	4612	VG	BDVG		x							
OM10_Gid_A12_2d	4612	VG			x	x	x	x		x	x	x
OM10_Gid_A12_1a	4532	VG			x			x		x	x	x
OM10_Gid_A12_1b	4532	SD	BDVG		x			x		x	x	x
OM10_Gid_A12_1c	4532	VG			x			x		x	x	x
OM12_Gid_213	4460	VG				x						
OM10_Gid_A14a	4389	VG			x	x	x	x		x	x	x
OM10_Gid_A14b	4389	VG				x	x	x		x		
OM10_Gid_A15	4129	VG			x	x	x	x		x		
OM10_Gid_A16	3924	FG	UFG		x	x	x	x		x	x	x
OM10_Gid_A17	3734	FG	UFG		x	x	x	x		x	x	x
OM10_Gid_A17_2	3577	FG	UFG		x	x	x	x		x	x	x
OM10_Gid_A17_3a	3574	FG	UFG		x			x		x		
OM12_Gid_215	3573	FG	UFG/MG			x						
OM10_Gid_A17_1	3550	FG	UFG		x	x	x	x		x	x	x
OM10_Gid_A18	3423	FG	LFG		x	x	x	x		x	x	x
OM10_Gid_A18_1	3230	FG	LFG		x	x	x	x		x	x	x
OM12_Gid_217	2979	FG	LFG			x						
OM10_Gid_A18_2a	2900	FG	LFG		x	x	x	x		x	x	x
OM10_Gid_A18_2b	2900	FG	LFG					x				
OM12_Gid_218	2788	FG	LFG			x						
OM10_Gid_A19	2700	FG	LFG		x	x	x	x		x	x	x
OM12_Gid_219	2656	FG	LFG			x						
OM12_Gid_057	2610	LG				x		x				
OM12_Gid_058	2610	LG				x		x				
OM12_Gid_059	2610	LG	MG			x		x		x	x	x
OM10_Gid_A20	2394	LG			x	x	x	x		x	x	x
OM10_Gid_A20a	2394	LG				x						
OM10_Gid_A20b	2394	LG				x						
OM12_Gid_055	2259	LG				x	x	x		x	x	x
OM10_Gid_A21	2124	LG			x	x	x	x		x		
OM11_Gid_A21A	2124	LG				x	x	x		x		
OM11_Gid_A21B	2124	LG				x						
OM12_Gid_054	2040	LG				x	x	x		x	x	x
OM12_Gid_052	2004	LG				x	x	x				

Sample	Depth[1]	Lithology[2]	Sub-Lithology[3]	Qualifier[4]	XRF	EPMA	EBSD	ICP OES ICP-MS	LA-ICP-MS	$^{87}Sr/^{86}Sr$	$^{176}Hf/^{177}Hf$	$^{143}Nd/^{144}Nd$
OM12_Gid_053	2004	LG				x	x	x		x	x	x
OM10_Gid_A22	1936	LG				x		x		x	x	x
OM11_Gid_A22	1936	LG				x	x	x		x		
OM12_Gid_049	1919	LG				x		x				
OM12_Gid_050	1919	LG				x		x				
OM12_Gid_051	1919	LG				x		x				
OM12_Gid_048	1792	LG				x	x	x		x	x	x
OM12_Gid_046	1727	LG				x		x		x	x	x
OM12_Gid_043	1671	LG				x		x				
OM12_Gid_045	1630	LG				x	x	x		x	x	x
OM10_Gid_A23	1659	LG			x	x	x	x		x	x	x
OM10_Gid_A23a	1659	LG				x				x		
OM10_Gid_A23b	1659	LG				x						
OM12_Gid_044	1626	LG				x	x	x		x	x	x
OM12_Gid_047	1787	LG	MG			x		x				
OM12_Gid_042	1562	LG	MG			x		x				
OM12_Gid_040	1508	LG				x	x	x		x	x	x
OM12_Gid_041	1508	LG				x		x				
OM10_Gid_A24	1431	LG			x	x	x	x		x	x	x
OM12_Gid_039	1289	LG				x		x		x	x	x
OM12_Gid_027	1222	LG				x	x	x				
OM10_Gid_A25	1210	LG				x	x	x		x		
OM12_Gid_026	1231	LG			x	x	x	x		x	x	x
OM12_Gid_Hy0	1190	LG		Hydroprofile		x						
OM12_Gid_Hy018	1190	LG		Hydroprofile		x						
OM12_Gid_Hy023	1190	LG	MG	Hydroprofile		x		x		x	x	x
OM12_Gid_Hy025	1190	LG		Hydroprofile	x	x						
OM12_Gid_Hy030	1190	LG		Hydroprofile		x						
OM12_Gid_Hy032A	1190	LG		Hydroprofile		x						
OM12_Gid_Hy032B	1190	LG		Hydroprofile		x						
OM12_Gid_Hy032C	1190	LG		Hydroprofile		x						
OM12_Gid_Hy032D	1190	LG		Hydroprofile		x						
OM12_Gid_Hy038	1190	LG		Hydroprofile		x						
OM12_Gid_Hy039	1190	LG		Hydroprofile		x						
OM12_Gid_Hy042	1190	LG		Hydroprofile		x						
OM12_Gid_Hy055B	1190	LG		Hydroprofile		x						
OM12_Gid_Hy058.5	1190	LG		Hydroprofile		x		x				
OM12_Gid_Hy059	1190	LG		Hydroprofile		x		x				
OM12_Gid_Hy059.5	1190	LG	MG	Hydroprofile	x	x		x		x	x	x
OM12_Gid_Hy062	1190	LG	MG	Hydroprofile		x		x		x	x	x
OM12_Gid_Hy068	1190	LG	MG	Hydroprofile	x	x		x		x	x	x
OM12_Gid_Hy077	1190	LG	MG	Hydroprofile	x	x		x		x	x	x
OM12_Gid_Hy080	1190	LG	MG	Hydroprofile	x	x		x		x	x	x
OM12_Gid_Hy080.5	1190	LG	MG	Hydroprofile	x	x		x				
OM12_Gid_Hy096	1190	LG	MG	Hydroprofile		x		x		x	x	x
OM12_Gid_Hy102	1190	LG		Hydroprofile	x	x		x				
OM12_Gid_Hy103	1190	LG	MG	Hydroprofile		x		x		x	x	x
OM12_Gid_Hy108	1190	LG	MG	Hydroprofile	x	x		x		x	x	x
OM12_Gid_Hy154	1190	LG		Hydroprofile	x	x						
OM12_Gid_Hy166	1190	LG		Hydroprofile		x						
OM12_Gid_025	1197	LG				x	x	x		x	x	x
OM12_Gid_038	1121	LG				x	x	x		x	x	x
OM10_Gid_A26	1079	LG			x	x	x	x		x	x	x
OM12_Gid_036	1064	LG				x		x				
OM12_Gid_037	1064	LG	MG			x		x				
OM12_Gid_035	991	LG				x	x	x		x	x	x
OM11_Gid_A26	930	LG				x	x	x		x		
OM12_Gid_033	890	LG	MG			x		x				
OM11_Gid_A27	816	LG				x		x		x		
OM10_Gid_A27	804	LG				x	x	x		x		
OM12_Gid_034	813	LG	MG		x	x		x				
OM12_Gid_032	749	LG	MG			x		x				
OM11_Gid_A27_1	714	LG				x		x		x		
OM11_Gid_A28B	703	LG	MG			x		x		x		
OM10_Gid_A28	696	LG			x	x	x	x		x	x	x
OM12_Gid_031	684	LG	MG			x		x				
OM11_Gid_A28	625	LG						x		x		
OM12_Gid_029	631	LG	MG			x		x				
OM12_Gid_030	631	LG	MG			x		x				
OM12_Gid_201	598	LG				x	x	x		x	x	x
OM12_Gid_202	594	LG	MG			x		x				
OM12_Gid_028	564	LG	MG			x		x				
OM10_Gid_A29	545	LG			x	x	x	x		x	x	x
OM11_Gid_A29_1	518	LG				x						
OM11_Gid_A29	517	LG				x	x	x		x		
OM12_Gid_204	434	LG	MG			x						
OM12_Gid_203	433	LG				x						
OM11_Gid_A29_2	401	LG				x	x	x		x		
OM10_Gid_A30	257	LG			x	x	x	x		x		
OM12_Gid_205	222	LG				x						
OM12_Gid_206	210	LG				x						

| | | | | | | Analytical technique | | | ICP OES | | | | |
Sample	Depth[1]	Lithology[2]	Sub-Lithology[3]	Qualifier[4]	XRF	EPMA	EBSD	ICP-MS	LA-ICP-MS	[87]Sr/[86]Sr	[176]Hf/[177]Hf	[143]Nd/[144]Nd
OM12_Gid_207	210	LG				x						
OM12_Gid_208	147	LG	MG			x						
OM12_Gid_209	147	LG				x						
OM12_Gid_211	135	LG	MG			x		x				
OM10_Gid_A31	123	LG			x	x	x	x		x		
OM12_Gid_210	88	LG				x						
OM10_Gid_A32	49	LG			x	x	x	x		x	x	x

[1] Depth: Calculated height above MOHO [m]

[2] Lithologies: PB = Pillow basalt; SD = Sheeted dike; ML = Melt lens; VG = Varitextured gabbro; FG = Foliated gabbro; LG = Layered gabbro

[3] Sub-Lithologies: USD = Upper sheeted dikes; LSD = Lower sheeted dikes; SG = Spotty gabbro; VG = Varitextuted gabbro; XE = Xenolith; BDVG = Basaltic dike in varitextured gabbro; PGXE = Xenolith bearing plagiogranite; UFG = Upper foliated gabbros; LFG = Lower; MG = Metagabbro

[4] ext = sampled out of Wadi Gideah

Table 2. Detection limits of electron probe micro analysis for minerals analysed

Mineral	SiO_2	Al_2O_3	FeO	MnO	MgO	CaO	Na_2O	K_2O	TiO_2	Cl	F	NiO	Cr_2O_3	V_2O_3
Plagioclase	0.09	0.08	0.14	0.12	0.06	0.07	0.07	0.02	0.04	-	-	-	-	-
Pyroxene	0.09	0.06	0.15	0.13	0.09	0.07	0.07	0.02	0.04	-	-	-	0.14	-
Olivine	0.09	0.07	0.16	0.13	0.11	0.04	0.07	0.02	0.04	-	-	0.12	-	-
Amphibole	0.09	0.07	0.15	0.13	0.08	0.07	0.08	0.02	0.04	0.01	0.19	-	-	-
Magnetite/Ilmenite	0.05	0.05	0.12	0.08	0.05	0.05	-	-	0.03	-	-	0.00	0.08	0.25

all detection limits in wt%

Table 3. Comparison of ICP-OES results with standard material

Standard		SiO_2	Al_2O_3	FeO	MnO	MgO	CaO	Na_2O	K_2O	TiO_2	P_2O_5	L.O.I.	Total
BHVO-2	recomm.	49.94	13.80	12.23	0.17	7.23	11.40	2.26	0.52	2.71	0.27	0.21	100.74
	this study	48.93	13.73	12.37	0.17	7.30	11.57	2.23	0.52	2.72	0.25	0.21	100.00
BIR-1	recomm.	47.77	15.35	11.26	0.17	9.68	13.24	1.75	0.03	0.96	0.05	0.20	100.45
	this study	47.25	15.53	11.27	0.17	9.54	13.28	1.77	0.01	0.96	< 0.08	0.20	99.98
JGB-2	recomm.	46.68	23.32	6.85	0.13	6.24	14.10	0.92	0.06	0.56	0.01	1.36	100.22
	this study	46.92	23.11	6.73	0.12	6.20	14.11	0.84	0.05	0.57	< 0.08	1.36	100.00

all values in wt%

Table A4. Comparison of ICP-MS results with standard material

	BHVO-2		BIR-1		JGb-1		JGb-2	
	recomm.	this study	recomm.	this study	recomm.	this study	recomm.	this study
Li	4.60	4.54	3.40	3.28	4.30	4.76	15.20	16.86
Sc	31.80	31.44	44.00	43.49	36.60	33.92	24.70	23.56
V	317.00	316.78	313.00	314.08	640.00	539.30	174.00	172.69
Cr	289.00	289.17	382.00	381.90	59.30	49.43	125.00	120.00
Co	45.00	44.67	51.40	51.53	61.60	59.05	25.80	25.16
Ni	119.00	118.11	166.00	166.79	25.40	22.91	13.60	12.75
Cu	127.00	128.73	126.00	117.44	86.80	80.06	11.00	10.53
Zn	103.00	106.41	71.00	69.08	111.00	105.33	48.00	47.31
Ga	21.70	21.85	16.00	15.41	18.90	18.72	15.90	16.12
Rb	9.20	9.24	0.21	0.21	4.00	5.85	2.85	2.32
Sr	395.00	392.81	104.00	108.55	321.00	326.04	435.00	437.97
Y	25.50	25.64	16.00	15.49	10.75	9.23	4.53	3.32
Zr	174.00	174.98	14.00	13.80	33.50	26.18	11.60	7.36
Nb	18.00	18.35	0.55	0.54	2.80	2.34	1.91	0.79
Mo	4.00	3.94	0.50	0.08	0.45	0.39	0.42	0.56
Sb	0.13	0.11	0.58	0.49	0.11	0.08	0.11	0.10
Cs	0.11	0.11	0.01	0.01	0.27	0.22	0.51	0.59
Ba	130.00	130.20	5.83	6.04	63.00	64.18	34.10	33.46
La	15.20	15.34	0.62	0.62	3.74	3.52	1.45	1.53
Ce	38.00	37.47	1.95	1.91	7.86	8.26	2.98	3.18
Pr	5.30	5.35	0.38	0.38	1.14	1.17	0.39	0.41
Nd	25.00	25.01	2.50	2.45	5.65	5.41	1.84	1.91
Sm	6.20	6.19	1.10	1.12	1.49	1.48	0.51	0.53
Eu	2.06	2.10	0.54	0.53	0.63	0.63	0.59	0.62
Gd	6.30	6.21	1.85	1.82	1.63	1.67	0.55	0.60
Tb	0.93	0.94	0.36	0.36	0.31	0.26	0.15	0.10
Dy	5.25	5.36	2.50	2.62	1.53	1.62	0.60	0.66
Ho	0.99	0.98	0.57	0.58	0.32	0.34	0.15	0.14
Er	2.50	2.44	1.70	1.64	1.07	0.95	0.36	0.39
Tm	0.34	0.33	0.26	0.25	0.15	0.13	0.05	0.06
Yb	2.00	1.99	1.65	1.65	0.97	0.90	0.39	0.40
Lu	0.28	0.28	0.26	0.25	0.15	0.13	0.06	0.06
Hf	4.07	4.34	0.58	0.58	0.88	0.74	0.25	0.23
Ta	1.13	1.02	0.04	0.04	0.17	0.13		0.06
W	0.25	0.25	0.07	0.02	0.81	4.69	1.45	1.49
Pb	1.70	1.60	3.08	2.92	1.90	1.62	1.46	0.97
Th	1.21	1.18	0.03	0.03	0.53	0.36	0.19	0.19
U	0.41	0.41	0.01	0.01	0.15	0.09	0.03	0.03

all values in ppm

Table 5. Petrographic features of Wadi Gideah samples

Sample	#[1]	Dom.[2]	Lith.[3]	S-Lith.[4]	Depth[5]	Pl	Cpx	Opx	Ol	Amph	Ox	Qtz	perv	vein	Pl	Cpx	Opx	Ol	Chl	Tr/Act	Hbl	Srp	Idd	Tlc	Ep/Czo	Ox	Ttn	Prh
						Modal proportions [vol%][6]							Alteration [vol%][7]		Grain size [mm][8]				Secondary minerals[9]									
OM10_Gid_A02			SD	USD	6449	94	22				22	6	32		1.0	0.3			p	p		p	p	p		p		
OM10_Gid_B06			SD	USD	6300	56	25					25	30		0.4	0.3			p	p	p	p	p	p		p		
OM10_Gid_A03			SD	USD	6288	50	25						96		2.5	0.2			p	r	r		p			p		
OM10_Gid_A10			SD	LSD	5321	50	47				3		72		0.2	0.2			r	r	r					r		
OM10_Gid_A11_3			SD	LSD	5094	50	50						70		0.5	0.4			r	r	r					r		
OM10_Gid_A11_2			SD	LSD	5062	95					5		70		0.2				r,p	p	r,p			r,p		r,p		
OM10_Gid_A11_1a		2	ML	VG	4994	91	3				6		37		1.2	2.3			r,p	r,p	r,p					r,v		
OM10_Gid_A11_1b		1	ML	VG	4994	98					2		54		0.6				r,p	r,p	r,p					r,p		
OM10_Gid_A11_1b		2	ML	VG	4994	97					3		40		3.0				r,p	r,p	r,p					r,p		
OM10_Gid_A11_1c		2	ML	VG	4994	94					6		41	1	0.6				r,p	r,p	r,p				v	r,v		
OM10_Gid_A11_1c		1	ML	VG	4994	96				2	2		50	1	1.9				r,p	r,p	r,p				?	r,v	?	?
OM10_Gid_A11_1d			ML	VG	4994	81	14				5		42		0.8				r,p	r,p	r,p					r,p		
OM10_Gid_A11_1e		2	ML	VG	4994	88					12		48		0.7				r,p	r,p	r,p					r,p		
OM10_Gid_A11_1e		1	ML	VG	4994	97					3		27	23	3.0	1.0			r,v,p	r,v,p	r,v,p				?	r,v,p	r,p	?
OM10_Gid_A11_1f			ML	BDVG	4994	91					9		45	1	0.2				r,p	r,v,p	r,p				?	r,v,p		?
OM10_Gid_A11_1ia		2	ML	XE	4994	67				6	6	22	16		0.3				?	?	r,p			r		r,p		
OM10_Gid_A11_1ia		1	ML	PG	4994	89				2	3	6	7		1.0				?	r,p	r,p					r,p		
OM10_Gid_A11_1j			ML	BDVG	4994	94				0	6		57		0.2				?	?	r,v					r,p	p	
OM10_Gid_A11_1m		2	ML	PG	4994	95				2	3		51		0.7				?	?	r,p			?		r,p		
OM10_Gid_A11_1m		1	ML	VG	4994	91				4	5		48		0.2				r,p	?	r,p			?	r	r,v,p	?	
OM10_Gid_A11_1n		1	ML	TR	4994	100							99		0.4					r,p	r,p			r,p	r	r,p		
OM10_Gid_A11_1n		2	ML	PG	4994	58					3	42	38		0.9				r	r,p	r				r,p	r,p	?	
OM10_Gid_A11_1o		1	ML	PG	4994	95					3	2	14		0.6				r	r,p	r,p					r,p		
OM10_Gid_A11_1o		2	ML	PG	4994	97					3		12		1.2				r	r,p	r,p					r,p		
OM10_Gid_A11_1p		2	ML	PG	4994	87				2	5	5	56		0.6				r	r,p	r,p					r,p	p	
OM10_Gid_A11_1p		1	ML	PG	4994	93				2	2	3	39		1.1				r	r,p	r,p			?	?	r,p	p	
OM10_Gid_A11_1q			ML	PG	4994	89				2	4	5	26		0.6				r		r,p				r,p	r,p		p
OM10_Gid_A11_1r		2	ML	VG	4994	89					11		75		0.5				r,p	r,p	r,p			?	?	r,p	?	?
OM10_Gid_A11_1r		1	ML	VG	4994	91				9			84		2.0				r	r,p	r,p					r,p		
OM10_Gid_A11_1s			ML	BDVG	4994	96					4		78		0.2				r,p	r,p	r,p					r,p	p	
OM10_Gid_A11_1t			ML	BDVG	4994	100							53		0.1				r,p	r,p	r,p					r,p		
OM10_Gid_A11_1u			ML	BDVG	4994	98					2		59		0.3				r	r,p	r,p					r,p		
OM10_Gid_A11_1v			ML	VG	4994	95					5		52		0.5				r	r,p	r,p			?		r,p		
OM10_Gid_A11_1w			ML	VG	4994	98					2		57		0.7				r	r,p	r,p					r,p		
OM10_Gid_A11_1x			ML	VG	4994	90					10		49		0.6				r,p	r,p	r,p					r,p		
OM10_Gid_A11			VG	BDVG	4954	100					6		75		0.4				r	r	r			r		r		
OM10_Gid_A12_3			SD	BDVG	4780	94					8		41		0.4				r	r						r		
OM10_Gid_A12_2c			SD	BDVG	4612	50				42			3		0.1				r	r						r		
OM10_Gid_A12_2a			VG	VG	4612	100							10		0.7				r	r						r		p
OM10_Gid_A13			SD	VG	4602	39	19	35		6	1		38		1.0	1.2	2.5		r	r	r			r		r		
OM10_Gid_A12_1b			SD	SD	4532	50	50	1					54		0.4	0.5			r,p	r,p	r,p					r,p		
OM10_Gid_A14a			VG	VG	4389	47	46			5			37		0.4	0.4	1.0		r,p	r,p	r,p					r,p		
OM10_Gid_A14b			VG	VG	4389	53	39			7	1		36		0.4	0.5			r,p	r,p	r,p			?		r,p		
OM10_Gid_A15			VG	VG	4129	59	33			6	3		48		0.8	0.8			r	r	r					r		
OM10_Gid_A16			FG	UFG	3924	55	39	1	5		0		7		1.0	0.7	1.4	0.9	r	r		r		r		r		
OM10_Gid_A17			FG	UFG	3734	79	14	5	5		2		51		0.6	0.8	1.5		r	r	r	r		r		r		
OM10_Gid_A17_2			FG	UFG	3577	56	39				5		56		2.1	1.8			r	r	r					r		
OM12_Gid_215			FG	MG	3573	100							95		4.0													p
OM10_Gid_A17_1			FG	UFG	3550	50	40		10		10		5		1.2	0.6		0.4	r	r	r	r				r		
OM10_Gid_A18		1	FG	LFG	3423	60	30		10				4		0.8	0.5			r	r	r	r				r		
OM10_Gid_A18		2	FG	LFG	3423	59	30				1		4		1.9	1.2		1.2	r,p	r,p	r,p	r		r		r,p		
OM10_Gid_A18_1			FG	LFG	3230	51	49		20				25	15	1.0	0.7		1.0	r,p	r,p	r,p	r				r,p		
OM12_Gid_217			FG	LFG	2979	45	33		5		2		30		1.0	0.8		2.0	r	r	r	r		r		r		
OM10_Gid_A18_2a			FG	LFG	2900	50	45						9		1.0	1.3						r		r		r		
OM12_Gid_218			FG	LFG	2788	50	44		6				3		0.8	0.4		0.5	r	r	r	r		r		r		

Table 5. continued

Sample	#[1]	Dom.[2]	Lith.[3]	S-lith.[4]	Depth[5]	Pl	Cpx	Opx	Ol	Amph	Ox	Qtz	perv	vein	Pl	Cpx	Opx	Ol	Chl	Tr / Act	Hbl	Srp	Idd	Tlc	Ep / Czo	Ox	Ttn	Prh
						Modal proportions [vol%][6]							Alteration [vol%][7]		Grain size [mm][8]				Secondary minerals[9]									
OM10_Gid_A19			FG	LFG	2700	52	40		8				7		0.9	0.4		1.0	r		r			r		r		
OM12_Gid_219			FG	LFG	2656	50	41		8		1		3		0.6	0.5		0.4	r	r	r	r				r		
OM12_Gid_057			LG	MG	2610	50	50						23		1.5	1.7					r	r				p		
OM12_Gid_058			LG	MG	2610	57	40				2		51	3	1.8	1.8				p,v	r	p,v				p		p,v
OM12_Gid_059			LG	MG	2610	53	45				3		49	4	1.2	1.3				r	r	r				r,p		
OM10_Gid_A20			LG		2394	60	20	5	15				14		1.8	2.0	1.5	2.0			r					r		
OM10_Gid_A20a			LG		2394	40	51		9				6		0.8	1.1		1.1	r	r	r	r		r		r		
OM10_Gid_A20b			LG		2394	50	45		5				4		0.9	1.0		0.9	r	r	r	r	r			r		
OM12_Gid_055			LG		2259	40	55		5				7		1.0	0.7		1.2	r	r	r	r				r,v		
OM10_Gid_A21			LG		2124	47	53						9	15	1.2	1.3			r	r,v	v			r,v		r,v		
OM11_Gid_A21A			LG		2124	49	27	11	8				19		1.8	1.1		1.8	r	r	r	r	r			r		
OM11_Gid_A21B			LG		2124	55	45						23	4	1.7	1.3			r,v	p	r	p,v		p		r		p,v
OM12_Gid_054			LG		2040	51	45		4		5		2	1	1.3	0.8		1.2	r,v	r,v	r	r				r,p		
OM12_Gid_052			LG		2004	35	41	24					55		1.2	1.0	0.8		r,p	r,p		r		p	v	r,p		
OM12_Gid_053			LG		2004	46	47		6				5		1.5	1.6		1.6	r,p	r,p	r					r,v		
OM10_Gid_A22			LG		1936	59	39		2				3	3	1.0	1.5		1.2	r	r,v	r,v			r,v		r,v		
OM11_Gid_A22			LG		1936	56	37		7				7	1	1.5	2.0		2.0			v	r		r		r		
OM12_Gid_049			LG		1919	60	40						28	4	1.2	1.8					r					r		
OM12_Gid_048			LG		1792	49	47		3				4		1.0	0.8		1.2	r,p	r,p	r	r,p	r,p	r,p	v	r,p		
OM12_Gid_047			LG	MG	1787	62	38						43	7	0.9	1.0			r,p	r,p	r	r,v,p	r,p			r,p		
OM12_Gid_046			LG		1727	53	47						7	6	0.9	1.2			r,v	r,v					v	r,v		
OM12_Gid_043			LG		1671	56	44						13	5	2.0	2.0				p,v	r	p,v	r,p	p				
OM10_Gid_A23			LG		1659	53	47						3		1.0	0.9			r	p	r			p		r,p		
OM10_Gid_A23a			LG		1659	60	40						5		1.0	1.0			r		r	r		r		r		
OM12_Gid_045			LG		1630	50	50						2	4	1.0	1.0			r,v	r,v	r	r			v	r,v		
OM12_Gid_044			LG		1626	62	30		8				6		1.4	1.8		1.4	r		r	r				r		
OM12_Gid_042	1		LG		1562	52	39		9				12		2.0	1.3							r					
OM12_Gid_042	2		LG		1562	53	47						22		1.3	1.7							r					
OM12_Gid_040			LG		1508	50	50						2	1	1.0	1.0			r,v,p	r,p		r,p	r			r,v,p		
OM12_Gid_041			LG		1508	50	50						3	1	1.0	1.1			r,v	p,v		r	r	r	v	r,v		
OM10_Gid_A24			LG		1431	30	58		12				4		0.9	1.1		0.9	r		r	r	r	r		r		
OM12_Gid_039			LG		1289	44	47		9				6		0.9	1.1		0.8	r		r	r	r			r		
OM12_Gid_026			LG		1231	55	43		0	13			18	8	1.2	2.5		0.9	p,v		r,p		p	p,v				
OM12_Gid_027			LG		1222	48	42		8	2			31	6	1.8	1.7			r		r	r	r	p		r		
OM10_Gid_025			LG		1210	45	45		10				5		0.9	1.0		0.8	r	r	r	r	r	r				
OM12_Gid_025			LG		1197	50	35		15				24		2.5	1.8		0.8		r	r		r					
OM12_Gid_Hy0			LG		1190	51	44		5				28		1.8	2.4			r	p	r		r	p				p
OM12_Gid_Hy018			LG		1190	57	40		3				12		1.8	2.3			r	r	r	r	r					
OM12_Gid_Hy023			LG	MG	1190	57	43						43	10	1.5	1.4			r,p	r,p	r	r,p	r,p	r		r		p,v
OM12_Gid_Hy025			LG		1190	50	45		5				14		1.2	2.5				r	r	r	r			p		p
OM12_Gid_Hy030			LG	MG	1190	53	47						96		0.7				p		r,p		r					
OM12_Gid_Hy032A			LG	MG	1190	41	34		26				32	2	1.9	2.4			r	r	r		r	r				
OM12_Gid_Hy032B			LG	MG	1190	43	43			13			87		4.0	2.3			r	r,p	r	p	r			r		
OM12_Gid_Hy032C			LG	MG	1190	0	80			20			95			2.4				r,p	r	p	r			r		
OM12_Gid_Hy032D			LG	MG	1190	0	81			19			89	5		2.5			p,v	p	r	p	r			r,p		r,p
OM12_Gid_Hy038			LG	MG	1190	44	36		14	6			37		1.8	2.3			r	p	r	r	r			r		p
OM12_Gid_Hy039	2		LG	MG	1190	43	57						88		5.0	5.0			r,v,p	r	r	p	r	p		r,p		p
OM12_Gid_Hy42			LG		1190	51	38		11				26	5	1.6	2.0		0.5		r,p	r	r,v	r			r		
OM12_Gid_Hy055B			LG	MG	1190	0	100						82	15		4.0			r,p	r,p		r,p	r,p	r,p		r,p		r,v,p
OM12_Gid_Hy058.5			LG		1190	55	45						38	4	1.8	2.2				r		r	r			p		
OM12_Gid_Hy059			LG		1190	66	34						24	7	2.3	2.1				r	r			r				
OM12_Gid_Hy059.5			LG	MG	1190	58	42						43	5	1.5	1.5				p		p,v		p,v				v
OM12_Gid_Hy062			LG	MG	1190	38	62						39	5	1.3	1.8			r,p	v		p		p				v
OM12_Gid_Hy068			LG	MG	1190	54	46						30		1.8	2.2				p		p	r	p		p		
OM12_Gid_Hy077			LG		1190	50	40		10				12		2.0	2.5										r		

Table 5, continued

Sample	#[1]	Dom.[2]	Lith.[3]	S-Lith.[4]	Depth[5]	Pl	Cpx	Opx	Ol	Amph	Ox	Qtz	perv	vein	Pl	Cpx	Opx	Ol	Chl	Tr/Act	Hbl	Srp	Idd	Tlc	Ep/Czo	Ox	Ttn	Prh
						Modal proportions [vol%][6]							Alteration [vol%][7]		Grain size [mm][8]				Secondary minerals[9]									
OM12_Gid_Hy080			LG	LG	1190	47	46		6		1		32	4	2.0	1.2				r	r	r,p	r	p		r		r
OM12_Gid_Hy080.5			LG	MG	1190	45	42		7	4	1		48	4	1.5	2.4				r	r	p	r,p	r,p		r		
OM12_Gid_Hy096			LG	MG	1190	51	49						40	2	1.2	1.3				r	p	r	p					
OM12_Gid_Hy102	1		LG	LG	1190	55	44				1		35		1.5	1.8			p	p		p	r			r		v
OM12_Gid_Hy102	2		LG	LG	1190	55	45						48	3	1.2	1.8		v	p		p							v
OM12_Gid_Hy103			LG	MG	1190	47	53						54	3	2.3	4.5		p,v	p	r	p,v	r					
OM12_Gid_Hy108			LG	LG	1190	51	49						34		1.3	2.3		p	p		p						
OM12_Gid_Hy154	1		LG	LG	1190	50	45		5				9		1.5	1.6									p	
OM12_Gid_Hy154	2		LG	MG	1190	34	56		9				53	28	1.1	1.8	p,v	p,v		p,v	p,v	p				
OM12_Gid_Hy166			LG	LG	1190	45	48		7				8		1.4	1.2		r		r	r					
OM12_Gid_Hy039	1		LG	LG	1190	43	57						88		5.0	5.0	r,v,p	r,p		p	r,v,p	p					p
OM12_Gid_038			LG	LG	1121	45	42		13				11	5	1.8	2.2	r	r		r,v	r	p				
OM10_Gid_A26			LG	LG	1079	48	44		8				8		1.0	1.1	2.3	r	r		r	r			r	
OM12_Gid_036			LG	LG	1064	71	29						36		1.5	1.6	0.8	p	p,v		p,v		p,v			
OM12_Gid_037			LG	MG	1064	54	46						15	2	0.9	1.5	p	p		p	r	p		r		v
OM12_Gid_035			LG	LG	991	53	47						57		1.8	1.0	p	p		p	r	p		r	
OM11_Gid_A26			LG	LG	930	45	40		15				17		2.3	1.4	2.0		r						
OM12_Gid_033			LG	MG	890	60	40						67		2.0	2.2		p	r	p		p		
OM12_Gid_034	1		LG	MG	813	52	48						50	4	1.3	1.5	p,v	r,p		p,v		p		r,p	
OM12_Gid_034	2		LG	LG	813	67	33						31		1.9	1.7	p,v	p,v	r,v	p,v		p,v			
OM10_Gid_A27			LG	LG	804	50	50		15				2	10	0.9	1.0	r,v	v		r,p				r,v		v
OM12_Gid_032			LG	MG	749	58	42						61	6	1.8	1.2	r,p	p		r,p				
OM11_Gid_A27_1			LG	LG	714	48	37		15				13		1.9	2.1	3.0	r	r		r,p	r			
OM11_Gid_A28B			LG	MG	703	50	50	14					86	4	0.7	0.8	p,v	r,p	r	r,p		p		r,p		v
OM10_Gid_A28			LG	LG	696	43	43						42		1.0	1.4	1.3	p	p	r	p		p		r
OM12_Gid_031			LG	MG	684	53	47						25	2	1.7	1.7	v	r,p	r	r,p		p		
OM12_Gid_030			LG	MG	631	50	50						28	1	2.0	1.7	p	r		r				
OM12_Gid_029			LG	MG	631	53	45				2		29		0.6	0.7		p	r	r	r,p			r,p	
OM12_Gid_201			LG	LG	598	45	50		5				4		1.0	3.0	0.8	r	r	r	r			r
OM12_Gid_202			LG	MG	594	50	50						45		1.0	0.6					r	r
OM12_Gid_028			LG	MG	564	53	47						63	5	1.2	1.0		p,v		r,p		p		p
OM10_Gid_A29			LG	LG	545	51	49						10		0.8	0.5	r,v	r,v		r		r,v		r
OM11_Gid_A29			LG	LG	517	47	24	12					33		1.0	1.3	1.0	p	p,v	r	r		r,v		
OM12_Gid_204			LG	MG	434	63	37		18				41	4	1.5	1.2	1.8	r,v	p,v	r	p,v	r	p		p		v
OM12_Gid_203			LG	LG	433	50	43		7				1	1	0.8	1.5	1.0	r,v	r		r		r		r,v
OM11_Gid_A29_2			LG	LG	401	46	43		11				16		1.2	1.2	2.5	r	r	r	r			
OM10_Gid_A30			LG	LG	257	53	29	12	6				24		2.0	1.9	1.4		p		p	r	p		
OM12_Gid_205			LG	LG	222	50	40		10				15		0,2/2	0.9	1.2	r			p		r		
OM12_Gid_206			LG	LG	210	49	49		2				3	1	1.0	0.9	0.5					r			r
OM12_Gid_207			LG	LG	210	61	32	2	5				12		0.8	1.1	3.0	r	r		r	r	p		r,v
OM12_Gid_208			LG	LG	147	60	40						30		1.0	1.3					r		r		r
OM12_Gid_211			LG	MG	135	53	47		10				66	5	1.4	1.6	p	r		r,p				
OM10_Gid_A31			LG	LG	123	60	30						3		1.0	0.8	0.5	r	r		r		r		r
OM12_Gid_210		1	LG	LG	88	5	92		3				3		0.3	1.0	0.7			r	r				r
OM12_Gid_210		2	LG	LG	88	50	45		5				2		0.3	0.4	0.9		r	r	r				r
OM12_Gid_210		3	LG	LG	88	85	15						2		0.3	0.5								
OM10_Gid_A32			LG	LG	49	51	33	11	5				30		1.1	0.9	0.8	1.4	p			p			

[1] Thin section number for multiple thin sections per sample

[2] Domain

[3] Lithologies: PB = Pillow basalt; SD = Sheeted dike; ML = Melt lens; VG = Varitextured gabbro; FG = Foliated gabbro; LG = Layered gabbro

[4] Sub-Lithologies: USD = Upper sheeted dikes; LSD = Lower sheeted dikes; TR = Trondhjemite; VG = Varitextuted gabbro; PGXE = Xenolith bearing plagiogranite; UFG = Upper foliated gabbros; LFG = Lower; MG = Metagabbro

[5] Depth: Calculated height avove MOHO

[6] Modal proportions in [vol%]: Pl = Plagioclase; Cpx = Clinopyroxene; OPX = Orthopyroxene; Ol = Olivine; Amph = Amphibole; Ox = Oxides; Qtz = Quartz

[7] Alteration in [vol%]; perv = pervasive; vein = vein alteration

[8] Grain size in [mm]: Pl =Plagioclase; Cpx = Clinopyroxene; Opx = Orthopyroxene; Ol = Olivine

[9] Secondary minerals: Chl = Chlorite; Tr/Act = Tremolite/Actinolithe; Hbl = Hornblende; Srp = Serpentinite; Idd = Iddingsite; Tlc = Talc; Ep/Czs = Epidote/Clinozoisite; Ox = Oxides; Ttn = Titanite; Prh = Prehnite; p = pervasive; r = pervasive; v = vein; ? = in question

Table 6. Visual estimation in comparison with point counting for determination of modal proportions

Sample	H.a.M. [1] [m]	CU [2]	Dom [3]	Phase [4]	Visual estimation [vol%]	Point counting [cts]	Point counting [vol%]	Point counting 2σ [vol%]	Deviation [5] %
OM12_Gid_201	618	LG		Pl	41.70	3965	43.95	1.05	-5.13
				Pl alt.	1.30	136	1.51	0.26	-13.77
				Cpx	46.50	3893	43.15	1.04	7.75
				Cpx alt.	2.50	128	1.42	0.25	76.19
				Ol	7.80	852	9.44	0.62	-17.41
				Ol alt.	0.20	47	0.52	0.15	-61.61
OM12_Gid_203	459	LG		Pl	49.00	3897	46.07	1.08	6.35
				Pl alt.	1.00	133	1.57	0.27	-36.41
				Cpx	42.20	3679	43.50	1.08	-2.98
				Cpx alt.	1.80	119	1.41	0.26	27.94
				Ol	5.90	587	6.94	0.55	-14.99
				Ol alt.	0.10	43	0.51	0.15	-80.33
OM12_Gid_205	272	LG		Pl	49.00	3864	45.90	1.09	6.76
				Pl alt.	1.00	57	0.68	0.18	47.70
				Cpx	41.80	3853	45.77	1.09	-8.66
				Cpx alt.	2.20	64	0.76	0.19	189.40
				Ol	5.00	483	5.74	0.51	-12.85
				Ol alt.	1.00	98	1.16	0.23	-14.09
OM12_Gid_206	262	LG		Pl	51.00	3932	48.47	1.11	5.22
				Pl alt.	1.00	124	1.53	0.27	-34.58
				Cpx	43.20	3642	44.90	1.10	-3.78
				Cpx alt.	1.80	98	1.21	0.24	49.00
				Ol	2.90	293	3.61	0.41	-19.71
				Ol alt.	0.10	23	0.28	0.12	-64.73
OM12_Gid_210	182	LG	1	Pl	4.90	436	5.54	0.52	-11.53
				Pl alt.	0.10	93	1.18	0.24	-91.54
				Cpx	89.10	7062	89.71	0.68	-0.68
				Cpx alt.	2.90	56	0.71	0.19	307.66
				Ol	2.90	205	2.60	0.36	11.36
				Ol alt.	0.10	20	0.25	0.11	-60.64
OM12_Gid_210	182	LG	2	Pl	49.00	3993	47.25	1.09	3.69
				Pl alt.	1.00	123	1.46	0.26	-31.30
				Cpx	43.65	3734	44.19	1.08	-1.22
				Cpx alt.	1.35	59	0.70	0.18	93.35
				Ol	4.90	452	5.35	0.49	-8.40
				Ol alt.	0.10	89	1.05	0.22	-90.51
OM12_Gid_210	182	LG	3	Pl	83.30	5942	66.85	1.00	24.61
				Pl alt.	1.70	67	0.75	0.18	125.54
				Cpx	14.55	2843	31.98	0.99	-54.51
				Cpx alt.	0.45	37	0.42	0.14	8.11
OM12_Gid_218	2799	FG		Pl	49.00	4073	47.99	1.08	2.11
				Pl alt.	1.00	79	0.93	0.21	7.44
				Cpx	41.80	3683	43.39	1.08	-3.67
				Cpx alt.	2.20	138	1.63	0.27	35.32
				Ol	5.90	471	5.55	0.50	6.33
				Ol alt.	0.10	44	0.52	0.16	-80.71

[1] Height above Moho [m]

[2] Crustal unit: FG - Foliated gabbro; LG - Layered gabbro

[3] Domain

[4] Phase: Pl - Plagioclase; Cpx - Clinopyroxene; Ol - Olivine; alt. - altered

[5] Reltive deviation of visual estimation from point counting

Table 7. Results for bulk major and trace element analysis

	Method[2]	OM10_Gid_B01a	OM10_Gid_B01b	OM10_Gid_B04a	OM10_Gid_B04e	OM10_Gid_B04c	OM10_Gid_B05a	OM10_Gid_B05b	OM10_Gid_B00	OM10_Gid_B02	OM10_Gid_B03	OM10_Gid_B06	OM10_Gid_A02	OM10_Gid_A03
Lithology[1]		PB	PB	PB	PB	PB	PB	PB	SD	SD	SD	SD	SD	SD
Major Elements [wt%]														
SiO_2calc		64.46	67.10	54.92	54.03	54.09	68.44	58.89	62.18	59.99	64.55	55.08	57.22	59.46
Al_2O_3		14.77	15.13	16.30	15.56	15.89	13.83	14.88	15.02	15.69	14.95	14.67	15.56	15.83
FeO		7.56	5.44	4.63	4.73	5.15	4.51	4.16	9.30	9.04	7.67	11.13	10.04	9.00
MnO		0.18	0.23	0.21	0.23	0.23	0.12	0.27	0.14	0.21	0.15	0.11	0.18	0.19
MgO		2.48	0.86	1.19	1.22	1.52	0.83	1.11	2.28	3.86	1.69	4.77	4.09	4.35
CaO		1.80	2.26	11.73	13.79	12.12	3.99	13.21	4.64	2.92	2.31	5.17	3.48	2.24
Na_2O		7.19	6.08	8.31	7.87	8.32	6.61	5.24	4.54	6.14	7.20	6.80	7.12	6.86
K_2O		0.04	1.46	0.41	0.32	0.43	0.55	0.33	0.38	0.38	0.17	0.11	0.24	0.23
TiO_2		1.21	1.15	2.09	2.06	2.05	0.92	1.69	1.32	1.57	1.01	1.98	1.87	1.66
P_2O_5		0.30	0.29	0.23	0.19	0.21	0.21	0.21	0.20	0.20	0.30	0.19	0.20	0.20
Total		100.00	100.00	100.00	100.00	100.00	100.00	100.00	100.00	100.00	100.00	100.00	100.00	100.00
Trace elements [ppm]														
Li	AD	2.27	8.54	3.78	4.97	4.40	13.55	18.07	2.16	2.29	1.45	1.99	1.91	5.25
Sc	AD	15.00	16.29	25.45	25.91	25.39	12.04	18.76	20.08	21.87	14.58	33.49	22.56	21.86
V	AD	71.86	65.96	188.36	201.84	190.13	27.44	126.82	75.06	196.90	34.37	394.98	192.65	207.75
Cr	AD	29.68	14.00	15.75	13.28	36.39	50.49	26.40	209.51	29.68	17.69	13.10	16.51	12.66
Co	AD	7.30	11.50	42.37	44.63	36.90	6.13	25.01	16.13	10.67	10.34	24.91	20.53	16.70
Ni	AD	15.41	6.00	6.73	6.03	18.55	25.51	8.80	117.04	10.79	7.09	12.03	10.98	6.89
Cu	AD	319.44	5.82	18.34	20.81	45.28	3.10	5.61	3.59	5.38	1.85	4.49	24.96	4.26
Zn	AD	82.55	99.93	104.19	111.72	105.10	94.27	131.69	41.44	99.84	40.27	29.38	87.26	83.40
Ga	AD	16.56	15.89	16.25	16.87	15.88	17.02	16.42	15.88	16.92	17.04	16.82	19.87	16.71
Rb	AD	<0.2	18.53	3.78	3.09	4.31	7.46	2.19	1.58	1.64	0.87	0.49	1.67	1.05
Sr	AD	73.83	231.99	242.03	148.90	265.10	267.13	217.35	181.99	221.45	197.41	217.96	90.89	128.35
Y	PT	64.88	58.13	43.39	41.63	41.67	58.33	40.25	42.53	43.95	52.82	42.36	38.45	41.52
Zr	PT	175.39	201.90	148.55	134.65	150.35	223.52	133.35	63.67	88.72	62.47	20.74	132.34	147.39
Nb	AD	5.87	4.70	4.09	3.78	3.90	5.15	3.39	2.73	3.71	5.00	1.34	3.53	3.57
Mo	AD	1.87	2.10	2.18	1.85	4.15	6.73	3.46	28.24	1.79	2.74	0.00	1.29	0.92
Sb	AD	0.02	0.26	0.05	0.04	0.03	0.07	0.05	0.04	0.04	0.02	<0.01	0.03	0.02
Cs	AD	<0.01	0.27	0.30	0.26	0.39	0.23	0.11	0.03	0.02	0.02		0.03	0.01
Ba	AD	14.00	202.64	71.43	42.80	79.35	72.56	75.57	33.93	50.09	13.87	10.42	8.31	33.04
La	AD	10.22	8.44	6.08	5.73	6.11	8.80	5.59	5.33	6.09	8.70	5.35	5.86	6.35
Ce	AD	28.56	22.86	17.23	16.11	17.10	24.23	15.81	15.78	17.42	25.23	14.55	16.13	17.86
Pr	AD	4.69	3.87	2.83	2.64	2.80	3.96	2.62	2.62	2.81	4.14	2.33	2.68	2.98
Nd	AD	24.10	19.69	14.44	13.50	14.54	19.90	13.59	13.71	14.45	21.19	12.54	13.71	15.17
Sm	AD	7.44	6.14	4.58	4.33	4.62	6.18	4.36	4.53	4.57	6.63	4.34	4.34	4.82
Eu	AD	2.23	1.94	1.58	1.50	1.59	1.85	1.55	1.58	1.52	1.99	1.52	1.52	1.63
Gd	AD	9.33	7.77	5.83	5.57	5.94	7.71	5.57	5.91	5.82	8.17	5.87	5.58	6.09
Tb	PT	1.63	1.36	1.04	0.98	1.05	1.35	0.98	1.04	1.03	1.41	1.08	0.94	1.06
Dy	PT	10.82	8.98	6.83	6.54	7.00	8.98	6.43	6.94	6.85	8.97	7.38	6.19	6.98
Ho	PT	2.26	1.91	1.44	1.38	1.46	1.90	1.33	1.44	1.43	1.81	1.56	1.38	1.54
Er	PT	6.29	5.37	3.98	3.82	4.03	5.35	3.66	3.96	3.98	4.77	4.35	4.09	4.49
Tm	PT	0.92	0.81	0.59	0.57	0.59	0.80	0.54	0.58	0.59	0.68	0.64	0.60	0.67
Yb	PT	5.90	5.41	3.83	3.69	3.77	5.31	3.48	3.66	3.76	4.45	4.18	3.87	4.30
Lu	PT	0.86	0.80	0.56	0.54	0.56	0.78	0.51	0.52	0.53	0.62	0.63	0.59	0.64
Hf	PT	4.40	4.83	3.56	3.29	3.42	5.23	3.15	2.14	2.62	2.14	0.92	3.26	3.74
Ta	PT	0.35	0.29	0.26	0.24	0.23	0.31	0.22	0.18	0.23	0.31	0.20	0.23	0.24
W	AD	0.14	0.14	0.13	0.12	0.23	0.32	0.15	1.23	0.12	0.15	0.12	0.13	0.10
Pb	AD	0.38	10.98	1.04	1.35	1.05	1.18	1.22	0.17	0.33	0.24	<0.1	0.43	0.36
Th	PT	0.56	0.53	0.40	0.37	0.40	0.56	0.32	0.24	0.29	0.19	0.21	0.36	0.36
U	PT	0.22	0.91	0.29	0.26	0.28	0.24	0.27	0.09	0.11	0.09	0.05	0.15	0.19
Sn	AD	1.66				0.98						2.24	1.25	1.03

[1] Lithology: PB = Pillow basalt; SD = Sheeted dike; VG = Varitextured gabbro; FG = Foliated gabbro; LG = Layered gabbro

[2] Method: AD = Acid Degestion (ICP-OES); PT = Powder Tablet (ICP-MS)

Table 7, continued

Major Elements [wt%] and Trace elements [ppm]

Lithology¹	SD	SD	SD	SD	SD	SD	SD	SD	SD	SD	VG	VG	VG	Method²
Sample	OM10_Gid_A04	OM10_Gid_A05a	OM10_Gid_A05b	OM10_Gid_A06	OM10_Gid_A10	OM10_Gid_A11_3	OM10_Gid_A11_2	OM10_Gid_A11	OM10_Gid_A12_3	OM10_Gid_A12_2c	OM10_Gid_A12_2d	OM10_Gid_A13	OM10_Gid_A12_1a	
SiO2calc	57.83	58.63	68.79	59.36	52.14	53.08	52.06	51.04	53.04	51.37	58.65	49.82	52.68	
Al2O3	14.59	15.36	13.88	15.08	16.56	15.88	16.13	16.39	16.26	17.01	15.89	17.20	15.43	
FeO	9.49	6.19	4.86	6.95	10.50	8.21	9.20	9.13	9.68	10.58	8.01	7.16	9.41	
MnO	0.13	0.15	0.06	0.11	0.17	0.15	0.12	0.18	0.12	0.12	0.07	0.13	0.14	
MgO	4.08	1.62	0.85	0.72	6.24	8.58	6.96	7.94	5.77	5.69	3.55	9.10	7.74	
CaO	4.46	8.49	2.88	7.47	8.71	9.64	10.57	11.51	9.31	9.78	6.70	14.48	10.37	
Na2O	7.43	7.73	7.85	8.20	4.18	3.20	3.53	2.53	4.10	3.88	5.00	1.50	3.06	
K2O	0.08	0.16	0.03	0.05	0.22	0.38	0.18	0.24	0.16	0.10	0.29	0.10	0.15	
TiO2	1.74	1.44	0.65	1.82	1.19	0.88	1.15	1.05	1.45	1.33	1.64	0.52	1.03	
P2O5	0.15	0.22	0.14	0.23	0.10	0.00	0.10	0.00	0.11	0.13	0.21	0.00	0.00	
Total	100.00	100.00	100.00	100.00	100.00	100.00	100.00	100.00	100.00	100.00	100.00	100.00	100.00	
					29.28	44.57					25.41	50.85		
Li	1.11	1.70	1.56	2.84	2.87	2.35	2.40	2.08	1.68	1.38	1.37	1.61	0.73	AD
Sc	26.18	18.80	10.34	20.08	36.08	37.02	37.73	40.15	32.32	35.00	22.86	39.52	38.18	AD
V	336.12	140.31	30.75	110.67	312.30	227.45	283.12	287.36	320.88	319.49	223.15	220.66	272.78	AD
Cr	20.50	11.91	48.43	30.10	84.65	256.53	157.60	304.09	113.41	205.61	21.48	367.65	423.30	AD
Co	15.56	6.26	4.05	6.50	33.39	36.39	34.78	35.54	34.70	32.28	19.10	41.12	37.19	AD
Ni	17.60	6.79	25.77	15.44	49.42	94.44	84.94	112.22	70.44	93.59	10.42	109.54	83.31	AD
Cu	3.48	1.19	29.10	51.68	15.66	16.09	9.51	75.21	6.91	3.53	3.12	65.63	4.45	AD
Zn	45.36	21.65	17.23	27.83	36.61	35.89	28.70	26.96	18.69	16.83	13.63	33.54	18.12	AD
Ga	13.73	15.32	14.20	12.23	16.46	13.85	15.63	13.91	17.26	19.36	18.23	12.83	14.84	AD
Rb	0.43	0.65	<0.2	0.24	0.75	1.98	0.71	0.87	0.80	0.56	1.19	0.75	0.51	AD
Sr	110.03	141.67	39.91	77.51	278.09	202.29	324.82	298.14	248.56	174.93	263.95	113.89	150.52	PT
Y	36.21	48.52	62.38	46.77	21.99	19.01	21.20	17.47	27.41	30.87	40.98	9.98	24.62	PT
Zr	121.12	147.33	257.87	146.47	67.28	50.90	56.98	41.19	79.65	86.52	184.03	20.17	44.64	PT
Nb	3.19	3.63	6.19	4.02	1.52	1.98	1.30	1.03	1.76	2.14	3.45	0.48	1.26	AD
Mo	2.50	1.46	5.82	3.86	3.57	1.98	11.38	12.01	12.61	15.19	1.70	0.22	2.51	AD
Sb	0.03	0.04	0.00	0.07	0.00	0.00	0.03	0.02	0.03	0.03	0.00	0.02	0.00	AD
Cs	<0.01	0.02	<0.01	0.01	<0.01	0.02	0.04	0.01	0.02	<0.01	0.02	<0.01	0.02	AD
Ba	11.32	19.14	6.84	12.31	31.57	73.02	20.12	18.21	19.57	27.76	33.60	12.42	19.48	AD
La	4.64	7.31	8.87	5.26	3.34	2.45	2.72	2.22	3.64	5.20	5.93	0.85	3.00	AD
Ce	14.29	19.79	25.51	15.77	8.84	6.84	7.51	6.30	10.14	14.68	16.22	2.51	8.48	AD
Pr	2.43	3.24	4.17	2.77	1.44	1.15	1.29	1.08	1.75	2.39	2.75	0.45	1.49	AD
Nd	12.58	16.67	20.69	14.57	7.32	6.06	6.87	5.74	9.18	11.94	14.23	2.56	7.95	AD
Sm	3.97	5.14	6.42	4.84	2.34	2.02	2.36	1.97	3.02	3.65	4.49	0.96	2.70	AD
Eu	1.40	1.82	1.68	1.67	0.93	0.83	0.94	0.84	1.23	1.29	1.45	0.44	0.98	AD
Gd	5.06	6.67	7.79	6.51	3.05	2.66	3.18	2.62	4.04	4.61	5.71	1.42	3.62	AD
Tb	0.95	1.21	1.57	1.14	0.54	0.47	0.54	0.44	0.68	0.79	1.00	0.24	0.62	PT
Dy	6.22	7.99	10.34	7.62	3.52	3.15	3.54	2.80	4.49	5.13	6.49	1.62	4.08	PT
Ho	1.36	1.71	2.24	1.71	0.78	0.68	0.78	0.61	0.95	1.14	1.40	0.36	0.92	PT
Er	3.83	4.85	6.57	4.97	2.27	1.91	2.23	1.70	2.68	3.28	4.05	1.04	2.65	PT
Tm	0.59	0.74	1.02	0.73	0.35	0.29	0.32	0.25	0.40	0.48	0.65	0.15	0.39	PT
Yb	3.92	4.85	6.70	4.70	2.27	1.93	2.12	1.68	2.65	3.18	4.23	1.02	2.55	PT
Lu	0.58	0.71	1.01	0.73	0.34	0.28	0.31	0.25	0.39	0.47	0.66	0.15	0.38	PT
Hf	3.18	3.73	6.33	3.65	1.76	1.32	1.47	1.07	1.95	2.19	4.19	0.56	1.27	PT
Ta	0.21	0.24	0.42	0.26	0.09	0.08	0.08	0.06	0.11	0.14	0.21	0.03	0.08	AD
W	0.18	0.14	0.37	0.26	0.25	0.22	0.55	0.58	0.64	0.64	0.19	0.07	0.17	AD
Pb	0.22	0.23	0.10	0.22	0.11	<0.1	0.14	0.10	<0.1	0.12	<0.1	0.17	0.14	AD
Th	0.34	0.42	0.68	0.43	0.24	0.13	0.14	0.10	0.18	0.30	0.41	0.05	0.12	PT
U	0.17	0.20	0.30	0.22	0.08	0.06	0.07	0.05	0.09	0.12	0.16	0.03	0.07	PT
Sn	2.05	1.15	1.40	1.31	0.66	0.59	0.81	0.59	1.01		0.72	0.37	1.49	AD

¹ Lithology: PB = Pillow basalt; SD = Sheeted dike; VG = Varitextured gabbro; FG = Foliated gabbro; LG = Layered gabbro

² Method: AD = Acid Degestion (ICP-OES); PT = Powder Tablet (ICP-MS)

Table 7. continued

Major Elements [wt%]

Sample	OM10 Gid A14a (VG)	OM10 Gid A14b (VG)	OM10 Gid A15 (VG)	OM10 Gid A16 (FG)	OM10 Gid A17 (FG)	OM10 Gid A17_2 (FG)	OM10 Gid A17_1 (FG)	OM10 Gid A18 (FG)	OM10 Gid A18_1 (FG)	OM10 Gid A18_2a (FG)	OM10 Gid A19 (FG)	OM10 Gid A20 (LG)	OM12 Gid 055 (LG)
SiO2calc	49.26	52.35	48.94	47.91	48.03	47.97	48.36	49.89	48.32	48.67	48.32	48.00	49.08
Al2O3	16.27	16.94	15.31	16.74	20.08	15.55	20.04	16.84	17.75	17.77	17.14	19.29	14.32
FeO	7.52	7.39	10.40	6.37	6.94	11.13	8.93	7.08	5.94	5.37	6.10	4.65	5.23
MnO	0.14	0.14	0.17	0.12	0.14	0.17	0.11	0.14	0.12	0.11	0.12	0.09	0.11
MgO	10.12	6.91	8.36	10.87	7.04	8.80	4.27	9.11	9.94	9.71	10.95	10.01	11.55
CaO	14.53	11.99	12.93	16.71	14.67	12.69	13.42	14.22	16.00	16.78	15.76	16.56	18.58
Na2O	1.52	3.21	2.31	0.97	2.28	2.31	3.03	2.28	1.56	1.28	1.32	1.10	0.72
K2O	0.12	0.20	0.17	0.00	0.03	0.08	0.06	0.00	0.02	0.00	0.00	0.03	0.00
TiO2	0.52	0.86	1.41	0.32	0.79	1.30	1.79	0.43	0.35	0.31	0.30	0.28	0.41
P2O5	0.00	0.00	0.00	0.00	0.00	0.00	0.00	0.00	0.00	0.00	0.00	0.00	0.00
Total	100.00	100.00	100.00	100.00	100.00	100.00	100.00	100.00	100.00	100.00	100.00	100.00	100.00
				26.90	58.19							43.90	67.68

Trace elements [ppm]

Element	Method	OM10 Gid A14a (VG)	OM10 Gid A14b (VG)	OM10 Gid A15 (VG)	OM10 Gid A16 (FG)	OM10 Gid A17 (FG)	OM10 Gid A17_2 (FG)	OM10 Gid A17_1 (FG)	OM10 Gid A18 (FG)	OM10 Gid A18_1 (FG)	OM10 Gid A18_2a (FG)	OM10 Gid A19 (FG)	OM10 Gid A20 (LG)	OM12 Gid 055 (LG)
Li	AD	0.83	0.90	1.32	2.49	1.04	1.11	0.61	1.62	0.78	1.12	1.06	1.25	0.95
Sc	AD	45.68	37.57	45.43	48.75	38.71	46.86	35.56	42.61	47.74	50.13	44.19	41.05	73.16
V	AD	178.05	229.51	335.19	159.14	220.47	411.71	580.79	169.84	157.19	153.80	142.28	128.42	221.58
Cr	AD	129.14	79.40	202.44	444.38	255.98	355.36	20.41	209.22	505.65	63.64	626.66	421.62	733.66
Co	AD	43.90	33.05	46.24	46.83	31.72	48.10	29.89	42.98	39.62	37.29	46.72	35.01	35.66
Ni	AD	55.36	63.01	75.69	181.07	77.02	53.15	51.45	75.26	119.92	66.30	172.04	136.85	145.54
Cu	AD	140.20	31.96	51.88	102.78	69.68	47.15	17.09	91.61	103.39	212.00	152.26	67.23	289.63
Zn	AD	43.58	32.78	56.99	33.88	45.03	68.72	52.62	36.35	28.04	21.08	28.92	21.52	22.84
Ga	AD	12.11	15.40	14.79	10.34	14.45	13.91	18.12	12.95	10.78	11.99	11.44	11.02	9.26
Rb	AD	0.95	0.86	1.78	<0.2	0.26	0.46	0.32	<0.2	<0.2	<0.2	<0.2	<0.2	0.08
Sr	AD	248.72	182.13	152.89	134.49	228.82	192.04	218.12	150.62	145.04	161.02	152.77	145.47	107.33
Y	PT	11.58	22.00	18.61	6.39	9.37	14.81	10.43	10.25	6.87	6.65	6.05	4.53	8.45
Zr	PT	24.65	43.02	34.66	5.99	11.78	18.43	19.39	8.57	7.00	5.60	4.66	5.33	5.52
Nb	AD	0.54	1.37	1.31	0.07	0.17	0.36	0.64	0.05	0.07	0.05	0.03	0.09	0.05
Mo	AD	7.76	6.01	2.33	10.51	0.17	0.80	1.74	0.11	0.17	0.25	2.46	0.08	0.10
Sb	AD	0.00	0.00	0.00	0.00	0.03	0.02	0.00	0.00	0.03	0.00	0.00	0.00	0.01
Cs	AD	0.01	0.01	<0.01	<0.01	<0.01	0.01	<0.01	<0.01	0.01	<0.01	<0.01	<0.01	<0.01
Ba	AD	28.23	34.94	21.46	4.61	8.38	31.04	13.62	6.39	4.87	3.15	3.42	7.75	2.55
La	AD	1.10	2.93	1.83	0.26	0.86	0.95	1.04	0.46	0.41	0.23	0.26	0.31	0.34
Ce	AD	3.14	8.04	5.27	0.99	2.49	3.06	2.97	1.60	1.29	0.90	0.99	1.03	1.14
Pr	AD	0.57	1.39	0.94	0.22	0.47	0.62	0.54	0.35	0.27	0.21	0.22	0.20	0.23
Nd	AD	3.21	7.39	5.25	1.42	2.76	3.80	3.04	2.24	1.67	1.39	1.44	1.22	1.58
Sm	AD	1.20	2.50	1.93	0.63	1.10	1.53	1.15	1.00	0.74	0.65	0.66	0.51	0.74
Eu	AD	0.55	1.01	0.92	0.35	0.74	0.77	0.71	0.58	0.42	0.37	0.39	0.30	0.36
Gd	AD	1.70	3.34	2.68	0.98	1.58	2.26	1.62	1.53	1.12	1.02	1.02	0.76	1.14
Tb	PT	0.30	0.56	0.49	0.17	0.25	0.40	0.27	0.27	0.18	0.18	0.17	0.12	0.22
Dy	PT	1.95	3.75	3.33	1.15	1.64	2.65	1.83	1.84	1.20	1.22	1.10	0.83	1.52
Ho	PT	0.44	0.81	0.70	0.24	0.35	0.57	0.40	0.40	0.24	0.26	0.24	0.17	0.32
Er	PT	1.19	2.28	1.91	0.69	0.99	1.65	1.13	1.13	0.72	0.68	0.67	0.50	0.85
Tm	PT	0.18	0.35	0.28	0.10	0.14	0.24	0.17	0.17	0.10	0.10	0.09	0.07	0.12
Yb	PT	1.18	2.23	1.82	0.63	0.88	1.51	1.03	1.01	0.65	0.62	0.60	0.46	0.77
Lu	PT	0.16	0.33	0.27	0.09	0.13	0.21	0.15	0.14	0.09	0.09	0.08	0.06	0.11
Hf	PT	0.69	1.24	1.04	0.24	0.35	0.62	0.58	0.35	0.26	0.22	0.20	0.19	0.29
Ta	PT	0.04	0.09	0.09	0.01	0.02	0.03	0.05	<0.005	0.01	<0.005	<0.005	0.01	0.01
W	AD	0.37	0.29	0.16	0.52	0.08	0.07	0.14	0.04	0.09	0.05	0.13	0.04	0.02
Pb	AD	0.29	0.27	0.24	0.16	0.16	0.14	0.21	<0.1	0.14	0.13	0.12	<0.1	31.37
Th	PT	0.07	0.13	0.11	0.01	0.02	0.03	0.04	<0.1	0.01	0.01	<0.005	0.01	0.01
U	PT	0.05	0.06	0.04	0.01	0.01	0.02	0.02	0.02	0.01	0.01	<0.005	0.01	0.01
Sn	AD	0.41	0.74	0.58	0.21	0.25	0.41	0.40	0.19	0.17	0.18	0.16	0.20	0.75

[1] Lithology: PB = Pillow basalt; SD = Sheeted dike; VG = Varitextured gabbro; FG = Foliated gabbro; LG = Layered gabbro

[2] Method: AD = Acid Degestion (ICP-OES); PT = Powder Tablet (ICP-MS)

Table 7, continued

Method[2]	Lithology[1]	LG	LG	LG	LG	LG	LG	LG	LG	LG	LG	LG	LG	LG
	Sample	OM11_Gid_A21A	OM10_Gid_A21	OM12_Gid_054	OM12_Gid_052	OM12_Gid_053	OM11_Gid_A22	OM10_Gid_A22	OM12_Gid_048	OM12_Gid_046	OM12_Gid_045	OM10_Gid_A23	OM12_Gid_044	OM12_Gid_040
	Major Elements [wt%]													
	SiO_2calc	47.27	49.14	48.57	44.75	47.90	47.81	48.53	47.33	48.16	48.46	46.76	48.12	49.87
	Al_2O_3	17.14	16.44	18.52	11.31	16.72	19.81	18.54	20.20	16.78	17.01	20.57	17.58	17.07
	FeO	9.05	5.77	5.22	12.64	6.24	3.78	4.43	4.58	4.89	5.08	4.59	5.17	3.97
	MnO	0.14	0.11	0.10	0.19	0.11	0.08	0.09	0.08	0.10	0.11	0.08	0.10	0.08
	MgO	9.21	11.04	8.95	20.89	11.35	8.97	9.37	9.47	11.37	9.59	10.97	11.26	9.79
	CaO	14.85	16.10	16.80	9.39	16.42	18.20	17.45	16.98	17.41	18.20	15.82	16.56	18.10
	Na_2O	1.51	1.10	1.50	0.64	0.97	1.11	1.31	1.11	1.04	1.13	1.05	0.97	0.85
	K_2O	0.00	0.00	0.00	0.00	0.00	0.00	0.00	0.00	0.00	0.00	0.00	0.00	0.00
	TiO_2	0.83	0.30	0.34	0.19	0.29	0.23	0.28	0.25	0.25	0.43	0.15	0.24	0.26
	P_2O_5	0.00	0.00	0.00	0.00	0.00	0.00	0.00	0.00	0.00	0.00	0.00	0.00	0.00
	Total	100.00	100.00	100.00	100.00	100.00	100.00	100.00	100.00	100.00	100.00	100.00	100.00	100.00
	Trace elements [ppm]													
AD	Li	0.55	<0.5	1.12	0.74	0.73	0.91	0.47	0.67	0.71	0.54	0.45	1.08	0.51
AD	Sc	47.55	23.07	53.80	30.85	51.99	46.99	52.15	41.66	46.54	57.62	29.25	43.00	57.95
AD	V	396.36	159.51	178.31	91.51	154.83	127.94	135.84	124.14	130.40	220.63	73.89	128.91	148.68
AD	Cr	351.71	218.86	171.42	115.75	683.54	382.96	247.74	446.11	720.94	747.75	591.47	642.08	349.67
AD	Co	52.40	40.02	34.41	111.50	46.92	29.36	29.86	33.31	36.44	28.69	39.48	39.69	29.62
AD	Ni	124.04	105.99	46.62	284.84	199.58	112.77	95.93	113.39	176.73	170.34	231.43	172.44	97.19
AD	Cu	107.19	11.91	16.78	218.64	303.80	173.92	11.56	45.58	225.50	119.04	209.93	93.72	96.14
AD	Zn	49.80	20.47	19.28	43.46	24.61	14.70	15.44	18.76	23.63	23.58	17.75	26.27	15.48
AD	Ga	14.12	9.35	12.76	7.27	10.29	11.37	10.63	11.61	9.61	10.63	10.89	10.30	10.31
AD	Rb	0.07	<0.2	0.05	0.06	0.05	0.09	0.08	0.06	0.06	0.03	0.08	0.05	0.04
AD	Sr	163.72	77.07	161.33	89.42	132.41	157.47	158.13	160.92	128.15	139.96	140.82	121.18	140.19
PT	Y	8.39	6.17	6.61	3.64	5.53	5.18	6.00	4.77	5.52	8.23	3.06	5.75	5.75
PT	Zr	2.01	4.40	2.97	0.69	2.21	1.19	3.84	2.24	1.83	5.81	0.61	1.91	1.96
AD	Nb	0.03	0.02	0.03	0.03	0.03	0.05	0.06	0.04	0.03	0.14	0.05	0.02	0.02
AD	Mo	0.08	0.10	0.10	0.08	0.10	0.12	0.10	0.05	0.09	0.06	0.13	0.10	0.05
AD	Sb	0.02	0.00	0.01	0.01	0.01	0.02	0.01	0.01	0.02	0.02	0.02	0.01	0.01
AD	Cs	<0.01	<0.01	<0.01	<0.01	<0.01	<0.01	<0.01	<0.01	<0.01	<0.01	<0.01	<0.01	<0.01
AD	Ba	2.67	1.94	4.01	1.63	2.70	2.70	3.56	3.33	1.76	2.39	2.70	2.16	2.21
AD	La	0.23	0.21	0.29	0.18	0.27	0.24	0.29	0.29	0.24	0.28	0.11	0.26	0.24
AD	Ce	0.83	0.76	0.88	0.52	0.81	0.75	0.94	0.84	0.74	0.95	0.48	0.80	0.75
AD	Pr	0.20	0.16	0.18	0.10	0.16	0.16	0.19	0.16	0.15	0.21	0.10	0.16	0.15
AD	Nd	1.37	1.09	1.21	0.68	1.05	1.01	1.26	1.01	1.03	1.48	0.64	1.07	1.05
AD	Sm	0.69	0.53	0.58	0.32	0.49	0.46	0.57	0.44	0.49	0.73	0.29	0.51	0.50
AD	Eu	0.42	0.30	0.35	0.20	0.30	0.28	0.33	0.28	0.29	0.39	0.21	0.31	0.29
AD	Gd	1.10	0.87	0.91	0.49	0.76	0.71	0.88	0.67	0.76	1.15	0.46	0.78	0.80
PT	Tb	0.21	0.16	0.17	0.09	0.14	0.13	0.17	0.12	0.14	0.22	0.08	0.15	0.15
PT	Dy	1.43	1.12	1.19	0.65	0.99	0.90	1.15	0.85	1.00	1.51	0.57	1.03	1.06
PT	Ho	0.30	0.24	0.25	0.14	0.21	0.19	0.24	0.18	0.21	0.32	0.12	0.22	0.22
PT	Er	0.80	0.69	0.66	0.37	0.56	0.50	0.64	0.48	0.57	0.85	0.32	0.58	0.59
PT	Tm	0.12	0.10	0.09	0.05	0.08	0.07	0.09	0.07	0.08	0.12	0.05	0.08	0.08
PT	Yb	0.73	0.59	0.59	0.35	0.50	0.45	0.58	0.43	0.51	0.74	0.29	0.53	0.52
PT	Lu	0.10	0.08	0.09	0.05	0.07	0.07	0.08	0.06	0.08	0.11	0.04	0.08	0.08
PT	Hf	0.24	0.18	0.22	0.12	0.19	0.18	0.22	0.18	0.17	0.29	0.11	0.17	0.18
PT	Ta	0.01	<0.005	0.01	0.01	0.01	0.01	0.02	0.01	0.01	0.14	0.01	0.01	0.01
AD	W	0.02	0.05	0.02	0.02	0.02	0.02	0.05	0.02	0.03	0.21	0.06	0.02	0.01
AD	Pb	0.34	<0.1	3.49	26.06	37.02	0.23	0.06	42.17	74.02	45.37	0.06	33.96	9.39
PT	Th	0.01	0.01	0.01	0.01	0.01	0.01	0.01	0.01	0.01	0.00	0.01	0.01	0.00
PT	U	0.01	0.01	0.00	0.00	0.00	0.01	0.00	0.01	0.00	0.03	0.00	0.00	0.00
AD	Sn	0.12	0.12	1.02	0.84	0.66	0.01	0.14	1.41	0.81	35.39	0.14	1.39	0.62

[1] Lithology: PB = Pillow basalt; SD = Sheeted dike; VG = Varitextured gabbro; FG = Foliated gabbro; LG = Layered gabbro
[2] Method: AD = Acid Degestion (ICP-OES); PT = Powder Tablet (ICP-MS)

Table 7, continued

Lithology[1]:		LG	LG	LG	LG	LG	LG	LG	LG	LG	LG	LG	LG	LG
Sample	Method[2]	OM12_Gid_041	OM10_Gid_A24	OM12_Gid_039	OM12_Gid_027	OM10_Gid_A25	OM12_Gid_026	OM12_Gid_025	OM12_Gid_038	OM11_Gid_A26	OM10_Gid_A26	OM10_Gid_A26	OM12_Gid_036	OM12_Gid_035
Major Elements [wt%]														
SiO2calc		48.85	47.68	47.21	49.01	48.75	48.23	47.17	46.97	48.25	47.98	48.52	47.74	48.31
Al2O3		17.16	17.84	18.47	16.92	15.05	19.86	20.68	18.56	17.97	17.52	17.49	28.58	18.87
FeO		3.95	4.52	4.94	5.58	5.00	3.66	3.94	5.35	4.81	5.21	5.10	1.79	4.34
MnO		0.09	0.09	0.09	0.11	0.11	0.08	0.08	0.10	0.10	0.10	0.10	0.03	0.09
MgO		9.81	11.33	12.22	10.51	12.71	8.66	10.25	12.37	10.73	10.93	10.77	3.25	9.84
CaO		19.02	17.43	16.07	16.36	17.38	18.11	16.83	15.40	16.88	17.00	16.74	16.54	16.84
Na2O		0.85	0.90	0.81	1.21	0.74	1.16	0.89	1.05	1.02	1.01	1.05	1.95	1.49
K2O		0.00	0.00	0.00	0.00	0.00	0.00	0.00	0.00	0.00	0.00	0.00	0.00	0.00
TiO2		0.27	0.21	0.20	0.30	0.25	0.24	0.17	0.20	0.25	0.25	0.24	0.11	0.22
P2O5		0.00	0.00	0.00	0.00	0.00	0.00	0.00	0.00	0.00	0.00	0.00	0.00	0.00
Total		100.00	100.00	100.00	100.00	100.00	100.00	100.00	100.00	100.00	100.00	100.00	100.00	100.00
Trace elements [ppm]														
Li	AD	0.47	0.89	0.95	1.32	1.06	0.48	0.82	0.82	0.48	1.06	1.15	0.20	0.83
Sc	AD	59.59	45.84	35.99	49.52	53.87	44.77	33.51	34.78	45.23	53.17	51.30	10.54	38.77
V	AD	152.13	124.52	99.80	158.54	148.53	124.74	91.38	98.41	140.31	147.96	141.96	33.41	114.73
Cr	AD	366.78	590.72	807.28	322.79	749.88	1070.25	475.91	757.19	620.80	468.70	467.78	100.60	588.63
Co	AD	28.07	37.05	41.43	39.72	41.87	24.08	33.11	45.32	39.21	44.55	43.10	11.25	30.58
Ni	AD	97.63	185.25	240.34	114.80	203.86	89.92	171.75	227.40	163.99	172.56	171.11	43.73	143.69
Cu	AD	83.78	145.95	130.58	80.77	150.77	68.96	89.89	108.44	154.78	200.40	199.30	7.89	108.83
Zn	AD	15.79	19.22	23.96	30.34	21.74	15.22	17.17	21.61	22.48	22.83	21.40	9.54	21.08
Ga	AD	10.22	9.65	10.06	11.00	9.01	11.21	10.87	10.49	11.00	10.88	10.49	15.41	10.24
Rb	AD	0.04	<0.2	0.06	0.09	<0.2	0.04	0.08	0.08	0.07	0.09	0.10	0.05	0.08
Sr	AD	147.77	126.02	118.96	130.78	100.65	154.81	140.40	142.31	138.10	140.21	137.91	246.29	136.63
Y	PT	5.86	4.57	4.13	6.74	5.56	5.12	3.47	3.97	5.41	5.17	5.10	1.46	4.61
Zr	PT	2.01	3.53	0.85	4.09	4.06	1.66	0.98	1.13	2.65	2.24	1.04		1.16
Nb	PT	0.03	0.03	0.02	0.05	0.03	0.02	0.05	0.04	0.03	0.07	0.03	0.02	0.02
Mo	AD	0.09	0.15	0.06	0.10	0.16	0.09	0.06	0.07	0.07	0.07	0.09	0.08	0.05
Sb	AD	0.01	0.00	0.01	0.01	0.02	0.02	0.01	0.01	0.01	0.01	0.03	0.01	0.01
Cs	AD	<0.01	<0.01	<0.01	<0.01	<0.01	<0.01	<0.01	<0.01	<0.01	<0.01	<0.01	<0.01	<0.01
Ba	AD	2.30	3.27	2.13	3.06	2.03	2.54	3.28	2.21	2.41	2.21	1.29	3.47	1.93
La	AD	0.25	0.19	0.21	0.31	0.13	0.24	0.20	0.20	0.28	0.26	0.18	0.24	0.21
Ce	AD	0.77	0.62	0.61	0.97	0.62	0.72	0.56	0.58	0.81	0.74	0.62	0.56	0.64
Pr	AD	0.16	0.13	0.12	0.19	0.16	0.15	0.11	0.11	0.16	0.15	0.14	0.09	0.13
Nd	AD	1.06	0.90	0.78	1.28	1.06	0.97	0.69	0.77	1.05	1.00	0.95	0.48	0.90
Sm	AD	0.52	0.44	0.37	0.59	0.53	0.46	0.31	0.37	0.48	0.47	0.45	0.18	0.42
Eu	AD	0.31	0.27	0.25	0.35	0.29	0.30	0.22	0.24	0.29	0.29	0.28	0.24	0.29
Gd	AD	0.80	0.69	0.57	0.91	0.86	0.71	0.48	0.57	0.75	0.73	0.69	0.24	0.65
Tb	PT	0.15	0.12	0.11	0.17	0.15	0.14	0.09	0.11	0.14	0.14	0.13	0.04	0.12
Dy	PT	1.06	0.83	0.74	1.21	1.02	0.95	0.62	0.74	0.96	0.93	0.88	0.27	0.84
Ho	PT	0.22	0.17	0.15	0.25	0.22	0.20	0.13	0.15	0.20	0.20	0.18	0.06	0.17
Er	PT	0.59	0.49	0.42	0.68	0.61	0.52	0.35	0.41	0.55	0.52	0.49	0.15	0.47
Tm	PT	0.08	0.07	0.06	0.10	0.09	0.08	0.05	0.06	0.08	0.07	0.07	0.02	0.07
Yb	PT	0.52	0.41	0.37	0.61	0.54	0.47	0.31	0.37	0.49	0.46	0.44	0.13	0.42
Lu	PT	0.08	0.06	0.06	0.09	0.07	0.07	0.05	0.06	0.07	0.07	0.06	0.02	0.06
Hf	PT	0.19	0.14	0.13	0.24	0.18	0.18	0.13	0.15	0.18	0.18	0.18		0.15
Ta	PT	0.01	<0.005	0.01	0.01	<0.005	0.01	0.01	0.01	0.01	0.01	0.01	0.01	0.02
W	AD	0.02	0.07	0.02	0.03	0.05	0.03	0.02	0.02	0.02	0.06	0.03	0.02	0.02
Pb	AD	50.60	0.10	8.54	22.98	<0.005	20.14	32.34	13.12	0.22	0.15	0.11	25.82	44.00
Th	PT	0.01	0.01	0.01	0.01	0.01	0.01	0.01	0.01	0.01	0.01	0.01	0.01	0.01
U	PT	0.00	0.01	0.00	0.01	0.01	0.01	0.01	0.00	0.00	0.00	0.01	0.01	0.00
Sn	AD	0.68	0.11	0.59	1.34	0.17	1.69	1.08	0.34	0.71	0.13		0.83	0.61

Table 7. continued

Method[2]	Lithology[1]	LG	LG	LG	LG	LG	LG	LG	LG	LG	LG	LG	LG	MG
	Sample	OM11_Gid_A27	OM10_Gid_A27	OM11_Gid_A27_1	OM10_Gid_A28	OM11_Gid_A28	OM12_Gid_201	OM10_Gid_A29	OM11_Gid_A29_1	OM11_Gid_A29_2	OM10_Gid_A30	OM10_Gid_A31	OM10_Gid_A32	OM12_Gid_057
	Major Elements [wt%]													
	SiO2calc	47.39	49.51	48.08	48.04	46.75	48.33	48.52	47.75	47.71	47.40	49.17	49.25	48.55
	Al2O3	16.75	18.40	13.32	18.28	16.61	13.82	16.71	18.92	17.58	19.53	18.51	17.89	19.94
	FeO	5.51	3.48	6.49	4.85	5.87	5.72	4.83	4.85	4.87	4.04	4.21	4.13	3.85
	MnO	0.10	0.08	0.12	0.10	0.11	0.11	0.10	0.09	0.09	0.08	0.09	0.09	0.07
	MgO	12.74	9.10	16.20	10.84	14.87	14.73	11.92	11.59	12.18	11.01	9.35	10.70	7.71
	CaO	16.45	17.91	14.86	16.45	14.85	16.42	16.69	15.68	16.56	16.97	16.93	16.20	18.24
	Na2O	0.83	1.26	0.69	1.18	0.76	0.61	1.00	0.93	0.79	0.79	1.52	1.60	1.33
	K2O	0.00	0.00	0.00	0.00	0.00	0.00	0.00	0.00	0.00	0.00	0.00	0.00	0.00
	TiO2	0.23	0.26	0.23	0.26	0.17	0.25	0.24	0.19	0.23	0.17	0.23	0.14	0.30
	P2O5	0.00	0.00	0.00	0.00	0.00	0.00	0.00	0.00	0.00	0.00	0.00	0.00	0.00
	Total	100.00	100.00	100.00	100.00	100.00	100.00	100.00	100.00	100.00	100.00	100.00	100.00	100.00
														59.88
	Trace elements [ppm]													
AD	Li	1.09	0.41	1.12	0.50	0.96	1.19	0.26	0.87	0.61	0.25	0.68	0.72	0.70
AD	Sc	48.41	50.04	47.69	45.03	36.23	52.80	48.59	37.06	45.96	38.77	48.54	48.40	52.79
AD	V	134.40	139.56	145.48	138.69	105.67	155.86	137.04	102.88	134.35	105.25	142.95	126.23	190.13
AD	Cr	462.53	519.29	810.82	536.32	740.07	930.67	647.67	588.67	624.20	1295.09	287.02	355.72	303.72
AD	Co	48.81	24.54	61.14	34.06	54.64	47.64	38.67	45.47	42.86	33.88	31.78	40.86	25.88
AD	Ni	204.42	110.27	323.99	164.69	279.62	257.35	187.06	199.88	203.18	216.87	100.39	125.57	110.94
AD	Cu	170.27	28.23	111.89	90.00	121.01	133.94	122.41	145.52	83.16	63.73	135.86	60.21	33.45
AD	Zn	22.96	15.50	32.84	24.27	26.91	28.46	20.89	21.79	19.42	16.95	16.36	11.39	14.27
AD	Ga	9.86	10.20	8.40	10.13	9.23	8.39	9.31	10.65	9.99	9.63	11.43	10.78	11.90
AD	Rb	0.24	0.08	0.06	<0.2	0.08	0.06	0.09	0.07	0.08	<0.2	<0.2	<0.2	<0.2
AD	Sr	135.18	152.77	77.09	162.63	105.09	72.83	132.86	150.97	124.21	131.16	160.47	161.48	188.52
PT	Y	5.01	5.61	5.49	5.10	3.77	5.80	5.06	3.91	4.69	3.12	4.94	2.95	4.62
PT	Zr	0.84	2.87	0.20	4.06	-0.74	1.18	2.32	0.15	0.73	2.52	2.10	0.92	1.59
AD	Nb	0.05	0.04	0.02	0.03	0.03	0.02	0.06	0.04	0.05	0.02	<0.01	<0.01	0.04
AD	Mo	0.11	0.10	0.09	0.20	0.10	0.11	0.09	0.08	0.10	0.12	0.09	0.16	0.06
AD	Sb	0.03	0.01	0.02	0.00	0.03	0.01	0.02	0.02	0.03	0.00	0.00	0.00	0.00
AD	Cs	<0.01	<0.01	<0.01	<0.01	0.01	<0.01	<0.01	<0.01	<0.01	<0.01	<0.01	<0.01	<0.01
AD	Ba	1.69	2.50	0.61	2.63	0.72	1.16	6.62	1.55	1.59	2.18	3.34	1.73	2.80
AD	La	0.22	0.23	0.13	0.24	0.13	0.18	0.10	0.17	0.17	0.14	0.12	<0.2	0.22
AD	Ce	0.69	0.78	0.49	0.77	0.42	0.58	0.56	0.54	0.56	<0.5	<0.5	<0.5	0.60
AD	Pr	0.15	0.17	0.13	0.17	0.10	0.13	0.14	0.12	0.13	0.09	0.11	<0.05	0.12
AD	Nd	0.97	1.12	0.86	1.14	0.65	0.91	0.94	0.78	0.84	0.62	0.82	0.35	0.82
AD	Sm	0.45	0.53	0.44	0.52	0.32	0.47	0.46	0.36	0.42	0.30	0.45	0.24	0.40
AD	Eu	0.26	0.31	0.24	0.30	0.20	0.26	0.26	0.23	0.24	0.21	0.31	0.18	0.24
AD	Gd	0.69	0.81	0.71	0.80	0.50	0.75	0.73	0.54	0.65	0.48	0.75	0.43	0.64
PT	Tb	0.13	0.15	0.13	0.14	0.09	0.15	0.14	0.10	0.12	0.08	0.13	0.08	0.12
PT	Dy	0.87	1.06	0.93	0.92	0.65	1.03	0.94	0.68	0.83	0.54	0.88	0.53	0.84
PT	Ho	0.18	0.22	0.20	0.20	0.14	0.22	0.20	0.14	0.17	0.12	0.19	0.12	0.17
PT	Er	0.48	0.59	0.53	0.54	0.37	0.60	0.53	0.38	0.46	0.33	0.53	0.31	0.46
PT	Tm	0.07	0.08	0.08	0.08	0.05	0.09	0.08	0.06	0.07	0.05	0.07	0.04	0.07
PT	Yb	0.44	0.53	0.49	0.48	0.34	0.54	0.47	0.34	0.41	0.28	0.45	0.26	0.41
PT	Lu	0.06	0.08	0.07	0.07	0.05	0.08	0.07	0.05	0.06	0.04	0.06	0.04	0.06
PT	Hf	0.18	0.19	0.16	0.15	0.12	0.16	0.18	0.14	0.17	0.09	0.12	0.04	0.16
PT	Ta	0.01	0.02	0.01	<0.005	0.01	0.01	0.01	0.01	0.01	<0.005	<0.005	<0.015	0.01
AD	W	0.03	0.06	0.02	0.08	0.02	0.02	0.04	0.02	0.02	0.08	0.08	<0.005	0.03
AD	Pb	0.23	0.07	0.29	<0.1	0.16	7.43	0.06	0.14	4.03	<0.1	<0.1	<0.1	65.00
PT	Th	0.03	0.01	0.01	0.00	0.01	0.00	0.01	0.01	0.01	<0.005	<0.005	<0.005	0.01
PT	U	0.01	0.00	0.01	0.01	0.01	0.00	0.01	0.01	0.01	0.01	0.01	0.01	0.01
AD	Sn	0.12		0.13	0.13	0.01	0.84	0.13			0.10	0.09	0.11	5.42

Table 7. continued

	Method[2]	Lithology[1]:	MG	MG	MG	MG	MG	MG	MG	MG	MG	MG	MG	MG	MG
		Sample	OM12_Gid_O58	OM12_Gid_O59	OM12_Gid_O49	OM12_Gid_O43	OM12_Gid_O47	OM12_Gid_O42	OM12_Gid_Hy023	OM12_Gid_Hy058_5	OM12_Gid_Hy059	OM12_Gid_Hy059_5	OM12_Gid_Hy062	OM12_Gid_Hy068	OM12_Gid_Hy077
Major Elements [wt%]															
SiO2calc			49.35	49.03	49.80	48.77	48.07	48.25	48.92	48.60	48.61	48.80	46.94	50.97	47.59
Al2O3			17.73	18.13	19.31	20.58	18.71	17.89	18.25	16.80	21.16	17.71	18.71	17.23	17.02
FeO			4.17	4.60	3.66	3.07	5.22	4.36	3.97	4.35	3.71	5.38	4.26	3.55	5.27
MnO			0.08	0.09	0.08	0.07	0.10	0.09	0.08	0.09	0.07	0.06	0.09	0.08	0.10
MgO			8.73	8.93	7.45	7.72	10.88	9.99	10.36	11.25	9.10	11.68	10.99	9.34	13.13
CaO			17.74	16.51	17.78	18.40	15.51	18.06	17.01	17.73	15.68	15.09	17.72	17.33	15.92
Na2O			1.67	2.07	1.64	1.18	1.26	1.07	1.18	0.93	1.50	1.02	1.07	1.27	0.77
K2O			0.16	0.02	0.00	0.00	0.00	0.00	0.00	0.00	0.00	0.00	0.00	0.00	0.00
TiO2			0.38	0.61	0.29	0.21	0.25	0.30	0.21	0.25	0.16	0.26	0.22	0.23	0.20
P2O5			0.00	0.00	0.00	0.00	0.00	0.00	0.00	0.00	0.00	0.00	0.00	0.00	0.00
Total			100.00	100.00	100.00	100.00	100.00	100.00	100.00	100.00	100.00	100.00	100.00	100.00	100.00
			70.70												
Trace elements [ppm]															
Li	AD		0.77	0.71	0.78	0.58	0.60	<0.5	0.77	<0.5	<0.5	<0.5	0.63	<0.5	0.78
Sc	AD		59.52	53.52	56.78	44.30	43.60	58.34	40.73	52.15	31.28	57.81	49.13	50.45	42.06
V	AD		209.42	208.41	156.59	122.11	122.46	155.46	122.10	143.08	88.59	144.71	136.33	142.18	119.70
Cr	AD		298.53	377.44	683.37	541.40	541.71	425.71	793.27	515.38	339.33	348.29	562.58	596.20	888.28
Co	AD		25.81	29.87	23.53	20.35	41.83	28.90	30.78	33.44	33.93	46.19	36.12	27.54	49.18
Ni	AD		70.90	102.89	53.64	100.87	133.78	89.38	164.43	142.36	138.31	174.41	191.42	144.67	297.08
Cu	AD		6.07	26.18	6.66	139.08	26.58	52.43	176.43	65.50	101.44	4.34	151.91	164.61	167.15
Zn	AD		11.98	19.92	16.75	13.51	21.67	17.26	23.49	19.78	17.70	8.57	23.34	15.92	25.78
Ga	AD		11.06	10.30	12.30	11.51	10.63	10.62	9.13	9.68	11.76	11.22	10.98	10.01	9.74
Rb	AD		0.62	0.28	<0.2	<0.2	<0.2	<0.2	<0.2	<0.2	<0.2	<0.2	<0.2	<0.2	<0.2
Sr	AD		209.55	243.21	191.30	156.55	174.37	140.03	197.69	120.13	186.41	172.60	144.77	145.75	103.33
Y	PT		6.71	8.71	5.74	4.76	4.95	6.18	4.79	5.56	3.21	5.87	4.97	5.28	4.35
Zr	PT		6.37	12.58	2.39	1.20	3.01	2.60	1.63	1.87	0.19	2.84	1.26	1.51	0.87
Nb	PT		0.10	0.54	0.06	0.02	0.05	0.03	0.02	0.10	0.02	0.05	0.02	0.03	0.02
Mo	AD		0.07	0.08	0.06	0.09	0.06	0.04	0.08	0.06	0.08	0.07	0.07	0.07	0.08
Sb	AD		0.00	0.02	0.00	0.00	0.00	0.00	0.00	0.03	0.00	0.00	0.00	0.00	0.00
Cs	AD		0.02	<0.01	<0.01	<0.01	<0.01	<0.01	<0.01	<0.01	<0.01	<0.01	<0.01	<0.01	<0.01
Ba	AD		8.03	4.56	4.07	13.40	5.36	3.75	3.75	1.93	3.71	3.75	14.73	15.19	1.54
La	AD		0.44	0.73	0.29	0.22	0.30	0.26	0.22	0.24	0.22	0.27	0.22	0.22	0.20
Ce	AD		1.24	2.07	0.81	0.65	0.85	0.82	0.63	0.70	0.55	0.87	0.63	0.63	0.56
Pr	AD		0.23	0.36	0.16	0.13	0.16	0.17	0.13	0.14	0.10	0.17	0.13	0.13	0.11
Nd	AD		1.43	2.12	1.08	0.88	1.02	1.15	0.87	1.00	0.65	1.13	0.87	0.92	0.76
Sm	AD		0.61	0.85	0.51	0.42	0.46	0.55	0.42	0.50	0.30	0.52	0.43	0.46	0.37
Eu	AD		0.33	0.34	0.31	0.27	0.28	0.31	0.24	0.28	0.24	0.29	0.28	0.27	0.24
Gd	AD		0.94	1.22	0.81	0.65	0.70	0.85	0.66	0.78	0.47	0.81	0.69	0.73	0.60
Tb	PT		0.17	0.23	0.15	0.13	0.13	0.16	0.13	0.15	0.09	0.15	0.13	0.14	0.11
Dy	PT		1.21	1.55	1.06	0.85	0.89	1.13	0.86	1.04	0.59	1.05	0.90	0.96	0.79
Ho	PT		0.25	0.32	0.22	0.18	0.19	0.23	0.18	0.21	0.12	0.22	0.18	0.20	0.16
Er	PT		0.68	0.89	0.59	0.48	0.50	0.63	0.48	0.58	0.33	0.59	0.50	0.54	0.44
Tm	PT		0.10	0.13	0.08	0.07	0.07	0.09	0.07	0.08	0.05	0.08	0.07	0.06	0.06
Yb	PT		0.62	0.83	0.52	0.43	0.45	0.57	0.43	0.52	0.29	0.54	0.44	0.48	0.40
Lu	PT		0.09	0.13	0.08	0.06	0.07	0.08	0.07	0.08	0.04	0.08	0.07	0.07	0.06
Hf	PT		0.28	0.48	0.20	0.15	0.19	0.21	0.16	0.19	0.11	0.20	0.15	0.16	0.14
Ta	PT		0.02	0.04	0.05	0.01	0.01	0.01	0.01	0.08	0.01	0.01	0.01	0.01	0.01
W	AD		0.03	0.40	0.07	<0.03	0.08	0.06	<0.03	0.12	<0.03	<0.03	<0.03	<0.03	<0.03
Pb	AD		44.31	13.17	30.06	29.14	9.67	50.04	8.47	2.21	4.29	27.47	15.54	5.37	5.80
Th	PT		0.02	0.07	0.01	0.01	0.01	0.01	0.01	0.01	0.01	0.01	0.01	0.01	0.01
U	PT		0.02	0.02	0.01	0.01	0.01	<0.005	0.01	0.01	<0.005	0.01	0.01	<0.005	<0.005
Sn	AD		5.43	1.80	18.38	0.57	3.21	0.37	1.03	26.34	4.39	1.95	2.57	0.78	2.94

[1] Lithology: PB = Pillow basalt; SD = Sheeted dike; VG = Varitextured gabbro; FG = Foliated gabbro; LG = Layered gabbro
[2] Method: AD = Acid Degestion (ICP-OES); PT = Powder Tablet (ICP-MS)

Table 7, continued

	Method[2]	MG OM12_Gid_Hy080	MG OM12_Gid_Hy080_5	MG OM12_Gid_Hy096	MG OM12_Gid_Hy102	MG OM12_Gid_Hy103	MG OM12_Gid_Hy108	MG OM12_Gid_037	MG OM12_Gid_033	MG OM12_Gid_034	MG OM12_Gid_032	MG OM12_Gid_030	MG OM12_Gid_031	MG OM12_Gid_028
Major Elements [wt%]														
SiO2calc		49.17	48.46	48.91	47.80	49.18	49.58	48.21	48.02	46.95	47.62	47.53	49.20	47.90
Al2O3		14.56	17.04	16.91	22.00	18.57	18.61	21.28	17.47	19.11	18.73	19.74	15.76	18.43
FeO		4.94	4.45	3.94	3.41	3.85	3.82	3.75	4.10	5.62	4.30	4.45	5.17	4.43
MnO		0.10	0.09	0.08	0.06	0.08	0.08	0.07	0.07	0.10	0.09	0.09	0.11	0.09
MgO		12.85	11.03	12.35	8.58	9.79	10.26	9.27	11.42	11.55	10.01	10.51	11.48	11.38
CaO		17.20	17.41	17.05	16.92	17.23	16.42	15.74	17.52	15.48	18.30	16.31	16.88	16.38
Na2O		0.91	1.19	0.55	1.07	1.10	1.05	1.51	1.17	1.01	0.67	1.18	1.12	1.15
K2O		0.00	0.00	0.00	0.00	0.00	0.00	0.00	0.00	0.00	0.00	0.00	0.00	0.00
TiO2		0.26	0.33	0.21	0.16	0.18	0.18	0.17	0.24	0.18	0.27	0.19	0.29	0.25
P2O5		0.00	0.00	0.00	0.00	0.00	0.00	0.00	0.00	0.00	0.00	0.00	0.00	0.00
Total		100.00	100.00	100.00	100.00	100.00	100.00	100.00	100.00	100.00	100.00	100.00	100.00	100.00
Trace elements [ppm]														
Li	AD	1.02	0.76	0.57	<0.5	0.77	0.56	<0.5	<0.5	<0.5	<0.5	<0.5	<0.5	<0.5
Sc	AD	56.17	50.59	43.86	30.19	34.92	38.80	30.99	41.82	30.11	44.50	32.52	53.65	44.58
V	AD	154.23	154.10	128.66	84.01	101.94	111.02	86.80	133.45	90.08	148.92	96.96	158.19	134.30
Cr	AD	870.89	798.40	793.41	434.00	443.55	727.24	339.55	503.93	657.36	495.39	718.64	703.55	632.90
Co	AD	37.75	38.78	37.25	29.08	30.98	34.98	33.94	29.64	44.12	30.23	35.46	36.57	38.92
Ni	AD	186.84	185.17	221.29	143.45	159.61	174.36	136.11	194.46	218.46	150.22	184.77	139.38	160.33
Cu	AD	220.27	408.09	17.18	126.38	131.03	120.62	102.07	50.43	108.01	40.23	101.08	99.88	30.23
Zn	AD	22.06	22.25	17.98	15.36	23.48	16.79	17.76	14.05	25.62	17.65	18.22	22.56	18.06
Ga	AD	8.21	10.27	9.88	11.71	10.29	10.22	11.74	9.77	10.30	11.73	10.70	9.40	9.58
Rb	AD	<0.2	<0.2	<0.2	<0.2	<0.2	<0.2	<0.2	<0.2	<0.2	<0.2	<0.2	<0.2	<0.2
Sr	AD	115.48	137.77	156.48	160.95	128.48	140.99	186.93	178.99	158.71	230.01	205.24	119.73	233.81
Y	PT	5.83	7.44	4.41	3.13	3.79	3.89	3.19	5.06	3.43	5.65	3.56	6.36	5.02
Zr	PT	2.26	5.61	1.21	0.28	0.76	0.75	0.37	1.67	0.21	2.12	0.67	2.08	2.05
Nb	AD	0.04	0.22	0.03	0.05	0.20	0.03	0.04	0.03	0.02	0.03	0.09	0.04	0.04
Mo	AD	0.07	0.08	0.07	0.06	0.06	0.06	0.07	0.08	0.10	0.06	0.08	0.00	0.06
Sb	AD	0.00	0.00	0.00	0.00	0.04	0.00	0.00	0.00	0.00	0.03	0.00	0.00	0.00
Cs	AD	<0.01	<0.01	<0.01	<0.01	<0.01	<0.01	<0.01	<0.01	<0.01	<0.01	<0.01	<0.01	<0.01
Ba	AD	42.11	28.14	2.50	2.21	10.02	2.68	3.82	1.41	1.68	1.51	10.04	2.02	1.34
La	AD	0.25	0.53	<0.2	0.23	0.23	0.20	0.23	0.25	<0.2	0.22	0.29	0.21	0.20
Ce	AD	0.73	1.54	0.52	0.55	0.60	0.53	0.57	0.74	0.51	0.66	0.74	0.70	0.63
Pr	AD	0.15	0.28	0.11	0.10	0.11	0.10	0.10	0.15	0.10	0.14	0.13	0.15	0.13
Nd	AD	1.02	1.66	0.76	0.66	0.74	0.71	0.67	1.01	0.66	0.99	0.79	1.07	0.92
Sm	AD	0.51	0.68	0.38	0.30	0.35	0.34	0.30	0.47	0.31	0.49	0.34	0.55	0.45
Eu	AD	0.28	0.34	0.21	0.23	0.24	0.22	0.24	0.27	0.23	0.29	0.25	0.30	0.23
Gd	AD	0.81	1.02	0.60	0.46	0.55	0.54	0.45	0.72	0.47	0.79	0.52	0.86	0.71
Tb	PT	0.15	0.19	0.12	0.08	0.10	0.10	0.09	0.13	0.09	0.15	0.10	0.17	0.13
Dy	PT	1.06	1.28	0.81	0.58	0.69	0.70	0.58	0.92	0.62	1.04	0.67	1.16	0.90
Ho	PT	0.22	0.27	0.17	0.12	0.15	0.14	0.12	0.19	0.13	0.22	0.14	0.24	0.19
Er	PT	0.60	0.73	0.45	0.32	0.39	0.39	0.33	0.52	0.35	0.58	0.37	0.65	0.50
Tm	PT	0.08	0.11	0.06	0.05	0.05	0.06	0.05	0.07	0.05	0.08	0.05	0.09	0.07
Yb	PT	0.53	0.67	0.40	0.29	0.35	0.35	0.29	0.47	0.31	0.51	0.34	0.58	0.45
Lu	PT	0.08	0.10	0.06	0.04	0.05	0.05	0.04	0.07	0.05	0.08	0.05	0.09	0.07
Hf	PT	0.19	0.27	0.15	0.11	0.19	0.12	0.11	0.16	0.11	0.18	0.13	0.20	0.17
Ta	PT	0.02	0.02	0.01	0.04	0.20	0.02	0.02	0.01	0.01	0.02	0.05	0.01	0.01
W	AD	0.03	<0.03	<0.03	0.07	0.33	0.04	0.03	<0.03	<0.03	0.04	0.05	<0.03	<0.03
Pb	AD	5.81	16.16	34.64	1.83	3.01	1.84	5.84	24.06	31.85	11.22	19.43	12.72	11.68
Th	PT	0.01	0.03	0.01	0.01	0.01	<0.005	0.01	0.01	<0.005	0.01	0.01	<0.005	0.01
U	PT	0.01	0.01	0.01	0.01	0.02	<0.005	0.01	0.01	<0.005	0.01	0.01	<0.005	0.01
Sn	AD	1.10	0.75	3.69	12.65	128.71	8.02	3.72	2.73	1.15	4.88	20.22	0.77	1.57

Table 7. continued

Lithology[1]:		MG	MG	MG
Sample		OM12_Gid_029	OM12_Gid_202	OM12_Gid_211
Major Elements [wt%]				
	SiO2calc	48.28	47.62	48.86
	Al2O3	17.15	17.27	17.70
	FeO	4.87	4.59	5.42
	MnO	0.10	0.09	0.11
	MgO	11.58	12.81	11.29
	CaO	16.89	16.55	14.37
	Na2O	0.90	0.80	1.99
	K2O	0.00	0.00	0.00
	TiO2	0.24	0.28	0.26
	P2O5	0.00	0.00	0.00
	Total	100.00	100.00	100.00
Method[2]	**Trace elements [ppm]**			
AD	Li	<0.5	<0.5	0.56
AD	Sc	44.22	50.64	45.25
AD	V	129.72	157.26	157.47
AD	Cr	896.06	735.33	485.06
AD	Co	37.37	43.62	40.53
AD	Ni	202.97	202.08	138.51
AD	Cu	158.77	31.42	3.46
AD	Zn	20.35	18.53	19.08
AD	Ga	9.47	10.00	9.38
AD	Rb	<0.2	<0.2	<0.2
AD	Sr	126.15	151.93	243.93
PT	Y	4.94	5.71	5.83
PT	Zr	1.59	2.38	0.28
PT	Nb	0.03	0.03	0.02
AD	Mo	0.10	0.07	0.06
AD	Sb	0.00	0.00	0.05
AD	Cs	<0.01	<0.01	<0.01
AD	Ba	4.71	2.32	1.67
AD	La	0.20	0.22	<0.2
AD	Ce	0.63	0.68	<0.5
AD	Pr	0.13	0.15	0.11
AD	Nd	0.90	1.01	0.83
AD	Sm	0.44	0.50	0.47
AD	Eu	0.26	0.26	0.21
AD	Gd	0.69	0.78	0.80
PT	Tb	0.13	0.15	0.15
PT	Dy	0.91	1.01	1.06
PT	Ho	0.19	0.21	0.22

Table 8a. Results for strontium isotopy

Sample	Litho.[1]	Depth[2]	87Sr/86Sr [mbc]	2 σ [abs]	σ [%]	2 σ [%]	σ [ppm]	2 σ [abs ppm]	87Sr/86Srini[3]	W/R[4]
OM10_Gid_B01a	PB	6600	0.70594	0.00001	0.00074	0.00147	7.37	14.73	0.70593	21.1
OM10_Gid_B01b	PB	6600	0.70565	0.00001	0.00067	0.00133	6.66	13.32	0.70535	12.0
OM10_Gid_B04a	PB	6600	0.70638	0.00001	0.00125	0.00250	12.51	25.02	0.70632	33.3
OM10_Gid_B04c	PB	6600	0.70637	0.00001	0.00125	0.00250	12.51	25.02	0.70630	32.4
OM10_Gid_B04e	PB	6600	0.70650	0.00001	0.00084	0.00167	8.35	16.70	0.70642	38.0
OM10_Gid_B05b	PB	6600	0.70550	0.00001	0.00066	0.00132	6.59	13.18	0.70546	13.4
OM10_Gid_A02	USD	6449	0.70570	0.00001	0.00073	0.00146	7.28	14.56	0.70563	15.6
OM10_Gid_A03	USD	6288	0.70554	0.00001	0.00125	0.00250	12.51	25.02	0.70551	14.0
OM10_Gid_A04	USD	6106	0.70543	0.00001	0.00071	0.00142	7.08	14.17	0.70542	12.8
OM10_Gid_A05a	USD	6001	0.70543	0.00001	0.00071	0.00143	7.13	14.26	0.70541	12.7
OM10_Gid_A05b	USD	6001	0.70549	0.00002	0.00125	0.00250	12.51	25.02	0.70547	13.5
OM10_Gid_A06	USD	5891	0.70516	0.00001	0.00066	0.00132	6.58	13.15	0.70515	10.0
OM10_Gid_B00	Sdext	5800	0.70574	0.00001	0.00064	0.00128	6.38	12.75	0.70571	16.9
OM10_Gid_B02	Sdext	5800	0.70548	0.00001	0.00079	0.00159	7.94	15.88	0.70545	13.2
OM10_Gid_B03	Sdext	5800	0.70535	0.00002	0.00125	0.00250	12.51	25.02	0.70533	11.8
OM10_Gid_B06	Sdext	5800	0.70558	0.00001	0.00070	0.00140	7.02	14.03	0.70558	14.9
OM10_Gid_A10	LSD	5321	0.70518	0.00001	0.00125	0.00250	12.51	25.02	0.70517	10.2
OM10_Gid_A11_3	LSD	5094	0.70452	0.00001	0.00081	0.00161	8.07	16.14	0.70448	5.2
OM10_Gid_A11_2	LSD	5062	0.70532	0.00002	0.00107	0.00215	10.74	21.48	0.70531	11.6
OM10_Gid_A11_2	LSD	5062	0.70531	0.00001	0.00125	0.00250	12.51	25.02	0.70530	11.5
OM10_Gid_A12_3	BDVG	4780	0.70486	0.00002	0.00125	0.00250	12.51	25.02	0.70485	7.5
OM10_Gid_A12_2c	BDVG	4612	0.70383	0.00002	0.00119	0.00239	11.95	23.89	0.70382	2.3
OM10_Gid_A12_1b	BDVG	4532	0.70388	0.00002	0.00115	0.00230	11.49	22.97	0.70387	2.5
OM10_Gid_A11	VG	4954	0.70518	0.00001	0.00080	0.00160	8.00	16.01	0.70517	10.1
OM10_Gid_A12_2a	VG	4612	0.70443	0.00001	0.00065	0.00130	6.48	12.95	0.70442	4.9
OM10_Gid_A12_2d	VG	4612	0.70545	0.00001	0.00077	0.00154	7.70	15.41	0.70543	13.0
OM10_Gid_A13	VG	4602	0.70384	0.00001	0.00125	0.00250	12.51	25.02	0.70381	2.3
OM10_Gid_A12_1a	VG	4532	0.70376	0.00001	0.00063	0.00127	6.34	12.68	0.70375	2.0
OM10_Gid_A12_1c	VG	4532	0.70427	0.00001	0.00073	0.00146	7.31	14.62	0.70427	4.1
OM10_Gid_A14a	VG	4389	0.70567	0.00001	0.00060	0.00119	5.95	11.90	0.70566	16.1
OM10_Gid_A14b	VG	4389	0.70373	0.00001	0.00125	0.00250	12.51	25.02	0.70371	1.9
OM10_Gid_A15	VG	4129	0.70355	0.00001	0.00125	0.00250	12.51	25.02	0.70350	1.2
OM10_Gid_A16	UFG	3924	0.70323	0.00001	0.00073	0.00145	7.25	14.50	0.70323	0.5
OM10_Gid_A17	UFG	3734	0.70373	0.00001	0.00125	0.00250	12.51	25.02	0.70372	2.0
OM10_Gid_A17_2	UFG	3577	0.70465	0.00001	0.00084	0.00167	8.37	16.75	0.70464	6.2
OM10_Gid_A17_3a	UFG	3574	0.70411	0.00001	0.00125	0.00250	12.51	25.02	0.70411	3.4
OM10_Gid_A17_1	UFG	3550	0.70339	0.00001	0.00067	0.00134	6.68	13.36	0.70339	0.9
OM10_Gid_A18	LFG	3423	0.70337	0.00001	0.00125	0.00250	12.51	25.02	0.70336	0.8
OM10_Gid_A18_1	LFG	3230	0.70351	0.00001	0.00070	0.00141	7.04	14.07	0.70351	1.3
OM10_Gid_A18_2a	LFG	2900	0.70329	0.00001	0.00070	0.00139	6.97	13.93	0.70329	0.6
OM10_Gid_A19	LFG	2700	0.70310	0.00001	0.00125	0.00250	12.51	25.02	0.70310	0.1
OM10_Gid_A20	LG	2394	0.70350	0.00001	0.00065	0.00131	6.54	13.08	0.70349	1.2
OM12_Gid_055	LG	2259	0.70333	0.00002	0.00113	0.00226	11.31	22.62	0.70332	0.7

[1] Lithology: USD = Upper sheeted dikes; SDext = samples out of Wadi Gideah; LSD = Lower sheeted dikes; VG = Varitextuted gabbro; BDVG = Basaltic dike in varitextured gabbro; UFG = Upper foliated gabbro; LFG = Lower foliated gabbro; MG = Metagabbro; LG = Layered gabbro

[2] Depth: Calculated height avove MOHO

[3] 87Sr/86Srini was calculated following Bosch (2004)

[4] W/R ratios were calculated following McCulloch et al. (1980), using 87Sr/86Srini and CSr Seawater given by these authors, 87Sr/86SrSeawater given by Burke et al. (1982), and CSr MORB given by Höfig et al. (2014)

Table 8a. Continued

Sample	Litho.[1]	Depth[2]	87Sr/86Sr [mbc]	2 σ [abs]	σ [%]	2 σ [%]	σ [ppm]	2 σ [abs ppm]	87Sr/86Srini[3]	W/R[4]
OM10_Gid_A21	LG	2124	0.70348	0.00002	0.00125	0.00250	12.51	25.02	0.70347	1.1
OM11_Gid_A21A	LG	2124	0.70319	0.00002	0.00125	0.00250	12.51	25.02	0.70319	0.4
OM12_Gid_054	LG	2040	0.70317	0.00002	0.00113	0.00227	11.35	22.70	0.70317	0.3
OM12_Gid_053	LG	2004	0.70318	0.00001	0.00088	0.00176	8.81	17.62	0.70318	0.4
OM10_Gid_A22	LG	1936	0.70333	0.00001	0.00125	0.00250	12.51	25.02	0.70333	0.7
OM11_Gid_A22	LG	1936	0.70317	0.00002	0.00125	0.00250	12.51	25.02	0.70317	0.3
OM12_Gid_048	LG	1792	0.70319	0.00002	0.00128	0.00256	12.81	25.63	0.70319	0.4
OM12_Gid_046	LG	1727	0.70357	0.00002	0.00107	0.00214	10.68	21.36	0.70357	1.5
OM10_Gid_A23	LG	1659	0.70336	0.00001	0.00065	0.00131	6.54	13.08	0.70336	0.8
OM10_Gid_A23	LG	1659	0.70331	0.00002	0.00125	0.00250	12.51	25.02	0.70331	0.7
OM12_Gid_045	LG	1630	0.70331	0.00002	0.00132	0.00265	13.25	26.49	0.70331	0.7
OM12_Gid_044	LG	1626	0.70317	0.00002	0.00119	0.00238	11.92	23.84	0.70316	0.3
OM12_Gid_040	LG	1508	0.70345	0.00002	0.00108	0.00217	10.84	21.68	0.70345	1.1
OM10_Gid_A24	LG	1431	0.70314	0.00002	0.00125	0.00250	12.51	25.02	0.70313	0.2
OM12_Gid_039	LG	1289	0.70303	0.00002	0.00112	0.00224	11.19	22.38	0.70303	0.0
OM12_Gid_026	LG	1231	0.70328	0.00001	0.00106	0.00212	10.60	21.20	0.70327	0.6
OM10_Gid_A25	LG	1210	0.70313	0.00001	0.00125	0.00250	12.51	25.02	0.70312	0.2
OM12_Gid_025	LG	1197	0.70335	0.00002	0.00130	0.00261	13.03	26.05	0.70335	0.8
OM12_Gid_Hy077	LG	1190	0.70319	0.00001	0.00070	0.00139	6.97	13.94	0.70318	0.4
OM12_Gid_Hy108	LG	1190	0.70350	0.00001	0.00063	0.00127	6.33	12.65	0.70349	1.2
OM12_Gid_038	LG	1121	0.70302	0.00002	0.00109	0.00218	10.91	21.82	0.70302	0.0
OM10_Gid_A26	LG	1079	0.70312	0.00001	0.00125	0.00250	12.51	25.02	0.70312	0.2
OM12_Gid_035	LG	991	0.70334	0.00002	0.00125	0.00250	12.50	25.00	0.70334	0.8
OM11_Gid_A26	LG	930	0.70323	0.00001	0.00125	0.00250	12.51	25.02	0.70323	0.5
OM11_Gid_A27	LG	816	0.70312	0.00001	0.00125	0.00250	12.51	25.02	0.70312	0.2
OM10_Gid_A27	LG	804	0.70335	0.00002	0.00125	0.00250	12.51	25.02	0.70335	0.8
OM11_Gid_A27_1	LG	714	0.70319	0.00002	0.00125	0.00250	12.51	25.02	0.70319	0.4
OM10_Gid_A28	LG	696	0.70357	0.00001	0.00125	0.00250	12.51	25.02	0.70357	1.4
OM11_Gid_A28	LG	625	0.70302	0.00001	0.00125	0.00250	12.51	25.02	0.70302	0.0
OM12_Gid_201	LG	598	0.70319	0.00002	0.00112	0.00224	11.21	22.41	0.70318	0.4
OM10_Gid_A29	LG	545	0.70342	0.00001	0.00080	0.00161	8.03	16.06	0.70342	1.0
OM11_Gid_A29	LG	517	0.70310	0.00002	0.00125	0.00250	12.51	25.02		
OM11_Gid_A29_2	LG	401	0.70308	0.00001	0.00125	0.00250	12.51	25.02	0.70308	0.1
OM10_Gid_A30	LG	257	0.70328	0.00002	0.00125	0.00250	12.51	25.02	0.70327	0.6
OM10_Gid_A31	LG	123	0.70319	0.00002	0.00125	0.00250	12.51	25.02	0.70318	0.4
OM10_Gid_A32	LG	49	0.70321	0.00001	0.00125	0.00250	12.51	25.02	0.70321	0.4
OM12_Gid_059	MG	2610	0.70474	0.00002	0.00141	0.00282	14.12	28.25	0.70473	6.7
OM12_Gid_Hy023	MG	1190	0.70456	0.00001	0.00075	0.00149	7.45	14.90	0.70456	5.6
OM12_Gid_Hy059.5	MG	1190	0.70430	0.00002	0.00126	0.00251	12.56	25.13	0.70430	4.3
OM12_Gid_Hy062	MG	1190	0.70351	0.00001	0.00080	0.00159	7.96	15.92	0.70350	1.2
OM12_Gid_Hy068	MG	1190	0.70380	0.00001	0.00081	0.00162	8.10	16.20	0.70379	2.2
OM12_Gid_Hy080	LG	1190	0.70398	0.00002	0.00125	0.00250	12.51	25.02	0.70397	2.9
OM12_Gid_Hy096	MG	1190	0.70400	0.00001	0.00074	0.00148	7.39	14.77	0.70399	2.9
OM11_Gid_A28B	MG	703	0.70460	0.00001	0.00125	0.00250	12.51	25.02	0.70459	5.9

[1] Lithology: USD = Upper sheeted dikes; SDext = samples out of Wadi Gideah; LSD = Lower sheeted dikes; VG = Varitextuted gabbro; BDVG = Basaltic dike in varitextured gabbro; UFG = Upper foliated gabbro; LFG = Lower foliated gabbro; MG = Metagabbro; LG = Layered gabbro

[2] Depth: Calculated height avove MOHO

[3] 87Sr/86Srini was calculated following Bosch (2004)

[4] W/R ratios were calculated following McCulloch et al. (1980), using 87Sr/86Srini and CSr Seawater given by these authors, 87Sr/86SrSeawater given by Burke et al. (1982), and CSr MORB given by Höfig et al. (2014)

Table 8b. Results for neodymium isotopy

Sample ID:	Lith.[1]	Depth[2]	143Nd/144Nd	143Nd/144Nd σ [abs]	143Nd/144Nd 2σ [abs]	εNd	εNd σ [abs]	εNd 2σ [abs]	εNd σ [%]	εNd 2σ [%]	εNd σ [ppm]	εNd 2σ [ppm]	143Nd/144Ndini[3]	εNdini
OM10_Gid_B01a	PB	6600	0.5130	0.0000	0.0000	8.05	0.00	0.00	0.00	0.00	22.85	45.69	0.51	8.02
OM10_Gid_B01b	PB	6600	0.5130	0.0000	0.0000	7.98	0.00	0.00	0.00	0.00	23.15	46.29	0.51	7.93
OM10_Gid_B04e	PB	6600	0.5130	0.0000	0.0000	8.04	0.00	0.00	0.00	0.00	23.28	46.56	0.51	7.92
OM10_Gid_B05b	PB	6600	0.5130	0.0000	0.0000	8.15	0.00	0.00	0.00	0.00	23.46	46.92	0.51	8.04
OM10_Gid_A02	USD	6449	0.5130	0.0000	0.0000	8.10	0.00	0.00	0.00	0.00	23.22	46.43	0.51	8.01
OM10_Gid_A04	USD	6106	0.5130	0.0000	0.0000	8.05	0.00	0.00	0.00	0.00	23.55	47.09	0.51	7.97
OM10_Gid_A05a	USD	6001	0.5130	0.0000	0.0000	8.18	0.00	0.00	0.00	0.00	23.21	46.42	0.51	8.15
OM10_Gid_A06	USD	5891	0.5130	0.0000	0.0000	8.08	0.00	0.00	0.00	0.00	23.28	46.56	0.51	7.87
OM10_Gid_B00	Sdext	5800	0.5131	0.0000	0.0000	8.35	0.00	0.00	0.00	0.00	23.24	46.48	0.51	10.61
OM10_Gid_B02	Sdext	5800	0.5130	0.0000	0.0000	8.16	0.00	0.00	0.00	0.00	23.53	47.07	0.51	10.42
OM10_Gid_B06	Sdext	5800	0.5131	0.0000	0.0000	8.34	0.00	0.00	0.00	0.00	22.88	45.76	0.51	10.59
OM10_Gid_A11_2	LSD	5062	0.5130	0.0002	0.0004	7.77	0.00	0.01	0.04	0.08	375.87	751.74	0.51	7.49
OM10_Gid_A11_3	LSD	5094	0.5130	0.0000	0.0000	8.12	0.00	0.00	0.00	0.00	23.30	46.61	0.51	7.92
OM10_Gid_A12_1b	BDVG	4532	0.5130	0.0002	0.0004	7.88	0.00	0.01	0.04	0.08	375.58	751.16	0.51	7.67
OM10_Gid_A12_2c	BDVG	4612	0.5130	0.0002	0.0004	7.08	0.00	0.01	0.04	0.08	375.75	751.49	0.51	7.08
OM10_Gid_A11	VG	4954	0.5131	0.0000	0.0000	8.36	0.00	0.00	0.00	0.00	23.07	46.14	0.51	8.08
OM10_Gid_A12_2a	VG	4612	0.5130	0.0000	0.0000	7.88	0.00	0.00	0.00	0.00	22.78	45.56	0.51	8.05
OM10_Gid_A12_1a	VG	4532	0.5131	0.0000	0.0000	8.40	0.00	0.00	0.00	0.00	26.01	52.01	0.51	8.15
OM10_Gid_A12_1c	VG	4532	0.5130	0.0000	0.0000	8.13	0.00	0.00	0.00	0.01	26.12	52.24	0.51	7.88
OM10_Gid_A12_2d	VG	4612	0.5130	0.0000	0.0000	8.08	0.00	0.00	0.00	0.01	22.98	45.96	0.51	8.00
OM10_Gid_A13	VG	4602	0.5131	0.0000	0.0000	8.52	0.00	0.00	0.00	0.00	31.60	63.21	0.51	7.98
OM10_Gid_A14a	VG	4389	0.5131	0.0000	0.0000	8.32	0.00	0.00	0.00	0.01	27.44	54.88	0.51	7.82
OM10_Gid_A16	UFG	3924	0.5131	0.0000	0.0000	8.79	0.00	0.00	0.00	0.01	38.32	76.64	0.51	7.73
OM10_Gid_A17	UFG	3734	0.5131	0.0000	0.0000	8.38	0.00	0.00	0.00	0.00	31.29	62.58	0.51	7.69
OM10_Gid_A17_1	UFG	3550	0.5131	0.0000	0.0000	8.27	0.00	0.00	0.00	0.01	27.04	54.07	0.51	7.73
OM10_Gid_A17_2	UFG	3577	0.5131	0.0000	0.0000	8.64	0.00	0.00	0.00	0.01	26.59	53.17	0.51	7.90
OM10_Gid_A18	LFG	3423	0.5131	0.0000	0.0000	9.19	0.00	0.00	0.00	0.00	31.80	63.61	0.51	8.15
OM10_Gid_A18_1	LFG	3230	0.5132	0.0001	0.0001	10.42	0.00	0.00	0.01	0.03	144.95	289.90	0.51	9.39
OM10_Gid_A18_2a	LFG	2900	0.5131	0.0000	0.0000	8.69	0.00	0.00	0.00	0.01	29.54	59.08	0.51	7.48
OM10_Gid_A19	LFG	2700	0.5131	0.0000	0.0000	9.12	0.00	0.00	0.00	0.00	31.74	63.49	0.51	7.96

[1] Lithology: USD = Upper sheeted dikes; LSD = Lower sheeted dikes; SDext = samples out of Wadi Gideah; VG = Varitextured gabbro; UFG = Upper foliated gabbro; BDVG = Basaltic dike in varitextured gabbro; UFG = Upper foliated gabbro; LFG = Lower foliated gabbro ; MG = Metagabbro; LG = Layered gabbro

[2] Depth: Calculated height avove MOHO

[3] ^{143}Nd/^{144}Ndini was calculated following Bosch (2004)

Table 8b. continued

Sample ID:	Lith.[1]	Depth[2]	143Nd/144Nd	143Nd/144Nd σ [abs]	143Nd/144Nd 2σ [abs]	εNd	εNd σ [abs]	εNd 2σ [abs]	εNd σ [%]	εNd 2σ [%]	εNd σ [ppm]	εNd 2σ [ppm]	143Nd/144Ndini[3]	εNdini
OM10_Gid_A20	LG	2394	0.5130	0.0000	0.0000	8.04	0.00	0.00			35.73	71.47	0.51	7.19
OM10_Gid_A22	LG	1936	0.5131	0.0000	0.0000	9.33	0.00	0.00			30.76	61.52	0.51	8.22
OM10_Gid_A23	LG	1659	0.5131	0.0000	0.0000	8.28	0.00	0.00			36.31	72.62	0.51	7.15
OM10_Gid_A24	LG	1431	0.5130	0.0000	0.0000	8.17	0.00	0.00	0.00	0.01	43.46	86.92	0.51	6.83
OM10_Gid_A26	LG	1079	0.5131	0.0000	0.0000	9.71	0.00	0.00			31.42	62.83	0.51	8.51
OM10_Gid_A28	LG	696	0.5131	0.0000	0.0000	9.61	0.00	0.00			31.19	62.39	0.51	8.47
OM10_Gid_A29	LG	545	0.5131	0.0000	0.0000	8.51	0.00	0.00			32.16	64.31	0.51	7.10
OM10_Gid_A32	LG	49	0.5132	0.0000	0.0000	10.69	0.00	0.00	0.00	0.01	31.83	63.66	0.51	7.83
OM12_Gid_025	LG	1197	0.5131	0.0002	0.0004	9.05	0.00	0.01	0.04	0.08	376.47	752.94	0.51	7.92
OM12_Gid_026	LG	1231	0.5131	0.0000	0.0000	8.36	0.00	0.00	0.00	0.01	44.34	88.69	0.51	7.09
OM12_Gid_035	LG	991	0.5131	0.0002	0.0004	9.19	0.00	0.01	0.04	0.08	376.10	752.19	0.51	8.01
OM12_Gid_038	LG	1121	0.5131	0.0000	0.0000	8.26	0.00	0.00	0.00	0.01	47.87	95.74	0.51	6.99
OM12_Gid_039	LG	1289	0.5130	0.0002	0.0004	7.64	0.00	0.01	0.04	0.08	376.60	753.19	0.51	6.38
OM12_Gid_040	LG	1508	0.5130	0.0002	0.0004	7.13	0.00	0.01	0.04	0.08	380.50	761.00	0.51	5.83
OM12_Gid_044	LG	1626	0.5131	0.0002	0.0004	9.02	0.00	0.01	0.04	0.08	376.17	752.35	0.51	7.76
OM12_Gid_045	LG	1630	0.5131	0.0002	0.0004	9.13	0.00	0.01	0.04	0.08	375.77	751.55	0.51	7.74
OM12_Gid_046	LG	1727	0.5131	0.0002	0.0004	9.01	0.00	0.01	0.04	0.08	376.04	752.07	0.51	7.73
OM12_Gid_048	LG	1792	0.5130	0.0000	0.0000	7.90	0.00	0.00	0.00	0.01	44.90	89.80	0.51	6.94
OM12_Gid_053	LG	2004	0.5131	0.0000	0.0000	8.45	0.00	0.00	0.00	0.01	42.67	85.33	0.51	10.70
OM12_Gid_054	LG	2040	0.5130	0.0000	0.0000	8.00	0.00	0.00	0.00	0.01	49.22	98.44	0.51	10.25
OM12_Gid_055	LG	2259	0.5130	0.0000	0.0000	7.99	0.00	0.00	0.00	0.01	40.08	80.16	0.51	10.25
OM12_Gid_201	LG	598	0.5131	0.0002	0.0004	8.88	0.00	0.01	0.04	0.08	376.69	753.39	0.51	7.34
OM12_Gid_Hy080	LG	1190	0.5131	0.0002	0.0004	8.76	0.00	0.01	0.04	0.08	375.86	751.72	0.51	7.35
OM12_Gid_059	MG	2610	0.5130	0.0000	0.0000	7.88	0.00	0.00	0.00	0.01	41.54	83.08	0.51	7.17
OM12_Gid_Hy059.5	MG	1190	0.5130	0.0000	0.0000	8.08	0.00	0.00	0.00	0.01	43.98	87.95	0.51	6.92
OM12_Gid_Hy062	MG	1190	0.5131	0.0000	0.0000	8.49	0.00	0.00	0.00	0.01	32.86	65.73	0.51	7.10
OM12_Gid_Hy096	MG	1190	0.5131	0.0000	0.0000	8.79	0.00	0.00	0.00	0.01	29.80	59.59	0.51	7.39
OM12_Gid_Hy103	MG	1190	0.5131	0.0000	0.0000	8.41	0.00	0.00	0.00	0.01	31.21	62.43	0.51	7.19

1 Lithology: USD = Upper sheeted dikes; SDext = samples out of Wadi Gideah; LSD = Lower sheeted dikes; VG = Varitextuted gabbro; BDVG = Basaltic dike in varitextured gabbro; UFG = Upper foliated gabbro; LFG = Lower foliated gabbro ; MG = Metagabbro ; LG = Layered gabbro

2 Depth: Calculated height avove MOHO

3 143Nd/144Ndini was calculated following Bosch (2004)

Table 8c. Results for hafnium isotopy

Sample	Litho.[1]	Depth[2]	176Hf/177Hf	176Hf/177Hf σ [abs]	εHf	εHf σ [abs]	εHf 2σ [abs]	εHf σ [%]	εHf 2σ [%]	εHf σ [ppm]	εHf 2σ [ppm]
OM10_Gid_B01a	PB	6600	0.28	0.00	14.64	0.00	0.00	0.00	0.01	41.76	83.51
OM10_Gid_B01b	PB	6600	0.28	0.00	14.73	0.00	0.00	0.00	0.01	41.83	83.66
OM10_Gid_B04e	PB	6600	0.28	0.00	13.98	0.00	0.00	0.00	0.01	42.48	84.95
OM10_Gid_B05b	PB	6600	0.28	0.00	14.50	0.00	0.00	0.00	0.01	42.36	84.73
OM10_Gid_A02	USD	6449	0.28	0.00	17.09	0.00	0.00	0.00	0.01	48.06	96.12
OM10_Gid_A04	USD	6106	0.28	0.00	15.02	0.00	0.00	0.00	0.01	41.57	83.15
OM10_Gid_A05a	USD	6001	0.28	0.00	16.13	0.00	0.00	0.00	0.01	45.45	90.89
OM10_Gid_A06	USD	5891	0.28	0.00	14.95	0.00	0.00	0.00	0.01	42.73	85.46
OM10_Gid_B00	Sdext	5800	0.28	0.00	15.68	0.00	0.00	0.00	0.01	42.45	84.90
OM10_Gid_B02	Sdext	5800	0.28	0.00	14.91	0.00	0.00	0.00	0.01	42.68	85.36
OM10_Gid_B06	Sdext	5800	0.28	0.00	19.15	0.00	0.00	0.00	0.01	48.44	96.87
OM10_Gid_A11_3	LSD	5094	0.28	0.00	15.26	0.00	0.00	0.00	0.01	42.42	84.85
OM10_Gid_A11_2	LSD	5062	0.28	0.00	15.59	0.00	0.00	0.01	0.01	54.45	108.90
OM10_Gid_A12_2c	BDVG	4612	0.28	0.00	16.65	0.00	0.00	0.01	0.01	53.01	106.01
OM10_Gid_A12_1b	BDVG	4532	0.28	0.00	15.96	0.00	0.00	0.01	0.01	54.36	108.72
OM10_Gid_A11	VG	4954	0.28	0.00	15.37	0.00	0.00	0.00	0.01	46.91	93.82
OM10_Gid_A12_2a	VG	4612	0.28	0.00	18.81	0.00	0.00	0.00	0.01	42.46	84.93
OM10_Gid_A12_2d	VG	4612	0.28	0.00	15.80	0.00	0.00	0.00	0.01	41.41	82.81
OM10_Gid_A13	VG	4602	0.28	0.00	15.43	0.00	0.00	0.00	0.01	42.22	84.44
OM10_Gid_A12_1a	VG	4532	0.28	0.00	17.48	0.00	0.00	0.00	0.01	48.98	97.95
OM10_Gid_A12_1c	VG	4532	0.28	0.00	20.22	0.00	0.00	0.01	0.01	50.40	100.80
OM10_Gid_A14a	VG	4389	0.28	0.00	15.55	0.00	0.00	0.00	0.01	46.93	93.86
OM10_Gid_A16	UFG	3924	0.28	0.00	16.55	0.00	0.00	0.01	0.01	59.20	118.40
OM10_Gid_A17	UFG	3734	0.28	0.00	12.12	0.00	0.00	0.00	0.01	43.71	87.42
OM10_Gid_A17_2	UFG	3577	0.28	0.00	16.05	0.00	0.00	0.01	0.01	50.31	100.62
OM10_Gid_A17_1	UFG	3550	0.28	0.00	14.86	0.00	0.00	0.00	0.01	49.57	99.14
OM10_Gid_A18	LFG	3423	0.28	0.00	16.93	0.00	0.00	0.00	0.01	41.32	82.65
OM10_Gid_A18_1	LFG	3230	0.28	0.00	16.62	0.00	0.00	0.00	0.01	48.66	97.31
OM10_Gid_A18_2a	LFG	2900	0.28	0.00	16.61	0.00	0.00	0.01	0.01	62.10	124.21
OM10_Gid_A19	LFG	2700	0.28	0.00	16.30	0.00	0.00	0.00	0.01	46.00	91.99

[1] Lithology: USD = Upper sheeted dikes; SDext = samples out of Wadi Gideah; LSD = Lower sheeted dikes; VG = Varitextuted gabbro; BDVG = Basaltic dike in varitextured gabbro; UFG = Upper foliated gabbro; LFG = Lower foliated gabbro ; MG = Metagabbro; LG = Layered gabbro

[2] Depth: Calculated height avove MOHO

Table 8c. Continued

Sample	Litho.[1]	Depth[2]	176Hf/177Hf	176Hf/177Hf σ [abs]	εHf	εHf σ [abs]	εHf 2σ [abs]	εHf σ [%]	εHf 2σ [%]	εHf σ [ppm]	εHf 2σ [ppm]
OM10_Gid_A20	LG	2394	0.28	0.00	16.03	0.00	0.00	0.00	0.01	47.57	95.13
OM12_Gid_055	LG	2259	0.28	0.00	19.72	0.00	0.00	0.01	0.02	94.91	189.83
OM12_Gid_054	LG	2040	0.28	0.00	20.32	0.00	0.00	0.01	0.02	111.63	223.26
OM12_Gid_053	LG	2004	0.28	0.00	20.26	0.00	0.00	0.01	0.02	120.25	240.49
OM10_Gid_A22	LG	1936	0.28	0.00	16.28	0.00	0.00	0.00	0.01	46.00	91.99
OM12_Gid_048	LG	1792	0.28	0.00	20.52	0.00	0.00	0.01	0.02	93.46	186.91
OM12_Gid_046	LG	1727	0.28	0.00	16.02	0.00	0.00	0.01	0.02	93.26	186.53
OM12_Gid_045	LG	1630	0.28	0.00	11.02	0.00	0.00	0.01	0.02	75.86	151.72
OM12_Gid_044	LG	1626	0.28	0.00	16.65	0.00	0.00	0.01	0.02	90.07	180.14
OM12_Gid_040	LG	1508	0.28	0.00	17.04	0.00	0.00	0.01	0.02	84.90	169.81
OM10_Gid_A24	LG	1431	0.28	0.00	17.86	0.00	0.00	0.01	0.01	51.09	102.19
OM12_Gid_039	LG	1289	0.28	0.00	16.66	0.00	0.00	0.01	0.02	115.71	231.42
OM12_Gid_026	LG	1231	0.28	0.00	19.71	0.00	0.00	0.01	0.03	126.48	252.97
OM12_Gid_025	LG	1197	0.28	0.00	15.97	0.00	0.00	0.01	0.02	112.35	224.69
OM12_Gid_Hy077	LG	1190	0.28	0.00	17.85	0.00	0.00	0.01	0.01	61.58	123.16
OM12_Gid_Hy080	LG	1190	0.28	0.00	19.03	0.00	0.00	0.01	0.03	125.94	251.88
OM12_Gid_Hy108	LG	1190	0.28	0.00	16.22	0.00	0.00	0.01	0.01	68.51	137.02
OM12_Gid_038	LG	1121	0.28	0.00	20.07	0.00	0.01	0.01	0.03	132.39	264.78
OM10_Gid_A26	LG	1079	0.28	0.00	16.75	0.00	0.00	0.00	0.01	48.69	97.38
OM12_Gid_035	LG	991	0.28	0.00	15.89	0.00	0.00	0.01	0.02	89.55	179.09
OM10_Gid_A28	LG	696	0.28	0.00	16.51	0.00	0.00	0.01	0.01	50.47	100.95
OM12_Gid_201	LG	598	0.28	0.00	21.32	0.00	0.01	0.01	0.03	132.83	265.66
OM10_Gid_A29	LG	545	0.28	0.00	13.76	0.00	0.00	0.01	0.01	70.52	141.03
OM10_Gid_A32	LG	49	0.28	0.00	17.88	0.00	0.00	0.01	0.02	78.81	157.61
OM12_Gid_059	MG	2610	0.28	0.00	17.29	0.00	0.00	0.01	0.01	65.15	130.30
OM12_Gid_Hy023	MG	1190	0.28	0.00	15.23	0.00	0.00	0.01	0.01	61.61	123.22
OM12_Gid_Hy059.5	MG	1190	0.28	0.00	18.13	0.00	0.00	0.01	0.02	99.46	198.91
OM12_Gid_Hy062	MG	1190	0.28	0.00	17.66	0.00	0.00	0.01	0.02	79.81	159.62
OM12_Gid_Hy068	MG	1190	0.28	0.00	15.99	0.00	0.00	0.01	0.01	59.88	119.76
OM12_Gid_Hy096	MG	1190	0.28	0.00	16.42	0.00	0.00	0.01	0.01	65.19	130.37

[1] Lithology: USD = Upper sheeted dikes; SDext = samples out of Wadi Gideah; LSD = Lower sheeted dikes; VG = Varitextuted gabbro; BDVG = Basaltic dike in varitextured gabbro; UFG = Upper foliated gabbro; LFG = Lower foliated gabbro ; MG = Metagabbro; LG = Layered gabbro

[2] Depth: Calculated height avove MOHO

Table 9. Results for mineral major element composition of Wadi Gideah (wt%) obtained by EPMA with StdDev added.

Sample	Depth[1]	Litho.[2]	Min[3]	Qual[4]	No[5]	SiO_2	TiO_2	Al_2O_3	Cr_2O_3	Fe_2O_3	FeO	MnO	Cl	F	NiO	MgO	CaO	Na_2O	K_2O	V_2O_3	Total	An[6]	XMg[7]
OM10_Gid_A03	6288	SD	Cpx	c	14	50.89	0.95	2.87	0.03	0.00	9.99	0.30			0.00	15.12	19.79	0.30	0.00		100.25		0.73
					14	*0.28*	*0.06*	*0.16*	*0.03*	*0.00*	*0.38*	*0.07*			*0.00*	*0.20*	*0.53*	*0.05*	*0.01*		*0.32*		*0.01*
			Cpx	r	6	50.33	1.09	3.02	0.02	0.00	11.14	0.30			0.00	14.49	19.37	0.32	0.01		100.10		0.70
					6	*0.24*	*0.08*	*0.36*	*0.02*	*0.00*	*1.33*	*0.06*			*0.00*	*0.52*	*0.52*	*0.03*	*0.01*		*0.23*		*0.03*
			Pl	c	13	68.06	0.00	21.15		0.18		0.00				0.01	0.85	10.08	0.16		100.50	4.43	0.00
					13	*1.16*		*0.59*		*0.13*		*0.04*				*0.49*	*0.95*	*0.38*			*0.87*	*2.63*	*0.00*
			Pl	r	3	68.62	0.00	20.43		0.10		0.00				0.00	1.21	10.01	0.04		100.42	6.17	0.00
					3	*1.66*		*1.39*		*0.07*		*0.00*				*0.45*	*0.78*	*0.01*			*0.96*	*1.98*	*0.00*
OM10_Gid_A05a	6001	SD	Pl	c	5	67.93	0.00	21.30		0.20		0.00				0.03	0.75	9.35	0.35		99.91	4.19	0.00
					5	*1.66*		*0.89*		*0.14*		*0.00*				*0.07*	*0.16*	*0.94*	*0.57*		*0.96*	*1.04*	*0.00*
OM10_Gid_A10	5321	SD	Amph		24	43.45	0.03	22.02	0.00	0.00	3.26	0.04	0.00	0.02	0.00	0.00	26.78	0.06	0.01		97.72		0.47
					24	*0.23*	*0.01*	*0.75*	*0.00*	*0.00*	*0.98*	*0.03*	*0.00*	*0.03*	*0.00*	*0.00*	*0.22*	*0.03*	*0.00*		*0.23*		*0.02*
			Pl	c	7	68.32	0.00	21.05		0.15		0.00				0.00	0.69	10.76	0.03		101.00	3.39	0.00
					7	*0.51*		*0.23*		*0.10*		*0.00*				*0.00*	*0.18*	*0.20*	*0.01*		*0.45*	*0.82*	*0.00*
			Pl	r	2	67.56	0.00	21.41		0.08		0.00				0.00	1.39	10.55	0.03		101.02	6.77	0.00
					2	*0.86*		*0.11*		*0.08*		*0.00*				*0.00*	*0.46*	*0.55*	*0.00*		*0.55*	*2.19*	*0.00*
OM10_Gid_A11	4954	ML	Pl		26	50.61	0.04	30.55		0.77		0.02				0.11	14.14	3.76	0.03		100.03	67.43	0.00
					26	*0.81*	*0.02*	*0.64*		*0.09*		*0.02*				*0.03*	*0.76*	*0.45*	*0.01*		*0.42*	*3.75*	*0.00*
OM10_Gid_A11_3	5094	SD	Pl	c	80	53.10	0.03	29.42		0.73		0.00				0.05	12.72	4.49	0.03		100.58	60.92	0.00
					80	*0.66*	*0.03*	*0.35*		*0.08*		*0.01*				*0.04*	*0.49*	*0.24*	*0.01*		*0.32*	*2.16*	*0.00*
			Pl	r	20	62.07	0.01	24.97		0.48		0.00				0.00	6.10	6.93	0.10		100.67	32.32	0.00
					20	*2.43*	*0.02*	*1.10*		*0.09*		*0.00*				*0.01*	*1.61*	*1.09*	*0.02*		*0.67*	*6.48*	*0.00*
OM10_Gid_A12_3	4780	SD	Pl	c	38	55.78	0.06	27.81		0.67		0.00				0.01	10.53	5.77	0.04		100.68	50.11	0.00
					38	*0.43*	*0.01*	*0.26*		*0.08*		*0.00*				*0.02*	*0.34*	*0.19*	*0.04*		*0.33*	*1.59*	*0.00*
			Pl	r	57	58.16	0.04	26.72		0.60		0.00				0.01	8.71	6.50	0.06		100.80	42.30	0.00
					57	*1.45*	*0.03*	*0.60*		*0.19*		*0.00*				*0.02*	*0.96*	*0.34*	*0.01*		*0.44*	*3.29*	*0.00*
OM10_Gid_A13	4602	VG	Amph		6	50.56	0.57	5.19	0.04	10.79	2.51	0.22	0.00	0.00	0.00	16.51	10.96	1.00	0.09		100.58		0.92
					6	*0.36*	*0.13*	*0.42*	*0.04*	*1.19*	*1.05*	*0.04*	*0.00*	*0.00*	*0.00*	*0.43*	*0.24*	*0.12*	*0.02*		*0.36*		*0.03*
			Cpx		7	51.52	0.57	2.61	0.25	0.00	7.09	0.20			0.00	16.20	20.81	0.24	0.01		99.51		0.80
					7	*0.45*	*0.22*	*0.07*	*0.19*		*1.24*	*0.05*			*0.00*	*0.63*	*0.46*	*0.02*	*0.01*		*0.36*		*0.03*
			Pl	c	6	45.82	0.01	33.82		0.54		0.02				0.01	17.75	1.56	0.03		99.51	86.08	0.00
					6	*0.66*		*0.35*		*0.03*						*0.02*	*0.48*	*0.27*	*0.01*		*0.41*	*2.36*	*0.00*
			Pl	r	5	52.99	0.04	28.88		0.66		0.02				0.01	12.16	4.89	0.14		99.73	57.42	0.00
					5	*0.24*	*0.02*	*0.31*		*0.03*		*0.03*				*0.01*	*0.29*	*0.14*	*0.03*		*0.37*	*1.26*	*0.00*
OM10_Gid_A14a	4389	VG	Amph		24	42.93	3.39	10.71	0.00	0.00	12.25	0.15	0.28	0.06	0.00	14.00	11.43	2.52	0.47		100.25		0.50
					24	*0.43*	*0.33*	*0.17*	*0.00*	*0.00*	*0.29*	*0.04*	*0.04*	*0.05*	*0.00*	*0.24*	*0.13*	*0.13*	*0.02*		*0.42*		*0.02*
			Amph		10	43.30	3.49	10.91	0.00	0.00	12.42	0.13	0.27	0.19	0.00	14.03	11.47	2.58	0.45		101.32		0.58
					10	*0.17*	*0.19*	*0.17*	*0.00*		*0.29*	*0.05*	*0.01*	*0.02*	*0.00*	*0.22*	*0.17*	*0.16*	*0.01*		*0.57*		*0.01*
			Cpx	c	5	51.67	0.82	2.61	0.03	0.00	8.27	0.22			0.00	15.39	21.14	0.31	0.00		100.47		0.77
					5	*0.18*	*0.02*	*0.06*	*0.03*	*0.00*	*0.07*	*0.03*			*0.00*	*0.09*	*0.25*	*0.02*	*0.00*		*0.37*		*0.00*
			Cpx	r	3	51.66	0.81	2.38	0.00	0.00	8.25	0.24			0.00	15.40	21.23	0.33	0.00		100.31		0.77
					3	*0.37*	*0.02*	*0.18*	*0.00*	*0.00*	*0.19*	*0.06*			*0.00*	*0.02*	*0.29*	*0.01*	*0.00*		*0.30*		*0.00*
			Ol		8	37.38	0.01	0.02	0.00	0.00	29.54	0.47			0.02	33.62	0.10	0.01	0.01		101.17		0.67
					8	*0.15*	*0.01*	*0.01*	*0.00*	*0.00*	*0.16*	*0.02*			*0.02*	*0.20*	*0.01*	*0.01*	*0.01*		*0.28*		*0.00*
			Opx		8	54.00	0.04	1.04	0.02	0.00	18.65	0.42			0.00	25.48	0.73	0.01	0.00		100.37		0.71
					8	*0.27*	*0.03*	*0.34*	*0.02*	*0.00*	*0.45*	*0.09*			*0.00*	*0.14*	*0.23*	*0.01*	*0.00*		*0.23*		*0.01*
			Pl		8	48.30	0.03	32.82		0.60		0.00				0.00	16.48	2.29	0.03		100.56	79.74	0.00
					8	*0.56*	*0.03*	*0.39*		*0.05*		*0.00*				*0.00*	*0.41*	*0.22*	*0.01*		*0.34*	*1.93*	*0.00*

[1] Depth_ calculated height above MOHO
[2] Lithology: SD = Sheeted dike; VG = Varitextured gabbro; MG = Metagabbro; FG = Foliated gabbro
[3] Mineral analysed
[4] Qualifier: r = rim; c = core
[5] Number of analyses
[6] Anorthite content of plagioclase
[7] XMg for Cpx, Opx, and Amph

Table 9. continued

Sample	Depth[1]	Litho.[2]	Min[3]	Qual[4]	No[5]	SiO_2	TiO_2	Al_2O_3	Cr_2O_3	Fe_2O_3	FeO	MnO	Cl	F	NiO	MgO	CaO	Na_2O	K_2O	V_2O_3	Total	An[6]	XMg[7]
OM10_Gid_A14b	4389	VG	Amph		7	49.29	1.21	4.50	0.00	0.00	13.96	0.27	0.15	0.26	0.00	15.04	10.73	1.32	0.25		99.06		0.50
					7	*0.60*	*0.11*	*0.43*	*0.00*	*0.00*	*0.21*	*0.02*	*0.02*	*0.06*	*0.00*	*0.16*	*0.12*	*0.10*	*0.03*		*0.30*		*0.01*
			Cpx		7	52.41	0.66	1.99	0.00	0.00	8.59	0.30			0.00	15.11	21.04	0.32	0.00		100.42		0.76
					7	*0.89*	*0.10*	*0.21*	*0.00*	*0.00*	*0.34*	*0.02*			*0.00*	*0.43*	*0.58*	*0.04*	*0.00*		*0.93*		*0.01*
			Mag		4	0.05	2.74	1.13	0.18	59.71	32.94	0.11			0.00	0.03	0.02	0.00	0.00	1.43	98.35		0.00
					4	*0.01*	*1.44*	*0.29*	*0.03*	*3.24*	*1.16*	*0.08*				*0.03*	*0.01*	*0.00*	*0.00*	*0.10*	*0.53*		*0.00*
			Pl		5	52.17	0.04	29.82		0.57		0.00			0.00	0.00	13.04	4.32	0.06		100.01	62.32	0.00
					5	*1.11*	*0.02*	*1.11*		*0.04*		*0.00*				*0.00*	*1.18*	*0.61*	*0.02*		*0.57*	*5.44*	
OM10_Gid_A15	4129	VG	Amph		15	43.11	3.44	10.15	0.00	0.00	13.59	0.18	0.26	0.22	0.00	13.07	11.02	2.57	0.43		100.11		0.63
					15	*0.25*	*0.18*	*0.08*	*0.00*	*0.00*	*0.14*	*0.02*	*0.02*	*0.03*		*0.19*	*0.15*	*0.05*	*0.02*		*0.47*		*0.02*
			Amph		9	43.74	3.40	10.39	0.00	0.00	13.95	0.17			0.00	13.29	11.12	2.59	0.42		101.63		0.57
					9	*0.24*	*0.07*	*0.24*	*0.00*	*0.00*	*0.22*	*0.02*			*0.00*	*0.17*	*0.22*	*0.08*	*0.02*		*0.29*		*0.03*
			Cpx		10	53.32	0.10	0.50	0.04	0.00	7.98	0.29			0.00	13.69	23.66	0.16	0.01		99.74		0.75
					10	*0.52*	*0.08*	*0.31*	*0.04*	*0.00*	*0.61*	*0.05*			*0.00*	*0.28*	*0.78*	*0.06*	*0.01*		*0.55*		*0.02*
			Ilm		10	0.01	49.78	0.05	0.05	4.79	42.70	1.40			0.00	0.37	0.01	0.00	0.00		99.14		0.00
					10	*0.01*	*0.13*	*0.02*	*0.04*	*0.30*	*0.20*	*0.10*			*0.00*	*0.08*	*0.01*	*0.00*	*0.00*		*0.45*		*0.00*
			Mag		7	0.10	1.48	1.05	0.67	62.99	32.14	0.03			0.00	0.05	0.03	0.00	0.00		98.55		0.00
					7	*0.10*	*0.31*	*0.09*	*0.07*	*0.81*	*0.49*	*0.03*			*0.00*	*0.05*	*0.04*	*0.00*	*0.00*		*0.40*		*0.00*
			Pl		15	51.28	0.06	30.58		0.43		0.02			0.00	0.03	13.84	3.70	0.08		99.96	67.10	0.00
					15	*0.57*	*0.01*	*0.37*		*0.06*		*0.02*				*0.02*	*0.37*	*0.22*	*0.01*		*0.33*	*1.86*	
OM10_Gid_A16	3924	FG	Amph		18	44.84	2.37	9.21	0.00	0.00	10.05	0.12			0.00	15.04	11.72	2.30	0.17		98.14		0.73
					18	*2.14*	*0.88*	*1.37*	*0.00*	*0.00*	*0.54*	*0.12*			*0.00*	*0.88*	*0.18*	*0.41*	*0.15*		*0.25*		*0.02*
			Cpx	c	21	51.73	0.58	2.59	0.05	0.00	6.97	0.17			0.00	15.19	21.92	0.29	0.00		99.49		0.80
					21	*0.51*	*0.14*	*0.45*	*0.05*	*0.00*	*0.36*	*0.04*			*0.00*	*0.16*	*0.43*	*0.03*	*0.00*		*0.33*		*0.01*
			Cpx	r	9	51.56	0.75	2.50	0.14	0.00	7.22	0.17			0.00	15.07	21.65	0.31	0.01		99.38		0.79
					9	*0.47*	*0.12*	*0.29*	*0.03*	*0.00*	*0.46*	*0.03*			*0.00*	*0.14*	*0.48*	*0.05*	*0.00*		*0.45*		*0.01*
			Ilm		12	0.04	50.30	0.05	0.23	3.16	41.52	3.15			0.00	0.20	0.18	0.00	0.00		98.81		0.00
					12	*0.03*	*0.39*	*0.05*	*0.08*	*0.37*	*0.87*	*1.24*			*0.00*	*0.25*	*0.13*	*0.00*	*0.00*		*0.65*		*0.00*
			Mag		12	0.05	3.09	2.03	2.06	57.34	32.94	0.33			0.00	0.22	0.17	0.00	0.00		98.23		0.00
					12	*0.03*	*17.67*	*0.85*	*1.19*	*20.52*	*3.38*	*1.24*			*0.00*	*0.16*	*0.12*	*0.00*	*0.00*		*0.63*		*0.00*
			Ol	c	25	38.18	0.02	0.01	0.00	0.00	24.07	0.35			0.06	36.43	0.07	0.01	0.00		99.19		0.73
					25	*0.15*	*0.01*	*0.01*	*0.00*	*0.00*	*0.30*	*0.04*			*0.03*	*0.36*	*0.01*	*0.01*	*0.00*		*0.50*		*0.00*
			Ol	r	10	38.13	0.02	0.02	0.00	0.00	23.94	0.35			0.06	36.15	0.09	0.01	0.00		98.77		0.73
					10	*0.25*	*0.01*	*0.01*		*0.00*	*0.46*	*0.07*			*0.05*	*0.46*	*0.03*	*0.01*	*0.00*		*0.39*		*0.01*
			Pl		25	46.94	0.03	33.40		0.60		0.01			0.05	0.02	17.13	1.93	0.02		100.02	82.94	0.00
					25	*0.38*	*0.01*	*0.33*		*0.10*		*0.02*				*0.04*	*0.32*	*0.15*	*0.01*		*0.29*	*1.32*	
OM10_Gid_A17	3734	FG	Amph		15	43.85	3.04	9.97	0.00	0.00	12.26	0.19			0.00	13.61	12.27	2.35	0.20		100.23		0.66
					15	*2.56*	*0.79*	*2.49*	*0.00*	*0.00*	*1.39*	*0.03*			*0.00*	*0.56*	*2.94*	*0.57*	*0.06*		*0.63*		*0.04*
			Cpx		16	52.41	0.47	1.65	0.02	0.03	7.92	0.29			0.00	14.00	21.95	0.27	0.01		99.01		0.76
					16	*0.34*	*0.12*	*0.33*	*0.03*	*0.08*	*0.40*	*0.06*			*0.00*	*0.26*	*0.54*	*0.05*	*0.01*		*0.37*		*0.01*
			Ilm		5	0.02	49.49	0.01	0.09	5.82	40.80	3.55			0.00	0.07	0.01	0.00	0.00		99.87		0.00
					5	*0.01*	*0.16*	*0.01*	*0.02*	*0.57*	*0.09*	*0.09*			*0.00*	*0.02*	*0.02*	*0.01*	*0.00*		*0.42*		*0.00*
			Mag		2	0.07	6.39	2.57	0.65	51.62	36.26	0.56			0.00	0.06	0.05	0.00	0.00		98.24		0.00
					2	*0.04*	*1.09*	*0.59*	*0.00*	*2.78*	*0.91*	*0.17*				*0.02*	*0.01*	*0.00*	*0.00*		*0.09*		*0.00*
			Pl		14	50.42	0.03	31.36		0.33		0.02			0.00	0.01	14.68	3.30	0.03		100.15	70.95	0.00
					14	*0.41*	*0.04*	*0.27*		*0.06*		*0.02*				*0.01*	*0.34*	*0.19*	*0.01*		*0.24*	*1.63*	

[1] Depth_ calculated height above MOHO
[2] Lithology: SD = Sheeted dike; VG = Varitextured gabbro; MG = Metagabbro; FG = Foliated gabbro
[3] Mineral analysed
[4] Qualifier: r = rim; c = core
[5] Number of analyses
[6] Anorthite content of plagioclase
[7] XMg for Cpx, Opx, and Amph

Table 9. continued

Sample	Depth[1]	Litho.[2]	Min[3]	Qual[4]	No[5]	SiO_2	TiO_2	Al_2O_3	Cr_2O_3	Fe_2O_3	FeO	MnO	Cl	F	NiO	MgO	CaO	Na_2O	K_2O	V_2O_3	Total	An[6]	XMg[7]
OM10_Gid_A17_1	3550	FG	Amph	c	10	44.51	2.65	9.66	0.00	0.00	13.74	0.21	0.23	0.07	0.00	13.49	11.37	2.23	0.29		100.52		0.64
						0.76	0.39	0.39	0.00	0.00	0.14	0.06	0.02	0.05	0.00	0.44	0.14	0.11	0.02		0.63		0.01
			Amph	r	3	45.08	2.17	9.28	0.00	0.00	13.56	0.20	0.22	0.02	0.00	13.78	11.37	2.05	0.30		100.11		0.64
					3	0.21	0.09	0.23	0.00	0.00	0.19	0.01	0.01	0.01	0.00	0.38	0.02	0.10	0.01		0.27		0.01
			Cpx	c	22	52.97	0.34	1.21	0.02	0.00	8.63	0.30			0.00	14.68	22.29	0.27	0.00		100.71		0.75
					22	0.64	0.19	0.49	0.03		0.55	0.05			0.00	0.24	0.92	0.10	0.01		0.52		0.01
			Cpx	r	5	52.60	0.43	1.53	0.02	0.00	8.85	0.29			0.00	14.35	21.89	0.35	0.01		100.30		0.74
					5	0.57	0.15	0.38	0.02		0.31	0.04			0.00	0.13	0.47	0.07	0.01		0.26		0.01
			Ilm		21	0.02	35.25	0.54	0.06	16.09	45.86	0.71			0.00	0.19	0.01	0.00	0.00	0.64	99.37		0.00
					21	0.03	19.14	0.90	0.06	25.53	6.37	0.37			0.00	0.15	0.01	0.00	0.00	0.51	1.09		0.00
			Mag		6	0.04	6.46	2.41	0.16	52.86	37.21	0.19			0.00	0.11	0.01	0.00	0.00	1.43	100.89		0.00
					6	0.02	0.58	0.24	0.03	0.97	0.60	0.04				0.01	0.01	0.00	0.00	0.05	0.48		0.00
			Pl	c	17	53.03	0.05	30.16		0.40		0.01				0.01	12.80	4.69	0.08		101.22	59.91	0.00
					17	0.52	0.01	0.27		0.08		0.02				0.01	0.30	0.24	0.01		0.30	1.70	0.00
			Pl	r	9	54.08	0.03	29.57		0.41		0.02				0.01	11.92	5.10	0.08		101.22	56.11	0.00
					9	0.61	0.02	0.21		0.08		0.02				0.01	0.38	0.25	0.01		0.47	1.73	0.00
OM10_Gid_A17_2	3577	FG	Amph		30	43.06	3.77	10.82	0.00	0.00	13.13	0.19	0.13	0.03	0.00	13.08	11.39	2.69	0.21		100.57		0.64
					30	0.35	0.14	0.24	0.00	0.00	0.39	0.04	0.03	0.03	0.00	0.37	0.18	0.11	0.02		0.40		0.01
			Cpx	c	16	53.08	0.30	1.11	0.04	0.00	8.24	0.29			0.00	14.99	22.32	0.25	0.01		100.64		0.76
					16	0.43	0.11	0.35	0.04		0.30	0.05			0.00	0.23	0.44	0.08	0.01		0.42		0.01
			Cpx	r	2	53.09	0.16	1.11	0.00	0.00	8.34	0.27			0.00	14.79	22.26	0.27	0.02		100.32		0.76
					2	0.15	0.01	0.27	0.00		0.27	0.04			0.00	0.16	0.69	0.01	0.02		0.05		0.00
			Ilm		6	0.00	0.35	0.05	0.03	0.71	0.35	0.07			0.00	0.02	0.01	0.00	0.00	0.08	0.18		0.00
					6	0.00	0.35	0.05	0.03	0.71	0.35	0.07			0.00	0.02	0.07	0.00	0.00	0.08	0.18		0.00
			Mag		7	1.05	8.90	2.19	0.77	44.26	39.39	0.48			0.00	0.08	0.78	0.00	0.00	2.83	100.74		0.00
					7	1.52	1.14	1.46	0.07	3.82	1.32	0.15				0.10	1.19	0.00	0.00	0.13	0.91		0.00
			Pl	c	23	53.33	0.05	29.97		0.33		0.02				0.01	12.49	4.88	0.05		101.11	58.43	0.00
					23	1.13	0.01	0.74		0.07		0.02				0.01	0.92	0.51	0.01		0.38	4.31	0.00
			Pl		6	54.49	0.05	29.53		0.41		0.03				0.01	11.74	5.31	0.06		101.60	54.82	0.00
					6	0.56	0.01	0.35		0.13		0.02				0.01	0.43	0.23	0.01		0.39	1.95	0.00
OM10_Gid_A18	3423	FG	Cpx	c	14	51.35	0.84	2.38	0.07	0.00	8.42	0.26			0.00	14.63	21.00	0.39	0.01		99.33		0.76
					14	0.27	0.05	0.06	0.03	0.00	0.41	0.03			0.00	0.38	0.71	0.02	0.01		0.32		0.01
			Cpx	r	6	51.59	0.69	2.15	0.05	0.00	8.06	0.25			0.00	14.75	21.65	0.37	0.01		99.57		0.77
					6	0.29	0.05	0.06	0.04	0.00	0.28	0.06			0.00	0.23	0.22	0.03	0.01		0.43		0.00
			Ilm		5	0.00	49.85	0.07	0.11	6.32	41.39	1.36			0.00	1.15	0.01	0.00	0.00		100.27		0.00
					5	0.13	0.20	0.01	0.04	0.30	0.21	0.12			0.00	0.08	0.01	0.00	0.00		0.28		0.00
			Mag		5	0.02	6.09	3.35	1.56	51.51	35.70	0.26			0.00	0.73	0.02	0.00	0.00		99.25		0.00
					5	0.01	1.24	0.48	0.21	3.05	0.96	0.12			0.00	0.11	0.04	0.00	0.00		0.47		0.00
			Ol	c	15	37.06	0.02	0.02	0.00	0.00	29.48	0.44			0.05	32.96	0.04	0.01	0.00		100.06		0.67
					15	0.16	0.02	0.01	0.00	0.00	0.32	0.05			0.04	0.20	0.04	0.01	0.00		0.39		0.00
			Ol	r	6	37.23	0.01	0.01	0.00	0.00	29.03	0.43			0.03	32.73	0.04	0.00	0.01		99.52		0.67
					6	0.13	0.01	0.01	0.00	0.00	0.34	0.04			0.02	0.21	0.04	0.00	0.01		0.34		0.00
			Pl		16	52.30	0.04	29.73		0.36		0.02				0.02	12.93	4.28	0.04		99.69	62.41	0.00
					16	0.19	0.02	0.28		0.03		0.03				0.01	0.19	0.10	0.01		0.47	0.79	0.00
OM10_Gid_A18_1	3230	FG	Amph		14	42.68	3.09	10.75	0.00	0.00	10.77	0.11				14.23	11.51	2.52	0.24		98.29		0.70
					14	0.28	0.20	0.18	0.00	0.00	0.16	0.02				0.18	0.17	0.05	0.02		0.48		0.00
			Amph		5	43.80	2.86	10.91	0.29	0.00	11.05	0.10	0.16	0.20	0.00	15.09	11.43	2.59	0.25		100.81		0.59
					5	0.13	0.04	0.10	0.03	0.00	0.20	0.06	0.03	0.01	0.00	0.20	0.17	0.04	0.02		0.16		0.02
			Cpx	c	15	51.48	0.59	2.05	0.09	0.00	6.77	0.19				15.03	21.85	0.34	0.01		98.39		0.80
					15	0.54	0.15	0.37	0.07		0.37	0.04				0.19	0.56	0.04	0.01		0.32		0.01
			Cpx	r	6	51.03	0.66	2.62	0.10	0.00	7.08	0.17				14.93	21.04	0.38	0.01		98.01		0.79
					6	0.35	0.07	0.56	0.08	0.00	0.31	0.06				0.19	0.76	0.07	0.01		0.36		0.01
			Pl		15	48.14	0.03	32.09		0.44		0.01				0.01	15.61	2.66	0.03		98.98	76.30	0.00
					15	0.45	0.01	0.28		0.06		0.01				0.01	0.27	0.16	0.01		0.42	1.31	0.00

[1] Depth_ calculated height above MOHO

[5] Number of analyses

Table 9. continued

Sample	Depth[1]	Litho.[2]	Min[3]	Qual[4]	No[5]	SiO₂	TiO₂	Al₂O₃	Cr₂O₃	Fe₂O₃	FeO	MnO	Cl	F	NiO	MgO	CaO	Na₂O	K₂O	V₂O₃	Total	An[6]	XMg[7]
OM10_Gid_A18_2a	2900	FG	Amph		17	43.18	2.91	10.96	0.00	0.00	11.16	0.13			0.00	14.11	11.73	2.32	0.16		99.13		0.69
					17	*0.20*	*0.10*	*0.14*	*0.00*	*0.00*	*0.37*	*0.03*			*0.00*	*0.30*	*0.16*	*0.13*	*0.01*		*0.44*		*0.01*
			Amph		10	43.86	2.72	10.68	0.00	0.00	11.26	0.14	0.07	0.15	0.00	15.10	11.61	2.34	0.15		100.17		0.59
					10	*0.31*	*0.28*	*0.15*	*0.00*	*0.00*	*0.33*	*0.02*	*0.01*	*0.01*	*0.00*	*0.15*	*0.15*	*0.10*	*0.01*		*0.64*		*0.02*
			Cpx	c	12	51.94	0.60	2.14	0.03	0.00	6.58	0.19			0.00	15.59	22.43	0.30	0.00		99.80		0.81
					12	*0.42*	*0.12*	*0.32*	*0.03*	*0.00*	*0.50*	*0.03*			*0.00*	*0.22*	*0.62*	*0.06*	*0.00*		*0.31*		*0.01*
			Cpx	r	4	51.75	0.66	2.25	0.03	0.00	6.66	0.19			0.00	15.78	22.24	0.34	0.01		99.90		0.81
					4	*0.23*	*0.01*	*0.02*	*0.02*	*0.00*	*0.03*	*0.02*			*0.00*	*0.19*	*0.33*	*0.05*	*0.00*		*0.51*		*0.00*
			Ol	c	15	38.27	0.01	0.01	0.00	0.00	23.73	0.37			0.05	38.10	0.04	0.01	0.00		100.60		0.74
					15	*0.15*	*0.01*	*0.01*	*0.00*	*0.00*	*0.23*	*0.05*			*0.03*	*0.22*	*0.23*	*0.01*	*0.00*		*0.42*		*0.01*
			Ol	r	6	38.21	0.01	0.00	0.00	0.00	23.34	0.32			0.07	38.50	0.05	0.02	0.00		100.53		0.75
					6	*0.22*	*0.01*	*0.00*	*0.00*	*0.00*	*0.27*	*0.03*			*0.04*	*0.28*	*0.02*	*0.02*	*0.00*		*0.26*		*0.00*
			Pl		10	47.94	0.03	32.75		0.45		0.02				0.01	16.48	2.31	0.02		99.95	79.72	0.00
					10	*0.45*	*0.01*	*0.31*		*0.08*		*0.02*					*0.32*	*0.16*	*0.01*		*0.17*	*1.43*	*0.00*
OM10_Gid_A19	2700	FG	Amph		20	43.26	2.89	10.90	0.00	0.00	10.33	0.13			0.00	14.22	11.85	2.21	0.21		98.31		0.71
					20	*0.52*	*0.18*	*0.53*	*0.00*	*0.00*	*0.13*	*0.02*			*0.00*	*0.26*	*0.14*	*0.15*	*0.01*		*0.49*		*0.00*
			Amph		5	43.50	3.07	11.22	0.61	0.00	10.30	0.10	0.14	0.15	0.00	14.84	11.76	2.56	0.19		100.53		0.57
					5	*0.17*	*0.11*	*0.27*	*0.14*	*0.00*	*0.34*	*0.01*	*0.04*	*0.02*	*0.00*	*0.11*	*0.14*	*0.12*	*0.01*		*0.44*		*0.01*
			Amph		5	45.85	2.48	9.46	0.21	0.00	10.00	0.12	0.04	0.15	0.00	16.13	11.62	2.18	0.16		100.53		0.59
					5	*0.57*	*0.12*	*0.33*	*0.03*	*0.00*	*0.30*	*0.01*	*0.04*	*0.02*	*0.00*	*0.16*	*0.14*	*0.12*	*0.01*		*0.33*		*0.02*
			Cpx	c	28	51.54	0.72	2.49	0.34	0.00	7.00	0.19	0.00		0.00	14.98	21.25	0.38	0.01		98.91		0.79
					28	*0.24*	*0.04*	*0.18*	*0.12*	*0.00*	*0.48*	*0.03*			*0.00*	*0.41*	*0.94*	*0.04*	*0.01*		*0.42*		*0.01*
			Cpx	r	12	51.62	0.69	2.34	0.26	0.00	6.52	0.21			0.00	14.57	21.99	0.38	0.01		98.59		0.80
					12	*0.34*	*0.02*	*0.08*	*0.04*	*0.00*	*0.33*	*0.05*			*0.00*	*0.24*	*0.33*	*0.03*	*0.01*		*0.39*		*0.01*
			Ol	c	30	38.37	0.01	0.01	0.00	0.00	23.10	0.35			0.10	36.66	0.04	0.01	0.01		98.66		0.74
					30	*0.18*	*0.01*	*0.01*	*0.00*	*0.00*	*0.32*	*0.05*			*0.03*	*0.58*	*0.01*	*0.01*	*0.01*		*0.70*		*0.00*
			Ol	r	12	38.23	0.02	0.02	0.00	0.00	22.95	0.37			0.08	36.91	0.08	0.01	0.01		98.68		0.74
					12	*0.33*	*0.01*	*0.01*	*0.00*	*0.00*	*0.29*	*0.05*			*0.05*	*0.67*	*0.04*	*0.01*	*0.01*		*0.36*		*0.00*
			Pl		15	48.62	0.03	32.12		0.48		0.02				0.02	15.60	2.77	0.03		99.64	75.57	0.00
					15	*0.40*	*0.01*	*0.15*		*0.07*		*0.02*				*0.01*	*0.19*	*0.11*	*0.00*		*0.28*	*0.91*	*0.00*
OM10_Gid_A20	2394	LG	Cpx	c	21	52.35	0.53	2.64	0.20	0.00	5.43	0.14			0.00	15.94	22.52	0.30	0.00		100.04		0.84
					21	*0.30*	*0.15*	*0.20*	*0.07*	*0.00*	*0.32*	*0.05*			*0.00*	*0.52*	*0.53*	*0.04*	*0.00*		*0.43*		*0.01*
			Cpx	r	9	52.04	0.78	2.57	0.20	0.00	6.01	0.14			0.00	15.54	22.47	0.39	0.00		100.14		0.82
					9	*0.33*	*0.11*	*0.04*	*0.05*	*0.00*	*0.20*	*0.02*			*0.00*	*0.22*	*0.27*	*0.04*	*0.00*		*0.43*		*0.00*
			Ol	c	20	39.06	0.01	0.06	0.00	0.00	20.46	0.31			0.10	40.10	0.04	0.01	0.00		100.15		0.78
					20	*0.31*	*0.01*	*0.17*	*0.00*	*0.00*	*0.59*	*0.04*			*0.03*	*0.71*	*0.01*	*0.01*	*0.01*		*0.54*		*0.01*
			Ol	r	8	39.03	0.01	0.02	0.00	0.00	20.27	0.28			0.09	39.88	0.04	0.01	0.00		99.64		0.78
					8	*0.38*	*0.00*	*0.03*	*0.00*	*0.00*	*0.56*	*0.04*			*0.03*	*0.51*	*0.01*	*0.01*	*0.00*		*0.36*		*0.01*
			Pl	c	14	47.48	0.04	33.57		0.49		0.00				0.01	17.50	2.02	0.02		101.09	82.61	0.00
					14	*0.41*	*0.01*	*0.25*		*0.07*		*0.01*				*0.02*	*0.31*	*0.11*	*0.01*		*0.39*	*1.02*	*0.00*
			Pl	r	9	47.40	0.04	33.65		0.42		0.01				0.01	17.58	1.96	0.02		101.04	83.12	0.00
					9	*0.30*	*0.01*	*0.26*		*0.09*		*0.01*				*0.01*	*0.36*	*0.13*	*0.01*		*0.40*	*1.21*	*0.00*

[1] Depth_calculated height above MOHO
[2] Lithology: SD = Sheeted dike; VG = Varitextured gabbro; MG = Metagabbro; FG = Foliated gabbro
3 Mineral analysed
[4] Qualifier: r = rim; c = core
[5] Number of analyses
[6] Anorthite content of plagioclase
[7] XMg for Cpx, Opx, and Amph

Table 9. continued

Sample	Depth[1]	Litho.[2]	Min[3]	Qual[4]	No[5]	SiO₂	TiO₂	Al₂O₃	Cr₂O₃	Fe₂O₃	FeO	MnO	Cl	F	NiO	MgO	CaO	Na₂O	K₂O	V₂O₃	Total	An[6]	XMg[7]
OM10_Gid_A20a	2394	LG	Amph		15	43.76	2.57	10.81	0.00	0.00	9.69	0.10			0.00	15.22	11.87	2.21	0.22		98.93		0.74
					15	*0.71*	*0.57*	*0.36*	*0.00*	*0.00*	*0.25*	*0.02*			*0.00*	*0.25*	*0.16*	*0.12*	*0.05*		*0.48*		*0.00*
			Amph		5	43.79	2.70	11.19	0.30	0.00	9.60	0.13	0.21	0.15	0.00	15.83	11.61	2.42	0.28		100.31		0.59
					5	*0.06*	*0.10*	*0.13*	*0.04*	*0.00*	*0.12*	*0.02*	*0.01*	*0.01*	*0.00*	*0.11*	*0.09*	*0.03*	*0.01*		*0.38*		*0.01*
			Cpx	c	25	52.54	0.41	2.07	0.19	0.00	5.31	0.14			0.00	16.52	22.93	0.24	0.01		100.37		0.85
					25	*0.57*	*0.14*	*0.60*	*0.08*	*0.00*	*0.33*	*0.05*			*0.00*	*0.34*	*0.87*	*0.05*	*0.01*		*0.54*		*0.01*
			Cpx	r	5	52.28	0.55	1.98	0.20	0.00	5.74	0.18			0.00	16.13	22.77	0.32	0.01		100.14		0.83
					5	*0.74*	*0.28*	*0.55*	*0.09*	*0.00*	*0.49*	*0.03*			*0.00*	*0.34*	*0.65*	*0.08*	*0.00*		*0.47*		*0.01*
			Ilm		3	0.03	50.16	0.04	0.05	2.83	38.66	5.63			0.00	0.19	0.35	0.00	0.00		97.94		0.00
					3	*0.01*	*0.97*	*0.02*	*0.02*	*1.50*	*0.34*	*0.58*				*0.02*	*0.02*	*0.00*	*0.00*		*0.45*		*0.00*
			Ol	c	30	38.87	0.01	0.01	0.00	0.00	20.89	0.32			0.10	40.94	0.05	0.02	0.01		101.20		0.78
					30	*0.21*		*0.01*			*0.37*	*0.05*			*0.04*	*0.30*	*0.02*	*0.02*	*0.01*		*0.41*		*0.00*
			Ol	r	10	39.22	0.01	0.02	0.00	0.00	20.22	0.28			0.08	40.78	0.16	0.01	0.01		100.79		0.78
					10	*0.84*	*0.01*	*0.02*			*1.36*	*0.05*			*0.03*	*0.82*	*0.29*	*0.01*	*0.01*		*0.99*		*0.01*
			Pl		25	46.90	0.03	33.27		0.49		0.02				0.01	17.22	1.98	0.03		99.90	82.66	0.00
					25	*0.45*	*0.01*	*0.44*		*0.05*		*0.02*				*0.01*	*0.42*	*0.25*	*0.03*		*0.34*	*2.13*	*0.00*
OM10_Gid_A20b	2394	LG	Cpx	c	20	52.28	0.54	2.36	0.18	0.00	5.75	0.16			0.00	15.89	21.82	0.29	0.01		99.27		0.83
					20	*0.53*	*0.27*	*0.43*	*0.06*	*0.00*	*0.49*	*0.04*			*0.00*	*0.31*	*0.85*	*0.08*	*0.01*		*0.61*		*0.01*
			Cpx	r	10	52.06	0.59	1.99	0.13	0.00	5.82	0.15			0.00	15.69	22.34	0.31	0.00		99.09		0.83
					10	*1.06*	*0.28*	*0.56*	*0.05*	*0.00*	*0.67*	*0.04*			*0.00*	*0.48*	*1.13*	*0.10*	*0.00*		*0.77*		*0.02*
			Ol	c	19	39.02	0.01	0.01	0.00	0.00	21.05	0.31			0.10	39.56	0.06	0.01	0.00		100.15		0.77
					19	*0.35*	*0.01*	*0.01*			*0.36*	*0.04*			*0.04*	*0.46*	*0.01*	*0.01*	*0.00*		*0.63*		*0.00*
			Ol	r	8	39.67	0.01	0.01	0.00	0.00	20.75	0.31			0.09	39.33	0.07	0.01	0.01		100.25		0.77
					8	*1.01*	*0.01*	*0.01*			*0.58*	*0.04*			*0.02*	*0.37*	*0.04*	*0.01*	*0.01*		*0.53*		*0.00*
			Pl		19	47.69	0.04	33.16		0.59		0.02				0.02	16.48	2.17	0.03		100.13	80.57	0.00
					19	*0.40*	*0.01*	*0.39*		*0.09*		*0.03*				*0.03*	*0.40*	*0.17*	*0.01*		*0.67*	*1.51*	*0.00*
OM10_Gid_A21	2124	LG	Cpx	c	17	51.55	0.69	2.69	0.09	0.00	6.94	0.17			0.00	15.51	21.60	0.35	0.01		99.62		0.80
					17	*0.70*	*0.03*	*0.27*	*0.04*	*0.00*	*0.26*	*0.03*			*0.00*	*0.38*	*0.42*	*0.03*	*0.01*		*0.69*		*0.01*
			Pl	c	18	47.48	0.03	32.53		0.52		0.02				0.01	16.40	2.36	0.03		99.34	79.20	0.00
					18	*0.53*	*0.01*	*0.27*		*0.07*		*0.03*				*0.02*	*0.25*	*0.13*	*0.01*		*0.71*	*1.07*	*0.00*
			Pl	r	3	46.80	0.03	33.23		0.47		0.02				0.05	17.10	1.96	0.03		99.62	82.69	0.00
					3	*0.53*	*0.01*	*0.36*		*0.07*		*0.01*				*0.04*	*0.50*	*0.33*	*0.01*		*0.54*	*2.81*	*0.00*
OM10_Gid_A22	1936	LG	Cpx	c	24	51.42	0.62	2.64	0.11	0.00	6.25	0.14			0.00	15.93	21.88	0.32	0.01		99.32		0.82
					24	*0.43*	*0.10*	*0.40*	*0.04*	*0.00*	*0.30*	*0.04*			*0.00*	*0.31*	*0.33*	*0.04*	*0.01*		*0.56*		*0.01*
			Ol		16	38.13	0.01	0.01	0.00	0.00	21.11	0.29			0.09	40.25	0.05	0.01	0.01		99.98		0.77
					16	*0.24*	*0.01*	*0.01*			*0.25*	*0.05*			*0.03*	*0.17*	*0.01*	*0.01*	*0.01*		*0.37*		*0.00*
			Pl	c	30	47.19	0.03	32.58		0.54		0.02				0.01	16.40	2.23	0.02		98.97	80.16	0.00
					30	*0.42*	*0.01*	*0.34*		*0.07*		*0.03*				*0.02*	*0.31*	*0.12*	*0.02*		*0.60*	*1.09*	*0.00*
			Pl	r	3	47.09	0.03	33.06		0.55		0.04				0.00	16.82	2.12	0.03		99.68	81.30	0.00
					3	*0.28*	*0.00*	*0.10*		*0.12*		*0.03*				*0.00*	*0.08*	*0.06*	*0.00*		*0.43*	*0.45*	*0.00*
OM10_Gid_A23	1659	LG	Cpx	c	31	52.59	0.45	2.53	0.35	0.00	5.31	0.14			0.00	15.58	22.94	0.32	0.00		100.21		0.84
					31	*0.59*	*0.07*	*0.39*	*0.10*	*0.00*	*0.33*	*0.04*			*0.00*	*0.43*	*0.57*	*0.06*	*0.00*		*0.46*		*0.01*
			Cpx	r	6	52.73	0.49	2.28	0.31	0.00	5.83	0.14			0.00	15.98	22.43	0.33	0.00		100.51		0.83
					6	*0.14*	*0.02*	*0.10*	*0.03*	*0.00*	*0.26*	*0.03*			*0.00*	*0.42*	*0.72*	*0.04*	*0.00*		*0.14*		*0.00*
			Pl	c	22	47.47	0.02	33.63		0.49		0.02				0.02	17.55	1.94	0.01		101.10	83.25	0.00
					22	*0.19*	*0.01*	*0.18*		*0.06*		*0.02*				*0.02*	*0.13*	*0.06*	*0.01*		*0.21*	*0.52*	*0.00*
			Pl	r	8	47.30	0.02	33.52		0.48		0.01				0.01	17.66	1.97	0.02		100.93	83.12	0.00
					8	*0.24*	*0.01*	*0.12*		*0.05*		*0.02*				*0.01*	*0.12*	*0.06*	*0.01*		*0.26*	*0.47*	*0.00*

[1] Depth_ calculated height above MOHO
[2] Lithology: SD = Sheeted dike; VG = Varitextured gabbro; FG = Foliated gabbro; MG = Metagabbro; FG = Foliated gabbro
3 Mineral analysed
[4] Qualifier: r = rim; c = core
[5] Number of analyses
[6] Anorthite content of plagioclase
[7] XMg for Cpx, Opx, and Amph

Table 9. continued

Sample	Depth[1]	Litho.[2]	Min[3]	Qual[4]	No[5]	SiO₂	TiO₂	Al₂O₃	Cr₂O₃	Fe₂O₃	FeO	MnO	Cl	F	NiO	MgO	CaO	Na₂O	K₂O	V₂O₃	Total	An[6]	XMg[7]
OM10_Gid_A23a	1659	LG	Cpx		17	52.57	0.43	2.21	0.35	0.00	5.21	0.14			0.00	16.23	22.58	0.29	0.00		99.99		0.85
					17	0.49	0.11	0.59	0.11	0.00	0.39	0.05			0.00	0.47	0.80	0.05	0.00		0.44		0.01
			Pl	c	22	46.70	0.02	33.61		0.46		0.02				0.01	17.40	1.75	0.02		99.95	84.51	0.00
					22	0.33	0.01	0.36		0.06		0.02				0.01	0.29	0.16	0.01		0.42	1.35	0.00
			Pl	r	3	46.37	0.01	33.66		0.42		0.02				0.02	17.60	1.69	0.02		99.76	85.14	0.00
					3	0.05	0.01	0.14		0.05		0.02				0.03	0.11	0.04	0.01		0.30	0.25	0.00
			Cpx	c	15	52.19	0.45	2.69	0.32	0.00	5.40	0.14			0.00	16.11	22.51	0.29	0.01		100.11		0.84
					15	0.26	0.04	0.21	0.10	0.00	0.20	0.03			0.00	0.23	0.43	0.03	0.00		0.28		0.00
OM10_Gid_A23b	1659	LG	Cpx	r	6	52.58	0.47	2.33	0.34	0.00	5.13	0.13			0.00	16.28	22.81	0.30	0.00		100.37		0.85
					6	0.15	0.04	0.21	0.08	0.00	0.18	0.02			0.00	0.12	0.40	0.02	0.00		0.23		0.00
			Ol	c	15	39.60	0.01	0.01	0.00		18.23	0.24			0.17	42.54	0.05	0.01	0.00		100.87		0.81
					15	0.17	0.01	0.01	0.00		0.32	0.04			0.04	0.25	0.01	0.01	0.00		0.41		0.00
			Ol	r	4	39.74	0.00	0.01	0.00		18.21	0.29			0.16	42.21	0.06	0.01	0.01		100.69		0.81
					4	0.29	0.00	0.00	0.00		0.14	0.03			0.05	0.08	0.01	0.01	0.00		0.32		0.00
			Pl		15	47.22	0.02	33.40		0.46		0.02				0.03	17.16	1.94	0.02		100.23	82.90	0.00
					15	0.20	0.01	0.23		0.06		0.02				0.01	0.19	0.07	0.01		0.26	0.63	0.00
OM10_Gid_A24	1431	LG	Cpx	c	15	52.31	0.47	2.49	0.24	0.00	5.38	0.15			0.00	16.04	22.03	0.27	0.01		99.38		0.84
					15	0.25	0.04	0.08	0.06	0.00	0.27	0.03			0.00	0.26	0.46	0.02	0.01		0.33		0.01
			Cpx	r	4	52.50	0.50	2.09	0.27	0.00	5.38	0.17			0.00	16.09	22.29	0.30	0.01		99.60		0.84
					4	0.03	0.01	0.02	0.00		0.12	0.05			0.00	0.25	0.47	0.01	0.01		0.43		0.00
			Ol	c	14	39.37	0.01	0.01	0.00		18.25	0.25			0.11	41.63	0.07	0.00	0.01		99.72		0.80
					14	0.20	0.01	0.01	0.00		0.27	0.04			0.03	0.32	0.02	0.01	0.01		0.37		0.00
			Ol	r	6	39.37	0.01	0.02	0.00		18.19	0.25			0.10	41.33	0.09	0.01	0.00		99.39		0.80
					6	0.17	0.01	0.01	0.00		0.36	0.04			0.02	0.32	0.02	0.01	0.00		0.18		0.00
OM10_Gid_A24	1431	LG	Pl		15	46.97	0.02	33.23		0.48		0.01				0.03	17.10	1.83	0.02		99.66	83.64	0.00
					15	0.25	0.01	0.19		0.08		0.02				0.01	0.26	0.12	0.01		0.29	1.05	0.00
OM10_Gid_A25	1210	LG	Cpx	c	15	52.94	0.39	2.27	0.19	0.00	5.40	0.19			0.00	16.50	22.31	0.27	0.01		100.46		0.84
					15	0.60	0.09	0.37	0.10	0.00	0.28	0.04			0.00	0.29	0.72	0.04	0.01		0.50		0.01
			Cpx	r	4	53.01	0.42	1.93	0.25	0.00	5.03	0.15			0.00	16.47	22.64	0.29	0.01		100.20		0.85
					4	0.58	0.11	0.34	0.04	0.00	0.28	0.05			0.00	0.24	0.36	0.05	0.00		0.44		0.01
			Ol	c	15	39.66	0.01	0.01	0.00		18.51	0.28			0.14	42.76	0.05	0.01	0.00		101.43		0.80
					15	0.19	0.01	0.01	0.00		0.24	0.05			0.03	0.25	0.02	0.01	0.01		0.36		0.00
			Ol	r	6	39.45	0.01	0.02	0.00		17.77	0.23			0.12	43.35	0.06	0.01	0.00		101.02		0.81
					6	0.50	0.01	0.01	0.00		0.27	0.04			0.03	0.75	0.03	0.01	0.00		0.63		0.00
			Opx		3	55.09	0.16	1.79	0.03	0.00	13.03	0.32			0.00	29.19	0.90	0.02	0.01		100.53		0.80
					3	0.10	0.00	0.01	0.02	0.00	0.22	0.04			0.00	0.12	0.03	0.01	0.00		0.34		0.00
			Pl		15	47.19	0.02	33.57		0.46		0.02				0.02	16.82	1.95	0.02		100.04	82.56	0.00
					15	0.22	0.01	0.15		0.06		0.02				0.01	0.16	0.09	0.01		0.25	0.69	0.00
OM10_Gid_A25_1a	1199	LG	Amph		10	43.63	3.54	11.49	0.38	0.00	9.15	0.05	0.23	0.09	0.00	15.75	11.84	2.45	0.39		101.09		0.59
					10	0.47	0.31	0.29	0.11	0.00	0.21	0.06	0.01	0.05	0.00	0.29	0.09	0.11	0.04		0.30		0.01
OM10_Gid_A26	1079	LG	Cpx	c	20	51.92	0.54	2.58	0.15	0.00	6.27	0.16			0.00	16.19	21.87	0.31	0.00		100.00		0.82
					20	0.37	0.08	0.34	0.11	0.00	0.31	0.04			0.01	0.23	0.44	0.04	0.00		0.35		0.01
			Cpx	r	8	52.13	0.64	2.22	0.11	0.00	6.22	0.17			0.00	16.17	22.08	0.32	0.01		100.08		0.82
					8	0.22	0.05	0.15	0.07	0.00	0.23	0.03			0.01	0.12	0.29	0.04	0.00		0.26		0.01
			Ol	c	10	38.83	0.01	0.00	0.00		21.44	0.30			0.09	40.42	0.05	0.02	0.00		101.18		0.77
					10	0.19	0.01	0.00	0.00		0.24	0.05			0.04	0.22	0.02	0.02	0.00		0.52		0.00
			Ol	r	4	38.70	0.01	0.01	0.00		21.45	0.30			0.11	40.56	0.07	0.02	0.01		101.22		0.77
					4	0.07	0.00	0.00	0.00		0.24	0.03			0.05	0.15	0.01	0.02	0.01		0.28		0.00
			Pl		15	47.80	0.03	32.69		0.55		0.02				0.03	16.45	2.30	0.02		99.84	79.69	0.00
					15	0.27	0.01	0.17		0.08		0.02				0.01	0.23	0.08	0.01		0.33	0.74	0.00

[1] Depth_calculated height above MOHO
[2] Lithology: SD = Sheeted dike; VG = Varitextured gabbro; FG = Foliated gabbro; MG = Metagabbro; FG = Foliated gabbro
[3] Mineral analysed
[4] Qualifier: r = rim; c = core
[5] Number of analyses
[6] Anorthite content of plagioclase
[7] XMg for Cpx, Opx, and Amph

Table 9. continued

Sample	Depth[1]	Litho.[2]	Min[3]	Qual[4]	No[5]	SiO₂	TiO₂	Al₂O₃	Cr₂O₃	Fe₂O₃	FeO	MnO	Cl	F	NiO	MgO	CaO	Na₂O	K₂O	V₂O₃	Total	An[6]	XMg[7]
OM10_Gid_A27	804	LG	Cpx	c	18	51.17	0.52	2.42	0.17	0.00	5.36	0.13			0.00	14.87	22.07	0.29	0.01		97.00		0.83
					18	*0.49*	*0.03*	*0.27*	*0.07*	*0.00*	*0.25*	*0.04*			*0.00*	*0.29*	*0.55*	*0.02*	*0.01*		*0.73*		*0.01*
			Cpx	r	3	51.08	0.54	2.18	0.20	0.00	5.26	0.18			0.00	14.64	21.76	0.31	0.01		96.17		0.83
					3	*0.10*	*0.04*	*0.17*	*0.03*		*0.18*	*0.04*					*0.60*	*0.04*	*0.01*		*0.06*		*0.01*
			Pl		21	46.38	0.03	32.99	0.03	0.45	0.18	0.04				0.02	16.72	1.99	0.02		98.58	82.24	0.00
					21	*0.16*	*0.01*	*0.17*		*0.09*		*0.01*				*0.03*	*0.17*	*0.06*	*0.01*		*0.28*	*0.44*	*0.00*
OM10_Gid_A28	696	LG	Pl		9	45.92	0.02	33.19		0.49						0.03	16.88	1.90	0.02		98.40	83.01	0.00
					9	*0.35*	*0.01*	*0.14*		*0.04*		*0.03*				*0.01*	*0.13*	*0.05*	*0.00*		*0.55*	*0.40*	*0.00*
OM10_Gid_A29	545	LG	Cpx	c	16	52.81	0.49	2.60	0.24	0.00	5.71	0.16			0.00	16.27	21.68	0.28	0.00		100.24		0.84
					16	*0.33*	*0.03*	*0.08*	*0.04*	*0.00*	*0.17*	*0.05*			*0.00*	*0.26*	*0.43*	*0.04*	*0.00*		*0.43*		*0.00*
			Cpx	r	12	53.02	0.51	2.29	0.21	0.00	5.44	0.15			0.00	16.25	22.39	0.27	0.00		100.53		0.84
					12	*0.37*	*0.06*	*0.22*	*0.06*	*0.00*	*0.24*	*0.03*			*0.00*	*0.23*	*0.53*	*0.04*	*0.00*		*0.55*		*0.01*
			Pl	c	20	47.28	0.02	33.78		0.43		0.02				0.02	17.09	1.88	0.01		100.49	83.35	0.00
					20	*0.67*	*0.01*	*0.40*		*0.08*		*0.02*				*0.03*	*0.39*	*0.26*	*0.01*		*0.74*	*2.21*	*0.00*
			Pl	r	12	47.18	0.01	34.00		0.46		0.02				0.01	17.31	1.79	0.01		100.75	84.23	0.00
					12	*0.65*	*0.01*	*0.41*		*0.07*		*0.02*				*0.02*	*0.43*	*0.28*	*0.00*		*0.56*	*2.44*	*0.00*
OM10_Gid_A30	257	LG	Cpx	c	15	52.06	0.42	2.96	0.70	0.00	5.05	0.12			0.00	16.05	21.44	0.28	0.01		99.08		0.85
					15	*0.11*	*0.04*	*0.08*	*0.07*	*0.00*	*0.20*	*0.04*			*0.00*	*0.36*	*0.66*	*0.03*	*0.00*		*0.32*		*0.00*
			Cpx	r	5	52.61	0.46	2.45	0.64	0.00	5.02	0.15			0.00	15.99	21.60	0.25	0.01		99.19		0.85
					5	*0.19*	*0.04*	*0.15*	*0.05*	*0.00*	*0.21*	*0.03*			*0.00*	*0.27*	*0.27*	*0.02*	*0.01*		*0.40*		*0.01*
			Ol	c	15	40.02	0.01	0.01	0.00	0.00	16.93	0.22			0.16	42.94	0.05	0.01	0.00		100.35		0.82
					15	*0.22*	*0.01*	*0.01*	*0.00*	*0.00*	*0.31*	*0.05*			*0.03*	*0.44*	*0.01*	*0.01*	*0.00*		*0.42*		*0.00*
			Ol	r	5	40.17	0.01	0.02	0.00	0.00	16.63	0.36			0.16	42.80	0.20	0.02	0.00		100.35		0.82
					5	*0.42*	*0.01*	*0.01*	*0.00*	*0.00*	*0.72*	*0.19*			*0.04*	*0.28*	*0.23*	*0.00*	*0.01*		*0.17*		*0.01*
			Pl		14	46.51	0.02	34.07		0.42		0.02				0.02	17.38	1.61	0.02		100.02	85.60	0.00
					14	*0.35*	*0.01*	*0.13*		*0.06*		*0.02*				*0.02*	*0.21*	*0.05*	*0.01*		*0.55*	*0.36*	*0.00*
OM10_Gid_A31	123	LG	Cpx	c	13	52.17	0.53	2.57	0.08	0.00	6.59	0.17			0.00	16.63	20.66	0.27	0.00		99.68		0.82
					13	*0.50*	*0.03*	*0.11*	*0.04*	*0.00*	*0.31*	*0.04*			*0.00*	*0.47*	*0.63*	*0.03*	*0.00*		*0.52*		*0.01*
			Cpx	r	6	52.68	0.50	2.08	0.07	0.00	5.82	0.19			0.00	16.43	21.89	0.25	0.00		99.92		0.83
					6	*0.30*	*0.03*	*0.08*	*0.03*	*0.00*	*0.36*	*0.03*			*0.00*	*0.29*	*0.80*	*0.03*	*0.00*		*0.39*		*0.01*
			Ol	c	14	39.08	0.01	0.01	0.00	0.00	20.19	0.30			0.07	40.60	0.03	0.01	0.00		100.29		0.78
					14	*0.22*	*0.01*	*0.01*	*0.00*	*0.00*	*0.34*	*0.05*			*0.03*	*0.13*	*0.01*	*0.01*	*0.01*		*0.42*		*0.00*
			Ol	r	6	39.09	0.01	0.01	0.00	0.00	20.13	0.28			0.07	40.42	0.10	0.01	0.01		100.13		0.78
					6	*0.16*	*0.01*	*0.01*		*0.00*	*0.34*	*0.02*			*0.04*	*0.37*	*0.08*	*0.01*	*0.01*		*0.59*		*0.00*
			Pl		15	48.97	0.04	32.03		0.55		0.02				0.05	15.51	2.74	0.01		99.84	75.74	0.00
					15	*0.21*	*0.01*	*0.12*		*0.17*		*0.02*				*0.03*	*0.14*	*0.06*	*0.01*		*0.24*	*0.52*	*0.00*
OM10_Gid_A32	49	LG	Cpx	c	23	52.85	0.24	2.18	0.12	0.00	5.61	0.17			0.00	17.49	21.15	0.33	0.00		100.14		0.85
					23	*0.26*	*0.02*	*0.17*	*0.04*	*0.00*	*0.51*	*0.04*			*0.00*	*0.65*	*1.12*	*0.04*	*0.00*		*0.40*		*0.00*
			Cpx	r	8	52.38	0.24	2.28	0.12	0.00	5.27	0.16			0.00	17.57	21.45	0.30	0.01		99.79		0.86
					8	*1.13*	*0.03*	*0.64*	*0.04*	*0.00*	*0.55*	*0.04*			*0.00*	*0.82*	*1.16*	*0.04*	*0.00*		*0.90*		*0.01*
			Ol	c	25	39.35	0.00	0.01	0.00	0.00	18.76	0.26			0.10	42.81	0.03	0.01	0.00		101.34		0.80
					25	*0.21*	*0.01*	*0.01*	*0.00*	*0.00*	*0.34*	*0.04*			*0.04*	*0.25*	*0.02*	*0.02*	*0.00*		*0.44*		*0.00*
			Ol	r	10	39.45	0.01	1.07	0.00	0.00	17.90	0.25			0.11	41.47	0.57	0.07	0.00		100.88		0.81
					10	*0.46*	*0.01*	*2.70*	*0.00*	*0.00*	*1.45*	*0.04*			*0.03*	*3.36*	*1.32*	*0.15*	*0.00*		*0.41*		*0.00*
			Opx		13	55.56	0.10	1.06	0.07	0.00	11.98	0.28			0.00	30.53	0.88	0.01	0.00		100.48		0.82
					13	*0.25*	*0.03*	*0.20*	*0.03*	*0.00*	*0.30*	*0.04*			*0.00*	*0.24*	*0.10*	*0.01*	*0.01*		*0.31*		*0.00*
			Pl		18	49.81	0.01	31.57		0.33		0.01				0.03	14.96	3.38	0.01		100.08	70.93	0.00
					18	*0.25*	*0.01*	*0.24*		*0.05*		*0.02*				*0.03*	*0.23*	*0.13*	*0.01*		*0.16*	*1.02*	*0.00*

[1] Depth_calculated height above MOHO
[2] Lithology: SD = Sheeted dike; VG = Varitextured gabbro; MG = Metagabbro; FG = Foliated gabbro
[3] Mineral analysed
[4] Qualifier: r = rim; c = core
[5] Number of analyses
[6] Anorthite content of plagioclase
[7] XMg for Cpx, Opx, and Amph

Table 9. continued

Sample	Depth[1]	Litho.[2]	Min[3]	Qual[4]	No[5]	SiO$_2$	TiO$_2$	Al$_2$O$_3$	Cr$_2$O$_3$	Fe$_2$O$_3$	FeO	MnO	Cl	F	NiO	MgO	CaO	Na$_2$O	K$_2$O	V$_2$O$_3$	Total	An[6]	XMg[7]
OM11_Gid_A21a	2124	LG	Cpx		19	51.16	0.83	2.50	0.03	0.00	8.70	0.24			0.00	15.71	20.94	0.33	0.00		100.45		0.76
					19	*0.50*	*0.14*	*0.37*	*0.05*	*0.00*	*0.51*	*0.04*			*0.00*	*0.41*	*0.81*	*0.06*	*0.01*		*0.44*		*0.01*
			Ol	c	8	37.55	0.01	0.02	0.00	0.00	27.15	0.46			0.05	36.64	0.06	0.01	0.00		101.95		0.71
					8	*0.20*	*0.01*	*0.01*		*0.00*	*0.23*	*0.04*			*0.03*	*0.31*	*0.01*	*0.01*	*0.01*		*0.47*		*0.00*
			Ol	r	8	37.85	0.01	0.01	0.00	0.00	26.95	0.41			0.07	36.50	0.07	0.00	0.00		101.87		0.71
					8	*0.30*	*0.01*	*0.01*			*0.21*	*0.05*			*0.04*	*0.25*	*0.02*	*0.01*	*0.00*		*0.42*		*0.00*
			Pl	c	10	49.42	0.05	31.13		0.47		0.02				0.01	14.93	3.19	0.02		99.19	72.04	0.00
					10	*0.68*	*0.01*	*0.25*		*0.07*		*0.02*				*0.03*	*0.31*	*0.16*	*0.01*		*0.52*	*1.44*	*0.00*
			Pl	r	10	48.12	0.03	32.00		0.55		0.02				0.00	15.93	2.70	0.02		99.30	76.48	0.00
					10	*1.07*	*0.02*	*0.68*		*0.10*		*0.03*				*0.00*	*0.81*	*0.42*	*0.01*		*0.65*	*3.70*	*0.00*
OM11_Gid_A21b	2124	LG	Cpx	c	11	51.27	0.77	2.73	0.04	0.00	8.24	0.20			0.00	14.57	21.82	0.37	0.01		100.02		0.76
					11	*0.24*	*0.03*	*0.13*	*0.04*		*0.27*	*0.03*			*0.00*	*0.20*	*0.47*	*0.04*	*0.01*		*0.33*		*0.01*
			Cpx	r	5	52.48	0.65	2.67	0.06	0.00	7.83	0.20			0.00	14.53	21.61	0.42	0.01		100.46		0.77
					5	*1.27*	*0.08*	*0.44*	*0.04*		*0.30*	*0.03*				*0.95*	*0.33*	*0.16*	*0.01*		*0.25*		*0.01*
			Pl	c	14	49.25	0.04	31.98		0.50		0.01				0.01	15.59	2.93	0.02		100.29	74.54	0.00
					14	*0.23*	*0.01*	*0.25*		*0.04*		*0.02*				*0.01*	*0.26*	*0.16*	*0.01*		*0.36*	*1.21*	*0.00*
			Pl	r	7	49.09	0.03	32.15		0.52		0.01				0.06	15.76	2.75	0.03		100.34	75.89	0.00
					7	*0.60*	*0.03*	*0.54*		*0.08*		*0.01*				*0.33*	*0.17*	*0.01*			*0.19*	*1.49*	*0.00*
			Sp		4	0.01	47.35	0.02	0.33	1.92	45.26	2.91			0.00	0.14	0.07	0.00	0.00	1.21	99.23		0.00
					4	*0.01*	*2.42*	*0.01*	*0.15*	*2.06*	*3.81*	*0.07*			*0.00*	*0.02*	*0.02*	*0.00*	*0.00*	*0.56*	*0.30*		
OM11_Gid_A22	1936	LG	Cpx		20	51.55	0.48	2.48	0.15	0.00	5.70	0.15			0.00	16.34	21.95	0.28	0.00		99.10		0.84
					20	*0.44*	*0.06*	*0.34*	*0.05*		*0.29*	*0.04*			*0.00*	*0.39*	*0.62*	*0.03*	*0.01*		*0.61*		*0.01*
			Ol	c	10	38.71	0.01	0.00	0.00	0.00	19.15	0.28			0.11	42.25	0.04	0.01	0.00		100.56		0.80
					10	*0.26*	*0.01*	*0.00*			*0.23*	*0.06*			*0.03*	*0.21*	*0.02*	*0.01*	*0.00*		*0.47*		*0.01*
			Ol	r	10	38.90	0.01	0.00	0.00	0.00	18.87	0.28			0.10	42.21	0.03	0.01	0.00		100.42		0.80
					10	*0.25*	*0.01*	*0.01*			*0.44*	*0.04*			*0.02*	*0.54*	*0.01*	*0.02*	*0.00*		*0.63*		*0.01*
			Pl	c	15	46.51	0.02	33.32		0.55		0.02				0.00	17.14	1.85	0.02		99.36	83.61	0.00
					15	*0.28*	*0.02*	*0.26*		*0.12*		*0.01*				*0.00*	*0.21*	*0.10*	*0.02*		*0.42*	*0.85*	*0.00*
			Pl	r	5	45.92	0.03	33.32		0.53		0.03				0.00	17.20	1.79	0.01		98.78	84.06	0.00
					5	*0.41*	*0.01*	*0.21*		*0.05*		*0.02*					*0.17*	*0.11*	*0.01*		*0.68*	*0.76*	
OM11_Gid_A26	930	LG	Cpx		20	51.57	0.60	2.46	0.20	0.00	5.92	0.14			0.00	16.54	21.86	0.30	0.00		99.58		0.83
					20	*0.40*	*0.11*	*0.33*	*0.08*		*0.39*	*0.05*			*0.00*	*0.40*	*0.74*	*0.04*	*0.00*		*0.41*		*0.01*
			Ol	c	10	38.67	0.01	0.01	0.00	0.00	20.08	0.28			0.10	41.68	0.06	0.01	0.00		100.89		0.79
					10	*0.27*	*0.01*	*0.01*			*0.24*	*0.04*			*0.04*	*0.41*	*0.02*	*0.01*	*0.00*		*0.54*		*0.01*
			Ol	r	10	38.55	0.01	0.02	0.00	0.00	20.18	0.32			0.08	41.41	0.06	0.00	0.00		100.63		0.79
					10	*0.33*	*0.01*	*0.02*			*0.52*	*0.04*			*0.03*	*0.62*	*0.02*	*0.00*	*0.00*		*0.59*		*0.01*
			Pl	c	14	47.21	0.03	32.70		0.52		0.02				0.00	16.59	2.17	0.03		99.22	80.75	0.00
					14	*0.44*	*0.02*	*0.30*		*0.08*		*0.02*				*0.01*	*0.24*	*0.15*	*0.02*		*0.58*	*1.25*	*0.00*
			Pl	r	5	47.05	0.04	33.06		0.47		0.03				0.00	16.71	2.11	0.02		99.45	81.33	0.00
					5	*0.41*	*0.01*	*0.21*		*0.05*		*0.03*					*0.14*	*0.09*	*0.01*		*0.34*	*0.74*	
OM11_Gid_A27	816	LG	Cpx		19	51.17	0.52	2.54	0.14	0.00	5.57	0.17			0.00	16.28	22.06	0.28	0.00		98.74		0.84
					19	*0.31*	*0.03*	*0.12*	*0.06*		*0.15*	*0.05*			*0.00*	*0.28*	*0.36*	*0.03*	*0.00*		*0.57*		
			Ol	c	10	38.10	0.01	0.01	0.00	0.00	18.94	0.27			0.10	41.74	0.05	0.01	0.00		99.24		0.80
					10	*0.49*	*0.01*	*0.01*			*0.19*	*0.05*			*0.03*	*0.42*	*0.01*	*0.01*	*0.00*		*0.95*		
			Ol	r	8	38.45	0.00	0.01	0.00	0.00	18.50	0.26			0.11	42.27	0.08	0.01	0.00		99.70		0.80
					8	*0.47*	*0.00*	*0.01*			*0.23*	*0.04*			*0.04*	*0.64*	*0.02*	*0.01*	*0.00*		*0.86*		
			Pl	c	15	46.42	0.02	33.07		0.52		0.01				0.00	17.01	1.88	0.02		98.90	83.23	0.00
					15	*0.30*	*0.02*	*0.17*		*0.07*		*0.02*				*0.00*	*0.10*	*0.08*	*0.01*		*0.44*	*0.67*	*0.00*
			Pl	r	4	46.25	0.02	33.28		0.72		0.03				0.00	17.18	1.78	0.01		99.19	84.12	0.00
					4	*0.21*	*0.01*	*0.37*		*0.06*		*0.02*				*0.00*	*0.17*	*0.03*	*0.01*		*0.49*	*0.14*	*0.00*

[1] Depth_calculated height above MOHO
[2] Lithology: SD = Sheeted dike; VG = Varitextured gabbro; FG = Foliated gabbro; MG = Metagabbro; FG = Foliated gabbro
[3] Mineral analysed
[4] Qualifier: r = rim; c = core
[5] Number of analyses
[6] Anorthite content of plagioclase
[7] XMg for Cpx, Opx, and Amph

Table 9. continued

Sample	Depth[1]	Litho.[2]	Min[3]	Qual[4]	No[5]	SiO₂	TiO₂	Al₂O₃	Cr₂O₃	Fe₂O₃	FeO	MnO	Cl	F	NiO	MgO	CaO	Na₂O	K₂O	V₂O₃	Total	An[6]	XMg[7]
OM12_Gid_025	1197	LG	Cpx	c	21	52.90	0.44	2.38	0.34	0.00	5.26	0.13			0.00	16.53	22.35	0.30	0.01		100.64		0.85
						0.39	*0.07*	*0.30*	*0.14*	*0.00*	*0.25*	*0.03*			*0.00*	*0.32*	*0.71*	*0.04*	*0.01*		*0.36*		*0.01*
			Cpx	r	9	52.93	0.49	2.12	0.37	0.00	5.04	0.13			0.00	16.58	22.53	0.29	0.00		100.48		0.85
						0.36	*0.05*	*0.19*	*0.07*	*0.00*	*0.30*	*0.03*			*0.00*	*0.26*	*0.50*	*0.04*	*0.00*		*0.44*		*0.01*
			Ol		28	39.58	0.01	0.01	0.00	0.00	17.98	0.25			0.14	43.24	0.04	0.01	0.00		101.26		0.81
						0.37	*0.01*	*0.02*	*0.00*		*0.23*	*0.04*			*0.03*	*0.33*	*0.01*	*0.01*	*0.00*		*0.49*		*0.00*
			Pl	c	20	46.81	0.02	33.99		0.48		0.01				0.01	17.54	1.78	0.02		100.65	84.41	0.00
						0.37	*0.01*	*0.25*		*0.07*		*0.02*				*0.01*	*0.17*	*0.13*	*0.01*		*0.36*	*1.07*	*0.00*
			Pl	r	7	47.11	0.03	34.10		0.48		0.02				0.01	17.49	1.79	0.02		101.05	84.27	0.00
						0.44	*0.02*	*0.32*		*0.11*		*0.02*				*0.01*	*0.16*	*0.07*	*0.00*		*0.75*	*0.50*	*0.00*
OM12_Gid_026	1231	LG	Cpx	c	15	51.40	0.45	2.78	0.45	0.00	5.71	0.15			0.00	16.26	21.71	0.30	0.00		99.22		0.84
						0.74	*0.08*	*0.40*	*0.23*	*0.00*	*0.22*	*0.07*			*0.00*	*0.62*	*0.45*	*0.05*	*0.00*		*0.61*		*0.01*
			Cpx	r	8	51.33	0.74	2.69	0.44	0.00	6.07	0.16			0.00	15.76	21.63	0.36	0.01		99.19		0.82
						0.40	*0.09*	*0.14*	*0.08*	*0.00*	*0.23*	*0.04*				*0.73*		*0.03*	*0.02*		*0.68*		*0.01*
			Pl	c	15	47.11	0.01	32.90		0.48		0.00				0.00	16.70	2.10	0.03		99.34	81.31	0.00
						0.36	*0.01*	*0.26*		*0.06*		*0.00*					*0.31*	*0.11*	*0.01*		*0.63*	*0.97*	*0.00*
			Pl	r	8	47.21	0.01	33.00		0.50		0.00				0.00	16.69	2.13	0.02		99.57	81.10	0.00
						0.26	*0.02*	*0.24*		*0.04*		*0.00*					*0.27*	*0.13*	*0.02*		*0.36*	*1.04*	*0.00*
OM12_Gid_027	1222	LG	Amph		18	41.79	3.60	10.98	0.00	0.00	10.99	0.10			0.00	14.60	11.47	2.51	0.31		98.68		0.51
						0.54	*0.34*	*0.11*	*0.00*	*0.00*	*0.29*	*0.04*			*0.00*	*0.16*	*0.16*	*0.08*	*0.02*		*0.52*		*0.02*
			Amph		10	42.48	3.67	11.09	0.07	0.00	11.25	0.12			0.00	14.58	11.28	2.61	0.31		99.88		0.58
						0.50	*0.44*	*0.14*	*0.11*	*0.00*	*0.13*	*0.02*			*0.00*	*0.27*	*0.14*	*0.10*	*0.03*		*0.49*		*0.01*
			Cpx	c	15	51.07	0.63	2.56	0.16	0.00	6.99	0.19			0.00	15.73	21.42	0.35	0.00		99.10		0.80
						0.44	*0.08*	*0.17*	*0.10*	*0.00*	*0.38*	*0.03*			*0.00*	*0.42*	*0.81*	*0.05*	*0.00*		*0.53*		*0.01*
			Cpx	r	9	51.08	0.77	2.52	0.11	0.00	7.02	0.20			0.00	15.71	21.31	0.37	0.00		99.12		0.80
						0.43	*0.05*	*0.05*	*0.05*	*0.00*	*0.34*	*0.03*			*0.00*	*0.25*	*0.54*	*0.03*	*0.00*		*0.64*		*0.01*
			Ol		26	37.46	0.01	0.01	0.00	0.00	22.87	0.31			0.07	39.46	0.04	0.01	0.00		100.24		0.75
						0.39	*0.01*	*0.01*	*0.00*		*0.42*	*0.05*			*0.03*	*0.49*	*0.01*	*0.01*	*0.00*		*0.56*		
			Opx		15	53.30	0.40	1.29	0.05	0.00	14.52	0.33			0.00	27.79	1.45	0.03	0.00		99.15		0.77
						0.38	*0.02*	*0.04*	*0.04*		*0.19*	*0.05*			*0.00*	*0.18*	*0.07*	*0.02*	*0.00*		*0.55*		
			Pl	c	34	47.86	0.01	32.14		0.56		0.00	0.24	0.06		0.00	16.01	2.53	0.04		99.16	77.62	0.00
						0.42	*0.02*	*0.29*		*0.08*		*0.02*	*0.02*	*0.05*			*0.30*	*0.14*	*0.03*		*0.53*	*1.26*	
			Pl	r	11	47.76	0.01	32.05		0.65		0.00	0.23	0.13		0.03	15.97	2.53	0.03		99.03	77.60	0.00
						0.39	*0.03*	*0.29*		*0.10*		*0.00*	*0.03*	*0.02*		*0.06*	*0.29*	*0.09*	*0.01*		*0.46*	*0.92*	
OM12_Gid_028	564	LG	Cpx	c	32	52.34	0.54	2.75	0.21	0.00	5.44	0.13			0.00	16.46	22.08	0.21	0.01		100.17		0.84
						0.52	*0.03*	*0.26*	*0.05*	*0.00*	*0.30*	*0.05*			*0.00*	*0.44*	*0.58*	*0.07*	*0.02*		*0.70*		*0.00*
			Pl		28	43.85	0.00	35.54		0.01		0.00				0.00	19.69	0.43	0.00		99.53	96.20	0.00
						0.86	*0.00*	*0.65*		*0.04*		*0.02*					*0.39*	*0.22*	*0.00*		*1.14*	*1.92*	
OM12_Gid_029	631	LG	Cpx	r	5	52.61	0.49	2.21	0.26	0.00	5.60	0.17			0.00	16.72	21.80	0.25	0.01		100.11		0.84
						0.11	*0.05*	*0.10*	*0.05*	*0.00*	*0.24*	*0.04*			*0.00*	*0.31*	*0.61*	*0.05*	*0.01*		*0.41*		*0.00*
			Cpx	c	17	52.49	0.53	2.52	0.32	0.00	5.54	0.15			0.00	16.41	22.19	0.23	0.01		100.38		0.84
						0.53	*0.02*	*0.19*	*0.04*	*0.00*	*0.33*	*0.04*			*0.00*	*0.36*	*0.53*	*0.11*	*0.01*		*0.44*		*0.01*
			Pl	r	5	47.41	0.00	33.25		0.38		0.00				0.00	17.12	1.99	0.01		100.17	82.56	0.00
						0.39	*0.00*	*0.27*		*0.03*		*0.00*					*0.25*	*0.21*	*0.01*		*0.45*	*1.62*	
			Pl	c	38	47.24	0.00	33.00		0.42		0.00				0.00	17.10	1.96	0.01		99.74	82.74	0.00
						0.64	*0.01*	*0.40*		*0.06*		*0.00*					*0.47*	*0.27*	*0.02*		*0.60*	*2.23*	
OM12_Gid_030	631	LG	Amph		28	43.24	0.16	13.00	0.00	0.00	10.66	0.14	0.07	0.01	0.00	14.53	12.55	2.44	0.04		98.90		0.51
						0.90	*0.09*	*0.86*	*0.00*	*0.00*	*0.90*	*0.03*	*0.03*	*0.03*	*0.00*	*0.57*	*0.30*	*0.18*	*0.01*		*0.88*		*0.03*
			Pl		13	43.17	0.00	35.28		0.06		0.00				0.06	19.63	0.46	0.00		98.66	95.95	0.00
						0.61	*0.00*	*0.67*		*0.15*		*0.00*				*0.22*	*0.43*	*0.26*	*0.00*		*0.87*	*2.24*	

[1] Depth_calculated height above MOHO
[2] Lithology: SD = Sheeted dike; VG = Varitextured gabbro; FG = Foliated gabbro; MG = Metagabbro; FG = Foliated gabbro
[3] Mineral analysed
[4] Qualifier: r = rim; c = core
[5] Number of analyses
[6] Anorthite content of plagioclase
[7] XMg for Cpx, Opx, and Amph

Table 9. continued

Sample	Depth[1]	Litho.[2]	Min[3]	Qual[4]	No[5]	SiO$_2$	TiO$_2$	Al$_2$O$_3$	Cr$_2$O$_3$	Fe$_2$O$_3$	FeO	MnO	Cl	F	NiO	MgO	CaO	Na$_2$O	K$_2$O	V$_2$O$_3$	Total	An[6]	XMg[7]
OM12_Gid_025	1197	LG	Cpx	c	21	52.90	0.44	2.38	0.34	0.00	5.26	0.13			0.00	16.53	22.35	0.30	0.01		100.64		0.85
					21	*0.39*	*0.07*	*0.30*	*0.14*		*0.25*	*0.03*			*0.00*	*0.32*	*0.71*	*0.04*	*0.01*		*0.36*		*0.01*
			Cpx		9	52.93	0.49	2.12	0.37	0.00	5.04	0.13			0.00	16.58	22.53	0.29	0.00		100.48		0.85
					9	*0.36*	*0.05*	*0.19*	*0.07*		*0.30*	*0.03*			*0.00*	*0.26*	*0.50*	*0.04*	*0.00*		*0.44*		*0.01*
			Ol		28	39.58	0.01	0.01	0.00	0.00	17.98	0.25			0.14	43.24	0.04	0.01	0.00		101.26		0.81
					28	*0.37*	*0.01*	*0.02*	*0.00*		*0.23*	*0.04*			*0.03*	*0.33*	*0.01*	*0.01*	*0.00*		*0.49*		*0.00*
			Pl	c	20	46.81	0.02	33.99		0.48		0.01				0.01	17.54	1.78	0.02		100.65	84.41	0.00
					20	*0.26*	*0.01*	*0.25*		*0.07*		*0.02*				*0.01*	*0.17*	*0.13*	*0.01*		*0.36*	*1.07*	*0.00*
			Pl	r	7	47.11	0.03	34.10		0.48		0.02				0.01	17.49	1.79	0.02		101.05	84.27	0.00
					7	*0.44*	*0.02*	*0.32*		*0.11*		*0.02*				*0.01*	*0.16*	*0.07*	*0.00*		*0.75*	*0.50*	*0.00*
OM12_Gid_026	1231	LG	Cpx	c	15	51.40	0.45	2.78	0.45	0.00	5.71	0.15			0.00	16.26	21.71	0.30	0.00		99.22		0.84
					15	*0.74*	*0.08*	*0.40*	*0.23*		*0.22*	*0.07*			*0.00*	*0.62*	*0.45*	*0.05*	*0.00*		*0.61*		*0.01*
			Cpx	r	8	51.33	0.74	2.69	0.44	0.00	6.07	0.16			0.00	15.76	21.63	0.36	0.01		99.19		0.82
					8	*0.40*	*0.09*	*0.14*	*0.08*		*0.23*	*0.04*			*0.00*	*0.73*	*0.73*	*0.03*	*0.02*		*0.68*		*0.01*
			Pl	c	15	47.11	0.01	32.90		0.48		0.00				0.00	16.70	2.10	0.03		99.34	81.31	0.00
					15	*0.36*	*0.01*	*0.26*		*0.06*		*0.00*				*0.00*	*0.31*	*0.11*	*0.01*		*0.63*	*0.97*	*0.00*
			Pl	r	8	47.21	0.01	33.00		0.50		0.00				0.00	16.69	2.13	0.02		99.57	81.10	0.00
					8	*0.26*	*0.02*	*0.24*		*0.04*		*0.00*				*0.00*	*0.27*	*0.13*	*0.02*		*0.36*	*1.04*	*0.00*
OM12_Gid_027	1222	LG	Amph		18	41.79	3.60	10.98	0.00	0.00	10.99	0.10			0.00	14.60	11.47	2.51	0.31		98.68		0.51
					18	*0.54*	*0.34*	*0.11*		*0.29*	*0.04*	*0.00*			*0.16*	*0.16*	*0.08*	*0.02*			*0.52*		*0.02*
			Amph		10	42.48	3.67	11.09	0.07	0.00	11.25	0.12			0.00	14.58	11.28	2.61	0.31		99.88		0.58
					10	*0.50*	*0.44*	*0.14*	*0.11*		*0.13*	*0.02*			*0.00*	*0.27*	*0.14*	*0.10*	*0.03*		*0.49*		*0.01*
			Cpx	c	15	51.07	0.63	2.56	0.16	0.00	6.99	0.19			0.00	15.73	21.42	0.35	0.00		99.10		0.80
					15	*0.44*	*0.08*	*0.17*	*0.10*		*0.38*	*0.03*			*0.00*	*0.42*	*0.81*	*0.05*	*0.00*		*0.53*		*0.01*
			Cpx	r	9	51.08	0.77	2.52	0.11	0.00	7.02	0.20			0.00	15.71	21.31	0.37	0.00		99.12		0.80
					9	*0.43*	*0.05*	*0.11*	*0.05*		*0.34*	*0.03*			*0.00*	*0.25*	*0.54*	*0.03*	*0.00*		*0.64*		*0.01*
			Ol		26	37.46	0.01	0.01	0.00	0.00	22.87	0.31			0.07	39.46	0.04	0.01	0.00		100.24		0.75
					26	*0.39*	*0.01*	*0.01*	*0.00*		*0.42*	*0.05*			*0.03*	*0.49*	*0.01*	*0.01*	*0.00*		*0.56*		*0.01*
			Opx		15	53.30	0.40	1.29	0.05	0.00	14.52	0.33			0.00	27.79	1.45	0.03	0.00		99.15		0.77
					15	*0.38*	*0.02*	*0.04*	*0.04*		*0.19*	*0.05*			*0.00*	*0.18*	*0.07*	*0.02*	*0.00*		*0.55*		*0.00*
			Pl	c	34	47.86	0.01	32.14		0.56		0.00	0.24	0.06		0.00	16.01	2.53	0.04		99.16	77.62	0.00
					34	*0.42*	*0.02*	*0.29*		*0.08*		*0.02*	*0.02*	*0.05*		*0.00*	*0.30*	*0.14*	*0.03*		*0.53*	*1.26*	*0.00*
			Pl	r	11	47.76	0.01	32.05		0.65		0.00	0.23	0.13		0.03	15.97	2.53	0.03		99.03	77.60	0.00
					11	*0.39*	*0.03*	*0.29*		*0.10*		*0.00*	*0.03*	*0.02*		*0.06*	*0.29*	*0.09*	*0.01*		*0.46*	*0.92*	*0.00*
OM12_Gid_028	564	LG	Cpx	c	32	52.34	0.54	2.75	0.21	0.00	5.44	0.13			0.00	16.46	22.08	0.21	0.01		100.17		0.84
					32	*0.52*	*0.03*	*0.26*	*0.05*		*0.30*	*0.05*			*0.00*	*0.44*	*0.58*	*0.07*	*0.02*		*0.70*		*0.00*
			Pl		28	43.85	0.00	35.54		0.01		0.00				0.00	19.69	0.43	0.00		99.53	96.20	0.00
					28	*0.86*	*0.00*	*0.65*		*0.04*		*0.02*					*0.39*	*0.22*	*0.00*		*1.14*	*1.92*	*0.00*
OM12_Gid_029	631	LG	Cpx	r	5	52.61	0.49	2.21	0.26	0.00	5.60	0.17			0.00	16.72	21.80	0.25	0.01		100.11		0.84
					5	*0.11*	*0.05*	*0.10*	*0.05*		*0.24*	*0.04*			*0.00*	*0.31*	*0.61*	*0.05*	*0.01*		*0.41*		*0.00*
			Cpx	c	17	52.49	0.53	2.52	0.32	0.00	5.54	0.15			0.00	16.41	22.19	0.23	0.01		100.38		0.84
					17	*0.53*	*0.02*	*0.19*	*0.04*		*0.33*	*0.04*			*0.00*	*0.36*	*0.53*	*0.11*	*0.01*		*0.44*		*0.01*
			Pl	r	5	47.41	0.00	33.25		0.38		0.00				0.00	17.12	1.99	0.01		100.17	82.56	0.00
					5	*0.39*		*0.27*		*0.03*		*0.00*				*0.00*	*0.25*	*0.21*	*0.01*		*0.45*	*1.62*	*0.00*
			Pl	c	38	47.24	0.00	33.00		0.42		0.00				0.00	17.10	1.96	0.01		99.74	82.74	0.00
					38	*0.64*		*0.40*		*0.06*		*0.00*				*0.00*	*0.47*	*0.27*	*0.02*		*0.60*	*2.23*	*0.00*
OM12_Gid_030	631	LG	Amph		28	43.24	0.16	13.00	0.00	0.00	10.66	0.14	0.07	0.01	0.00	14.53	12.55	2.44	0.04		98.90		0.51
					28	*0.90*	*0.09*	*0.86*	*0.00*		*0.90*	*0.03*	*0.03*	*0.03*	*0.00*	*0.57*	*0.30*	*0.18*	*0.01*		*0.88*		*0.03*
			Pl		13	43.17	0.00	35.28	0.00	0.06		0.00			0.00	0.06	19.63	0.46	0.00		98.66	95.95	0.00
					13	*0.61*	*0.00*	*0.67*		*0.15*		*0.00*				*0.22*	*0.43*	*0.26*	*0.00*		*0.87*	*2.24*	*0.00*

[1] Depth_ calculated height above MOHO
[2] Lithology: SD = Sheeted dike; VG = Varitextured gabbro; FG = Foliated gabbro; MG = Metagabbro; FG = Foliated gabbro
3 Mineral analysed
[4] Qualifier: r = rim; c = core
[5] Number of analyses
[6] Anorthite content of plagioclase
[7] XMg for Cpx, Opx, and Amph

Table 9. continued

Sample	Depth[1]	Litho.[2]	Min[3]	Qual[4]	No[5]	SiO$_2$	TiO$_2$	Al$_2$O$_3$	Cr$_2$O$_3$	Fe$_2$O$_3$	FeO	MnO	Cl	F	NiO	MgO	CaO	Na$_2$O	K$_2$O	V$_2$O$_3$	Total	An[6]	XMg[7]
OM12_Gid_031	684	LG	Amph		16	44.44	0.12	12.36	0.00	0.00	11.29	0.16	0.00	0.00	0.00	13.96	12.71	2.03	0.04		99.17		0.51
						0.92	*0.03*	*0.85*	*0.00*	*0.00*	*0.40*	*0.03*	*0.00*	*0.00*	*0.00*	*0.52*	*0.17*	*0.17*	*0.01*		*0.61*		*0.02*
			Cpx	r	7	52.55	0.56	2.28	0.23	0.00	6.09	0.19				16.08	22.24	0.26	0.01		100.48		0.82
						0.42	*0.07*	*0.27*	*0.05*	*0.00*	*0.31*	*0.06*				*0.31*	*0.81*	*0.13*	*0.00*		*0.63*		*0.01*
			Cpx	c	36	51.94	0.55	2.82	0.24	0.00	6.19	0.16			0.00	15.85	21.96	0.25	0.01		99.97		0.82
						0.58	*0.06*	*0.43*	*0.05*	*0.00*	*0.43*	*0.04*			*0.00*	*0.68*	*0.87*	*0.09*	*0.01*		*0.90*		*0.01*
			Pl	r	6	47.73	0.00	32.85		0.43		0.00				0.00	16.69	2.27	0.00		99.97	80.23	0.00
						0.51	*0.00*	*0.16*		*0.09*		*0.00*				*0.00*	*0.55*	*0.21*	*0.01*		*0.93*	*1.87*	*0.00*
			Pl	c	53	48.19	0.01	32.66		0.49		0.00				0.01	16.61	2.21	0.00		100.18	80.61	0.00
						0.50	*0.02*	*0.28*		*0.09*		*0.00*				*0.04*	*0.19*	*0.13*	*0.01*		*0.79*	*0.98*	*0.00*
OM12_Gid_032	749	LG	Amph		14	44.17	1.95	10.62	0.00	0.00	7.67	0.08	0.06	0.05	0.00	16.81	12.07	2.44	0.17		98.16		0.51
						0.76	*0.93*	*0.50*	*0.00*	*0.00*	*0.14*	*0.05*	*0.01*	*0.04*	*0.00*	*0.81*	*0.16*	*0.27*	*0.03*		*0.47*		*0.02*
			Cpx	r	5	51.65	0.51	2.15	0.29	0.00	4.98	0.14			0.00	16.41	22.31	0.18	0.02		98.65		0.85
						0.31	*0.14*	*0.56*	*0.08*	*0.00*	*0.49*	*0.03*			*0.00*	*0.42*	*0.65*	*0.07*	*0.01*		*0.97*		*0.01*
			Cpx	c	22	50.82	0.52	3.17	0.28	0.00	5.45	0.13			0.00	16.75	20.61	0.39	0.01		98.14		0.85
						0.79	*0.13*	*1.56*	*0.12*	*0.00*	*0.47*	*0.04*			*0.00*	*0.94*	*3.45*	*0.39*	*0.02*		*1.52*		*0.01*
			Pl	r	6	46.79	0.02	33.09		0.35		0.00				0.00	16.86	2.02	0.03		99.15	82.09	0.00
						0.42	*0.02*	*0.24*		*0.09*		*0.00*				*0.00*	*0.32*	*0.17*	*0.05*		*0.71*	*1.63*	*0.00*
			Pl	c	21	46.86	0.00	33.11		0.33		0.00				0.00	16.96	2.03	0.01		99.31	82.16	0.00
						0.30	*0.01*	*0.18*		*0.06*		*0.00*				*0.00*	*0.19*	*0.12*	*0.01*		*0.38*	*0.97*	*0.00*
OM12_Gid_033	890	MG	Amph		5	43.70	3.02	11.11	0.36	0.00	9.05	0.09	0.12	0.16	0.00	16.15	12.05	2.59	0.10		100.60		0.61
					5	*0.19*	*0.16*	*0.06*	*0.02*	*0.00*	*0.22*	*0.05*	*0.01*	*0.02*	*0.00*	*0.11*	*0.06*	*0.08*	*0.01*		*0.22*		*0.02*
			Cpx		15	54.73	0.52	2.59	0.19	0.00	6.15	0.16			0.00	16.06	22.16	0.29	0.00		102.86		0.82
					15	*0.17*	*0.08*	*0.15*	*0.04*	*0.00*	*0.33*	*0.04*			*0.00*	*0.38*	*0.51*	*0.03*	*0.00*		*0.38*		*0.01*
			Pl		10	49.51	0.03	33.25		0.50		0.02				0.01	17.34	2.20	0.02		102.84	81.22	0.00
					10	*0.34*	*0.01*	*0.32*		*0.06*		*0.02*				*0.03*	*0.24*	*0.11*	*0.01*		*0.43*	*0.92*	*0.00*
OM12_Gid_034a	813	LG	Cpx	r	9	51.69	0.51	2.43	0.29	0.00	5.96	0.19			0.00	16.25	21.71	0.26	0.01		99.29		0.83
						0.32	*0.03*	*0.13*	*0.07*	*0.00*	*0.16*	*0.03*			*0.00*	*0.19*	*0.20*	*0.06*	*0.01*		*0.50*		*0.00*
			Cpx	c	39	51.42	0.46	2.66	0.33	0.00	6.05	0.15			0.00	16.15	21.70	0.27	0.01		99.20		0.83
						0.50	*0.06*	*0.27*	*0.09*	*0.00*	*0.30*	*0.05*			*0.00*	*0.34*	*0.42*	*0.06*	*0.00*		*0.68*		*0.01*
			Pl	r	7	46.36	0.01	32.98		0.48		0.00				0.00	17.11	1.88	0.00		98.82	83.43	0.00
						0.19	*0.02*	*0.10*		*0.05*		*0.00*				*0.00*	*0.17*	*0.10*	*0.01*		*0.25*	*0.87*	*0.00*
			Pl	c	31	46.53	0.01	32.75		0.50		0.00				0.00	16.89	1.99	0.01		98.67	82.41	0.00
						0.44	*0.02*	*0.24*		*0.10*		*0.00*				*0.00*	*0.17*	*0.11*	*0.01*		*0.69*	*0.88*	*0.00*
OM12_Gid_034b	813	LG	Cpx	r	9	51.83	0.55	2.42	0.14	0.00	6.02	0.20			0.00	16.28	22.09	0.19	0.00		99.74		0.83
						0.56	*0.17*	*0.29*	*0.06*	*0.00*	*0.53*	*0.09*			*0.00*	*1.03*	*1.28*	*0.08*	*0.00*		*0.80*		*0.02*
			Cpx	c	38	51.94	0.48	2.51	0.21	0.00	5.65	0.15			0.00	16.74	21.72	0.20	0.01		99.59		0.84
						0.65	*0.07*	*0.25*	*0.10*	*0.00*	*0.39*	*0.04*			*0.00*	*0.29*	*0.85*	*0.12*	*0.00*		*0.84*		*0.01*
			Pl	r	8	46.91	0.00	32.76		0.48		0.00				0.00	16.88	2.00	0.00		99.02	82.36	0.00
						0.56	*0.00*	*0.26*		*0.04*		*0.00*				*0.00*	*0.33*	*0.15*	*0.01*		*0.90*	*1.28*	*0.00*
			Pl	c	41	46.93	0.01	32.90		0.50		0.00				0.00	17.15	1.80	0.00		99.29	84.05	0.00
						0.49	*0.02*	*0.39*		*0.06*		*0.00*				*0.01*	*0.27*	*0.21*	*0.01*		*0.70*	*1.66*	*0.00*
OM12_Gid_035	991	LG	Cpx	c	15	52.44	0.48	2.53	0.24	0.00	6.01	0.13			0.00	16.61	21.58	0.31	0.00		100.33		0.83
					15	*0.31*	*0.04*	*0.10*	*0.05*	*0.00*	*0.22*	*0.03*			*0.00*	*0.27*	*0.46*	*0.04*	*0.00*		*0.47*		*0.02*
			Cpx	r	9	52.77	0.50	2.25	0.23	0.00	5.89	0.15			0.00	16.59	21.88	0.30	0.00		100.57		0.83
					9	*0.33*	*0.03*	*0.20*	*0.04*	*0.00*	*0.31*	*0.04*			*0.00*	*0.24*	*0.60*	*0.05*	*0.00*		*0.37*		*0.01*
			Pl	c	15	49.10	0.00	32.44		0.47		0.00				0.00	15.86	2.66	0.01		100.54	76.67	0.00
					15	*0.26*	*0.01*	*0.25*		*0.06*		*0.00*				*0.00*	*0.17*	*0.12*	*0.01*		*0.16*	*0.96*	*0.00*
			Pl	r	9	48.96	0.01	32.63		0.47		0.00				0.00	16.06	2.58	0.00		100.70	77.50	0.00
					9	*0.27*	*0.02*	*0.17*		*0.04*		*0.00*				*0.00*	*0.25*	*0.14*	*0.00*		*0.33*	*1.08*	*0.00*

[1] Depth_ calculated height above MOHO
[2] Lithology: SD = Sheeted dike; VG = Varitextured gabbro; FG = Foliated gabbro; MG = Metagabbro; FG = Foliated gabbro
[3] Mineral analysed
[4] Qualifier: r = rim; c = core
[5] Number of analyses
[6] Anorthite content of plagioclase
[7] XMg for Cpx, Opx, and Amph

Table 9. continued

Sample	Depth[1]	Litho.[2]	Min.[3]	Qual[4]	No[5]	SiO₂	TiO₂	Al₂O₃	Cr₂O₃	Fe₂O₃	FeO	MnO	Cl	F	NiO	MgO	CaO	Na₂O	K₂O	V₂O₃	Total	An[6]	XMg[7]
OM12_Gid_036	1064	LG	Pl	r	6	45.97	0.00	33.79		0.36		0.00				0.00	17.67	1.65	0.01		99.45	85.47	0.00
						0.76		*0.74*		*0.29*		*0.00*					*0.64*	*0.35*	*0.01*		*0.52*	*3.07*	*0.00*
			Pl	c	59	46.95	0.01	33.07		0.53		0.00				0.01	16.97	1.99	0.01		99.54	82.47	0.00
						0.55	*0.02*	*0.24*		*0.05*						*0.02*	*0.25*	*0.14*	*0.01*		*0.52*	*1.21*	*0.00*
OM12_Gid_037	1064	LG	Cpx		39	51.45	0.46	2.42	0.17	0.00	5.58	0.15			0.00	16.58	21.75	0.28	0.00		98.83		0.84
						0.50	*0.06*	*0.17*	*0.06*	*0.00*	*0.31*	*0.05*			*0.00*	*0.62*	*0.99*	*0.04*	*0.01*		*0.51*		*0.01*
			Pl		37	46.62	0.00	32.95		0.47		0.00				0.00	16.74	2.03	0.01		98.81	82.00	0.00
						0.41	*0.01*	*0.22*		*0.06*						*0.00*	*0.27*	*0.09*	*0.01*		*0.64*	*0.73*	*0.00*
OM12_Gid_038	1121	LG	Cpx	c	13	52.23	0.52	2.63	0.46	0.00	5.60	0.16			0.00	16.17	21.86	0.34	0.01		99.98		0.84
						0.27	*0.07*	*0.29*	*0.15*	*0.00*	*0.21*	*0.04*			*0.00*	*0.37*	*0.43*	*0.05*	*0.01*		*0.20*		*0.00*
			Cpx	r	8	52.43	0.55	2.34	0.40	0.00	5.55	0.15			0.00	16.32	22.00	0.32	0.00		100.06		0.84
						0.37	*0.01*	*0.13*	*0.06*	*0.00*	*0.27*	*0.03*			*0.00*	*0.36*	*0.47*	*0.03*	*0.00*		*0.53*		*0.00*
			Ol		24	39.33	0.01	0.01	0.00	0.00	18.88	0.28			0.13	41.67	0.04	0.01	0.00		100.37		0.80
						0.39	*0.01*	*0.01*	*0.00*		*0.25*	*0.04*			*0.03*	*0.58*	*0.01*	*0.02*	*0.00*		*0.69*		*0.00*
			Pl	c	13	47.35	0.01	33.13		0.50		0.00				0.02	16.76	2.13	0.00		99.90	81.28	0.00
						0.54	*0.02*	*0.39*		*0.06*						*0.06*	*0.33*	*0.16*	*0.01*		*0.59*	*1.41*	*0.00*
			Pl	r	7	47.37	0.00	32.96		0.51		0.00				0.00	16.53	2.25	0.01		99.64	80.07	0.00
						1.80		*1.17*		*0.11*						*0.00*	*1.70*	*0.80*	*0.02*		*0.87*	*7.48*	*0.00*
OM12_Gid_039	1289	LG	Cpx	c	15	51.38	0.51	2.61	0.42	0.00	5.51	0.15			0.00	16.64	21.55	0.31	0.00		99.08		0.84
						0.67	*0.05*	*0.17*	*0.08*	*0.00*	*0.27*	*0.04*			*0.00*	*0.23*	*0.44*	*0.04*	*0.00*		*0.75*		*0.01*
			Cpx	r	7	51.48	0.53	2.40	0.42	0.00	5.27	0.15			0.00	16.69	22.03	0.30	0.00		99.27		0.85
						0.27	*0.02*	*0.14*	*0.08*	*0.00*	*0.31*	*0.01*			*0.00*	*0.22*	*0.44*	*0.02*	*0.00*		*0.43*		*0.01*
			Ol		21	38.86	0.01	0.01	0.00	0.00	18.12	0.25			0.13	42.53	0.05	0.01	0.00		99.98		0.81
			Pl	c	8	46.52	0.00	33.48		0.50		0.00				0.00	17.29	1.86	0.00		99.65	83.71	0.00
						0.24		*0.25*		*0.07*						*0.00*	*0.15*	*0.08*	*0.01*		*0.43*	*0.59*	*0.00*
			Pl	r	6	46.69	0.00	33.57		0.58		0.00				0.00	17.22	1.84	0.00		99.90	83.82	0.00
						0.39		*0.23*		*0.11*						*0.00*	*0.16*	*0.06*	*0.00*		*0.57*	*0.55*	*0.00*
OM12_Gid_040	1508	LG	Cpx	c	15	52.14	0.47	2.57	0.13	0.00	5.62	0.13			0.00	16.10	22.06	0.28	0.00		99.51		0.84
						0.44	*0.06*	*0.10*	*0.06*	*0.00*	*0.28*	*0.04*			*0.00*	*0.40*	*0.38*	*0.04*	*0.00*		*0.53*		*0.01*
			Cpx	r	9	51.97	0.51	2.61	0.15	0.00	5.55	0.20			0.00	15.96	22.26	0.30	0.00		99.51		0.84
						0.48	*0.03*	*0.53*	*0.07*	*0.00*	*0.26*	*0.03*			*0.00*	*0.52*	*0.63*	*0.05*	*0.00*		*0.54*		*0.00*
			Pl	c	15	46.79	0.01	33.06		0.47		0.00				0.00	16.99	1.99	0.01		99.33	82.42	0.00
						0.43	*0.02*	*0.24*		*0.05*						*0.00*	*0.22*	*0.07*	*0.01*		*0.62*	*0.65*	*0.00*
			Pl	r	9	46.73	0.01	33.37		0.45		0.00				0.00	17.15	1.83	0.01		99.54	83.75	0.00
						0.30	*0.02*	*0.30*		*0.07*						*0.00*	*0.19*	*0.04*	*0.01*		*0.63*	*0.24*	*0.00*
OM12_Gid_041	1508	LG	Cpx	c	14	52.56	0.48	2.51	0.10	0.00	5.62	0.17			0.00	16.28	22.24	0.27	0.00		100.25		0.84
						0.24	*0.03*	*0.12*	*0.04*	*0.00*	*0.31*	*0.06*			*0.00*	*0.39*	*0.47*	*0.03*	*0.00*		*0.38*		*0.01*
			Cpx	r	9	52.76	0.51	2.16	0.14	0.00	5.53	0.16			0.00	16.27	22.54	0.27	0.00		100.34		0.84
						0.28	*0.01*	*0.07*	*0.03*	*0.00*	*0.17*	*0.03*			*0.00*	*0.20*	*0.20*	*0.03*	*0.00*		*0.48*		*0.00*
			Ol		15	39.35	0.01	0.01	0.00	0.00	19.30	0.26			0.08	41.97	0.05	0.01	0.00		101.05		0.79
						0.20	*0.01*	*0.02*	*0.00*	*0.00*	*0.26*	*0.05*			*0.03*	*0.40*	*0.01*	*0.01*	*0.01*		*0.63*		*0.00*
			Pl	c	15	47.14	0.00	33.76		0.52		0.00				0.00	17.42	1.81	0.01		100.66	84.14	0.00
						0.35	*0.01*	*0.17*		*0.05*						*0.00*	*0.15*	*0.11*	*0.01*		*0.43*	*0.86*	*0.00*
			Pl	r	9	46.97	0.00	33.82		0.58		0.00				0.02	17.52	1.73	0.01		100.65	84.76	0.00
						0.24	*0.00*	*0.21*		*0.10*						*0.04*	*0.25*	*0.05*	*0.01*		*0.29*	*0.54*	*0.00*

[1] Depth_ calculated height above MOHO
[2] Lithology: SD = Sheeted dike; VG = Varitextured gabbro; MG = Metagabbro; FG = Foliated gabbro
[3] Mineral analysed
[5] Number of analyses
[6] Anorthite content of plagioclase
[7] XMg for Cpx, Opx, and Amph

Table 9. continued

Sample	Depth[1]	Litho.[2]	Min[3]	Qual[4]	No[5]	SiO₂	TiO₂	Al₂O₃	Cr₂O₃	Fe₂O₃	FeO	MnO	Cl	F	NiO	MgO	CaO	Na₂O	K₂O	V₂O₃	Total	An[6]	XMg[7]
OM12_Gid_042_I	1562	LG	Amph		5	43.60	2.60	11.18	0.00	0.00	9.84	0.09	0.15	0.66	0.00	15.03	12.02	2.40	0.10		99.74		0.51
						0.32	*0.11*	*0.60*	*0.00*	*0.00*	*0.21*	*0.02*	*0.01*	*0.41*	*0.00*	*0.08*	*0.11*	*0.08*	*0.06*		*0.64*		*0.01*
			Cpx	r	3	51.61	0.70	2.55	0.24	0.00	6.22	0.13			0.00	15.84	22.49	0.32	0.00		100.08		0.82
						0.19	*0.04*	*0.17*	*0.07*		*0.24*	*0.06*				*0.03*	*0.06*	*0.02*			*0.25*		*0.01*
			Cpx	c	12	50.53	0.71	2.72	0.21	0.00	6.45	0.15			0.00	15.82	21.91	0.29	0.00		98.80		0.81
						0.37	*0.05*	*0.18*	*0.06*		*0.29*	*0.05*				*0.27*	*0.44*	*0.05*			*0.51*		*0.01*
			Ol		39	37.77	0.01	0.01	0.00		21.06	0.29			0.10	40.65	0.05	0.00	0.01		99.95		0.77
						0.63	*0.01*	*0.01*			*0.67*	*0.05*			*0.04*	*0.58*	*0.02*	*0.01*	*0.01*		*1.62*		*0.00*
			Pl	r	9	46.75	0.01	33.27		0.63		0.00				0.00	17.06	1.93	0.01		99.65	82.97	0.00
						0.35	*0.02*	*0.26*		*0.12*		*0.00*					*0.25*	*0.11*	*0.02*		*0.50*	*0.97*	*0.00*
			Pl	c	29	46.38	0.01	32.98		0.53		0.00				0.00	16.96	2.04	0.02		98.92	82.04	0.00
						0.94	*0.02*	*0.61*		*0.08*						*0.02*	*0.39*	*0.20*	*0.02*		*1.46*	*1.75*	*0.00*
OM12_Gid_042_II	1562	LG	Amph		11	30.03	0.01	19.54	0.00	0.00	12.71	0.15	0.01	0.24	0.00	24.48	0.28	0.03	0.02		89.42		0.52
						0.77	*0.01*	*1.12*	*0.00*		*0.46*	*0.05*	*0.00*	*0.42*	*0.00*	*1.17*	*0.55*	*0.04*	*0.02*		*1.23*		*0.02*
			Cpx	r	8	51.42	0.56	2.55	0.17	0.00	5.93	0.16			0.00	15.69	22.51	0.30	0.01		99.29		0.83
						0.38	*0.04*	*0.10*	*0.03*		*0.17*	*0.04*				*0.26*	*0.64*	*0.03*	*0.01*		*0.73*		*0.00*
			Cpx	c	35	51.36	0.53	2.72	0.16	0.00	6.14	0.15			0.00	15.82	22.31	0.29	0.01		99.48		0.82
						0.49	*0.06*	*0.23*	*0.07*		*0.24*	*0.04*				*0.40*	*0.62*	*0.03*	*0.01*		*0.50*		*0.00*
			Pl	r	9	46.98	0.00	33.28		0.50		0.00				0.00	17.10	1.97	0.02		99.85	82.66	0.00
						0.30	*0.00*	*0.19*		*0.06*		*0.00*					*0.20*	*0.09*	*0.02*		*0.26*	*0.81*	*0.00*
			Pl	c	38	47.16	0.00	32.99		0.60		0.00				0.04	16.91	2.09	0.02		99.81	81.57	0.00
						0.35	*0.01*	*0.69*		*0.35*		*0.00*				*0.22*	*0.48*	*0.16*	*0.02*		*0.59*	*1.60*	*0.00*
OM12_Gid_043	1671	LG	Cpx	r	6	52.06	0.54	2.59	0.21	0.00	5.47	0.14			0.00	16.06	21.87	0.24	0.00		99.19		0.84
						0.23	*0.13*	*0.73*	*0.03*		*0.52*	*0.05*				*0.76*	*1.00*	*0.07*	*0.01*		*0.62*		*0.01*
			Cpx	c	44	52.07	0.49	2.49	0.24	0.00	5.43	0.14			0.00	16.07	22.23	0.24	0.01		99.41		0.84
						0.49	*0.10*	*0.62*	*0.09*		*0.53*	*0.04*				*0.54*	*0.79*	*0.10*	*0.01*		*0.59*		*0.01*
			Pl	r	9	46.54	0.00	33.56		0.40		0.00				0.00	17.41	1.74	0.02		99.66	84.61	0.00
						0.36	*0.00*	*0.34*		*0.08*		*0.00*					*0.25*	*0.13*	*0.02*		*0.63*	*1.17*	*0.00*
			Pl	c	44	46.68	0.01	33.28		0.47		0.00				0.00	17.21	1.75	0.01		99.42	84.40	0.00
						0.53	*0.02*	*0.27*		*0.08*		*0.00*					*0.25*	*0.13*	*0.02*		*0.92*	*0.99*	*0.00*
OM12_Gid_044	1626	LG	Cpx	c	15	52.09	0.50	2.44	0.26	0.00	6.07	0.17			0.00	16.15	21.65	0.30	0.00		99.62		0.83
						0.34	*0.07*	*0.12*	*0.07*		*0.37*	*0.03*				*0.46*	*0.70*	*0.03*	*0.00*		*0.47*		*0.01*
			Cpx	r	9	51.98	0.66	2.32	0.23	0.00	6.02	0.15			0.00	15.87	21.84	0.31	0.00		99.40		0.82
						0.39	*0.05*	*0.11*	*0.06*		*0.30*	*0.03*				*0.36*	*0.65*	*0.03*	*0.00*		*0.42*		*0.01*
			Ol		24	38.52	0.01	0.01	0.00	0.00	20.68	0.30			0.10	40.00	0.05	0.01	0.00		99.68		0.78
						0.38	*0.01*	*0.01*		*0.00*	*0.25*	*0.05*			*0.04*	*0.57*	*0.02*	*0.01*	*0.00*		*0.55*		*0.00*
			Pl	c	15	47.50	0.00	32.81		0.49		0.00				0.00	16.66	2.20	0.01		99.68	80.67	0.00
						0.22	*0.01*	*0.21*		*0.06*		*0.00*					*0.15*	*0.08*	*0.01*		*0.32*	*0.60*	*0.00*
			Pl	r	8	46.92	0.01	33.23		0.51		0.00				0.03	17.14	1.94	0.01		99.78	82.95	0.00
						0.46	*0.02*	*0.37*		*0.04*						*0.08*	*0.36*	*0.15*	*0.01*		*0.23*	*1.32*	*0.00*
OM12_Gid_045	1630	LG	Cpx	c	15	51.63	0.80	2.91	0.24	0.00	7.14	0.16			0.00	15.66	21.82	0.33	0.00		100.71		0.80
						0.34	*0.06*	*0.10*	*0.04*		*0.35*	*0.05*				*0.34*	*0.57*	*0.03*	*0.00*		*0.40*		*0.01*
			Cpx	r	9	51.85	0.82	2.65	0.23	0.00	7.13	0.19			0.00	15.62	21.75	0.34	0.00		100.59		0.80
						0.25	*0.03*	*0.08*	*0.06*		*0.38*	*0.04*				*0.26*	*0.49*	*0.03*	*0.01*		*0.40*		*0.01*
			Pl	c	15	47.50	0.00	33.53		0.48		0.00				0.00	17.21	2.02	0.00		100.76	82.48	0.00
						0.69	*0.01*	*0.40*		*0.05*						*0.00*	*0.50*	*0.28*	*0.01*		*0.38*	*2.44*	*0.00*
			Pl	r	9	47.57	0.00	33.42		0.55		0.00				0.00	17.06	2.12	0.01		100.74	81.63	0.00
						0.31		*0.15*		*0.05*						*0.00*	*0.23*	*0.12*	*0.01*		*0.24*	*1.02*	*0.00*

[1] Depth_ calculated height above MOHO
[2] Lithology: SD = Sheeted dike; VG = Varitextured gabbro; MG = Metagabbro; FG = Foliated gabbro
[3] Mineral analysed
[4] Qualifier: r = rim; c = core
[5] Number of analyses
[6] Anorthite content of plagioclase
[7] XMg for Cpx, Opx, and Amph

Table 9. continued

Sample	Depth[1]	Litho.[2]	Min[3]	Qual[4]	No[5]	SiO_2	TiO_2	Al_2O_3	Cr_2O_3	Fe_2O_3	FeO	MnO	Cl	F	NiO	MgO	CaO	Na_2O	K_2O	V_2O_3	Total	An[6]	XMg[7]
OM12_Gid_046	1727	LG	Cpx	c	15	52.25	0.55	2.42	0.26	0.00	5.94	0.17			0.00	16.21	22.09	0.31	0.00		100.20		0.83
						0.24	*0.04*	*0.10*	*0.05*	*0.00*	*0.26*	*0.05*			*0.00*	*0.51*	*0.51*	*0.03*	*0.00*		*0.33*		*0.01*
			Cpx	r	9	52.37	0.55	2.16	0.26	0.00	5.64	0.14			0.00	16.32	22.37	0.31	0.00		100.12		0.84
						0.29	*0.06*	*0.12*	*0.03*	*0.00*	*0.12*	*0.05*				*0.24*	*0.59*	*0.03*	*0.00*		*0.54*		*0.00*
			Pl	c	15	47.33	0.01	33.35		0.48		0.00				0.00	16.99	2.02	0.01		100.20	82.25	0.00
						0.41	*0.02*	*0.27*		*0.07*		*0.00*				*0.00*	*0.19*	*0.07*	*0.02*		*0.65*	*0.64*	*0.00*
			Pl	r	9	47.22	0.01	33.48		0.43		0.00				0.00	17.18	1.98	0.01		100.30	82.72	0.00
						0.31	*0.02*	*0.25*		*0.06*						*0.00*	*0.11*	*0.08*	*0.01*		*0.49*	*0.61*	*0.00*
OM12_Gid_047	1787	MG	Amph		5	43.15	3.00	11.44	0.51	0.00	9.61	0.12	0.15	0.11	0.00	15.43	11.72	2.81	0.21		100.37		0.59
						0.18	*0.18*	*0.05*	*0.06*	*0.00*	*0.11*	*0.03*	*0.01*	*0.01*	*0.00*	*0.04*	*0.19*	*0.10*	*0.01*		*0.34*		*0.01*
			Cpx	c	16	52.33	0.48	2.10	0.19	0.00	5.66	0.16			0.00	15.89	22.88	0.28	0.01		99.97		0.83
						0.65	*0.14*	*0.49*	*0.05*	*0.00*	*0.47*	*0.05*			*0.00*	*0.24*	*0.62*	*0.06*	*0.01*		*0.38*		*0.01*
			Cpx	r	9	52.33	0.49	1.83	0.18	0.00	5.63	0.16			0.00	15.56	23.19	0.29	0.01		99.67		0.83
						0.64	*0.23*	*0.78*	*0.07*	*0.00*	*0.25*	*0.05*			*0.00*	*0.40*	*1.10*	*0.10*	*0.00*		*0.39*		*0.01*
			Ol		6	52.54	0.41	1.87	0.05	0.00	5.48	0.17			0.03	15.95	22.90	0.34	0.01		99.69		0.84
						0.85	*0.45*	*0.45*	*0.00*	*0.00*	*0.45*	*0.04*			*0.02*	*0.29*	*0.60*	*0.14*	*0.01*		*0.53*		*0.00*
			Pl		22	47.65	0.03	32.89	0.00	0.53		0.02				0.01	16.83	2.19	0.02		100.12	80.84	0.00
						0.29	*0.01*	*0.24*	*0.00*	*0.07*		*0.03*				*0.02*	*0.24*	*0.14*	*0.01*		*0.36*	*1.13*	*0.00*
OM12_Gid_048	1792	LG	Cpx	c	10	52.00	0.72	2.78	0.15	0.00	6.64	0.14			0.00	15.95	21.61	0.31	0.00		100.29		0.81
						0.45	*0.03*	*0.29*	*0.03*	*0.00*	*0.28*	*0.04*			*0.00*	*0.27*	*0.53*	*0.06*	*0.00*		*0.53*		*0.01*
			Cpx	r	6	52.76	0.61	2.37	0.20	0.00	6.23	0.14			0.00	16.00	22.00	0.30	0.00		100.61		0.82
						0.62	*0.10*	*0.44*	*0.04*	*0.00*	*0.36*	*0.04*			*0.00*	*0.22*	*0.44*	*0.09*	*0.01*		*0.49*		*0.01*
			Ol		16	39.54	0.01	0.01	0.00	0.00	21.37	0.29			0.10	41.21	0.06	0.00	0.00		102.60		0.77
						0.35	*0.01*	*0.01*	*0.00*	*0.00*	*0.21*	*0.05*			*0.03*	*0.32*	*0.02*	*0.01*	*0.00*		*0.50*		*0.00*
			Pl	c	10	47.82	0.00	33.01		0.55		0.00				0.00	16.94	1.88	0.00		100.19	83.29	0.00
						0.38	*0.00*	*0.20*		*0.06*						*0.00*	*0.16*	*0.14*	*0.01*		*0.44*	*1.13*	*0.00*
			Pl	r	6	47.56	0.00	32.96		0.59		0.00				0.00	16.99	1.89	0.00		99.99	83.24	0.00
						0.48	*0.00*	*0.16*		*0.05*						*0.00*	*0.22*	*0.08*	*0.00*		*0.36*	*0.74*	*0.00*
OM12_Gid_049	1919	LG	Cpx	c	19	52.33	0.48	2.10	0.19	0.00	5.66	0.16			0.00	15.89	22.88	0.28	0.01		99.97		0.83
						0.65	*0.14*	*0.49*	*0.05*	*0.00*	*0.47*	*0.05*			*0.00*	*0.24*	*0.62*	*0.06*	*0.01*		*0.38*		*0.01*
			Cpx	r	9	52.33	0.49	1.83	0.18	0.00	5.63	0.16			0.00	15.56	23.19	0.29	0.00		99.67		0.83
						0.64	*0.23*	*0.78*	*0.05*	*0.00*	*0.25*	*0.05*			*0.00*	*0.40*	*1.10*	*0.10*	*0.00*		*0.39*		*0.01*
			Ol		6	52.54	0.41	1.87	0.00	0.00	5.48	0.17			0.03	15.95	22.90	0.34	0.01		99.69		0.84
						0.85	*0.22*	*0.78*	*0.00*	*0.00*	*0.45*	*0.04*			*0.02*	*0.29*	*0.60*	*0.10*	*0.01*		*0.53*		*0.00*
			Pl		22	47.65	0.03	32.89	0.00	0.53		0.02				0.02	16.83	2.19	0.02		100.12	80.84	0.00
						0.29	*0.01*	*0.24*	*0.00*	*0.07*		*0.03*				*0.02*	*0.24*	*0.14*	*0.01*		*0.36*	*1.13*	*0.00*
OM12_Gid_050	1919	LG	Amph		34	42.60	3.81	11.14	0.00	0.00	11.17	0.12	0.22	0.03	0.00	13.71	11.55	2.51	0.35		99.25		0.51
						0.67	*0.38*	*0.38*	*0.00*	*0.00*	*1.09*	*0.07*	*0.04*	*0.03*	*0.00*	*1.00*	*0.23*	*0.25*	*0.06*		*0.85*		*0.02*
			Amph		10	43.00	3.90	11.53	0.04	0.00	11.29	0.11	0.24	0.14	0.00	14.58	11.57	2.60	0.35		101.44		0.59
						1.20	*0.28*	*0.12*	*0.07*	*0.00*	*0.24*	*0.04*	*0.02*	*0.02*	*0.00*	*0.22*	*0.12*	*0.07*	*0.02*		*0.41*		*0.01*
			Cpx		35	52.86	0.36	1.60	0.08	0.00	6.26	0.16			0.00	14.88	22.99	0.25	0.01		99.44		0.81
						0.85	*0.20*	*0.75*	*0.07*	*0.00*	*0.69*	*0.04*			*0.00*	*0.82*	*0.92*	*0.09*	*0.03*		*1.09*		*0.03*
			Pl		12	48.72	0.02	32.69	0.00	0.60		0.01				0.00	15.77	2.63	0.03		100.48	76.66	0.00
						0.47	*0.02*	*0.33*	*0.04*	*0.07*		*0.03*				*0.00*	*0.55*	*0.28*	*0.01*		*0.44*	*2.51*	*0.00*
			Sp		9	54.63	0.06	0.36	0.01	0.00	5.01	0.16			0.00	15.02	24.89	0.00	0.00	0.10	100.25		0.00
						1.09	*0.07*	*0.28*	*0.02*	*0.05*	*0.48*	*0.03*			*0.00*	*0.29*	*0.66*	*0.00*	*0.00*	*0.06*	*0.78*		*0.00*
OM12_Gid_051	1919	LG	Amph		8	46.53	1.96	8.87	0.00	0.00	10.68	0.14	0.12	0.02	0.00	15.01	11.91	1.75	0.18		99.23		0.52
						3.34	*1.45*	*2.20*	*0.00*	*0.00*	*1.73*	*0.07*	*0.08*	*0.02*	*0.00*	*1.90*	*0.39*	*0.52*	*0.12*		*0.68*		*0.01*
			Cpx		24	52.83	0.21	1.21	0.06	0.00	6.22	0.24			0.00	14.96	23.40	0.20	0.01		99.33		0.81
						0.70	*0.17*	*0.64*	*0.05*	*0.00*	*1.17*	*0.13*			*0.00*	*0.96*	*0.80*	*0.08*	*0.01*		*0.79*		*0.04*
			Pl		6	48.52	0.02	32.62	0.05	0.57		0.00				0.01	15.58	2.70	0.03		100.06	75.96	0.00
						0.18	*0.02*	*0.14*		*0.06*						*0.02*	*0.17*	*0.06*	*0.02*		*0.40*	*0.52*	*0.00*

[1] Depth_ calculated height above MOHO
[2] Lithology: SD = Sheeted dike; VG = Varitextured gabbro; FG = Foliated gabbro; MG = Metagabbro; FG = Foliated gabbro
3 Mineral analysed
[4] Qualifier: r = rim; c = core
[5] Number of analyses
[6] Anorthite content of plagioclase
[7] XMg for Cpx, Opx, and Amph

Table 9. continued

Sample	Depth[1]	Litho.[2]	Min[3]	Qual[4]	No[5]	SiO₂	TiO₂	Al₂O₃	Cr₂O₃	Fe₂O₃	FeO	MnO	Cl	F	NiO	MgO	CaO	Na₂O	K₂O	V₂O₃	Total	An[6]	XMg[7]
OM12_Gid_052	2004	LG	Cpx	c	19	52.24	0.54	2.75	0.40	0.00	5.17	0.13			0.00	15.76	22.64	0.29	0.01		99.94		0.84
						0.32	*0.05*	*0.26*	*0.08*	*0.00*	*0.26*	*0.04*			*0.00*	*0.45*	*0.52*	*0.03*	*0.01*		*0.42*		*0.01*
			Cpx	r	12	52.52	0.50	2.21	0.31	0.00	4.78	0.15			0.00	15.74	23.14	0.25	0.01		99.61		0.85
						0.54	*0.10*	*0.70*	*0.08*	*0.00*	*0.21*	*0.03*			*0.00*	*0.27*	*0.92*	*0.08*	*0.01*		*0.68*		*0.01*
			Pl	c	18	47.24	0.02	33.19		0.40		0.02				0.01	17.29	1.95	0.02		100.10	82.95	0.00
						0.45	*0.01*	*0.28*		*0.07*		*0.02*				*0.01*	*0.27*	*0.13*	*0.01*		*0.56*	*1.05*	*0.00*
			Pl	r	9	46.54	0.01	33.62		0.39		0.02				0.00	17.66	1.65	0.01		99.85	85.50	0.00
						0.78	*0.01*	*0.46*		*0.10*		*0.02*				*0.00*	*0.33*	*0.22*	*0.01*		*0.63*	*1.84*	*0.00*
OM12_Gid_053	2004	LG	Cpx	c	15	51.81	0.51	2.84	0.33	0.00	6.08	0.14			0.00	15.67	22.19	0.33	0.00		99.91		0.82
						0.42	*0.08*	*0.10*	*0.05*	*0.00*	*0.62*	*0.06*			*0.00*	*0.40*	*0.33*	*0.05*	*0.00*		*0.51*		*0.02*
			Cpx	r	9	51.25	0.78	2.74	0.22	0.00	7.16	0.18			0.00	15.19	21.89	0.37	0.00		99.78		0.79
						0.28	*0.06*	*0.12*	*0.05*	*0.00*	*0.29*	*0.04*			*0.00*	*0.23*	*0.27*	*0.04*	*0.00*		*0.37*		*0.01*
			Ol		24	38.61	0.01	0.01	0.00	0.00	23.43	0.36			0.09	38.00	0.06	0.00	0.00		100.56		0.74
						0.21	*0.01*	*0.01*	*0.00*	*0.00*	*0.28*	*0.05*			*0.04*	*0.19*	*0.01*	*0.01*	*0.00*		*0.42*		*0.01*
			Pl	c	14	47.29	0.01	33.28		0.57		0.00				0.00	16.98	2.00	0.01		100.14	82.38	0.00
						0.49	*0.02*	*0.34*		*0.06*		*0.00*				*0.00*	*0.52*	*0.25*	*0.01*		*0.37*	*2.21*	*0.00*
			Pl	r	9	47.78	0.00	33.02		0.60		0.00				0.01	16.69	2.27	0.01		100.37	80.23	0.00
						0.17	*0.00*	*0.30*		*0.09*		*0.00*				*0.03*	*0.40*	*0.17*	*0.01*		*0.34*	*1.54*	*0.00*
OM12_Gid_054	2040	LG	Cpx	c	23	50.94	0.70	2.80	0.08	0.00	7.66	0.17			0.00	15.30	21.53	0.34	0.00		99.52		0.78
						0.66	*0.08*	*0.33*	*0.04*	*0.00*	*0.43*	*0.03*			*0.00*	*0.40*	*0.77*	*0.04*	*0.00*		*0.63*		*0.01*
			Cpx	r	15	51.24	0.73	2.63	0.07	0.00	7.18	0.18			0.00	15.31	22.04	0.37	0.01		99.76		0.79
						0.31	*0.09*	*0.21*	*0.04*	*0.00*	*0.25*	*0.06*			*0.00*	*0.53*	*0.27*	*0.05*	*0.01*		*0.50*		*0.01*
			Pl	c	15	48.46	0.01	32.43		0.58		0.00				0.00	16.09	2.62	0.02		100.21	77.16	0.00
						0.56	*0.02*	*0.59*		*0.10*		*0.00*				*0.00*	*0.57*	*0.33*	*0.02*		*0.48*	*2.86*	*0.00*
			Pl	r	9	48.16	0.01	32.70		0.61		0.00				0.01	16.43	2.44	0.01		100.37	78.72	0.00
						1.11	*0.01*	*0.70*		*0.07*		*0.00*				*0.04*	*1.02*	*0.49*	*0.01*		*0.34*	*4.40*	*0.00*
OM12_Gid_055	2259	LG	Cpx	c	28	51.84	0.55	2.69	0.29	0.00	6.39	0.15			0.00	16.25	21.84	0.32	0.00		100.32		0.82
						0.58	*0.13*	*0.35*	*0.23*	*0.00*	*0.50*	*0.04*			*0.00*	*0.58*	*0.81*	*0.05*	*0.00*		*0.56*		*0.01*
			Cpx	r	11	51.66	0.80	2.58	0.20	0.00	6.63	0.18			0.00	16.01	21.93	0.33	0.01		100.32		0.81
						0.61	*0.10*	*0.31*	*0.05*	*0.00*	*0.41*	*0.03*			*0.00*	*0.31*	*0.63*	*0.03*	*0.01*		*0.71*		*0.01*
			Ol		23	38.67	0.01	0.01	0.00	0.00	21.34	0.32			0.09	40.74	0.05	0.01	0.00		101.25		0.77
						0.42	*0.01*	*0.01*	*0.00*	*0.00*	*0.22*	*0.04*			*0.04*	*0.52*	*0.01*	*0.01*	*0.00*		*0.37*		*0.00*
			Pl	c	10	46.70	0.02	33.60		0.55		0.00				0.00	17.58	1.80	0.00		100.26	84.35	0.00
						0.66	*0.02*	*0.26*		*0.06*		*0.00*				*0.00*	*0.26*	*0.17*	*0.00*		*0.49*	*1.38*	*0.00*
			Pl	r	5	47.50	0.01	33.75		0.71		0.00				0.00	17.08	2.04	0.01		101.09	82.20	0.00
						0.30	*0.02*	*0.33*		*0.13*		*0.00*				*0.00*	*0.21*	*0.10*	*0.01*		*0.36*	*0.89*	*0.00*
OM12_Gid_057	2610	MG	Amph		9	44.32	2.96	10.40	0.25	0.00	10.01	0.09	0.07	0.15	0.00	15.64	11.84	2.24	0.07		100.13		0.60
						0.17	*0.13*	*0.14*	*0.06*	*0.00*	*0.25*	*0.03*	*0.01*	*0.01*	*0.00*	*0.21*	*0.36*	*0.07*	*0.04*		*0.36*		
			Cpx		21	52.03	0.65	2.89	0.11	0.00	7.11	0.16			0.00	15.62	22.08	0.28		0.00	100.94		0.80
						0.89	*0.12*	*0.27*	*0.05*	*0.00*	*0.50*	*0.04*			*0.00*	*0.60*	*0.90*	*0.05*		*0.00*	*0.82*		*0.01*
			Pl		26	47.30	0.02	33.42		0.56		0.01				0.00	17.55	1.81	0.02		100.64	84.21	0.00
						0.32	*0.01*	*0.24*		*0.09*		*0.02*				*0.00*	*0.27*	*0.09*	*0.01*		*0.59*	*0.79*	*0.00*
OM12_Gid_058	2610	LG	Amph		26	45.95	2.67	10.11	0.00	0.00	10.88	0.11			0.00	13.03	12.23	2.58	0.19		99.82		0.68
						1.06	*1.09*	*0.68*	*0.00*	*0.00*	*0.46*	*0.03*			*0.00*	*0.60*	*0.20*	*0.27*	*0.09*		*0.89*		*0.02*
			Amph		10	43.93	3.46	10.83	0.06	0.00	11.26	0.10	0.20	0.12	0.00	14.83	11.77	2.53	0.25		101.45		0.58
						0.56	*0.34*	*0.44*	*0.09*	*0.00*	*0.24*	*0.04*	*0.01*	*0.02*	*0.00*	*0.26*	*0.10*	*0.14*	*0.01*		*0.44*		*0.02*
			Cpx		15	55.99	0.26	1.11	0.07	0.00	5.62	0.17			0.00	15.72	24.46	0.21	0.01		103.61		0.83
						0.62	*0.12*	*0.52*	*0.05*	*0.00*	*0.59*	*0.04*			*0.00*	*0.33*	*0.42*	*0.06*	*0.01*		*0.49*		*0.02*
			Pl		16	49.61	0.03	33.37		0.51		0.01				0.00	17.40	2.14	0.02		103.04	81.72	0.00
						0.33	*0.01*	*0.24*		*0.07*		*0.02*				*0.00*	*0.25*	*0.13*	*0.01*		*0.34*	*1.05*	*0.00*

[1] Depth_ calculated height above MOHO
[2] Lithology: SD = Sheeted dike; VG = Varitextured gabbro; FG = Foliated gabbro; MG = Metagabbro; FG = Foliated gabbro
[3] Mineral analysed
[4] Qualifier: r = rim; c = core
[5] Number of analyses
[6] Anorthite content of plagioclase
[7] XMg for Cpx, Opx, and Amph

Table 9. continued

Sample	Depth[1]	Litho.[2]	Min[3]	Qual[4]	No[5]	SiO₂	TiO₂	Al₂O₃	Cr₂O₃	Fe₂O₃	FeO	MnO	Cl	F	NiO	MgO	CaO	Na₂O	K₂O	V₂O₃	Total	An[6]	XMg[7]
OM12_Gid_059	2610	LG	Amph		32	47.76	1.85	7.06	0.00	0.00	10.47	0.11			0.00	15.78	12.54	1.31	0.28		99.33		0.73
						2.53	*0.83*	*2.20*	*0.00*	*0.00*	*1.26*	*0.04*			*0.00*	*0.97*	*2.87*	*0.44*	*0.12*		*1.05*		*0.03*
			Amph		5	48.44	1.85	7.39	0.09	0.00	11.13	0.12	0.21	0.14	0.00	16.43	11.78	1.40	0.32		101.42		0.60
						1.82	*0.46*	*1.20*	*0.11*	*0.00*	*0.58*	*0.02*	*0.03*	*0.03*	*0.00*	*0.80*	*0.09*	*0.25*	*0.08*		*0.30*		*0.02*
			Amph		5	44.12	3.28	10.53	0.04	0.00	11.30	0.09	0.25	0.14	0.00	14.49	11.77	2.02	0.48		100.59		0.57
						0.09	*0.04*	*0.08*	*0.08*	*0.00*	*0.18*	*0.05*	*0.01*	*0.01*	*0.00*	*0.15*	*0.09*	*0.07*	*0.01*		*0.26*		*0.02*
			Cpx	c	11	52.77	0.42	1.46	0.07	0.00	6.21	0.19	0.01	0.01	0.00	15.25	23.42	0.22	0.00		100.02		0.81
						1.21	*0.33*	*0.93*	*0.06*	*0.00*	*0.61*	*0.04*				*0.31*	*1.08*	*0.11*	*0.00*		*0.54*		*0.02*
			Cpx	r	3	51.76	0.80	2.37	0.15	0.00	6.99	0.19			0.00	15.29	22.20	0.31	0.00		100.06		0.80
						0.30	*0.04*	*0.05*	*0.05*	*0.00*	*0.25*	*0.02*			*0.00*	*0.25*	*0.63*	*0.04*	*0.00*		*0.59*		*0.00*
			Pl	c	20	47.49	0.02	33.08	0.05	0.46		0.02			0.00	0.00	17.06	2.07	0.04		100.20	81.78	0.00
						0.59	*0.02*	*0.50*		*0.10*		*0.02*				*0.01*	*0.52*	*0.59*	*0.01*		*0.39*	*2.24*	*0.00*
			Pl	r	3	48.05	0.02	32.87		0.65		0.02				0.03	16.78	2.21	0.03		100.61	80.62	0.00
						0.16	*0.00*	*0.05*		*0.06*		*0.02*				*0.04*	*0.14*	*0.06*	*0.00*		*0.03*	*0.49*	*0.00*
OM12_Gid_104g	6300	VG	Amph		24	43.94	2.38	9.81	0.00	0.00	14.11	0.20	0.26	0.03	0.00	13.45	11.20	2.36	0.26		100.06		0.49
						1.21	*1.01*	*0.56*	*0.00*	*0.00*	*0.68*	*0.04*	*0.11*	*0.05*	*0.00*	*0.57*	*0.26*	*0.37*	*0.09*		*0.53*		*0.02*
			Cpx		11	45.47	0.71	8.40	0.00	0.00	19.90	0.26			0.00	10.06	11.76	1.57	0.23		98.37		0.47
						1.44	*0.38*	*1.00*	*0.00*	*0.00*	*1.24*	*0.07*			*0.00*	*1.03*	*0.18*	*0.44*	*0.05*		*0.46*		*0.04*
			Ilm		5	0.01	50.10	0.03	0.04	4.50	42.29	2.52			0.00	0.05	0.11	0.00	0.00	0.19	99.84		0.00
						0.01	*0.31*	*0.01*	*0.03*	*0.46*	*0.31*	*0.00*			*0.00*	*0.02*	*0.04*	*0.00*	*0.00*	*0.01*	*0.13*		*0.00*
			Mag		5	0.09	5.51	0.50	0.29	56.68	35.97	0.25			0.00	0.05	0.09	0.00	0.00	1.31	100.74		0.00
						0.07	*2.17*	*0.13*	*0.04*	*3.82*	*1.98*	*0.10*			*0.00*	*0.04*	*0.05*	*0.00*	*0.00*	*0.04*	*0.57*		*0.00*
			Pl	c	6	53.11	0.07	29.61		0.65		0.00			0.00	0.03	12.58	4.60	0.07		100.72	59.92	0.00
						0.76	*0.01*	*0.39*		*0.12*		*0.00*				*0.05*	*0.53*	*0.28*	*0.03*		*0.40*	*2.43*	*0.00*
			Pl	r	3	53.47	0.06	29.70		0.54		0.00				0.00	12.77	4.60	0.06		101.20	60.37	0.00
						0.19	*0.00*	*0.13*		*0.04*		*0.00*				*0.00*	*0.08*	*0.23*	*0.01*		*0.14*	*1.38*	*0.00*
OM12_Gid_104s	6300	SD	Amph		24	51.70	0.40	3.85	0.00	0.00	15.37	0.28	0.04	0.01	0.00	14.02	11.56	0.42	0.06		99.80		0.49
						0.72	*0.19*	*0.84*	*0.00*	*0.00*	*0.80*	*0.04*	*0.01*	*0.02*	*0.00*	*0.49*	*0.79*	*0.10*	*0.02*		*0.66*		*0.02*
			Pl	c	21	53.86	0.04	29.05		0.69		0.00			0.00	0.04	12.11	4.92	0.04		100.75	57.53	0.00
						0.95	*0.03*	*0.70*		*0.13*		*0.00*				*0.04*	*0.74*	*0.49*	*0.01*		*0.42*	*3.88*	*0.00*
			Pl	r	6	63.37	0.01	23.26		0.48		0.00				0.01	4.79	9.18	0.08		101.18	22.28	0.00
						0.85	*0.02*	*0.69*		*0.13*		*0.00*				*0.02*	*0.73*	*0.46*	*0.01*		*0.48*	*3.50*	*0.00*
OM12_Gid_105	6300	SD	Amph		26	50.85	0.55	3.97	0.00	0.00	17.86	0.28	0.12	0.06	0.00	12.36	11.43	0.56	0.10		100.21		0.49
						1.19	*0.23*	*1.23*	*0.00*	*0.00*	*1.07*	*0.06*	*0.04*	*0.18*	*0.00*	*0.93*	*0.50*	*0.28*	*0.04*		*0.47*		*0.02*
			Pl	c	19	53.74	0.06	28.91		0.89		0.00				0.01	12.11	4.92	0.04		100.67	57.52	0.00
						0.83	*0.02*	*0.57*		*0.09*		*0.00*				*0.03*	*0.79*	*0.46*	*0.01*		*0.30*	*3.84*	*0.00*
			Pl	r	3	61.46	0.03	24.38		0.47		0.00				0.00	6.09	8.58	0.11		101.12	28.07	0.00
						1.21	*0.05*	*0.78*		*0.13*		*0.00*				*0.00*	*0.98*	*0.67*	*0.01*		*0.37*	*4.84*	*0.00*
OM12_Gid_106	6300	SD	Amph		15	51.49	0.26	3.22	0.00	0.00	18.58	0.49	0.05	0.01	0.00	12.75	10.10	0.41	0.08		99.52		0.49
						1.31	*0.10*	*0.88*	*0.00*	*0.00*	*0.84*	*0.11*	*0.02*	*0.02*	*0.00*	*0.58*	*0.78*	*0.09*	*0.05*		*0.86*		*0.01*
			Ilm		8	0.64	48.71	0.07	0.02	5.48	39.15	4.21			0.00	0.09	0.78	0.00	0.00	0.16	99.29		0.00
						0.77	*0.73*	*0.07*	*0.01*	*1.75*	*0.78*	*0.98*			*0.00*	*0.16*	*0.54*	*0.00*	*0.00*	*0.07*	*0.72*		*0.00*
			Mag		16	0.51	1.82	0.31	0.12	62.76	32.78	0.07			0.00	0.06	0.19	0.00	0.00	0.76	99.39		0.00
						0.22	*0.88*	*0.08*	*0.03*	*1.81*	*0.84*	*0.04*				*0.03*	*0.10*			*0.11*	*1.05*		*0.00*
			Pl	c	7	64.84	0.00	18.59		0.11		0.00			0.00	0.00	0.30	0.24	15.95		100.03	1.53	0.00
						0.73	*0.00*	*0.42*		*0.10*		*0.00*				*0.00*	*0.45*	*0.11*	*0.55*		*0.39*	*2.31*	*0.00*
			Pl	r	3	61.30	0.06	24.22		0.47		0.00				0.00	6.40	8.21	0.11		100.77	29.93	0.00
						0.18	*0.00*	*0.16*		*0.07*		*0.00*				*0.00*	*0.18*	*0.14*	*0.01*		*0.16*	*0.96*	*0.00*

[1] Depth_ calculated height above MOHO
[2] Lithology: SD = Sheeted dike; VG = Varitextured gabbro; MG = Metagabbro; FG = Foliated gabbro
[3] Mineral analysed
[4] Qualifier: r = rim; c = core
[5] Number of analyses
[6] Anorthite content of plagioclase
[7] XMg for Cpx, Opx, and Amph

Table 9. continued

Sample	Depth[1]	Litho.[2]	Min[3]	Qual[4]	No[5]	SiO_2	TiO_2	Al_2O_3	Cr_2O_3	Fe_2O_3	FeO	MnO	Cl	F	NiO	MgO	CaO	Na_2O	K_2O	V_2O_3	Total	An[6]	XMg[7]
OM12_Gid_110	6300	SD	Mag		12	0.81	0.59	0.19	0.02	65.25	32.05	0.12			0.00	0.06	0.21	0.00	0.00	0.18	99.47		0.00
					12	*0.32*	*0.39*	*0.06*	*0.02*	*1.60*	*0.49*	*0.05*			*0.00*	*0.03*	*0.14*	*0.00*	*0.00*	*0.09*	*0.84*		*0.00*
			Pl	c	15	65.16	0.00	18.47		0.12		0.00				0.01	0.00	0.06	16.53		100.34	0.00	0.00
					15	*0.41*	*0.00*	*0.18*		*0.13*		*0.00*				*0.02*	*0.00*	*0.08*	*0.14*		*0.68*	*0.00*	
OM12_Gid_111	6300	SD	Mag		12	1.49	0.65	0.32	0.01	64.26	33.29	0.14			0.00	0.15	0.15	0.00	0.00	0.10	100.57		0.00
					12	*0.93*	*0.35*	*0.18*	*0.02*	*2.44*	*1.36*	*0.04*			*0.00*	*0.16*	*0.06*	*0.00*	*0.00*	*0.08*	*0.65*		*0.00*
			Pl	c	6	60.58	0.03	25.07		0.59		0.00				0.00	7.08	7.80	0.10		101.26	33.24	0.00
					6	*0.63*	*0.02*	*0.35*		*0.05*		*0.00*				*0.00*	*0.41*	*0.26*	*0.01*		*0.42*	*2.00*	
			Pl	r	2	66.30	0.00	20.88		0.56		0.00				0.00	2.31	10.47	0.46		100.98	10.58	0.00
					2	*0.25*	*0.00*	*0.09*		*0.02*		*0.00*				*0.00*	*0.37*	*0.10*	*0.11*		*0.20*	*1.69*	
OM12_Gid_112	6300	SD	Amph		10	51.21	0.49	3.41	0.00	0.00	19.23	0.40	0.04	0.02	0.00	11.14	11.73	0.50	0.11		100.33		0.48
					10	*0.84*	*0.18*	*0.75*	*0.00*	*0.00*	*0.60*	*0.10*	*0.02*	*0.02*	*0.00*	*0.38*	*0.34*	*0.20*	*0.02*		*0.40*		*0.02*
			Mag		10	1.02	2.82	0.85	0.11	59.06	33.67	0.29			0.00	0.09	0.64	0.00	0.00	0.89	99.44		0.00
					10	*1.33*	*1.65*	*0.38*	*0.03*	*4.95*	*1.40*	*0.13*			*0.00*	*0.15*	*0.96*	*0.00*	*0.00*	*0.19*	*0.85*		*0.00*
			Pl		19	65.55	0.00	18.30		0.07		0.00				0.00	0.00	0.12	16.40		100.44	0.00	0.00
					19	*0.54*	*0.00*	*0.20*		*0.10*		*0.00*				*0.00*	*0.00*	*0.12*	*0.22*		*0.62*	*0.00*	
OM12_Gid_113	6300	SD	Amph		8	49.98	0.27	4.71	0.00	0.00	22.65	0.81	0.04	0.04	0.00	7.99	10.09	0.68	0.10		99.39		0.48
					8	*0.92*	*0.04*	*1.29*	*0.00*	*0.00*	*0.88*	*0.13*	*0.02*	*0.03*	*0.00*	*0.63*	*0.79*	*0.46*	*0.06*		*0.95*		*0.01*
			Mag		3	0.92	0.79	0.31	0.02	63.49	31.93	0.06			0.00	0.02	0.32	0.00	0.00	0.05	97.92		0.00
					3	*0.40*	*0.18*	*0.11*	*0.02*	*1.17*	*0.72*	*0.00*				*0.02*	*0.05*	*0.00*	*0.00*	*0.04*	*0.48*		*0.00*
			Pl	c	14	59.00	0.04	25.98		0.68		0.00				0.02	8.18	7.23	0.07		101.19	38.33	0.00
					14	*0.53*	*0.02*	*0.25*		*0.12*		*0.00*				*0.03*	*0.29*	*0.19*	*0.01*		*0.52*	*1.16*	
			Pl	r	5	63.70	0.02	23.48		0.75		0.00				0.00	5.04	9.16	0.14		102.29	23.15	0.00
					5	*0.93*	*0.02*	*0.33*		*0.11*		*0.00*				*0.00*	*0.44*	*0.36*	*0.02*		*0.43*	*1.79*	
OM12_Gid_201	598	LG	Cpx	c	16	52.67	0.50	2.40	0.36	0.00	5.50	0.16			0.00	16.83	21.93	0.29	0.00		100.65		0.85
					16	*0.27*	*0.03*	*0.16*	*0.08*	*0.00*	*0.36*	*0.03*			*0.00*	*0.44*	*0.72*	*0.03*	*0.00*		*0.49*		*0.01*
			Cpx	r	9	53.26	0.49	2.08	0.32	0.00	5.00	0.14			0.00	16.71	22.62	0.28	0.00		100.89		0.86
					9	*0.22*	*0.02*	*0.10*	*0.05*	*0.00*	*0.21*	*0.04*			*0.00*	*0.25*	*0.30*	*0.02*	*0.00*		*0.38*		*0.00*
			Ol	c	9	39.67	0.01	0.01	0.00	0.00	18.12	0.27			0.13	42.72	0.03	0.03	0.00		100.99		0.81
					9	*0.24*	*0.01*	*0.01*	*0.00*	*0.00*	*0.32*	*0.02*			*0.03*	*0.24*	*0.01*	*0.03*	*0.00*		*0.40*		*0.00*
			Ol	r	4	39.74	0.01	0.02	0.00	0.00	17.67	0.31			0.13	42.75	0.07	0.04	0.00		100.73		0.81
					4	*0.30*	*0.01*	*0.01*	*0.00*	*0.00*	*0.42*	*0.09*			*0.05*	*0.32*	*0.03*	*0.03*	*0.00*		*0.81*		*0.00*
			Pl	c	21	47.44	0.02	33.25		0.45		0.02				0.02	17.20	2.03	0.02		100.40	82.31	0.00
					21	*0.25*	*0.01*	*0.21*		*0.07*		*0.02*				*0.04*	*0.18*	*0.09*	*0.01*		*0.34*	*0.72*	
			Pl	r	14	46.99	0.02	33.51		0.47		0.02				0.12	17.71	1.82	0.02		100.63	84.26	0.00
					14	*0.57*	*0.01*	*0.58*		*0.09*		*0.03*				*0.20*	*0.40*	*0.20*	*0.01*		*0.57*	*1.74*	
OM12_Gid_202	594	LG	Cpx	r	9	52.82	0.58	2.35	0.28	0.00	4.84	0.12			0.00	16.69	22.49	0.30	0.01		100.47		0.86
					9	*0.19*	*0.06*	*0.23*	*0.04*	*0.00*	*0.32*	*0.05*			*0.00*	*0.22*	*0.49*	*0.04*	*0.01*		*0.38*		*0.01*
			Cpx	c	46	52.61	0.59	2.58	0.26	0.00	4.91	0.13			0.00	16.59	22.32	0.29	0.01		100.30		0.86
					46	*0.70*	*0.12*	*0.64*	*0.06*	*0.00*	*0.47*	*0.04*			*0.00*	*0.58*	*0.92*	*0.10*	*0.01*		*0.82*		*0.01*
			Pl	r	3	47.18	0.00	34.46		0.44		0.00				0.00	17.33	1.71	0.00		101.12	84.84	0.00
					3	*0.24*	*0.00*	*0.17*		*0.05*							*0.07*	*0.05*			*0.33*	*0.32*	
			Pl	c	59	47.54	0.00	34.09		0.42		0.00				0.00	16.95	1.95	0.01		100.97	82.73	0.00
					59	*0.32*	*0.01*	*0.28*		*0.08*							*0.30*	*0.13*	*0.05*		*0.55*	*1.08*	

[1] Depth_ calculated height above MOHO
[2] Lithology: SD = Sheeted dike; VG = Varitextured gabbro; MG = Metagabbro; FG = Foliated gabbro
[3] Mineral analysed
[4] Qualifier: r = rim; c = core
[5] Number of analyses
[6] Anorthite content of plagioclase
[7] XMg for Cpx, Opx, and Amph

Table 9, continued

Sample	Depth[1]	Litho.[2]	Min[3]	Qual[4]	No[5]	SiO$_2$	TiO$_2$	Al$_2$O$_3$	Cr$_2$O$_3$	Fe$_2$O$_3$	FeO	MnO	Cl	F	NiO	MgO	CaO	Na$_2$O	K$_2$O	V$_2$O$_3$	Total	An[6]	XMg[7]
OM12_Gid_203	433	LG	Cpx	c	15	52.53	0.52	2.67	0.26	0.00	5.88	0.13			0.00	16.82	21.56	0.30	0.00		100.67		0.84
						0.54	*0.06*	*0.29*	*0.09*		*0.49*	*0.05*			*0.00*	*0.47*	*1.10*	*0.04*	*0.01*		*0.63*		*0.01*
			Cpx	r	9	52.73	0.50	2.31	0.25	0.00	5.33	0.17			0.00	16.46	22.69	0.34	0.00		100.79		0.85
						0.37	*0.07*	*0.24*	*0.04*		*0.20*				*0.00*	*0.18*	*0.53*	*0.04*	*0.00*		*0.37*		*0.00*
			Ol	c	14	39.41	0.01	0.01	0.00	0.00	18.56	0.28			0.14	42.56	0.04	0.09	0.01		101.10		0.80
						0.29	*0.01*	*0.01*	*0.04*		*0.23*	*0.03*			*0.03*	*0.22*	*0.01*	*0.08*	*0.01*		*0.40*		*0.00*
			Ol	r	6	39.39	0.01	0.01	0.00		18.46	0.25			0.11	42.39	0.06	0.08	0.00		100.76		0.80
						0.21	*0.01*	*0.01*			*0.23*	*0.05*			*0.04*	*0.49*	*0.01*	*0.09*	*0.00*		*0.79*		*0.00*
			Pl	c	20	47.79	0.02	33.28		0.52		0.02				0.00	17.04	2.25	0.02		100.89	80.65	0.00
						0.29	*0.01*	*0.21*		*0.09*		*0.02*				*0.01*	*0.26*	*0.18*	*0.01*		*0.41*	*1.31*	*0.00*
			Pl	r	9	47.35	0.02	33.25		0.47		0.02				0.00	17.27	2.04	0.01		100.38	82.30	0.00
						0.31	*0.01*	*0.19*		*0.03*		*0.02*				*0.01*	*0.24*	*0.05*	*0.01*		*0.26*	*0.56*	*0.00*
OM12_Gid_204	434	LG	Cpx		12	52.25	0.63	2.43	0.13	0.00	6.01	0.17			0.00	16.12	22.26	0.29	0.00		100.28		0.83
						0.35	*0.04*	*0.24*	*0.03*		*0.18*	*0.04*			*0.00*	*0.37*	*0.30*	*0.03*	*0.00*		*0.48*		*0.00*
			Pl		10	48.55	0.00	33.54		0.51		0.00				0.00	16.32	2.37	0.01		101.30	79.18	0.00
						0.19	*0.01*	*0.15*		*0.06*		*0.00*				*0.00*	*0.18*	*0.04*	*0.01*		*0.32*	*0.42*	*0.00*
OM12_Gid_205	222	LG	Cpx	c	15	52.43	0.47	2.70	0.30	0.00	5.54	0.20			0.00	16.35	21.87	0.28	0.01		100.15		0.84
						0.21	*0.02*	*0.14*	*0.05*		*0.25*	*0.07*			*0.00*	*0.27*	*0.51*	*0.03*	*0.00*		*0.32*		*0.00*
			Cpx	r	9	52.52	0.47	2.34	0.28	0.00	5.38	0.23			0.00	16.42	22.04	0.27	0.01		99.95		0.84
						0.24	*0.03*	*0.13*	*0.06*		*0.14*	*0.05*			*0.00*	*0.14*	*0.27*	*0.04*	*0.01*		*0.29*		*0.00*
			Ol	c	14	39.29	0.01	0.01	0.00	0.00	18.73	0.41			0.09	41.61	0.07	0.00	0.00		100.24		0.80
						0.38	*0.01*	*0.01*			*0.45*	*0.07*			*0.04*	*0.41*	*0.11*	*0.01*	*0.00*		*0.51*		*0.01*
			Ol	r	6	39.31	0.01	0.01	0.00	0.00	18.71	0.39			0.10	41.38	0.07	0.00	0.00		99.99		0.80
						0.22	*0.01*	*0.01*			*0.53*	*0.08*			*0.03*	*0.50*	*0.03*	*0.00*	*0.00*		*0.40*		*0.01*
			Pl	c	14	47.43	0.02	33.15		0.43		0.05				0.01	17.02	2.01	0.01		100.09	82.31	0.00
						0.29	*0.01*	*0.19*		*0.09*		*0.05*				*0.01*	*0.20*	*0.09*	*0.01*		*0.34*	*0.81*	*0.01*
			Pl	r	8	46.99	0.01	33.61		0.38		0.01				0.01	17.41	1.75	0.01		100.16	84.51	0.00
						0.33	*0.01*	*0.28*		*0.07*		*0.02*				*0.01*	*0.33*	*0.14*	*0.01*		*0.29*	*1.27*	*0.00*
OM12_Gid_206	210	LG	Cpx	c	15	52.53	0.48	2.62	0.39	0.00	5.49	0.14			0.00	16.79	21.96	0.28	0.00		100.69		0.84
						0.28	*0.03*	*0.18*	*0.04*		*0.20*	*0.03*			*0.00*	*0.24*	*0.30*	*0.04*	*0.00*		*0.37*		*0.00*
			Cpx	r	9	52.53	0.45	2.64	0.39	0.00	4.99	0.14			0.00	16.49	22.63	0.28	0.00		100.53		0.85
						0.55	*0.05*	*0.64*	*0.02*		*0.30*	*0.05*			*0.00*	*0.41*	*0.39*	*0.02*	*0.00*		*0.58*		*0.01*
			Ol	c	15	39.61	0.01	0.01	0.00	0.00	17.86	0.25			0.15	43.16	0.02	0.03	0.00		101.10		0.81
						0.22	*0.01*	*0.01*			*0.21*	*0.04*			*0.04*	*0.17*	*0.01*	*0.07*	*0.00*		*0.31*		*0.00*
			Ol	r	9	39.47	0.01	0.01	0.00	0.00	17.64	0.23			0.13	43.22	0.09	0.01	0.00		100.81		0.81
						0.27	*0.01*	*0.01*			*0.32*	*0.04*			*0.03*	*0.38*	*0.09*	*0.01*	*0.00*		*0.52*		*0.00*
			Pl	c	20	46.95	0.02	33.59		0.48		0.01				0.01	17.48	1.82	0.01		100.32	84.07	0.00
						0.30	*0.01*	*0.19*		*0.09*		*0.02*				*0.02*	*0.14*	*0.07*	*0.01*		*0.41*	*0.52*	*0.00*
			Pl	r	12	46.66	0.02	33.82		0.47		0.01				0.01	17.73	1.66	0.01		100.35	85.45	0.00
						0.41	*0.02*	*0.21*		*0.12*		*0.01*				*0.03*	*0.26*	*0.10*	*0.01*		*0.57*	*0.83*	*0.00*
OM12_Gid_207	210	LG	Cpx	c	21	52.72	0.40	2.57	0.21	0.00	5.26	0.12			0.00	16.80	22.18	0.25	0.01		100.53		0.85
						0.50	*0.05*	*0.20*	*0.14*		*0.42*	*0.04*			*0.00*	*0.51*	*0.81*	*0.04*	*0.00*		*0.45*		*0.01*
			Cpx	r	9	52.78	0.47	2.33	0.31	0.00	5.27	0.13			0.00	16.65	22.44	0.27	0.00		100.65		0.85
						0.41	*0.08*	*0.13*	*0.06*		*0.38*	*0.05*			*0.00*	*0.46*	*0.71*	*0.04*	*0.00*		*0.51*		*0.01*
			Ol	c	18	39.78	0.01	0.01	0.00	0.00	17.65	0.24			0.15	43.39	0.03	0.00	0.01		101.25		0.81
						0.20	*0.01*	*0.01*			*0.56*	*0.04*			*0.03*	*0.42*	*0.01*	*0.00*	*0.01*		*0.45*		*0.00*
			Ol	r	6	39.70	0.00	0.01	0.00	0.00	16.88	0.26			0.12	43.84	0.06	0.00	0.01		100.88		0.82
						0.17	*0.01*	*0.01*			*0.43*	*0.03*			*0.03*	*0.30*	*0.00*	*0.00*	*0.00*		*0.32*		*0.00*
			Pl	c	15	46.73	0.01	33.83		0.48		0.02				0.00	17.67	1.68	0.01		100.40	85.23	0.00
						0.39	*0.01*	*0.17*		*0.08*		*0.02*				*0.30*	*0.16*	*0.15*	*0.01*		*0.40*	*1.11*	*0.00*
			Pl	r	9	46.62	0.02	33.92		0.46		0.02				0.10	17.75	1.64	0.01		100.50	85.63	0.00
						0.24	*0.02*	*0.44*		*0.09*		*0.03*				*0.27*	*0.31*	*0.10*	*0.01*		*0.55*	*0.88*	*0.00*

[1] Depth, calculated height above MOHO
[2] Lithology: SD = Sheeted dike; VG = Varitextured gabbro; FG = Foliated gabbro; MG = Metagabbro; FG = Foliated gabbro
[3] Mineral analysed
[4] Qualifier: r = rim; c = core
[5] Number of analyses
[6] Anorthite content of plagioclase
[7] XMg for Cpx, Opx, and Amph

Table 9. continued

Sample	Depth[1]	Litho.[2]	Min[3]	Qual[4]	No[5]	SiO$_2$	TiO$_2$	Al$_2$O$_3$	Cr$_2$O$_3$	Fe$_2$O$_3$	FeO	MnO	Cl	F	NiO	MgO	CaO	Na$_2$O	K$_2$O	V$_2$O$_3$	Total	An[6]	XMg[7]
OM12_Gid_208	147	LG	Cpx	c	10	51.19	0.58	2.32	0.00	0.00	7.04	0.23			0.00	14.87	22.38	0.35	0.01		98.98		0.79
					10	*0.61*	*0.18*	*0.66*	*0.00*	*0.00*	*0.51*	*0.04*			*0.00*	*0.45*	*1.18*	*0.09*	*0.00*		*0.58*		*0.01*
			Cpx	r	6	51.17	0.60	2.23	0.00	0.00	7.53	0.21			0.00	14.97	22.08	0.36	0.01		99.17		0.78
					6	*0.22*	*0.02*	*0.33*	*0.00*		*0.38*	*0.04*			*0.00*	*0.29*	*1.15*	*0.05*	*0.02*		*0.51*		*0.01*
			Pl	c	13	43.96	0.00	35.29		0.11		0.04				0.00	19.05	0.77	0.01		99.19	93.17	0.00
					13	*0.69*	*0.01*	*0.42*		*0.07*		*0.02*				*0.01*	*0.44*	*0.28*	*0.01*		*0.48*	*2.43*	*0.00*
			Pl	r	2	44.80	0.01	34.45		0.19		0.01				0.00	18.24	1.31	0.00		99.00	88.44	0.00
					2	*0.25*	*0.01*	*0.34*		*0.02*		*0.01*				*0.00*	*0.14*	*0.05*	*0.00*		*0.52*	*0.48*	*0.00*
OM12_Gid_209	147	LG	Cpx	c	28	52.04	0.68	2.60	0.00	0.00	7.65	0.19			0.20	14.94	21.35	0.36	0.00		100.02		0.78
					28	*0.28*	*0.03*	*0.16*	*0.03*	*0.00*	*0.51*	*0.05*			*0.04*	*0.45*	*0.87*	*0.02*	*0.00*		*0.41*		*0.01*
			Cpx	r	3	52.33	0.64	2.21	0.00	0.00	7.19	0.25			0.13	15.07	21.51	0.36	0.02		99.72		0.79
					3	*0.06*	*0.02*	*0.11*			*0.20*	*0.02*			*0.03*	*0.18*	*0.48*	*0.07*	*0.00*		*0.13*		*0.00*
			Pl	c	16	46.56	0.00	34.50		0.10		0.01				0.00	17.91	1.50	0.00		100.60	86.83	0.00
					16	*0.55*	*0.01*	*0.45*		*0.06*		*0.02*				*0.01*	*0.46*	*0.27*	*0.00*		*0.33*	*2.34*	*0.00*
			Pl	r	3	52.66	0.05	29.91		0.41		0.01				0.02	13.03	4.35	0.04		100.44	62.19	0.00
					3	*0.04*	*0.00*	*0.34*		*0.04*		*0.01*				*0.02*	*0.18*		*0.00*		*0.14*	*0.52*	*0.00*
OM12_Gid_210	88	LG	Cpx	c	29	51.56	0.67	2.69	0.07	0.00	7.95	0.20			0.00	15.63	20.90	0.36	0.00		100.02		0.78
					29	*0.36*	*0.07*	*0.16*	*0.04*	*0.00*	*0.42*	*0.04*			*0.00*	*0.38*	*0.73*	*0.03*	*0.01*		*0.43*		*0.01*
			Cpx	r	18	51.80	0.63	2.32	0.09	0.00	7.44	0.19			0.00	15.59	21.55	0.36	0.00		99.97		0.79
					18	*0.28*	*0.07*	*0.21*	*0.05*		*0.52*	*0.05*			*0.00*	*0.49*	*0.76*	*0.05*	*0.01*		*0.39*		*0.01*
			Ol	c	20	38.13	0.01	0.02	0.00	0.00	24.89	0.37			0.09	37.20	0.03	0.01	0.00		100.74		0.73
					20	*0.27*	*0.01*	*0.02*				*0.04*			*0.04*	*0.26*	*0.01*	*0.02*	*0.00*		*0.31*		*0.00*
			Ol	r	12	38.26	0.01	0.04	0.00	0.00	24.53	0.34			0.08	37.11	0.15	0.00	0.00		100.54		0.73
					12	*0.46*	*0.01*	*0.09*			*0.49*	*0.05*			*0.03*	*0.69*	*0.21*	*0.01*	*0.01*		*0.52*		*0.01*
			Pl	c	25	52.36	0.04	29.94		0.49		0.01				0.02	12.97	4.49	0.04		100.30	61.35	0.00
					25	*0.40*	*0.01*	*0.25*		*0.12*		*0.01*				*0.03*	*0.33*	*0.19*	*0.01*		*0.42*	*1.54*	*0.00*
			Pl	r	12	52.09	0.03	30.21		0.47		0.01				0.04	13.19	4.33	0.04		100.35	62.61	0.00
					12	*0.37*	*0.01*	*0.31*		*0.11*		*0.02*				*0.10*	*0.38*	*0.20*	*0.01*		*0.30*	*1.67*	*0.00*
OM12_Gid_211	135	LG	Cpx	r	14	52.27	0.60	2.96	0.19	0.00	6.78	0.20			0.00	15.41	21.40	0.33	0.01		100.15		0.80
					14	*0.71*	*0.03*	*0.66*	*0.04*		*0.58*	*0.04*			*0.00*	*0.69*	*0.85*	*0.03*	*0.02*		*0.82*		*0.01*
			Cpx	c	42	52.11	0.62	3.05	0.19	0.00	6.86	0.18			0.00	15.40	21.77	0.34	0.01		100.53		0.80
					42	*0.57*	*0.07*	*0.46*	*0.05*		*0.57*	*0.04*			*0.00*	*0.58*	*0.82*	*0.04*	*0.02*		*0.67*		*0.01*
			Pl	r	5	51.99	0.00	31.27	0.16	0.36		0.00				0.00	13.31	3.86	0.04		100.84	65.44	0.00
					5	*0.31*	*0.00*	*0.19*	*0.03*	*0.07*						*0.00*	*0.34*	*0.14*	*0.01*		*0.33*	*1.38*	*0.00*
			Pl	c	42	52.12	0.03	31.01	0.05	0.49		0.00				0.01	13.23	3.96	0.04		100.89	64.69	0.00
					42	*0.51*	*0.03*	*0.28*		*0.33*						*0.03*	*0.55*	*0.13*	*0.04*		*0.96*	*0.89*	*0.00*
OM12_Gid_213	4460	VG	Cpx	c	5	51.93	0.70	1.87	0.05	0.00	9.31	0.27			0.00	14.85	20.58	0.26	0.00		99.82		0.74
					5	*0.17*	*0.04*	*0.13*	*0.03*	*0.00*	*0.20*	*0.03*			*0.00*	*0.12*	*0.21*	*0.03*	*0.00*		*0.25*		*0.00*
			Cpx	r	4	52.05	0.67	1.84	0.03	0.00	9.80	0.29			0.00	14.90	20.21	0.30	0.00		100.09		0.73
					4	*0.17*	*0.03*	*0.08*	*0.02*	*0.00*	*0.18*	*0.01*			*0.00*	*0.17*	*0.37*	*0.01*	*0.00*		*0.32*		*0.00*
			Ilm		5	0.04	51.13	0.04	0.16	3.29	43.64	1.93			0.00	0.18	0.09	0.00	0.00	1.07	101.56		0.00
					5	*0.05*	*0.31*	*0.03*	*0.03*	*0.38*	*0.23*	*0.15*			*0.00*	*0.03*	*0.10*	*0.00*	*0.00*	*0.02*	*0.33*		*0.00*
			Ol	c	8	37.26	0.02	0.01	0.00	0.00	30.23	0.50			0.07	32.29	0.08	0.01	0.00		100.46		0.66
					8	*0.22*	*0.01*	*0.01*			*0.22*	*0.04*			*0.04*	*0.20*	*0.03*	*0.01*	*0.00*		*0.17*		*0.00*
			Pl	c	9	47.67	0.04	32.80		0.56		0.01				0.00	16.53	2.21	0.02		99.79	80.48	0.00
					9	*1.11*	*0.01*	*0.75*		*0.08*		*0.01*				*0.00*	*0.71*	*0.50*	*0.01*		*0.34*	*4.20*	*0.00*
			Pl	r	2	54.56	0.03	28.46		0.66		0.01				0.01	11.23	5.05	0.03		99.99	55.02	0.00
					2	*0.25*	*0.02*	*0.34*		*0.12*		*0.01*				*0.01*	*0.40*	*0.18*	*0.02*		*0.15*	*1.83*	*0.00*

[1] Depth_ calculated height above MOHO
[2] Lithology: SD = Sheeted dike; VG = Varitextured gabbro; MG = Metagabbro; FG = Foliated gabbro; LG = Foliated gabbro
[3] Mineral analysed
[4] Qualifier: r = rim; c = core
[5] Number of analyses
[6] Anorthite content of plagioclase
[7] XMg for Cpx, Opx, and Amph

Table 9. continued

Sample	Depth[1]	Litho.[2]	Min[3]	Qual[4]	No[5]	SiO₂	TiO₂	Al₂O₃	Cr₂O₃	Fe₂O₃	FeO	MnO	Cl	F	NiO	MgO	CaO	Na₂O	K₂O	V₂O₃	Total	An[6]	XMg[7]
OM12_Gid_217	2979	FG	Cpx	c	19	52.12	0.51	2.53	0.38	0.00	5.74	0.16			0.00	16.23	22.18	0.32	0.00		100.19		0.83
					19	*0.44*	*0.04*	*0.25*	*0.11*	*0.00*	*0.32*	*0.05*			*0.00*	*0.37*	*0.63*	*0.04*	*0.01*		*0.37*		*0.01*
			Cpx	r	12	52.40	0.54	2.34	0.34	0.00	5.46	0.13			0.00	16.15	22.56	0.33	0.00		100.26		0.84
					12	*0.20*	*0.03*	*0.13*	*0.03*		*0.20*	*0.05*			*0.00*	*0.12*	*0.27*	*0.05*	*0.00*		*0.39*		*0.00*
			Ol	c	15	39.35	0.01	0.01	0.00		19.36	0.29			0.12	41.72	0.05	0.00	0.00		100.92		0.79
					15	*0.35*	*0.01*	*0.01*			*0.22*	*0.04*			*0.03*	*0.24*	*0.01*	*0.01*			*0.38*		*0.00*
			Ol	r	7	39.43	0.01	0.02	0.00		19.13	0.29			0.10	41.71	0.07	0.00	0.00		100.77		0.80
					7	*0.31*	*0.01*	*0.01*			*0.24*	*0.02*			*0.04*	*0.28*	*0.03*	*0.01*			*0.46*		*0.00*
			Pl	c	14	46.55	0.02	33.81		0.50		0.01			0.04	0.00	17.87	1.68	0.01		100.41	85.37	0.00
					14	*0.30*	*0.01*	*0.17*		*0.06*		*0.02*				*0.01*	*0.20*	*0.06*	*0.01*		*0.41*	*0.56*	*0.00*
			Pl	r	8	46.00	0.01	33.70		0.50		0.02				0.15	18.03	1.54	0.01		99.92	86.59	0.00
					8	*0.56*	*0.01*	*0.79*		*0.12*		*0.03*				*0.30*	*0.33*	*0.22*	*0.00*		*0.80*	*1.83*	*0.00*
OM12_Gid_218	2788	FG	Cpx	c	19	52.25	0.54	2.47	0.24	0.00	5.95	0.16			0.00	15.93	22.53	0.30	0.00		100.36		0.83
					19	*0.96*	*0.14*	*0.69*	*0.07*		*0.50*	*0.04*			*0.00*	*0.40*	*0.60*	*0.04*	*0.00*		*0.64*		*0.01*
			Cpx	r	12	52.70	0.50	2.10	0.23	0.00	5.50	0.15			0.00	16.13	22.87	0.29	0.01		100.47		0.84
					12	*0.90*	*0.17*	*0.62*	*0.10*		*0.75*	*0.04*			*0.00*	*0.24*	*0.93*	*0.07*	*0.00*		*0.48*		*0.02*
			Ol	c	15	38.88	0.02	0.01	0.00		20.80	0.31			0.10	40.37	0.04	0.01	0.00		100.54		0.78
					15	*0.27*	*0.01*	*0.01*			*0.31*	*0.05*			*0.02*	*0.24*	*0.01*	*0.01*			*0.39*		*0.00*
			Ol	r	9	38.95	0.01	0.01	0.00		20.74	0.33			0.11	40.52	0.08	0.01	0.00		100.77		0.78
					9	*0.25*	*0.01*	*0.01*			*0.15*	*0.04*			*0.03*	*0.26*	*0.02*	*0.02*			*0.28*		*0.00*
			Pl	c	15	46.80	0.03	33.57		0.50		0.01				0.00	17.46	1.79	0.01		100.12	84.30	0.00
					15	*0.17*	*0.01*	*0.12*		*0.05*		*0.02*				*0.01*	*0.23*	*0.06*	*0.01*		*0.30*	*0.51*	*0.00*
			Pl	r	9	46.52	0.01	33.97		0.44		0.03				0.00	17.76	1.63	0.01		100.33	85.72	0.00
					9	*0.65*	*0.01*	*0.45*		*0.10*		*0.03*				*0.01*	*0.44*	*0.27*	*0.01*		*0.28*	*2.37*	*0.00*
OM12_Gid_219	2656	FG	Cpx	c	15	52.02	0.72	2.48	0.20	0.00	6.95	0.27			0.00	15.75	21.53	0.36	0.01		100.28		0.80
					15	*0.20*	*0.03*	*0.13*	*0.08*		*0.54*	*0.06*			*0.00*	*0.48*	*0.98*	*0.03*	*0.01*		*0.34*		*0.01*
			Cpx	r	6	52.23	0.70	2.22	0.22	0.00	6.28	0.23			0.00	15.55	22.12	0.38	0.01		99.92		0.82
					6	*0.11*	*0.02*	*0.07*	*0.06*		*0.24*	*0.06*			*0.00*	*0.11*	*0.24*	*0.02*	*0.00*		*0.22*		*0.01*
			Ol	c	21	38.69	0.01	0.02	0.00		22.79	0.50			0.08	38.24	0.04	0.02	0.00		100.38		0.75
					21	*0.21*	*0.01*	*0.01*			*0.21*	*0.09*			*0.03*	*0.20*	*0.02*	*0.02*			*0.39*		*0.00*
			Ol	r	2	38.85	0.00	0.01	0.00		22.41	0.55			0.06	38.01	0.07	0.02	0.00		99.99		0.75
					2	*0.02*		*0.01*			*0.04*	*0.01*			*0.02*	*0.10*	*0.01*	*0.02*			*0.03*		*0.00*
			Pl	c	19	49.28	0.03	31.76		0.53		0.03				0.01	15.38	2.90	0.05		99.91	74.35	0.00
					19	*0.46*	*0.01*	*0.23*		*0.08*		*0.04*				*0.02*	*0.18*	*0.13*	*0.03*		*0.58*	*1.07*	*0.00*
			Pl	r	3	49.42	0.05	31.75		0.42		0.03				0.00	15.56	2.91	0.04		100.13	74.54	0.00
					3	*0.20*	*0.01*	*0.14*		*0.04*		*0.04*				*0.01*	*0.05*	*0.07*	*0.01*		*0.03*	*0.54*	*0.00*
OM12_Gid_Hy_0	1190	LG	Cpx	r	11	52.45	0.44	2.42	0.21	0.00	5.32	0.15			0.00	16.97	22.19	0.26	0.00		100.41		0.85
					11	*0.85*	*0.03*	*0.44*	*0.05*		*0.18*	*0.05*			*0.00*	*0.38*	*0.48*	*0.03*	*0.00*		*0.77*		*0.01*
			Cpx	c	28	52.35	0.40	2.42	0.21	0.00	5.16	0.14			0.00	16.98	22.28	0.25	0.00		100.20		0.85
					28	*0.64*	*0.06*	*0.28*	*0.05*		*0.25*	*0.04*			*0.00*	*0.36*	*0.76*	*0.03*	*0.01*		*0.66*		*0.00*
			Ol	r	3	39.60	0.00	0.02	0.00		17.37	0.29			0.12	43.30	0.05	0.00	0.00		100.74		0.82
					3	*0.44*	*0.01*	*0.01*			*0.25*	*0.05*			*0.05*	*0.31*	*0.01*	*0.00*			*0.88*		*0.01*
			Ol	c	14	39.12	0.01	0.01	0.00		17.60	0.26			0.12	43.55	0.05	0.01	0.00		100.73		0.82
					14	*0.52*	*0.01*	*0.01*			*0.36*	*0.05*			*0.03*	*0.59*	*0.01*	*0.01*			*0.56*		*0.00*
			Pl	r	12	46.38	0.00	33.59		0.82		0.00				0.42	17.37	1.69	0.01		100.30	84.88	0.00
					12	*0.38*	*0.01*	*0.77*		*0.86*						*0.96*	*1.06*	*0.14*	*0.02*		*0.49*	*1.91*	*0.00*
			Pl	c	26	46.57	0.00	33.58		0.51		0.00				0.03	17.50	1.78	0.01		99.97	84.42	0.00
					26	*0.37*	*0.01*	*0.26*		*0.14*		*0.00*				*0.10*	*0.24*	*0.10*	*0.01*		*0.43*	*0.87*	*0.00*

[1] Depth_ calculated height above MOHO
[2] Lithology: SD = Sheeted dike; VG = Varitextured gabbro; FG = Foliated gabbro; MG = Metagabbro; FG = Foliated gabbro
[3] Mineral analysed
[4] Qualifier: r = rim; c = core
[5] Number of analyses
[6] Anorthite content of plagioclase
[7] XMg for Cpx, Opx, and Amph

Table 9. continued

Sample	Depth[1]	Litho.[2]	Min[3]	Qual[4]	No[5]	SiO_2	TiO_2	Al_2O_3	Cr_2O_3	Fe_2O_3	FeO	MnO	Cl	F	NiO	MgO	CaO	Na_2O	K_2O	V_2O_3	Total	An[6]	XMg[7]
OM12_Gid_Hy_018	1190	LG	Cpx	c	21	52.72	0.43	2.53	0.11	0.00	5.39	0.15			0.00	16.58	22.22	0.27	0.00		100.41		0.85
						0.47	*0.07*	*0.28*	*0.06*	*0.00*	*0.26*	*0.04*			*0.00*	*0.39*	*0.50*	*0.03*	*0.00*		*0.42*		*0.01*
			Cpx	r	9	52.86	0.51	2.67	0.16	0.00	5.41	0.14			0.00	16.31	22.58	0.30	0.01		100.95		0.84
						0.68	*0.10*	*0.62*	*0.07*	*0.00*	*0.20*	*0.05*			*0.00*	*0.66*	*0.76*	*0.06*	*0.01*		*0.47*		*0.01*
			Ol	r	2	47.66	1.80	10.23	0.00	0.00	7.78	0.12			0.03	16.47	12.19	1.86	0.06		98.19		0.79
						0.59	*0.05*	*0.46*	*0.00*	*0.00*	*0.09*	*0.01*			*0.01*	*0.02*	*0.03*	*0.12*	*0.00*		*0.06*		*0.00*
			Ol	c	6	54.94	0.15	2.18	0.00	0.00	13.71	0.35			0.03	28.64	0.81	0.01	0.01		100.83		0.79
						0.49	*0.03*	*0.47*	*0.00*	*0.00*	*0.22*	*0.04*			*0.03*	*0.35*	*0.05*	*0.01*	*0.01*		*0.36*		*0.00*
			Pl	r	5	47.23	0.00	34.05	0.00	0.48		0.00			0.03	0.00	17.33	1.76	0.01		100.87	84.41	0.00
						0.45	*0.00*	*0.53*		*0.08*						*0.00*	*0.26*	*0.03*	*0.01*		*0.97*	*0.27*	*0.00*
			Pl	c	14	47.03	0.00	34.09		0.68		0.00				0.18	17.13	1.83	0.01		100.95	83.77	0.00
						0.50	*0.00*	*0.36*		*0.64*		*0.00*				*0.65*	*0.50*	*0.12*	*0.01*		*0.73*	*0.80*	*0.00*
OM12_Gid_Hy_023	1190	LG	Amph	r	2	45.68	0.86	22.21	0.00	0.00	6.84	0.08	0.05	0.05	0.00	13.34	12.00	1.85	0.09		105.32		0.54
						0.11	*0.48*	*5.83*	*0.00*	*0.00*	*1.45*	*0.00*	*0.01*	*0.01*	*0.00*	*3.48*	*0.35*	*0.60*	*0.02*		*0.41*		*0.01*
			Amph	c	7	45.98	1.38	15.82	0.00	0.00	8.20	0.11	0.08	0.04	0.00	16.95	12.08	2.41	0.11		105.42		0.52
						1.55	*0.62*	*1.51*	*0.00*	*0.00*	*0.29*	*0.06*	*0.01*	*0.04*	*0.00*	*0.48*	*0.19*	*0.27*	*0.04*		*0.69*		*0.01*
			Cpx	r	4	53.36	0.43	3.10	0.28	0.00	5.22	0.13	0.01	0.03	0.00	16.34	22.51	0.34	0.01		101.74		0.85
						0.25	*0.14*	*0.83*	*0.05*	*0.00*	*0.52*	*0.08*			*0.00*	*0.10*	*0.95*	*0.08*	*0.00*		*0.56*		*0.01*
			Cpx	c	11	52.97	0.43	3.47	0.23	0.00	5.44	0.15			0.00	16.54	22.34	0.29	0.00		101.86		0.84
						0.46	*0.06*	*0.70*	*0.07*	*0.00*	*0.49*	*0.04*			*0.00*	*0.62*	*1.19*	*0.03*	*0.00*		*0.28*		*0.01*
			Pl	r	3	39.74	0.00	45.12		0.15		0.00			0.00	0.00	12.87	3.03	0.00		100.91	70.18	0.00
						0.09	*0.00*	*0.17*		*0.13*					*0.00*	*0.00*	*0.20*	*0.17*	*0.00*		*0.47*	*1.10*	*0.00*
			Pl	c	6	39.58	0.00	45.17		0.11		0.00				0.00	12.80	3.28	0.00		100.95	68.38	0.00
						0.55	*0.00*	*0.64*		*0.15*		*0.00*				*0.00*	*0.21*	*0.30*	*0.00*		*0.56*	*2.24*	*0.00*
OM12_Gid_Hy_025	1190	LG	Cpx	r	6	52.49	0.44	2.27	0.24	0.00	5.29	0.17			0.00	17.27	21.93	0.25	0.01		100.35		0.85
						0.27	*0.02*	*0.18*	*0.03*	*0.00*	*0.40*	*0.04*			*0.00*	*0.57*	*0.92*	*0.04*	*0.01*		*0.33*		*0.01*
			Cpx	c	24	52.58	0.43	2.36	0.24	0.00	5.36	0.13			0.00	16.98	22.28	0.29	0.01		100.66		0.85
						0.35	*0.06*	*0.29*	*0.08*	*0.00*	*0.25*	*0.03*			*0.00*	*0.40*	*0.62*	*0.04*	*0.01*		*0.39*		*0.01*
			Ol	r	4	39.52	0.01	0.00	0.00	0.00	17.76	0.28			0.10	43.69	0.05	0.01	0.00		101.43		0.81
						0.29	*0.01*	*0.00*	*0.00*	*0.00*	*0.69*	*0.03*			*0.04*	*0.42*	*0.01*	*0.01*	*0.00*		*0.60*		*0.01*
			Ol	c	9	39.61	0.01	0.01	0.00	0.00	17.66	0.27			0.11	43.70	0.05	0.00	0.01		101.42		0.82
						0.17	*0.01*	*0.01*	*0.00*	*0.00*	*0.20*	*0.06*			*0.02*	*0.28*	*0.01*	*0.01*	*0.01*		*0.36*		*0.00*
			Pl	r	13	47.44	0.00	33.41	0.00	0.51		0.00			0.02	0.02	17.18	2.03	0.03		100.60	82.29	0.00
						0.70	*0.00*	*0.41*		*0.08*						*0.05*	*0.51*	*0.24*	*0.03*		*0.53*	*2.27*	*0.00*
			Pl	c	32	47.12	0.00	33.47		0.44		0.00				0.01	17.29	1.97	0.02		100.33	82.81	0.00
						0.39	*0.00*	*0.34*		*0.08*		*0.00*				*0.02*	*0.29*	*0.15*	*0.03*		*0.37*	*1.37*	*0.00*
OM12_Gid_Hy_030	1190	LG	Amph		46	51.60	1.13	4.01	0.00	0.00	10.94	0.17	0.14	0.18	0.00	17.19	11.32	1.02	0.15		99.97		0.51
						0.70	*0.17*	*0.48*	*0.00*	*0.00*	*0.36*	*0.05*	*0.02*	*0.27*	*0.00*	*0.51*	*0.30*	*0.16*	*0.03*		*0.66*		*0.02*
			Ilm	c	9	29.23	38.87	0.53	0.05	0.00	2.28	0.08			0.00	0.11	27.32	0.00	0.00	0.00	98.47		0.00
						2.73	*2.40*	*0.29*	*0.02*	*0.00*	*3.61*	*0.13*			*0.00*	*0.30*	*2.60*	*0.00*	*0.00*	*0.00*	*1.00*		*0.00*
			Cpx	r	4	52.33	0.52	3.75	0.30	0.00	5.00	0.22			0.00	16.04	21.71	0.34	0.00		100.23		0.85
						0.68	*0.07*	*2.60*	*0.06*	*0.00*	*0.15*	*0.04*			*0.00*	*1.34*	*0.51*	*0.09*	*0.01*		*0.44*		*0.01*
			Cpx	c	38	52.34	0.46	2.78	0.48	0.00	5.26	0.14			0.00	16.58	21.79	0.33	0.00		100.15		0.85
						0.86	*0.08*	*0.31*	*0.23*	*0.00*	*0.45*	*0.04*			*0.00*	*0.43*	*0.61*	*0.05*	*0.00*		*0.89*		*0.01*
			Pl		27	47.66	0.01	33.44		0.71		0.00				0.13	16.45	2.22	0.01		100.62	80.35	0.00
						0.69	*0.02*	*0.37*		*1.26*		*0.00*				*0.47*	*0.91*	*0.15*	*0.01*		*0.56*	*0.87*	*0.00*

[1] Depth_ calculated height above MOHO
[2] Lithology: SD = Sheeted dike; VG = Varitextured gabbro; FG = Foliated gabbro; MG = Metagabbro; FG = Foliated gabbro
[3] Mineral analysed
[4] Qualifier: r = rim; c = core
[5] Number of analyses
[6] Anorthite content of plagioclase
[7] XMg for Cpx, Opx, and Amph

Table 9. continued

Sample	Depth[1]	Litho.[2]	Min[3]	Qual[4]	No[5]	SiO_2	TiO_2	Al_2O_3	Cr_2O_3	Fe_2O_3	FeO	MnO	Cl	F	NiO	MgO	CaO	Na_2O	K_2O	V_2O_3	Total	An[6]	XMg[7]
OM12_Gid_Hy_032B	1190	LG	Amph		18	44.26	3.13	9.65	0.00	0.00	12.54	0.19	0.16	0.08	0.00	14.00	11.10	2.43	0.21		99.81		0.49
						0.76	*0.29*	*0.49*	*0.00*	*0.00*	*0.34*	*0.05*	*0.02*	*0.10*	*0.00*	*0.49*	*0.14*	*0.20*	*0.01*		*0.79*		*0.02*
			Pl		24	55.85	0.01	28.16		0.45		0.00				0.00	10.14	5.97	0.11		100.70	48.12	0.00
						0.83	*0.02*	*0.59*		*0.08*		*0.00*				*0.00*	*0.61*	*0.33*	*0.03*		*0.47*	*2.82*	*0.00*
OM12_Gid_Hy_032C	1190	LG	Amph	r	3	41.63	3.73	10.09	0.00	0.00	12.10	0.21	0.13	0.02	0.00	14.72	11.10	2.65	0.21		98.62		0.51
						0.06	*0.08*	*0.06*	*0.00*	*0.00*	*0.15*	*0.01*	*0.01*	*0.03*	*0.00*	*0.10*	*0.05*	*0.04*	*0.03*		*0.11*		*0.01*
		LG	Amph	c	29	42.53	3.70	10.06	0.00	0.00	11.81	0.16	0.12	0.04	0.00	14.99	11.18	2.75	0.21		99.63		0.50
						0.96	*0.24*	*0.43*	*0.00*	*0.00*	*0.29*	*0.04*	*0.02*	*0.05*	*0.00*	*0.27*	*0.22*	*0.24*	*0.09*		*1.08*		*0.02*
OM12_Gid_Hy_032D	1190	LG	Amph		26	42.48	3.54	9.95	0.00	0.00	12.03	0.16	0.12	0.03	0.00	14.95	11.28	2.66	0.19		99.46		0.50
						0.75	*0.70*	*0.48*	*0.00*	*0.00*	*0.40*	*0.05*	*0.02*	*0.04*	*0.00*	*0.35*	*0.26*	*0.29*	*0.01*		*0.60*		*0.01*
			Opx		10	49.02	1.47	5.22	0.09	0.00	10.93	0.19			0.00	17.75	11.13	1.54	0.24		97.60		0.74
						0.75	*0.12*	*0.55*	*0.05*	*0.00*	*0.34*	*0.04*			*0.00*	*0.41*	*0.17*	*0.02*	*0.02*		*0.40*		*0.01*
OM12_Gid_Hy_038	1190	LG	Amph		9	42.81	2.64	10.86	0.00	0.00	9.22	0.08	0.07	0.04	0.00	16.72	11.67	2.72	0.16		99.08		0.52
						0.96	*0.38*	*0.25*	*0.00*	*0.00*	*0.19*	*0.05*	*0.01*	*0.05*	*0.00*	*0.36*	*0.10*	*0.07*	*0.01*		*0.79*		*0.02*
			Cpx		8	51.56	0.44	2.54	0.33	0.00	5.21	0.11			0.00	17.70	21.68	0.33	0.00		99.90		0.86
						0.80	*0.15*	*0.12*	*0.06*	*0.00*	*0.68*	*0.02*			*0.00*	*0.87*	*1.09*	*0.05*	*0.01*		*0.93*		*0.01*
			Ol		20	38.21	0.01	0.01	0.06	0.00	19.86	0.27			0.17	43.72	0.05	0.01	0.00		102.31		0.80
						0.76	*0.01*	*0.02*	*0.00*	*0.00*	*0.29*	*0.04*			*0.03*	*0.56*	*0.02*	*0.01*	*0.00*		*0.55*		*0.00*
			Pl		28	47.45	0.03	32.47		0.47		0.00				0.03	16.56	2.35	0.01		99.37	79.50	0.00
						0.66	*0.03*	*0.39*		*0.08*		*0.00*				*0.15*	*0.41*	*0.20*	*0.01*		*0.71*	*1.74*	*0.00*
OM12_Gid_Hy_039_I	1190	LG	Cpx	r	3	51.93	0.62	2.79	0.31	0.00	5.84	0.14			0.00	17.00	21.13	0.37	0.02		100.14		0.84
						0.61	*0.05*	*0.46*	*0.04*	*0.00*	*0.26*	*0.03*			*0.00*	*0.16*	*0.62*	*0.02*	*0.01*		*0.63*		*0.01*
			Cpx	c	6	52.27	0.41	2.54	0.35	0.00	5.37	0.13			0.00	17.03	21.41	0.29	0.01		99.81		0.85
						0.48	*0.08*	*0.06*	*0.05*	*0.00*	*0.25*	*0.04*			*0.00*	*0.53*	*0.69*	*0.04*	*0.01*		*0.54*		*0.00*
			Pl	r	3	48.74	0.04	32.44		0.47		0.00				0.00	15.95	2.78	0.02		100.45	75.93	0.00
						0.26	*0.03*	*0.32*		*0.04*		*0.00*				*0.00*	*0.08*	*0.11*	*0.01*		*0.14*	*0.68*	*0.00*
			Pl	c	17	47.53	0.00	33.22		0.48		0.00				0.00	16.92	2.21	0.01		100.37	80.82	0.00
						0.34	*0.01*	*0.25*		*0.06*		*0.00*				*0.00*	*0.23*	*0.14*	*0.02*		*0.41*	*1.12*	*0.00*
OM12_Gid_Hy_039_II	1190	LG	Amph		26	42.64	4.28	11.34	0.00	0.00	8.64	0.09	0.20	0.06	0.00	15.40	11.64	2.96	0.32		99.65		0.53
						0.30	*0.57*	*0.13*	*0.00*	*0.00*	*0.26*	*0.03*	*0.01*	*0.05*	*0.00*	*0.29*	*0.17*	*0.08*	*0.02*		*0.58*		*0.02*
			Pl		23	47.64	0.01	33.24		0.49		0.00				0.00	16.84	2.20	0.01		100.43	80.85	0.00
						0.22	*0.02*	*0.26*		*0.05*		*0.00*				*0.00*	*0.23*	*0.10*	*0.02*		*0.51*	*0.79*	*0.00*
OM12_Gid_Hy_042	1190	LG	Cpx	r	9	52.76	0.49	2.22	0.24	0.00	5.44	0.13			0.00	16.49	22.14	0.31	0.01		100.21		0.84
						0.26	*0.04*	*0.10*	*0.05*	*0.00*	*0.26*	*0.05*			*0.00*	*0.25*	*0.47*	*0.03*	*0.01*		*0.40*		*0.01*
			Cpx	c	21	52.77	0.48	2.45	0.20	0.00	5.80	0.15			0.00	16.61	21.50	0.31	0.00		100.27		0.84
						0.35	*0.05*	*0.20*	*0.09*	*0.00*	*0.48*	*0.04*			*0.00*	*0.69*	*1.02*	*0.04*	*0.00*		*0.59*		*0.01*
			Ol	r	3	39.46	0.01	0.00	0.00	0.00	20.04	0.24			0.12	41.65	0.04	0.01	0.00		101.57		0.79
						0.25	*0.01*	*0.00*	*0.00*	*0.00*	*0.14*	*0.02*			*0.03*	*0.28*	*0.01*	*0.01*	*0.00*		*0.66*		*0.00*
			Ol	c	7	39.74	0.01	0.01	0.00	0.00	19.86	0.32			0.10	41.59	0.05	0.01	0.00		101.70		0.79
						0.30	*0.01*	*0.01*	*0.00*	*0.00*	*0.21*	*0.04*			*0.03*	*0.44*	*0.01*	*0.01*	*0.00*		*0.49*		*0.00*
			Pl	r	12	48.08	0.01	32.75		0.81		0.00				0.39	16.35	2.36	0.02		100.77	79.20	0.00
						0.79	*0.02*	*1.87*		*1.12*		*0.00*				*1.29*	*0.42*	*0.24*	*0.02*		*0.60*	*1.86*	*0.00*
			Pl	c	27	48.57	0.01	33.08		0.51		0.00				0.08	16.20	2.46	0.02		100.92	78.35	0.00
						0.71	*0.02*	*0.60*		*0.32*		*0.00*				*0.28*	*0.69*	*0.32*	*0.02*		*0.48*	*2.84*	*0.00*

[1] Depth_ calculated height above MOHO
[2] Lithology: SD = Sheeted dike; VG = Varitextured gabbro; MG = Metagabbro; FG = Foliated gabbro
[3] Mineral analysed
[4] Qualifier: r = rim; c = core
[5] Number of analyses
[6] Anorthite content of plagioclase
[7] XMg for Cpx, Opx, and Amph

Table 9. continued

Sample	Depth[1]	Litho.[2]	Min[3]	Qual[4]	No[5]	SiO_2	TiO_2	Al_2O_3	Cr_2O_3	Fe_2O_3	FeO	MnO	Cl	F	NiO	MgO	CaO	Na_2O	K_2O	V_2O_3	Total	An[6]	XMg[7]
OM12_Gid_Hy_055B	1190	LG	Cpx		22	51.85	0.54	2.74	0.58	0.00	5.28	0.14			0.00	17.12	21.83	0.31	0.00		100.40		0.85
						0.46	*0.11*	*0.22*	*0.29*	*0.00*	*0.51*	*0.04*			*0.00*	*0.35*	*0.55*	*0.04*	*0.01*		*0.50*		*0.01*
			Amph		10	52.12	0.51	2.70	0.00	0.00	5.92	0.14	0.02	0.04	0.00	16.28	21.94	0.33	0.01		102.14		0.53
						0.46	*0.07*	*0.51*	*0.00*	*0.00*	*0.79*	*0.04*	*0.03*	*0.04*	*0.00*	*0.33*	*0.92*	*0.09*	*0.01*		*0.43*		*0.02*
			Cpx	r	5	52.09	0.49	2.10	0.19	0.00	5.48	0.17			0.00	16.35	21.96	0.26	0.00		99.11		0.84
						0.44	*0.05*	*0.17*	*0.05*	*0.00*	*0.26*	*0.05*			*0.00*	*0.23*	*0.72*	*0.01*	*0.01*		*0.60*		*0.01*
			Cpx	c	22	52.42	0.49	2.44	0.18	0.00	5.50	0.14			0.00	16.38	22.14	0.26	0.01		99.97		0.84
						0.80	*0.07*	*0.37*	*0.06*	*0.00*	*0.32*	*0.04*				*0.54*	*0.71*	*0.05*	*0.01*		*0.77*		*0.01*
			Pl	r	5	46.83	0.00	33.47		0.39		0.00				0.00	16.46	2.09	0.08		99.31	80.96	0.00
						0.19	*0.00*	*0.13*		*0.03*							*0.30*	*0.17*	*0.12*		*0.33*	*1.86*	*0.00*
			Pl	c	19	46.92	0.00	33.56		0.40		0.00				0.00	16.67	2.10	0.00		99.65	81.43	0.00
						0.38	*0.00*	*0.21*		*0.10*							*0.25*	*0.21*	*0.01*		*0.53*	*1.07*	*0.00*
OM12_Gid_Hy_059	1190	LG	Cpx	r	6	52.47	0.52	2.39	0.14	0.00	5.20	0.14			0.00	16.57	22.24	0.27	0.01		99.95		0.85
						0.28	*0.04*	*0.23*	*0.04*	*0.00*	*0.19*	*0.03*			*0.00*	*0.24*	*0.34*	*0.03*	*0.01*		*0.29*		*0.00*
			Cpx	c	9	52.12	0.47	2.87	0.19	0.00	5.41	0.14			0.00	16.43	22.19	0.24	0.01		100.07		0.84
						0.58	*0.06*	*0.47*	*0.05*	*0.00*	*0.43*	*0.03*			*0.00*	*0.46*	*0.84*	*0.02*	*0.00*		*0.54*		*0.01*
			Pl	r	4	46.96	0.00	33.79		0.41		0.00				0.00	17.59	1.81	0.00		100.56	84.31	0.00
						0.17	*0.00*	*0.10*		*0.07*							*0.20*	*0.05*	*0.00*		*0.09*	*0.49*	*0.00*
			Pl	c	25	46.73	0.01	33.49		0.49		0.00				0.00	17.47	1.81	0.01		100.01	84.18	0.00
						0.34	*0.02*	*0.26*		*0.12*							*0.21*	*0.05*	*0.01*		*0.57*	*0.67*	*0.00*
OM12_Gid_Hy_059.5	1190	LG	Amph	r	3	47.63	0.86	9.36	0.00	0.00	8.41	0.07	0.14	0.01	0.00	16.97	12.51	1.75	0.06		99.89		0.51
						0.86	*0.61*	*0.74*	*0.00*	*0.00*	*0.04*	*0.05*	*0.04*	*0.01*	*0.00*	*0.16*	*0.37*	*0.16*	*0.01*		*0.40*		*0.01*
			Amph	c	5	46.16	0.20	10.66	0.00	0.00	9.37	0.06	0.12	0.03	0.00	16.17	12.79	1.96	0.08		99.70		0.54
						0.58	*0.03*	*0.16*	*0.00*	*0.00*	*0.46*	*0.04*	*0.03*	*0.06*	*0.00*	*0.25*	*0.16*	*0.14*	*0.01*		*0.39*		*0.01*
			Cpx	r	3	45.45	0.30	11.63	0.16	0.00	8.49	0.06			0.00	16.93	12.26	2.19	0.07		97.54		0.78
						0.38	*0.05*	*0.60*	*0.09*	*0.00*	*0.22*	*0.05*			*0.00*	*0.40*	*0.63*	*0.09*	*0.01*		*0.69*		*0.01*
			Cpx	c	4	45.54	0.29	11.50	0.09	0.00	8.92	0.03			0.00	16.44	12.49	2.28	0.08		97.65		0.77
						0.65	*0.04*	*0.42*	*0.05*	*0.00*	*0.22*	*0.02*			*0.00*	*0.29*	*0.12*	*0.11*	*0.02*		*0.31*		*0.01*
			Pl	r	6	43.80	0.00	36.21		0.03		0.00				0.00	19.86	0.42	0.00		100.32	96.29	0.00
						0.20	*0.00*	*0.17*		*0.08*							*0.17*	*0.08*	*0.00*		*0.54*	*0.69*	*0.00*
			Pl	c	14	43.78	0.00	36.12		0.00		0.00				0.00	20.02	0.39	0.00		100.30	96.60	0.00
						0.25	*0.00*	*0.26*		*0.00*							*0.25*	*0.09*	*0.00*		*0.48*	*0.83*	*0.00*
OM12_Gid_Hy_062	1190	LG	Cpx		20	52.89	0.45	2.55	0.21	0.00	5.44	0.14			0.00	16.55	22.48	0.26	0.01		100.98		0.84
						0.49	*0.05*	*0.26*	*0.06*	*0.00*	*0.51*	*0.04*			*0.00*	*0.56*	*1.00*	*0.03*	*0.01*		*0.71*		*0.01*
OM12_Gid_Hy_068	1190	LG	Cpx	r	11	53.33	0.47	3.16	0.25	0.00	5.35	0.16			0.00	16.86	22.19	0.27	0.00		102.04		0.85
						0.37	*0.02*	*0.14*	*0.06*	*0.00*	*0.26*	*0.04*			*0.00*	*0.28*	*0.40*	*0.03*	*0.00*		*0.59*		*0.00*
			Cpx	c	27	53.07	0.46	3.47	0.26	0.00	5.49	0.14			0.00	16.78	22.04	0.27	0.01		101.98		0.85
						0.66	*0.03*	*0.55*	*0.10*	*0.00*	*0.42*	*0.05*			*0.00*	*0.40*	*0.99*	*0.03*	*0.01*		*0.58*		*0.01*
			Pl	r	9	47.60	0.00	50.04		0.49		0.00				0.00	17.12	2.03	0.00		117.28	82.34	0.00
						0.34	*0.00*	*0.44*		*0.10*							*0.22*	*0.05*	*0.01*		*0.52*	*0.49*	*0.00*
			Pl	c	29	47.56	0.00	50.16		0.50		0.00				0.00	17.25	1.96	0.02		117.45	82.90	0.00
						0.35	*0.01*	*0.47*		*0.10*							*0.27*	*0.06*	*0.06*		*0.50*	*1.23*	*0.00*
OM12_Gid_Hy_077	1190	LG	Cpx		9	54.81	0.46	2.78	0.41	0.00	5.45	0.13			0.00	16.25	22.53	0.31	0.00		103.13		0.84
						0.30	*0.05*	*0.20*	*0.10*	*0.00*	*0.21*	*0.01*			*0.00*	*0.23*	*0.57*	*0.02*	*0.00*		*0.49*		*0.00*
			Ol		10	41.64	0.01	0.01	0.00	0.00	18.33	0.26			0.14	42.18	0.07	0.01	0.00		102.66		0.80
						0.30	*0.01*	*0.01*	*0.00*	*0.00*	*0.36*	*0.03*			*0.04*	*0.37*	*0.01*	*0.01*	*0.00*		*0.55*		*0.00*
			Pl		9	49.54	0.02	33.53		0.51		0.00				0.01	17.54	2.02	0.02		103.15	82.64	0.00
						0.17	*0.01*	*0.24*		*0.06*						*0.02*	*0.17*	*0.08*	*0.01*		*0.42*	*0.65*	*0.00*

[1] Depth_ calculated height above MOHO
[2] Lithology: SD = Sheeted dike; VG = Varitextured gabbro; FG = Foliated gabbro; MG = Metagabbro; FG = Foliated gabbro
[3] Mineral analysed
[4] Qualifier: r = rim; c = core
[5] Number of analyses
[6] Anorthite content of plagioclase
[7] XMg for Cpx, Opx, and Amph

Table 9. continued

Sample	Depth[1]	Litho.[2]	Min[3]	Qual[4]	No[5]	SiO2	TiO2	Al2O3	Cr2O3	Fe2O3	FeO	MnO	Cl	F	NiO	MgO	CaO	Na2O	K2O	V2O3	Total	An[6]	XMg[7]
OM12_Gid_Hy_102_I	1190	LG	Cpx	r	6	52.63	0.48	2.61	0.27	0.00	5.37	0.15			0.00	16.85	21.41	0.38	0.01		100.15		0.85
						0.59	*0.13*	*1.15*	*0.03*	*0.00*	*0.63*	*0.04*			*0.00*	*0.51*	*2.25*	*0.25*	*0.01*		*0.59*		*0.01*
			Cpx	c	16	52.77	0.43	2.52	0.24	0.00	5.22	0.14			0.00	16.99	22.08	0.27	0.00		100.67		0.85
						0.36	*0.05*	*0.15*	*0.06*	*0.00*	*0.33*	*0.03*			*0.00*	*0.70*	*1.24*	*0.05*	*0.00*		*0.74*		*0.00*
			Ol	r	3	38.88	0.01	0.03	0.00	0.00	18.07	0.24			0.11	43.73	0.08	0.00	0.00		101.15		0.81
						0.31	*0.01*	*0.00*			*0.22*	*0.01*			*0.05*	*0.17*	*0.01*				*0.72*		*0.81*
			Ol	c	9	38.23	0.01	0.01	0.00		18.24	0.28			0.13	44.37	0.06	0.00	0.00		101.34		0.81
						0.23	*0.01*	*0.01*	*0.00*		*0.23*	*0.06*			*0.04*	*0.28*	*0.02*				*0.35*		*0.00*
			Pl	r	6	46.56	0.01	34.44		0.42		0.00				0.00	17.75	1.73	0.01		100.91	84.99	0.00
						0.40	*0.02*	*0.27*		*0.03*							*0.11*	*0.13*	*0.01*		*0.42*	*0.99*	*0.00*
			Pl	c	14	47.16	0.00	34.03		0.44		0.00				0.00	17.42	1.85	0.01		100.90	83.85	0.00
						0.21	*0.00*	*0.14*		*0.07*							*0.14*	*0.04*	*0.01*		*0.28*	*0.35*	*0.00*
OM12_Gid_Hy_102_II	1190	LG	Cpx	r	6	52.52	0.39	2.35	0.18	0.00	4.96	0.13			0.00	16.59	22.85	0.28	0.01		100.25		0.86
						0.67	*0.10*	*0.98*	*0.07*	*0.00*	*0.35*	*0.05*			*0.00*	*0.76*	*0.68*	*0.05*	*0.01*		*0.73*		*0.01*
			Cpx	c	14	52.33	0.41	2.50	0.25	0.00	5.17	0.14			0.00	16.89	22.19	0.28	0.01		100.17		0.85
						0.33	*0.03*	*0.18*	*0.08*	*0.00*	*0.20*	*0.04*			*0.00*	*0.43*	*0.46*	*0.04*	*0.01*		*0.68*		*0.01*
			Pl	r	8	46.53	0.00	33.93		0.45		0.00				0.00	17.52	1.81	0.01		100.25	84.21	0.00
						0.23	*0.00*	*0.31*		*0.05*							*0.26*	*0.11*	*0.01*		*0.55*	*0.91*	*0.00*
			Pl	c	26	46.75	0.00	34.13		0.40		0.00				0.00	17.47	1.86	0.01		100.62	83.80	0.00
						0.33	*0.00*	*0.21*		*0.07*							*0.17*	*0.10*	*0.01*		*0.31*	*0.81*	*0.00*
OM12_Gid_Hy_108	1190	LG	Cpx		10	51.99	0.43	2.16	0.27	0.00	5.30	0.13			0.00	16.94	21.63	0.27	0.00		99.13		0.85
						0.36	*0.03*	*0.18*	*0.03*	*0.00*	*0.58*	*0.04*			*0.00*	*0.78*	*1.48*	*0.02*	*0.01*		*0.43*		*0.01*
OM12_Gid_Hy_154_I	1190	LG	Cpx	r	9	53.22	0.49	2.25	0.15	0.00	5.46	0.14			0.00	16.89	22.08	0.29	0.01		100.97		0.85
						0.12	*0.03*	*0.23*	*0.05*	*0.00*	*0.17*	*0.03*			*0.00*	*0.26*	*0.66*	*0.05*	*0.01*		*0.55*		*0.00*
			Cpx	c	29	53.06	0.45	2.41	0.14	0.00	5.58	0.15			0.00	16.78	22.09	0.28	0.00		100.93		0.84
						0.32	*0.06*	*0.24*	*0.07*	*0.00*	*0.46*	*0.04*			*0.00*	*0.53*	*0.93*	*0.04*	*0.01*		*0.42*		*0.01*
			Ol		24	39.71	0.01	0.01	0.00	0.00	18.38	0.27			0.14	42.92	0.05	0.01	0.00		101.51		0.81
						0.21	*0.01*	*0.01*	*0.00*		*0.34*	*0.04*			*0.03*	*0.31*	*0.02*				*0.44*		*0.00*
			Pl	r	12	47.28	0.00	34.36		0.51		0.00				0.04	17.59	1.80	0.01		101.60	84.32	0.00
						0.44	*0.01*	*0.20*		*0.07*						*0.09*	*0.27*	*0.14*	*0.01*		*0.37*	*1.23*	*0.00*
			Pl	c	45	47.23	0.00	34.15		0.51		0.00				0.01	17.42	1.87	0.02		101.20	83.64	0.00
						0.52	*0.00*	*0.35*		*0.07*						*0.05*	*0.36*	*0.16*	*0.02*		*0.57*	*1.43*	*0.00*
OM12_Gid_Hy_154_II	1190	LG	Cpx	r	3	52.78	0.60	2.05	0.06	0.00	5.55	0.14			0.00	16.24	22.41	0.29	0.00		100.13		0.84
						0.25	*0.01*	*0.08*	*0.04*	*0.00*	*0.05*	*0.05*			*0.00*	*0.12*	*0.13*	*0.01*	*0.00*		*0.55*		*0.00*
			Cpx	c	13	52.99	0.50	2.25	0.08	0.00	5.58	0.15			0.00	16.55	22.31	0.30	0.01		100.74		0.84
						0.30	*0.05*	*0.15*	*0.04*	*0.00*	*0.28*	*0.05*			*0.00*	*0.28*	*0.50*	*0.03*	*0.01*		*0.38*		*0.01*
			Pl	r	3	48.07	0.02	33.66		0.46		0.00				0.00	16.91	2.23	0.04		101.38	80.58	0.00
						0.16	*0.02*	*0.08*		*0.03*						*0.00*	*0.13*	*0.05*	*0.00*		*0.35*	*0.22*	*0.00*
			Pl	c	13	47.64	0.01	33.85		0.48		0.00				0.01	17.25	1.99	0.04		101.27	82.54	0.00
						0.41	*0.02*	*0.33*		*0.10*						*0.02*	*0.35*	*0.12*	*0.03*		*0.66*	*1.07*	*0.00*
OM12_Gid_Hy_166	1190	LG	Cpx	r	4	53.37	0.50	2.23	0.29	0.00	5.33	0.15			0.00	16.76	22.19	0.29	0.00		101.12		0.85
						0.14	*0.02*	*0.17*	*0.05*	*0.00*	*0.26*	*0.03*			*0.00*	*0.06*	*0.46*	*0.01*	*0.00*		*0.33*		*0.01*
			Cpx	c	7	52.97	0.49	2.38	0.27	0.00	5.78	0.17			0.00	16.93	21.45	0.28	0.00		100.74		0.84
						0.30	*0.02*	*0.14*	*0.05*	*0.00*	*0.32*	*0.06*			*0.00*	*0.44*	*0.93*	*0.03*	*0.01*		*0.65*		*0.01*
			Ol	r	6	53.71	0.45	2.06	0.00	0.00	5.45	0.16			0.02	16.94	22.04	0.26	0.00		101.11		0.85
						0.81	*0.09*	*0.37*	*0.00*	*0.00*	*0.53*	*0.04*			*0.01*	*0.63*	*1.12*	*0.06*	*0.00*		*0.59*		*0.01*
			Ol	c	17	39.80	0.01	0.01	0.00	0.00	18.43	0.26			0.12	42.34	0.04	0.02	0.00		101.03		0.80
						0.26	*0.01*	*0.01*	*0.00*	*0.00*	*0.27*	*0.05*			*0.04*	*0.44*	*0.01*				*0.50*		*0.00*
			Pl	r	9	47.19	0.00	33.95		0.64		0.00				0.11	17.27	1.84	0.01		101.01	83.80	0.00
						0.45	*0.00*	*0.43*		*0.36*						*0.21*	*0.54*	*0.10*	*0.01*		*0.85*	*0.83*	*0.00*
			Pl	c	21	47.44	0.00	33.93		0.48		0.00				0.00	17.25	1.90	0.01		101.02	83.31	0.00
						0.24	*0.00*	*0.24*		*0.07*						*0.00*	*0.15*	*0.09*	*0.01*		*0.27*	*0.69*	*0.00*

[1] Depth_ calculated height above MOHO
[2] Lithology: SD = Sheeted dike; VG = Varitextured gabbro; MG = Metagabbro; FG = Foliated gabbro; FG = Foliated gabbro
[3] Mineral analysed
[4] Qualifier: r = rim; c = core
[5] Number of analyses
[6] Anorthite content of plagioclase
[7] XMg for Cpx, Opx, and Amph

Table 9. continued

Sample	Depth[1]	Litho.[2]	Min[3]	Qual[4]	No[5]	SiO2	TiO2	Al2O3	Cr2O3	Fe2O3	FeO	MnO	Cl	F	NiO	MgO	CaO	Na2O	K2O	V2O3	Total	An[6]	XMg[7]
OM12_Gid_Hy000	1190	MG	Amph		5	45.69	1.51	11.15	0.33	0.00	7.98	0.03	0.16	0.16	0.00	17.14	12.26	2.20	0.16		100.91		0.59
						0.68	*0.10*	*0.77*	*0.05*	*0.00*	*0.24*	*0.04*	*0.01*	*0.02*	*0.00*	*0.57*	*0.56*	*0.13*	*0.02*		*0.43*		*0.01*
OM12_Gid_Hy023	1190	MG	Amph		10	44.76	1.71	10.46	0.72	0.00	8.23	0.04	0.12	0.10	0.00	16.71	11.79	2.43	0.17		99.33		0.60
						1.26	*0.48*	*0.84*	*0.24*	*0.00*	*0.24*	*0.06*	*0.08*	*0.04*	*0.00*	*0.49*	*0.23*	*0.25*	*0.04*		*0.46*		*0.02*
OM12_Gid_Hy030	1190	MG	Amph		10	52.33	1.14	4.04	0.00	0.00	10.82	0.18	0.14	0.19	0.00	17.73	11.43	1.07	0.16		101.39		0.60
						0.34	*0.11*	*0.31*	*0.00*	*0.00*	*0.17*	*0.02*	*0.02*	*0.03*	*0.00*	*0.34*	*0.23*	*0.05*	*0.02*		*0.36*		*0.02*
OM12_Gid_Hy032D	1190	MG	Amph		8	43.69	3.74	10.58	0.00	0.00	11.71	0.15	0.12	0.15	0.00	14.70	11.35	2.74	0.19		101.20		0.58
						0.40	*0.29*	*0.40*	*0.00*	*0.00*	*0.47*	*0.03*	*0.02*	*0.01*	*0.00*	*0.14*	*0.13*	*0.08*	*0.01*		*0.36*		*0.01*
OM12_Gid_Hy038	1190	LG	Amph		5	44.36	2.44	11.43	0.38	0.00	9.28	0.05	0.08	0.14	0.00	16.32	11.82	2.62	0.15		101.19		0.59
						0.16	*0.45*	*0.08*	*0.06*	*0.00*	*0.09*	*0.06*	*0.01*	*0.02*	*0.00*	*0.28*	*0.09*	*0.05*	*0.01*		*0.38*		*0.02*
OM12_Gid_Hy038	1190	MG	Amph		5	43.41	3.91	11.37	0.03	0.00	9.65	0.12	0.10	0.11	0.00	15.37	11.58	2.76	0.19		100.68		0.59
						0.18	*0.29*	*0.16*	*0.06*	*0.00*	*0.23*	*0.01*	*0.00*	*0.02*	*0.00*	*0.12*	*0.20*	*0.05*	*0.01*		*0.11*		*0.01*
OM12_Gid_Hy039_II	1190	MG	Amph		10	43.40	4.11	11.48	0.31	0.00	8.67	0.03	0.22	0.12	0.00	15.85	11.90	2.72	0.31		101.23		0.58
						0.86	*0.92*	*0.21*	*0.18*	*0.00*	*0.24*	*0.05*	*0.06*	*0.03*	*0.00*	*0.34*	*0.21*	*0.15*	*0.04*		*0.49*		*0.01*
OM12_Gid_Hy042	1190	LG	Amph		5	44.35	2.24	12.57	0.39	0.00	8.96	0.03	0.08	0.18	0.00	15.32	11.84	2.58	0.05		100.70		0.59
						0.77	*0.32*	*0.59*	*0.06*	*0.00*	*0.13*	*0.05*	*0.01*	*0.02*	*0.00*	*0.36*	*0.12*	*0.13*	*0.01*		*0.21*		*0.01*
OM12_Gid_Hy102_I	1190	LG	Amph		5	45.07	2.04	10.61	0.55	0.00	7.82	0.04	0.08	0.15	0.00	16.94	11.81	2.55	0.19		99.96		0.59
						0.40	*0.05*	*0.31*	*0.07*	*0.00*	*0.20*	*0.05*	*0.00*	*0.03*	*0.00*	*0.19*	*0.17*	*0.15*	*0.01*		*0.32*		*0.01*
OM12_Gid_Hy103	1190	MG	Amph		10	43.77	3.07	10.98	0.60	0.00	8.64	0.03	0.22	0.15	0.00	16.14	11.85	2.55	0.17		100.26		0.60
						0.22	*0.16*	*0.17*	*0.09*	*0.00*	*0.19*	*0.04*	*0.02*	*0.03*	*0.00*	*0.15*	*0.13*	*0.10*	*0.05*		*0.51*		*0.02*
OM12_Gid_Hy166	1190	LG	Amph		5	44.20	2.56	12.17	0.34	0.00	8.78	0.10	0.10	0.15	0.00	15.58	11.80	2.41	0.11		100.39		0.59
						0.22	*0.12*	*0.27*	*0.08*	*0.00*	*0.24*	*0.05*	*0.00*	*0.01*	*0.00*	*0.20*	*0.09*	*0.07*	*0.00*		*0.32*		*0.01*

[1] Depth_calculated height above MOHO

[2] Lithology: SD = Sheeted dike; VG = Varitextured gabbro; FG = Foliated gabbro; MG = Metagabbro; FG = Foliated gabbro

[3] Mineral analysed

[4] Qualifier: r = rim; c = core

[5] Number of analyses

[6] Anorthite content of plagioclase

[7] XMg for Cpx, Opx, and Amph

Table 10. Clinopyroxene core trace element data (in ppm)

Sample	Lith.¹	Depth²	Rb	Ba	Th	U	Nb	Ta	La	Ce	Pr	Sr	Nd	Zr	Hf	Sm	Eu	Gd	Tb	Dy	Y	Ho	Er	Tm	Yb	Lu
OM10_Gid_A11_1w	VG	4994	0.04	0.46	0.01	0.01	0.01	0.01	0.28	1.49	0.40	8.79	3.10	11.20	0.53	1.73	0.64	2.90	0.54	4.01	19.27	0.77	2.32	0.32	1.92	0.28
OM10_Gid_A11-1w	VG	4994	0.03	0.18	0.01		0.02	0.01	0.39	2.13	0.58	10.30	4.37	19.49	1.05	2.51	0.89	4.29	0.77	5.71	28.90	1.16	3.34	0.45	2.87	0.43
OM10_Gid_A13	VG	4602	0.07	0.03			0.02		0.05	0.31	0.08	6.00	0.66	2.30	0.13	0.38	0.16	0.71	0.15	1.08	5.99	0.24	0.67	0.09	0.63	0.09
OM10_Gid_A13	VG	4602	0.03	0.54	0.01		0.02	0.00	0.10	0.32	0.08	5.93	0.66	2.02	0.13	0.34	0.16	0.74	0.15	1.02	6.02	0.23	0.68	0.10	0.58	0.09
OM10_Gid_A14b	VG	4389	0.01	0.02	0.01	0.00	0.02	0.01	0.39	1.84	0.46	11.87	3.37	14.55	0.78	1.75	0.62	3.06	0.56	3.91	20.59	0.83	2.38	0.32	1.94	0.29
OM10_Gid_A14b	VG	4389		0.10	0.01	0.00	0.01		0.29	1.86	0.46	11.45	3.48	13.78	0.61	1.77	0.64	2.99	0.60	4.13	21.47	0.84	2.50	0.34	2.10	0.32
OM10_Gid_A14b	VG	4389	0.02	0.21	0.01		0.01		0.31	1.67	0.41	12.88	3.02	11.45	0.62	1.41	0.56	2.50	0.46	3.30	17.01	0.69	2.03	0.27	1.60	0.23
OM10_Gid_A15	VG	4129	0.05	1.62	0.02	0.05	0.03	0.00	0.26	1.48	0.37	12.62	2.72	16.19	0.56	1.43	0.53	3.29	0.47	3.19	16.44	0.69	1.91	0.27	1.58	0.22
OM10_Gid_A15	VG	4129	0.17	0.59	0.02	0.01	0.03		0.44	2.14	0.52	12.88	3.80	18.02	1.06	1.99	0.74	3.90	0.61	4.19	21.60	0.85	2.51	0.34	2.19	0.33
OM10_Gid_A15	VG	4129	0.06	1.01	0.16	0.05	0.04	0.00	0.70	4.48	0.89	9.97	5.43	18.02	1.06	2.53	0.74	3.90	0.71	4.87	26.88	0.99	3.04	0.41	2.89	0.42
OM10_Gid_A16	FG	3924	0.08	0.50	0.01	0.01	0.03		0.24	1.28	0.31	12.12	2.14	10.16	0.51	1.00	0.45	1.58	0.31	2.18	11.58	0.46	1.28	0.17	1.11	0.16
OM10_Gid_A16	FG	3924	0.07	0.91	0.01	0.00	0.02		0.18	0.88	0.22	10.41	1.62	5.71	0.33	0.87	0.34	1.37	0.27	1.86	9.23	0.40	1.09	0.14	1.00	0.14
OM10_Gid_A16	FG	3924	0.06	0.85	0.02	0.01	0.04	0.00	0.20	1.00	0.24	10.65	1.72	6.77	0.33	0.89	0.34	1.48	0.27	1.94	10.09	0.41	1.11	0.15	0.92	0.14
OM10_Gid_A17	FG	3734	0.05	0.44	0.02	0.01	0.03	0.00	0.42	2.13	0.53	8.19	3.88	15.05	0.65	1.96	0.61	3.31	0.60	4.16	22.06	0.89	2.55	0.35	2.13	0.33
OM10_Gid_A17	FG	3734	0.03	0.06	0.02	0.01	0.02		0.19	0.93	0.21	5.01	1.51	5.20	0.35	0.71	0.28	1.14	0.23	1.50	7.74	0.32	0.90	0.12	0.80	0.12
OM10_Gid_A17	FG	3734	0.05	0.37	0.03	0.01	0.01		0.19	0.87	0.22	7.22	1.53	7.67	0.39	0.81	0.32	1.38	0.25	1.79	9.05	0.38	1.06	0.15	0.88	0.13
OM10_Gid_A18	FG	3423	0.02	0.32	0.03	0.01	0.03	0.01	0.57	3.10	0.70	11.07	4.67	12.83	0.33	2.01	0.65	2.73	0.53	3.59	19.04	0.73	2.14	0.32	2.10	0.31
OM10_Gid_A18	FG	3423	0.05	0.27	0.01	0.01	0.02		0.47	2.43	0.64	8.91	4.63	19.55	0.87	2.43	0.75	4.14	0.78	5.57	29.40	1.17	3.36	0.46	2.87	0.41
OM10_Gid_A18_1	FG	3230		0.14	0.02	0.01	0.02	0.01	0.57	3.30	0.83	8.63	6.22	29.99	1.37	3.12	0.88	5.37	0.96	6.89	35.90	1.47	4.17	0.56	3.39	0.53
OM10_Gid_A18_1	FG	3230	0.03	0.20	0.01	0.01	0.02	0.01	0.56	3.01	0.77	8.42	5.60	30.02	1.06	2.85	0.84	4.99	0.91	6.37	36.57	1.39	3.97	0.55	3.28	0.50
OM10_Gid_A18_1	FG	3230	0.01	0.09	0.02	0.01	0.08	0.01	0.30	1.83	0.45	9.94	3.34	16.44	0.78	1.68	0.61	2.76	0.52	3.52	20.86	0.75	2.17	0.31	1.80	0.26
OM10_Gid_A18_2a	FG	2900	0.02	0.12	0.02	0.01	0.09	0.01	0.35	2.00	0.51	8.93	3.55	17.94	0.75	1.72	0.65	2.86	0.58	3.80	19.38	0.81	2.32	0.29	1.93	0.30
OM10_Gid_A18_2a	FG	2900	0.01	0.08	0.02	0.01	0.07	0.01	0.33	1.85	0.47	10.61	3.44	17.51	0.75	1.67	0.61	2.83	0.52	3.65	19.38	0.79	2.23	0.29	1.84	0.28
OM10_Gid_A18_2a	FG	2900	0.05	0.65	0.02	0.01	0.03	0.00	0.28	1.51	0.38	13.60	2.78	12.33	0.61	1.48	0.55	2.58	0.48	3.25	16.97	0.68	1.97	0.26	1.61	0.24
OM10_Gid_A19	FG	2700	0.11	1.37	0.01	0.01	0.03	0.00	0.27	1.50	0.37	11.17	2.75	11.09	0.50	1.40	0.53	2.37	0.44	3.06	16.12	0.66	1.84	0.25	1.55	0.23
OM10_Gid_A19	FG	2700	0.04	0.62	0.01	0.00	0.04	0.00	0.27	1.55	0.38	10.99	2.84	13.02	0.60	1.47	0.55	2.53	0.47	3.23	16.91	0.68	1.96	0.27	1.66	0.25
OM10_Gid_A19	FG	2700	0.01	0.08	0.01	0.00	0.05	0.01	0.28	1.58	0.42	11.11	3.20	14.26	0.67	1.69	0.61	2.86	0.53	3.60	19.45	0.78	2.23	0.30	1.81	0.28
OM10_Gid_A19	FG	2700		0.04	0.01		0.05	0.01	0.31	1.75	0.45	11.04	3.13	14.09	0.68	1.71	0.60	2.96	0.55	3.74	19.61	0.81	2.29	0.31	1.92	0.28
OM10_Gid_A20	LG	2394	0.01	0.03	0.02	0.02	0.01	0.01	0.31	1.70	0.45	11.43	3.13	14.79	0.68	1.71	0.60	2.81	0.56	3.69	19.01	0.78	2.24	0.29	1.81	0.29
OM10_Gid_A20	LG	2394	0.26	0.30	0.02	0.01	0.01	0.00	0.15	0.75	0.16	12.50	1.23	4.91	0.28	0.71	0.30	1.46	0.26	1.76	8.91	0.39	1.07	0.14	0.92	0.15
OM10_Gid_A20	LG	2394	0.05	0.28	0.01	0.01	0.03	0.00	0.13	0.68	0.17	11.27	1.21	4.59	0.22	0.72	0.29	1.22	0.23	1.63	8.21	0.33	0.90	0.13	0.76	0.12
OM11_Gid_A21	LG	2124	0.06	0.24	0.01	0.01	0.02	0.00	0.12	0.55	0.15	11.55	1.10	4.55	0.24	0.69	0.28	1.18	0.23	1.70	8.25	0.36	0.97	0.12	0.78	0.12
OM11_Gid_A21	LG	2124	0.02	0.18	0.02	0.01	0.03	0.01	0.28	1.31	0.40	11.78	3.13	10.83	0.59	1.78	0.69	3.13	0.59	4.13	21.41	0.84	2.49	0.35	2.14	0.31
OM11_Gid_A21	LG	2124	0.04	0.20	0.01	0.01	0.03	0.00	0.28	1.61	0.42	11.28	3.28	12.27	0.61	1.69	0.63	3.02	0.56	3.90	19.92	0.77	2.35	0.32	1.98	0.29
OM11_Gid_A22	LG	1936	0.01	0.03			0.01		0.29	1.66	0.45	10.53	3.54	13.93	0.69	2.02	0.72	3.63	0.67	4.67	23.58	0.97	2.79	0.38	2.39	0.34
OM11_Gid_A22	LG	1936	0.03	0.17	0.01	0.00	0.02	0.00	0.15	0.77	0.21	11.52	1.54	5.77	0.30	0.88	0.33	1.45	0.28	1.98	10.66	0.43	1.14	0.15	0.94	0.14
OM11_Gid_A22	LG	1936	0.05	0.27	0.01	0.00	0.03	0.00	0.19	0.84	0.21	14.22	1.48	6.07	0.29	0.81	0.31	1.33	0.25	1.80	9.77	0.37	1.02	0.14	0.89	0.13
OM12_Gid_046	LG	1727	0.05	0.20	0.00	0.00	0.02	0.00	0.19	0.97	0.24	14.08	1.68	6.84	0.31	0.85	0.35	1.52	0.29	1.99	10.79	0.44	1.20	0.17	1.02	0.15
OM12_Gid_046	LG	1727	0.01	0.05	0.01		0.05	0.00	0.22	1.06	0.27	11.01	1.93	8.42	0.36	1.07	0.38	1.81	0.33	2.36	12.65	0.49	1.43	0.19	1.12	0.16
OM12_Gid_046	LG	1727	0.01	0.03	0.01		0.02	0.01	0.16	0.89	0.24	13.70	1.65	6.62	0.31	0.90	0.37	1.60	0.31	2.11	11.12	0.45	1.25	0.17	1.06	0.17
OM12_Gid_044	LG	1626	0.05	0.19			0.02	0.01	0.17	0.88	0.23	10.82	1.78	6.67	0.33	0.95	0.38	1.67	0.31	2.17	11.75	0.46	1.33	0.18	1.11	0.18
OM12_Gid_044	LG	1626	0.07	0.04			0.03	0.01	0.19	0.90	0.24	11.32	1.67	6.30	0.31	0.86	0.36	1.56	0.29	2.14	11.16	0.43	1.22	0.17	1.04	0.15
OM12_Gid_044	LG	1626	0.01	0.03			0.03	0.01	0.20	1.05	0.27	9.85	1.95	7.52	0.37	1.01	0.40	1.75	0.33	2.21	12.49	0.48	1.39	0.18	1.15	0.18
OM12_Gid_039	LG	1289	0.01	0.07		0.00	0.01	0.00	0.29	1.08	0.27	10.53	2.10	8.76	0.40	1.08	0.40	2.01	0.36	2.54	14.28	0.54	1.56	0.21	1.28	0.20
OM12_Gid_039	LG	1289	0.03	0.01	0.01	0.00	0.04	0.00	0.15	0.77	0.21	9.91	1.60	6.13	0.29	0.83	0.34	1.48	0.28	1.93	10.15	0.41	1.14	0.15	0.96	0.14
OM12_Gid_039	LG	1289	0.05	0.17	0.01		0.05	0.00	0.17	0.87	0.22	9.76	2.14	10.10	0.32	0.91	0.37	2.01	0.31	2.63	14.14	0.56	1.60	0.22	1.35	0.21
OM12_Gid_026	LG	1231	0.01	0.17	0.01	0.01	0.04	0.00	0.16	0.86	0.23	10.18	1.69	6.50	0.32	0.91	0.37	1.60	0.30	2.11	11.25	0.45	1.25	0.17	1.07	0.16
OM12_Gid_026	LG	1231	0.02	0.19	0.01	0.01	0.07	0.00	0.19	0.93	0.24	10.36	1.71	7.67	0.42	0.97	0.37	1.65	0.31	2.10	11.12	0.45	1.29	0.17	1.06	0.17
OM12_Gid_026	LG	1231	0.03	0.02	0.02	0.01	0.07	0.01	0.23	1.01	0.30	10.58	1.88	8.10	0.39	0.97	0.37	1.79	0.34	2.28	14.80	0.48	1.35	0.19	1.16	0.17
OM12_Gid_Hy080.5	LG	1190	0.25	0.28	0.01	0.01	0.10	0.01	0.21	1.19	0.30	15.87	2.22	10.19	0.50	1.19	0.47	2.09	0.40	2.81	14.80	0.58	1.73	0.22	1.44	0.21
OM12_Gid_Hy080.5	LG	1190	0.07	0.26	0.02	0.01	0.05	0.00	0.21	1.06	0.26	10.51	1.84	9.00	0.53	0.98	0.39	1.69	0.31	2.21	11.77	0.46	1.32	0.18	1.10	0.16
OM12_Gid_038	LG	1121	0.03	0.23	0.01	0.00	0.04	0.01	0.22	0.98	0.26	9.11	1.83	7.78	0.40	0.96	0.37	1.72	0.32	2.21	12.39	0.46	1.36	0.19	1.18	0.17
OM12_Gid_038	LG	1121	0.05	0.27	0.01	0.01	0.04	0.00	0.18	0.98	0.24	9.07	1.79	10.38	0.46	1.03	0.37	1.67	0.32	2.27	13.07	0.49	1.36	0.18	1.14	0.17
OM12_Gid_039	LG	1121	0.03	0.01	0.01	0.00	0.05	0.01	0.14	0.83	0.22	11.36	1.70	7.83	0.37	0.57	0.36	1.78	0.33	2.30	12.45	0.49	1.38	0.19	1.13	0.17
OM10_Gid_038	LG	1079	0.01	0.03	0.00	0.00	0.06	0.00	0.20	1.11	0.30	11.86	2.23	10.50	0.38	1.15	0.45	2.07	0.38	2.64	14.32	0.54	1.56	0.20	1.30	0.18
OM10_Gid_A26	LG	1079	0.05	0.54	0.00		0.05	0.00	0.17	1.01	0.28	11.99	2.07	9.60	0.42	1.13	0.42	1.95	0.38	2.57	13.58	0.53	1.52	0.21	1.25	0.18
OM10_Gid_A26	LG	1079	0.01	0.10	0.01		0.04	0.01	0.17	0.91	0.24	10.18	1.74	6.76	0.37	0.91	0.37	1.67	0.31	2.13	11.40	0.47	1.28	0.18	1.13	0.16
OM10_Gid_A28	LG	696	0.05	0.05	0.01		0.07	0.01	0.17	0.93	0.25	13.41	1.81	7.85	0.39	0.96	0.39	1.66	0.31	2.11	11.13	0.45	1.25	0.17	1.04	0.15
OM10_Gid_A28	LG	696	0.01	0.05			0.02	0.01	0.17	0.50	0.23	12.59	1.73	7.18	0.36	0.50	0.38	1.58	0.30	2.06	10.49	0.43	1.20	0.16	0.99	0.15
OM10_Gid_A28	LG	696	0.05	0.76	0.01	0.01	0.04	0.01	0.27	1.42	0.35	11.22	2.50	10.66	0.52	1.31	0.48	2.10	0.40	2.77	13.97	0.58	1.67	0.23	1.41	0.21
OM10_Gid_A29	LG	545	0.07	0.88	0.02	0.01	0.04	0.00	0.26	1.37	0.35	12.30	2.46	10.10	0.48	1.24	0.50	2.15	0.40	2.76	13.95	0.58	1.67	0.22	1.42	0.20
OM10_Gid_A29	LG	545	0.03	0.23	0.01		0.04	0.01	0.21	1.37	0.36	11.29	2.68	10.76	0.58	1.38	0.50	2.31	0.42	2.96	14.87	0.62	1.77	0.24	1.45	0.22
OM10_Gid_A29	LG	545	0.05	0.27	0.01	0.01	0.04	0.01	0.19	0.92	0.25	11.57	1.86	7.75	0.41	0.99	0.38	1.70	0.32	2.29	12.13	0.48	1.38	0.19	1.10	0.17
OM10_Gid_A30	LG	257	0.01	0.01	0.00	0.01	0.03		0.18	0.88	0.22	12.04	1.84	7.46	0.37	1.02	0.38	1.65	0.31	2.21	11.26	0.46	1.30	0.18	1.08	0.16
OM10_Gid_A30	LG	257	0.03	0.27	0.01		0.04		0.16	0.95	0.26	10.28	1.80	7.81	0.39	0.95	0.38	1.69	0.31	2.11	11.68	0.46	1.25	0.17	1.10	0.15
OM10_Gid_A30	LG	257	0.01	0.08	0.00		0.03		0.17	1.01	0.28	10.75	2.23	8.58	0.38	1.13	0.42	2.07	0.38	2.64	14.32	0.53	1.56	0.20	1.30	0.18
OM10_Gid_A32	LG	49	0.01	0.05	0.01		0.03		0.12	0.65	0.18	11.19	1.16	5.88	0.27	0.74	0.27	1.32	0.24	1.68	9.31	0.36	1.00	0.14	0.83	0.12
OM10_Gid_A32	LG	49	0.01	0.14		0.00	0.01	0.00	0.01	0.11	0.05	11.64	0.54	1.18	0.15	0.48	0.24	0.98	0.18	1.32	6.60	0.27	0.73	0.09	0.71	0.08
OM10_Gid_A32	LG	49	0.01	0.02			0.01	0.00	0.01	0.10	0.05	10.90	0.50	1.08	0.13	0.43	0.24	0.98	0.18	1.29	6.58	0.27	0.73	0.10	0.55	0.08

¹ Lithology: VG = Varitextured gabbro; FG = Foliated gabbro; LG = Layered gabbro

² Depth: calculated height above Moho

Table 11. Clinopyroxene rim trace element data (in ppm)

Sample	Lith.[1]	Depth[2]	Rb	Ba	Th	U	Nb	Ta	La	Ce	Pr	Sr	Nd	Zr	Hf	Sm	Eu	Gd	Tb	Dy	Y	Ho	Er	Tm	Yb	Lu
OM10_Gid_A11_1w	VG	4994	0.02	0.02	0.02		0.01	0.01	0.25	1.39	0.38	8.26	2.96	9.90	0.53	1.51	0.62	2.86	0.53	3.78	19.04	0.75	2.19	0.32	1.97	0.28
OM10_Gid_A11-1w	VG	4994	0.04	0.26	0.01		0.01	0.01	0.32	1.58	0.40	8.99	3.16	12.56	0.55	1.84	0.61	3.01	0.57	3.98	20.68	0.83	2.51	0.35	2.06	0.30
OM10_Gid_A13	VG	4602	0.02	0.25	0.01	0.01	0.03	0.01	0.15	0.60	0.14	6.75	1.04	3.25	0.16	0.56	0.21	1.49	0.30	2.13	8.82	0.48	1.44	0.15	1.21	0.13
OM10_Gid_A13	VG	4602	0.03	0.42	0.01	0.01	0.03		0.19	0.68	0.17	6.11	1.24	3.86	0.21	0.75	0.28	1.38	0.28	2.01	10.88	0.44	1.28	0.18	1.09	0.16
OM10_Gid_A14b	VG	4389	0.04	0.04			0.03	0.00	0.45	2.46	0.66	11.87	4.80	16.89	0.75	2.38	0.76	4.18	0.76	5.33	27.99	1.16	3.47	0.45	3.06	0.45
OM10_Gid_A14b	VG	4389	0.03	0.09			0.01		0.39	2.00	0.53	12.33	3.97	14.81	0.66	1.90	0.68	3.43	0.64	4.63	24.79	0.97	2.78	0.39	2.31	0.35
OM10_Gid_A14b	VG	4389		0.25			0.01		0.33	1.92	0.46	11.63	3.36	12.57	0.53	1.77	0.62	2.80	0.54	3.87	20.33	0.79	2.34	0.33	1.96	0.29
OM10_Gid_A15	VG	4129	0.06	0.06			0.01		0.26	1.54	0.40	11.76	2.90	12.17	0.62	1.57	0.61	2.93	0.56	3.89	20.40	0.85	2.34	0.32	1.96	0.28
OM10_Gid_A15	VG	4129	0.08	0.53	0.09	0.04	0.03	0.00	1.05	5.35	1.24	11.50	8.06	34.21	1.16	4.13	1.04	5.91	1.06	7.85	38.00	1.58	4.74	0.66	4.54	0.64
OM10_Gid_A16	FG	3924	0.11	1.21	0.06	0.04	0.03	0.01	1.04	4.93	1.15	11.36	7.69	32.22	1.13	3.71	0.99	5.88	1.10	7.55	40.57	1.58	4.78	0.69	4.28	0.66
OM10_Gid_A16	FG	3924	0.04	0.74	0.01	0.01	0.03		0.29	1.55	0.43	10.96	2.92	14.22	0.63	1.51	0.50	2.40	0.45	3.06	16.30	0.61	1.87	0.26	1.60	0.24
OM10_Gid_A16	FG	3924	0.01	0.09	0.02	0.01	0.02		0.25	1.32	0.36	11.80	2.64	11.20	0.54	1.32	0.51	2.26	0.43	2.69	15.29	0.56	1.54	0.21	1.45	0.22
OM10_Gid_A16	FG	3924	0.04	0.72	0.02	0.01	0.01	0.01	0.29	1.65	0.39	10.87	3.00	19.52	0.46	1.47	0.50	2.49	0.48	3.28	17.43	0.69	1.93	0.26	1.34	0.20
OM10_Gid_A17	FG	3734	0.06	0.05	0.02	0.01	0.03	0.01	0.50	2.61	0.65	10.05	4.72	19.71	0.84	2.33	0.64	4.01	0.74	5.16	27.15	1.07	3.13	0.44	2.68	0.41
OM10_Gid_A17	FG	3734	0.03	0.13	0.04	0.01	0.04		0.66	3.21	0.80	11.49	5.70	29.00	1.02	2.70	0.81	4.37	0.80	5.55	30.76	1.17	3.37	0.49	3.07	0.44
OM10_Gid_A17	FG	3734	0.11	0.47	0.03	0.02	0.01		0.61	3.34	0.91	12.40	6.90	28.10	1.28	3.74	0.97	6.46	1.16	8.17	42.69	1.74	4.87	0.68	4.20	0.62
OM10_Gid_A17	FG	3734	0.03	0.11	0.03	0.02	0.02		0.67	3.86	1.00	12.88	7.03	39.39	1.22	3.57	0.98	5.69	1.06	7.39	37.84	1.36	4.19	0.62	3.67	0.50
OM10_Gid_A18	FG	3423	0.03	0.27	0.01	0.01	0.02		0.49	2.72	0.71	9.87	5.29	23.55	1.05	2.70	0.85	4.63	0.87	6.16	32.88	1.35	3.86	0.52	3.25	0.49
OM10_Gid_A18	FG	3423	0.03	0.20	0.01	0.01	0.02	0.01	0.59	3.17	0.80	9.23	5.89	33.24	1.14	2.91	0.85	4.74	0.91	6.29	33.24	1.34	3.74	0.54	3.40	0.47
OM10_Gid_A18_1	FG	3230	0.03	0.10	0.01	0.01	0.02	0.01	0.53	2.94	0.77	8.06	5.72	31.39	1.37	2.84	0.84	5.06	0.95	6.55	36.51	1.42	4.07	0.55	3.25	0.49
OM10_Gid_A18_1	FG	3230	0.01	0.12	0.01	0.01	0.07		0.30	1.79	0.45	10.59	3.32	16.16	0.77	1.67	0.60	2.81	0.51	3.44	18.58	0.73	2.11	0.29	1.74	0.25
OM10_Gid_A18_1	FG	3230	0.02	0.08	0.02		0.08		0.33	1.89	0.47	12.30	3.29	16.96	0.73	1.72	0.61	2.77	0.53	3.60	19.44	0.77	2.22	0.31	1.82	0.26
OM10_Gid_A18_2a	FG	2900	0.01	0.05	0.01	0.01	0.08	0.01	0.34	1.85	0.47	10.16	3.42	16.36	0.72	1.73	0.64	2.81	0.54	3.71	19.80	0.80	2.24	0.27	1.92	0.28
OM10_Gid_A18_2a	FG	2900	0.03	0.05	0.01		0.03	0.00	0.26	1.48	0.37	12.12	2.68	12.54	0.58	1.42	0.54	2.47	0.47	3.17	16.82	0.71	1.96	0.26	1.61	0.24
OM10_Gid_A18_2a	FG	2900	0.03	0.31	0.01		0.03	0.00	0.26	1.43	0.37	11.79	2.81	12.38	0.56	1.47	0.53	2.53	0.46	3.23	16.87	0.69	1.55	0.26	1.62	0.24
OM10_Gid_A19	FG	2700	0.01	0.13	0.01	0.00	0.03	0.00	0.28	1.46	0.38	11.35	2.80	11.84	0.55	1.46	0.54	2.46	0.47	3.13	16.78	0.69	1.96	0.30	1.64	0.24
OM10_Gid_A19	FG	2700	0.01	0.09	0.01		0.05	0.01	0.28	1.51	0.42	11.51	3.10	14.83	0.67	1.69	0.62	2.89	0.53	3.79	20.08	0.82	2.24	0.33	1.90	0.28
OM10_Gid_A19	FG	2700	0.01	0.02	0.01		0.06	0.01	0.32	1.77	0.46	10.35	3.64	14.77	0.62	1.80	0.67	3.20	0.60	4.19	20.98	0.88	2.43	0.33	2.01	0.30
OM10_Gid_A20	LG	2394	0.03	0.21	0.02	0.02	0.06	0.01	0.28	1.61	0.42	11.76	3.25	14.16	0.68	1.61	0.64	2.81	0.54	3.54	19.09	0.76	2.11	0.30	1.82	0.26
OM10_Gid_A20	LG	2394	0.18	0.68	0.02	0.02	0.02	0.00	0.22	1.21	0.29	11.70	2.11	10.47	0.39	1.03	0.46	1.79	0.34	2.51	12.78	0.51	1.52	0.20	1.26	0.19
OM10_Gid_A20	LG	2394	0.31	0.37	0.02	0.01	0.02	0.00	0.29	1.69	0.42	10.16	3.14	17.29	0.73	1.51	0.46	2.64	0.48	3.46	18.63	0.75	2.12	0.31	1.91	0.29
OM11_Gid_A21	LG	2124	0.06	0.06	0.01	0.01	0.02	0.00	0.20	1.18	0.28	10.62	2.09	9.00	0.30	1.04	0.37	1.85	0.32	2.40	12.40	0.49	1.46	0.21	1.31	0.20
OM11_Gid_A21	LG	2124		0.07			0.01		0.27	1.53	0.44	11.57	3.38	13.28	0.63	1.88	0.72	3.41	0.62	4.41	23.18	0.91	2.73	0.38	2.36	0.34
OM11_Gid_A21	LG	2124	0.01	0.11		0.00	0.01		0.25	1.48	0.42	10.82	3.23	11.06	0.56	1.77	0.66	3.06	0.57	3.97	20.29	0.84	2.42	0.31	2.04	0.30
OM11_Gid_A22	LG	1936	0.03	0.06	0.01		0.01		0.26	1.52	0.42	11.23	3.29	11.83	0.57	1.87	0.71	3.27	0.60	4.41	22.39	0.88	2.67	0.35	2.22	0.33
OM11_Gid_A22	LG	1936	0.01	0.13		0.00	0.02	0.00	0.19	1.01	0.26	10.87	1.89	8.60	0.43	1.05	0.39	1.73	0.32	2.26	12.25	0.48	1.32	0.19	1.18	0.18
OM11_Gid_A22	LG	1936	0.01	0.30	0.01	0.00	0.02	0.00	0.19	0.99	0.27	11.54	1.97	8.71	0.37	1.03	0.38	1.63	0.33	2.24	12.33	0.48	1.38	0.18	1.13	0.17
OM12_Gid_046	LG	1727	0.04	0.18	0.01	0.00	0.02	0.00	0.20	1.08	0.27	11.65	2.03	9.22	0.39	1.03	0.40	1.81	0.34	2.39	12.64	0.51	1.42	0.20	1.22	0.18
OM12_Gid_046	LG	1727	0.01	0.06	0.01	0.00	0.03	0.00	0.21	1.12	0.30	12.30	2.26	10.53	0.46	1.10	0.45	1.96	0.38	2.60	13.85	0.56	1.54	0.22	1.37	0.20
OM12_Gid_046	LG	1626	0.01	0.04	0.01	0.00	0.05	0.01	0.18	1.05	0.29	10.61	2.09	9.86	0.45	1.19	0.42	2.05	0.39	2.68	14.31	0.57	1.60	0.22	1.61	0.20
OM12_Gid_026	LG	1231	0.01	0.05	0.01	0.00	0.05	0.02	0.18	1.05	0.29	9.95	2.01	8.92	0.40	1.07	0.41	1.83	0.37	2.46	12.82	0.52	1.51	0.20	1.21	0.19
OM12_Gid_026	LG	1231	0.02	0.29	0.02	0.01	0.14	0.02	0.19	1.40	0.36	8.94	2.50	19.39	0.71	1.32	0.45	2.13	0.41	2.74	14.52	0.67	1.91	0.23	1.38	0.24
OM12_Gid_026	LG	1231	0.03	0.18	0.03	0.00	0.11	0.01	0.29	1.54	0.39	10.48	2.78	22.16	0.88	1.41	0.48	2.42	0.45	3.10	16.87	0.67	1.91	0.25	1.60	0.21
OM12_Gid_044	LG	1626	0.01	0.20	0.03	0.00	0.04	0.01	0.27	1.40	0.36	11.82	2.51	16.64	0.57	1.26	0.47	2.27	0.43	2.87	15.59	0.62	1.75	0.25	1.52	0.22
OM12_Gid_044	LG	1626	0.04	0.14	0.03	0.00	0.04	0.01	0.21	1.07	0.27	8.83	2.00	11.33	0.53	1.08	0.39	1.83	0.34	2.34	13.64	0.52	1.78	0.19	1.57	0.24
OM12_Gid_Hy080.5	LG	1190	0.02	0.17	0.01	0.00	0.04	0.01	0.21	0.90	0.22	11.12	1.73	12.47	0.39	0.93	0.35	1.54	0.31	2.12	11.92	0.46	1.26	0.18	1.01	0.17
OM12_Gid_Hy080.5	LG	1190	0.02	0.01	0.00	0.00	0.05	0.00	0.14	0.81	0.23	11.03	1.77	8.26	0.30	0.96	0.37	1.73	0.33	2.29	12.50	0.47	1.37	0.18	1.15	0.16
OM12_Gid_038	LG	1121	0.01	0.02	0.00	0.00	0.04		0.14	0.95	0.26	11.87	1.98	8.55	0.40	1.09	0.41	1.93	0.37	2.35	13.72	0.54	1.54	0.21	1.27	0.19
OM12_Gid_038	LG	1121		0.17	0.01	0.01	0.04		0.15	0.99	0.24	11.87	1.99	10.31	0.48	1.08	0.40	2.00	0.38	2.64	13.90	0.56	1.56	0.22	1.31	0.19
OM12_Gid_039	LG	1289	0.03	0.03	0.00	0.00	0.02		0.18	1.05	0.29	9.09	2.09	9.86	0.45	1.15	0.42	1.99	0.37	2.66	13.94	0.55	1.53	0.22	1.30	0.20
OM12_Gid_039	LG	1289	0.01	0.13	0.01	0.01	0.02	0.01	0.19	1.10	0.30	11.17	2.23	14.68	0.45	1.23	0.45	2.02	0.38	2.61	13.92	0.57	1.60	0.20	1.36	0.20
OM10_Gid_A26	LG	1079	0.01	0.08	0.01	0.00	0.03		0.18	1.04	0.28	12.99	2.08	10.44	0.44	1.06	0.42	1.90	0.36	2.46	12.86	0.52	1.51	0.20	1.22	0.19
OM10_Gid_A26	LG	1079	0.04	0.10	0.01		0.02	0.01	0.28	1.42	0.38	9.84	2.81	13.98	0.64	1.48	0.51	2.44	0.47	3.15	16.86	0.69	1.98	0.26	1.63	0.23
OM10_Gid_A28	LG	696	0.04	0.48	0.01	0.01	0.04	0.01	0.28	1.44	0.36	11.58	2.84	11.33	0.57	1.45	0.54	2.33	0.43	3.02	14.85	0.67	1.78	0.25	1.55	0.21
OM10_Gid_A28	LG	696	0.02	0.03	0.01		0.04	0.01	0.25	1.41	0.37	11.12	2.91	12.47	0.62	1.51	0.53	2.45	0.46	3.15	16.12	0.66	1.90	0.25	1.65	0.24
OM10_Gid_A29	LG	545	0.02	0.24	0.01	0.01	0.05	0.01	0.21	0.96	0.25	11.24	2.01	9.09	0.43	1.14	0.42	1.88	0.31	2.50	13.49	0.52	1.26	0.20	1.19	0.18
OM10_Gid_A29	LG	545	0.12	0.43	0.01	0.01	0.05	0.01	0.17	0.94	0.23	10.60	1.73	8.33	0.40	0.93	0.37	1.60	0.30	2.16	12.07	0.45	1.26	0.17	1.09	0.16
OM10_Gid_A30	LG	257	0.01	0.07	0.01	0.01	0.04	0.00	0.13	0.88	0.24	9.33	1.81	7.84	0.36	0.99	0.37	1.66	0.30	2.09	11.52	0.45	1.27	0.17	1.04	0.16
OM10_Gid_A30	LG	257	0.01	0.13		0.00	0.04		0.12	0.66	0.18	10.18	1.36	5.61	0.26	0.78	0.31	1.30	0.25	1.73	9.39	0.37	1.05	0.13	0.89	0.13
OM10_Gid_A30	LG	257	0.01	0.05	0.01		0.03		0.11	0.67	0.17	10.19	1.38	5.54	0.27	0.76	0.32	1.33	0.24	1.73	9.42	0.36	1.06	0.15	0.87	0.13
OM10_Gid_A32	LG	49	0.01	0.02			0.01		0.01	0.09	0.04	10.59	0.49	1.03	0.11	0.43	0.22	0.93	0.18	1.27	6.09	0.26	0.71	0.09	0.54	0.08
OM10_Gid_A32	LG	49		0.02			0.01		0.01	0.10	0.05	11.36	0.55	1.16	0.14	0.47	0.25	0.97	0.19	1.37	6.97	0.28	0.77	0.10	0.58	0.08

[1] Lithology: VG = Varitextured gabbro; FG = Foliated gabbro; LG = Layered gabbro

[2] Depth: calculated height above Moho

Table 12. Intitial compositions used for MELTS modeling (in wt%)

	GBC[1]	A11_1U[2]	NMORB[3]
$SiO2_{calc}$	51.44	51.35	50.77
Al_2O_3	16.85	16.07	15.24
FeO_{tot}	7.22	8.45	9.88
MnO	0.12	0.13	0.17
MgO	8.14	8.69	7.81
CaO	12.02	11.96	11.43
Na_2O	3.18	2.33	2.85
K_2O	0.08	0.15	0.14
TiO_2	0.89	0.78	1.54
P_2O_5	0.06	0.07	0.17

[1] Gideah Bulk Crust, calculated after Gillis et al. (2014)
[2] Gideah basaltic dike
[3] NMORB by Gale (2013)

Table A13. Modal composition (in wt%), and CPO characteristics from EBSD analysis.

Sample	Litho.[1]	Depth[2]	Pl	Cpx	Opx	Ol	Ox	Hbl	Act	Ni	max. Dens. [100]	max. Dens. <010>	max. Dens. <001>	BA index	ODF J	pfJ [100]	pfJ <010>	pfJ <001>	ODF J (Cpx)
OM10_Gid_A11	ML	4954	27.66	0.01	0.00	0.01	0.00	3.85	6.54	61.92	1.41	1.61	1.29	0.63	1.25	1.12	1.07	1.26	46.41
OM10_Gid_A12_2a	ML	4612	75.21	0.01	0.00	0.01	0.00	0.04	0.07	24.66	1.34	1.24	1.31	0.60	1.35	1.03	1.01	1.02	51.03
OM10_Gid_A12_2d	VG	4612	54.65	0.01	0.00	0.05	0.01	0.16	0.31	44.82	1.56	1.45	1.22	0.41	1.12	1.04	1.03	1.01	68.39
OM10_Gid_A13	VG	4602	44.56	11.38	1.77	0.00	0.23	8.83	7.64	25.59	1.66	1.85	1.38	0.20	1.28	1.08	1.09	1.01	2.71
OM10_Gid_A14a	VG	4389	35.95	15.84	0.54	0.01	0.10	9.52	6.11	31.94	2.38	3.50	1.51	0.38	1.75	1.29	1.57	1.06	1.72
OM10_Gid_A14b	VG	4389	42.98	10.29	0.00	0.01	0.21	4.16	3.80	38.55	1.82	2.26	1.29	0.30	1.30	1.14	1.24	1.02	1.57
OM10_Gid_A15	VG	4129	37.11	10.11	0.67	0.00	1.53	13.58	9.69	27.98	3.65	4.84	1.83	0.29	2.87	1.63	2.00	1.11	2.55
OM10_Gid_A16	FG	3924	37.81	27.53	0.00	6.04	0.01	0.38	0.37	27.18	2.17	3.53	1.47	0.36	1.88	1.23	1.53	1.06	1.46
OM10_Gid_A17	FG	3734	48.74	23.36	0.00	0.00	0.07	2.28	1.14	24.40	2.62	2.88	1.39	0.35	1.88	2.62	2.88	1.39	154.91
OM10_Gid_A17_2	FG	3577	33.24	24.75	0.00	0.01	0.04	2.35	0.85	38.75	2.11	2.78	1.76	0.51	2.05	1.23	1.33	1.04	2.28
OM10_Gid_A17_1	FG	3550	53.86	18.43	0.00	0.05	1.12	0.82	0.50	25.23	2.09	1.70	1.62	0.35	2.09	1.09	1.05	1.04	1.65
OM10_Gid_A18	FG	3423	46.12	24.24	1.22	4.20	0.02	0.21	0.20	23.79	2.66	4.31	1.72	0.27	2.31	1.47	1.79	1.06	1.48
OM10_Gid_A18_1	FG	3230	41.18	30.07	0.00	0.00	0.00	0.99	0.78	26.97	2.80	7.59	1.91	0.07	3.91	2.80	2.95	1.91	1.67
OM10_Gid_A18_2a	FG	2900	43.54	27.44	0.31	3.07	0.00	0.43	0.27	24.93	2.38	5.35	1.77	0.18	2.49	2.38	5.35	1.77	1.47
OM10_Gid_A19	FG	2700	45.28	29.38	0.33	6.30	0.00	0.08	0.05	18.57	3.37	6.99	1.91	0.30	3.09	3.37	6.99	1.91	1.45
OM10_Gid_A20	LG	2394	46.24	22.33	0.06	5.10	0.00	0.14	0.10	26.03	2.69	4.41	1.77	0.18	2.56	2.69	4.41	1.77	3.52
OM12_Gid_055	LG	2259	33.12	34.94	0.15	1.27	0.01	0.32	0.16	30.04	2.83	4.37	1.80	0.23	3.17	1.54	1.65	1.08	2.40
OM10_Gid_A21	LG	2124	41.39	23.24	0.01	0.55	0.01	0.06	0.01	34.72	3.24	5.29	1.70	0.30	3.47	1.61	2.07	1.10	5.65
OM11_Gid_A21a	LG	2124	41.87	25.02	0.03	0.25	0.12	0.51	0.40	31.80	5.22	4.20	1.86	0.53	3.76	2.16	1.72	1.15	4.85
OM12_Gid_054	LG	2040	43.10	34.30	0.13	0.98	0.00	0.02	0.01	21.46	3.70	4.02	1.87	0.26	3.34	1.60	1.59	1.08	2.84
OM12_Gid_052	LG	2004	34.16	19.89	0.02	0.00	0.05	1.43	1.27	43.25	5.70	7.08	2.62	0.46	6.86	2.42	2.78	1.24	5.62
OM12_Gid_053	LG	2004	44.11	32.71	0.02	3.35	0.00	0.20	0.07	19.53	3.12	4.62	1.78	0.31	3.47	1.58	1.76	1.08	6.34
OM11_Gid_A22	LG	1936	49.39	30.29	0.08	2.70	0.00	0.01	0.01	17.52	3.32	4.93	1.92	0.29	3.11	3.32	4.93	1.92	3.11
OM12_Gid_048	LG	1792	57.03	25.50	0.06	3.22	0.00	0.12	0.06	14.01	3.93	6.25	2.06	0.20	3.52	1.86	2.37	1.14	2.44
OM10_Gid_A23	LG	1659	55.60	29.05	0.00	0.01	0.00	0.05	0.08	15.21	3.64	6.48	1.81	0.25	4.20	1.85	2.47	1.14	3.18
OM12_Gid_045	LG	1630	29.11	34.01	0.00	0.00	0.10	0.11	0.07	36.61	4.09	3.40	1.88	0.55	3.47	4.09	3.40	1.88	3.72
OM12_Gid_044	LG	1626	50.09	23.92	0.07	5.70	0.00	0.02	0.02	20.18	2.50	3.02	1.47	0.45	3.44	1.29	2.37	1.03	6.69
OM12_Gid_040	LG	1508	40.02	34.50	0.00	0.00	0.00	0.47	0.23	24.78	4.14	5.09	1.89	0.32	3.57	1.84	2.21	1.14	3.52
OM10_Gid_A24	LG	1431	42.94	29.65	0.08	5.98	0.00	0.45	0.11	20.78	4.65	5.09	1.94	0.45	3.76	4.65	5.09	1.94	3.60
OM12_Gid_039	LG	1289	51.34	25.23	0.12	9.53	0.00	0.13	0.03	13.61				0.38	3.41				
OM12_Gid_026	LG	1231	48.94	27.71	0.04	0.00	0.05	0.20	0.21	22.86	3.91	3.43	1.59	0.70	3.28	1.96	2.55	1.19	6.16
OM12_Gid_027	LG	1222	43.41	19.27	4.66	1.47	0.00	2.60	2.16	26.44	3.78	3.35	1.85	0.63	3.11	1.79	1.63	1.06	6.39
OM10_Gid_A25	LG	1210	41.20	28.18	0.05	6.79	0.00	0.00	0.01	23.76	4.94	3.60	2.80	0.59	3.55	1.63	1.51	1.07	3.43
OM12_Gid_025	LG	1197	58.34	18.81	0.07	1.87	0.00	0.02	0.02	20.87	4.70	5.72	2.20	0.44	5.19	1.95	1.56	1.18	4.67
OM12_Gid_038	LG	1121	51.23	18.23	0.22	12.60	0.00	0.05	0.01	17.66	3.55	5.12	1.71	0.42	3.75	2.21	2.34	1.19	6.51
OM10_Gid_A26	LG	1079	47.94	35.07	0.02	3.46	0.00	0.06	0.15	13.29	3.35	3.47	1.68	0.54	3.54	1.59	1.91	1.71	4.95
OM12_Gid_035	LG	991	0.88	25.15	0.00	0.00	0.00	0.42	0.57	72.97	4.80	10.03	3.42	0.24	15.58	1.57	1.59	1.08	1.77
OM11_Gid_A26	LG	930	48.93	27.33	0.01	2.81	0.00	0.31	0.25	20.36	3.15	2.81	1.54	0.68	2.84	1.82	3.46	1.56	4.08
OM11_Gid_A27	LG	816	37.62	27.42	0.08	10.15	0.00	0.01	0.00	24.72				0.44	2.94				
OM10_Gid_A27	LG	804	42.02	33.70	0.00	0.00	0.00	0.01	0.01	24.24	4.23	7.69	2.12	0.29	5.88	1.39	1.37	1.04	2.91
OM10_Gid_A28	LG	696	39.30	34.36	0.17	0.00	0.00	0.26	0.17	25.91	4.26	3.62	2.11	0.62	4.58	1.67	1.88	1.07	4.94
OM12_Gid_201	LG	598	35.13	30.83	0.00	8.70	0.00	0.00	0.00	25.17	3.60	4.30	1.99	0.40	4.11	1.95	2.86	1.17	5.99
OM10_Gid_A29	LG	545	35.35	32.63	0.00	0.00	0.00	0.51	0.45	31.06	3.76	4.70	1.79	0.57	3.38	1.90	1.77	1.11	2.42
OM11_Gid_A29	LG	517	46.88	17.78	0.09	3.75	0.00	1.09	0.40	30.02	4.24	5.66	2.04	0.35	3.98	1.68	1.83	1.11	3.07
OM11_Gid_A29_2	LG	401	37.61	25.88	0.08	5.06	0.00	0.18	0.07	31.12	4.76	4.35	2.06	0.57	4.14	1.64	2.05	1.08	4.26
OM10_Gid_A30	LG	257	45.15	20.87	0.01	1.20	0.00	0.14	0.16	32.48	3.78	4.22	2.12	0.49	4.12	1.88	2.31	1.11	5.25
OM10_Gid_A31	LG	123	50.05	24.81	0.18	3.94	0.00	0.05	0.08	20.89	3.85	3.81	2.04	0.51	4.35	1.89	1.85	1.10	2.67
OM10_Gid_A32	LG	49	44.96	23.01	1.07	5.48	0.00	0.01	0.01	25.45	2.93	2.76	1.92	0.60	2.81	1.32	1.35	1.07	1.86

[1] Lithology: ML = Melt lens; VG = Varitextured gabbro; FG = Foliated gabbro; LG = Layered gabbro
[2] Depth: calculated height above MOHO

Table 14. Results for bulk major element composition of Gideah South (wt%)

Sample:	Litho.[1]	SiO$_2$	Al$_2$O$_3$	FeOtot	MnO	MgO	CaO	Na$_2$O	K$_2$O	TiO$_2$	P$_2$O$_5$	SO$_3$	Total	Mg#
OM10-A11-1a	SG	51.85	16.31	11.41	0.14	4.93	8.48	4.40	0.20	2.17	0.09	0.01	100	43.53
OM10-A11-1v	SG	50.03	15.87	12.94	0.14	5.20	9.19	4.22	0.14	2.11	0.13	0.01	100	41.76
OM10-A11-1x	SG	52.74	15.95	11.30	0.13	4.55	7.53	5.24	0.27	2.09	0.14	0.06	100	41.82
OM10-A11-1b	VG	51.93	15.70	12.26	0.15	4.86	7.99	4.47	0.22	2.27	0.12	0.01	100	41.42
OM10-A11-1c	VG	51.13	15.57	12.61	0.15	5.04	8.79	4.05	0.22	2.34	0.10	0.01	100	41.59
OM10-A11-1d	VG	49.24	15.18	13.77	0.16	5.58	9.80	3.51	0.17	2.49	0.07	0.01	100	41.94
OM10-A11-1iA	XE	60.63	15.36	8.16	0.09	2.90	5.34	5.61	0.22	1.53	0.15	0.03	100	38.76
OM10-A11-1iB	PG	63.62	16.98	5.51	0.05	1.47	4.21	6.73	0.21	0.99	0.22	0.01	100	32.21
OM10-A11-1l	PG	61.47	17.77	6.06	0.05	1.32	3.24	8.77	0.04	1.02	0.25	0.01	100	27.92
OM10-A11-1n	TR	74.51	13.09	2.55	0.04	0.99	2.63	5.19	0.29	0.58	0.12	0.01	100	40.97
OM10-A11-1p	PG	63.60	16.01	5.90	0.06	1.95	4.25	6.38	0.31	1.24	0.30	0.01	100	37.14
OM10-A11-1t	BD	53.50	16.40	8.31	0.10	6.39	10.05	4.10	0.09	0.97	0.07	0.01	100	57.81
OM10-A11-1u	BD	51.35	16.07	8.45	0.13	8.69	11.96	2.33	0.15	0.78	0.07	0.01	100	64.73
OM10-A11-1f	BD	51.10	16.93	9.08	0.12	6.98	11.65	2.73	0.12	1.16	0.10	0.01	100	57.80
OM10-A11-1j	BD	54.76	16.28	9.20	0.10	5.47	7.55	5.04	0.21	1.30	0.09	0.01	100	51.47

[1] Lithology: BD = basaltic dike; XE = xenolith; PG = plagiogranite; SG = spotty gabbro; TR = trondhjemite; VG = varitextured gabbros

Table 15. Results for bulk trace element composition of Gideah South (ppm)

Sample:	Litho.[1]	Cs	Rb	Ba	Th	U	Nb	Ta	La	Ce	Pr	Sr	Nd	Zr	Hf	Sm	Eu	Gd	Tb	Dy	Y	Ho	Er	Tm	Yb	Lu
OM10-A11-1a	SG	0.01	0.94	27.12	0.21	0.09	2.18	0.14	3.25	10.12	1.64	215.86	8.81	75.96	1.93	2.97	1.03	4.11	0.72	4.93	30.37	1.06	3.20	0.45	3.00	0.45
OM10-A11-1v	SG	0.01	0.59	23.83	0.17	0.06	1.65	0.10	3.00	7.69	1.35	227.36	7.40	61.27	1.58	2.56	0.96	3.44	0.62	3.99	24.74	0.89	2.50	0.38	2.48	0.37
OM10-A11-1x	SG	0.02	1.19	37.30	0.16	0.09	2.46	0.15	3.78	10.40	1.71	225.08	9.16	100.00		3.12	1.20	4.22	0.77	5.21	31.90	1.10	3.05	0.45	2.93	0.43
OM10-A11-1b	VG	0.01	1.02	30.32	0.22	0.08	2.62	0.17	4.03	11.89	1.85	219.43	9.79	77.77	1.90	3.19	1.09	4.36	0.75	5.12	32.99	1.09	3.26	0.45	3.01	0.46
OM10-A11-1c	VG	0.01	0.86	23.27	0.18	0.06	2.20	0.13	3.08	9.28	1.48	184.69	7.87	78.17	1.82	2.56	0.87	3.47	0.60	4.06	27.14	0.87	2.65	0.37	2.45	0.37
OM10-A11-1d	VG	0.01	0.82	21.80	0.18	0.08	1.93	0.11	2.85	8.79	1.44	176.69	7.79	61.06	1.47	2.64	0.93	3.65	0.65	4.45	29.61	0.95	2.82	0.39	2.62	0.40
OM10-A11-1iA	XE	0.03	0.84	44.21	0.51	0.14	5.57	0.33	7.14	22.63	3.67	165.03	18.37	85.00		5.68	1.48	7.28	1.35	9.14	56.71	1.96	5.52	0.84	5.62	0.83
OM10-A11-1iB	PG	0.02	0.87	41.95	0.35	0.14	3.95	0.23	5.80	17.83	2.84	175.71	14.83	294.56	5.06	4.51	1.53	5.85	0.99	6.60	49.88	1.43	4.37	0.62	4.12	0.65
OM10-A11-1l	PG	0.01	0.30	10.05	0.71	0.23	5.50	0.37	5.30	15.26	2.88	91.65	16.45	240.25	6.19	5.95	1.77	8.25	1.49	9.85	62.25	2.23	6.49	1.00	6.68	1.03
OM10-A11-1p	PG	0.02	1.21	40.41	0.68	0.16	4.02	0.26	6.74	18.25	3.25	175.81	17.44	150.68	3.72	5.76	1.67	7.48	1.33	8.51	54.80	1.90	5.37	0.81	5.30	0.80
OM10-A11-1n	TR	0.03	1.16	31.17	1.10	0.16	4.15	0.40	5.98	13.74	2.22	149.06	11.27	281.44	7.44	3.58	1.16	4.65	0.84	5.53	37.36	1.28	3.81	0.60	4.18	0.65
OM10-A11-1f	BD	0.01	0.52	14.63	0.12	0.06	1.52	0.09	2.83	8.07	1.26	206.14	6.64	64.45	1.32	2.15	0.88	2.88	0.49	3.30	23.38	0.69	2.06	0.28	1.86	0.28
OM10-A11-1j	BD	0.02	1.01	20.79	0.12	0.06	1.22	0.08	3.39	8.45	1.23	213.59	6.30	76.05	1.53	1.99	0.93	2.70	0.47	3.18	24.14	0.68	2.05	0.29	1.90	0.30
OM10-A11-1t	BD	0.01	0.39	23.94	0.13	0.08	0.95	0.06	3.22	7.75	1.25	213.22	6.48	53.98	1.41	2.14	0.87	2.84	0.52	3.35	21.03	0.76	2.18	0.33	2.21	0.34
OM10-A11-1u	BD	0.02	0.72	43.27	0.12	0.07	0.84	0.05	1.85	5.13	0.90	178.57	4.78	43.42	1.11	1.63	0.65	2.18	0.40	2.56	16.08	0.58	1.64	0.24	1.63	0.25

[1] Lithology: BD = basaltic dike; XE = xenolith; PG = plagiogranite; SG = spotty gabbro; TR = trondhjemite; VG = varitextured gabbros

Table 16. Results for major element mineral analyses of Gideah South (in wt%) obtained by EPMA with StdDev added.

Sample	Litho.[1]	Min[2]	Qual[3]	No[4]	SiO₂	TiO₂	Al₂O₃	Cr₂O₃	Fe₂O₃	FeO	MnO	Cl	F	MgO	CaO	Na₂O	K₂O	V₂O₃	Total	An[5]	XMg[6]
OM10_Gid_A11_1a	VGgr	Pl	c	65	53.34	0.05	29.38		0.69					0.03	12.64	4.56	0.07		100.75	60.30	
					0.67	*0.03*	*0.44*		*0.13*					*0.06*	*0.45*	*0.27*	*0.12*		*0.63*	*2.08*	
		Pl	r	22	65.23	0.00	22.24		0.36					0.01	3.51	9.75	0.15		101.27	16.47	
					0.75	*0.02*	*0.38*		*0.09*						*0.47*	*0.31*	*0.03*		*0.43*	*2.19*	
		Pl	c	5	51.84	0.05	29.09		0.76					0.04	12.46	4.45	0.04		98.68	60.62	
					0.51	*0.03*	*0.41*		*0.05*						*0.48*	*0.20*	*0.02*		*0.47*	*2.01*	
		Pl	r	2	57.52		25.43		0.56						7.82	7.30	0.08		98.71	37.00	
					0.10		*0.15*		*0.01*						*0.11*	*0.04*	*0.01*		*0.23*	*0.20*	
		Amph		29	50.23	1.28	5.08	0.12		13.62	0.26	0.13	0.11	15.24	11.25	1.24	0.12		100.66		0.43
					3.62	*0.93*	*2.97*	*0.03*		*1.63*	*0.05*	*0.13*	*0.13*	*1.75*	*0.70*	*0.72*	*0.07*		*0.44*		*0.02*
		Mag		21	0.05	1.46	0.54		65.87	32.66	0.07			0.02	0.02				100.81		
					0.02	*0.47*	*0.11*		*1.11*	*0.48*	*0.04*			*0.02*	*0.02*				*0.68*		
		Ilm		25	0.07	49.11	0.09	0.04	3.61	45.57	1.79			0.16	0.04				100.47		
					0.19	*0.61*	*0.21*	*0.03*	*3.29*	*3.67*	*0.42*			*0.07*	*0.05*				*0.56*		
OM10_Gid_A11_1a	VGso	Pl	c	19	52.86	0.06	29.25		0.63					0.02	12.32	4.78	0.05		99.97	58.58	
					0.64	*0.02*	*0.35*		*0.09*					*0.04*	*0.34*	*0.25*	*0.01*		*0.71*	*1.87*	
		Pl	r	3	60.70		24.78		0.44					0.00	6.52	8.17	0.14		100.74	30.35	
					0.70		*0.27*		*0.07*					*0.00*	*0.26*	*0.18*	*0.01*		*0.39*	*1.31*	
		Cpx		24	51.62	0.67	1.93	0.03		8.18	0.28			15.47	21.91	0.18	0.00		100.35		0.77
					1.69	*0.49*	*1.27*	*0.03*		*1.26*	*0.04*			*0.97*	*1.66*	*0.09*	*0.00*		*0.72*		*0.03*
		Ilm		5	0.01	45.95	0.04	0.03		50.60	1.50			0.25	0.02			0.21	98.61		
					0.00	*0.35*	*0.01*	*0.02*		*0.17*	*0.16*			*0.02*				*0.07*	*0.29*		
OM10_Gid_A11_1b	VGmg	Pl	c	5	60.83	0.01	24.38		0.46						6.73	8.06	0.11		100.58	31.39	
					0.77	*0.03*	*0.41*		*0.05*						*0.50*	*0.30*	*0.01*		*0.31*	*2.40*	
		Pl	r	3	64.81	0.02	22.10		0.37						3.73	9.73	0.14		100.89	17.33	
					0.30	*0.02*	*0.16*		*0.05*						*0.18*	*0.08*	*0.02*		*0.40*	*0.82*	
		Cpx		13	54.16	0.03	0.21	0.01		9.48	0.35			13.59	23.43	0.23	0.00		101.50		0.72
					0.37	*0.02*	*0.10*	*0.01*		*1.23*	*0.05*			*0.75*	*0.65*	*0.08*	*0.00*		*0.32*		*0.04*
		Amph	brown	10	44.23	3.26	10.46	0.02		13.08	0.21	0.07	0.27	13.73	11.32	2.57	0.11		101.42		0.50
					0.50	*0.47*	*0.24*	*0.05*		*0.27*	*0.03*	*0.01*	*0.02*	*0.18*	*0.16*	*0.12*	*0.01*		*0.45*		*0.01*
		Amph		7	52.24	0.81	3.04			14.44	0.24	0.15	0.15	15.78	11.20	0.84	0.10		101.11		0.43
					1.68	*0.34*	*1.10*			*0.66*	*0.06*	*0.05*	*0.18*	*0.51*	*0.65*	*0.38*	*0.04*		*0.43*		*0.02*
OM10_Gid_A11_1b	VGfg	Pl	c	3	57.77		26.30		0.48						8.97	6.64	0.09		100.25	42.53	
					0.45		*0.22*		*0.05*						*0.33*	*0.22*	*0.00*		*0.05*	*1.42*	
		Pl	r	3	61.31	0.04	23.99		0.70						6.22	8.25	0.11		100.62	29.23	
					0.75	*0.03*	*0.59*		*0.01*						*0.62*	*0.27*	*0.01*		*0.21*	*2.74*	
		Amph	green	7	51.77	1.11	3.82			14.21	0.19	0.16	0.32	15.72	10.76	1.17	0.12		101.50		0.50
					0.56	*0.10*	*0.51*			*0.57*	*0.02*	*0.03*	*0.03*	*0.33*	*0.16*	*0.12*	*0.02*		*0.51*		*0.01*
		Amph		2	52.00	1.08	3.31			13.56	0.23	0.15	0.09	16.29	11.17	1.00	0.13		101.13		0.41
					0.32	*0.03*	*0.03*			*0.06*	*0.02*	*0.03*	*0.06*	*0.13*	*0.18*	*0.02*	*0.01*		*0.52*		*0.02*
		Mag		3	0.04	1.60	0.35	0.11	65.35	32.57	0.03			0.02	0.03				100.10		
					0.02	*0.47*	*0.01*	*0.00*	*1.07*	*0.31*	*0.02*			*0.01*	*0.01*				*0.29*		
		Ilm		2	0.09	48.85	0.04			49.41	1.61			0.16	0.05				100.22		
					0.08		*0.01*			*0.11*	*0.13*			*0.05*	*0.04*				*0.51*		

[1] Lithology: BD = basaltic dike; Bdrel = relictic in basaltic dike; PG = plagiogranite; VGfg = fine grained varitextured gabbro; VGgr = granular varitextured gabbro; VGmg = medium grained varitextured gabbro; VGso = subophitic varitextured gabbro; XEBD = xenolith of formed basaltic dike;

[2] Mineral analysed

[3] Qualifier: r = rim; c = core

[4] number of analyses

[5] content of plagioclase

[6] XMg for Cpx and Amph

Table 16. continued

Sample	Litho.[1]	Min[2]	Qual[3]	No[4]	SiO₂	TiO₂	Al₂O₃	Cr₂O₃	Fe₂O₃	FeO	MnO	Cl	F	MgO	CaO	Na₂O	K₂O	V₂O₃	Total	An[5]	XMg[6]
OM10_Gid_A11_1c	VGmg	Pl	c	5	65.41 (0.55)		22.19 (0.36)		0.34 (0.10)						3.47 (0.38)	9.70 (0.31)	0.15 (0.03)		101.26 (0.34)	16.35 (1.90)	
		Pl	r	3	66.40 (0.55)		21.84 (0.41)		0.35 (0.02)						2.86 (0.45)	10.03 (0.22)	0.15 (0.01)		101.63 (0.41)	13.47 (2.09)	
		Cpx		10	53.36 (0.56)	0.40 (0.31)	1.15 (0.77)	0.03 (0.03)		9.67 (0.64)	0.34 (0.04)			14.80 (1.35)	21.34 (1.43)	0.35 (0.05)	0.00 (0.01)		101.44 (0.50)		0.73 (0.03)
		Amph		10	53.21 (0.46)	0.46 (0.10)	2.25 (0.11)			17.24 (1.66)	0.36 (0.08)	0.14 (0.05)	0.21 (0.02)	15.24 (0.61)	9.31 (1.15)	0.62 (0.06)	0.06 (0.02)		101.25 (0.43)		0.50 (0.02)
		Amph		9	52.59 (0.52)	0.84 (0.13)	2.97 (0.30)			14.43 (0.39)	0.24 (0.02)	0.14 (0.01)	0.07 (0.05)	15.21 (0.55)	10.91 (0.16)	0.84 (0.06)	0.10 (0.04)		100.45 (0.42)		0.44 (0.03)
		Ilm		3	0.00 (0.00)	46.72 (0.08)	0.01 (0.01)	0.05 (0.02)		51.09 (0.37)	1.38 (0.06)			0.18 (0.01)	0.03 (0.02)				99.46 (0.21)		
OM10_Gid_A11_1c	VGfg	Pl	c	6	57.41 (0.36)	0.01 (0.02)	26.40 (0.46)		0.46 (0.06)						8.41 (0.50)	6.83 (0.28)	0.11 (0.02)		99.65 (0.44)	40.23 (2.37)	
		Pl	r	3	67.10 (0.09)		20.67 (0.13)		0.15 (0.11)						1.49 (0.01)	10.69 (0.07)	0.17 (0.00)		100.27 (0.24)	7.07 (0.05)	
		Amph		5	52.87 (0.77)	0.65 (0.19)	2.53 (0.53)			13.46 (0.86)	0.27 (0.04)	0.12 (0.03)	0.02 (0.04)	15.96 (0.22)	11.05 (0.18)	0.65 (0.20)	0.09 (0.03)		99.78 (0.75)		0.42 (0.01)
		Amph		6	52.27 (0.54)	0.89 (0.12)	2.92 (0.18)			15.87 (0.23)	0.30 (0.02)	0.10 (0.01)	0.33 (0.04)	15.29 (0.48)	10.14 (0.20)	0.93 (0.10)	0.26 (0.04)		101.43 (0.45)		0.52 (0.01)
		Ilm		3	0.02 (0.01)	47.90 (0.41)	0.03 (0.02)	0.02 (0.02)		50.38 (0.35)	1.33 (0.05)			0.11 (0.00)	0.01 (0.01)				99.81 (0.19)		
OM10_Gid_A11_1d	VGfg	Pl	c	17	54.56 (2.12)	0.05 (0.03)	28.47 (1.30)		0.55 (0.13)						10.97 (1.67)	5.45 (0.97)	0.06 (0.04)		100.11 (0.71)	52.52 (8.24)	
		Pl	ri	4	59.63 (0.30)		24.58 (0.10)		0.46 (0.04)						6.34 (0.18)	7.81 (0.15)	0.15 (0.01)		98.98 (0.21)	30.71 (0.99)	
		Pl	ro	6	64.98 (0.79)		22.73 (0.61)		0.33 (0.04)						3.28 (0.38)	9.54 (0.33)	0.24 (0.12)		101.10 (0.24)	15.74 (1.86)	
		Cpx		17	52.84 (0.32)	0.08 (0.07)	0.37 (0.26)	0.02 (0.02)		8.96 (0.77)	0.36 (0.09)			12.63 (0.36)	23.53 (0.62)	0.26 (0.08)	0.00 (0.00)		99.05 (0.71)		0.72 (0.02)
		Amph		10	52.67 (0.73)	0.62 (0.18)	2.66 (0.80)			14.60 (0.53)	0.32 (0.03)	0.12 (0.04)	0.23 (0.04)	16.15 (0.52)	10.51 (0.52)	0.76 (0.08)	0.08 (0.02)		100.85 (0.41)		0.50 (0.02)
		Mag		25	0.06 (0.03)	1.82 (1.18)	0.44 (0.11)	0.15 (0.03)	63.80 (2.44)	32.61 (1.02)	0.12 (0.09)			0.03 (0.03)	0.02 (0.02)			1.29 (0.08)	100.34 (0.41)		
		Ilm		10	0.02 (0.01)	46.31 (1.18)	0.03 (0.01)	0.04 (0.02)		50.16 (0.97)	1.32 (0.04)			0.24 (0.02)	0.01 (0.01)			0.28 (0.09)	98.42 (0.28)		
OM10_Gid_A11_1e	VGmg	Pl	c	11	63.37 (0.54)	0.00 (0.01)	23.41 (0.38)		0.33 (0.07)						5.00 (0.31)	8.90 (0.24)	0.15 (0.01)		101.17 (0.25)	23.50 (1.57)	
		Pl	r	5	65.80 (0.46)		21.95 (0.32)		0.25 (0.15)						3.03 (0.44)	9.93 (0.17)	0.18 (0.04)		101.14 (0.64)	14.28 (1.98)	
		Amph		6	53.47 (0.32)	0.69 (0.10)	2.41 (0.10)			12.95 (0.52)	0.27 (0.04)	0.10 (0.01)	0.22 (0.04)	17.09 (0.23)	10.34 (0.30)	0.83 (0.06)	0.06 (0.01)		100.59 (0.39)		0.51 (0.01)
		Amph		6	52.72 (0.51)	0.89 (0.15)	2.95 (0.33)			12.95 (0.55)	0.26 (0.03)	0.12 (0.03)	0.25 (0.03)	16.76 (0.31)	10.41 (0.41)	1.05 (0.11)	0.08 (0.02)		100.59 (0.49)		0.50 (0.02)
		Mag		5	0.14 (0.19)	0.60 (0.18)	0.26 (0.05)	0.15 (0.01)	65.89 (1.39)	31.36 (0.12)	0.02 (0.02)			0.00 (0.00)	0.18 (0.14)			1.25 (0.06)	99.85 (0.91)		
		Ilm		5	0.03 (0.02)	48.25 (0.17)	0.02 (0.01)	0.03 (0.03)	4.68 (3.83)	43.71 (3.74)	2.45 (0.22)			0.09 (0.03)	0.10 (0.03)			0.16 (0.06)	99.51 (0.39)		

[1] Lithology: BD = basaltic dike; Bdrel = relictic in basaltic dike; PG = plagiogranite; VGfg = fine grained varitextured gabbro; VGgr = granular varitextured gabbro; VGmg = medium grained varitextured gabbro; VGso = subophitic varitextured gabbro; XEBD = xenolith of formed basaltic dike;
[2] Mineral analysed   [4] number of analyses
[3] Qualifier: r = rim; c = core   [5] content of plagioclase   [6] XMg for Cpx and Amph

Table 16. continued

Sample	Litho.[1]	Min[2]	Qual[3]	No[4]	SiO₂	TiO₂	Al₂O₃	Cr₂O₃	Fe₂O₃	FeO	MnO	Cl	F	MgO	CaO	Na₂O	K₂O	V₂O₃	Total	An[5]	XMg[6]
OM10_Gid_A11_1e	VGfg	Pl	c	10	56.71	0.03	27.12		0.46						9.29	6.44	0.08		100.12	44.19	
				sd	*1.55*	*0.03*	*0.82*		*0.06*						*1.08*	*0.61*	*0.02*		*0.43*	*5.17*	
		Pl	r	7	63.14	0.01	23.43		0.29						4.50	8.98	0.16		100.51	21.48	
				sd	*0.99*	*0.02*	*0.81*		*0.04*						*0.98*	*0.56*	*0.01*		*0.38*	*4.67*	
		Amph		8	42.45	3.52	10.49	0.13		12.87	0.19	0.05	0.08	12.76	11.53	2.55	0.14		98.65		0.51
				sd	*0.56*	*0.36*	*0.34*	*0.02*		*0.22*	*0.04*	*0.01*	*0.09*	*0.15*	*0.19*	*0.20*	*0.04*		*0.52*		*0.01*
		Mag		6	0.07	0.95	0.17	0.04	65.90	31.75	0.06			0.01	0.13			1.19	100.36		
				sd	*0.01*	*0.58*	*0.03*	*0.02*	*1.36*	*0.41*	*0.05*			*0.01*	*0.03*			*0.07*	*0.57*		
		Ilm		8	0.05	47.85	0.02	0.02	1.36	48.77	1.65			0.17	0.16			0.22	98.91		
				sd	*0.01*	*0.51*	*0.01*		*0.33*		*0.11*				*0.07*			*0.08*	*0.28*		
OM10_Gid_A11_1f	BDrel	Pl		18	47.66	0.00	33.00		0.54					0.14	17.08	2.05	0.01		100.50	82.11	
				sd	*0.85*	*0.01*	*0.51*		*0.08*					*0.04*	*0.57*	*0.36*	*0.02*		*0.35*	*3.01*	
OM10_Gid_A11_1f	BD	Pl	c	34	49.82	0.03	30.97		0.74					0.12	14.53	3.35	0.03		99.59	70.49	
				sd	*1.89*	*0.03*	*1.34*		*0.12*					*0.04*	*1.56*	*0.89*	*0.02*		*0.42*	*7.75*	
		Pl	r	3	58.40	0.01	25.89		0.48						8.08	7.11	0.08		100.06	38.41	
				sd	*0.20*	*0.02*	*0.07*		*0.03*						*0.18*	*0.14*	*0.01*		*0.36*	*0.97*	
		Amph		8	50.32	0.57	5.27	0.49		14.99	0.24	0.06	0.17	13.61	11.96	0.81	0.08		100.65		0.49
				sd	*1.68*	*0.10*	*1.15*	*0.56*		*0.61*	*0.02*	*0.03*	*0.02*	*1.03*	*0.20*	*0.26*	*0.03*		*0.32*		*0.02*
		Mag		3	0.26	0.90	0.19	0.15	66.00	31.58	0.10			0.06	0.28				99.52		
				sd	*0.16*	*0.23*	*0.09*	*0.01*	*1.33*	*0.21*	*0.08*			*0.07*	*0.07*				*0.91*		
		Sp		10	29.91	36.35	1.62	0.12		1.68	0.04			0.04	28.24				98.01		
				sd	*0.48*	*1.39*	*0.59*	*0.09*		*0.68*	*0.02*			*0.11*	*0.33*				*0.75*		
OM10_Gid_A11_1i	PG	Pl	c	11	61.80		23.83		0.38						5.31	8.59	0.13		100.05	25.27	
				sd	*0.92*		*0.58*		*0.09*						*0.78*	*0.47*	*0.03*		*0.28*	*3.78*	
		Pl	r	8	66.90		20.99		0.49						1.40	10.83	0.10		100.70	6.61	
				sd	*0.88*		*0.63*		*0.10*						*0.75*	*0.41*	*0.02*		*0.36*	*3.49*	
		Amph		6	52.72	0.82	2.77	0.04		14.45	0.28	0.11	0.33	16.01	10.56	0.73	0.09		101.02		0.50
				sd	*0.40*	*0.18*	*0.26*	*0.03*		*0.43*	*0.05*	*0.01*	*0.06*	*0.19*	*0.35*	*0.17*	*0.02*		*0.59*		*0.02*
		Mag		4	0.39	0.48	0.35	0.03	66.47	31.58	0.02			0.02	0.27				99.61		
				sd	*0.43*	*0.18*	*0.19*		*1.08*	*0.40*	*0.02*			*0.02*	*0.19*				*0.36*		
		Sp		2	30.32	36.71	1.37	0.03		1.74	0.03			0.04	28.70				98.90		
				sd	*0.17*	*0.75*	*0.24*		*0.34*					*0.11*	*0.10*				*0.23*		
OM10_Gid_A11_1i	XEBD	Pl	c	3	62.78	0.01	23.41		0.41						4.46	9.07	0.11		100.26	21.25	
				sd	*0.18*	*0.02*	*0.29*		*0.13*						*0.27*	*0.31*	*0.02*		*0.14*	*1.57*	
		Pl	r	4	67.09	0.03	20.71		0.45						1.18	11.05	0.11		100.63	5.57	
				sd	*0.22*	*0.03*	*0.41*		*0.13*						*0.27*	*0.32*	*0.02*		*0.23*	*1.32*	
		Amph		9	51.87	0.90	3.26	0.00		14.59	0.27	0.14	0.40	15.54	10.48	0.91	0.18		100.66		0.50
				sd	*1.21*	*0.13*	*0.81*	*0.00*		*1.10*	*0.05*	*0.03*	*0.11*	*1.03*	*0.29*	*0.19*	*0.07*		*0.49*		*0.02*
		Ilm		2	0.04	48.28	0.01	0.00	3.59	44.64	2.24			0.10	0.19				99.08		
				sd	*0.03*	*0.10*	*0.01*	*0.00*	*3.59*	*3.56*	*0.15*			*0.00*	*0.02*				*0.01*		
		Sp		3	30.34	37.20	1.25	0.03		1.20	0.05				28.38				98.44		
				sd	*0.14*	*0.71*	*0.32*	*0.02*		*0.20*	*0.02*				*0.19*				*0.47*		
OM10_Gid_A11_1j	BD	Pl	c	3	53.77		28.95		0.83					0.06	11.73	4.95	0.04		100.33	56.58	
				sd	*0.63*		*0.23*		*0.06*					*0.04*	*0.48*	*0.30*	*0.01*		*0.28*	*2.50*	
		Pl	r	6	62.74		23.57		0.44					0.02	4.83	9.06	0.09		100.75	22.63	
				sd	*0.88*		*0.54*		*0.08*						*0.65*	*0.22*	*0.02*		*0.45*	*2.81*	
		Pl	r	4	68.82		20.93		0.41					0.03	0.72	10.96	0.02		101.86	3.47	
				sd	*0.31*		*0.08*		*0.04*						*0.08*	*0.04*	*0.01*		*0.30*	*0.36*	
		Amph		10	51.51	0.48	3.30	0.32		15.61	0.28	0.04	0.21	13.99	11.92	0.55	0.14		100.42		0.50
				sd	*0.61*	*0.15*	*0.55*	*0.27*		*1.11*	*0.03*	*0.01*	*0.02*	*0.71*	*0.15*	*0.11*	*0.06*		*0.63*		*0.02*

[1] Lithology: BD = basaltic dike; BDrel = relictic in basaltic dike; PG = plagiogranite; VGfg = fine grained varitextured gabbro; VGgr = granular varitextured gabbro; VGmg = medium grained varitextured gabbro; VGso = subophitic varitextured gabbro; XEBD = xenolith of formed basaltic dike;

[2] Mineral analysed

[3] Qualifier: r = rim; c = core

[4] Number of analyses

[5] An: content of plagioclase

[6] XMg for Cpx and Amph

Table 16. continued

Sample	Litho.[1]	Min[2]	Qual[3]	No[4]	SiO$_2$	TiO$_2$	Al$_2$O$_3$	Cr$_2$O$_3$	Fe$_2$O$_3$	FeO	MnO	Cl	F	MgO	CaO	Na$_2$O	K$_2$O	V$_2$O$_3$	Total	An[5]	XMg[6]
OM10_Gid_A11_1m	PG	Pl		18	68.14 (0.83)		20.29 (0.42)							0.05 (0.07)	0.25 (0.16)	11.44 (0.27)	0.04 (0.08)		100.21 (0.71)	1.18 (0.78)	
		Amph		4	51.17 (0.65)	0.30 (0.05)	2.79 (0.39)	0.06 (0.02)		18.62 (0.83)	0.26 (0.03)	0.05 (0.02)	0.23 (0.01)	12.51 (0.80)	11.78 (0.15)	0.44 (0.09)	0.06 (0.01)	0.37 (0.09)	100.26 (0.42)		0.50 (0.02)
		Mag		13	0.10 (0.09)	0.75 (0.70)	0.28 (0.03)	0.02 (0.02)	66.76 (1.43)	31.70 (0.57)	0.09 (0.10)			0.03 (0.03)	0.08 (0.09)	0.09	0.01		100.22 (0.49)		
		Ilm		7	0.03 (0.01)	45.19 (0.20)	0.04 (0.01)	0.02 (0.02)		50.58 (0.52)	2.23 (0.38)			0.10 (0.01)	0.01 (0.01)			0.11 (0.05)	98.31 (0.26)		
OM10_Gid_A11_1m	XEBD	Pl		20	67.83 (0.54)		19.98 (0.22)		0.46 (0.09)						0.67 (0.26)	11.60 (0.18)	0.12 (0.03)		100.65 (0.41)	3.07 (1.19)	
		Amph		20	52.34 (1.05)	0.67 (0.18)	2.31 (0.59)			13.73 (1.39)	0.28 (0.09)	0.11 (0.03)	0.14 (0.09)	16.15 (1.15)	10.82 (0.23)	0.56 (0.20)	0.11 (0.04)		99.34 (0.56)		0.49 (0.02)
		Ilm		6	0.12 (0.11)	47.85 (0.11)	0.01 (0.00)	0.01 (0.02)	8.04 (0.45)	37.62 (0.26)	5.07 (0.26)			0.03 (0.02)	0.30 (0.15)	0.20	0.04	0.04 (0.04)	99.09 (0.58)		
OM10_Gid_A11_1n	PG	Pl		7	64.36 (0.46)	0.01 (0.02)	22.94 (0.24)	0.02 (0.02)	0.29 (0.13)						3.80 (0.33)	9.29 (0.29)	0.18 (0.02)		100.87 (0.49)	18.27 (1.71)	
		Amph		10	49.95 (0.39)	1.18 (0.19)	4.39 (0.24)	0.04		13.66 (0.27)	0.51 (0.03)	0.12 (0.02)	0.97 (0.18)	16.12 (0.40)	10.20 (0.29)	1.45 (0.24)	0.18 (0.13)		100.87 (0.60)		0.51 (0.01)
OM10_Gid_A11_1o	PG	Pl	c	6	56.75 (0.32)	0.05 (0.03)	27.50 (0.14)		0.39 (0.05)						9.55 (0.12)	6.25 (0.07)	0.07 (0.01)		100.59 (0.25)	45.57 (0.46)	
		Pl	r	3	68.11 (0.67)		20.74 (0.36)		0.27 (0.19)						0.97 (0.53)	11.10 (0.65)	0.12 (0.05)		101.30 (0.23)	4.65 (2.59)	
		Amph		5	50.92 (0.71)	0.78 (0.14)	3.24 (0.42)	0.05 (0.02)		16.70 (2.03)	0.30 (0.07)	0.16 (0.03)	0.50 (0.14)	14.73 (1.12)	9.81 (1.06)	0.92 (0.15)	0.10 (0.03)		100.26 (0.41)		0.51 (0.02)
		Mag		15	0.12 (0.07)	0.77 (0.52)	0.41 (0.08)		66.48 (1.23)	31.80 (0.34)	0.02 (0.04)			0.01 (0.03)	0.05 (0.03)	0.15	0.03	0.47 (0.06)	100.25 (0.43)		
OM10_Gid_A11_1o	PG	Pl	c	6	60.23 (0.63)		25.06 (0.39)		0.31 (0.06)						7.01 (0.45)	7.83 (0.34)	0.09 (0.01)		100.54 (0.15)	32.94 (2.37)	
		Pl	r	3	67.65 (0.30)		20.65 (0.10)		0.42 (0.00)						1.20 (0.07)	11.36 (0.22)	0.12 (0.01)		101.39 (0.38)	5.47 (0.39)	
		Amph		5	51.50 (0.32)	0.16 (0.03)	3.15 (0.09)	0.05 (0.03)		18.62 (0.43)	0.31 (0.03)	0.04 (0.01)	0.24 (0.02)	12.04 (0.30)	11.57 (0.23)	0.42 (0.04)	0.05 (0.01)		100.16 (0.29)		0.48 (0.01)
		Mag		14	0.05 (0.02)	0.76 (0.70)	0.26 (0.06)	0.03	67.20 (1.60)	31.83 (0.61)	0.06 (0.07)			0.04 (0.05)	0.09 (0.07)	0.04	0.01	0.37 (0.06)	100.66 (0.58)		
		Ilm		5	0.32 (0.57)	48.21 (0.67)	0.03 (0.03)	0.00 (0.00)	4.50 (2.62)	41.40 (2.95)	3.32 (0.30)			0.00 (0.01)	0.43 (0.46)			0.06 (0.07)	98.30 (0.59)		
OM10_Gid_A11_1p	PG	Pl	c	7	62.11 (0.42)	0.01 (0.01)	23.85 (0.22)		0.31 (0.03)						5.29 (0.27)	8.54 (0.22)	0.16 (0.01)		100.27 (0.32)	25.29 (1.44)	
		Pl	r	5	68.37 (0.63)		20.34 (0.37)		0.19 (0.17)						0.61 (0.36)	11.27 (0.25)	0.10 (0.05)		100.88 (0.29)	2.87 (1.69)	
		Amph		10	52.95 (0.95)	0.73 (0.18)	2.64 (0.53)	0.04 (0.04)		14.64 (0.72)	0.32 (0.04)	0.11 (0.03)	0.37 (0.07)	16.02 (0.66)	10.33 (0.41)	0.77 (0.21)	0.09 (0.02)		101.12 (0.30)		0.51 (0.02)
		Mag		2	0.86 (0.35)	0.65 (0.26)	0.47 (0.12)	0.04	65.54 (0.06)	32.51 (0.18)	0.06 (0.02)			0.19 (0.11)	0.11 (0.07)	0.21	0.02		100.42 (0.53)		
OM10_Gid_A11_1p	PG	Pl	c	15	63.22 (1.07)		23.60 (0.55)		0.32 (0.07)						5.03 (0.73)	8.81 (0.46)	0.14 (0.02)		101.12 (0.48)	23.80 (3.57)	
		Pl	r	5	67.30 (0.66)		21.08 (0.19)		0.38 (0.05)						1.98 (0.28)	10.52 (0.34)	0.16 (0.03)		101.43 (0.62)	9.34 (1.43)	
		Amph		10	53.55 (0.50)	0.63 (0.10)	2.10 (0.19)	0.04		14.92 (0.80)	0.34 (0.04)	0.04 (0.04)	0.22 (0.07)	15.66 (0.47)	10.31 (0.30)	0.68 (0.11)	0.18 (0.04)		100.79 (0.40)		0.50 (0.01)

[1] Lithology: BD = basaltic dike; Bdrel = relictic in basaltic dike; PG = plagiogranite; VGfg = fine grained varitextured gabbro; VGgr = granular varitextured gabbro; VGmg = medium grained varitextured gabbro; VGso = subophitic varitextured gabbro; XEBD = xenolith of formed basaltic dike;

[2] Mineral analysed

[3] Qualifier: r = rim; c = core

[4] Number of analyses

[5] content of plagioclase

[6] XMg for Cpx and Amph

Table 16. continued

Sample	Litho.[1]	Min.[2]	Qual.[3]	No.[4]	SiO_2	TiO_2	Al_2O_3	Cr_2O_3	Fe_2O_3	FeO	MnO	Cl	F	MgO	CaO	Na_2O	K_2O	V_2O_3	Total	An[5]	XMg[6]
OM10_Gid_A11_1q	PG	Pl	c	13	61.34	0.01	24.06		0.30						5.49	8.47	0.15		99.82	26.11	
					1.24	*0.02*	*0.50*		*0.08*						*1.03*	*0.50*	*0.02*		*0.65*	*4.72*	
		Pl	r	8	67.09	0.00	21.10		0.22						1.57	10.36	0.10		100.44	7.66	
					1.26	*0.01*	*0.76*		*0.10*						*0.72*	*0.43*	*0.03*		*0.52*	*3.49*	
		Amph		10	52.54	0.72	2.77	0.03		13.56	0.24	0.10	0.31	16.75	10.95	0.78	0.10		101.01		0.52
					1.18	*0.28*	*0.77*	*0.03*		*1.22*	*0.06*	*0.03*	*0.05*	*0.99*	*0.48*	*0.29*	*0.02*		*0.53*		*0.02*
		Mag		15	0.09	0.96	0.29	0.02	66.50	31.93	0.12			0.01	0.04		0.02	0.18	100.14		0.02
					0.03	*0.92*	*0.07*	*0.02*	*1.87*	*0.73*	*0.18*			*0.02*	*0.03*			*0.07*	*0.58*		
		Ilm		5	0.06	44.69	0.02	0.02		51.10	1.61			0.09	0.01			0.04	97.65		
					0.02	*0.24*	*0.01*			*0.23*	*0.06*			*0.06*					*0.11*		
OM10_Gid_A11_1r	PG	Pl		7	64.01		22.30		0.27						3.56	9.31	0.19		99.64	17.25	
					0.36		*0.11*		*0.11*						*0.23*	*0.13*	*0.01*		*0.41*	*1.08*	
		Amph		5	52.76	0.61	2.78			15.16	0.31	0.11	0.20	15.79	10.46	0.72	0.07		100.70		0.51
					0.17	*0.18*	*0.51*			*1.04*	*0.07*	*0.02*	*0.02*	*0.23*	*0.62*	*0.12*	*0.03*		*0.39*		*0.02*
OM10_Gid_A11_1r	VGgr	Amph		5	51.96	0.72	3.24			14.18	0.25	0.12	0.20	15.79	11.05	0.81	0.10		100.54		0.50
					0.35	*0.19*	*0.28*			*0.38*	*0.03*	*0.02*	*0.02*	*0.18*	*0.17*	*0.07*	*0.02*		*0.45*		*0.02*
		Mag		11	0.08	1.32	0.36	0.14	65.28	32.36	0.08			0.03	0.03			1.08	100.77		
					0.03	*0.55*	*0.06*	*0.02*	*1.06*	*0.53*	*0.05*			*0.03*	*0.03*			*0.06*	*0.72*		
		Ilm		9	0.03	47.09	0.03	0.03		49.45	1.43			0.14	0.03			0.22	98.45		
					0.02	*0.85*	*0.01*	*0.02*		*0.63*	*0.05*			*0.05*	*0.03*			*0.06*	*0.32*		
OM10_Gid_A11_1s	BD	Pl	r	4	61.75	0.01	24.00		0.36						5.66	8.48	0.11		100.37	26.81	
					0.62	*0.02*	*0.52*		*0.09*						*0.63*	*0.42*	*0.02*		*0.21*	*3.14*	
		Pl	c	11	54.54	0.05	27.69		0.67						10.93	5.42	0.05		99.40	52.63	
					1.51	*0.03*	*0.76*		*0.12*						*1.13*	*0.76*	*0.02*		*0.93*	*6.13*	
		Amph		10	51.50	0.38	3.84			16.35	0.28	0.09	0.21	13.58	12.03	0.75	0.09		101.19		0.50
					0.45	*0.04*	*0.32*			*0.40*	*0.03*	*0.01*	*0.01*	*0.20*	*0.15*	*0.07*	*0.01*		*0.42*		*0.02*
OM10_Gid_A11_1t	BD	Pl	c	12	53.59	0.02	29.24		0.75					0.07	12.10	4.70	0.04		100.52	58.63	
					1.50	*0.03*	*0.83*		*0.10*					*0.06*	*1.08*	*0.65*	*0.01*		*0.50*	*5.48*	
		Pl	r	9	63.44		23.67		0.15					0.01	4.59	8.90	0.11		100.87	22.04	
					0.98		*0.63*		*0.11*					*0.04*	*0.83*	*0.45*	*0.02*		*0.25*	*3.92*	
OM10_Gid_A11_1u	BD	Pl	c	13	50.38	0.03	30.36		0.88					0.19	14.24	3.44	0.04		99.57	69.43	
					1.27	*0.03*	*0.94*		*0.12*					*0.10*	*1.10*	*0.61*	*0.02*		*0.23*	*5.40*	
		Pl	r	8	56.73	0.01	26.87		0.54					0.06	9.27	6.35	0.08		99.91	44.44	
					1.39	*0.02*	*1.11*		*0.17*					*0.12*	*1.22*	*0.61*	*0.03*		*0.44*	*5.47*	
		Amph		10	50.37	0.52	5.51	0.15		12.38	0.20	0.04	0.14	15.63	11.91	0.82	0.07		99.84		0.51
					0.41	*0.07*	*0.53*	*0.22*		*0.57*	*0.02*	*0.01*	*0.02*	*0.54*	*0.32*	*0.09*	*0.02*		*0.66*		*0.02*
		Sp		3		0.57	18.28	37.27	7.42	32.70				1.14	0.10				97.48		
						0.01	*0.09*	*0.13*	*0.24*	*0.02*				*0.05*	*0.01*				*0.31*		
OM10_Gid_A11_1v	VGgr	Pl	c	7	53.37	0.02	29.05		0.63						12.27	4.83	0.04		100.20	58.30	
					0.49	*0.03*	*0.28*		*0.05*						*0.30*	*0.28*	*0.00*		*0.37*	*1.67*	
		Pl	r	2	65.17		21.81		0.37						3.01	9.87	0.15		100.38	14.31	
					0.54		*0.47*		*0.04*						*0.56*	*0.26*	*0.01*		*0.28*	*2.60*	
OM10_Gid_A11_1v		Cpx		4	54.49	0.02	0.21	0.00		8.69	0.30	0.07	0.27	14.30	23.49	0.32	0.00		101.81		0.75
					0.30	*0.01*	*0.01*	*0.00*		*1.19*	*0.02*	*0.01*	*0.02*	*0.56*	*0.68*	*0.10*	*0.00*		*0.39*		*0.03*
		Amph		5	54.07	0.61	2.05			14.24	0.31			16.64	10.20	0.81	0.09		101.53		0.51
					0.27	*0.05*	*0.19*			*0.65*	*0.03*			*0.28*	*0.41*	*0.07*	*0.02*		*0.66*		*0.01*
		Amph		5	50.94	0.91	4.35			13.15	0.25	0.11	0.27	16.55	10.39	1.33	0.10		100.48		0.51
					1.56	*0.42*	*1.30*			*0.92*	*0.07*	*0.04*	*0.02*	*0.45*	*0.74*	*0.30*	*0.03*		*0.42*		*0.01*
		Mag		8	0.04	0.99	0.49	0.13	66.24	32.26	0.08			0.01	0.01			1.13	101.38		
					0.02	*0.34*	*0.07*	*0.02*	*0.73*	*0.30*	*0.05*			*0.01*	*0.01*			*0.09*	*0.20*		

[1] Lithology: BD = basaltic dike; Bdrel = relictic in basaltic dike; PG = plagiogranite; VGfg = fine grained varitextured gabbro; VGgr = granular varitextured gabbro; VGmg = medium grained varitextured gabbro; VGso = subophitic varitextured gabbro; XEBD = xenolith of formed basaltic dike;
[2] Mineral analysed
[3] Qualifier: r = rim; c = core
[4] number of analyses
[5] content of plagioclase
[6] XMg for Cpx and Amph

Table 16. continued

Sample	Litho.[1]	Min[2]	Qual[3]	No[4]	SiO_2	TiO_2	Al_2O_3	Cr_2O_3	Fe_2O_3	FeO	MnO	Cl	F	MgO	CaO	Na_2O	K_2O	V_2O_3	Total	An[5]	XMg[6]
OM10_Gid_A11_1v	VGso	Pl	c	10	51.44 *1.20*	0.04 *0.03*	30.38 *1.05*		0.78 *0.13*						13.60 *1.13*	3.76 *0.61*	0.03 *0.02*		100.02 *0.56*	66.57 *5.47*	
		Pl	r	3	58.64 *1.20*		25.74 *0.74*		0.51 *0.51*						7.91 *0.87*	6.91 *0.62*	0.08 *0.01*		99.80 *0.38*	38.60 *4.78*	
		Amph		5	49.20 *0.63*	0.99 *0.21*	5.01 *0.49*		0.04	14.72 *0.11*	0.24 *0.03*	0.19 *0.03*	0.55 *0.18*	15.02 *0.28*	10.59 *0.20*	1.69 *0.22*	0.32 *0.03*		100.61 *0.47*		0.51 *0.01*
		Cpx		9	53.58 *0.25*	0.07 *0.03*	0.43 *0.15*	0.02 *0.02*		7.90 *0.93*	0.33 *0.05*			14.24 *0.56*	23.75 *0.58*	0.31 *0.16*	0.00 *0.01*		100.63 *0.22*		0.76 *0.03*
OM10_Gid_A11_1w	VGgr	Pl	c	24	53.29 *2.10*	0.03 *0.03*	29.48 *1.25*		0.67 *0.15*					0.03 *0.04*	12.53 *1.56*	4.57 *0.96*	0.13 *0.27*		100.73 *0.53*	59.87 *7.78*	
		Pl	r	5	61.78 *2.10*		23.71 *0.86*		0.50 *0.12*					0.13 *0.16*	5.53 *1.06*	8.64 *0.62*	0.14 *0.02*		100.43 *0.69*	25.93 *5.03*	
		Pl	c	13	50.62 *0.55*	0.04 *0.03*	30.17 *0.44*		0.77 *0.12*					0.02 *0.06*	13.50 *0.43*	3.86 *0.24*	0.05 *0.03*		99.03 *0.35*	65.71 *2.03*	
		Pl	ri	7	53.42 *1.62*	0.04 *0.03*	28.54 *1.06*		0.73 *0.19*					0.01 *0.02*	11.24 *1.35*	5.23 *0.78*	0.05 *0.01*		99.23 *0.44*	54.18 *6.69*	
		Pl	ro	3	59.47 *0.17*		24.85 *0.13*		0.24 *0.06*						6.37 *0.08*	8.17 *0.08*	0.08 *0.01*		99.18 *0.09*	29.96 *0.08*	
		Amph		14	50.29 *2.20*	0.83 *0.43*	5.03 *1.92*			13.51 *1.70*	0.22 *0.04*	0.14 *0.05*	0.16 *0.12*	15.19 *1.63*	11.69 *1.01*	1.19 *0.36*	0.21 *0.09*		100.57 *0.95*		0.43 *0.02*
OM10_Gid_A11_1w	VGso	Pl	c	7	61.91 *0.78*	0.01 *0.02*	24.37 *0.45*		0.37 *0.04*						5.94 *0.64*	8.17 *0.39*	0.13 *0.03*		100.90 *0.23*	28.44 *3.16*	
		Pl	c	5	58.64 *0.24*	0.01 *0.02*	26.13 *0.17*		0.37 *0.05*						8.23 *0.08*	6.90 *0.18*	0.09 *0.01*		100.37 *0.29*	39.53 *0.84*	
		Pl	r	5	66.14 *0.32*	0.01 *0.02*	21.83 *0.41*		0.31 *0.05*					0.03 *0.05*	2.81 *0.34*	9.93 *0.20*	0.21 *0.06*		101.26 *0.40*	13.37 *1.60*	
		Cpx		12	54.02 *0.35*	0.12 *0.08*	0.70 *0.37*	0.06 *0.04*		6.49 *0.51*	0.22 *0.04*			15.00 *0.26*	23.59 *0.78*	0.13 *0.06*	0.00		100.35 *0.45*		0.80 *0.01*
		Mag		12	0.08 *0.07*	0.88 *0.60*	0.39 *0.09*	0.21 *0.01*	66.19 *1.38*	31.97 *0.52*	0.08 *0.06*			0.03 *0.03*	0.07 *0.04*		0.00	1.09 *0.07*	100.97 *0.58*		
		Ilm		4	0.02 *0.02*	47.51 *0.27*	0.03 *0.01*	0.04 *0.02*		48.67 *0.08*	2.87 *0.17*			0.17 *0.03*	0.15 *0.05*			1.12 *0.04*	100.58 *0.13*		
		Sp		6	30.94 *0.22*	34.36 *1.63*	3.09 *0.95*	0.07 *0.03*		1.75 *0.52*	0.01 *0.01*				28.13 *0.24*			1.22 *0.17*	99.57 *0.42*		
OM10_Gid_A11_1x	VGgr	Pl	c	10	60.38 *2.10*	0.02 *0.02*	24.90 *1.27*		0.37 *0.08*						6.70 *1.54*	7.79 *0.89*	0.13 *0.03*		100.29 *0.41*	32.03 *7.48*	
		Pl	ri	3	63.86 *0.22*		22.73 *0.20*		0.27 *0.06*						4.03 *0.15*	9.35 *0.07*	0.18 *0.00*		100.43 *0.41*	19.05 *0.68*	
		Pl	r	6	67.87 *0.86*		20.69 *0.49*		0.22 *0.11*						1.11 *0.54*	10.90 *0.37*	0.13 *0.03*		100.92 *0.31*	5.29 *2.61*	
		Amph		5	51.67 *1.25*	0.43 *0.22*	3.99 *1.65*			15.74 *0.78*	0.22 *0.02*	0.04 *0.02*	0.20 *0.01*	13.91 *0.62*	12.17 *0.23*	0.70 *0.21*	0.07 *0.01*		101.23 *0.12*		0.50 *0.02*
		Amph		10	51.86 *0.34*	0.21 *0.21*	2.94 *0.27*			15.42 *0.60*	0.24 *0.03*	0.08 *0.01*	0.02 *0.04*	14.05 *0.41*	12.57 *0.17*	0.54 *0.05*	0.09 *0.01*		100.08 *0.36*		0.49 *0.01*
		Mag		8	0.11 *0.12*	0.65 *0.31*	0.29 *0.08*	0.11 *0.03*	66.98 *0.90*	31.78 *0.39*	0.05 *0.02*			0.03 *0.04*	0.13 *0.15*			0.92 *0.12*	101.05 *0.57*		
		Ilm		10	0.02 *0.12*	46.17 *0.40*	0.04 *0.01*	0.03 *0.03*		50.44 *0.54*	1.72 *0.12*			0.19 *0.05*	0.05 *0.03*			0.20 *0.08*	98.85 *0.24*		

[1] Lithology: BD = basaltic dike; Bdrel = relictic in basaltic dike; PG = plagiogranite; VGfg = fine grained varitextured gabbro; VGgr = granular varitextured gabbro; VGmg = medium grained varitextured gabbro; VGso = subophitic varitextured gabbro; XBD = xenolith of formed basaltic dike;

[2] Mineral analysed

[3] Qualifier: r = rim; c = core

[4] number of analyses

[5] content of plagioclase

[6] XMg for Cpx and Amph

Table 16. continued

Sample	Litho.[1]	Min[2]	Qual[3]	No[4]	SiO$_2$	TiO$_2$	Al$_2$O$_3$	Cr$_2$O$_3$	Fe$_2$O$_3$	FeO	MnO	Cl	F	MgO	CaO	Na$_2$O	K$_2$O	V$_2$O$_3$	Total	An[5]	XMg[6]
OM10_Gid_A11_1x	VGso	Pl	c	10	56.84	0.02	27.24		0.60						9.58	6.17	0.06		100.52	46.02	
					0.67	*0.02*	*0.47*		*0.08*						*0.43*	*0.30*	*0.01*		*0.30*	*2.29*	
		Pl	r	6	62.36		24.18		0.39						5.41	8.61	0.10		101.04	25.66	
					0.89		*0.66*		*0.10*						*0.70*	*0.46*	*0.01*		*0.26*	*3.42*	
		Cpx		8	53.76	0.06	0.26	0.02		7.07	0.29			14.58	24.70	0.13	0.01		100.87		0.79
					0.23	*0.03*	*0.09*	*0.03*		*0.53*	*0.08*			*0.41*	*0.59*	*0.09*	*0.01*		*0.36*		*0.02*
		Cpx		5	53.94	0.04	0.37	0.03		9.93	0.36			13.56	23.35	0.28	0.00		101.87		0.71
					0.29	*0.03*	*0.06*	*0.02*		*1.44*	*0.10*			*0.82*	*0.68*	*0.08*	*0.01*		*0.15*		*0.04*

[1] Lithology: BD = basaltic dike; Bdrel = relictic in basaltic dike; PG = plagiogranite; VGfg = fine grained varitextured gabbro; VGgr = granular varitextured gabbro; VGmg = medium grained varitextured gabbro; VGso = subophitic varitextured gabbro; XEBD = xenolith of formed basaltic dike;

[2] Mineral analysed

[3] Qualifier: r = rim; c = core

imber of analyses

content of plagioclase

[6] XMg for Cpx and Amph

Acknowledgements

Curriculum Vitae

Personal details

Name	Tim Müller
Address	An der Questenhorst 14, 30173 Hannover
E-Mail	mueller-tim@gmx.net
Date of Birth	15.02.1984
Place of Birth	Güstrow

Education

Since 04/2012	PhD (Dr. rer. nat., Docteur de l`Université Montpellier [Géosciences]) at the Institute of Mineralogy at the Leibniz University Hannover and Géosciences Montpellier at the Université Montpellier
11/2011	Diploma in Geosciences (MSc equivalent). Institute of Mineralogy, Leibniz University Hannover, Germany
10/2005 – 11/2011	Postgraduates studies in Geosciences, Leibniz University Hannover, Germany
05/2004	Secondary school (Abitur, Kaiser Karl Gymnasium, Itzehoe)

List of Publications

Journals:

Koepke, J., France, L., **Müller, T.**, Faure, F., Goetze, N., Dziony, W., & Ildefonse, B. (2011). Gabbros from IODP Site 1256, equatorial Pacific: Insight into axial magma chamber processes at fast spreading ocean ridges. *Geochemistry, Geophysics, Geosystems*, 12(9).

Conference Abstracts:

Mueller, T., Koepke, J., Garbe-Schönberg, D., Strauss, H., and Ildefonse, B. Petrological and geochemical investigation related to the "Wadi Gideah" cross-section in the southern Oman ophiolite: constraints on fast-spreading crust accretion processes in the frame of the ICDP project "The Oman drilling project". *ICDP/IODP Kolloquium*, Bonn, 2015

Garbe-Schoenberg, C. D., Koepke, J., **Mueller, T.**, Wolff, P. E., & Strauss, H. (2014, December). Trace element systematics in the plutonic section of fast-spread oceanic crust-evidence from the Wadi Gideah reference profile (Wadi Tayin Massif, Oman ophiolite). In *AGU Fall Meeting Abstracts* (Vol. 1, p. 4728).

Koepke, J., **Mueller, T.**, Linsler, S., Schuth, S., Garbe-Schoenberg, C. D., & McCaig, A. M. (2014, December). Invasion of Seawater-Derived Fluids at Very High Temperatures in the Oman Ophiolite-a Key for Cooling the Deep Crust at Fast-Spreading Ridges. In *AGU Fall Meeting Abstracts* (Vol. 1, p. 03).

Müller, T., Koepke, J., Garbe-Schoenberg, C. D., Schuth, S., & Wolff, P. E. (2014, December). Oman Ophiolite: Petrological and Geochemical Investigation of Fast-Spreading Crust Formation Processes. In *AGU Fall Meeting Abstracts* (Vol. 1, p. 4727).

Mueller, T., Koepke, J., Garbe-Schönberg, D., and Strauss, H. Establishing a reference profile for fast-spreading oceanic crust: Petrology and geochemistry of the Wadi Gideah cross section in the Oman Ophiolite. *ICDP/IODP Kolloquium*, Universität Erlangen, 2014

Mueller, T., Koepke, J., Garbe-Schönberg, D., Wolff, P.E., and Strauss, H. Formation processes of fast-spreading oceanic crust: Evidence from the "Wadi Gideah" cross section in the Oman Ophiolite. *ICDP Kolloquium*, Freiberg, 2013

Linsler, S., Mueller, T., Schuth, S., Wolff., P.E., Koepke, J., Garbe-Schönberg, D., and Strauss, H. Focused fluid flow zones in the Oman ophiolite (Wadi Gideah, Wadi Tayin Massif) – A key for cooling the deep crust at fast-spreading ridges. *DMG Tagung*, Universität Tübingen, 2013

Mueller, T., Koepke, J., Garbe-Schönberg, D., Wolff, P.E., and Strauss, H. Melt/rock interaction in the deep crust of fast-spreading ridges: evidence from the Wadi Gideah in the Oman Ophiolite. *DMG Tagung*, Universität Tübingen, 2013

Mueller, T., Wolff, P.E., Koepke, J., Garbe-Schönberg, D., and Strauss, H. Petrology and geochemistry of the "Wadi Gideah" cross section in the Southern Oman Ophiolite: a reference profile for fast-spreading crust. *EMC Tagung*, Frankfurt am Main, 2012

Mueller, T., Wolff, P.E., Koepke, J., Garbe-Schönberg, D., and Strauss, H. The "Wadi Gideah" cross section in the Southern Oman ophiolite: a reference profile for the fast-spreading oceanic crust?. *ICDP Kolloquium*, Universität Kiel, 2012

Wolff, P.E., **Müller, T.**, Koepke, J., Garbe–Schönberg, D., and Strauss, H. Petrology and geochemistry of the "Wadi Gideah" cross section in the Southern Oman ophiolite *International Conference on the Geology of the Arabian Plate and the Oman Mountains*,Sultan Qaboos University, Muscat, Sultanate of Oman 2012

Abstract - A section of ancient fast-spreading ocean crust was sampled at Wadi Gideah, located in the Wadi Tayin Massif of the Oman ophiolite. This sample suite was used for generating a coherent data set combining various petro-geochemical and structural investigations, with the aim of building a reference section for advancing our understanding of crustal accretion processes at fast-spreading mid-ocean ridges. Additionally, this study focuses on one outcrop that represents part of the fossil axial melt lens (AML).

Major and trace element analyses reveal a trend of chemical evolution up section in the lower crust, with a marked difference between the layered gabbros and the foliated gabbros above. Petrological modeling shows that the chemical evolution up section can be produced by hydrous fractionation crystallization, with melt H_2O contents of ~0.8 wt% and 0.8 to 1.2 wt% for the lower and upper crust, respectively. Together with the observed very steep bulk Zr/Hf vs. Zr gradient, high F and Cl content of magmatic amphibole, general Nb-Ta depletion of melts compared with NMORB, and high Sr^{87}/Sr^{86} ratio compared with modern fast-spread crust, this suggests that Wadi Gideah layered gabbros were accreted by crystallization of ascending melts in sills, in a context of subduction initiation. The distinct changes in chemical trends and average grain size at the layered to foliated gabbro transition are tentatively explained by enhanced hydrothermal cooling deeper than the AML. The gabbro/dike transition displays complex structural and lithological relationships that, together with fractional crystallization modeling, point to episodic vertical movements of the AML. Plagioclase crystallographic preferred orientations (CPO) measured over the whole gabbro section are always consistent with magmatic flow. The CPO strength generally increases downward, with more scattering in the layered gabbro section. From the top to the bottom of the layered gabbros, CPO become progressively more prolate, possibly reflecting increasing shear induced by active mantle flow underneath.

Wadi Gideah lower crust recorded a formation history consistent with a hybrid accretion model, combing several processes such as downward magmatic flow and/or upward melt migration in the upper foliated gabbros, sill intrusions in the layered gabbros, and deep hydrothermal circulation. The latter was presumably focused in channels, preserved today as several, up to 100 m wide zones of extensively altered former layered gabbro, cross-cutting the magmatic layering. These metagabbros display significantly higher Sr^{87}/Sr^{86} ratio, late stage magmatic phases, and evidence for high temperature partial melting.

Résumé - Une coupe d'ancienne croute océanique rapide a été échantillonnée dans le Wadi Gideah, situé dans le Massif de Wadi Tayin de l'Ophiolite d'Oman. Cette série d'échantillons a permis de générer un jeu de données cohérent, combinant des études pétro-géochimiques et structurales, dans le but de construire une coupe de référence pour mieux contraindre notre compréhension des processus d'accrétion crustale aux dorsales océaniques rapides. Ce travail intègre aussi l'étude détaillée d'un affleurement représentant en partie la lentille magmatique axiale (LMA) fossile.

Les analyses d'éléments majeurs et traces révèlent une évolution chimique dans la croûte inférieure, avec une nette différence entre les gabbros lités et les gabbros foliés sus-jacents. La modélisation pétrologique montre que l'évolution chimique vers le haut peut être produite par cristallisation fractionnée hydratée, avec des teneurs en H_2O des magmas de ~0.8 wt% dans la croute inférieure et 0.8 to 1.2 wt% dans la croute supérieure. Combiné aux forts gradients de Zr/Hf vs. Zr, aux teneurs élevées de F et Cl dans les amphiboles magmatiques, à l'appauvrissement général en Nb-Ta des magmas comparé aux NMORB, et aux rapports Sr^{87}/Sr^{86} élevés comparés à la croûte rapide moderne, ceci suggère que les gabbros lités du Wadi Gideah ont été formés par la cristallisation des magmas ascendants dans des sills, dans un contexte d'initiation de subduction. Les changements de signature géochimique et de taille de grain à la transition entre gabbros lités et gabbros foliés témoignent possiblement d'un fort refroidissement hydrothermal plus profond que la LMA. La transition complexe filonien/gabbro montre des relations structurale et lithologiques complexes, qui, combinées o la modélisation de la cristallisation fractionnée, traduisent les mouvements verticaux épisodiques de la LMA. Les orientations préférentielles cristallographiques (OPC) des plagioclases mesurées sur l'ensemble de la coupe dans les gabbros témoignent toujours d'une déformation magmatique. L'intensité des OPC a tendance à augmenter vers le bas, avec une plus forte variabilité dans les gabbros lités. Dans les gabbros lités, les OPC sont de plus en plus linéaires vers le bas, résultant possiblement d'un cisaillement plus fort induit par l'écoulement actif du manteau sous-jacent.

La croûte inférieure dans le Wadi Gideah a enregistré une histoire compatible avec un modèle d'accrétion hydride, combinant plusieurs processus tels que l'écoulement magmatique vers le bas et/ou la migration de liquides magmatiques vers le haut dans les gabbros foliés supérieurs, l'intrusion de sills dans les gabbros lités, et une circulation hydrothermale profonde. Cette dernière était probablement concentrée dans des chenaux, préservés aujourd'hui sous la forme de plusieurs zones, dont l'épaisseur atteint 100 m, de gabbros lités fortement altérés, recoupant le litage magmatique. Ces métagabbros ont des rapports Sr^{87}/Sr^{86} élevés, comportent des phases magmatiques tardives et montrent des évidences de fusion partielle.